FURNACE TAPPING 2022

EDITORS

Joalet D. Steenkamp

Dean Gregurek

Quinn G. Reynolds

Gerardo Alvear Flores

Hugo Joubert

Phillip J. Mackey

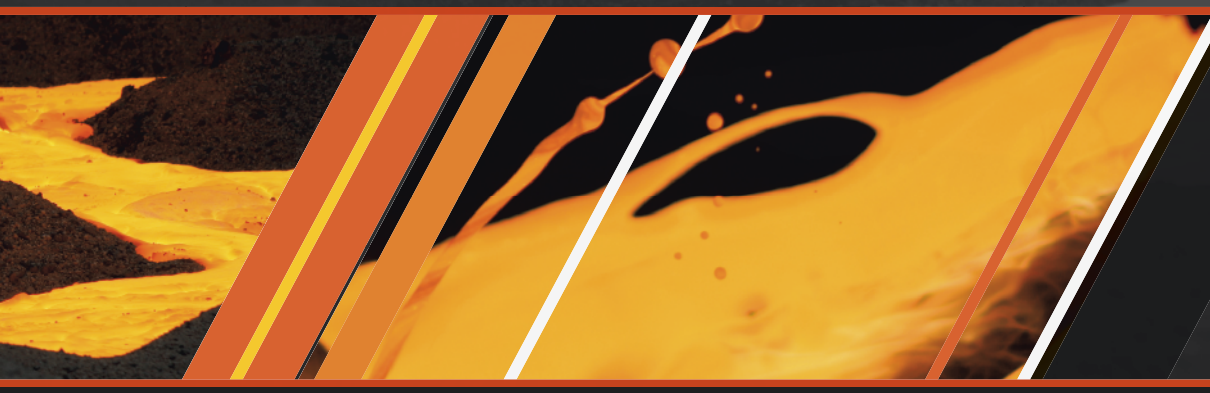

TMS

Springer

The Minerals, Metals & Materials Series

Joalet D. Steenkamp · Dean Gregurek ·
Quinn G. Reynolds · Gerardo Alvear Flores ·
Hugo Joubert · Phillip J. Mackey
Editors

Furnace Tapping 2022

TMS

Springer

Editors
Joalet D. Steenkamp
Mintek
Johannesburg, South Africa

Quinn G. Reynolds
Mintek
Johannesburg, South Africa

Hugo Joubert
Tenova Pyromet
Johannesburg, South Africa

Dean Gregurek
RHI Magnesita
Leoben, Austria

Gerardo Alvear Flores
Rio Tinto
Singapore, Singapore

Phillip J. Mackey
P. J. Mackey Technology, Inc.
Kirkland, QC, Canada

ISSN 2367-1181 ISSN 2367-1696 (electronic)
The Minerals, Metals & Materials Series
ISBN 978-3-030-92543-7 ISBN 978-3-030-92544-4 (eBook)
https://doi.org/10.1007/978-3-030-92544-4

This Springer imprint is published by the registered company Springer Nature Switzerland AG
The registered company address is: Gewerbestrasse 11, 6330 Cham, Switzerland

Preface

It is my honor and privilege to present to you the proceedings of Furnace Tapping 2022, the third event in the series and the first time it has been co-hosted with the TMS Annual Meeting & Exhibition.

The proceedings is the culmination of the efforts of the authors, peer reviewers, organizing committee, and TMS staff. Firstly, I would like to thank the authors for sharing their perspectives on a problem common to most pyrometallurgical smelter operations, namely the tapping of furnaces. The strength of the Furnace Tapping conference series lies in the diversity of the perspectives shared: across commodities, across disciplines, and across business type.

Secondly, I want to thank the organizing committee for the enthusiastic participation in the committee meetings and their hard work behind the scenes, first to solicit abstracts and then to manage the peer-reviewing process. All the papers published in the conference proceedings were independently peer reviewed. The organizers either reviewed the papers themselves or drew on the expertise and insights of a number of specialists, from around the world, who generously offered constructive criticism and suggestions. We are grateful for the inputs from these expert reviewers

Lastly, the support of the TMS staff, in particular Trudi Dunlap and Patricia Warren, was outstanding.

At the time of writing, the organizing committee is still hoping for an in-person event. Only time will tell whether or not travel restrictions, imposed by countries due to the ongoing COVID-19 pandemic, will allow us to meet in person or require us to go online. Either way, I trust that you will enjoy the event and that the proceedings will serve the pyrometallurgical industry at large, taking the tapping of furnaces from an art to science and engineering.

Joalet D. Steenkamp
Lead Organizer

Contents

About the Editors

Joalet D. Steenkamp is employed as a Technical Specialist in the Pyrometallurgy Division at Mintek, South Africa. Her research focus areas are Furnace Containment and Manganese Ferroalloys Production. She holds a Ph.D. in Metallurgical Engineering from the University of Pretoria and an appointment from the University of the Witwatersrand as Visiting Adjunct Professor. Joalet has 13 years of experience in the South African Industry/Private Sector (secondary steelmaking, ilmenite roasting and smelting, and manganese ferroalloy production) and 13 years in the Research/Public Sector. Dr Steenkamp has been a TMS member since 2009. At TMS, she has served on the Pyrometallurgy Committee since 2017, served on the Industrial Advisory Committee (2018–2021) for which she was the inaugural Chair (2018–2020), serves on the Extraction and Processing Division Council as a representative for the Professional Development Committee (2021–2023), and chairs the Organizing Committee for Furnace Tapping 2022. She is the founder of the Furnace Tapping Conference series for which she also chaired the Organizing Committees in 2014 and 2018 when the events were hosted by the Southern African Institute of Mining and Metallurgy in South Africa.

Dean Gregurek is a senior mineralogist in the RHI Magnesita Technology Center Leoben, Austria since 2001. Dr. Gregurek received his M.Sc. degree at the University of Graz in 1995 and his doctorate degree in Applied Mineralogy from the University of Leoben in 1999. Prior to RHI Magnesita, he worked for two years for Luzenac Europe in talc business. His current research interests and technical expertise are focused on chemical and mineralogical studies related to interactions between refractories, molten metals, and slags from pyrometallurgical furnaces. Dr. Gregurek has been a TMS member since 2012, *JOM* advisor (2014–2017), chair of the Pyrometallurgy Committee (2018–2020), and a co-organizer for the 7th–12th International Symposium on High-Temperature Metallurgical Processing (TMS Annual Meetings 2016–2021) and Furnace Tapping (TMS Annual Meetings 2022).

Quinn G. Reynolds holds an undergraduate degree in Chemical Engineering from the University of Kwazulu-Natal, a Masters in Engineering from the University of the Witwatersrand, and a Ph.D. in Applied Mathematics from the University of Cape Town. He has worked in the Pyrometallurgy Division at Mintek for the past 23 years. Mintek is a research institute conducting applied research and development to serve the extensive mineral processing and metallurgical industry in South Africa and worldwide.

Dr. Reynolds' expertise includes mathematical and computational modelling of complex coupled phenomena in high temperature processes and in particular the application of high-performance computing and open-source modelling software to pyrometallurgy. His current areas of research include magnetohydrodynamic modelling of electric arcs, multiphysics fluid flow problems in furnace tapping and phase separation, combustion modelling for metallurgical processing, and discrete element modelling for particle flow problems. He has also performed extensive work in the characterization of the dynamic behavior of direct-current plasma arcs using high-speed photography and electrical measurement techniques.

Gerardo Alvear Flores is a Chemical Engineer with a Doctor of Engineering degree in Materials Science and Processing. He has over 25 years of experience in non-ferrous metallurgy, with a focus in extractive metallurgy of copper, lead, zinc, and nickel and multi metal recovery.

Dr. Alvear initiated his carrier in the academic field in Chile. In 1990 he was awarded by the Japanese government with the Monbusho Ministry of Education scholarship to continue his education as a graduate student at Nagoya University, receiving his D.Eng. in Materials Science and Engineering in 1995.

In 1995 he joined NGK Metals in Japan for one year as a Post-Doctoral Fellow. After returning to Chile to work for Enami's Las Ventanas smelter in 1996, he joined the Research Centre for Advanced Waste and Emission Management in Japan, to work as assistant professor, with a special focus in pyrometallurgical processing of copper containing materials.

In 1999, he joined Codelco's Institute for Innovation in Mining and Metallurgy, where he worked as senior researcher, project manager, and finally as technology program leader to develop technical solutions to Codelco's copper smelters.

In 2005, he joined Xstrata technology (now, Glencore Technology) working in several roles until 2016, supporting the development and implementation of ISASMELT technology.

In 2016, he joined Aurubis as Executive Director Research, Development and Innovation supporting the development of Aurubis's multi-metal strategy.

In January 2021 he was appointed Adjunct Professor of the University of Queensland and joined Rio Tinto Singapore Holdings as Technical Marketing Manager for Copper.

Dr. Alvear Flores is an active member of professional societies in Canada and the US and is a member of the Copper Conference International Organizing Board. Dr. Alvear Flores has been selected by TMS as Co-Chairman of Copper 2025.

Hugo Joubert is a Mechanical Engineer with 28 years of furnace and smelter design experience. Working in numerous roles in production, technical development, business development, and management, Joubert specializes in furnace equipment design and solution development. He started his career as a plant engineer on iron blast furnaces in South Africa and completed his master's degree in 1998 on furnace lining/cooling system design including the use of Computational Fluid Dynamics. He first joined Tenova Pyromet in 1998 as a Design Engineer and, following a stint with Glencore Technology as Engineering Manager, rejoined Tenova Pyromet in 2015. His experience includes electric furnace as well as top submerged lance furnace technology.

Phillip J. Mackey obtained his B.Sc. (Honors) and Ph.D. degrees from the School of Metallurgy at the University of New South Wales, Australia. He then moved to Montreal, Canada to join Noranda to work on a new copper smelting process. As Pilot Plant Supervisor, Dr. Mackey helped develop the Noranda Process, which was first implemented at the Horne smelter in the early 1970s. Here he first learned the art and technique of tapping a high temperature melt—blister copper, copper matte, and slag. The Noranda Process, one of the most important copper smelting technologies of the twentieth century, also achieved early success in the United States, Australia, and China. Dr. Mackey was later instrumental in developing the Noranda Converting Process, of which he is a co-inventor, and which was installed at the Horne smelter in the late 1990s providing enhanced environmental performance.

At Noranda and Falconbridge, he was involved with other initiatives, including new developments for processing nickel laterites and concluding technology agreements with other nations, notably Chile. He conducted due diligence studies on a range of projects around the world.

He later formed his own consulting company, and this has led to a range of projects worldwide, including work on the development of a new nickel laterite project in Brazil.

He is a co-founder of the Copper-Cobre conferences, which expanded from a joint Canadian-Chilean enterprise to embrace the entire global industry. Dr. Mackey is on the Board of Hazen Research of Denver, USA. A Past-President of Metsoc of CIM and a Fellow of CIM and TMS, Dr. Mackey has authored or co-authored more than 100 technical papers covering diverse aspects of non-ferrous metallurgy. His CIM Awards include the Silver Medal, a Special Medal of Honour, the Selwyn G. Blaylock Medal, and the prestigious Airey Award for "outstanding contributions" to the field of extractive metallurgy. The Phillip Mackey Symposium was held in his honor at the 2019 Copper Conference in Vancouver. He presented the TMS EPD Distinguished Lecture in 2020 and received the John Elliott Lectureship Award of the Association for Iron and Steel Technology for 2021–2022. He will be inducted into the Canadian Mining Hall of Fame in 2022.

Part I
Session I

Controlled Tapping—The Research Project

Merete Tangstad, Michal Ksiazek, Jan Erik Olsen, Quinn Reynolds, and Eli Ringdalen

Abstract Controlled Tapping is a research project funded by the Norwegian Research Council and the Norwegian silicon and ferroalloy industry. The overall goal of the industry is to minimize the amount of uneven tappings and thus to reduce the energy consumption and the risk of hazardous events. In addition, the gassing, in the silicon industry, and the slag/metal separation in the ferroalloy industry, is a concern. The project Controlled Tapping will give fundamental and industrial knowledge to the industry, so these concerns can be addressed. The project focus is how the furnace interior, that is the furnace operation, is affecting the tapping. Tapping is an experience based sub-process that is developed over time at the various plants. To expand the knowledge into the scientific world, numerical modelling is a valuable tool and is the basis in the project. This has been done in SINTEF, NTNU in cooperation with Mintek. A variety of models have been developed calculating the tapping rate. Models describing the whole furnace with accumulated materials, e.g. TiC banks in the SiMn furnace, models that describes the slag metal separation in cascade tapping with various ladle positions, and models describing the tapping where the slag and metal properties are changed, has been developed. For a models to give the true picture, realistic input data is needed, and one of the Ph.D. projects has been to measure the interfacial tension between slag and metal in Mn-ferroalloy production. We also need to know the mechanisms affecting the tapping of industrial furnaces and on the consequences if furnaces accumulate metal and slag. Both industrial campaigns and investigations on mechanisms and material at the lab has been conducted. The industrial campaigns have been to excavate both Mn-ferroalloy and Si furnaces, to find that the tapped silicon is above 1800 °C when all literature says 1600 °C, to see the variances of the metal and slag during a tapping-cycle and over a year and investigating the energy in the gassing. In lab scale, the formation of

M. Tangstad (✉)
Norwegian University of Science and Technology, Trondheim, Norway
e-mail: merete.tangstad@ntnu.no

M. Ksiazek · J. E. Olsen · E. Ringdalen
SINTEF, Trondheim, Norway

Q. Reynolds
MINTEK, Randburg, South Africa

J. D. Steenkamp et al. (eds.), *Furnace Tapping 2022*, The Minerals, Metals & Materials Series, https://doi.org/10.1007/978-3-030-92544-4_1

TiC banks in the SiMn furnaces, the formation of slag, and the formation of SiO gas in Si furnaces and the pressure build up in charges by fines, have been investigated.

Keywords Tapping · Furnace excavations · Modelling · Mn-ferroalloy production · Si/FeSi production

Introduction

The Norwegian production of ferroalloys and silicon takes place in submerged arc furnaces. From these furnaces, up to 450 tons/day of metal is being tapped in liquid state at high temperatures, from 1400 to 1700 °C. In addition to the liquid metal, also liquid slag and furnace gas will follow the metal. Some producers tap their furnace continuously, like some of the silicon producers, and others tap the furnaces discontinuously, by closing and opening the tap-hole on a regular basis, e.g. every other hour. In the ideal case, the metal and slag will be tapped in the same rate as it is produced, it will be tapped in a controlled and steady mode and no furnace gas will exit the tap-hole. In the real world, there are a number of challenges when it comes to tapping.

Uneven drainage from furnace is often one of the major challenges. With unstable tapping, metal and slag may accumulate in the furnace and lead to variation of flow as well as variations in metal chemistry and back reactions inside the furnace. Large tappings will lead to disturbance of furnace operation and logistics, safety issues and diffuse emissions. In worst case the furnace load must be decreased, and this will hence have a major effect on production rate and cost. Back reactions lead to losses in yield and reduced production of metal.

Gassing from tap-hole is another challenge, maybe more detrimental in the high-temperature Si/FeSi process. In the silicon production, SiO/CO gas may exit the tap-hole at 2000 °C. First, this constitutes a serious safety risk for operators, as the operators may be exposed to the heat and dust. Next, it will lead to a lower silicon yield and loss of energy. Finally, it will lead to an increased maintenance cost on tapping equipment due to heat load and dust.

Slag and metal separation is a typical KPI in the slag producing processes. Slag droplets may be trapped in the metal, deteriorating the quality of the metal, and metal may be trapped in the slag, leading to a low metal yield and hence a higher energy consumption. The extent of these phenomenon is affected by the tapping process and the properties of the metal and, especially, the slag during the tapping process.

Physical geometry of the tap-hole will also affect the stability of the tappings. As the tap-hole is changing over time with increased wear followed by maintenance work, the geometry of the tap-hole will thus change both continuously and discontinuously, and thus effecting the above mentioned points.

The challenges described above are a result of the furnace operation, the geometry of the tap-hole and the tap-hole area, and the tapping process itself. The furnace operation and the tapping process are based on long-time experience in the industry.

The furnace operation has been summarized in textbooks [1–4] and the geometry close to the tap-hole have been investigated and reviewed in [5, 6] scientific studies. This project is however focusing on the interaction between the furnace state and its effect on tapping. Important input is of course the materials and zones in the furnace. This has previously been published for some industrial furnace excavations [7–11]. It is seen that zones in the furnaces will be different from furnace to furnace even with the same product, and hence more industrial excavations are necessary.

The basis for the tapping of the furnaces is a fluid flow phenomenon, and hence *numerical modelling* of fluid flow is one of the three platforms in the project. Some modelling on the whole furnace has previously been done, however, in the previous work the interior of the furnace are assumed ideal, with simplified zones [12–14]. The Controlled Tapping project are hence developing models both for sub-processes and for the entire furnace. There are however quite a lot of knowledge needed to input the model work, from phenomenon describing the model framework to boundary conditions to physical properties and reaction rates of the fluids involved. The other two parts of the project is hence *physical model* and *industrial data*. This paper will hence describe some of the work done in the *numerical modelling part*, the *physical model* as well as the *industrial data*.

For the industry the access of good students is essential, and recruitment is hence an important part of the project. Both B.Sc., M.Sc. and Ph.D. students are hence working in the project. Of the students finished so far, five of totally six of the B.Sc. and M.Sc. students have been employed by the project partners.

To seek the highest possible quality on the scientific work internationalization is essential, and the Norwegian partners NTNU and SINTEF have been not only working closely with especially MINTEK (South Africa) but also the University of Reykjavik (Iceland) and the University of Science and Technology Beijing (China) in this project. The dissemination through scientific journals and conferences are also important and so far 18 papers have been published [15–42] in addition to internal reports. It has also been focused on a "conceptual model" which described the main features affecting the tapping. This model is a simple model, where the main features may be transferred to both management and operators. An attempt to discuss the tapping in the Si/FeSi process on an overview level is shown in the publication "Conceptual model of tapping mechanisms in a FeSi/Si furnaces" at Infacon 2021 [35] (Fig. 1).

Modelling Concept and Implications to Tapping

In the Controlled Tapping project, two modelling techniques have been pursued: multiphase computational fluid dynamics (CFD) with interface tracking and reduced order modelling (ROM). The latter offers much shorter computational times, but the models are based on more assumptions and empirical correlations. When studying

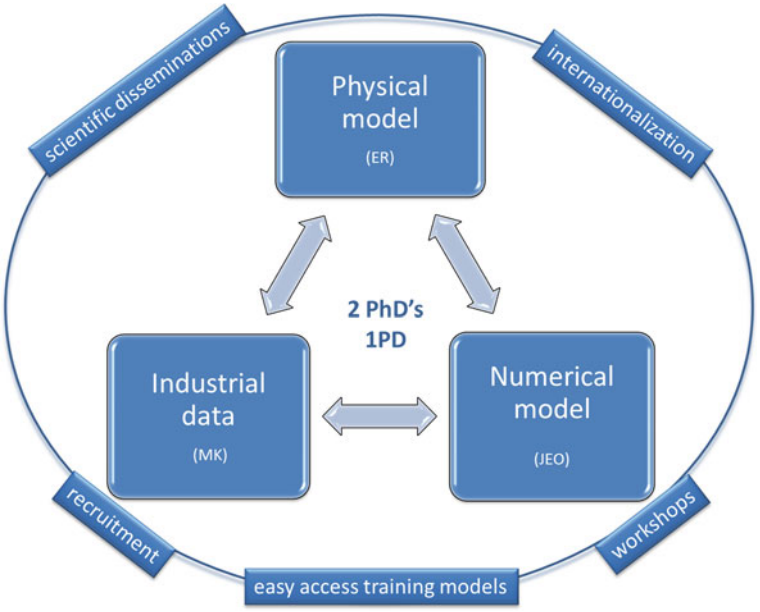

Fig. 1 Work packages of the controlled tapping process, also showing the focus on internationalization, recruitment and various dissemination levels

drainage of furnaces, both modelling concepts need to account for the flow resistance provided by the particle bed in the furnace. The modelling concept have been validated against drainage experiments with particle beds.

From basic physics (e.g., Bernoulli's equation) and earlier work, we know that the furnaces are drained by the hydrostatic pressure. The driving mechanism is gravity which increase with increasing density and level of the liquid being drained. In some furnaces, the gas pressure is also driving the drainage. The drag from the particle bed on the metal and slag reduces the driving force and the tapping rate. In the project a more accurate term for the pressure loss due to the particle bed has been introduced compared to earlier work. It has also been shown that the tapping rate is very sensitive to the particle configuration close to the tap-hole. This indicates that small variations due to closing and opening of tap-holes can cause variations in tapping rates.

Accumulated TiC-Banks in the SiMn Furnaces

Two SiMn furnaces were excavated where in the project FerroGlobe 2017 [29] and Kvinesdal 2020 [38]. They can be compared with the previous excavation in Elkem Sauda [11]. In addition to the observations in the active zones, that is the prereduction and the coke bed-zone, inactive banks containing carbides were observed in the

Ferroglobe furnace (Fig. 2) and one of the Kvinesdal furnaces. Of special interest was the observation of TiC in the banks, and though the Ti content was very low in the charge (<1%), the Ti was measured up to 12% in the bank material. As Fig. 3 shows, the sample was mainly containing slag, metal, and graphite precipitations in addition to the carbide.

The presence of inactive banks in the furnace will affect the tapping conditions as well as well as leaving less room for reduction work, and in general affect the energy and mass flows in the furnace. The formation of TiC and also the removal of carbides in the furnace is hence an interesting question. The stability of TiC in

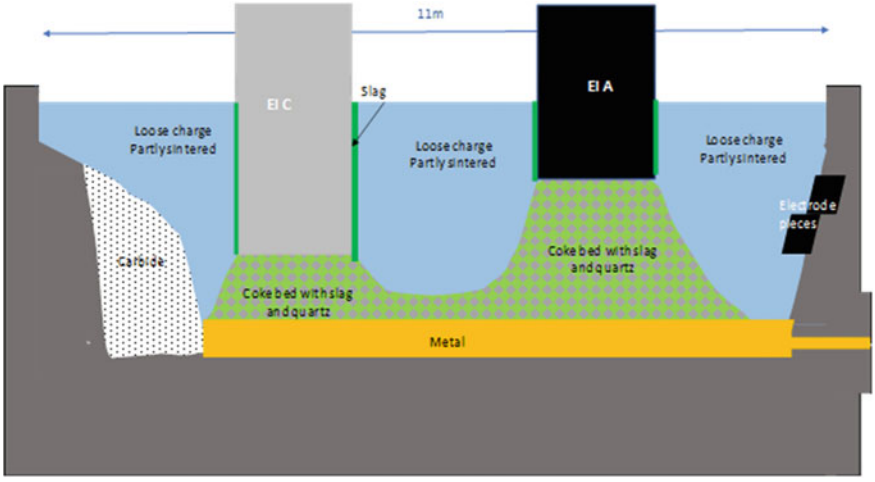

Fig. 2 Zones in the excavation of a furnace at Glencore Norway in 2017 (27.5 MW, 16% Si)

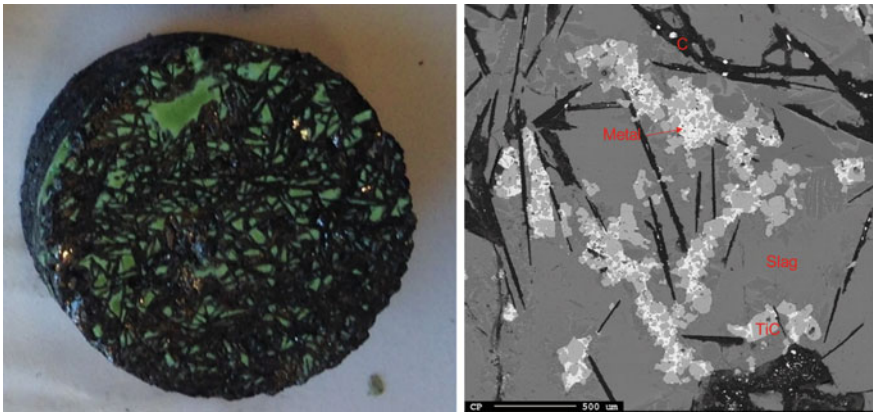

Fig. 3 Carbide banks containing 12%Ti is mixture of slag, metal, graphite, and TiC

the slag/metal/C SiMn system has hence been investigated both through lab-scale investigations and thermodynamic calculations [42].

The presence of banks in slag producing processes has also been modelled by CFD [41]. The results show that in principle all metal and slag produced around all electrodes are drained from the furnace if sufficient time for tapping is allowed. At the beginning of a tap, most of the products leaving the tap-hole emanate from the zone around the electrode close to the tap-hole, whereas towards the end of the tap most products emanate from the back electrodes. The products leaving from the back electrodes will thus have some longer residence time in the furnace. Normally, tapping is stopped somewhat before all slag and metal is drained. It is therefore expected that more products from the back electrodes are accumulated in the furnace than from the electrode close to the tap-hole.

Slag/Metal Separation in the Mn-Ferroalloy Processes

In all processes, the slag/metal separation is an important Key Performance Indicator affecting the productivity and hence the cost and environmental aspects. The slag/metal separation has in this project been investigated with various numerical models. One of the parameters affecting the slag/metal separation, that has not been well known, is the interfacial tension between the slag and the metal. The interfacial tension will affect the terminal velocity of metal droplets in the slag. One of the two Ph.D. candidates in the project is hence focusing on determining the interfacial tension experimentally between slag and metal, and some examples can be seen in Fig. 4. This is experimentally not trivial and new methods has been developed combining experimental and modelling work.

For studies on how to reduce metal loss in cascade tapping a multiphase CFD model was developed, and case studies performed [19]. This is illustrated in Fig. 5.

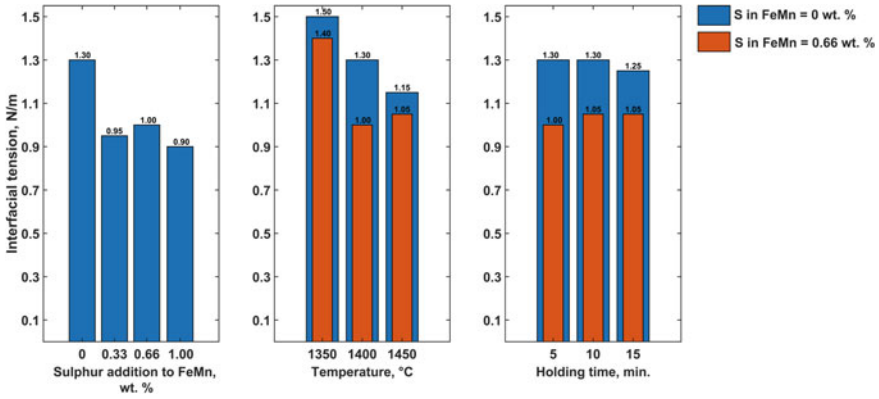

Fig. 4 Examples of interfacial tension as a function of temperature and S-content [16, 17]

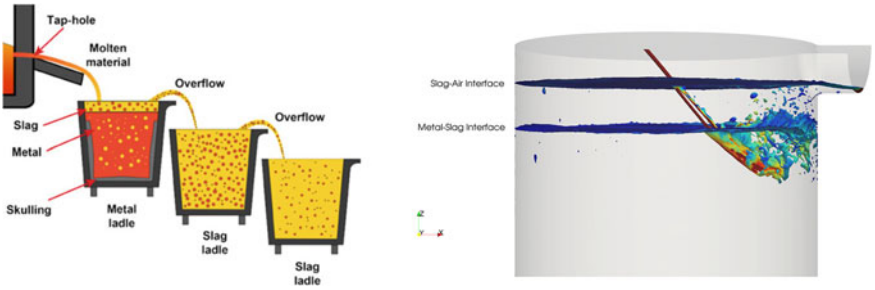

Fig. 5 Illustration of cascade tapping (left) and example of CFD results (right) for fluid interfaces colored by velocity

The amount of metal carried over from the metal ladle to the other ladles in the cascade during tapping of FeMn was extracted from the simulation data. Maintaining a significant thickness of slag layer on top of the metal layer reduced the quantity of metal entrained in the overflow stream from the metal ladle. Adjusting the position and layout of the ladles in the cascade was also seen to reduce metal losses. The density and viscosity of the tapped materials had a stronger impact on the results than surface tension, due to the momentum-dominated nature of the bulk flow in tapping streams and ladles. Although surface tension had no significant impact on cascade tapping, it is expected to have an impact on post-tapping slag/metal separation where settling and coalescence dynamics govern the separation.

Slag in Si/FeSi Furnaces

The Si and FeSi process is often referred to as a slag-free process, as the main impurities in the raw materials, Al and Ca, is dissolved in the metal tapped in about equal amounts. During previous excavations [7–9] and excavations done in this project [21], it is however seen large amounts of slag as accumulated in the furnaces, especially in the bottom of the furnace and in the periphery along the lining, sometimes from the bottom to the charge top. This will in the same manner as other high viscosity materials affect the mass flow in the furnace, and hence the tapping. In Fig. 6 one can see how the tapping channel is enveloped in a wide slag layer. This layer also contains SiC particles that adds to the viscosity.

The slag in the FeSi/Si furnaces contains about equal parts of CaO, Al_2O_3 and SiO_2. The CaO/Al_2O_3 ratio will however be dependent on the raw materials used, and the SiO_2 may vary from 40% and up. This means that the liquidus is typically around 1400–1500 °C and solidus 1100–1200 °C. As the high temperature area in the Si/FeSi furnaces are from 1800 to 2000 °C, it is also believed that the main part of the slag may be liquid/semi-liquid, except from very close to the lining. It is seen that the slag tapped from the furnace are close to the accumulated slag, and also that

Fig. 6 Tapping channel of silicon through a more than 1 m wide slag layer

the slag behind the various tap-holes are quite similar. As the slag from the furnace is not typically sampled, special equipment was made to sample this slag.

In FeSi production, the iron source may be metallic or oxidic. During experimental work, the iron is always reduced to metallic iron, long before the quartz melts above 1700 °C, and hence in experimental work FeO is typically not present in the slag phase. Industrially, it is however seen that FeO–SiO_2 slag is found on the charge top [36], and this is believed to be the case if there are very high temperatures high up in the charge, and so the iron oxide has not had time to be reduced before it dissolves the quartz, producing a liquid slag.

Temperatures and Heat Loss of Tapped Metal (Si/FeSi)

One of the large variables in understanding the process, as well as in fluid flow calculations, is the temperature. As the temperature in the ladle is typically measured to 1500–1600 °C, this is also the temperature that has been reported to be the tapping temperature. In this project the temperature close to the tap-hole has been measured for a semi-continues tapping at a FeSi furnace and continues tapping at a Si furnace [24]. The temperature from the tap-hole is seen to be above 1800–1900 °C, where the highest temperature is seen for the non-continues tappings (FeSi) and may be due to the higher flow rate. It is also seen that the composition may vary a bit during the tapping, especially in the beginning, and hence samples for analyses should not be taken to early after opening the tap-hole. The difference between the temperature out of the tap-hole and the ladle, which is the order of 100–300 K, has also been modelled and can be explained with radiation and conductive losses into the runner and ladle [29].

Quartz: Impurities, Melting, Fines- and SiO-Formation

As quartz/quartzite is the main raw material in Si/FeSi processes, several aspects of the raw material have been investigated. As previously seen [43], it is also here seen that the softening and melting of quartz may vary with 100 K and at a constant temperature at 1750 °C the melting may take between 20 and 80 min depending on the quartz type. With heating, the impurity phases will also change. The initial main impurities are CaO, Al_2O_3 phases and it is seen that with heating the impurity phases will start to dissolve SiO_2. When the temperature is 1800 °C it will be more than 75% SiO_2 in the impurity phases, and hence compared to the slag in the lower part of the furnace, the impurity phases will hence be reduced again wither to SiO gas or directly to silicon.

The fines formation of quartz has been investigated previously by among others Jusnes [44]. In this project, the crack formation during heating was investigated together with USTB (China) in a high-temperature confocal microscope. Crack formation in the quartz during heating to 1600 °C mainly happens at two temperature intervals, ~300–600 °C and ~1300–1600 °C and is mostly due to volume changes in the sample. The cracks occur from impurity areas, expanding grain boundaries, damaged or uneven surface and in some cases from the cavities from the escaped fluid inclusions. It can however be mentioned that not all crack formation leads to higher fines production [20].

In furnaces where tapping is hindered and an accumulation of Si/FeSi happens, a higher SiO-loss is experienced industrially. The rate of the SiO production from Si and quartz ($SiO_2 + Si = 2SiO(g)$) was experimentally determined and modelled for a number of various commercial quartz types. No difference was however found between the quartz types, even at both high and low impurity concentrations [30].

Present Activities

Though several of the above-mentioned activities will finish by the end of 2021, the activities of gassing during tapping in the Si-furnace and excavation of a HC FeMn furnace will also be investigated before the project end.

Summary

Controlled tapping is a 5-year project funded by the Norwegian ferroalloy and silicon industry and the Norwegian Research Council. The main focus is to get more knowledge regarding the fundamental aspects of the tapping process, as a basis for the industry to reduce the amount of uneven tappings. Industrial campaigns and physical laboratory work set the input to numerical sub-models, describing the various

features of the tapping process. The project is a cooperation between the Norwegian industry, the Norwegian University of Science and Technology, SINTEF (Norway), and Mintek (South Africa).

References

1. Schei A, Tuset JK, Tveit H (1998) Production of high silicon alloys. Tapir Forlag, Trondheim. ISBN 82-519-1317-9
2. Tangstad M (2013) Ferrosilicon and silicon technology. In: Gasik M (ed) Handbook of ferroalloys: theory and technology. Elsevier Ltd., Butterworth-Heinemann, Oxford, pp 179–220
3. Olsen S, Tangstad M, Lindstad T (2007) Production of manganese ferroalloys. Tapir Forlag, Trondheim. ISBN-978-82-519-2191-6
4. Tangstad M (2013) Manganese ferroalloys technology. In: Gasik M (ed) Handbook of ferroalloys: theory and technology. Elsevier Ltd., Butterworth-Heinemann, Oxford, pp 221–266
5. Nelson LR, Hundermark RJ (2016) The tap-hole—key to furnace performance. SAIMM 116. https://doi.org/10.17159/2411-9717/2016/v116n5a12
6. Steenkamp J (2014) Chemical wear of carbon-based refractory materials in a silicomanganese furnace tap-hole. PhD-thesis, University of Pretoria
7. Tranell G, Andersson M, Ringdalen E, Ostrovski O, Steimo JJ (2010) Reaction zones in a FeSi75 furnace-results from industrial excavation. In: Infacon XII, Helsinki, Finland
8. Tangstad M, Ksiazek M, Andersen JE (2014) Zones and materials in the Si furnace. Silicon for the chemical and solar industry XII. Trondheim, Norway
9. Ksiazek M, Tangstad M, Ringdalen E (2016) Five furnaces five different stories. Silicon for the chemical and solar industry XIII. Kristiansand, Norway
10. Barcza NA, Koursaris A, See JB, Gericke WA (1979) The “dig out” of a 75 MVA high carbon ferromanganese electric furnace. In: 37th Electric furnace conference proceedings, Detroit, AIME, 1979, pp 19–33
11. Olsen SE, Tangstad M (2004) Silicomanganese production—process understanding. In: Proceedings/INFACON 2004, vol 10, pp 231–238
12. Kadkhodabeigi M (2010) Modeling of tapping processes in submerged arc furnaces. PhD thesis, NTNU, Trondheim, Norway
13. Kadkhodabeigi M, Tveit H, Johansen ST (2011) Modelling of the tapping process in submerged arc furnaces used in high silicon alloys production. ISIJ Int 51(2):193–202
14. Kadkhodabeigi M, Tveit H, Johansen ST (2011) Modelling of the effect of furnace crater pressure on the melt and gas flows in the submerged arc furnaces used for silicon production. J Pro Comp Fluid Dyn 10(5/6):374–383
15. Bao S, Tangstad M, Tang K et al (2021) Investigation of two immiscible liquids wetting at elevated temperature: interaction between liquid FeMn alloy and liquid slag. Metall Mater Trans B. https://doi.org/10.1007/s11663-021-02222-6
16. Bublik S, Bao S, Tangstad M, Einarsrud KE (2019) Slag-metal interactions in the FeMn tapping process: interfacial properties and wetting. In: Liquid metal processing & casting conference, England, 8–11 Sept 2019
17. Bublik S, Einarsrud KE (2020) Inverse modelling of interfacial tension between ferroalloy and slag using OpenFOAM. In: 14th International conference on computational fluid dynamics in the oil & gas. Metallurgical and Process Industries (CFD 2020), 12–14 Oct 2020
18. Bublik S, Olsen JE, Loomba V et al (2021) A review of ferroalloy tapping models. Metall Mater Trans B 52:2038–2047. https://doi.org/10.1007/s11663-021-02134-5
19. Reynolds QG, Olsen JE (2021) Modelling of metal loss in ferromanganese furnace tapping operations, materials processing fundamentals 2021, pp 83–92

20. Folstad MB, Tangstad M, Ringdalen E, Fredriksli R, Dalum S (2018) Tapping procedures in silicon production, and the role of female tapping operators. In: Tapping conference, South Africa, 14–17 Oct 2018
21. Folstad MB, Yu H, Wang H, Tangstad M (2021) Formation of slag in Si furnaces. In: Molten 2021, South Korea, 21–25 Feb 2021
22. Folstad MB, Ksiazek MT, Tangstad M (2020) Slag in the tapping area in a Si furnace. I: Silicon for the chemical and solar industry XV. NTNU, Trondheim, pp 119–127. ISBN 978-82-997357-9-7
23. Folstad MB, Ringdalen E, Tveit H et al (2021) Effect of different SiO_2 polymorphs on the reaction between SiO_2 and SiC in Si production. Metall Mater Trans B 52:792–803. https://doi.org/10.1007/s11663-020-02053-x
24. Johansen ST, Ringdalen E (2018) Reduced metal loss to slag in HC FeCr production—by redesign based on mathematical modelling. In: Furnace tapping 2018, South Africa, 14–17 Oct 2018
25. Ksiazek MT, Tangstad M, Ringdalen E, Grådahl S, Hustad HM, Holtan J, Nymoen AB, Kaukonen S (2018) Measurement of metal temperature during tapping of an industrial FeSi furnace. In: Furnace tapping conference, South Africa, 14–17 Oct 2018
26. Olsen JE (2020) A CFD study on the impact of barriers and nonuniformities on furnace tapping. In: 14th International conference on computational fluid dynamics in the oil & gas, metallurgical and process industries, 12–14 Oct 2020
27. Olsen JE, Reynolds Q, Erwee M (2018) Temperature field at the tap-hole in manganese furnace—a computational modelling study. In: Furnace tapping 2018, 14–17 Oct 2018
28. Olsen JE, Reynolds QG (2020) Mathematical modeling of furnace drainage while tapping slag and metal through a single tap-hole. Metall Mater Trans B 51:1750–1759
29. Reynolds Q, Olsen JE, Erwee M, Oxtoby O (2018) Phase effects in tap-hole flow—a computational modelling study. In: Furnace tapping 2018, South Africa, 14–17 Oct 2018
30. Olsen JE, Hoem M (2018) Modelling heat loss in metal runner during furnace tapping. In: CFD 2018. SINTEF Industry, Melbourne, p 273
31. Ringdalen EK, Tomasz M (2018) Excavation of SiMn-furnace. In: Furnace tapping 2018, South Africa, 14–18 Oct 2018
32. Sindland C, Tangstad M (2021) Production rate of SiO gas from industrial quartz and silicon. Metall Mater Trans B 52:1755–1771
33. Tesfahunegn Y, Magnusson T, Tangstad M, Saevarsdottir G (2018) Effect of electrode shape on the current distribution in submerged arc furnaces for silicon production—a modelling approach. In: Symposium series—Southern African Institute of Mining and Metallurgy 2018, vol 118, no 6, pp 595–600
34. Tveit H, Ringdalen E, Edfeldt H (2020) Important parameters that control the crater pressure in a silicon furnace. In: Digital conference, Silicon for chemical and solar industry, Trondheim, Norway, 15–18 June 2020
35. Tangstad M et al (2021) Conceptual model of tapping mechanisms in a FeSi/Si furnaces. In: InfaconXVI, Trondheim, Norway, 27–29 Sept 2021
36. Jusnes KF et al (2021) Investigation of slag composition and possible relation to furnace operation of a FeSi75 furnace. In: InfaconXVI, Trondheim, Norway, 27–29 Sept 2021
37. Folstad MB, Tangstad M (2021) SiO_2-CaO-Al_2O_3 slags in Si/FeSi furnaces. In: InfaconXVI, Trondheim, Norway, 27–29 Sept 2021
38. Øvrelid S et al (2021) Excavation and analysis of a 31 MW SiMn-furnace at Eramet Kvinesdal. In: InfaconXVI, Trondheim, Norway, 27–29 Sept 2021
39. Reynolds Q et al (2021) Variability in ferroalloy furnace tapping—insights from modelling. In: InfaconXVI, Trondheim, Norway, 27–29 Sept 2021
40. Olsen JE et al (2021) CFD modelling of inconsistent furnace tappings. In: InfaconXVI, Trondheim, Norway, 27–29 Sept 2021
41. Loomba V et al (2021) Simulation of metal and slag in a SiMn furnace during production and tapping. In: InfaconXVI, Trondheim, Norway, 27–29 Sept 2021

42. Canaguier V, Ringdalen E (2021) Carbide formation and accumulation in SiMn furnaces. In: InfaconXVI, Trondheim, Norway, 27–29 Sept 2021
43. Nordnes E (2019) Softening and melting properties of quartz. Master's thesis in Chemical Engineering and Biotechnology, NTNU
44. Jusnes KF (2020) Phase transformations and thermal degradation in industrial quartz. Doctoral thesis 2020:205, Norwegian University of Science and Technology (NTNU), Trondheim. ISBN 978-82-326-4759-0 (electronic ver.)

MIRS Robotic Tapping and Plugging of Non-ferrous Smelting Furnaces

Rodrigo Madariaga, Luis Arevalo, Thomas Gabardi, and Phillip Mackey

Abstract The tapping operation of a metal, matte, or slag at a non-ferrous smelting furnace has a number of common aspects from one facility to another. In simple terms, the tap-hole initially requires the safe opening, the molten phase is allowed to flow through the tap-hole, and then the tap-hole needs to be safely closed. Until now, tapping in non-ferrous smelting operations is largely performed by an operator. Safe operations around the tap-hole require proper process control of the smelting furnaces, the proper tap-hole design for the required duty, and high-quality, robust tapping equipment. The present paper describes the successful development of a robotic system for automating the slag tapping operation at a full commercial scale on a large copper flash furnace. The development of this robotic tapping machine is described, and the operating features and performance are discussed.

Keywords Robot · Automation · Mining · Furnace · Smelter · Tapping · Lancing · Plugging · Mud gun · Tap-hole · MIRS

R. Madariaga · T. Gabardi (✉)
MIRS Robotics, 222 South Main Street, 5th Floor, Salt Lake City, UT 84101, USA
e-mail: Tom.Gabardi@mirsrobotics.com

R. Madariaga
e-mail: Rodrigo.madariaga@mirsrobotics.com

L. Arevalo
MIRS Robotics, Av Presidente Kennedy 6660, 765067 Vitacura, Santiago, Chile
e-mail: Luis.Arevalo@mirsrobotics.com

P. Mackey
P.J. Mackey Technology, Inc., 295 Kirkland Blvd, Kirkland, QC H9J 1P7, Canada

J. D. Steenkamp et al. (eds.), *Furnace Tapping 2022*, The Minerals, Metals & Materials Series, https://doi.org/10.1007/978-3-030-92544-4_2

Introduction

Throughout the world, the metallurgical industry is in the process of transforming the way plants are designed and operated. A number of changes have prompted this trend, including responses to climate change and global warming, cost reduction, and improved safety at plants; higher computing power and connectivity and automation technologies; and the shift in metal demand—and also production—from west to east. It has been stated that the trend to the so-called "smart automation" is part of the fourth-generation industrial revolution which is also referred to as "Industry 4.0" [1]. Briefly, it is generally considered that the first generation was motive power production (initially steam, later electricity) along with early mechanical machines (mid-end 1800s), the second was wide-scale industrialization (most of the twentieth century), the third was the beginnings of automation and digitalization, and now, the fourth—as stated above—smart automation through connectivity. Most mining and metallurgical companies are embracing this transformative trend.

Furnace tapping is a critical step in the operation of all pyrometallurgical processes involving molten phases—both the tap-hole design and operation are vitally important. As companies embark on new stages of transformation, automation of operating processes at the non-ferrous smelter is anticipated, including the steps of concentrate feeding and furnace tapping, which typically involves manual operation in fairly high-risk plant areas.

Virtually all non-ferrous pyrometallurgical furnaces today rely on manually operated tapping machines—some remotely operated—for tap-hole opening and closing. Combining the unrivalled quality and performance of foundry model industrial robots and the technological skills at MIRS, the company has pioneered the successful development of a new robotic tapping and plugging machine. This paper briefly describes the development of the world's first robotic furnace tapping machine for non-ferrous furnaces. The paper then describes the successful commercial operation of this tapping equipment for slag tapping at the flash furnace at the large Chuquicamata copper smelter in Chile. The installation is described together with operational results.

The History of MIRS

In 2001, MIRS's parent company, HighService Corporation, entered into a commercial and technological agreement with KUKA Roboter to begin the development of robotic applications for the mining industry. After the successful implementation of several industrial robotic solutions, MIRS was founded in 2007 to provide robotic solutions to the global mining industry. MIRS provides conceptual development, design engineering, manufacturing, integration, and support services for state-of-the-art robotic solutions and has developed applications for mines, concentrators,

tank houses, smelters, and refineries. The applications are specially designed to withstand the harsh environments associated with heavy industrial operations, including acid environments, extreme high temperature and high-altitude conditions, severe vibration, and highly dusty conditions. They also cover a broad range of industrial processes and are aimed at providing the following benefits:

- Lowering operating costs.
- Increasing plant availability and lowering maintenance costs.
- Increasing process reliability.
- Improving occupational health and safety aspects and reducing risks to personnel.

Development of the MIRS Robotic Tapping Machine and Testing at Chuquicamata

The Chuquicamata Smelter

Chile produced 5.73 million tonnes of copper in 2020 and is the world's largest copper-producing country, representing some 32% of the world's mined copper. About one-third of Chilean mined copper is smelted at one of the country's seven smelters. The Chuquicamata smelter, part of the largest mine-smelter complexes in Chile operated by Codelco, began operations in 1953 based on reverberatory furnace smelting with a capacity of about 145,000 tonnes of copper per year. The plant has undergone numerous expansions and improvements since that time. The following is a brief outline and is included in part here to illustrate the progressive changes and improvements at the smelter.

Oxy-fuel burners were introduced in 1979 on the reverberatory furnaces, and a moderate-sized El Teniente converter for smelting was built in 1984 (and replaced by a much larger El Teniente unit in 1993). In 1988, an Outokumpu flash furnace was commissioned. In 2004, HighService entered discussions with Chuquicamata for consideration of robotic tapping at the smelter. It is noted that by 2018 following the initial tapping trials as discussed below, Codelco undertook further changes at the Chuquicamata smelter which necessitated several plant shutdowns. These ongoing changes would, also as discussed below, impact the sequencing of the robotic tapping trials. The plant changes Codelco introduced starting about 2018 included closing the El Teniente converter and expanding the capacity of the flash furnace (by enlarging the physical size of the reaction shaft) to maintain smelting capacity and yet meet the D28 environmental regulations [2].

In 2004, Codelco entered into an agreement with HighService to begin the development of a robotic tapping machine. In 2007, the world's first robotic tapping and plugging system was installed and used on a slag tap-hole at Chuquicamata flash furnace. In 2008, a jackhammer tool was developed and in 2009 this tool was added to the robotic system.

Initial Test Work—Development of Tap-Hole Lancing and Plugging Systems

Starting in 2004, laboratory test work began on the development of the system and the associated tools. The work included testing all the individual steps involved in the tap-hole opening and closing operations. Some of the tests were carried out on a specially constructed "pilot" rig before initiating the work at the smelter. In 2007, when the on-site program at Chuquicamata commenced, the typical slag composition and conditions of the tapping operation were as follows (Table 1).

Table 1 2007 Slag condition and composition

2007 flash furnace Slag conditions	
Condition	Details
Tapping method	Manual lancing with hollow 14 mm outer diameter lance and occasional 25 mm solid bar, no machine
Plugging method	Manual with clay cone, no machine
Cu Conc	Up to 3,000 tpd (nominal)
Slag	1,220–1,575 tpd
Shift schedule	Three, 8-h shifts
Slag tap temp	1250–1330 °C
Length of tap-hole[a]	700 mm
Number of slag tap-holes used	4, each one ~150 mm
Approximate slag tonnage/tap	30–40 tonnes
Approximate number of taps/day	35–45
Opening time for slag tap-hole	10 min for the first tap, 1 min for successive taps during shift

2007 Typical flash furnace Slag composition	
Component	Assay range, wt%
Cu	1.5–2.5%
Fe	37.5–45.5%
Fe_3O_4	10.0–25.0%
Zn	1.0–5.0%
S	0.5–1.5%
SiO_2	28.0–35.0%
CaO	0.8–2.0%

[a] The horizontal length from the faceplate to the inside of the wall of the furnace, refer to Fig. 1

The following general procedure was used at Chuquicamata to manually open the slag tap-hole:

- The hardened clay plug is removed from the tap-hole using a steel bar.
- Operator 1 connects the oxygen supply to the lance and places the lance near the igniter.
- Operator 2 slightly opens the oxygen valve allowing a small oxygen flow and moves the lance in front of the igniter until the flame is established.
- Operator 1 places the lance in front of the tap-hole.
- Operator 2 increases the oxygen flow while Operator 1 inserts the lance into the tap-hole to initiate burning.
- Occasionally, Operator 1 will introduce a 25 mm solid steel bar to improve the slag flow.
- Operator 2 pushes the lance into the tap-hole with a circular motion until slag starts to flow.

With manual slag tap-hole closing, it is common to stop the slag flow using a clay plug on a steel, conical-shaped stopper mounted on a steel bar. Typically, when a clay plug is used, the clay plug is formed in the shape of a cone and affixed at its base to a steel disk about 75–100 mm in diameter welded to the tap-hole bar. Manual clay plugging was used at the Chuquicamata flash furnace at the time of the tests.

The following general procedure was used at Chuquicamata to manually close the slag tap-hole:

- Operator 1 places the bar with the clay plug affixed in front of the tap-hole.
- With a swift forceful action, Operator 1 rams the clay cone into the tap-hole, thus stopping the flow of slag.
- Operator 2 immediately hammers by hand the far end of the steel bar, safely securing slag stoppage.

For typical operations in 2007, the normal operating procedure was to use one slag tap-hole for the duration of the shift, then switch to another tap-hole the following shift. As is typical for flash furnace operations, slag is tapped periodically. In Chuquicamata's case, slag is tapped to a ladle, then when the ladle is full, the tap-hole is closed until being re-opened for the next slag tap.

A schematic diagram of the tap-hole design in use at the time is shown in Fig. 1.

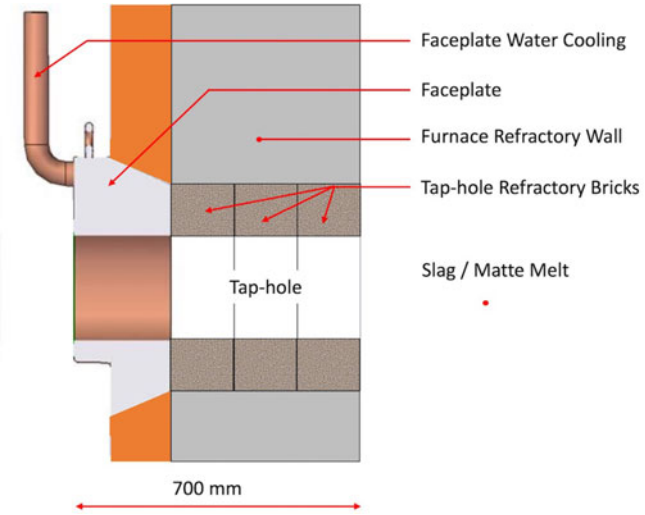

Fig. 1 Schematic diagram of tap-hole

New Tapping Machine Development

Beginning in 2004, a development program for a robust, robotic tapping and plugging machine began. Slag tapping and plugging operations were carefully observed and the processes at the smelter were studied. The robotic system was designed based on this study work. This preliminary work also included the design and testing of each system component, including the tools to be used by the robot.

Robot Selection

The considerations for selecting the robot included: area layout and space, tool and clay payload (for the system at Chuquicamata, this was 150 kg—the approximate weight of the mud gun assembly), robot reach, and environmental conditions to provide necessary protection against extreme heat, gas, and dust.

The most suitable robot given the above selection criteria was a KUKA KR 210 R2700-2 F machine. This robot has a payload capacity of 210 kg and a reach of 2.7 m. The lance length selected, based on the selected robot, was 3 m.

Lancing Tool Development

The first tests of lancing were carried out on a special pilot rig built at the MIRS laboratory in Santiago, Chile. A short section of circular steel pipe was fashioned as the tap-hole "block". Initially, concrete formed inside the pipe was selected to simulate solidified slag along with a clay plug. Later, solidified flash furnace slag plus a clay plug was used. These initial tests and the above-noted observations at the flash furnace established the main lancing strategy that would ensure the correct opening of the furnace slag tap-hole. Deviations from "standard" conditions were also identified and understood. For example, this approach defined how to open a "deep" tap-hole, such as the tap-hole full of solidified slag rather than clay, which involves using more than one lance. The required movements to withdraw the lance, dispose of it, and collect a new lance were optimized to ensure no undue cooling of the tap block occurred (Fig. 2).

Fig. 2 Lance testing

After many tests and advancing through several prototype stages, a final lance system for slag tapping was ready to be tested on the simulated tap-hole arrangement with solidified slag. The lance tool adopted is a pneumatically operated system that together with the pre-programmed robot automatically picks up the lance, safely connects to the oxygen piping, controls the axial forces to "feel" the opposing forces on the lance tip, ignites the lance, burns through the tap-hole, drops off the used lance section, and changes lances whenever necessary. After these final stages of prototype testing, the system, including a suitable protective covering for the robot to guard against the plant environment, was ready to be installed and tested on site.

Plugging Tool Development

At Chuquicamata, the tap-hole is closed with a clay plug or clay cone mounted on a steel bar. The robotic system was designed to use a constant force, higher than that employed manually, rather than the hammering procedure as described above.

A first task was to determine the required plugging force which consists of the movement and the extrusion action of the clay entering the tap-hole as well as the static head of the melt in the furnace. The force for clay extrusion is considered the main component of the forces involved. This force was measured in a compression apparatus while the melt head was calculated from the depth of liquid slag inside the furnace and the slag density.

The hydraulic cylinder used for the extrusion movement was selected based in part on the known forces involved and knowledge of the tap-hole operation. After determining these forces, the hydraulic cylinder used for clay extrusion was carefully selected. Even though the robot can handle higher forces than an operator, it was deemed desirable to use a latching mechanism for the frame of the hydraulic cylinder to the furnace structure. This latching mechanism provided a safe means for the robot to remain completely stable and free of excessive lateral forces. The hydraulic cylinder and assembly are referred to here as the "mud gun" (Fig. 3).

Fig. 3 Mud gun development test work

Jackhammer Tool Development

Following observations and measurements during the early tests at the smelter, it was decided to include a "jackhammer" tool as part of the tap-hole toolbox. Typically, a jackhammer operates with a rapid "up and down" movement of a hammer. The tap-hole tool developed for the present application included an electric hammering machine that the robot can use as needed. A damping mechanism was included to avoid excessive alternating high loads on the robot (Fig. 4).

Fig. 4 Jackhammer tool test work

Sampling Tool Development

Typically, the tap-hole operator takes a slag sample for analysis from the flowing molten stream. At Chuquicamata, an experienced operator could also visually judge the level of oxidation of the slag. However, this can now be done with a portable Satmagan instrument [3]. The slag sample collected by the robot as described below can be used to obtain a quick determination of the magnetite content of the slag. A robotic sampler was designed employing a steel bar with a flat plate at the end for collecting/retaining a suitable slag sample. This is similar to that used manually. The robotic movement includes securely returning the sample to a sample canister located at the side of the tap-hole (Fig. 5).

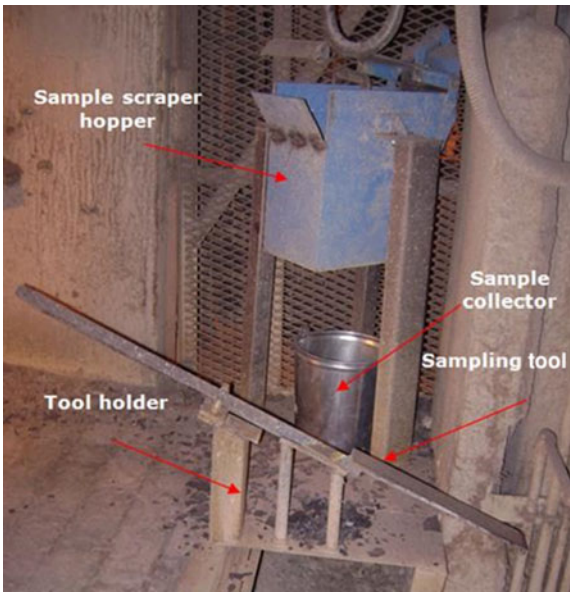

Fig. 5 Sampling tool, collector, and scraper

First Industrial Trial

The objective of the first, full-scale industrial trial was to validate the robotic system tapping and plugging operations on the original two slag tap-holes (numbers 3 and 4). The site installation and commissioning began in 2007.

Description of Operation

Tapping

The first industrial trial was conducted in two phases. For the first phase of the test in 2007, the equipment was installed and tested. Several changes were made and later an upgraded design was made for the second phase in 2009.

The steps involved robotic slag tapping essentially mimicking manual tapping. The robotic steps described here are programmable. In the sequence, the operator initiates the various robotic steps from a distance, thereby ensuring a safe operation and improved furnace control. The operator can also adjust and modify the sequence as needed.

The lance with an initial low oxygen flow is first ignited using an electric spark device. With ignition, the lance is pulled away slowly and moved to the front of the tap-hole. To ensure the lance remains straight as it goes into the tap-hole, a metal

Fig. 6 Lance ignition (left), lancing operation (right)

"v-shaped" guide mounted on the faceplate is used during lancing. Once the lance touches the slag inside the tap-hole, it automatically increases the oxygen flow to commence burning the clay/slag (Fig. 6).

The system carries out pre-defined movements and, in conjunction with the force feedback, correctly positions the tool. The system moves the lance forward until the tool sensors, with further small movements, indicate no opposing force. This determines that the tap-hole is correctly open.

When the lance has been consumed to its limit, the system first shuts off the oxygen and removes the lance from the tap-hole. The robot then deposits the lance piece into the used lance receiver. The robot then moves to pick up a new lance unless the operator presses the "stop tapping" button. When the tap-hole has opened, the system deposits the remaining lance in the lance receiver, and the robot moves to the "home position" to await the next instruction.

Sampling

Once the slag is flowing, the robot then takes the sampling tool and obtains a sample by moving the flat plate section of the tool across the flow and then depositing it in the sample canister.

Plugging

When the slag ladle is deemed by the operator to be about three-quarters full, the tap-hole plugging operation is typically activated. The jackhammer tool may be used to clean the faceplate if there is an obstruction. The robot then takes the mud gun and slowly moves it in a diagonal direction so it will not get in the way of the molten flow until it contacts the pivot point on the furnace wall where the plugging tool is attached. This position can shift a few centimeters daily, so the robot uses the force control system to locate the current position.

Upon making contact, the mud gun is activated, and the clay starts to move out as the robot pivots towards the tap-hole. This action allows minimum slag splash. After the load of clay has been fully extruded, the system stays in position until the

Fig. 7 Mud gun

operator indicates that the tool can be withdrawn. The robot takes the tool to the holder, moves to the home position, and waits for the next instruction (Fig. 7).

Intermediate Tapping

In the case when the tap-hole has been plugged for less than about 15 min, the jackhammer tool may be used to open the tap-hole. The jackhammer tapping sequence is activated by the operator and the robot takes the jackhammer tool from its support and moves it to the furnace. The system carries out pre-defined movements in conjunction with the force feedback and position of the tool. The system moves forward with the jackhammer until the tool sensors indicate no opposition from the tap-hole, which is when the robot determines that the tap-hole is open (Fig. 8).

Fig. 8 Robot operating jackhammer tap-hole opening tool

Design Changes

This first trial thus completed was considered by both Codelco and MIRS a success. Two necessary improvements from the first industrial trial were identified and later implemented during the next trial. They are as follows:

1. Lance Design

The first lance chosen was a thermal lance consisting of a 17 mm outer diameter steel pipe filled with 3 mm steel wires. This worked satisfactorily; however, during the test, a new type of lance was brought to the attention of MIRS and was tested and subsequently used for the remainder of the work. The new lance, referred to as a "trefilated" lance, consisted of a 21 mm outer diameter steel pipe with an internal steel star-shaped cross section to provide a more efficient oxygen flame [4]. This allowed a much faster and cleaner tap-hole opening and overall represented better performance.

2. Tapping after First Opening

The tapping operation on a tap-hole that has remained plugged for an extended period usually requires multiple lances to open the tap-hole. For a tap-hole that has been plugged for less than about 15 min, such tapping does not require the use of a full 3 m lance. To reduce waste, a modified jackhammer tool was developed during the second phase of the industrial trial and used in this case to remove clay instead of using a lance.

Test Results

The first industrial test returned excellent results. Figure 9 presents the events related to robotic tapping during the second phase of the tests. The pie segments denote the proportion of time in each of the categories shown.

It is seen that over a total period of 204 shifts, normal robotic tapping was carried out 61% of the time. The remaining 39% of the time was distributed according to the labels on the pie diagram in Fig. 9. If the period the smelter was down (24% of the time) and the non-robot related causes (11% of the time) are taken into account, the normal robotic availability was then 96% of the time.

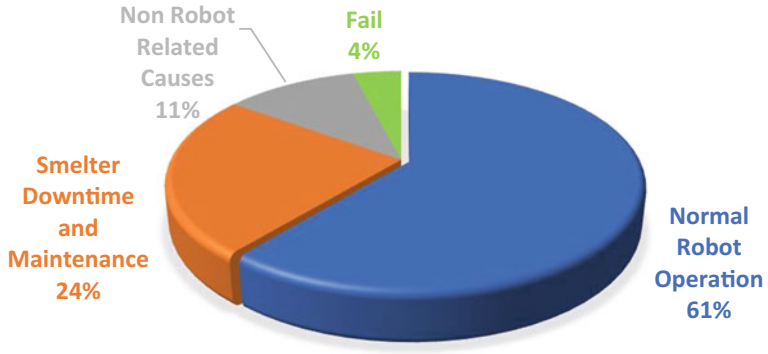

Fig. 9 Results from 204 shifts of operation during phase 2 testing, April–June 2009

Below is a further explanation of the segments in Fig. 9.

- Normal Robot Operation (61%)—shifts when the robotic system operated correctly during the entire shift, tapping, and plugging without issues.
- Non-Robot-Related Causes (11%)—shifts when the robot was available but was not used because there were no trained operators at the time, or when there were insufficient lances available.
- Smelter Downtime and Maintenance (24%)—shifts when the robot was available but not used because of smelter operational reasons such as unavailability of concentrate, or one of the tap-holes required unscheduled maintenance.
- Fail (4%)—shifts when the robotic system required assistance. In most cases, the system continued operating after corrective measures were taken. An example of the "fail" condition is when the mud gun support was incorrectly positioned after a faceplate change, such that the robotic mud gun could not couple to the bar on the furnace structure.

The benefits realized from the industrial trial with the robot are summarized below:

- Lower operating cost—the manpower required to operate the robotic system is less than that for the manual operation. This also allows personnel to focus on tasks having a higher impact on the operation instead of repetitive manual labor.
- Increased plant availability—the straighter lancing achieved with the robot increases the faceplate life cycle reducing maintenance frequency.
- Increased process reliability—the robotic system always carries out the operations in the same way, leading to better maintenance planning.
- Improved occupational health and safety aspects and reduced risks to personnel—the robot operator worked from the Human Machine Interface (HMI) outside of the fenced area and only accessed the area when the robot was locked out and when there was no molten material flowing. This eliminates the risk of an operator being splashed by hot slag when plugging or by hot particles ejected during the lancing operation.

At the end of 2009, Codelco recognized the value of the system and was interested in retaining the robotic equipment, so the equipment was kept at the smelter. It was successfully used intermittently by Chuquicamata personnel until 2011, when as part of a major smelter overhaul, the equipment was removed and placed in storage, but not re-installed at smelter start-up. As discussed below, due to a variety of factors, plant testing resumed in 2021.

Second Industrial Trial

The objectives of the planned second industrial trial were to further prove that the system could operate the original two slag tap-holes (numbers 3 and 4) and extend its capabilities to the other two tap-holes (numbers 5 and 6). To fulfil these objectives, the trial was split into two phases. In the first phase, the same system from the first industrial trial with specific upgrades was re-installed for operation in the same location. In the second phase, the system was to be expanded to include operation on the two other tap-holes, either by moving the existing robot or by adding an additional robot.

During 2019–2020, the robotic system was returned to the MIRS laboratory in Santiago, refurbished, and upgraded. The improvements included the following:

1. An upgrade to the lancing tool. The internal carriage used wheels which allowed it to move only horizontally; by changing the design to linear bearings over tubes, it allowed the tool to operate at any angle. This also gave it a smoother movement which reduced maintenance work.
2. Improvements to the mud gun head and latch to the faceplate. The faceplate is changed every 200 slag taps or slag ladles. The mud gun latch was originally connected to the faceplate so at every maintenance activity it had to be moved and not always put back in the same place so the mud gun could not latch or couple correctly. The improvements made were to move the latch away from the faceplate and locate it on a fixed section of the furnace wall, so that whenever the faceplate was changed, the latch position was not affected. This also required that the mud gun head bar be somewhat longer.
3. Complete closure of the operating area. On the first trial, the slag launders were adopted as a “barrier” because they did not allow access to the robot area. For the second trial, a fence was added to that section.

The second industrial trial with robotic tapping/plugging commenced on the same two slag tap-holes of the Chuquicamata flash furnace during January 2021 which was also at a time when work on the furnace overhaul was on-going. Initially, the overhaul work was believed to not influence the areas around slag tapping. However, due to this and other factors, only part of the first phase of this industrial trial could be accomplished as the smelter overhaul required more work than expected. In addition, the COVID-19 pandemic affected the ability to install and test the system. Finally, during the short trial, the flash furnace experienced an episode of significant solids

build-up on the hearth, arising in part due to the start-stop operations from the aforementioned situation. The build-up encroached up to the slag tap-hole level thereby prohibiting normal tap-hole procedures. In fact, heavy manual effort was required to effect tapping.

Due to this unusual condition, robotic tapping was stopped, and the robot was removed to provide room for working around the tap-hole. The robotic system was, therefore, only operational for a few days; however, during this time, the system was successful in all the tapping and plugging operations.

In correspondence to MIRS regarding the situation, smelter management acknowledged that the robotic system conducted proper tapping and plugging operations in automatic mode without any major operator intervention and that the system was removed solely based on smelter operational conditions and not related at all to the robotic system.

Conclusions

MIRS has developed and commercially tested, over a sustained period a robust, reliable robotic slag tapping and plugging machine. The step-by-step stages of this development were described in this paper, and the unit can now provide a new approach for improved and safer non-ferrous furnace tapping operations worldwide. The benefits realized from the industrial trials of the robotic machine described in this paper include: lower operating costs, increased plant availability, lower maintenance cost, increased process reliability, and improved occupational health and safety.

MIRS is continuing development of the system, extending the application to melts other than slag, plus additional improvements, including an optional drill tool for tap-hole opening.

Acknowledgements The development of the MIRS robotic tapping machine is the result of a dedicated team effort of many individuals. Several individuals within MIRS and at supporting organizations are to be thanked for providing valuable input and inspiration aiding the numerous developments described in this paper. The untiring contributions and support of all Chuquicamata personnel who assisted with the industrial trials are acknowledged. The authors wish to thank Codelco-Chile for its support and for permission to publish this paper. The authors also thank MIRS for permission to publish this paper. Finally, the authors acknowledge and thank the management of MIRS for the vision in identifying and supporting improved ways of operating non-ferrous plants.

References

1. Arias L, Balladares E, Parra R, Sbarbaro D, Torres S (2021) Sensors and process control in copper smelters: a review of current systems and some opportunities. Minerals 11:1
2. Meneses LB (2018) Potenciamiento horno flash fundicion Chuquicamata, paper at Smelter Seminar, IIMCH, October 2018

3. Satmagan Model 135 instrument. https://www.rapiscansystems.com/en/products/satmagan-135
4. Morales D, Morales C, Nunez S (2018) Tap-hole opening: advances and improvements. In: Steenkamp JD, Cowey A (eds) Furnace tapping. South African Institute of Mining and Metallurgy, Kruger National Park, 14–17 October 2018, pp 231–249

Theoretical Framework and Practical Recommendations for Proper Thermal Lance Use and Selection

Sebastián Núñez, Antonio Umaña, and Darwin Morales

Abstract Drill bits and thermal lances are both perforation tools used in a variety of situations. For drill bit solutions, there exists a lot of theory regarding the proper drill bit selection for each application. However, for thermal lances, despite being a century-old tool, there is no technical information nor a theoretical framework that allows to understand its underlying science, required to properly select a thermal lance for a specific application. This article presents a theoretical framework, developing the concepts and variables that rule the thermal lances behaviour and performance. The proposed framework fits well with experimental results, therefore could be used as a guide to select the proper thermal lance for each tapping process, potentially allowing time savings leading to an increase in the profitability of furnaces operation.

Keywords Tap-hole · Thermal lance · Thermal resistance · Furnace stopped

Introduction

Whereas there are different thermal lances optimized for different tap-hole operation conditions, normally, a fixed thermal lance model is defined and used, leading to several process inefficiencies. In other words, there is an opportunity for improvement just by selecting the proper thermal lance for each tap-hole operation condition. However, the relation between these conditions and the proper lance properties is not completely clear.

This article presents a theoretical framework that clarifies the relation between operation conditions and proper lance properties. The determination of the proper thermal lance properties, such as diameter, length, and its profile configuration, depends on several factors regarding the tap-hole process requirements and conditions. Typically, the main requirements are related to the geometry of the required perforation, determined by length and diameter. And the more relevant condition

S. Núñez (✉) · A. Umaña · D. Morales
Trefimet S.A., Santiago, Chile
e-mail: snunez@trefimet.cl

J. D. Steenkamp et al. (eds.), *Furnace Tapping 2022*, The Minerals, Metals & Materials Series, https://doi.org/10.1007/978-3-030-92544-4_3

factors are, on one hand, the kind of material to be melted and, on the other hand, the quality, quantity, and pressure of the oxygen influx available on site.

The remaining of this document is organized as follows. In section "Theory and Concepts", the influence of the condition's factors over the thermal lance properties is detailed. In section "Theoretical Framework for Thermal Lance Performance Characterization", a theoretical framework to evaluate the thermal efficiency of the process is presented and used to estimate the amount of lance required. The proposed theoretical framework is used, contrasted, and experimentally validated. Finally, in section "Conclusions", the principal conclusions, the scope of the results, and future work are summarized.

Theory and Concepts

Given a perforation diameter requirement, the conditions of the tap-hole operation such as the kind of material to be melted and the oxygen supply play a fundamental role in the proper thermal lance selection. This section presents and details these conditions and their relation with thermal lance's properties.

Kind of Material to Be Melted

One of the key factors regarding the properties of the material to be melted is if it reacts with oxygen at the tapping process temperatures, reactive material from here on. If the material is reactive, such as iron, titanium, or zinc, it will demand more oxygen from the thermal lance than non-reactive material. The heat required to complete the perforation is obtained primarily from the material reaction itself. Therefore, the thermal lance primary objective is not to provide heat, but sufficient oxygen to sustain the material self-reaction. The most suitable lance cross-sectional configuration for this purpose is mainly confined free space, typically achievable by an oxygen pipe.

Conversely, if the material is non-reactive, the thermal energy required to melt it come from the thermal lance combustion. The calculation of the required energy to melt the non-reactive material could be obtained knowing its density [kg/m^3], molar mass [g/mol], melting point [K], specific heat [$J/(mol * K)$], and latent heat of fusion [kJ/mol]. To get a precise result, it is recommended to use databases with specific heat (C_p) at different temperatures, as the NIST tables.

Typically, specific heat units are [$J/(mol * K)$]. With the material density and its molar mass, the specific heat value could be expressed in [kg/m^3] units. The heat required to raise the temperature of the material from ambient temperature to its melting point (Q) could be obtained by integrating its specific heat:

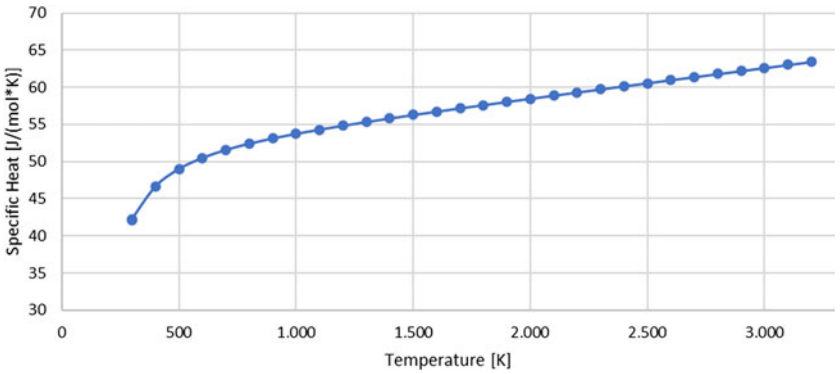

Fig. 1 Graphic of specific heat at different temperatures

$$Q_{298\,\mathrm{K}\rightarrow T_{fusion}} = \int_{298}^{T_{fusion}} C_p dt \tag{1}$$

With the latent heat of fusion (λ_{fusion}) of the material and knowing the mass to be melted (m), the energy required to change its state from solid to liquid can be calculated as follows:

$$Q_{fusión} = m * \lambda_{fusion} \tag{2}$$

Finally, the total heat required to melt the material is given by

$$Q_{Total} = Q_{298\,\mathrm{K}\rightarrow T_{fusion}} + Q_{fusion} \tag{3}$$

Example 1: Energy Calculation to Melt a Material

In this example, the energy required to melt 1 m^3 of Calcium oxide (CaO) is calculated.

Step 1: Get CaO properties.

Density: 3,340 kg/m^3. Molar mass: 56.08 g/mol. Melting point: 3,200 K.

Step 2: Calculate the energy required to raise 1 m^3 CaO temperature from ambient temperature to its melting point.

Values of Calcium oxide specific heat are obtained from NIST Tables as a function of temperature, with steps of 100 K. These values are shown in the following graph.

The energy required to raise CaO temperature from ambient temperature to its melting point corresponds to the area under the curve shown in Fig. 1. This area, given by Eq. (1), could be obtained from discrete data using the integral Riemann approximation, which results in

$$Q_{298\rightarrow T_{fusion}} = \int_{298}^{3,200} c_{pCaO}\,dt = \sum_{298}^{3,200}\left(\frac{C_{pi+1}+C_{pi}}{2}\right)(T_{i+1}-T_i) \quad = 164.575\,\frac{\text{J}}{\text{mol}} \tag{4}$$

Step 3: Energy calculation to raise 1 m^3 of CaO from ambient temperature to its melting point.

Using the CaO density and molar mass, both detailed in Step 1, the energy required to raise CaO temperature from ambient temperature to its melting point evaluates to 9,802,183 kJ.

Step 4: Calculate heat required to produce the change of state (solid to liquid).

When the material reaches its melting point, it will continue to absorb energy at a constant temperature until the change of state is complete. The energy required to change the material state corresponds to the latent heat of fusion. On the next NIST table extract, enthalpy of fusion (latent heat of fusion) can be found from the column "H–H° (Tr)" subtracting the final enthalpy value (244.117 kJ/mol) and the initial enthalpy value (164.621 kJ/mol) at the melting temperature of the CaO (3,200 K) (Table 1).

Then, the latent heat of fusion for CaO is 79.5 kJ/mol, which rewritten in units of mass results in 1,418 kJ/kg. Considering the mass of 1 m^3 of CaO, the energy required for the fusion is 4,734,824 kJ. Thus, the total energy (heat) required to melt 1 m^3 of CaO is

$$Q_{Total} = Q_{25\,^\circ\text{C}\rightarrow T_{fusion}} + Q_{fusion} = 14{,}537{,}008\,\text{kJ} \tag{5}$$

This means that to melt 1 m^3 of CaO, it is necessary to transfer **14,537,008** kJ of thermal energy from the thermal lance to the material.

Thermal lances designs could be optimized either for oxygen delivery, more appropriate for reactive materials, or to generate more energy per unit of cross-sectional area (CSA), adequate for non-reactive materials. There exists a trade-off between

Table 1 CaO NIST table extract to find the enthalpy of fusion

T [K]	H–H° (Tr) [kJ/mol]
3,100	158.298
3,200	**168.621**
3,200	**244.117**
3,300	250.393
3,400	256.669

these two optimization objectives, given by the fact that a smaller free cross-sectional area would lead to an increase in energy density but also to a reduction of the free flow of oxygen delivered by the lance. This trade-off could be characterized by the energy at the tip normalized by the cross-sectional area of the lance.

Energy/Surface Ratio (RE/A) and Free Area for Oxygen Flow

The $R_{E/A}$ ratio is defined as the available theoretical energy at 1 mm of length, normalized by the cross-section of a thermal lance, and its units are [J/mm^2]. The available energy is the amount of energy when iron reacts with oxygen. The amount of iron that is in consideration is the amount of iron in the cross-section given that there is enough oxygen flux to enable its reaction. This ratio is expressed as follows (see also Fig. 2):

$$R_{E/A} = \frac{Energy\ contained\ at\ the\ thermal\ lance\ in\ 1\ [mm]\ length}{Thermal\ lance\ cross\ section}\left[\frac{\mathrm{J}}{\mathrm{mm}^2}\right] \quad (6)$$

Note that the energy of the $R_{E/A}$ is calculated based on the iron fraction **that can react** in the cross-section, which is not necessarily equal to the total iron mass contained on it. The fraction of iron that can react is given by the balance between the thickness of the inserts and the cross-section of the interstices through which oxygen is conducted. This balance represents the science behind the design of efficient thermal lances. Although is tempting to increase the amount of iron, to increase the $R_{E/A}$ ratio, there is a point when more iron will not only have no effect on the $R_{E/A}$ ratio, but also will be counterproductive given that a fraction of the produced energy would be used for heating and melting the iron in excess that can't react. The reaction of iron occurs in solid state, and unlike the most common combustions in the gas state, there is no need for a mixture between iron and oxygen. In other words, if the iron is at its ignition point (1,143.15 K), it will react with the surrounding

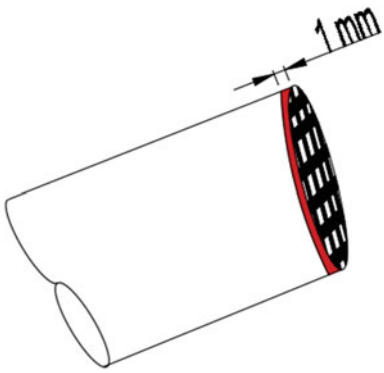

Fig. 2 Reaction volume in the $R_{E/A}$ calculation

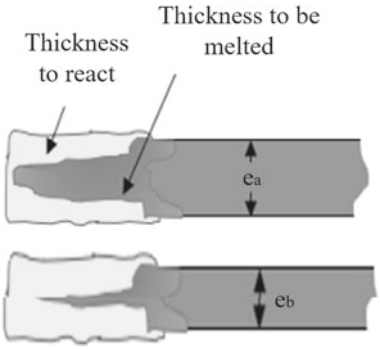

Fig. 3 Thickness scheme. e_a: deficient thickness; e_b: efficient thickness ($e_a > e_b$)

oxygen. Once the reaction is concluded, iron oxides isolate the inner unreacted iron from other oxygen molecules, thus inhibiting further reactions (see Fig. 3). However, a fraction of the released heat of formation melts both iron oxides and unreacted iron. When melted, the iron oxide layer drains and left the inner iron available again to react. This process repeats continuously and can be modelled by a layer of unreacted iron and a layer of iron under reaction. The latest with a thickness that increase with the oxygen flow rate.

While there is still work to be done regarding the determination of the thickness of the layer of iron under reaction, experimental results conducted by authors show that a $R_{E/A}$ must be lower than 25 J/mm^2 to assure a complete combustion of the available iron. In particular, the preliminary experiment results show that a performance increase of 23% can be achieved when iron walls of 0.9 mm of thickness are used instead of 1.35 mm (see Table 2).

For practical oxygen supplies, with maximum inlet pressure limits, there exists a minimum fraction of free space required to provide sufficient oxygen to sustain the combustion of the lance. For this purpose, experimental results determined by the authors suggest a free cross-sectional area greater than 35%. Lower free cross-sectional areas limit the amount of oxygen required to ensure a complete reaction of the available iron, therefore, highly reducing the performance of the thermal lance.

Table 2 Thermal lances information

General information	Unit	Lance type A	Lance type B
External tube thickness	[mm]	0.9	1.35
Internal tube thickness	[mm]	0.9	1.35
Unitary mass	[kg/m]	0.5	0.73
Perforation performance	[mm/kg]	107.44	82.5
Mean diameter	[mm]	64.37	76.51

This restriction could be interpreted in terms of $R_{E/A}$ as a practical upper-bound of 28 J/mm^2.

Classification of the Thermal Lance's Profile Configuration Based on $R_{E/A}$ Ratio

Based on the $R_{E/A}$ ratio, the thermal lances' profile configuration could be classified under three categories, each one of them fitting well for a particular application.

High $R_{E/A}$ thermal lances (23 J/mm^2 < $R_{E/A}$ < 25 J/mm^2): Designed to work in materials with high thermal requirements at facilities with proper oxygen flow and pressure supply that allows the thermal lance to have the oxygen required to achieve a complete combustion of iron. A $R_{E/A}$ over 38 J/mm^2 will not perform well because the oxygen flow is limited by a small free area for oxygen flow in the cross-section; therefore, the amount of oxygen is insufficient to the reaction of all the iron.

Medium $R_{E/A}$ thermal lances (20 J/mm^2 < $R_{E/A}$ < 23 J/mm^2): Designed to work in materials with high thermal requirements at facilities that do not dispose the proper oxygen flow and pressure conditions to use high $R_{E/A}$ thermal lances.

Low $R_{E/A}$ thermal lances ($R_{E/A}$ < 20 J/mm^2): Designed to work in materials that react with oxygen or at facilities that do not dispose the proper pressure of the oxygen to reach the oxygen flow required at the ignition tip of the lance.

Effect of $R_{E/A}$ on the Tap-Hole Perforation Diameter

Experimental results conducted by authors show that thermal lances with a higher $R_{E/A}$ ratio produce perforation holes with a diameter of 1.8 and 3.5 times greater than the diameter of the thermal lances. In contrast, thermal lances with a lower $R_{E/A}$ ratio produce perforation holes 3–6 times or more. Also, the hole perforation in the latter is more uneven and unpredictable. Hence, with higher chances of damaging components of the passage. In summary, for efficiency, economy, and security reasons, when sufficient oxygen flow is available, it is recommended to choose a high $R_{E/A}$ thermal lance for the operation.

Thermal Lance Length

Given a pressure at the input of the thermal lance, the length of the lance itself will affect the flow of oxygen, therefore, its performance. The thermal lance length generally depends on the space limitations at the tapping zone and the number of

lances to be used. Sometimes to minimize the number of lances changes, two or more lances are coupled serially before the start of the operation; however, this is not recommended since the losses by friction are considerably increased, and therefore, the oxygen flow will drop, and the efficiency of the thermal lance with it. Depending on the thermal lance defined, it will be advisable to use a secondary lance station when multiple thermal lances lengths are required.

Oxygen Supply

The oxygen supply disposed by the facilities for tapping operations is a very important factor in thermal lance definition and it has 3 features that should always be considered:

Oxygen purity: The efficiency of the iron reaction depends on the purity of the oxygen; it means iron will have the best combustion with oxygen at 100% of purity and the worst or even null reaction with less than 95% of purity.
Available oxygen flow at the line: Each thermal lance requires a determined oxygen flow depending on the iron that reacts in the cross-section. If the available oxygen flow is insufficient for the reaction of the defined thermal lance, a lance with a lower $R_{E/A}$ must be selected, but if the oxygen flow is higher than required by the reaction of the defined thermal lance, it must be adjusted to proper flow since an excess of flow reduces the performance of the thermal lance, as will be explained forward.
Available oxygen pressure at the line: To transport the oxygen flow to the ignition tip of the thermal lance, a certain pressure is required to overcome the losses due to the cross-section and length of the thermal lance. The higher the $R_{E/A}$, the higher the pressure must be to transport oxygen through the lance. If the pressure in the line is not capable to generate the required oxygen flow, a thermal lance with a lower $R_{E/A}$ must be defined; on the other hand, if the pressure is high and generates higher oxygen flow than required by the reaction of the thermal lance, it is necessary to reduce the pressure in the line.
Oxygen required in the thermal lance for its best efficiency: The equations and concepts required to calculate the thickness of the oxygen layer available for the reaction are detailed in the theory introduced in [1].

The oxygen flow in a thermal lance will be distributed at each duct depending on its shape and size. The main design criteria for these ducts are to consider that each one of them should carry the required oxygen to ensure a complete reaction of the surrounding iron available for combustion.

Example 2: Calculus and Comparison of Two Lances Using the $R_{E/A}$ Ratio

A thermal lance with an efficient design, with steel profiles that have an appropriate thickness so that 100% of the iron reacts, is a "TR-38" (see Fig. 4), which has a free area for oxygen flow of 43.8% in an external diameter of 17 mm, it can generate 5,535 J/mm. Compared to another thermal lance called "Superoxibar 3/8" (SOB 38) with the same external diameter, but with 73.9% free area for oxygen flow, which can generate 3,825 J/mm. Using Eq. (6), each $R_{E/A}$ can be calculated obtaining the following results:

$R_{E/A}$ TR-38: 24 J/mm^2.

$R_{E/A}$ SOB 38: 17 J/mm^2.

Albeit both thermal lances have the same external diameter, the TR-38 generates 1.45 times more energy than the SOB 38. Now, while the generated energy is a good start point for proper lance selection, it is worth to be noted that not all the generated energy is effectively transferred to the material to be melted. Furthermore, the relation between the finally delivered energy of TR-38 and SOB-38 lance is in practice even greater (see Table 3). The efficiency of the energy transfer is detailed in the following section.

Theoretical Framework for Thermal Lance Performance Characterization

There are inefficiencies in this energy transfer that could be summarized in two efficiency terms, (i) the thermal efficiency of the lance, which describes the losses within the lance, and (ii) the thermal efficiency of the operation, which describes the losses related to the operation outside the thermal lance.

Fig. 4 Different thermal lance profiles used in the examples of this document. Model 1: SOB 38 (3/8 in.) (left), model 2: TR-38 (3/8 in.) (center) and model 3: TR-50 (1/2 in.) (right). Lance model 2, have a unitary mass per length of 1.23 kg/m and a total required oxygen inlet flow of 58.26 Nm^3/h

Table 3 Test block perforation samples. Low $R_{E/A}$ Pipe 3/8" (at top) produces a higher diameter and more irregular perforation than a higher $R_{E/A}$ thermal lance such as TR-38 (third from top to bottom)

Test block perforation sample	Parameter	Result
	OD lance [mm]	17.3
	Re/a [kJ/mm^2]	3
	Free oxygen CSA [%]	100
	Max perf. diam [mm]	128.37
	Performance [mm_{Perf}/m_{Lance}]	28.75
	$D_{Perforation}/D_{Lance}$	7.42
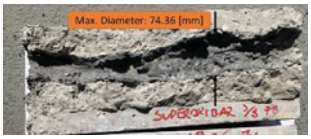	OD lance [mm]	16.9
	Re/a [kJ/mm^2]	17
	Free oxygen CSA [%]	73.90
	Max perf. diam [mm]	74.36
	Performance [mm_{Perf}/m_{Lance}]	92.63
	$D_{Perforation}/D_{Lance}$	4.40
	OD lance [mm]	16.9
	Re/a [kJ/mm^2]	24
	Free oxygen CSA [%]	43.8
	Max perf. diam [mm]	62.14
	Performance [mm_{Perf}/m_{Lance}]	176.60
	$D_{Perforation}/D_{Lance}$	3.68
	OD lance [mm]	20.9
	Re/a [kJ/mm^2]	25
	Free oxygen CSA [%]	37.4
	Max perf. diam [mm]	70.30
	Performance [mm_{Perf}/m_{Lance}]	180.97
	$D_{Perforation}/D_{Lance}$	3.36

Thermal Efficiency of the Lance (η_{TL})

The efficiency of a thermal lance is calculated from (i) the theoretical energy contained in the thermal lance (ECTL), this is assuming 100% of iron would react, (ii) on how much energy is spent to maintain the reaction (ECC), (iii) on how much energy is lost by melting unreacted iron (EFFe), and (iv) on how much energy is lost by heating the remaining free oxygen after the iron combustion (ECO_2). The efficiency of a thermal lance is then given by

$$n_{TL} = \frac{ECTL - (ECC + EFFe + ECO_2)}{ECTL} \tag{7}$$

In the following, mathematical expressions for each one of these terms will be developed and exemplified.

Theoretical Heat Energy Contained in the Thermal Lance (ECTL)

This energy corresponds to the enthalpy of formation released during the iron oxidation process. The ETCL varies with the oxidation state (see Table 4). Hereafter and for sake of simplicity, only the maximum enthalpy of formation (literal (e) on Table 4) is considered for calculations [2].

With the reaction information, plus the molar mass of the reactants and product, it can be shown that for 1 g of iron to react completely, it is necessary to add 0.43 g of oxygen. This reaction has an enthalpy of formation of 7.356 kJ, that is to say

$$1\,\mathrm{g\,Fe} + 0.43\,\mathrm{g\,O_2} = 1.43\,\mathrm{g\,Fe_2O_3} \rightarrow 7.356\,\mathrm{kJ/g_{Fe}} \tag{8}$$

Given the energy released by each gram of iron and knowing the unitary mass per length [kg/m] of the thermal lance, the available energy, expressed in [kJ/m] units, can be obtained by

$$\mathrm{ECTL}\left[\frac{\mathrm{kJ}}{\mathrm{m}}\right] = \text{Mass per length}\left[\frac{\mathrm{kg}}{\mathrm{m}}\right] * \text{Energy per gram}\left[\frac{\mathrm{kJ}}{\mathrm{g}}\right] * 1{,}000\left[\frac{\mathrm{g}}{\mathrm{kg}}\right] \tag{9}$$

For lance model 2, Eq. (9) evaluates to 9,047.9 kJ/m.

Table 4 Iron oxides equation and enthalpy of formation [2, 3, 4]

Equation	ΔH°Enthalpy of formation	**N°**
$Fe_{(s)} + \frac{1}{2}O_{2(g)} \rightarrow FeO(s)$	$\Delta H^\circ_{comb.} = -265.61\,\mathrm{kJ/mol_{Fe}}$	(a)
$FeO_{(s)} + \frac{1}{6}O_{2(g)} \rightarrow \frac{1}{3}Fe_3O_4(s)$	$\Delta H^\circ_{comb.} = -97.31\,\mathrm{kJ/mol_{Fe}}$	(b)
$FeO_{(s)} + \frac{1}{4}O_{2(g)} \rightarrow \frac{1}{2}Fe_2O_3(s)$	$\Delta H^\circ_{comb.} = -138.46\,\mathrm{kJ/mol_{Fe}}$	(c)
$Fe_{(s)} + \frac{2}{3}O_{2(g)} \rightarrow \frac{1}{3}Fe_3O_4(s)$	$\Delta H^\circ_{comb.} = -362.92\,\mathrm{kJ/mol_{Fe}}$	(d)
$Fe_{(s)} + \frac{3}{4}O_{2(g)} \rightarrow \frac{1}{2}Fe_2O_3(s)$	$\Delta H^\circ_{comb.} = -404.07\,\mathrm{kJ/mol_{Fe}}$	(e)

Energy Spent to Sustain the Thermal Lance Reaction (ECC)

This term resumes all the energy required to keep the iron reaction active. The energy required is given by three terms, (i) energy to raise the iron from ambient temperature to its ignition point (1,143.15 K) (EFFe), (ii) the energy to raise the oxygen temperature from ambient temperature up to 473.15 K (EO_2), and (iii) the latent heat of fusion of the iron oxides (Eprod) with a melting point at 1,833.14 K. For lance model 2, these terms, normalized by each gram of reacting iron, are 0.64 kJ/g_{Fe}, 0.4523 kJ/g_{Fe}, and 3.0433 kJ/g_{Fe} respectively [1]; thus, for lance model 2, the energy required to sustain the thermal lance reaction is given by

$$\mathrm{ECC}_{\mathrm{TR}-38} = \mathrm{Efe} + \mathrm{EO}_2 + \mathrm{Eprod} = 4.1356 \frac{\mathrm{kJ}}{\mathrm{g}_{\mathrm{Fe}}} \tag{10}$$

Rewriting Eq. (10) by unitary mass results in 5,086.79 kJ/m.

Energy Lost by Melting the Unreacted Iron at the Thermal Lance (EFFe)

This loss occurs when the oxygen flow rate at the combustion zone is not high enough to enable all the iron to react. Under this condition, a fraction of the energy produced by the reaction is spent on melting the unreacted iron. Since thermal lance model 2 has both proper thicknesses and profile design that minimize the losses given by this phenomenon, EFFe can be despised.

Energy Lost by Heating the Unreacted Oxygen (ECO_2)

Due to the lance design or because of the oxygen supply, there could be oxygen that did not react at the tip of the lance, and this oxygen will absorb part of the heat produced by the reaction. As by each gram of iron that reacts, 0.43 g of oxygen are required (see Eq. (8)), any mass of oxygen value over this quantity will be considered as unreacted oxygen and its absorption of energy is given by

$$\dot{Q} = \dot{m} * C_p * (T_2 - T_1) \tag{11}$$

where: "Q" is the energy lost by heating the unreacted oxygen, "m" is the heated mass of oxygen, "C_p" is the specific heat of the oxygen, and "T_2" and "T_1" are oxygen temperatures before and after the energy absorption. Note that a constant pressure could be assumed in Eq. (11) because oxygen is released into the atmosphere at this point.

Considering T_1 as 298.15 K, T_2 as 473.15 K [1], C_p of the oxygen as 0.000934 kJ/(g ∗ K) [5], and an oxygen overflow at the thermal lance of 2.6 times (1.118 g) with respect to its stoichiometric mass (0.43 g), that is, that by each gram of iron that reacts, the mass of unreacted oxygen is 0.688 g; and then replacing these values at Eq. (11), and considering the thermal lance model 2 unitary mass per length, then ECO_2 term is 144.49 kJ/m.

Replacing the values for $ECTL_{TR\text{-}38}$, $EFFe_{TR\text{-}38,}$ and $ECO_{2\_TR\text{-}38}$ in Eq. (7), the thermal efficiency of lance model 2 results to be $\eta_{TL\_TR\text{-}38} = 42.2\%$. Then, the total useful delivered energy, $ET_{TR\text{-}38}$, evaluates to 3,816.7 kJ/m.

Thermal Efficiency of the Operation of a Thermal Lance Inside the Channel (η_{Op})

Outside the thermal lance, there exist additional inefficiencies related to the operation. These inefficiencies are summarized in the thermal efficiency of operation, η_{Op} and depend on three terms: (i) the useful energy delivered from the lance (ET), (ii) the waste of energy regarding the distance between the tip of the lance and material to be melted, introduced as Energy lost at operation due to heat transfer (POTC), and (iii) energy lost due to an excessive oxygen flow ($POEO_2$). Then, the thermal efficiency of the operation is given by

$$n_{Op} = \left(\frac{ET - (POTC + POEO_2)}{ET} \right) \tag{12}$$

Energy Lost at Operation Due to Heat Transfer (POTC)

As the reaction of iron is produced in the solid state, the energy released in this reaction occurs through a radiation process [1], and as the thermal energy in radiation processes is governed by a spherical geometry [6], then the maximum energy transmission is obtained when the tip of the lance is in contact with the material to be melted. If the lance tip is separated from the material, the transmission of thermal energy is given by [6]

$$\text{Energy received by Material} = \frac{\text{Energy at ignition lance tip}}{\left(\pi * \left(\frac{D}{2}\right)^2\right) + \left(4 * \pi * r^2\right)} * \left(\pi * \left(\frac{D}{2}\right)^2\right) \tag{13}$$

where "r" [mm] is the distance between the ignited tip of the thermal lance and the material to be melted, and "D" [mm] is the external diameter of the thermal lance (Fig. 5).

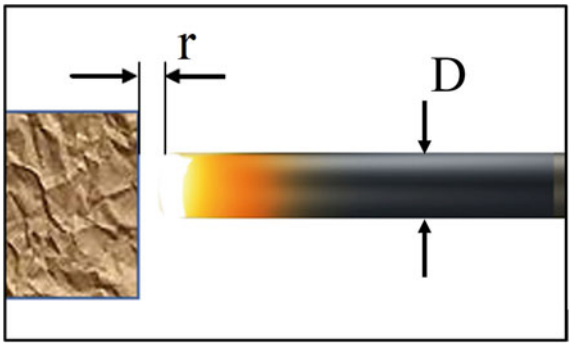

Fig. 5 Distance between the tip of the thermal lance and the material to be melted

For example, if the thermal lance model 2 is in contact with the material to be melted, the energy flow is 67.5 kJ/s and *POTC* term could be neglected, in contrast, if the lance is operated at r = 1 cm from to the material, the energy flow drops to 24.44 $\frac{\text{kJ}}{\text{s}}$, and the term POTC, considering a thermal lance consumption rate is of 1 m/min, turns out to be

$$POTC_{TR-38} = \left(67.5\frac{\text{kJ}}{\text{s}} - 24.44\frac{\text{kJ}}{\text{s}}\right) * 60\frac{\text{s}}{\text{m}} = 2{,}583.6\frac{\text{kJ}}{\text{m}} \tag{14}$$

Energy Lost Due to an Excessive Oxygen Flow ($POEO_2$)

If the oxygen flow is higher than the one required for the reaction of the iron in the thermal lance, the oxygen flow excess will come out of the lance, extracting heat from the material.

This term, named as $POEO_2$, can be also modelled by Eq. (11), but T_1 and T_2 are now defined on different points. As unreacted oxygen mass was defined as 0.68 g_{O_2}/g_{Fe}, given the unitary mass of the lance model 2, then it can be said that 20.5 g of iron are reacting each second, and consequently, the unreacted oxygen mass flow is 13.94 g/s. T_1 is the oxygen temperature at the exit of the lance and is assumed to be 473.15 K. T_2 is the oxygen temperature after being in contact with the material and is assumed to be 1,000 K. Replacing these values at Eq. (15) results in

$$\dot{Q} = 13.94\,\frac{\text{g}}{\text{s}} * 0.000934\,\frac{\text{kJ}}{\text{g} * \text{K}} * (1{,}000\,\text{K} - 473.15\,\text{K}) = 6.86\,\frac{\text{kJ}}{\text{s}}$$

If a thermal lance consumption rate of 1 m/min is considered, then

$$POEO_{2\,TR-38} = 6.86\,\frac{\text{kJ}}{\text{s}} * 60\,\frac{\text{s}}{\text{m}} = 411.57\,\frac{\text{kJ}}{\text{m}} \tag{16}$$

Finally, replacing the example values for the efficiency, the thermal efficiency of the operation inside the channel is 21.62% at r = 1 cm, equivalent to 826.35 kJ/m of effective heat transfer, and 89.23% with lance in contact, equivalent to 3,409.95 kJ/m of heat transfer. Note that when the lance is in contact, the effective transfer heat is 4.13 × times greater. Accordingly, the time required to do the perforation and the amount of thermal lance gets also reduced by this factor.

Calculation and Experimental Validation of the Required Length of Thermal Lance

With the thermal lance performance and the required energy to complete a perforation, it is possible to estimate the required number of thermal lances. As an example, and to validate results, perforation in a test block used in several experiments by the authors is considered here. The required perforation is of 60 mm in diameter and 0.5 m in Depth, equivalent to 0.0014137 m^3 of volume. The test block composition is 80% SiO_2 with a 20%bonding mixture, which in turn is composed of 67% CaO, 25% SiO_2, and 8% Al_2O_3. The tool used is the thermal lance model 2. Using the methodology presented in Example 1, the heat required to fusion 1 m^3 of each component was calculated, weighted by its proportion of the total mass, and finally, all of them were added, resulting in 6,968,076 kJ, the total heat required to fusion 1 m^3 of test block material. Hence, for the volume of the perforation, the proportion of required heat is 10,585 kJ. Dividing this term by the effective heat transferred when the lance is in contact with the material results in 3.1 m, the total amount of thermal lance required for this operation.

To validate these results, experimental tests were performed in triplicate. The same test block and lance were used as in the prior example. The experimental results show that for the same operation as described in the example, a 95% confidence interval for the required amount of thermal lance is 2.87–3.85 m, with a mean value of 3.36 m. Whereas the theoretical result is within this range, it is important to highlight that the number of essays is low to assure the significance of the interval. Also, note that the theoretical result has a percentual error of 7.7% with respect to the experiment average value. This difference could be explained by some energy losses that were not considered on this framework, such as the energy transferred to the non-melted part of the test bloc, or the energy transfer to the ambient when swapping lances during the operation.

Flow of molten materials: Just as for drill bit, in thermal lances processes, it is necessary to evacuate the material of the perforation, so the evacuation flow of molten materials must be equal or higher than the sum between the molten material from the passage and the iron oxides produced in the reaction of the thermal lance. If the evacuation flow is lower, a restriction inside the channel could take place slowing down the evacuation of the materials and consequently the operation. Evacuation of the material could benefit from an oxygen excess, but at the same time, this implies

a reduction in the perforation efficiency, so it is very important to achieve a balance between the thermal energy and the excess of oxygen to help in the evacuation of molten materials.

Considering thermal lance model 2 unitary mass and the optimal consumption rate, then each minute 1.23 kg of iron and 0.52 kg of oxygen are reacting, giving a thermal lance material melting rate of 1.75 kg/min of Fe_2O_3, which has density 5.24 g/cm^3 [7], and combining this information, then

$$FV_{Fe2O3} = \frac{1.75\frac{\text{kg}}{\text{min}} * 60\frac{\text{min}}{\text{h}}}{5.240\frac{\text{kg}}{\text{m}^3}} = 0.02014\frac{\text{m}^3}{\text{h}} \tag{17}$$

Considering the energy flow from the thermal lance, $\text{FE}_{\text{TR-38}} = 17.25$ kJ/s. Then, test block melting rate can be calculated as

$$TF_{TestBlock} = \frac{56.83\frac{\text{kJ}}{\text{s}} * 3,600\frac{\text{s}}{\text{h}}}{6,968,076\frac{\text{kJ}}{\text{m}^3}} = 0.02936\frac{\text{m}^3}{\text{h}} \tag{18}$$

Then, the total flow of molten materials (titanium carbide plus iron oxides) is

$$FM = FV_{Fe2O3} + TF_{TiC} = 0.02014\frac{\text{m}^3}{\text{h}} + 0.02936\frac{\text{m}^3}{\text{h}} = 0.0495\frac{\text{m}^3}{\text{h}} \tag{19}$$

Evacuation of Molten Materials

It is normally observed that the operators of the thermal lances utilize a high oxygen flow rate through the lances to assure a good molten material evacuation. However, this generates several drawbacks, for example an unnecessary and dangerous emission of molten material and sparks that, depending on the oxygen flow, could be easily projected up to 4, 5, 10 m and even further. Also, and typically unknown by the operators, with those levels of oxygen flow, the efficiency of the operation decreases due to the cooling effect of oxygen. Then, higher oxygen flow should only be added when a drop in the evacuation of molten material rate is detected.

There are many factors that affect the fluidity of molten material, the main are the viscosity and the surface tension, where both have a temperature dependence. Many studies, regarding the oxygen flow rate required to evacuate materials, conclude that the oxygen flow order to help the evacuation of molten materials will vary depending on perforation depth and cross-section up to 20 Nm^3/h.

Conclusions

In this work, a novel theoretical framework was introduced and detailed that helps to understand the principal variables involved in the tapping processes using thermal lances. This framework could be used for further studies and as a tool to objectively benchmark different lance performances. Also, it helps to understand the efficiency of a given operation in terms of thermal lance length and the time required to complete the tapping process and to determine which are the main inefficiencies of the processes and its relative impact on the overall efficiency, so it allows to focus improvements efforts to potentially reduce the operational costs and time.

Maximum tap-hole opening efficiency mainly depends on the use of the right thermal lance considering the material to be melted, to be always touching this material with the thermal lance ($r = 0$) and with the proper oxygen flow.

If the material to be melted is not reactive with oxygen, the proper thermal lance to operate will be one with a high E/A ratio ($R_{E/A}$). It is important to remind that an excessive $R_{E/A}$ ratio (higher than 25 J/mm^2) will drop the thermal lance efficiency due to the lack of oxygen to make react all the iron of the thermal lance.

If a low E/A ratio thermal lance is utilized in an oxygen unreactive material, operation performance will drop considerably, increasing the thermal lances quantity and the operation time.

As was detailed in this work, the feed of the oxygen flow plays a fundamental role in the performance of a thermal lance. The energy losses due to cooling both in the lance and at the attack point occupy a significant place within the total energy released and there are extremely important operational factors that are strongly influenced by this variable, such as the ability to sweep the molten material within the passage, as to maintain the lance at a desired burn/consumption rate.

The theoretical framework presented in this paper could be used to estimate different operation indicators such as the number of thermal lances and the time required to complete tap-hole operation. These indicators could be used in future works to analyse the economic impact of optimizing the tap-hole process in the context of the complete furnace operation. Preliminary analysis realized by authors suggests that when solving several drawbacks such as the uncertainty regarding the tap-hole operation and reducing the chances of damaging the furnace passages, time savings could be achieved with a positive impact on furnaces productivity. This analysis will be further analysed in future works.

References

1. Morales D (2018) Tap-hole opening: advances and improvements. In: Furnace tapping conference, South Africa
2. Saxena SK (1993) Thermodynamic data on oxides and silicates. Springer, Berlin
3. NIST-JANAF Thermochemical Tables 2013. https://janaf.nist.gov/tables/C-107.html. Consulted in July 2021

4. Barin I (1989) Thermochemical data of pure substances, Part I/II. VCH Verlagsgesellschaft, Weinheim
5. Perry (1934) Chemical engineer's handbook. McGraw-Hill Book, London and New York
6. Rybicki G, Lightman A (1979) Radiative processes in astrophysics. Harvard-Smithsonian Center for Astrophysics, Toronto
7. Doo W (2011) Magnetic signature of Siaolin Village, southern Taiwan, after burial by a catastrophic landslide due to Typhoon Morakot
8. Barin I (1993) Thermochemical data of pure substances, 2nd edn. VCH Verlagsgesellschaft, Weinheim

Data Analysis to Assess Carry-Over Slag

P. Chris Pistorius

Abstract "Carry-over slag" refers to steelmaking slag that is transferred to the steel ladle when tapping a steelmaking vessel (electric arc furnace or oxygen converter). Carry-over slag is oxidizing, causing consumption of deoxidizer (such as aluminum) during ladle processing, and leading to phosphorus reversion to the steel. In principle, mass balances based on the concentrations of several elements—phosphorus, manganese, and aluminum—could be used to assess the amount of carry-over slag. In this work, steel and slag compositions and the amounts of additions during tap were used to estimate the carry-over slag mass, using data from a large number of heats. It is concluded that—for aluminum-killed steel—an aluminum mass balance gives the only reliable estimate.

Keywords Slag carry-over · Electric furnace steelmaking · Data analysis

Introduction

As reviewed recently [1], the transfer of slag from a steelmaking vessel to the subsequent steel refining step must be limited. The reasons to limit slag transfer are that the slag contains reducible species such as FeO, MnO, and P_2O_5 that would consume deoxidizer (commonly aluminum) and would revert impurities (notably phosphorus) to the steel. Calculated effects of slag carry-over are shown in Fig. 1, indicating the sharp increase in aluminum consumption with increased slag carry-over, and the potential to revert tens of parts per million (by mass) of phosphorus to the steel. (The values used in calculating this figure correspond to the averages for the heats considered in this study.)

In the work presented here, data was obtained from an electric furnace operation to test a method to estimate the amount of carry-over slag from an Al mass balance. The principle is that the concentration of dissolved Al after deoxidation is what remains after Al has been consumed by reacting with dissolved oxygen in the steel,

P. Chris Pistorius (✉)
Department of Materials Science and Engineering, Center for Iron and Steelmaking Research, Carnegie Mellon University, 5000 Forbes Avenue, Pittsburgh, PA 15213, USA
e-mail: pistorius@cmu.edu

J. D. Steenkamp et al. (eds.), *Furnace Tapping 2022*, The Minerals, Metals & Materials Series, https://doi.org/10.1007/978-3-030-92544-4_4

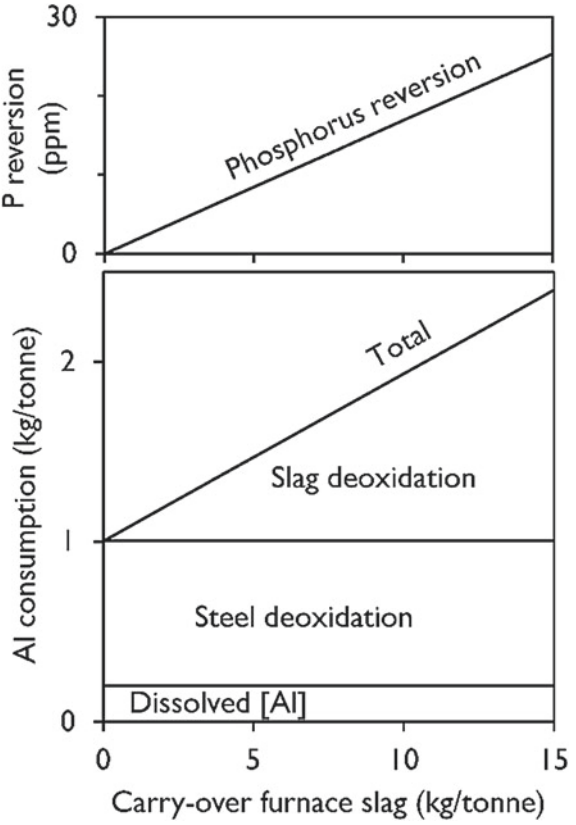

Fig. 1 Calculated effect of slag carry-over on the required mass of deoxidizer (aluminum), to obtain steel containing 0.02% dissolved Al and fully reducing FeO, MnO, and P_2O_5 from the slag. Calculated for steel containing 715 ppm dissolved oxygen before oxidation and slag with 37% (FeO + MnO) and 0.17% P

by reducing oxides from the carry-over slag, and by acting as reductant during initial desulfurization. In principle, the extent of phosphorus reversion (Fig. 1) and MnO reduction from the slag (increasing the Mn concentration in the steel) could also be used to estimate the amount of carry-over slag, and these approaches were evaluated.

Data Analysis Approach

Data Set

Production data from more than 200 heats produced at an electric arc furnace (EAF) steelmaking plant were obtained. The plant is a scrap-based operation. Shortly before furnace tapping, the concentration of dissolved oxygen is measured, and a steel sample is taken for chemical analysis. The median dissolved oxygen concentration before tapping is approximately 700 ppm (Fig. 2).

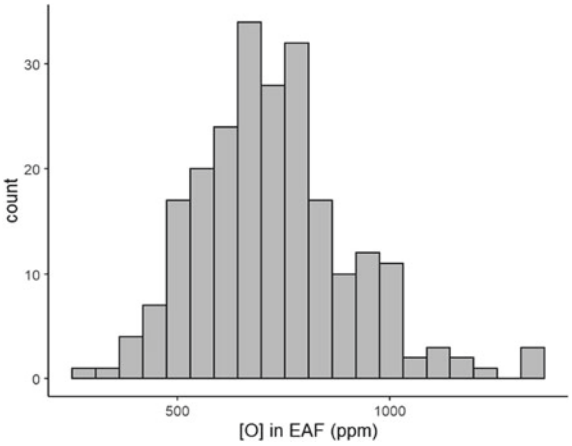

Fig. 2 Distribution of the concentration of dissolved oxygen in the steel, shortly before tapping the steel from the EAF

Upon tapping, aluminum and other additions are made to the steel in the ladle. Additions include ferroalloys (ferrosilicon, silicomanganese, ferromanganese, and ferrochromium) and fluxes to adjust the slag composition. The amount of aluminum added is adjusted according to the concentration of dissolved oxygen (Fig. 3). Each heat of steel was approximately 92 tonnes (Fig. 4).

After the additions, the steel is stirred using argon bubbling (through a stirring plug in the ladle), and a first ladle sample is taken. The median concentration of dissolved Al in this sample is 0.02% (Fig. 5).

In addition to the compositions of steel in the EAF and after deoxidation, and the masses of all tap additions, EAF and ladle slag samples from 25 heats were analyzed

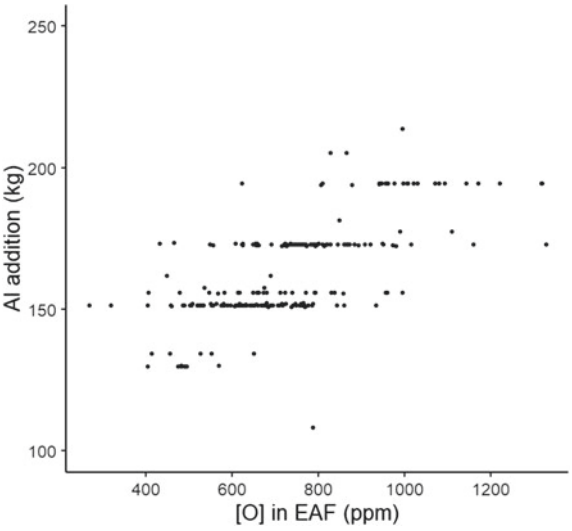

Fig. 3 Aluminum additions made upon tapping the steel from the EAF, for the heats considered in this study

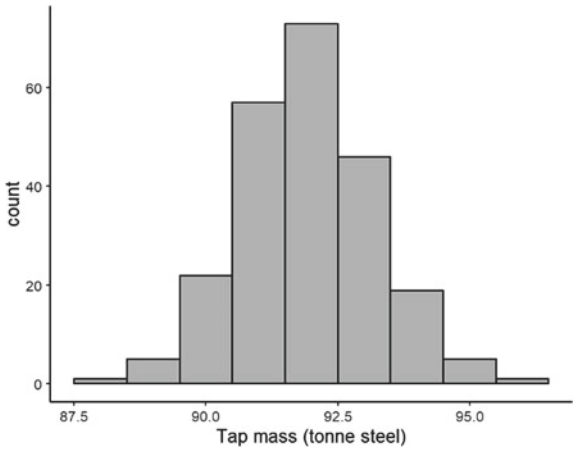

Fig. 4 Distribution of tap masses of the heats considered in this study

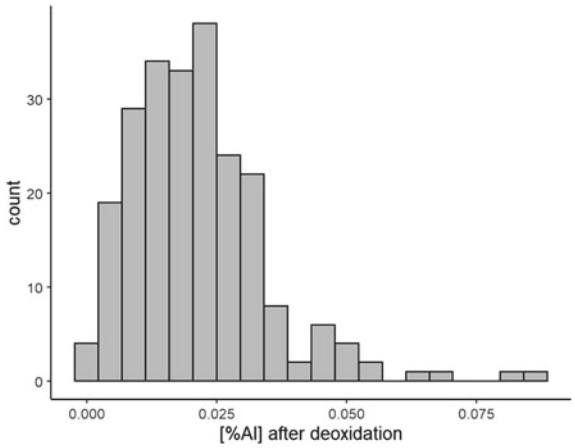

Fig. 5 Dissolved aluminum in the steel after deoxidation

(Fig. 6). The figure shows that the concentrations of FeO, MnO, Cr_2O_3, and P_2O_5 are much lower in the ladle slag than in the EAF slag, reflecting the deoxidation effect of aluminum. The higher concentrations of Al_2O_3 and CaO (in the ladle slag) result from Al_2O_3 formed during deoxidation, and fluxing additions.

Calculation Approach

The amount of carry-over slag was estimated from an aluminum mass balance, as described by Piva [2]. For each heat, the amount of aluminum consumed by reaction with dissolved oxygen in the steel and by desulfurization is calculated. The difference between the added aluminum (Fig. 3) and the sum of the reacted aluminum

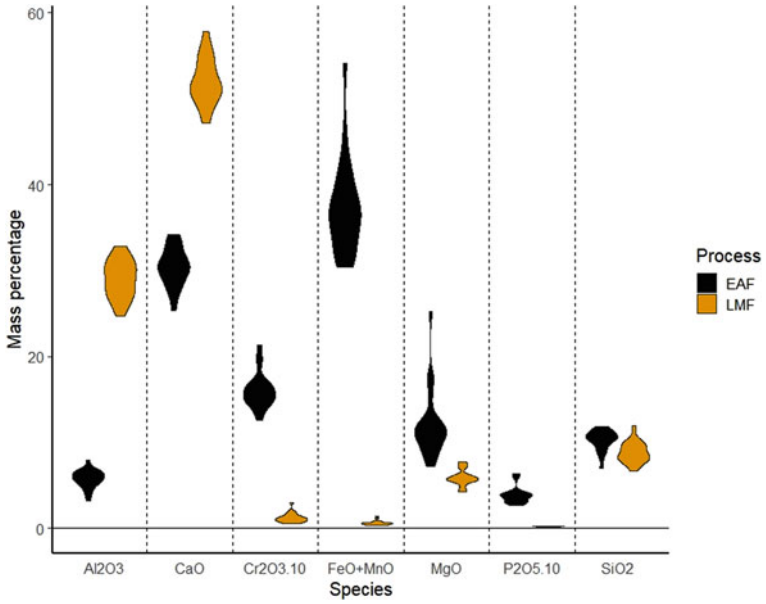

Fig. 6 Violin plots of the distributions of the compositions of the EAF and ladle slags. Note that the concentrations of Cr_2O_3 and P_2O_5 were multiplied by 10 to be visible in the graph

(Fig. 2, plus a small amount for desulfurization) and the aluminum remaining in solution (Fig. 5) is available to reduce the carry-over furnace slag. From the known concentrations of the reducible species (FeO, MnO, P_2O_5, and Cr_2O_3) in the furnace slag, the amount of reacted slag is found by stoichiometry.

Results and Discussion

Calculations Based on Aluminum Mass Balance

The calculated mass of carry-over slag is summarized in Fig. 7. The median (approximately 8 kg slag per tonne steel) is typical for a well-controlled EAF operation [1]. Based on the mass balance, the aluminum mostly reacted with dissolved oxygen and FeO + MnO, with a minor amount consumed by desulfurization and reduction of P_2O_5 and Cr_2O_3 (Fig. 8).

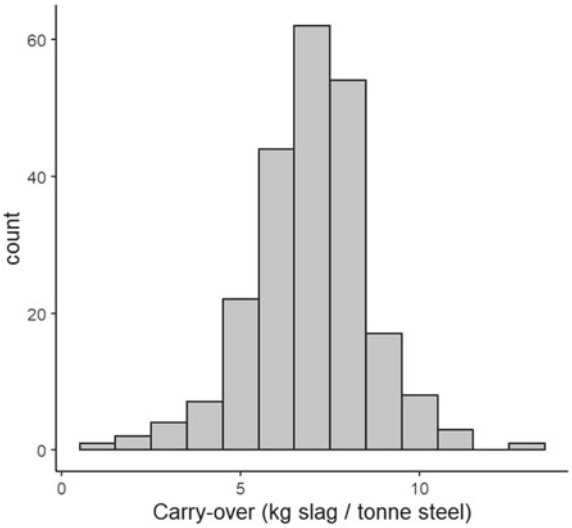

Fig. 7 Distribution of calculated mass of carry-over slag, calculated from an aluminum mass balance

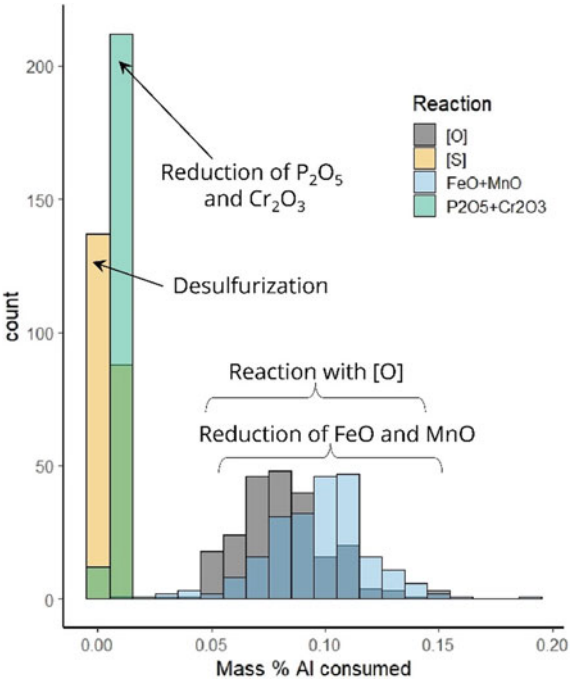

Fig. 8 Calculated consumption of aluminum by reaction with different species in the tapped steel and carried-over slag

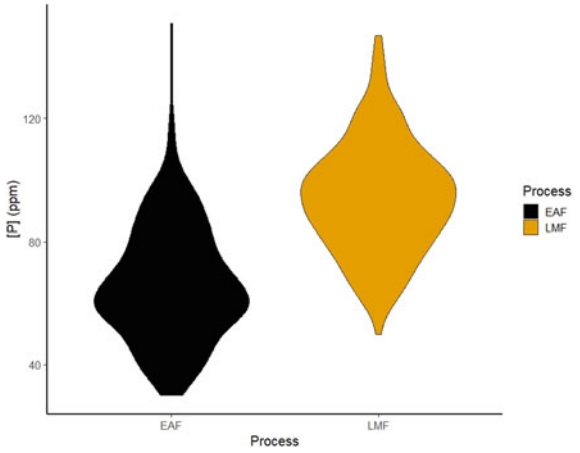

Fig. 9 Distributions of phosphorus concentrations in the steel in the EAF and in the ladle

Phosphorus and Manganese Mass Balances

Since the reduction of P_2O_5 from the carry-over slag causes the phosphorus concentration in steel to increase significantly (Fig. 1), the change in [P] could possibly be used as another way to estimate the amount of carry-over slag. The analyses confirm that the steel contains more phosphorus after deoxidation than in the EAF (Fig. 9). However, the average increase (approximately 30 ppm) is larger than that would be expected from the phosphorus concentration in the furnace slag and the calculated amount of carry-over slag. The likely source of the larger increase in phosphorus is the alloying additions made during tap: ferromanganese can contain as much as 0.35% P, and silicomanganese as much as 0.2% P [3, 4].

Reduction of MnO from the carried-over slag increases the Mn concentration in the steel; the calculated average mass of Mn recovered in this way is approximately 35 kg per heat (Fig. 10). However, as this figure shows the alloying additions of Mn are much greater than this, precluding the use of a Mn mass balance to estimate the mass of carry-over slag.

Conclusion

While manganese and phosphorus mass balances cannot be used to calculate the amount of furnace slag carried over to the ladle, a conceptually simple aluminum mass balance yields realistic estimates, of around 8 kg slag per tonne steel for the operation considered here.

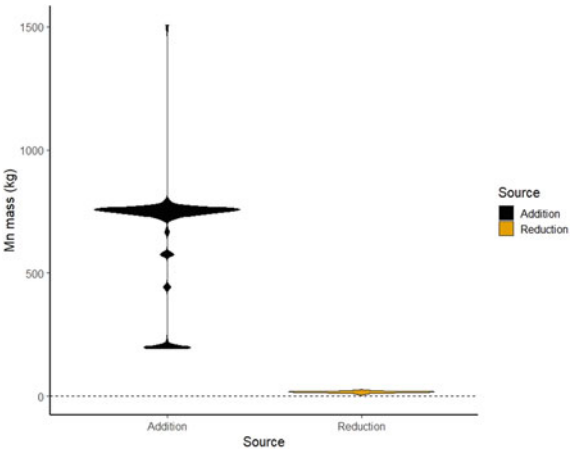

Fig. 10 Calculated amounts of manganese added to the steel by alloying additions and by reduction of MnO from carry-over slag

Acknowledgements Enlightening discussions with Stephano Piva are gratefully acknowledged, as is the support of this work by the industrial members of the Center for Iron and Steelmaking Research.

References

1. Pistorius PC (2019) Slag carry-over and the production of clean steel. J SAIMM 119:557–561
2. Piva SPT, Pistorius PC (2021) Data-driven study of desulfurization during ladle treatment and its impact on steel cleanliness. In: AISTech 2021—Proceedings of the iron & steel technology conference, pp 861–873
3. ASTM International (2019) ASTM Standard A99-03. Standard specification for ferromanganese
4. ASTM International (2020) A483/A483M-10. Standard specification for silicomanganese

An Overview of Submerged Arc Furnaces Tapping Operations and Tap-Hole Management at Assmang Manganese Cato Ridge Works

M. Cele and T. Nzima

Abstract Assmang Manganese Cato Ridge is an integrated manganese smelter in South Africa producing High Carbon Ferromanganese and Refined Alloys. It was constructed in 1956 and is jointly owned by African Rainbow Minerals and Assore Limited. This paper seeks to share critical considerations to ensure effective, efficient, and sustainable tapping operations. These considerations include tap-hole design, launder design, maintenance practices and procedures, daily operations, critical equipment required, and tapping employees' skills. The paper will also discuss the benefits of being an inclusive employer whereby more than 50 percent of employees who are tappers are females ranging from the age of 26 to over 50 years. The following are the outcomes of the well-managed tapping process: reduced health and safety risks, metal/slag separation, improved tap block life cycle, no production losses due to unplanned tap-hole blocks maintenance, no V-Shape repairs, and no runaway taps.

Keywords Runaway taps · Mud gun and drill · V-Shape repairs · Burn-through · Mickey block · Tap-hole clay

Introduction

Assmang Manganese Cato Ridge Smelter has six submerged arc furnaces where three are open furnaces and another three are closed. Assmang is currently operating three open furnaces; however, the paper will focus on the tapping operations of the two open submerged arc furnaces starting from the last complete furnace rebuilds. The two furnaces are Furnace 2 and Furnace 5, which are rated at 22 MVA and 30 MVA, respectively.

M. Cele (✉)
Assmang Manganese, Cato Ridge, South Africa
e-mail: musac@feralloys.co.za

T. Nzima
Assore Limited, Sandton, South Africa
e-mail: thabonzima@assore.com

J. D. Steenkamp et al. (eds.), *Furnace Tapping 2022*, The Minerals, Metals & Materials Series, https://doi.org/10.1007/978-3-030-92544-4_5

Assmang Furnace 2 is a 22 MVA furnace that underwent a major upgrade in February 2011. The main design change on the furnace was the incorporation of a slag tap-hole approximately 1000 mm above the metal tap-hole. The furnace was installed with a complete freeze lining supplied by Graftech. The dual tap-hole operation was officially discontinued approximately six months after the furnace start-up. The premise of maintaining a high enough metal bath in the furnace so that slag can be tapped from higher slag tap-hole led to lining metal line temperatures in excess of 800 °C. The furnace has since then operated very efficiently on a single tap-hole operation. There were no tap-hole change or partial repair done in the past 9 years. A decision was taken in February 2020 to reline Furnace 2 due to bottom plate lifting which was measured in excess of 200 mm in the proximity of electrode 1. Electrodes are numbered clockwise, where the tapping electrode is number 2 and back electrodes are numbers 1 and 3 as shown in Fig. 1.

Assmang Furnace 5 was in operation from November 2007 until May 2021 when it was switched out for a planned rebuild of the entire furnace after 14 years of operation. Furnace 5 was completely relined with a Graftech Freeze Lining in November 2007, the next scheduled repair of the tap block and a V-shape repair was done in July 2016, and lastly, a cold face reline was done in September 2018 due to the sill requiring replacement. The cold face repair is the removal and replacement of the top 60% Alumina bricks from the shell top steel ring or sill that became loose due to the bottom shell lifting. About 500 mm of Alumina bricks around the top diameter of the furnace from the top were replaced and a steel ring or sill was replaced which is used to keep alumina bricks in position. The Graftech® freeze lining concept design (Fig. 2) combines wall cooling and thermally conductive carbon and graphite refractories to cool the refractories by transferring heat away from the furnace lining. Effective water sidewall cooling, together with the efficiency of the heat dissipating conductive refractories, lowers the temperature of the lining below that of the molten materials. This causes a layer of slag and process metal to solidify and form a protective which

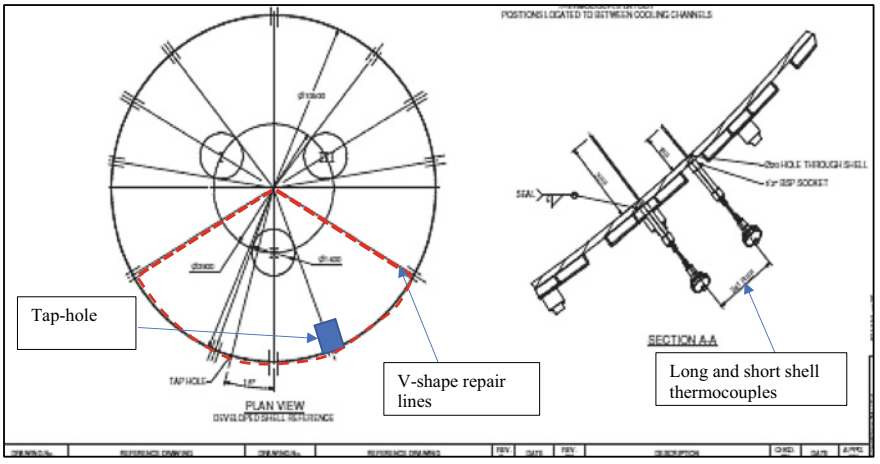

Fig. 1 Furnace diameter indicating electrode positions, V-shape, and thermocouples

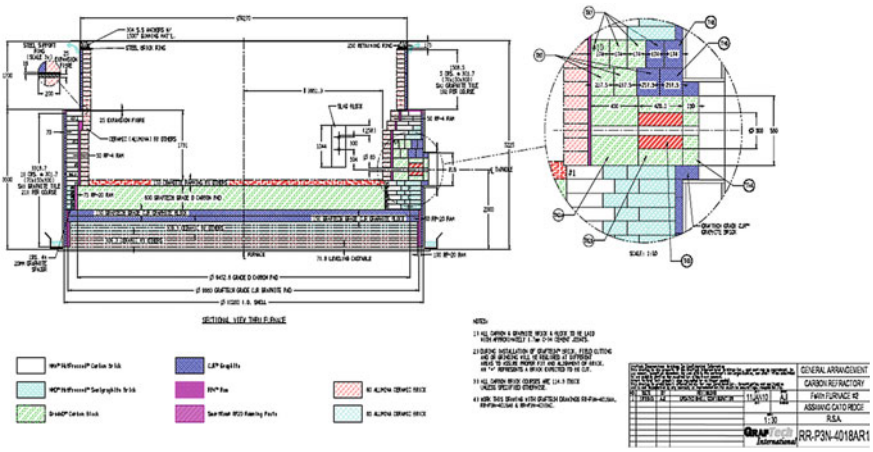

Fig. 2 Furnace Graftech freeze lining design

completely coats the refractory hot face. Once formed, the slag skull insulates the refractories, reducing heat loss and protecting the lining from erosion, chemical attack, thermal shock, and other stresses. The result is extended life and greatly improved refractory performance. The V-shape repair is the replacement of the entire tap block area from top to bottom including an angle of about 45° on both sides of electrode 2 as indicated by red dotted lines in Fig. 1.

Tap-Hole and Launder (Runner) Design

Design During Re-build

Both furnaces were relined with a full freeze lining design from Graftech, where a Carbon D grade tap-hole block with a graphite sleeve was installed. Graphite lintels were installed on top of the tap-hole towards water-cooled channel shell. Graphite tiles against the shell followed by semi graphite bricks above and below the tap-hole and then standard carbon bricks towards the furnace interior were installed (Fig. 2).

The furnace shell is cooled by forced water through channels and forced air under the hearth steel plate. The cooling water is chemically treated to control total water hardness, nitrite contents, conductivity, total dissolved solids, suspended solids, pH, and iron levels. The chemical treatment of the cooling water is crucial to maintain heat transfer by preventing the build-up in or corrosion of the pipes. In addition to the quality of water, the inlet temperature should be low enough (less than 25 °C) to ensure proper heat transfer. Water cooling equipment (cooling towers) should operate properly to ensure efficient cooling of the water. The shell channel cooling

inspection in Fig. 5 indicated a clean channel, as a result of the effective cooling water management, after 10 years of operation.

Three sacrificial Mickey blocks were installed from the tap block towards the short launder or spout, where the outside one is changed every 3 to 5 months to protect the tap block and ensure the smooth contact area or surface for the mud gun to close properly. Short launder or spout is the area joining the furnace shell and the runner or launder. One Mickey block which is indicated in Fig. 1 is in a water-cooled area and come the Graftech design whilst the two sacrificial Mickey blocks are located in the tap-hole arch (extension) and are not cooled. These two furnaces are tapping slag and metal simultaneously from the single-level tap-hole. Thermocouples are installed around the tap-hole to monitor heat transfer. Thermocouples are installed as a pair, long and short thermocouples at 300 mm and 150 mm deep in the carbon bricks, respectively, to assist with heat transfer calculations.

Sacrificial Mickey blocks (150 mm) were changed from standard carbon blocks that were lasting an average of 3 months to super micropore carbon sacrificial Mickey blocks type that last an average of 5 months. Micropore carbon sacrificial Mickey blocks performed better because of their superior heat transfer capabilities, high density, high strength, and high resistance to chemical attack compared to conventional carbon. Tomala and Batista concluded that micropore carbon materials, compared to the standard carbon, give better resistance to the attack by liquid metal and other wear factors, as they are characterised by a considerable share of pores of diameters below1 μm [4]. The high density, high strength, and high resistance to chemical properties give micropore Mickeys a better advantage to perform well rather than heat transfer capabilities.

Initially, the tap-hole in Furnace 5 was at 0 degrees to the Furnace centre and was changed to 15 degrees (Figs. 3 and 4) to match the Furnace 2 design. The zero

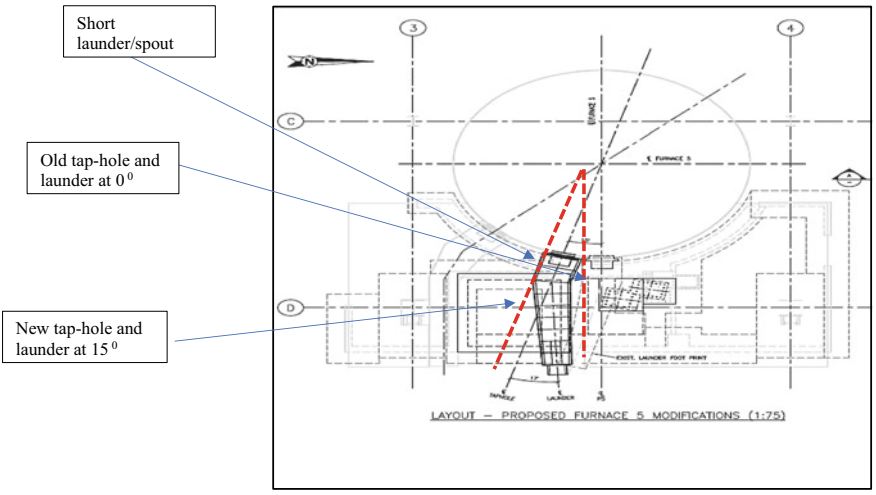

Fig. 3 Furnace launder or runner design

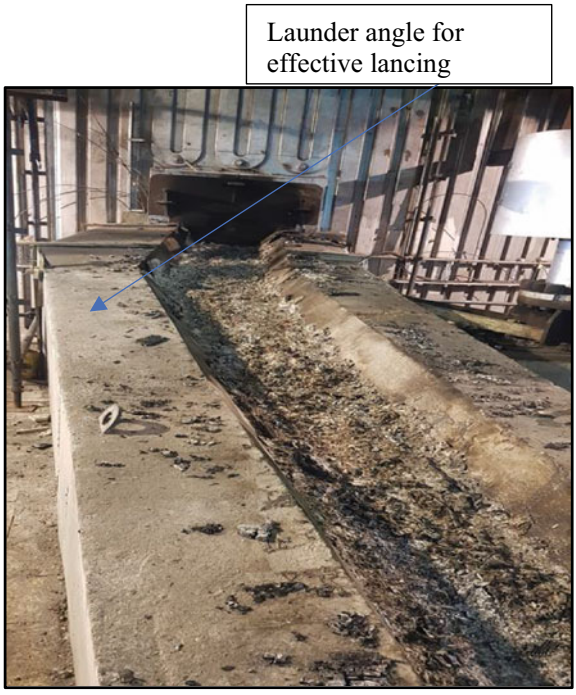

Fig. 4 Furnace launder or runner design

degrees tap-hole had a straight launder, which made it difficult to lance straight and caused the erosion of the launder. It resulted in a partial V-shaped repair where a tap block change was done after 8 years of operation. The opportunity was utilised to change the tap-hole angle to 15 degrees and the launder was re-designed. The design ensures that molten metal and slag flow away from the tappers which allows the tappers to lance straight.

Tap-Hole Condition During Dig Out

Coetzee et al. indicated that there was little wear on Furnace 2 metal tap-hole observed after 9 years, and lintels and carbon side blocks were perfectly intact (Fig. 6) [2]. Slag tap-hole abutment was in a very good condition, which means that tap-hole management was excellent. Metal and slag penetration into the lining was not observed in tap-hole abutments. This proved to show that lining wear on this furnace did not originate from the tap-holes. This is consistent with what Pal and Ciezki presented regarding TEMCO South 32 furnace 1 tap-hole condition after 11 years of operation in INFACON XV [3].

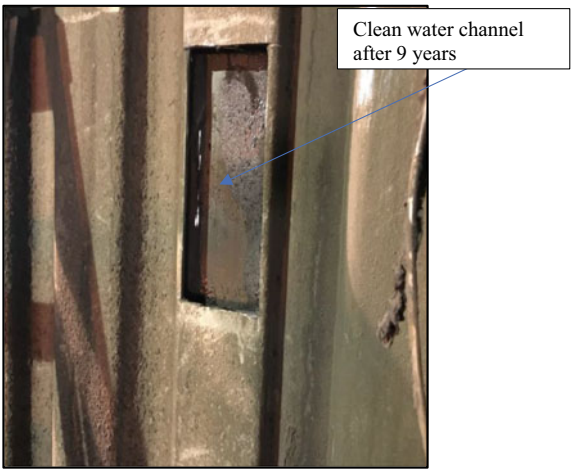

Fig. 5 Shell cooling channel inspection

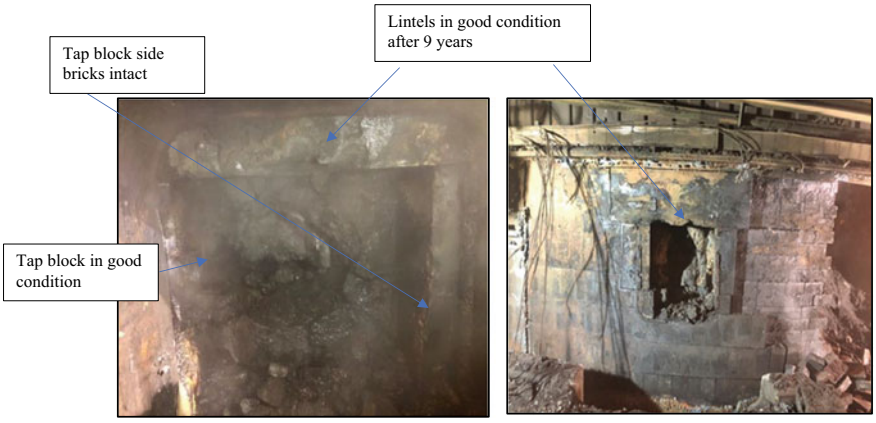

Fig. 6 Furnace 2 tap-hole condition during demolition

Maintenance Practices and Procedures

Tapping Procedures and Practices

Metal and slag streams are tapped simultaneously from a single-level tap-hole after every 2 h' intervals, usually based on the number of kilowatt-hours accumulated. Metal and slag are sampled and send to the laboratory to be analysed using X-ray fluorescence (XRF) as shown in Table 1 and used for process control. Furthermore, Assmang's furnace slag chemistry details were presented by Broekman and Ford [1]. The tapping process is performed every second hour and normally takes between 20 and 30 min from opening to closing the tap-hole. The smelter targets 12 taps of 15

tons of alloy per tap which is tapped into refractory lined ladle then slag overflow into the slag pot (Fig. 9a). The typical slag to alloy ratio (ton/ton) of 0.6 to 0.7 is achieved in Table 1 and the basicity equation in Eq. 1.

According to temperature measurements taken, the furnace tapping temperature averages between 1410 °C and 1445 °C. Henceforth, tapping operations are hazardous and need to be carried out in a safe manner. The tapping temperatures are measured at the launder on an ad hoc basis using Infra-Red images.

$$\text{Basicity} = \frac{(CaO + MgO)}{(SiO_2 + Al_2O_3)} \tag{1}$$

Maintenance Procedures and Practices

The graphs in Figs. 9 and 10 indicate sacrificial carbon Mickey block changes for Furnace 2 and Furnace 5 over the past 5 years. It also indicates changes in the life of sacrificial Mickey blocks when changing from the standard carbon Mickey block to super micropore carbon Mickey blocks from an average of 3 months to more than 5 months. Furnace 2 has used 3 standard carbon Micky campaigns with checker board pattern filled bars as shown in Fig. 9. Furnace 5 has used 5 standard carbon Micky campaigns with checker board pattern filled bars as shown in Fig. 10. The cost-effective microspore carbon sacrificial Mickeys also came at 8% cheaper per unit price. At least 1 h shut and labour are required to change sacrificial Mickey blocks. Typically, jackhammers are used to break out the old Mickey block and short launder. The removal of the tap-hole arch holding plate is also required (Figs. 7 and 8). Proper cleaning of the area is required to ensure the new Mickey block is installed and short launder repaired with castables. The Alumino silicate monolithic (castables) refractories used can withstand a temperature of 1650 °C with the following typical specification; Alumina = 64%, Silica = 27%, Calcium Oxide = 7%, and the balance as Iron Oxide.

Carbon tap-hole block change and partial reline is not a standard practice at Assmang Cato Ridge as the carbon tap-hole blocks last the lining life time, provided that the tap-hole and launder were designed correctly. This also indicates good tap-hole practises and procedures which include employee skills and furnace operation.

Critical Equipments Required

A pedestal-type mud gun and drill supplied by Dango & Dienenthal SA (PTY) LTD is the standard fixture in all Assmang Cato Ridge furnaces. The mud gun and drill can be operated in the control panel or using a remote control. Assmang Cato Ridge prefers to install pedestal-type mud gun and drill equipment on the opposite side of

Fig. 7 Tap-hole arch holding plate before installation

Fig. 8 Tap-hole holding plate installed

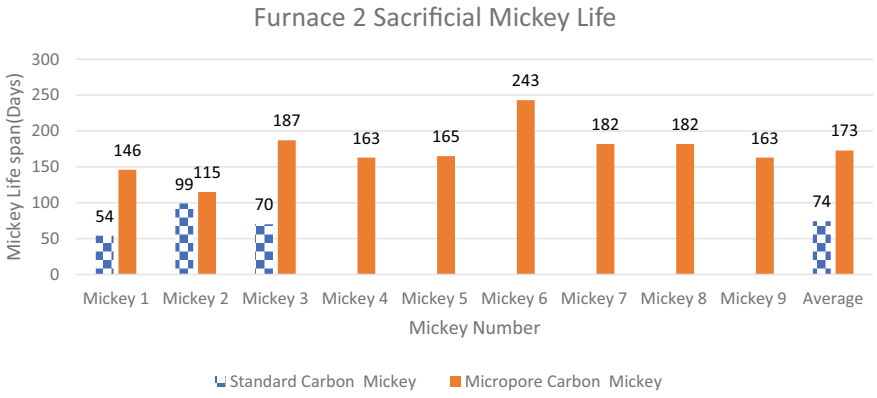

Fig. 9 Furnace 2 sacrificial Mickey blocks life in days

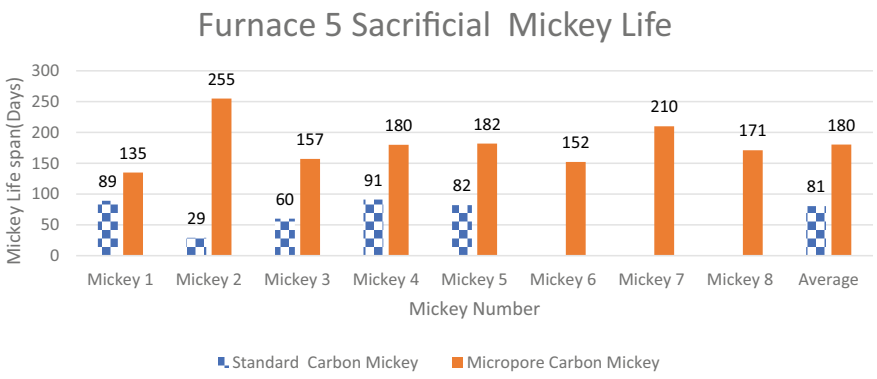

Fig. 10 Furnace 5 sacrificial Mickey blocks life in days

the tappers for safety reasons. At least three notches of clay (Calde Tap 010 FASX) are recommended when closing the tap-hole to ensure a more than 1 m of clay is extruded into the tap-hole. More paste in the tap results in an easier tap-hole opening. Mud gun alignment with tap-hole and mud gun nozzle maintenance is important. A drill should drill the tap-hole to more than 1 m and the drill bit (Fig. 11) should be inspected and changed regularly. Oxygen lancing is used for tap-hole opening as a back-up or a complement to drilling. To protect the drill, it is preferable to use the lance to complete opening the tap-hole.

Oxygen lancing is performed by two tapping operators to penetrate into the solidified clay. One operator is responsible for regulating oxygen flow through the lance pipe while the second operator burns through the tap-hole with a lance pipe until the liquid metal/slag mixture starts to flow. The standard tapping lance used is 7 m and can be connected into two using push lock connectors shown in Figs. 12 and 13 to provide uninterrupted lancing.

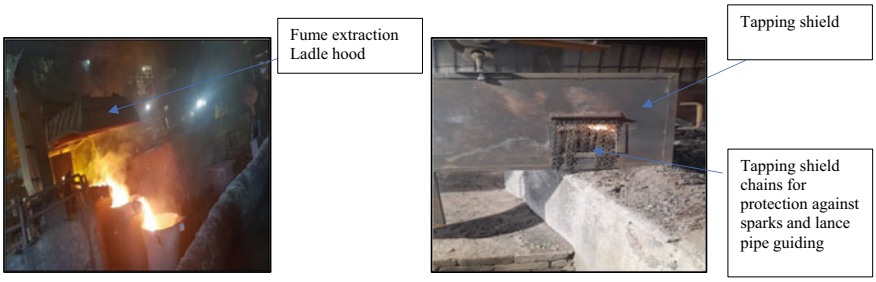

Fig. 11 **a** Tap-hole fume extraction ladle hood **b** Tapping shield

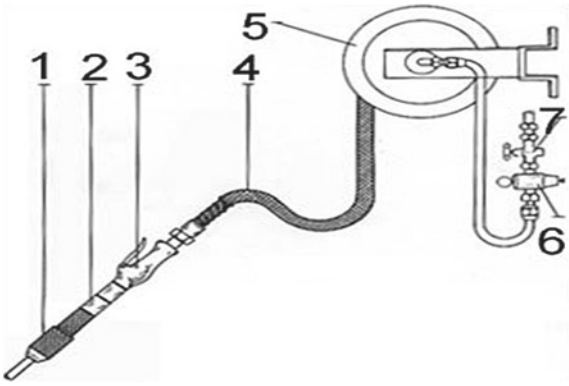

Fig. 12 Main oxygen lancing components

In addition to a full tapping protective clothing which includes tapping jacket, tapping pant, long gloves, respirators or air stream helmet, hard hat, tapping boots, and carbon monoxide analyser, a tapping shield provide extra protection. The tapping shield (Fig. 11b) which is pushed and positioned on the launder is crucial in protecting tappers from the blowing and sparks from the tap-hole. The tapping shield hole with chains also assists in positioning the oxygen lance pipe towards the tap-hole.

Assmang has trialled different parting agents to use to prepare launders; however, building or plaster sand remains the most cost-effective and safe material to utilise. Building or plaster sand is not only useful to prepare launders, but also assists in controlling runaway (uncontrolled tap) taps. It is important to ensure that the sand is dry enough to prevent the violent reaction of moisture and molten metal.

Tapping fumes are removed from the tap-hole hood, launder hood, and movable jip crane covering the ladle and slag pot (Fig. 11a). A fume extraction system is designed to limit the exposure of tapping operators/tappers to tapping fumes.

A revolutionary non-toxic tap-hole clay (THC), that puts all health and safety concerns associated with traditional tap-hole clay to rest, by eliminating all the toxins that are emitted when it is heated and grants the additional benefit of being more cost-effective, is used in the smelter (Calde Tap 010 FASX from Calderys Refractories). The following are the advantages associated with THC:

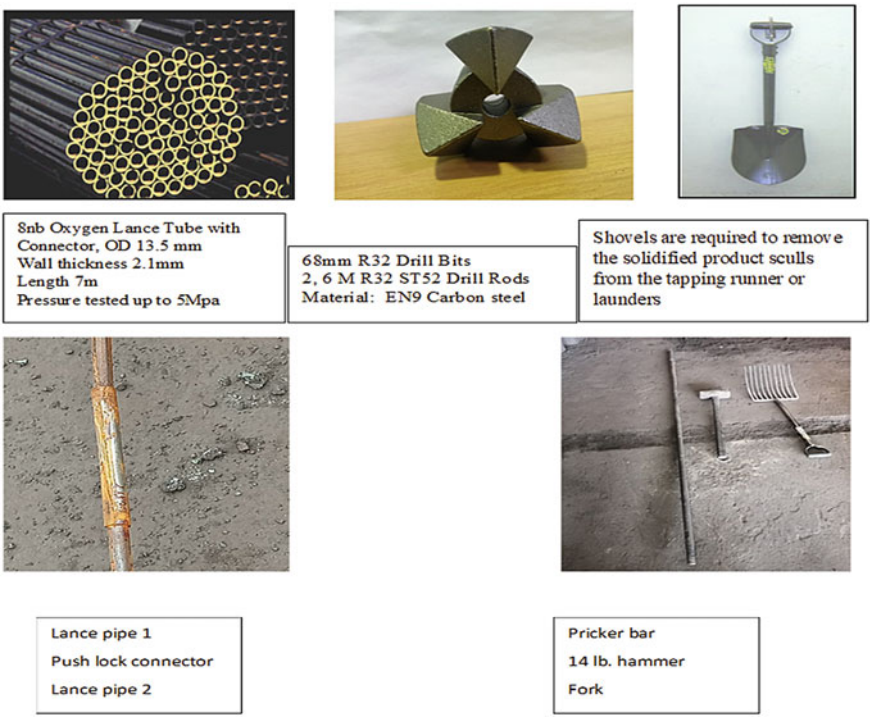

Fig. 13 Tapping equipment

- Less fumes and/or smoke when closing the tap-hole.
- Environmentally and personal friendly—less PAH (Polyromantic hydrocarbon levels).
- Better tap-hole management capabilities due to its expansion capacity.
- Number of lances can be reduced because one is able to open the tap-hole with the drill only.
- No uncontrolled opening of the tap-hole due to weak bonding and poor expansion of the clay.
- No constant flame on the tap-hole after closing.

Additional tapping equipment necessary are as follows: round bars, ballast forks, pointed hexagonal pricker bars, shovels, flashback arrestor and lance holder, changeable launder lips, oxygen hose connections, and 14-pound hammer shown in Figs. 12 and 13.

Main Components of Oxygen Lancing Equipment

The typical oxygen installation for the lancing of electrical arc furnace tap-holes is illustrated and listed below.

1. Lance Holder

It holds and seals the oxygen pipes. Holding is done by means of a chuck enabling usage of a larger range of tolerances on the pipe. Unthreaded pipe to be used thus eliminating cumbersome threading operation.

2. Flashback Arrestor or Backfire Safety Device

It is used to shut off the flow of oxygen, in case of backfire, slag return, or overheating. This does not allow for the flow of gas in either direction unless the lance is fully inserted and clamped. Flashback arrestors are ideal flashback safety devices for hot flames.

3. Quick Shut off Valve

The valve allows the flow of oxygen only when continuously engaged. Excellent valve giving full control to operator to open fully, close fully, or pass only required amount of oxygen.

4. Oxygen Hose

The hose used for oxygen is a special high-pressure hose, with a distinctive yellow colour, and conveys oxygen from the main supply valve to the lance.

5. Hose Drum

The hose drum ensures that the hoses are automatically wound on the drum by means of a coil spring and that hoses are not lying on the tapping floor. The Hose Drum is made from robust steel construction, complete with Rotary Coupling for the oxygen supply, and guides, which ensures reeling the hose smoothly in and out of the drum. This is useful equipment to avoid accidents on the tapping floor and also to keep the plant neat and tidy.

6. Pressure reducer for oxygen supply which is used to regulate oxygen pressure.
7. Main oxygen supply valve, which is used to open/close the oxygen supply to the oxygen lance.

Employee Skills and Training

Good tap-hole design, launder design, tapping equipment, and excellent maintenance practices and procedures are not enough to maximise the tap-hole life. Employee skills are crucial in the successful taping process. Assmang Cato Ridge is an inclusive employer where skilled tapping employees are predominantly females. The total number of tappers tapping all Assmang Cato Ridge Submerged Arc Furnaces (SAF)

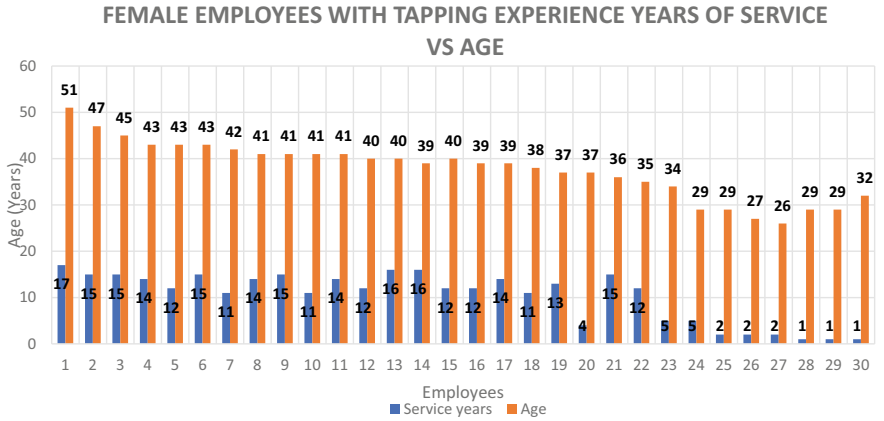

Fig. 14 Female employees with tapping skills and experience

is 24 (out of 24 tappers, 14 are female). As indicated in Fig. 14, more than 50% of tapping employees are female. The age ranges from 26 years to over 50 years and the most experienced employee has served the company for more than 17 years as an experience tapping crew member. In addition, all tapping employees are enrolling for the Metals Production Learnership program which is accredited by the Manufacturing, Engineering, and Related Service Sector Education and Training Authority (merSETA). The accredited qualification does not only enhance their competencies, but also opens more opportunities to market themselves in other industries and organisations.

Local youth, including females, enrol for a two-year Metals Production Learnership Program which when successfully completed can get opportunities in the organisation or can be absorbed by other industries. The qualification they achieve is called the Certificate in National Qualification Framework (NQF) Level 2. The above strategy ensures that Assmang has a succession plan to retain skilled employees.

Conclusion

The performance of tap-hole blocks life, which is equivalent to the life of the furnace lining campaigns, indicates that the current tap-hole design, launder design, operating conditions, and procedures are suitable for Assmang furnaces. All recent furnace lining campaigns were between 10 and 15 years and the reline decisions were mainly driven by hearth conditions rather than tap-hole condition. It also indicates that the slag chemistry was suitable as no tap-hole erosion or dissolution were observed and metal and slag separation were adequate with MnO of less than 25 wt% on average.

Table 1 Typical slag and metal analysis with basicity defined in Eq. 1

wt%												
	Mn	Fe	C	Si	P	Al_2O_3	Cao	MgO	SiO_2	MnO	Basicity	FeO
Average (wt%)	77.49	14.88	6.96	0.24	0.05	2.98	33.94	8.49	28.94	24.43	1.33	0.22
Std. dev. (+/)	1.22	0.29	0.07	0.12	0.01	0.20	0.69	0.48	0.82	1.67	0.03	0.16

Acknowledgements This paper is published with the permission of Assmang. The contributions of our colleagues are gratefully acknowledged.

References

1. Broekman BR, Ford KJR (2004) The development and application of a HCFeMn furnace simulation model for Assmang Ltd. Proceedings: Tenth International Ferroalloys Congress 1:4
2. Coetzee C, Taylor Q, Brisley A, Botha P, Cele M, Moodley S (2021) New insights Into refractory lining wear mechanisms on a 22MVA FeMn furnace. In: Paper presented at INFACON XVI, Norway, 27–29 September
3. Pal S, G Ciezki (2018) Temco F1 Operation on freeze lining 2001–2017. In: International Ferro-Alloys Congress, Cape Town, Infacon XV, pp 233–248.
4. Tomala J, Basista S (2007) Micropore carbon furnace lining. In: Innovation in Ferroalloy Industry, New Delhi, India, Infacon XI, pp 722–727

Aluminium Tapping and Molten Metal Handling in Primary Smelters

J. F. Grandfield, R. B. Wagstaff, and S. R. Wagstaff

Abstract This paper presents a review of tapping and melt handling technology of aluminium for those more familiar with steel and iron. The practice for light metals is substantially different to that used for iron and steel. For primary production using the Hall-Heroult technology, a variety of methods are used at the various stages of cell tapping, crucible transfer to the cast house, ladle treatment, liquid transfer to furnaces, furnace tapping and flow control during casting. Level sensor technology is examined including mechanical systems, lasers and capacitors. Refractory types and melt interactions are also covered. Trough design is covered. Future developments such as automated furnace skimming are mentioned.

Keywords Aluminium tapping · Tapping melt handling · Melt handling technology

Introduction

This paper presents a review of tapping and melt handling technology for aluminium in primary smelters. Aluminum melt handling practice is substantially different to that used for iron and steel. For primary aluminium production using the Hall-Heroult technology, a variety of metal handling methods are used at the various stages from tapping the electrolysis cell to the casting units. The general flowsheet for a primary aluminium smelter including alumina refining and bauxite mining is shown in Fig. 1. Most smelters do not include bauxite and alumina activities on site as they buy

J. F. Grandfield (✉)
Grandfield Technology, Melbourne, Australia
e-mail: JohnGrandfield@bigpond.com

R. B. Wagstaff
Oculatus Consulting, Spokane, WA, USA
e-mail: bob.wagstaff@oculatusconsulting.com

S. R. Wagstaff
Oculatus Consulting, Marietta, GA, USA
e-mail: sam.wagstaff@oculatusconsulting.com

J. D. Steenkamp et al. (eds.), *Furnace Tapping 2022*, The Minerals, Metals & Materials Series, https://doi.org/10.1007/978-3-030-92544-4_6

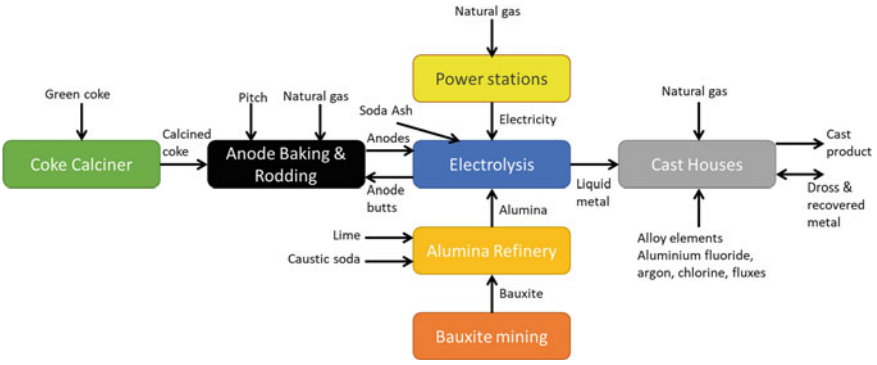

Fig. 1 Generalised flow of materials and processes in primary aluminium smelters

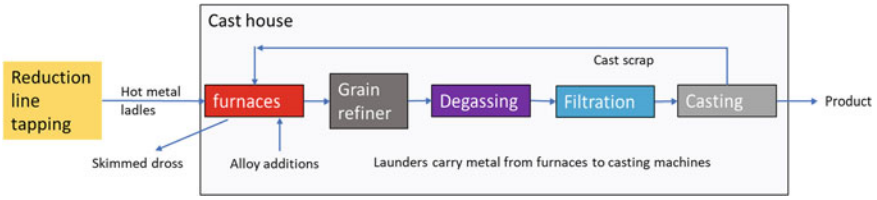

Fig. 2 Generalised cast house metal flow and unit operations

alumina or bauxite off site. There is no universal cast house layout as different smelters make different products (extrusion billets, rolling slabs, remelt ingots in the form of sows, T-bar and 23 kg ingots) which may require melt refining or not (Fig. 2).

Important fundamental differences between aluminium and steel are:

- Density-liquid aluminium 2,300 kg/m^3 is one third liquid steel ~ 6,900 kg/m^3[1]
- Operating temperatures are lower for aluminium (600 °C–900 °C) versus ~1,450 °C for steel
- Refractories need to be resistant to reaction with aluminium
- Total global tonnage handled per year is about ten times greater for steel than aluminium

Chapter 2 of "Direct-chill casting of light alloys" by J. F. Grandfield, D. G. Eskin and I. F. Bainbridge [1], has a review of aluminium and magnesium melt handling. Another review of melt handling operations was also given in 2021 [2]. A typical primary aluminium smelter produces around 500 ktpa and 1 million tpa smelters are not uncommon. Anywhere from 200 to 700 cells are used and the potlines are over a kilometer long. A note on terminology: within the aluminium industry, the ladles are often called crucibles and troughs are also called launders.

[1] Depending on temperature and composition.

Tapping Electrolysis Cells

Aluminium is produced by the Hall-Heroult process. Alumina is added to an electrolyte of molten cryolite at 950 °C and reduced to aluminium. The aluminium accumulates on the carbon cathode underneath the cryolite and the oxygen reacts with the carbon anode above the cryolite, to produce carbon dioxide. Aluminium accumulating in the cells is periodically tapped into ladles. Evacuated cast iron tubes transfer metal to the ladles. Ladles are typically 10–12 tonnes in capacity which are transported, when full, to the cast shop using dedicated vehicles.

In the cells, the liquid aluminium accumulates on the cathode on the bottom of the cell while the lighter cryolite electrolyte floats on top of the metal (Fig. 3). The depth of aluminium can be 10 to 25 mm depending on the cell technology. It is therefore difficult to position the tip of the spout exactly in the aluminium. It is not desirable to put the spout on the bottom of the cell as sludge can build up there which is pulled into the metal causing problems downstream. If the spout tip is too high vortexing occurs pulling electrolyte into the spout and ladle. Inevitably, some bath is tapped. Depending on operator skill, and the mass flow rate up to 40 kg per tonne is tapped but usual practice is more like 5–10 kg per tonne [3].

Initially, the bath is visible as a liquid floating on the aluminium liquid but as the crucible cools the bath solidifies and the density increases and then the bath sinks and accumulates in the crucible requiring periodic cleaning in order to maintain crucible capacity.

There has been some work on methods to sense and control bath carryover [4] however a reliable method remains elusive. Modelling of cell tapping both mathematical and physical has been carried out giving insight to the behaviour [5, 6]. The tapping flow rate is found to have a significant effect on the amount of bath tapped into the metal [7, 8].

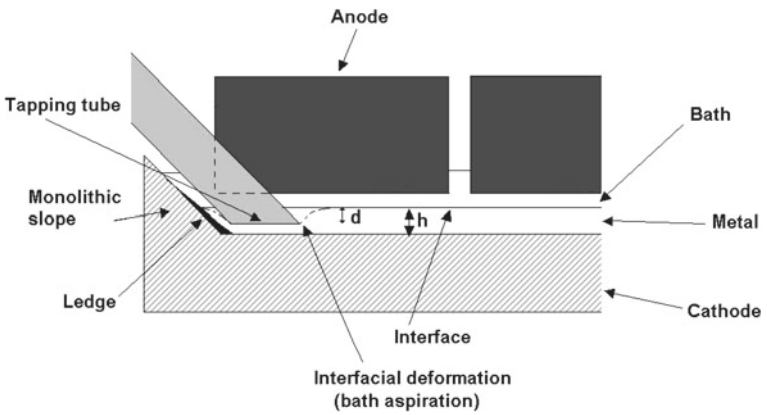

Fig. 3 General arrangement during cell tapping. After Walker 1997

Fig. 4 AGV Hot Metal Carrier in the process of picking up a small crucible. Source CSIRO

Ladle transport is by dedicated vehicles. Attempts (Fig. 4) have been made to convert these to AGV (automatically guided vehicles) [9] but has not yet been implemented.

Ladle Treatment

Some limited melt refining is carried out in the ladles in the case where low sodium alloys are produced and must be removed. Certain magnesium alloys suffer edge cracking during rolling if the sodium concentration is over 1 ppm and aluminium from the cells can have up to 150 ppm. One technology [10] uses aluminium fluoride additions to react with the sodium in the ladle with the reaction product skimmed off with an automated skimmer. Another version injects argon into the melt in the ladle. Bath carryover causes problems with the AlF_3 additions due to reaction with the AlF_3 which means less is available to react with sodium. The compound formed is chiolite which is hard and makes it more difficult to clean the crucibles. When preparing magnesium alloys, if any residual bath is transferred to the furnace will react with the magnesium putting sodium back into solution.

In general, alloying operations are made in the holding furnaces. The idea of alloying in the ladle has been around for a long time [11] but has not been adopted. Part of the problem is the possibility of the alloying elements finding their way back to the reduction cells via crucible cleanings, reducing performance along with the crucible cleaning product (oxides and cryolite). Contamination could also occur in the holding furnace where traces of elemental additions from one alloy product flow into another. As part of the ladle treatment, the crucibles are skimmed automatically to remove bath and oxides.

Ladle to Furnace Transfer

Holding furnaces buffer the metal flow from the reduction cells and the casting of alloy batches. Holding furnaces can be up to 100t capacity. Options for emptying the ladles into the holding furnaces include ladle tilt stations, pouring by using cranes, dedicated tilting apparatus on the transfer vehicles, pressurised crucibles and siphoning. The simple option is to tilt the ladles suspended from a crane to fill furnaces (Fig. 5). Dedicated ladle tilting vehicles are also used (Figs. 6 and 7). One of the main issues in transfer from ladle to furnace is the amount of dross generated causing melt loss. If the flow is turbulent and the metal flows from high up, in the order of 10-12 kg per tonne of dross is generated. This material is removed/skimmed from

Fig. 5 Crucible emptying into a furnace using a crane and a feeding trough

Fig. 6 Combined crucible tilter and transport vehicle

the furnace and cooled and sent to metal recovery. Dross is a mixture of aluminium oxide and entrapped unoxidised metal.

Siphon transfer (Fig. 8) significantly reduces the amount of dross generated by underpouring below the melt surface and only 3–5 kg of dross per tonne is generated [12]. Other trials reported 7.3 kg/t before siphoning and 2.2 kg/t when using siphoning [13]. Similar performance is obtained using a "huff and puff" crucible system where after tapping into the ladle it is pressurised to push the liquid back out into the furnace through the same spout (Fig. 8). Siphoning from ladle to furnace while casting from the furnace has also been developed [14].

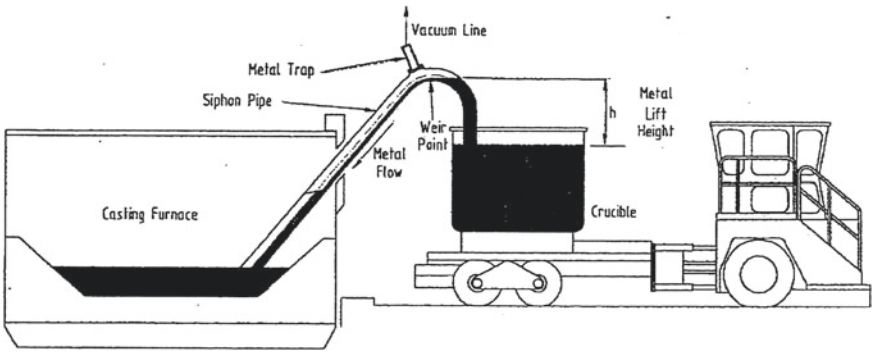

Fig. 7 Siphon arrangement for filling furnaces

Fig. 8 Pressurised crucible transport system

Ladle to Caster

Guthrie and Grandfield suggested in 1991 [15] that casting from a ladle as practiced in the steel industry, should be entirely possible for aluminium. It is only in recent years that this possibility has been realised. Fully automated melt transfer from ladles to sow casting conveyors without a furnace is fully automatic [16] and the need for a holding furnace is removed. This approach is only used for unalloyed melt.

Ladle Transport by Road

In some cases, liquid metal is sold to external operations and transported on public roads. The external customer may be situated literally over the fence or even 100 km away. The ladles obviously need a secure lid sealing system. In the case of a vehicle accident the crucible must withstand being knocked on its side without spilling.

Level Sensors

Trough Sensors

At the heart of the multi-level, metal level automation system, are the sensors, pin positioners and the control loops, which provide uniform metal delivery to each mould.

Contact flotation devices use a refractory float and control pin balanced over a fulcrum. The control pin remains full open during the fill until the float displaces enough molten metal to float. Eventually, as the metal level in the mould raises, the pin closes and then opens once again when the cast commences. Multi-strand casting systems require a fair level of operator control or intervention, so with the drive to remove humans from the dangerous start, these mechanisms have been replaced with more sophisticated sensors. Oxides can form around the float, and then release. These crude float systems are rarely used now.

Non-contact sensors combined with spout control-pin positioners allow simultaneous control of mould metal to prescribed level(s) in multiple ingot moulds throughout the cast, including the initial metal rush from the furnace, the start of cast, and during cast continuation. Metal level control in direct chill (DC) casting involves:

- The fill rate and level over time.
- Brings the metal level of all ingot positions to the start down metal levels at the same time.
- Automatically starts the cast when the metal reaches a practice-specified level. Controls the metal levels precisely and allows level adjustment during the cast.
- Can determine starting head position at the start of a cast.

The controlled fill sequence provides for a very consistent start, minimizes cracking, hang ups, bleed outs etc.

Capacitance metal level sensors typically have a wide range over which the sensor can detect metal. This technology is over 30 years old and has generally been replaced by inductive or laser sensors.

Inductive metal level sensors typically have a measuring range of about 50 mm. To increase the effective measuring range, the inductive sensor is attached to the end of a linear actuator and the elevation of the inductive coil above the molten metal surface is continuously controlled to about mid-range of the sensing range. The sensor and actuator position signals are summed, resulting in a measuring range equivalent to the actuator stroke (200 mm or more). With this newfound measuring range, metal level can be precisely controlled from early in the fill stage and throughout the cast, following complex recipe ramps, on large 5–7 strand ingot centers in the slab market, at the large rolling mills, and at a handful of smelters.

Laser metal level sensors fit well in confined spaces where a stable oxide is present and where steam and smoke are minimized. This technology is used commonly in molten metal level control in the trough. Lasers used in mould metal level control are also growing in use.

Radar based systems offer the potential to measure the level in the furnace and get a better estimate of the batch weight and are currently used in some plants.

Tilting and Stationary Holding Furnaces

Tap-holes are used on stationary holding furnaces. These tap-holes are opened manually using a cone and a tapping block located below the molten metal level. Some automated systems are used to remotely commence and terminate casting with minor operator intervention to fine tune control during steady state processes.

Tilting holding furnaces have steadily replaced stationary holders, currently seen only in older plants. When encountering an upset condition, during start or steady state conditions, the level pour design is the preferred choice as the casting trough can reverse molten metal back to the holder; whereas furnaces without the level pour feature can only vacate the molten metal via a series of strategically placed dump bins, which are always difficult to keep clean and preheated when not in continual use.

Tilting furnaces deliver metal to the launder via a flexible spout/joint. These were predominantly metal-to-metal joints, and sometimes these failed. The usual configuration these days is a flexible fiberglass joint. The molten metal-to-joint interface is or should be preheated and cleaned on a regular basis. Preheating the joint is best done by controlling the furnace pressure, so the molten metal does not collect or agglomerate at the joint, which complicates melt flow at the start of the cast. The furnace refractory on the inside of the furnace adjacent the pouring spout/joint must be cleaned on a regular basis. During casting, as the molten metal flows to the trough, any oxide is carried to the spout and collects against the refractory adjacent the spout, as the bulk of the oxide migrates to the spout during casting. This systematic agglomeration of oxides, cast after cast, eventually builds up and reduces the spout discharge area. This buildup transitions the molten stream from the designed laminar to transitional or even turbulent flow conditions, which naturally re-entrains oxides into the melt.

Trough/Launder Design

A general layout from the furnace to the casting machine showing the trough connections is shown in Fig. 9.

Launders need to be designed for Laminar flow so as not to generate oxides in the product. They are also crucial to temperature control -sometimes heating and sometimes cooling. The trough can be fitted with lids and these may contain heaters if the launder is long. Launder coating such as bone ash, and boron nitride are important for protecting the trough lining materials. Bone ash has been identified as a potential health hazard due to the formation of phosphides which react with water emitting toxic phosphine. The launder needs to be deskulled and recoated after each cast. A head is needed to get the metal to flow in the trough to the casting machine. Usually, the launder has a high point near the molten metal filter so at the end of the cast metal flows back to the furnace and to the casting unit i.e., is fully drained.

Fig. 9 General cast house layout. Ladle treatment at 1. Furnaces at 2 receive metal from the cells. At 3 is the rotary flux injector. The launders (4) transport metal from the furnaces. Metal flows to the inline degasser (5) and then the filter (6) along the trough and finally to the casting machine (not shown on left). Skimmed dross goes to the dross coolers (7). Source STAS

The filter removes non-metallic inclusions such as oxides which would cause various defects like pinholes in can body and foil. Filtration technology used depends on the final product and various types of filter are used; ceramic foam filters, rigid media filters and ball bed filters. Silicon carbide ceramic foam filters have been used for steel filtration. A slope of 1.5-2 mm/meter is normally used to help the liquid drain back to the holder from the filter at the end of the cast. Downstream of the filter the launder slopes down to the casting unit. Inclusion concentration measurements are also made at this point.

A recent innovation in trough design [17] is compression of the refractories to prevent aluminium ingress between joins and when cracks appear (Figs. 10 and 11).

Trough to Casting Machine

The connection from the trough to the casting machine depends on the type of machine and product being cast.

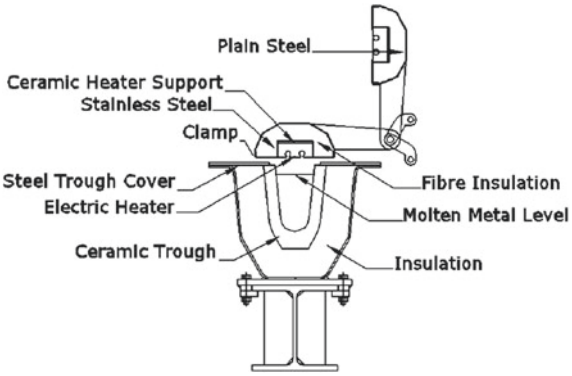

Fig. 10 Section through typical launder [18]

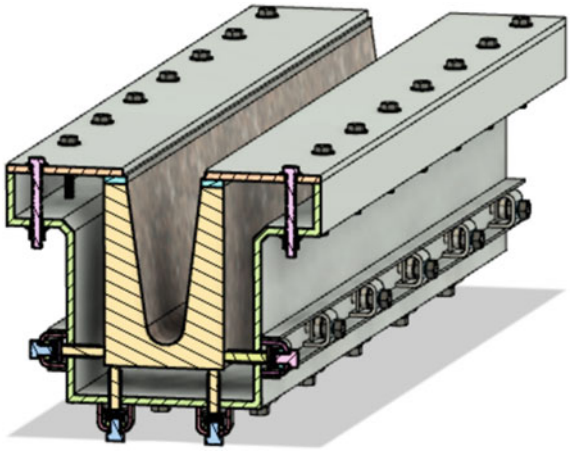

Fig. 11 Compressed trough section

Direct Chill (DC) Billet Casting

In direct chill casting, the mould can be open top or flooded table. The mould contains the molten metal and directs the water spray onto the emerging billet. Open top moulds in the past were used for both rolling slab casting or extrusion billet casting but these days flooded tables are the norm for billet casting. They offer productivity benefits by casting large numbers of strands at once. There are also fewer oxides generated during flow into the mould. For extrusion billet casting, a flooded table is connected to the trough and the same level runs through to the tilting furnace. This level is controlled by the furnace tilt and measured by a laser over the trough. Each strand of extrusion billet is a hot top mould usually gas pressurised moulds to achieve a good cast surface (Figs. 12, 13, 14, 15, 16, 17).

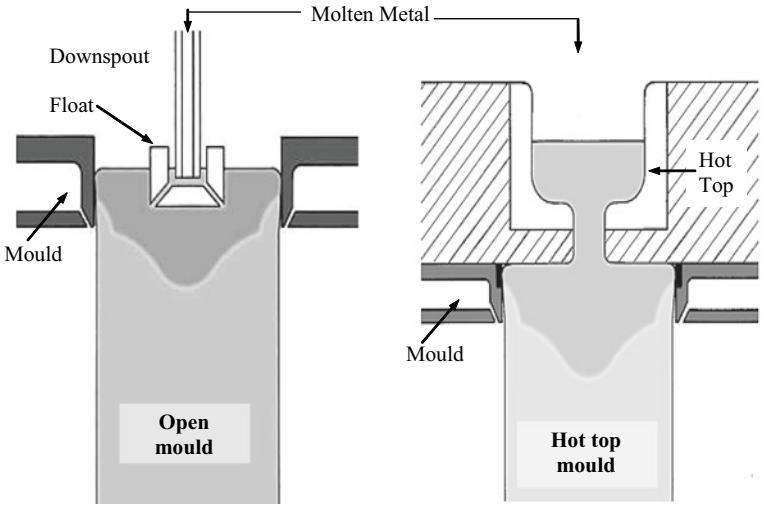

Fig. 12 DC casting with open top mould controlled by a float (left) and hot top casting (right)

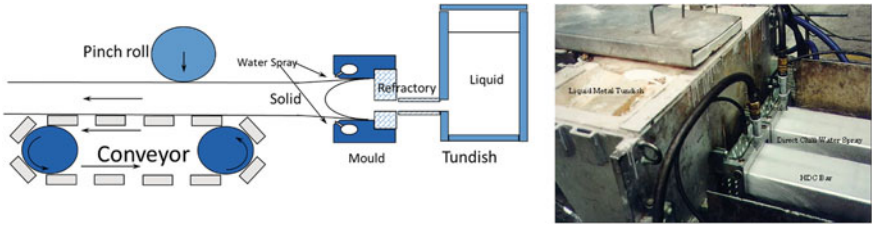

Fig. 13 Overall schematic (left) and small horizontal DC casting machine (right)

Rolling Slab Casting

Individual automatic metal level control is applied to rolling slab casting. A pin inside a spout opens and closes to control the metal level (better than ± 1 mm) usually with a laser level sensor.

Horizontal DC Casting

Horizontal DC casting is fully continuous whereby metal flows into a tundish and then into the mould. These machines are useful if only a small capacity is required e.g., in extrusion plants that recycle their scrap. They are also used for casting of T-Bar section aluminium silicon alloys.

Fig. 14 Flooded table direct chill extrusion billet casting

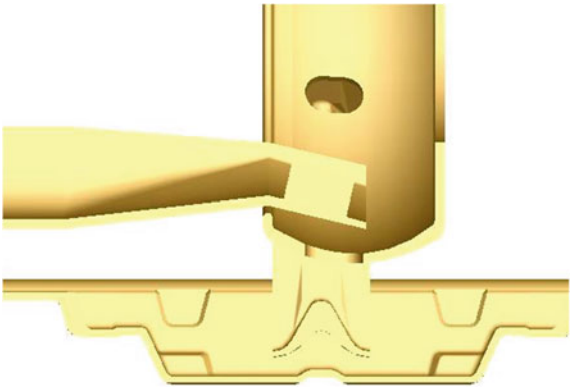

Fig. 15 Section through a typical wheel filling system. *Source* CASTcrc

Ingot Conveyor

23 kg remelt ingot casters consist of a long conveyor up to 40 m with the moulds moving along through a water bath to solidify the ingots for demoulding at the knockout end. The filling system consists of a wheel which distributes the liquid to the moulds and turns in synchronisation with the conveyor. Casting rates can be up to 40 t/hr.

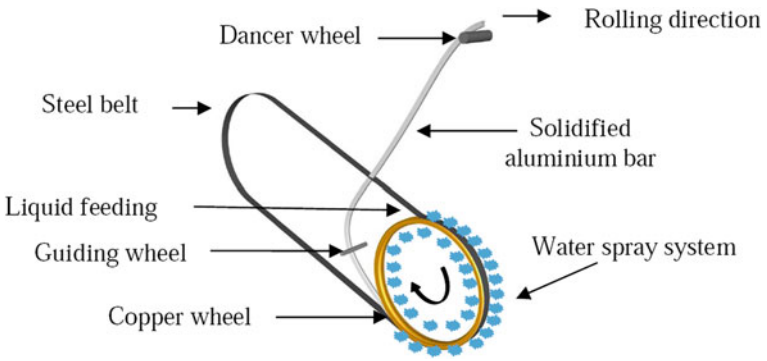

Fig. 16 Typical old style wheel and belt caster whereby the bar is pushed sideways to avoid hitting the belt

Fig. 17 Large wheel and belt caster for casting of 10 kg remelt ingots. Source Aluminium Bahrain

Fully Automated Sow Casting

In the last few years sow casting lines have become highly automated to the extent that a furnace is not needed. Mould filling and skimming are fully automated (zero manning).

Wheel and Belt Casting

Wheel and belt casters are generally used to produce a rod and wire but can also be used to make remelt foundry alloy bar.

Furnace to Furnace Transfer

In secondary operations a melting furnace feeds the liquid to a holding furnace. This is usually done by gravity feed in a connecting trough but siphoning from furnace to furnace with a fully automated system is possible [19].

Refractories

Refractories play a very important role in keeping the melt hot at different stages.

High purity fused silica components out-perform their peers in applications where electrical insulation is needed with a low dielectric value. Low coefficient of thermal expansion and excellent thermal shock resistance along with dimensional stability are hallmarks of these materials and perform well when low thermal conductivity is needed with thermal and chemical insulation.

Dense high purity silicon carbide components see use with high precision components requiring extremely high thermal shock resistance, high levels of corrosion resistance commonly used with indirect radiant heating systems which can elevate the component pre-molten contact temperature to mitigate the normally low shock resistance of this material.

Low density alumina components are commonly used in metal distribution systems where superior insulating values are needed without any crystalline silica. Components commonly constructed by these materials have very low shrinkage over time and little to no water absorption and the off gassing which follows water absorption. While components have moderate cost, they are easy to maintain, they have low thermal conductivity, low heat capacity and very low thermal expansion. The absence of crystalline silica corresponds to very low reactivity with the molten aluminium over time, generating the lowest possible inclusion profile over time.

Dense high purity alumina components are generally high precision with very high shock and thermal resistance. The density of these materials being somewhat higher than the high density silicon carbide restricts this family of refractories to applications demanding high thermal conductivity and thermal-chemical stability.

Hardened refractory fiber components are commonly in use where large and complicated shapes are needed at varying density.

Low strength-low density vacuum formed materials (traditional silica-starch compositions) are used without rigidizer treatments as refractory backer boards

against the steel in furnace or trough lining assemblies. After rigidizing treatments, these materials are used in molten contact situations distributing molten aluminium and in furnace design or operating situations requiring a disposable molten aluminium contact shell. Most of these materials are produced from totally inorganic compounds with high alumina in the range of 97% Alumina. It is quite common to pre-shrink and sinter these compositions, sometimes with blanket cast in as part of the component structure.

High strength reinforced silica matrix composite materials are used where high strength is needed and very abrasive situations.

Molten Metal Safety

Over-filling furnaces can occur. Furnace tap outs-generally occur as a result of overextending the furnace lining beyond the threshold common to the lining type. Overexuberant furnace operators, intending to do a thorough job cleaning the hearth, pops a brick with the cleaning tool or abrades the monolithic hearth past the hard-wear layer into the soft under-layer which normally acts as the molten freeze plane.

Molten metal water explosions can occur if water comes in contact with the liquid aluminium e.g., due to a furnace fill. This can be in the form of a steam generation event caused by the aluminium heating the water rapidly resulting in metal ejecting into the air. More serious explosions occur when the aluminium reduces the steam to hydrogen and then the hydrogen reacts with the oxygen in the air.

Tilting furnaces are far safer in terms of the ability to control the metal flow.

Future Developments

Melt handling systems are continuously improving as sensors get cheaper and automation increases.

The conduct of a cast can be entirely in handsfree automatic mode. Before the cast, the operator prepares the molten metal filter, cleans the trough, positions the mould and starting head, but once the cast start button is pushed, the cast process can be fully automated including the furnace tilt, the trough level, the casting speed etc. Sadly some operations still expose their personnel unnecessarily.

Automated furnace skimming is an emerging technology and announcements are to be made at the TMS Annual Meeting. AGV transfer of tapping crucibles will surely become standard.

References

1. Grandfield JF, Eskin DG, Bainbridge IF (2013) Direct-chill casting of light alloys. Wiley, Hoboken
2. Dion-Martin O et al (2021) Light metals 2021, TMS, p 769
3. Goutiere V et al (2007) Mapping bath carryover from cell tapping to casting in smelter operations. In: Grandfield & Taylor (eds) Aluminium cast house technology 2007. CSIRO publishing, p 231
4. Death D et al (2007) Prototype video system to monitor metal tapping from an aluminium production cell. In: Grandfield J, Taylor J (eds) Aluminium cast house technology 2007. CSIRO publishing, p 239
5. Walker M (1997) Visualisation of tapping flows. In: Huglen R (ed) Light metals 1997, TMS, p 215
6. Chen JJJ, Xu YS, Chen XD (1999) Numerical simulation of aluminum metal tapping. In: Second international conference on CFD in the minerals and process industries. CSIRO, Melbourne, Australia
7. Goutiere V, Dupuis CI (2008) Understanding the mechanisms of bath carry-over with molten aluminum in smelters. In: Light metals 2008. The Minerals & Materials Society, pp 563–567
8. Kabezya K et al (2019) A review of primary aluminium tapping models. SN Appl Sci 1:850
9. Roberts J et al (2007) Autonomous hot metal carrier. In: Grandfield J, Taylor J (eds) Aluminium cast house technology 2007, CSIRO Publishing, p 247
10. Maltais B et al (2009) Operational experience with a large capacity integrated tac (treatment of aluminium in a crucible) and a skimmer, Light metals 2009, TMS, pp 755–760
11. Gariepy B, Dube G (1989) Aluminium ladle metallurgy (ALM): A new process for efficient alloy preparation. In: Nilmani M (ed) Aluminium melt refining and alloying, University of Melbourne
12. Locatelli J (1996) Dross reduction through improved metal transfer from crucible to furnace, Fifth Australasian cast house technology conference, TMS, p 205
13. Locatelli J, Liu G (2010) Light metals 2010. In: Johnson J (ed) TMS, p 639
14. Locatelli J, Liu G (2010) Automated metal siphoning and cast house energy consumption. Mater Sci Forum 630:61–69
15. Guthrie RIL, Grandfield JF (1991) Aluminium cast house technology. University of Melbourne
16. Tremblay A et al (2020) Light metals 2020. In Tomsett A (ed) TMS, p 868
17. US10012443B2
18. Canullo V et al (2010) Mater Sci Forum V630:119–125
19. Dion-Martin O et al (2020) Light metals 2020, TMS, p 873

Part II
Session II

Furnace Tapping 101

Joalet Dalene Steenkamp, Jan Erik Olsen, and Quinn Gareth Reynolds

Abstract The Furnace Tapping Conference series is an example of problem-based conferencing. It focusses on tasks all smelters have in common, namely the tapping of liquid slag and alloy or matte from the reactor. The series draws on perspectives from across commodities and across disciplines in Science, Engineering, and Technology. It is a platform where ideas are exchanged between operators, engineering and support, and researchers on how to optimally manage the processes involved. The paper presented here is aimed at new-comers to the field, hence the title Furnace Tapping 101, and is written in two parts. In Part 1, Natural Language Processing (NLP), a branch of Artificial Intelligence (AI), is applied in the review of papers included in the Proceedings of Furnace Tapping 2014 and Furnace Tapping 2018 which took place in South Africa. In Part 2, terminology which newcomers to the field might be unfamiliar with, is explained in the form of a dialogue between a Mathematician and a Pyrometallurgist.

Keywords Extraction and processing · Pyrometallurgy · Modelling and simulation

J. D. Steenkamp (✉) · Q. G. Reynolds
200 Malibongwe Road, Randburg 2125, South Africa
e-mail: joalets@mintek.co.za

Q. G. Reynolds
e-mail: quinnr@mintek.co.za

J. D. Steenkamp
University of the Witwatersrand, 1 Jan Smuts Ave, Johannesburg 2000, South Africa

J. E. Olsen
SINTEF, SP Andersen vei 15B, 7031 Trondheim, Norway
e-mail: jan.e.olsen@sintef.no

Q. G. Reynolds
University of Stellenbosch, Private Bag X1, Matieland, Stellenbosch 7602, South Africa

J. D. Steenkamp et al. (eds.), *Furnace Tapping 2022*, The Minerals,
Metals & Materials Series, https://doi.org/10.1007/978-3-030-92544-4_8

Introduction

An example of problem-based conferencing, the Furnace Tapping Conference series was established to serve the pyrometallurgical industry at large, focusing on a very specific challenge namely the tapping of furnaces. In 2014 and 2018 respectively, the Southern African Institute of Mining and Metallurgy (SAIMM) hosted the First and Second Furnace Tapping Conferences. Both events were well attended with Tapping 2014 hosting 203 delegates and Furnace Tapping 2018, 144. Delegates came from five continents, representing 12 and 17 countries respectively [1, 2]. For both events, peer-reviewed Proceedings were published, containing nineteen papers each. The SAIMM made these papers available on-line as free, Open Access [3, 4]. Both conferences drew from various perspectives on the topic with authors and presenters representing industry, consultants, service providers, and especially for Furnace Tapping 2018, research institutions.

Part 1: Natural Language Processing

For the purpose of this paper, Natural Language Processing (NLP), a branch of Artificial Intelligence (AI), was applied in the review of papers included in the Proceedings of Furnace Tapping 2014 and Furnace Tapping 2018. The NLTK package (https://www.nltk.org/) written in the Python programming language was used for all NLP processing tasks unless otherwise indicated. Basic processing of the PDF documents was initially performed to extract sets of raw text, which were then processed to remove punctuation and tagged with part-of-speech identifiers. This information was used to filter the set by removing non-technical content such as prepositions and common English-language words. The filtered sets of text were condensed using lemmatisation and a manual list of synonyms for technical terms, and finally a word frequency chart was generated for each paper. Those were added up and visualises as bar charts: the totals over all events (Fig. 1) and per conference (Fig. 2) for the top 50 keywords. The frequency counts (Y-axis) are in *occurrences per total word count*, e.g. 0.01 means that word occurs on average once every hundred words in the original (non-filtered) text.

Not surprisingly the word *tap-hole* [5–7] was used most frequently followed by *furnace* and *tap* (Fig. 1). As an anecdote, the spelling of the word *tap-hole* was heavily debated during the editing of the Proceedings for Furnace Tapping 2014. The industry standard was considered to be *taphole*, but the hyphenated version was selected on the grounds of removing ambiguity and improving readability, as *taphole* requires a brief moment to decipher whether the 'ph' should be read as 'f'.

Next in line was *slag* [8–10] as many tapping problems during the *production process* are related to the *temperature* dependent properties and *phase* composition thereof, as well as those of *metal* and *matte* [11–13] but to a lesser extent, and the effects of these properties on *flow* during *tapping*.

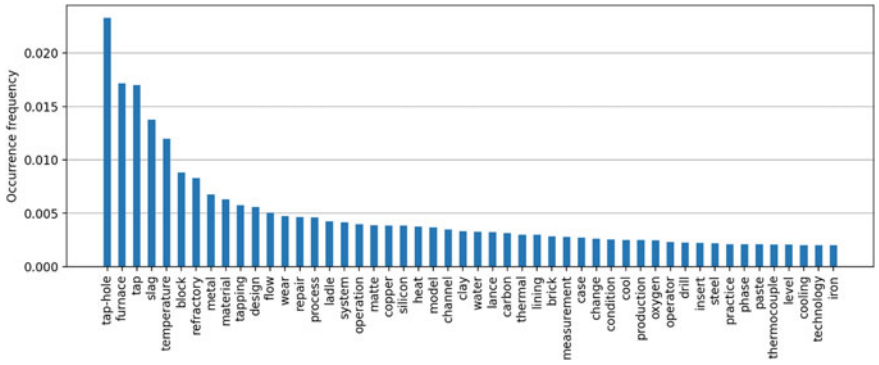

Fig. 1 Frequency chart indicating the occurrences per total word count for the top 50 keywords for Furnace Tapping 2014 and Furnace Tapping 2018 combined

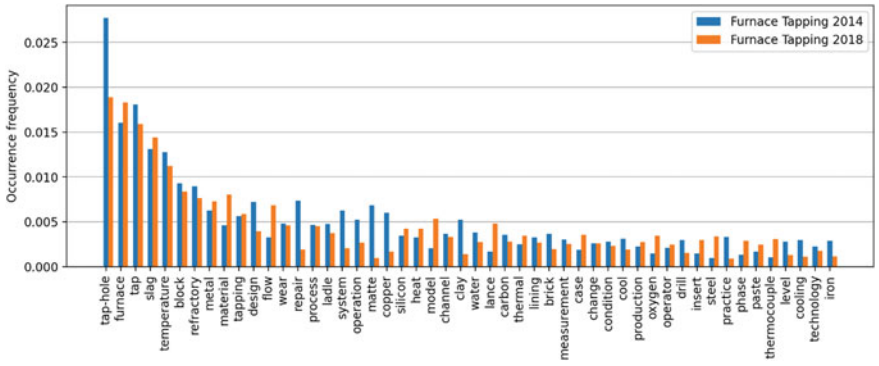

Fig. 2 Frequency chart indicating the occurrences per total word count for the top 50 keywords for Furnace Tapping 2014 versus Furnace Tapping 2018

Parts of the furnace containment system, the tap *block*, *refractory*/*carbon* [14, 15], *material*/*bricks*/*inserts* [16], and *steel* shell as well as the *design*, *wear*/*condition*, and *repair* [17–19] of the *lining*, were discussed. Included in the conversation around furnace containment was *cooling* by *water* or other fluids [20, 21] as provided by *copper* [22–24] components. The *channel* (launder) and *ladle* were also considered as part of the *system*. Specialised *measurement technology* applied included those related to *heat* transfer or *thermal* monitoring [25, 26] i.e. *thermocouples* [27, 28] and *level* sensors [29].

An important part of the tapping *practice* is the opening and closing of the tap-hole using a *drill* or *oxygen lance* [30] and *clay* gun [31] to inject tap-hole clay or *paste* [32, 33]. This is also where the *operator* plays an important role. *Models* [34–39] play an equally important part in studying and understanding the *changes* involved.

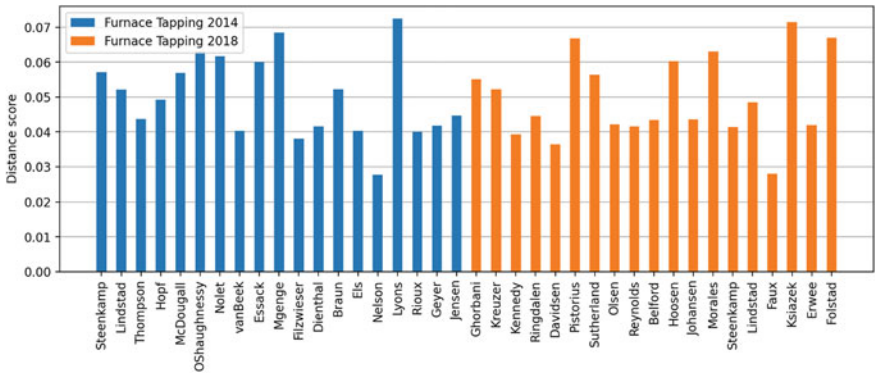

Fig. 3 Results from the distance score for each manuscript relative to the overall average

The main commodities which featured were *iron* making [40] and *silicon* smelting [41, 42] which could be an indication that these are the commodities that could potentially experience the most tapping problems during *operation.*

When comparing the frequency charts for Furnace Tapping 2014 against Furnace Tapping 2018 (Fig. 2) the influence of the increase in research papers can be seen in the reduction in the frequency of occurrence for words such as *design*, *repair*, *operation*, *practice*, *copper*, and *cooling*.

Another way of presenting the NLP results is to generate a *distance* number for each manuscript, which measures how close (or not) it is to the overall average (Fig. 3). It was found that more specialised papers obtained a higher score and more general or review papers lower scores.

Part 2: Conversation Between a Mathematician and a Pyrometallurgist

In the Journal Comment on Furnace Tapping 2014 [1], a call was issued for '*strong contributions from research institutions (focusing on the application of CFD modelling with associated assumptions, including properties of materials and validation of these models; studies on tap-hole clay; and studies on refractory interaction with slag/metal/matte specifically under the tap-hole conditions)*'. The Controlled Tapping project, funded by the Norwegian Research Council and Industry Partners, included a significant amount of modelling conducted by mathematicians experienced in computational fluid dynamic (CFD) but new to furnace tapping. As a textbook on tapping do not exist yet and papers collated in the Proceedings of the two Furnace Tapping Conferences assumes a basic understanding of the concepts

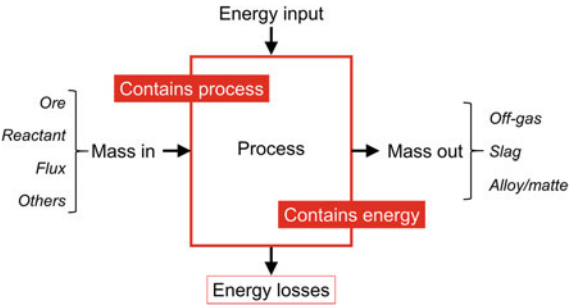

Fig. 4 Simplified schematic indicating the purpose of the furnace containment system in the context of a pyrometallurgical furnace

involved, an attempt is made here at addressing the short-coming in the form of a conversation between a Mathematician and a Pyrometallurgist.[1]

Furnace Containment System

Briefly describe the components of the furnace containment system (using an illustration)

Taking a step back, the purposes of the furnace containment system are to contain the process materials (solid, liquid, and gas), by receiving raw materials as inputs and releasing products as outputs in a controlled manner, and to minimize the losses of energy to atmosphere (Fig. 4). A detailed description of the different types of process inputs and outputs that apply to pyrometallurgical furnaces lies beyond the scope of this paper. For the context of furnace tapping it is necessary to focus on the liquid products tapped from the furnace. *Slag* typically consists of an ionic solution of oxides and can be a mixture of liquid with some solids. *Alloy* is a liquid solution of primarily metallic phases and *matte* a special type of alloy containing very high levels of sulphur.

For the purpose of the discussion, I am going to refer to the furnace containment system of a pilot-scale furnaces designed for the evaluation of the effect of pre-heating of manganese ores on the production of high carbon ferromanganese (HCFeMn) utilising a submerged arc furnace (SAF). The schematic drawing in Fig. 5 applies. In this example, the containment system consists of two types of materials: mild steel and refractory materials. The mild steel structure, often referred to as the *steel shell*, provides the furnace structure and interface with the surroundings. The refractory materials (high alumina castable, bubble alumina castable, carbon brick, and graphite tapblock) provides the insulation and protects the steel shell from the hot interior of the furnace (in this case temperatures of 1723–1823 K are typical).

What are refractory materials, bricks, and ramming materials?

Refractory materials are defined internationally as non-metallic ceramic materials with a certain refractoriness defined as a pyrometric cone equivalent (end point

[1] Keep in mind that a Wise Woman once said: "Three Metallurgists, four opinions…"

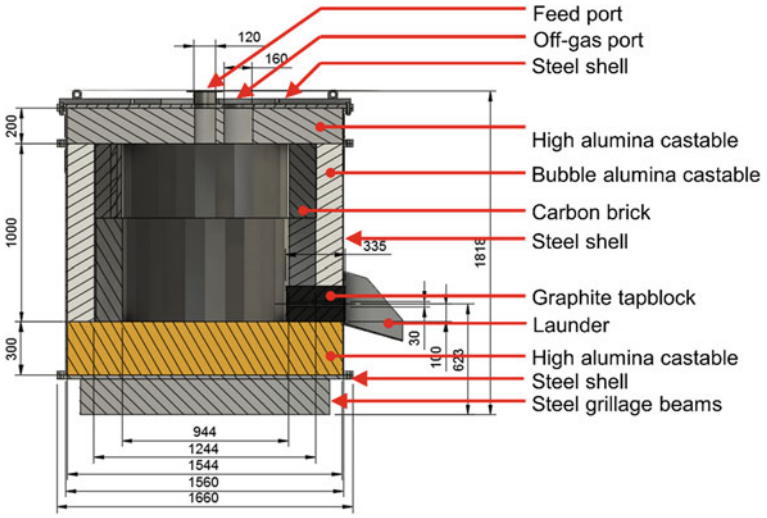

Fig. 5 Schematic drawing of a pilot-scale furnace indicating the components of the furnace containment system

temperature at which the tip of the pyrometric cone touches the supporting plaque) greater than 1773 K [43]. Examples of such materials in Fig. 5 are the high alumina castable and bubble alumina castable. Some materials are utilised in refractory applications but do not fulfil the definition based on the pyrometric cone equivalent i.e. the carbon brick and graphite tapblock in Fig. 5. These are considered *refractory products* [43]. For the remainder of the discussion, refractory materials and refractory products will be collectively referred to as *refractories.*

Refractories can be shaped as bricks or functional products i.e. the carbon bricks and graphite tapblock in Fig. 5 respectively. They can also be unshaped when purchased, i.e. high alumina castable and bubble alumina castable, and prepared and installed where applied on-site. Unshaped refractory materials and products are called *monolithics* [43]. Monolithics can be installed in the form of a powder which is referred to as a *rammable* or *ramming material*, or as a slurry which is referred to as a *castable* or *castable material*. The selection of shape depends on a number of factors including ease of installation, maintainability, durability, and cost.

How do refractory bricks, refractory ramming materials, steel and copper differ in properties and purpose (e.g. insulating or heat conductive)?

Two different types of philosophies can be applied in the design of a furnace containment system [22]. In an *insulating design* the refractories are typically in contact with liquid process materials i.e. slag, alloy, or matte. In a *conductive design* a layer of process materials is purposefully frozen onto the surface of the refractories. The latter is applied in cases where chemical compatibility between the process materials and refractories do not exist. Refractories have many properties to consider, but the main property in this instance is the thermal conductivity, k,

measured in $W \cdot m^{-1} \cdot K^{-1}$. For an insulating lining design, the chemical compatibility of the refractory with liquid alloy or slag is also important i.e. the refractory should neither dissolve in the liquid process material nor react with it to form an unwanted reaction product [14, 15, 19].

The example in Fig. 5 is an insulating lining design. The thermal conductivity of the bubble alumina is 0.5 $W \cdot m^{-1} \cdot K^{-1}$, of the carbon refractory 10 $W \cdot m^{-1} \cdot K^{-1}$, and of the high alumina castable 2.4 $W \cdot m^{-1} \cdot K^{-1}$. Although the chemical compositions of the bubble alumina and the high alumina castable are similar, the thermal conductivities differ significantly because of the air trapped in the bubbles (air is an excellent insulator). The carbon refractory has a relatively high thermal conductivity and was selected for its thermal compatibility with the liquid process materials, compared to the alumina-based refractories.

In conductive lining designs, refractories in combination with water-cooled elements manufactured from steel or copper, are designed in such a configuration that the layer of frozen process materials has the lowest thermal conductivity. The thermal conductivity for copper is high, in the order of 350 to 380 $W \cdot m^{-1} \cdot K^{-1}$ [23, 26], for steel approximately 45 $W \cdot m^{-1} \cdot K^{-1}$ (depending on the composition), for carbon-based refractory (including graphite) 5–85 $W \cdot m^{-1} \cdot K^{-1}$, magnesia-based refractory 6–11 $W \cdot m^{-1} \cdot K^{-1}$, alumina-based refractory 4–6 $W \cdot m^{-1} \cdot K^{-1}$ and insulating materials 0.1–1.5 $W \cdot m^{-1} \cdot K^{-1}$ [44]. All values quoted are for refractories at 473 K. It is important to note that the thermal conductivity of refractories are very much dependent on temperature. It is therefore important to take this temperature dependence into account and utilise reliable data sources.

Tapping Configuration

Why do some tap slag and metal through separate tap-holes and others not (dual-level vs single-level tapping)?

In furnace operations, it is important to separate the alloy or matte from the slag. Liquid slag typically has a much lower density than liquid alloy or matte [5]. One way to separate the two products is to tap them from tap-holes at different elevations, with the slag tap-hole above that of the metal or matte. Such a configuration is referred to as *dual-level tapping*. In other operations, separation of the liquid alloy from the slag occurs beyond the tap-hole and the two streams are tapped from the same tap-hole. Such a configuration is referred to as *single-level tapping* of which the design in Fig. 5 is an example. Single-level tapping is more common for processes with a slag-to-alloy ratio (ton/ton) of less than 1.5 [5].

How and why are there multiple tap-holes in some furnaces even if slag and metal are tapped through the same single-level tap-hole?

The tap-hole is typically one of the high wear areas in the furnace containment system and tap-hole wear is often the reason why the lining has to be repaired or rebuilt. A furnace rebuild is expensive, not only due to the cost of the materials of construction, but more so due to the loss in production associated with taking the

furnace out of operation, rebuilding the containment system, and getting the furnace back to full operation. By having more than on tap-hole, the wear can be spread between tap-holes resulting in extended lining lives.

What is continuous vs discontinuous tapping?

Continuous or near-continuous tapping typically occurs in furnace with a very high slag-to-alloy ratio, i.e. FeNi or PGM smelting, for which slag is tapped nearly continuously from the furnace or very low slag-to-alloy ratios, i.e. Si smelting, for which alloy is tapped nearly continuously. The tapblocks of the furnaces from which slag is tapped continuously are typically made of water-cooled copper blocks. *Discontinuous* tapping is when slag and/or alloy are tapped from the furnace in batches at discreet intervals.

Can we say something on which furnaces (commodities) use which of these configurations?

In their review papers, Nelson and Hundermark [5] and Nolet [11], provide excellent summaries of the type of configurations applied in the production of various commodities.

How long is the tap-hole open in discontinuous tapping?

The tap-time is very much dependent on the commodity being produced, and the configurations of the furnace and downstream handling systems. For matte smelters, matte tap durations of 10–15 min on average are typical with outliers of 3 min and 60 min also quoted [11]. For silicomanganese, tap durations of 30–46 min were quoted [7, 19].

At which frequency do operators change tap-hole and why is it necessary to change tap-hole?

Tap-hole maintenance and repair can include replacement of the cold face sections making up the tapblock (partial repair) [7, 11, 17], replacement of the full tapblock [7, 11, 17, 24] or replacement of the tapblock and sections of refractory above and around the tapblock (often referred to as a V-down) [15, 32] or a full reline.

Tapblock

What is a tapblock?

A tapblock is that part of the furnace containment system design which contains the tap-hole, as illustrated in Fig. 5.

How is it constructed?

Tapblock designs vary from being one large block [15, 18, 19, 22] to being constructed from a single material, using specific tapblock shapes [24] or regular refractory bricks [7], to being constructed from various types and shapes of materials [40] which often include copper blocks [5, 6, 12, 22, 23, 26, 32]. In some applications, the tapblock consist of water-cooled copper blocks only [13].

Are refractory bricks in a tapblock different than bricks in other parts of the furnace?

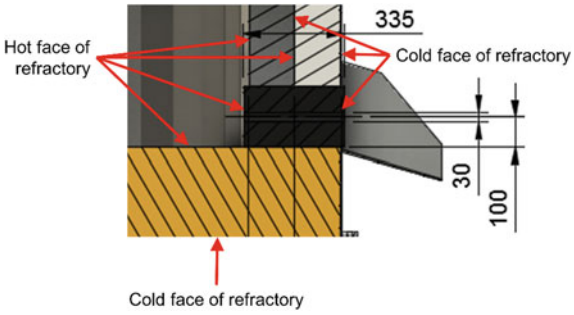

Fig. 6 Indication of hot and cold faces of various refractories in pilot-scale design in Fig. 5

More often than not, the refractory bricks in the tapblock differs from the bricks in other parts of the furnace, both in terms of shape and in terms of composition.

Why are sometimes copper parts used and which furnaces uses them?

In some applications, the life of the tap-hole is extended when using water-cooled copper blocks as part of the tapblock design. The reasons include lowering temperature of the refractory material which inhibits the potential for the liquid process materials to chemically react with it [12, 22, 24]. In other applications it promotes the formation of a protective frozen slag layer which renders the use of refractory materials obsolete [13, 23].

Define hot face and cold face.

The hot face of a refractory is the hottest side of the components and the cold face the coldest side of the same component. As indicated in Fig. 6, the hot face of the carbon brick, graphite tapblock, and high alumina castable face the furnace interior, whilst the hot face of the bubble alumina castable faces the cold face of the carbon brick.

What is meant by a series of blocks and a Mickey?

As discussed, in some tapblock designs [24, 32] a series of specially shaped, tap-hole bricks are utilised when building the tapblock (Fig. 7a). In other designs, a single tapblock is utilised with a *Mickey*, also called *quick replaceable carbon block*, installed on the cold face of the block. The Mickey is more easily replaced than an entire tapblock and is thus also replaced more frequently to allow for a clean, straight interface between the tap-hole and the claygun. The Mickey is typically made of the same, or similar, material as the tapblock [13, 15].

Closing of Tap-Hole

What is a claygun and how does it operate?

A *claygun*, also referred to as mudgun [5], closes the tap-hole by injecting tap-hole clay, also referred to as plugging paste [33], into the tap-hole at the end of a tap. The principle of operation of a clay-gun [31] is similar to that of a syringe injecting COVID-19 vaccine into one's arm. The barrel of the clay-gun is filled with tap-hole

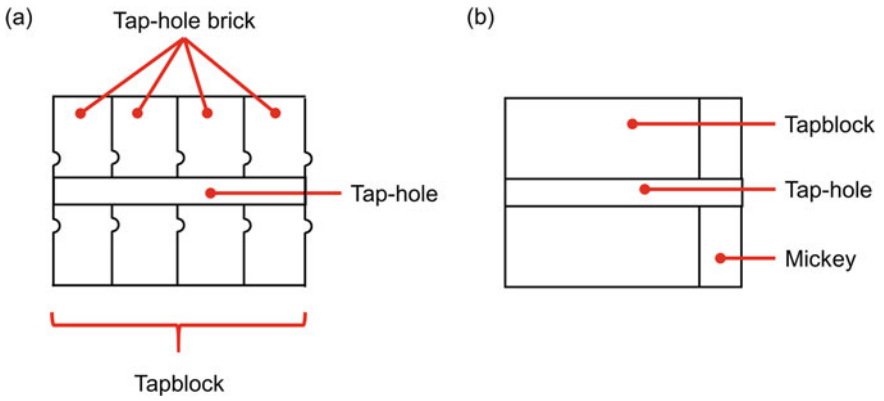

Fig. 7 **a** Tapblock constructed from a series of tap-hole bricks. **b** Tapblock with Mickey on its cold face

clay, the clay-gun is moved into position, and a piston applies the force that extrudes the clay into the tap-hole [45]. In the past, clayguns were steam, pneumatically or electrically driven, but in modern times hydraulic power is utilised [31].

How much (clay) is typically injected each time?

The amount of clay injected very much depends on the size of the operation, the size of the tap-hole, the condition of the tapblock, and the bulk density of the tap-hole clay utilised. A study conducted on five silicomanganese smelters found that between 30 and 46 kg of tap-hole clay per tap was used, where all five clayguns had a barrel capacity of 50 L [46].

How long does the claygun use to complete one closing operation?

The same study [46] found that the clay injection rate varied between 3.6 and 6.0 L per second, which meant that injecting the clay into the tap-hole took between 8 and 14 s. The clayguns remained in position at the tap-hole for around 2 min to allow the clay to set.

Difference between rail and pedestal support?

When supported by a rail, the claygun hangs from and move along a rail which follows the curvature of the furnace shell [13]. When supported by pedestal, the claygun is supported by a structure attached to a column [31]. The structure is utilised to move the claygun in position.

How does the tap-hole clay work? What makes it freeze (phase change, evaporation of liquid agents)?

Tap-hole clay is a specialised type of refractory material which can be dugout from the ground [11] or manufactured by refractory suppliers [5, 33]. For water-based clays, evaporation of the water bonded with the clay minerals, cause the clay to solidify. For tar-based clays, evaporation of the volatile matter will be the cause and for resin-bonded clays, it is assumed that chemical reactions are the cause. The scientific knowledge on tap-hole clays is very limited and the opportunities for research plentiful.

What is the composition of tap-hole clay?

The compositions of tap-hole clays vary depending on the source and/or how it was manufactured. Natural clays consist of clay minerals. Manufactured clays typically consist of an aggregate and a binder phase, similar to concrete utilised in the building industry. Aggregates can include calcined anthracite, Quartz, or Andalusite [47] and binder phases clay minerals, tar, or resin or a combination of these [5, 11].

Drilling and Lancing

What type of equipment is used?

Just as one would use a power-drill at home to drill a hole in a wall, a drill is used to drill a hole in the tap-hole filled with clay. In many instances the first part of the hole is drilled, using an expensive drill bit, and then a hammer action is applied with a simple rod to open the tap-hole [31]. Alternatively an oxygen lance is used to open the last part of the tap-hole [13]. The drill is often supplied by the same supplier as the claygun and installed as one unit. As with the claygun, the drill can be powered pneumatically, electro-mechanically or hydraulically although the latter is favoured in modern times [31].

How drill depth is defined (what is 0 depth)?

Drill depth is the first part where the hole is drilled with 0 depth being the cold face of the tapblock.

What is lancing and why do we lance?

Oxygen lancing is when oxygen is blown through a steel pipe and ignited. The flame that form can cut through tap-hole clay or slag and therefore opens the tap-hole [5, 30, 31]. Lancing is an effective way of opening the tap-hole, especially when alloy froze in the tap-hole, but can be very destructive towards the tapblock materials of construction. In order to minimize the impact of lancing on tap-hole wear, the use of lancing is combined with drill operation as described, and thermal lances—which have a higher steel density—are developed [30].

Post Tap-Hole

What happens with metal and slag after leaving the furnace?

The liquid alloy or slag flows along a shorter channel called a *launder* (see Fig. 5), and if a far distance away from the downstream equipment, along another longer channel called a *runner* from where several options of treatment exist. The words launder or runner are often used inter-changeably. Slag can be tapped into slag pots [7] or is granulated using water [13, 24] or air [5]. Alloy is tapped in ladles [7], granulated, or cast into large moulds formed by front-end loader in beds of metal fines (Fig. 8b).

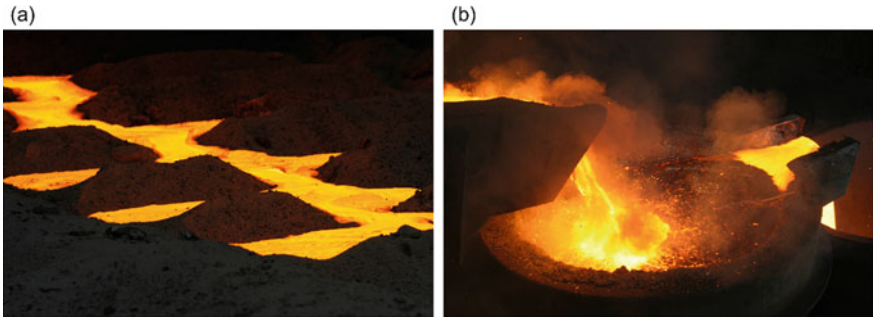

Fig. 8 **a** Liquid alloy cast into large moulds formed by front-end loader in beds of metal fines © Joalet Steenkamp. **b** Cascade tapping with liquid alloy and slag frowing from a launder into a ladle from which slag overflows into a slag pot © Joalet Steenkamp

What is cascade tapping?

Cascade tapping occurs when slag and alloy are tapped from a single-level tap-hole and both flow into a ladle from which the slag overflows into a slagpot (Fig. 8a).

Other

Which mechanisms degrades the tap-hole and the tap block?

Lancing is considered one of the major causes of wear of the tap-hole [5]. Thermal shock, due to the thermal cycles which the tap-hole is exposed to during discontinuous tapping, is another. For some processes, where the containment system design is based on a conductive philosophy, the refractory material chemically reacts with the liquid process materials [14, 15, 19].

What is a runaway tap?

A runaway tap occurs when the tap-hole has to be closed where there is liquid material remaining in the furnace, as would be the case for an alloy tap in a dual tap-hole configuration, and the tap-hole fails to close. The liquid alloy and slag continue to drain from the furnace and can overflow into the tapping hall, causing significant damage to equipment downstream of the furnace.

Conclusions

The Furnace Tapping Conference series provides a platform that allows for multi-disciplinary, multi-commodity conversations around a universal challenge, namely the tapping of furnaces. The set of peer-reviewed papers, contained in the Proceedings of the first two events, provides a useful resource for newcomers and seasoned participants alike.

Acknowledgements This paper is published with permission from Mintek and SINTEF.

References

1. Steenkamp JD (2016) Journal comment: furnace tapping 2014. J South Afr Inst Min Metall 116(1):iv–v
2. Steenkamp JD (2019) Journal comment: furnace tapping 2018. J South Afr Inst Min Metall 119(6):iv
3. Steenkamp JD, Cowey A (ed) (2014) Proceedings of the furnace tapping conference 2014. Southern African Institute of Mining and Metallurgy. http://www.saimm.co.za/Conferences/FurnaceTapping/. Accessed 8 Sept 2021
4. Steenkamp JD, Cowey A (ed) (2018) Proceedings of the furnace tapping conference 2018. Southern African Institute of Mining and Metallurgy. http://www.saimm.co.za/Conferences/FurnaceTapping2018/. Accessed 8 Sept 2021
5. Nelson LR, Hundermark RJ (2014) 'The tap-hole'—key to furnace performance. In: Proceedings of the furnace tapping conference 2014. Southern African Institute of Mining and Metallurgy. https://www.saimm.co.za/Conferences/FurnaceTapping/001-Nelson.pdf. Accessed 8 Sept 2021
6. Faux S, Walker C, Stober F, MacRosty R, Darini M, Katgutkar B (2018) Optimizing tap-hole performance using a risk-based asses management strategy. In: Proceedings of the furnace tapping conference 2014. Southern African Institute of Mining and Metallurgy. https://www.saimm.co.za/Conferences/FurnaceTapping2018/205-Faux.pdf. Accessed 8 Sept 2021
7. Sutherland JJ, Gous JP (2018) Managing the tap-hole life-cycle at five submerged arc furnaces producing silicomanganese at transalloys. In: Proceedings of the furnace tapping conference 2018. Southern African Institute of Mining and Metallurgy. https://www.saimm.co.za/Conferences/FurnaceTapping2018/117-Sutherland.pdf. Accessed 8 Sept 2021
8. Essack SC (2014) Closing your slag tap-hole. In: Proceedings of the furnace tapping conference 2014. Southern African Institute of Mining and Metallurgy. https://www.saimm.co.za/Conferences/FurnaceTapping/193-Essack.pdf. Accessed 8 Sept 2021
9. Pistorius PC (2018) Slag carry-over an the production of clean steel. In: Proceedings of the furnace tapping conference 2018. Southern African Institute of Mining and Metallurgy. https://www.saimm.co.za/Conferences/FurnaceTapping2018/001-Pistorius.pdf. Accessed 8 Sept 2021
10. Ringdalen E, Ksiazek M (2018) Excavation of a SiMn furnace. In: Proceedings of the furnace tapping conference 2018. Southern African Institute of Mining and Metallurgy. https://www.saimm.co.za/Conferences/FurnaceTapping2018/167-Ringdalen.pdf. Accessed 8 Sept 2021
11. Nolet I (2014) Tapping of PGM-Ni mattes: an industry survey. In: Proceedings of the furnace tapping conference 2014. Southern African Institute of Mining and Metallurgy. https://www.saimm.co.za/Conferences/FurnaceTapping/223-Nolet.pdf. Accessed 8 Sept 2021
12. Thomson L (2014) Monitoring, repair, and safety practices for electric furnace matte tapping. In: Proceedings of the furnace tapping conference 2014. Southern African Institute of Mining and Metallurgy. https://www.saimm.co.za/Conferences/FurnaceTapping/087-Thomson.pdf. Accessed 8 Sept 2021
13. Van Beek WSB, Goff TJ, Nel PE, Rex E (2014) An overview of the design, operation, and maintenance practices relating to tap-hole management ofa PGM smelting furnace. In: Proceedings of the furnace tapping conference 2014. Southern African Institute of Mining and Metallurgy. https://www.saimm.co.za/Conferences/FurnaceTapping/113-vanBeek.pdf. Accessed 8 Sept 2021
14. Steenkamp JD, Gous JP, Pistorius PC, Tangstad M, Zietsman JH (2014) Wear analysis of a tap-hole from a SiMn production furnace. In: Proceedings of the furnace tapping conference

2014. Southern African Institute of Mining and Metallurgy. https://www.saimm.co.za/Conferences/FurnaceTapping/051-Steenkamp.pdf. Accessed 8 Sept 2021
15. Steenkamp JD (2018) Wear analysis of tap-holes at two ferrochromium production furnaces. In: Proceedings of the furnace tapping conference 2018. Southern African Institute of Mining and Metallurgy. https://www.saimm.co.za/Conferences/FurnaceTapping2018/011-Steenkamp.pdf. Accessed 8 Sept 2021
16. Rioux DJ, Moore TA, McTeer GJ, Verhelst DL (2014) Teck's KIVCETTM lead tapping experience. In: Proceedings of the furnace tapping conference 2014. Southern African Institute of Mining and Metallurgy. https://www.saimm.co.za/Conferences/FurnaceTapping/233-Rioux.pdf. Accessed 8 Sept 2021
17. Lindstad L (2014) Maintenance and major repairs of tap-holes and tapping spouts. In: Proceedings of the furnace tapping conference 2014. Southern African Institute of Mining and Metallurgy. https://www.saimm.co.za/Conferences/FurnaceTapping/129-Lindstad.pdf. Accessed 8 Sept 2021
18. O'Shaughnessy P, Van der Merwe H, Botes S (20140 Tap-hole repair: the UCAR®V repair solution. In: Proceedings of the furnace tapping conference 2014. Southern African Institute of Mining and Metallurgy. https://www.saimm.co.za/Conferences/FurnaceTapping/079-O'Shaughnessy.pdf. Accessed 8 Sept 2021
19. Davidsen JE, Honstad M (2018) Tap-hole maintenance and management on furnace 10 at Eramet Norway Porsgrunn.
20. Filzwieser A, Konetschnik S, Dreyer E (2014) METTOP's ionic liquid cooling technology: the safest way of furnace tapping. In: Proceedings of the furnace tapping conference 2014. Southern African Institute of Mining and Metallurgy. https://www.saimm.co.za/Conferences/FurnaceTapping/217-Filzwieser.pdf. Accessed 8 Sept 2021
21. Kennedy MW, MacRae A, Olesen F (2018) Non-water-based metal tap-hole cooling—a safer alternative. In: Proceedings of the furnace tapping conference 2018. Southern African Institute of Mining and Metallurgy. https://www.saimm.co.za/Conferences/FurnaceTapping2018/101-Kennedy.pdf. Accessed 8 Sept 2021
22. Mc Dougall I (2014) Water-cooled tap-hole blocks. In: Proceedings of the furnace tapping conference 2014. Southern African Institute of Mining and Metallurgy. https://www.saimm.co.za/Conferences/FurnaceTapping/183-McDougall.pdf. Accessed 8 Sept 2021
23. Belford BN, Conradie P, Mwanza T (2018) Development, installation, and operation of a full-copper, deep-cooled slag tap-block for a six-in-line copper slag-cleaning electric furnace. In: Proceedings of the furnace tapping conference 2018. Southern African Institute of Mining and Metallurgy. https://www.saimm.co.za/Conferences/FurnaceTapping2018/057-Belford.pdf. Accessed 8 Sept 2021
24. Hoosen A, Sichone M, Rambiyana I (2018) Improvements to the Anglo Converting Process (ACP) tap-block management. In: Proceedings of the furnace tapping conference 2018. Southern African Institute of Mining and Metallurgy. https://www.saimm.co.za/Conferences/FurnaceTapping2018/049-Hoosen.pdf. Accessed 8 Sept 2021
25. Braun W, Gebski P, MacRosty R, Pula R, Sadri A, Ying W (2014) Tap-hole monitoring technologies. In: Proceedings of the furnace tapping conference 2014. Southern African Institute of Mining and Metallurgy. https://www.saimm.co.za/Conferences/FurnaceTapping/169-Braun.pdf. Accessed 8 Sept 2021
26. Hopf M (2014) Monitoring the wear of water-cooled tap-hole blocks by the OPTISAVE fibre-optic method. In: Proceedings of the furnace tapping conference 2014. Southern African Institute of Mining and Metallurgy. https://www.saimm.co.za/Conferences/FurnaceTapping/033-Hopf.pdf. Accessed 8 Sept 2021
27. Ghorbani H, Al-Dojayli M, Chomyn K (2018) Thermal assessment and identification of wear zones in a blast furnace hearth and tap-holes. In: Proceedings of the furnace tapping conference 2018. Southern African Institute of Mining and Metallurgy. https://www.saimm.co.za/Conferences/FurnaceTapping2018/039-Ghorbani.pdf. Accessed 8 Sept 2021
28. Ksiazek M, Hustad HM, Nymoen A, Holtan J, Gradahl S, Kaukonen S, Tangstad M (2018) Measurement of metal temperature during tapping of an industrial FeSi furnace.

In: Proceedings of the furnace tapping conference 2018. Southern African Institute of Mining and Metallurgy. https://www.saimm.co.za/Conferences/FurnaceTapping2018/083-Ksiazek.pdf. Accessed 8 Sept 2021
29. Rödfalk A, Nilsson JP, Brogden N, Bloemer P, Lyons A, Østensen OJ (2014) An automatic ladle level measurement system for monitoring ladle fill rate during tapping. In: Proceedings of the furnace tapping conference 2014. Southern African Institute of Mining and Metallurgy. https://www.saimm.co.za/Conferences/FurnaceTapping/065-Lyons.pdf. Accessed 8 Sept 2021
30. Morales D, Morales D, Nunez S (2018) Tap-hole opening: advances and improvements. In: Proceedings of the furnace tapping conference 2018. Southern African Institute of Mining and Metallurgy. https://www.saimm.co.za/Conferences/FurnaceTapping2018/231-Morales.pdf. Accessed 8 Sept 2021
31. Dienenthal A (2014) A short history of the development of tapping equipment. In: Proceedings of the furnace tapping conference 2014. Southern African Institute of Mining and Metallurgy. https://www.saimm.co.za/Conferences/FurnaceTapping/203-Dienenthal.pdf. Accessed 8 Sept 2021
32. Mgenge S, Steenkamp JD (2014) Furnace tapping practice at Tronox Namakwa Sands. In: Proceedings of the furnace tapping conference 2014. Southern African Institute of Mining and Metallurgy. https://www.saimm.co.za/Conferences/FurnaceTapping/137-Mgenge.pdf. Accessed 8 Sept 2021
33. Lindstad LH (2018) More health-friendly materials for the tapping area. In: Proceedings of the furnace tapping conference 2018. Southern African Institute of Mining and Metallurgy. https://www.saimm.co.za/Conferences/FurnaceTapping2018/095-Lindstad.pdf. Accessed 8 September 2021
34. Els L, Cowx P, Smith P, Nordhagen R (2014) Analysis and optimization of fume extraction from a ferromanganese furnace tapping operation. In: Proceedings of the furnace tapping conference 2014. Southern African Institute of Mining and Metallurgy. https://www.saimm.co.za/Conferences/FurnaceTapping/157-Els.pdf. Accessed 8 Sept 2021
35. Erwee MW, Reynolds QG, Zietsman JH, Bezuidenhout PJA (2018) Multiphase flow modelling of lancing of furnace tap-holes: validation of multiphase flow simulated in OpenFOAM. In: Proceedings of the furnace tapping conference 2018. Southern African Institute of Mining and Metallurgy. https://www.saimm.co.za/Conferences/FurnaceTapping2018/179-Erwee.pdf. Accessed 8 Sept 2021
36. Johansen ST, Ringdalen E (2018) Reduced metal loss to slag in HC FeCr production - by redesign based on mathematical modelling. In: Proceedings of the furnace tapping conference 2018. Southern African Institute of Mining and Metallurgy. https://www.saimm.co.za/Conferences/FurnaceTapping2018/029-Johansen.pdf. Accessed 8 Sept 2021
37. Kreuzer DR, Marschall HU, Wagner C (2018) Numeral simulation—a tap-hole refractory design study. In: Proceedings of the furnace tapping conference 2018. Southern African Institute of Mining and Metallurgy. https://www.saimm.co.za/Conferences/FurnaceTapping2018/189-Kreuzer.pdf. Accessed 8 Sept 2021
38. Olsen JE, Reynolds QG, Erwee MW (2018) Temperature field at the tap-hole in a manganese furnace—a computational modelling study. In: Proceedings of the furnace tapping conference 2018. Southern African Institute of Mining and Metallurgy. https://www.saimm.co.za/Conferences/FurnaceTapping2018/223-Olsen.pdf. Accessed 8 Sept 2021
39. Reynolds QG, Olsen JE, Erwee MW, Oxtoby OF (2018) Phase effects in tap-hole flow - a computational modelling study. In: Proceedings of the Furnace Tapping Conference 2018. Southern African Institute of Mining and Metallurgy. https://www.saimm.co.za/Conferences/FurnaceTapping2018/133-Reynolds.pdf. Accessed 8 Sept 2021
40. Geyer PG, Halifa Z (2014) Blast furnace tapping practices at ArcelorMittal South Afruca, Vanderbijlpark works. In: Proceedings of the furnace tapping conference 2014. Southern African Institute of Mining and Metallurgy. https://www.saimm.co.za/Conferences/FurnaceTapping/097-Geyer.pdf. Accessed 8 Sept 2021
41. Tveit H, Andersen V, Berget KH, Jensen R (2014) The tapping process in silicon production. In: Proceedings of the furnace tapping conference 2014. Southern African Institute of

Mining and Metallurgy. https://www.saimm.co.za/Conferences/FurnaceTapping/147-Jensen.pdf. Accessed 8 Sept 2021
42. Folstad MB, Tangstad M, Ringdalen E, Fredriksli R, Dalum S (2018) Tapping procedures in silicon production, and the role of female tapping operators. In: Proceedings of the furnace tapping conference 2018. Southern African Institute of Mining and Metallurgy. https://www.saimm.co.za/Conferences/FurnaceTapping2018/111-Folstad.pdf. Accessed 8 Sept 2021
43. Routschka G, Barthel H (2004) Introduction. In: Routschka G (ed) Pocket manual refractory materials basics—structures—properties, 2nd edn. Vulkan-Verlag, Essen, pp 1–16
44. Routschka G (ed) (2004) Pocket manual refractory materials basics—structures—properties, 2nd edn. Vulkan-Verlag, Essen
45. Steenkamp JD, Mnisi M, Skjeldestad A (2018) The workability index of three tap-hole clays. In: Proceedings of the international ferro-alloys congress XV. Southern African Institute of Mining and Metallurgy. https://www.pyrometallurgy.co.za/InfaconXV/249-Steenkamp.pdf. Accessed 8 Sept 2021
46. Steenkamp JD, Hayman DA, Bezuidenhout PJA (2019) Benchmark for tap-hole lifecycle management practices in silicomanganese production when submerged arc furnace technology of circular design is applied. JOM 71(7):2430–2434
47. Thobadi I, Mnisi M, Steenkamp JD, Matinde E, Clark W (2020) Chemical and phase chemical characterisation of three different tap-hole clays. In: Proceedings of IMPC 2020 XXX international minerals processing congress. Southern African Institute of Mining and Metallurgy. http://www.mintek.co.za/Pyromet/Files/2021Thobadi.pdf. Accessed 8 Sept 2021

CFD Study on Continuous Tapping of Silicon

Jan Erik Olsen, Michal Ksiazek, and Merete Tangstad

Abstract Silicon is mostly produced in rotating submerged arc furnaces with continuous tapping of metal. The burden is often dense due to condensates. Thus, furnace gas does not escape easily to the top of the burden and some gas escapes through the tap-hole. This can cause a hazardous flame jet out of the tap-hole which poses an HES threat to operators. A mathematical CFD model has been developed to study the flow of gas and metal in the furnace through the tap-hole. A modelling challenge is to account for the continuous tapping and the rotating furnace. These aspects differ from earlier CFD studies applied to furnace tapping. Results indicate the difference in tapping behaviour as the burden permeability varies and as the position of the tap-hole varies due to the rotation.

Keywords Furnace tapping · Continuous tapping · CFD model · Silicon

Introduction

Furnace tapping is the process of extracting products (metal, slag,…) from furnaces which is essential in metal production. The tapping process varies between furnaces producing different types of metal, but most of them operate on the principle of gravity draining liquid products out of a tap-hole (or several tap-holes) placed in the lower parts of the furnace. Although consistent tapping of alloys from furnaces is important for both furnace performance and downstream processing, many of the tapping configurations still fail to deliver a predictable output [1].

The tapping process may be continuous or discontinuous. In a discontinuous tapping process, all tap-holes remain closed for a specific time during which the products accumulate in the furnace. When tap-holes are opened, the liquid products drain through the tap-hole(s) and the amount of metal and slag in the furnace

J. E. Olsen (✉) · M. Ksiazek
SINTEF, Trondheim, Norway
e-mail: jan.e.olsen@sintef.no

M. Tangstad
Department of Material Science and Engineering, NTNU, Trondheim, Norway

J. D. Steenkamp et al. (eds.), *Furnace Tapping 2022*, The Minerals, Metals & Materials Series, https://doi.org/10.1007/978-3-030-92544-4_9

decreases. In continuous tapping, there is always (or most of the time) an open tap-hole. When there is a need to change the tap-hole to be open, the furnace is closed for tapping for a short time. Often submerged arc furnaces, for example, FeMn, SiMn, and FeCr are operated with discontinuous tapping and blast furnaces and submerged arc furnaces for Si are operated with continuous tapping.

In this study, we focus on continuous tapping of silicon, but it should be noted that many of the findings can be generalized to continuous tapping in general. There are, however, some additional features which are specific to tapping of silicon. Firstly, while the electrodes are static, the furnace shell is rotating. This continuously changes the relative position of the tap-hole with respect to the nearest electrode. Secondly, one of the by-products is a sticky condensate which reduces the permeability of the burden. This creates a resistance for the gas to escape upwards. Thus, some of the gas will escape through the tap-hole. The ratio of gas escaping through the tap-hole is relatively higher than for other submerged arc furnaces. This creates a potential for strong jets of hazardous gas through the tap-hole which poses a risk to operators [2]. Lastly, there is very little slag production in silicon furnaces.

To better understand the tapping behaviour and gas jet issue of silicon furnaces, a CFD model has been developed. This follows the approach of earlier tapping models [3], but modifications have been necessary since earlier work has only addressed discontinuous tapping. Also, the rotation of the furnace and the high velocities of the tap-hole gas jets needed special attention. The model and results from the case studies with the model are presented in the following.

Model

A CFD model was developed to represent the conditions during tapping of silicon from a submerged arc furnace. The model consists of a chosen representation of the furnace and the conditions inside the furnace and a mathematical description governing conservation laws and the chosen furnace conditions.

Furnace Conditions

Production of silicon in a submerged arc furnace is carried out by charging raw materials from the top of the furnace. The raw materials are minerals, mainly quartz (SiO2) and carbon-rich materials like coke, coal, charcoal, and wood chips (C). The key components of the raw materials react according to the overall reaction:

$$Si\,O_2 + (1+y)\,C = y\,Si + (1-y)\,Si\,O + (1+y)\,C\,O$$

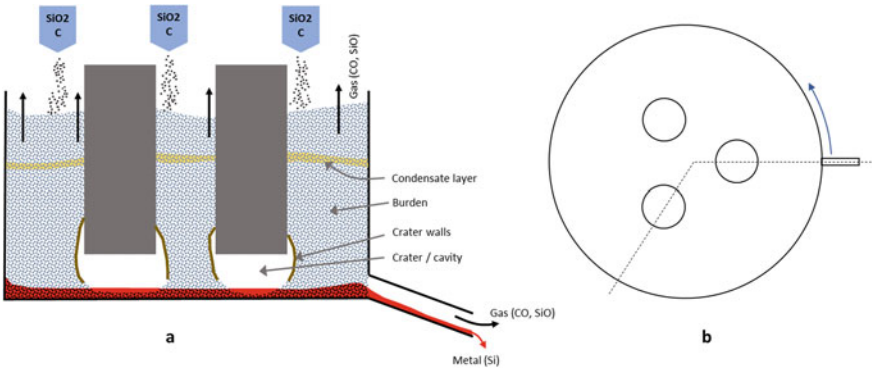

Fig. 1 **a** Vertical and horizontal **b** cross sections of a simplified typical silicon furnace. The vertical cross section is given by the dashed line in the horizontal cross section

where y is the silicon yield. This reaction is highly endothermic. Thus, energy is needed to drive the reaction. This is supplied via three electrodes submerged into the burden of raw materials and reaction products. A silicon furnace with its main features and operating principles is illustrated in Fig. 1.

There are several additional reactions and conditions which complicate the furnace operation. Further details are given by Schei et al. [4]. The implications of these which are of importance to metal tapping and gas flow in the furnace are as follows: underneath the electrodes a cavity is formed where electric arcs spark between the electrode tip and the metal pool at the bottom of the furnace. The cavity is also known as a crater. Highly viscous melted silica (SiO_2) drains downwards at the outside of the cavity forming a sticky crater wall together with the particles in the burden. The crater wall has a lower permeability than the main bulk of the burden. SiO gas created in the crater zones rises towards the top of the furnace where the temperatures are lower. The cooling of SiO promotes condensation. The condensate forms a sticky layer with low permeability known as the condensate layer.

Since the conditions inside a silicon furnace are highly complex and difficult to predict accurately, a simplified model is designed based on the description above of the true process and furnace. This model is illustrated in Fig. 2. To the left (part a) we see the furnace with electrodes, a burden, a condensate layer, craters with crater walls, and a metal layer at the bottom which drains out through a tap-hole. These zones are given different properties and permeabilities in the mathematical model. There is also a thin zone around the periphery of the electrodes. It is known that a significant amount of gas escapes upwards near the electrodes. Thus, a more permeable zone is created close to the electrodes. The mathematical model focuses on tapping and material flow. A full furnace model with species conservation and chemical reactions is out of scope. Still, we need to add the metal and gas continuously produced in the furnace. Without chemical reactions in the model, there are no source terms to provide a production of metal and gas. Instead, metal and gas is injected into the furnace by means of boundary conditions. Metal is injected from the bottom of

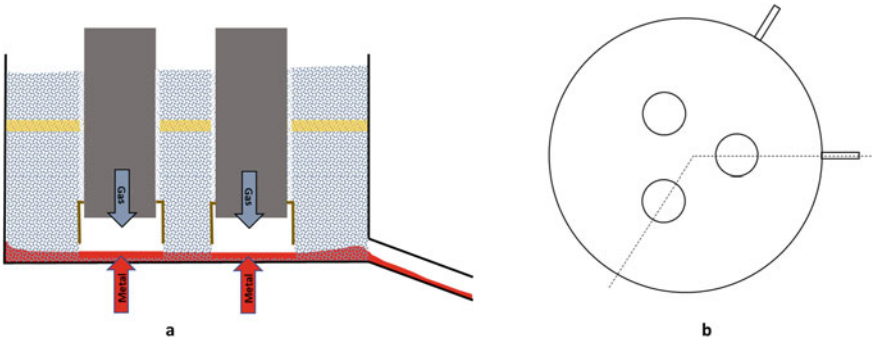

Fig. 2 **a** Vertical and horizontal **b** cross sections of the furnace model applied in the mathematical simulations

the furnace under each electrode and gas is injected underneath each electrode. It is computationally challenging to model the rotation of the furnace, both due to the long timeframe for this rotation and due to the complexity of moving parts. Therefore, we kept the furnace stagnant and included two tap-holes in the furnace as seen to the right (part b) of Fig. 2. These were only kept open one at a time. They represent the scenarios when the tap-hole is adjacent to the nearest electrode and as far as possible from the electrode.

Mathematical Model

To quantify tapping performance, a mathematical model has been developed based on the furnace model described above. The mathematical model solves a set of differential equations based on conservation laws for mass and momentum which is the basis for computational fluid dynamics (CFD). The solution gives quantitative values on pressure and velocity of the gas and metal flow and the location of the interface between gas and metal. In the current model, the temperature is assumed constant and no conservation law for energy is solved. A source term for the pressure loss due to the particle bed's resistance to flow is included in the model. Ergun's equation [5] is applied for the pressure loss. This depends on several parameters and variables including the particle bed porosity and the particle diameter which also defines the permeability of the burden. An overview of the equations is given by Bublik et.al. [3]. The mathematical model has been validated against the drainage experiment of Vångö et.al. [6] where water was drained through a bed of spherical wood chips. The model is consistent with the experiment [7]. The model is used to study tapping of silicon and gassing issues as described in the next section.

Table 1 Furnace geometry

Furnace diameter	8 m		Tap-hole diameter	0.1 m
Electrode diameter	1.2 m		Tap-hole length	1.0 m
Electrode height[1]	0.44 m		Tap-hole inclination	10°

Table 2 Material properties

	Viscosity (kg/m s)	Density (kg/m^3)
Silicon	2e-3	2450
Gas	1e-5	0.2

Solution Strategy

The above-mentioned model has been implemented in the commercial CFD software ANSYS/Fluent where the Geo-Reconstruct scheme is applied in the VOF approach to track the interface between metal and gas. If rapid variation in production is not of interest, the numerical solution we are interested in has a steady-state characteristic since we are studying continuous tapping. Thus, it might be tempting to apply a steady-state solver. However, mass is not properly conserved for the VOF approach with a steady-state solver and a transient solver is therefore applied. The high velocities of the gas jets escaping from the tap-hole force the simulations to apply a very short time step to avoid divergence in the solver. Typically, time steps as low as 0.1 ms are needed. The simulations are progressed in time until key parameters reach a steady state.

Results

To study continuous tapping of rotating silicon furnaces, a series of computational simulations has been performed. The simulations are based on the mathematical model described above. The case to which it is applied is a furnace with geometry as listed in Table 1 and material properties as listed in Table 2. The particle distribution and permeability of the burden vary and six cases representing different hypothesized configurations have been studied. These cases are founded on two base cases with different burden permeabilities. The permeability properties for Base Case 1 and Base Case 2 are defined in Table 3. They are quite similar with a slightly lower porosity around the electrodes for Case 2, making the burden of Case 2 less permeable than the burden of Case 1. These cases can be further varied by tapping from the tap-hole close to the front electrode and far away from the front electrode. These two variations will represent two stages in the rotation of the furnace. Another variation is the potential extension of the tap-hole into the furnace. This will depend upon

[1] Distance between electrode tip and furnace bottom.

Table 3 Permeability parameters for different furnace zones

	Case 1		Case 2	
	Porosity	Particle diameter (cm)	Porosity	Particle diameter (cm)
Main burden	0.35	2.5	0.35	2.5
Condensate layer	0.05	0.1	0.05	0.1
Crater and tap-hole	1.0	–	1.0	–
Crater walls	0.2	1.0	0.2	1.0
Electrode periphery	0.4	2.5	0.3	2.5

Fig. 3 Porosity distribution in idealized Si-furnace (left) and an alternative distribution with extended tap-hole (right)

the drilling operation when opening the tap-hole or to keep the tap-hole open. The extended tap-hole is a kind of cavity extending from the tap-hole into the furnace. These two variations are illustrated in Fig. 3. This leaves us with six cases:

Base Case 1

Case 1 with extended tap-hole.
Case 1 with tapping far from electrode.

Base Case 2 (less permeable than Case 1).

Case 2 with extended tap-hole.
Case 2 with tapping far from electrode.

For all of these six cases, the gas production rate was varied. A typical silicon furnace can produce 100 tonnes of metal per day (1.15 kg/s). When assuming a silicon yield of 0.9, the gas production is 2.6 kg/s with a mass fraction of 0.075 SiO. This is an average production number. In reality, the gas production varies. In this study, it varies between 0.026 and 5.22 kg/s. The gas amount is inserted through the bottom of the electrodes as a boundary condition. The metal production is kept constant at 1.15 kg/s and inserted from the bottom of the furnace underneath each electrode as indicated in Fig. 2.

The results from the simulations include the flow and distribution of metal and gas, pressure and velocities. An example of metal distribution is seen in Fig. 4 and a velocity field is seen in Fig. 5.

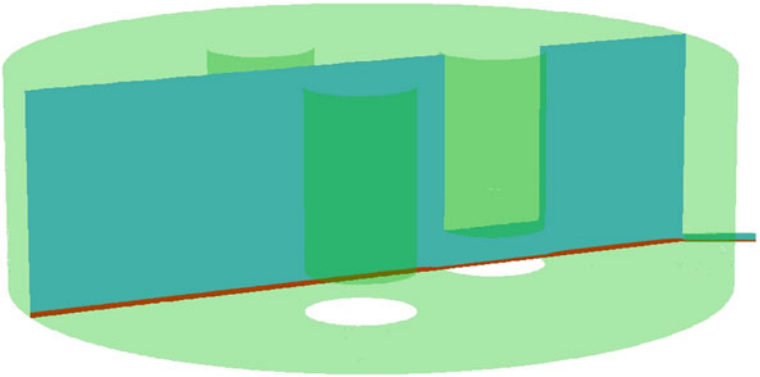

Fig. 4 Metal (red) distribution in furnace seen on cross section for Base Case 1. (Color figure online)

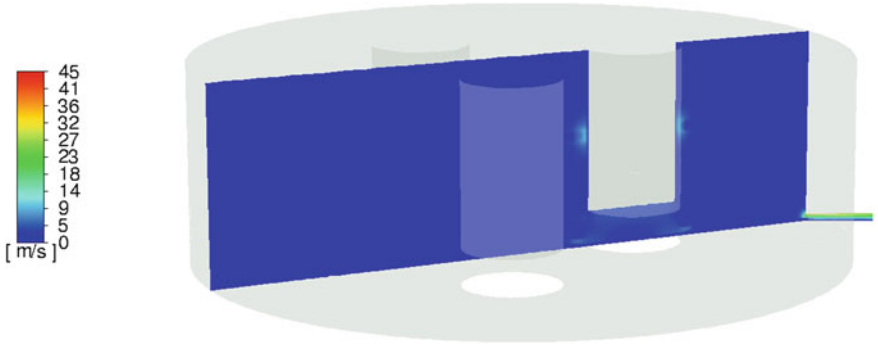

Fig. 5 Velocity magnitude plotted on cross section in furnace for Base Case 1

Several quantitative numbers can be extracted from the simulations. One of these is the crater pressure. Since the burden is quite dense, the gas cannot easily escape. Thus, a gas pressure is produced. The crater pressure as function of the gas production is seen in Fig. 6. As expected, the pressure increases with gas production. The increase is quite significant. From the results in Fig. 6, it can also be seen that the crater pressure is higher for Case 2 than Case 1. This is caused by the lower permeability of the burden in Case 2. Whether the tapping occurs through the near or far tap-hole or with an extended tap-hole does not influence the crater pressure as much as the gas production and burden permeability. The predicted pressures are consistent with measured values. That is not a proof of validation since the burden permeability was decided by calibrating against these measured values.

Most of the gas produced in the furnace escapes through the top of the furnace, but some escapes through the tap-hole as a gas jet. Figure 7 displays the maximum velocity of gas in the tap-hole exit as a function of the gas production. The gas jet velocity increases with increasing gas production since more gas is diverted to the

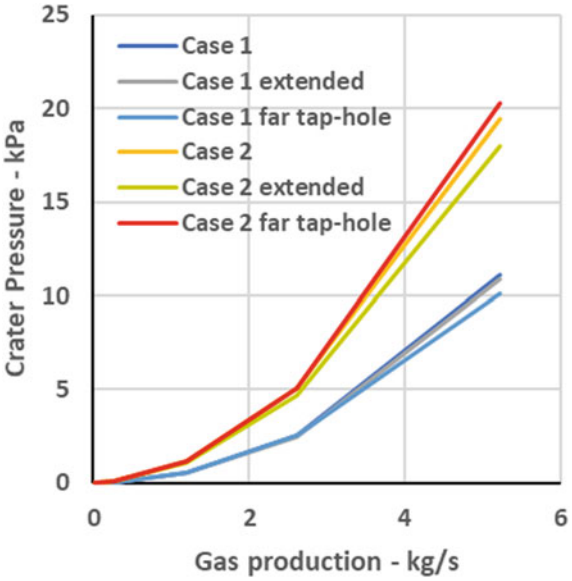

Fig. 6 Crater pressure as function of gas production rate

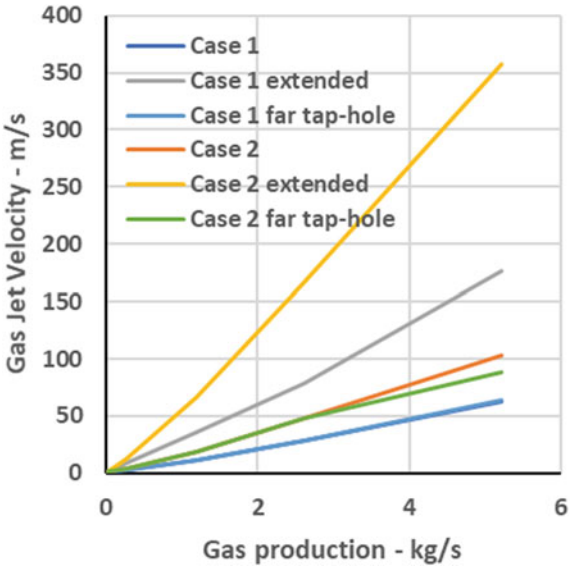

Fig. 7 Gas jet velocity as function of gas production rate

tap-hole with increasing gas production. The gas jet velocity is higher for the cases with less permeable burden (Case 2 variants) since the reduced permeability mostly restricts flow upwards. There is also a clear indication that the configurations with an extended tap-hole create the highest jet velocities. It has earlier been indicated that the particle configuration close to the tap-hole entrance is very important for

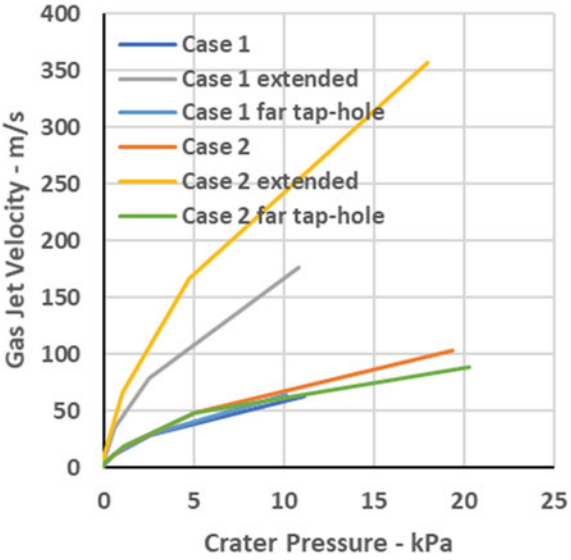

Fig. 8 Gas jet velocity as function of crater pressure

the pressure loss due to the flow acceleration at the entrance to the tap-hole. Some of these velocities are high and they should be of concern to operators close to the tap-hole. The velocities are consistent with observations in silicon plants. The gas jet velocity can also be plotted as function of crater pressure. This is done in Fig. 8.

To assess the impact of tap-hole position (furnace rotation) and tap-hole extension, a relative gas jet velocity can be studied. The relative gas jet velocity is the velocity normalized with the velocity of the base case of the chosen permeability configuration. This number will then filter out the impact of the permeability. The relative gas jet velocity is plotted in Fig. 9. It shows that tap-hole extension significantly affects the relative gas jet velocity while the tap-hole position is not of importance.

Summary and Discussion

A mathematical model has been developed to study continuous tapping from rotating silicon furnaces. Simulations based on the model have been carried out, and they have provided insight into the tapping of silicon, especially the accompanying gas flow through the tap-hole. Due to the condensate layer formed in silicon furnaces, the burden is less permeable than the burden in most other submerged arc furnaces. This creates a resistance to the flow of gas upwards to the furnace hood. The resistance causes an increased crater pressure and forces some of the gas to flow out through the tap-hole. Even a small fraction of the total gas can create a strong gas jet out of the tap-hole. This gas jet poses a severe risk to operators due to its high energy. The gas will very likely combust with surrounding air to create a flame jet.

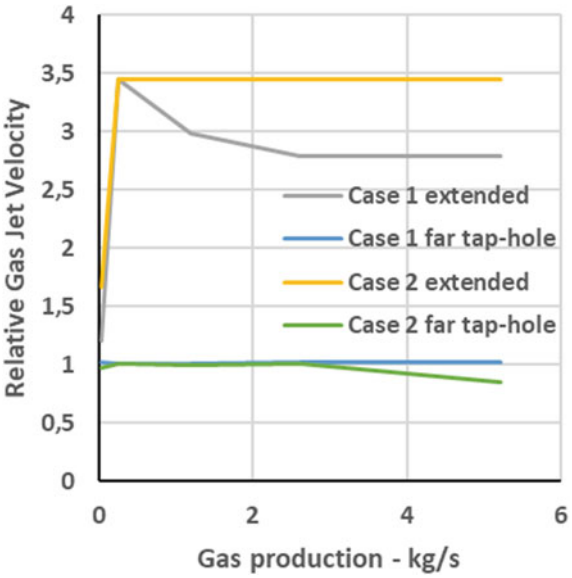

Fig. 9 Relative gas jet velocity as function of gas production rate

The simulation results show that the gas jet can be ejected with velocities up to 100 m/s. The severity increases with increasing gas production and decreasing burden permeability. If there is an extension of the tap-hole into the furnace, the gas jet will be even more severe. This extension is a type of cavity (particle-free zone) inside the furnace extending from the tap-hole in which metal and gas flows more freely. This extension can be created if drilling continues beyond the tap-hole or maybe by pushing rods into the tap-hole. Avoiding a cavity near the tap-hole entrance will reduce the risk of severe gas jets. The extension can also be prevented by the same operation with rods.

Gassing seems to be unaffected by the tap-hole position. This is somewhat contradictory to observations. It should be noted that in our studies on tap-hole position we have only varied the tap-hole position. The burden configuration and tap-hole extension have been kept constant. In reality, it might be that the furnace rotation alters the burden configuration as the tap-hole rotates away from the nearest electrode. This might favour reduced gassing (e.g. by destroying an extension of the tap-hole).

It should also be noted that this study has been conducted on an idealized furnace. The distribution of materials inside a silicon furnace is more complicated than what was assumed here. After some years of operation, materials (e.g. slag) will accumulate inside the furnace and affect the flow pattern of metal and gas. This will complicate the flow pattern. Future studies need to account for this.

References

1. Nelson LR, Hundermark R (2016) The tap-hole—key to furnace performance. J South Afr Inst Min Metall 116(5):465–490. https://doi.org/10.17159/2411-9717/2016/v116n5a12
2. Tveit H, Halland T, Landrø K-I, Johansen ST, Ravary B (2002) The tapping process in silicon production. In: Silicon for the chemical industry VI. Loen, Norway
3. Bublik S, Olsen JE, Loomba V, Reynolds QG, Einarsrud KE (2021) A review of ferroalloy tapping models. Metall Mater Trans B 52(4):2038–2047. https://doi.org/10.1007/s11663-021-02134-5
4. Schei A, Tuset JK, Tveit H (1998) Production of high silicon alloys. TAPIR, Trondheim
5. Ergun S (1952) Fluid flow through packed columns. Chem Eng Prog, vol 48
6. Vångö M, Pirker S, Lichtenegger T (2018) Unresolved CFD–DEM modeling of multiphase flow in densely packed particle beds. Appl Math Model 56:501–516
7. Olsen JE (2020) A CFD study on the impact of barriers and nonuniformities on furnace tapping. In: 14th International Conference on CFD in Oil & Gas, Metallurgical and Process Industries. Virtual: SINTEF akademisk forlag

Reduced-Order Models of Furnace Tapping Systems—A Case Study from a Submerged Arc Furnace Producing Silicomanganese

Quinn G. Reynolds, Joalet D. Steenkamp, and Jakobus Sutherland

Abstract With the advent of the fourth industrial revolution, advanced methods for control and automation of pyrometallurgical furnace plants are beginning to receive considerable attention. One aspect of such work is the development of predictive tools based on fundamental process modelling—such models are able to extrapolate furnace behaviour beyond what is available in historical data. In the present paper, a reduced-order model of tapping from a submerged arc furnace is developed for the case of silicomanganese production. The utility of the resulting model is assessed by comparison to tapping measurements obtained from an industrial furnace plant. Strengths and weaknesses of the model are subsequently identified and discussed in the context of the potential for such models to act as operator guidance and digital twinning tools.

Keywords Furnace tapping · Silicomanganese · Modelling

Introduction

Ferromanganese and silicomanganese are used extensively in the steel industry for alloying and purification, and the pyrometallurgical processing of manganese-containing ores to produce these ferroalloys is a significant economic activity in South Africa and worldwide [7, 8].

Q. G. Reynolds (✉) · J. D. Steenkamp
Mintek, Private Bag X3015, Randburg 2125, South Africa
e-mail: quinnr@mintek.co.za

Q. G. Reynolds
University of Stellenbosch, Private Bag X1, Matieland 7602, South Africa

J. D. Steenkamp
University of the Witwatersrand, Private Bag 3, Wits, Johannesburg 2050, South Africa

J. Sutherland
Transalloys, PO Box 856, Emalahleni 1035, South Africa

J. D. Steenkamp et al. (eds.), *Furnace Tapping 2022*, The Minerals, Metals & Materials Series, https://doi.org/10.1007/978-3-030-92544-4_10

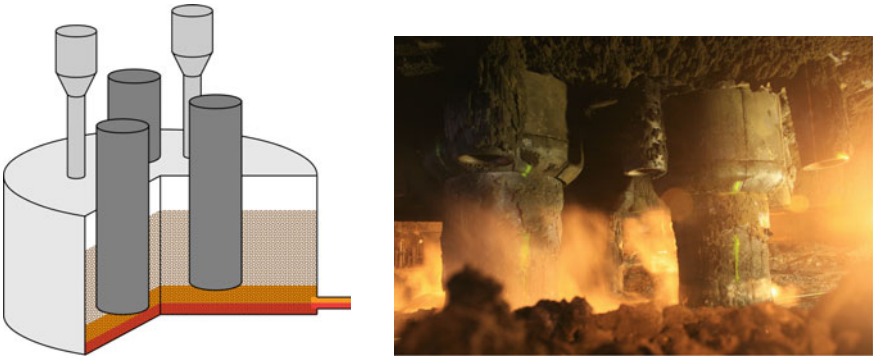

Fig. 1 (l) Cutaway schematic of a silicomanganese furnace showing burden, metal, and slag layers, (r) electrodes in an operating furnace ("Giants in the Dust", image ©Joalet Steenkamp)

In the silicomanganese industry, circular submerged arc furnaces (SAF) are commonly used [7]. These are a type of electric furnace vessel consisting of a cylindrical containment shell lined with refractory and three centrally located self-baking graphite electrodes. Power is supplied to the electrodes by an alternating current transformer which steps grid electricity down to the high-current, low-voltage levels required in furnace operations. Ore containing iron and manganese is fed to the furnace together with a source of silica (typically a quartz flux) and a carbonaceous reductant. These materials form a deep particulate bed or *burden* inside the furnace vessel. The burden is continuously consumed from below by melting and chemical reactions in the hot zones around each electrode tip, and replenished from feed chutes in the furnace roof. Counterflow of reaction gases from the hot zones facilitates preheating and solid-state prereduction reactions in the upper regions of the burden, improving overall efficiency of the unit. The smelting process generates a silicomanganese metal alloy and a waste slag (oxide), both of which are in the molten state at typical operating temperatures. The metal and slag phases are immiscible, and build up as separate liquid layers in the base of the furnace vessel. The interior structure of a typical SAF is shown in Fig. 1.

As in many other pyrometallurgical processes, extraction of the reaction products from the furnace vessel is achieved by *batch tapping* [5]. This involves the periodic opening (usually by drilling or thermal lancing) of a dedicated tap-hole channel in the furnace sidewall, allowing the molten products inside to drain out under gravity, and resealing the tap-hole to continue operation. Tapping of silicomanganese furnaces is phenomenologically complex due to the use of a single tap-hole through which metal and slag products are extracted simultaneously, and the presence of the burden layer which forms a porous bed through which the products must drain. Difficulties in understanding tapping dynamics are further exacerbated by the problem's high sensitivity to variables such as tap-hole diameter and disposition of the burden near to the tap-hole entrance, many of which may change randomly between successive taps and cause appreciable variability in the tapping process. Despite these challenges it

remains of interest to have some means of predicting the tapping behaviour of silicomanganese furnaces, as tapped mass of metal is a critical indicator of performance for industrial operations.

Current attempts to understand furnace tapping behaviour focus on the development of process models using one of two different approaches. In "bottom-up" modelling, mathematical descriptions of varying complexity are obtained from the fundamental physical principles governing the system, while in "top-down" modelling large quantities of historical data are analysed using advanced statistical and machine-learning methods in order to generate reliable empirical relationships. Research in the former is well advanced, whereas the latter remains at a nascent stage [3].

This paper details the application of a reduced-order bottom-up model to silicomanganese furnace tapping, and evaluation of the model's performance against data obtained from an operating plant. The intention of the present work is to demonstrate a simplified and lightweight bottom-up framework with flexible empirical parameterisation which would potentially be suitable for integration with data-driven techniques in the future.

Industrial Data Set

For testing purposes, a large set of data related to furnace tapping was obtained from a South African silicomanganese producer. The data covers a period of approximately a year and a half of operations on a 48 MVA SAF unit, and represents nearly three thousand distinct tapping events. Information recorded for each tap includes the time at which the tap-hole was opened and closed, tap masses of metal (measured) and slag (estimated), and a running total of the energy input to the furnace in MWh.

Furnace interruptions were identified using gaps of greater than 24 h between data entries, and served to divide the set into several distinct periods of continuous operation. Additional processing was performed to calculate tap-to-tap times (defined as the intervals between successive tap-hole closures) and tapping times (defined as the interval between opening and closing of the tap-hole) for each tap event. The average power setting for the furnace during each tap was also calculated using the energy totaliser reading and the tap-to-tap time. The entire data set was averaged to obtain estimates for the process energy requirement and ratio of slag to metal produced. These were found to be 4.19 MWh/ton metal and 1.13, respectively.

Subsets consisting of approximately 100 taps were then selected from the overall data set for comparison with models. Criteria for selection were that the subsets should contain no missing or error values, the subsets should not cross furnace interruption boundaries, and each of the operating periods should be represented by at least one subset. The full data set together with the nine subsets selected for the current study is shown in Fig. 2.

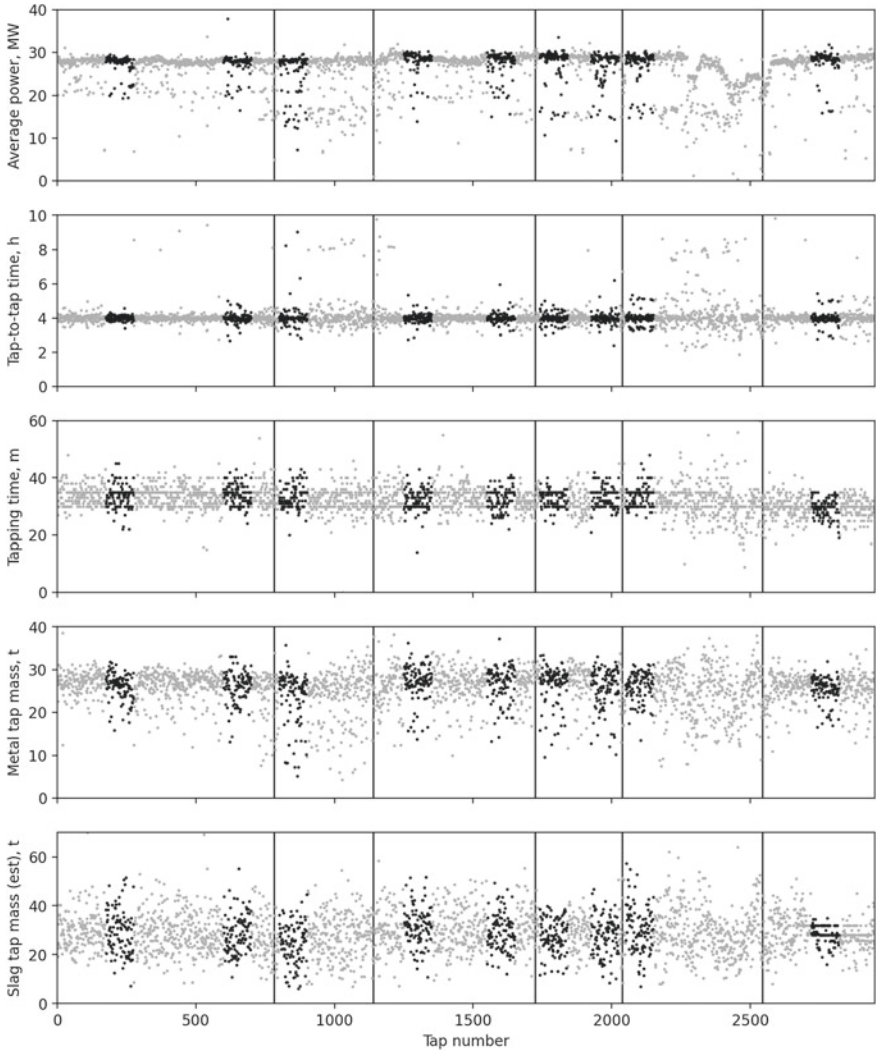

Fig. 2 Tap information from a 48 MVA silicomanganese smelter—vertical lines indicate periods of continuous operation, dark points show sample subsets selected for modelling study

Model Description

A reduced-order model for tapping from a silicomanganese furnace was developed according to the framework described in [6]. This framework combines dynamic mass balances on the furnace inventory with phenomenological descriptions of multiphase and porous media fluid flow effects during tapping. Tapping flowrates are governed by a pressure balance based on the levels of metal and slag in the furnace

Table 1 Parameters for silicomanganese tapping model

Parameter	Symbol	Value
Process-specific energy requirement	SER_m	4.19 MWh/t
Slag: metal production ratio	MSR	1.13
Furnace internal diameter	D_F	9.68 m
Furnace active area fraction[a]	α_A	0.75
Diameter of burden particles	$D_{p,b}$	0.03 m
Sphericity of burden particles	$\psi_{p,b}$	0.8
Burden void fraction	ϕ_b	0.5
Diameter of burden cavity at tap-hole entrance[b]	$D_{b,min}$	0.15 m
Tap-hole diameter	D_t	0.075 m
Tap-hole length	L_t	1.17 m
Tap-hole centreline height[c]	H_t	0.15 m
Tap-hole entry pressure loss coefficient	K_t	0.25
Tap-hole channel surface roughness	ϵ_t	0.001 m
Tap-hole channel friction factor correlation	f_D	Bellos et al. [2]
Metal density	ρ_m	4450 kg/m^3
Metal viscosity	μ_m	0.005 Pa s
Slag density	ρ_s	2550 kg/m^3
Slag viscosity	μ_s	1 Pa s

[a]Fraction of total furnace cross-sectional area occupied by molten bath
[b]Size of hemispherical region at tap-hole entrance which is clear of burden particles
[c]Relative to hearth level

interior, and a series of pressure drops defined by the properties of the burden and the geometry of the tap-hole. While power is supplied to the furnace, metal and slag are generated continuously according to the process energy requirement and the slag: metal production ratio; in this case, these were fixed by taking averages of the industrial data set as described earlier, however they could also be estimated from thermodynamic calculations.

All additional parameters needed for the silicomanganese tapping model were estimated from information supplied by the furnace operator together with literature sources [4, 7] and are given in Table 1.

The model was implemented as a self-contained package in the Python programming language [1]. The evolution of the metal and slag levels in the furnace over the duration of a tap were solved by explicit forward integration in time over a large number of small time steps (typically 5 s or less), producing filling and draining profiles according to the current state of the system. The fixed parameters in Table 1 were combined with information about tap-to-tap time, tapping time, and power

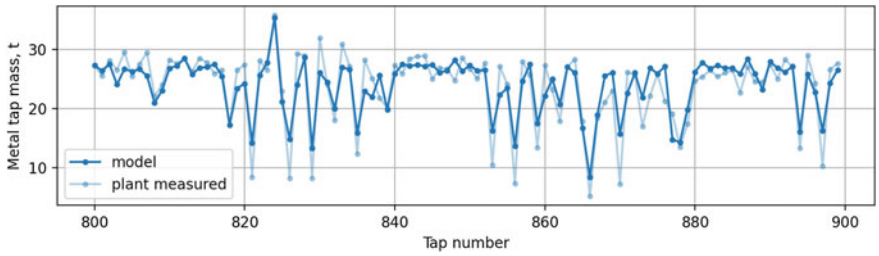

Fig. 3 Metal tap masses for tap data subset 3, showing measured values and model predictions

from the industrial data sets to generate a priori predictions of the system behaviour. These predictions were then compared to measured values in the data set to assess the model's performance.

Results and Discussion

For each of the nine subsets of plant data identified earlier, the tapping model was used to predict metal tap masses, slag tap masses, and the variation of metal and slag levels internal to the furnace. For each subset, the initial slag and metal levels in the simulated furnace were obtained by fitting to the data from the first tap in the sequence.

Metal Tap Masses

An example comparison between modelled metal tap mass and the values from the plant data set is shown in Fig. 3, for the third data subset. It can be seen that the model is in reasonable qualitative agreement with the measured tap masses, especially for capturing large deviations and irregular taps. Predictions at the end of the sequence appear to be of similar accuracy as those at the beginning, suggesting that errors are well controlled and the model is at least to some degree self-correcting. This is a desirable feature for a predictive tool, since it would potentially require less frequent recalibration.

Quantitative estimates of the model prediction error were generated for each data subset by calculating the relative difference between measured and predicted tap masses for each tap. In addition, the number of incorrect predictions of the direction of the change in mass between successive taps (i.e. will the following tap yield more or less metal than the current one?) was calculated. In both cases, smaller values are more desirable. The results are shown in Table 2.

Table 2 Model performance against measured metal tap masses

Data subset	Prediction error (%)	Direction error (%)
1	5.86	26
2	7.31	34
3	9.59	30
4	6.51	28
5	7.29	29
6	6.19	26
7	7.56	22
8	7.51	40
9	6.33	34

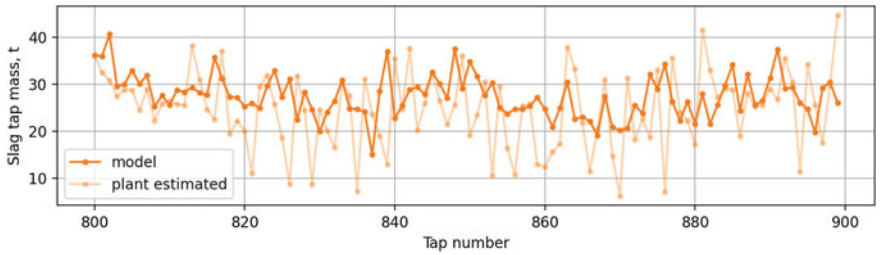

Fig. 4 Slag tap masses for tap data subset 3, showing plant estimates and model predictions

The average error in tap mass prediction for all data sets was found to be between 5 and 10%, while the error in direction change varied between 22 and 40%. These results are encouraging, and potential exists for further improvement by tuning some or all of the model parameters to best fit this particular furnace operation.

Slag Tap Masses

The furnace plant from which the data set was obtained does not measure tapped mass of slag directly, but rather infers it from the metal mass using empirical relationships. For interest, the tapping model predictions were compared to these empirical estimates. An example result is shown in Fig. 4, again for data subset 3.

Qualitatively it appears that the reduced-order model predicts the correct order of magnitude of values, and does track the broad long-term trends seen in the plant estimates—but it is obvious that there are significant differences on a per-tap basis. The plant estimates also exhibit a higher degree of variability with more outliers (similar to the metal tap masses) when compared to the model.

Quantitative error estimates were calculated as for the metal masses, and are given in Table 3. It can be seen that the average differences between the slag mass

Table 3 Model performance against estimated slag tap masses

Data subset	Prediction error (%)	Direction error (%)
1	26.4	55
2	25.0	51
3	28.7	51
4	20.6	53
5	21.7	64
6	21.4	52
7	23.7	54
8	26.4	55
9	14.8	49

estimates and the model predictions are much larger than those obtained for the metal tap masses, close to 25% across all data subsets. The direction change is also predicted poorly, being in error slightly more than 50% of the time.

Since the slag mass data were not directly measured [10], this raises the question of whether the data or model are in error here. Further investigation by performing slag tap mass measurement studies on the furnace plant (if feasible) would be advisable in order to resolve the issue and build further confidence in the model.

Furnace Levels

In order to demonstrate the type of additional information that can potentially be obtained from tapping system models, maximum and minimum of both the slag and metal levels inside the furnace were calculated from the model data for each tap. These represent the cyclic tidal changes in the furnace interior that occur during each tap, from empty (beginning of tap) to full (before tap-hole is opened) to empty again (after tap-hole is closed). The results for all data subsets are shown in Fig. 5.

It is interesting to observe that the metal levels in the furnace remain reasonably uniform. This is due to the fact that the furnace appears to be completely emptied of metal at each tap, and the level of the metal bath is therefore continuously "reset" to a fixed reference point. By contrast the slag inventory varies considerably over the tap sequences considered here, with evidence of both rapid dynamics between successive taps as well as slower variations and oscillations occurring over much longer time periods.

Bath levels cannot be easily measured on operating furnaces (although it may be possible to infer them to some degree from the position and movement of the three electrodes), and these results should therefore best be interpreted as qualitative rather than quantitative. A well-tuned and reliable model that is validated against tap mass

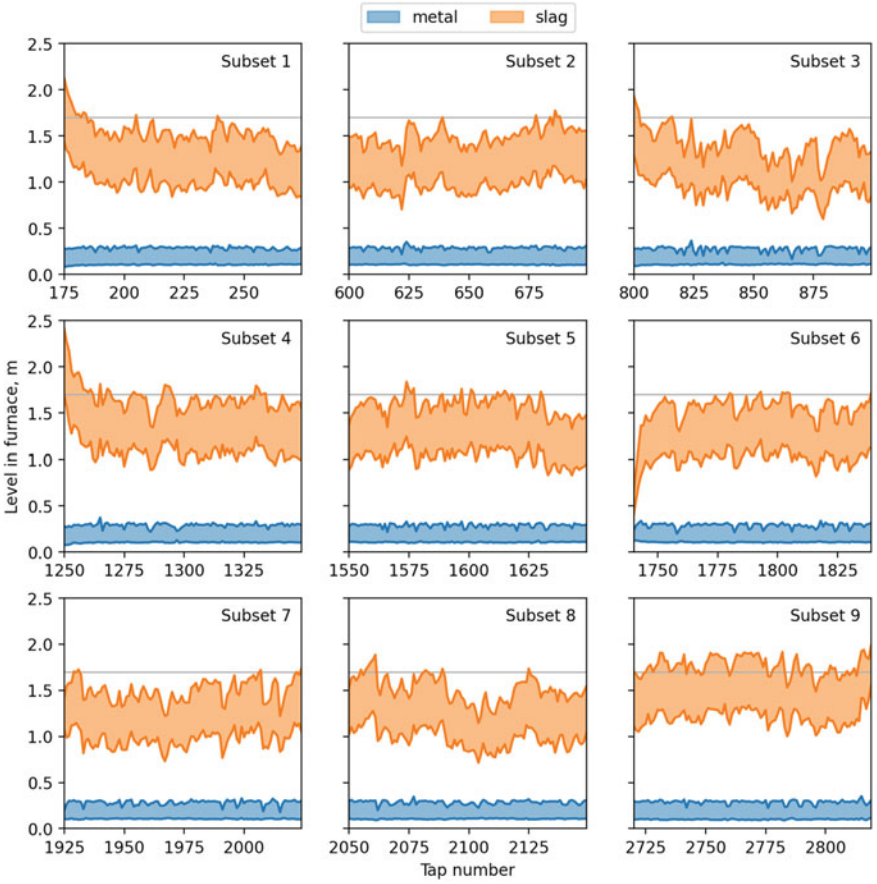

Fig. 5 Slag and metal furnace level variations as predicted by reduced-order model (grey lines indicate a representative 1.7 m electrode tip position [9]) (Color figure online)

data may nonetheless be of some utility by permitting operators to relate furnace inventory changes to other observed phenomena.

Conclusions

A reduced-order model of the silicomanganese furnace tapping process was successfully implemented. Model predictions were compared against several data sets extracted from plant data obtained from an operating 48 MVA silicomanganese furnace. Although only generic estimates of the model parameters were used, predictions agreed well with the observed dynamics in the measured metal tap masses. Com-

parison of the model with slag tap mass data was less convincing; however, an open question remains due to the fact that these masses are not directly measured on the plant. The slag and metal inventory behaviour was extracted from the model results and showed a number of interesting features including appreciable dynamics in the slag levels inside the furnace.

Much work still remains to be done in this area of study. In particular, extending the validation of the model with comparisons to measured metal tap masses from silicomanganese furnaces of a variety of designs and scales is currently being considered, and a measurement campaign to understand the reasons for the model's poor performance in predicting slag tap masses would be of value. In addition, new or existing furnace measurements that can be used to infer the accuracy (or lack thereof) of the bath-level predictions produced by the model will be explored. Finally, the integration of simple phenomenological models such as this with top-down, data-driven techniques in order to reach levels of accuracy and robustness that cannot be achieved by either approach in isolation is an exciting area of research—at present this appears to be the most likely path toward development of practical digital twins of furnace tapping systems in the future.

Acknowledgements This paper is published by permission of Mintek and Transalloys.

References

1. Python Software Foundation (2020). https://www.python.org/
2. Bellos V, Nalbantis I, Tsakiris G (2018) Friction modeling of flood flow simulations. J Hydraul Eng 144(12):04018073
3. Bublik S, Olsen JE, Loomba V, Reynolds QG, Einarsrud KE (2021) A review of ferroalloy tapping models. Metall Mater Trans B 52:2038–2047
4. Muller J, Zietsman JH, Pistorius PC (2015) Modeling of manganese ferroalloy slag properties and flow during tapping. Metall Mater Trans B 46B:2639–2651
5. Nelson LR, Hundermark RJ (2016) The tap-hole—key to furnace performance. J South Afr Inst Min Metall 116(5):465–490
6. Olsen JE, Reynolds QG (2020) Mathematical modeling of furnace drainage while tapping slag and metal through a single tap-hole. Metall Mater Trans B 51(4):1750–1759
7. Olsen SE, Tangstad M, Lindstad T (2007) Production of manganese ferroalloys. Tapir Academic Press, Trondheim, Norway
8. Steenkamp JD, Basson J (2013) The manganese ferroalloys industry in southern Africa. J South Afr Inst Min Metall 113:667–676
9. Steenkamp JD, Gous JP, Grote W, Cromarty RD, Gous HJ (2018) Process zones observed in a 48 MVA submerged arc furnace producing silicomanganese according to the ore-based process. In: Extraction 2018, Ottawa, Ontario, Canada, Aug 2018, pp 639–651. The Minerals, Metals & Materials Society
10. Steenkamp JD, Hayman DA, Bezuidenhout PJA (2019) Benchmark for tap-hole lifecycle management practices in silicomanganese production when submerged arc furnace technology of circular design is applied. JOM 71(7):2430–2434

Tapped Alloy Mass Prediction Using Data-Driven Models with an Application to Silicomanganese Production

Alexey Vladimirovich Cherkaev, Khutso Rampyapedi, Quinn Gareth Reynolds, and Joalet Dalene Steenkamp

Abstract The accounting mass balance on pyrometallurgical plants, to which the tapped masses of alloy and slag are essential inputs, forms an integral part of the process control and planning of any smelter. Thus, it is desirable to be able to predict tapped mass ahead of time. This paper examines three data-driven models that aim to predict tapped alloy mass for a submerged arc furnace producing silicomanganese. All the models are linear and based on lagged data and, thus, can be described as autoregressive models with exogenous inputs (ARX). They differ in the selection of the predictors. Ordinary least squares (OLS) model uses all of the available predictors, whereas least absolute shrinkage and selection operator (LASSO) model selects most important predictors and partial least squares (PLS) model finds best predictors in the latent space. Feature selection analysis is performed on the model results. It is shown that the model based on OLS with a reduced number of the predictors slightly outperforms other models. It is shown that power input is the strongest predictor of the tapped alloy mass, confirming current industry practice. Tap duration, energy input corresponding to the previous tap, and the previously tapped alloy mass are shown to be weak but statistically significant predictors. Using mutual information, it was shown that it was not possible to improve tapped mass prediction accuracy using tapping and recipe data alone.

Keywords Silicomanganese · Ferroalloys smelting · Tapped mass · Machine learning · ARX model · LASSO regression · PLS regression · Feature selection · Mutual information

A. V. Cherkaev (✉) · Q. G. Reynolds · J. D. Steenkamp
MINTEK, Randburg 2125, South Africa
e-mail: Alexey.Cherkaev@outlook.com

K. Rampyapedi
Transalloys, Emalahleni, South Africa

Q. G. Reynolds
University of Stellenbosch, Private Bag X1, Matieland, Stellenbosch 7602, South Africa

J. D. Steenkamp
University of the Witwatersrand, 1 Jan Smuts Ave, Johannesburg 2000, South Africa

J. D. Steenkamp et al. (eds.), *Furnace Tapping 2022*, The Minerals, Metals & Materials Series, https://doi.org/10.1007/978-3-030-92544-4_11

Introduction

Transalloys is a manganese ferroalloy producer situated in a coal mining town of eMalahleni, Mpumalanga Province, South Africa. Its main product is silicomanganese (SiMn) containing 16.4% Si, 66.5% Mn, 1.8% C, and 15.5% Fe on average [1]. Transalloys operations consist of 5 submerged arc furnaces (SAFs): one rated at 15 MVA, two at 22 MVA, and the last two at 48 MVA. All SAFs have an open-roof design [1]. For the purpose of this study, one of the 48 MVA SAFs was chosen for analyses.

Figure 1 presents a basic schematic of the inputs and outputs to the SAF. Blends of different types of manganese ores as well as briquettes, different types of carbonaceous reductants, and quartzite are fed into the furnace intermittently. Power, in the form of electricity, is added continuously through three electrodes, submerged into the burden of raw material, and an alternating current power supply. Slag and alloy, typically produced at a ratio of 1.1:1.0, are tapped intermittently, at 4 h intervals, through a single-level tap-hole. The CO-rich off-gas is combusted at the top of the burden to form CO_2. Not all of the electrical energy supplied is utilized in the process. Some of it is lost to atmosphere via the furnace containment system.

Currently, the main key performance indicator (KPI) for predicting the tapped alloy mass is the power efficiency of a particular SAF, i.e. the ratio of supplied energy to mass of tapped alloy (MWh/ton) with values of 3.5–4.5 MWh/ton typical for the process [2]. Practically, the power efficiency will vary from time-to-time based on the furnace condition. A poor efficiency (higher MWh/ ton alloy) is often an indication that energy is not applied correctly. This is often the case when operating on very short electrodes. Metallurgy also plays a role in power efficiency. A silicon content that is higher than the specified amount will lead to a higher MWh/ton alloy. It is also

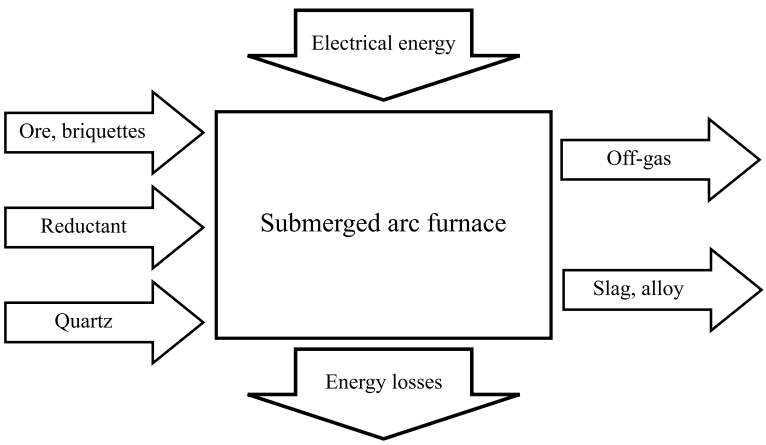

Fig. 1 Basic schematic of inputs and outputs of a submerged arc furnace applied in the production of silicomanganese

possible to experience a low power efficiency with a furnace that has correct electrode length and metallurgy. A furnace is normally tapped for 30 min and if there is an obstruction on the tap-hole then there will be a reduced flow rate of alloy and slag within the 30 min duration. This phenomenon is also responsible for a production backlog thus resulting in lower power efficiency.

Being able to reliably predict the tapped alloy mass to be expected at each tap, will allow for improved management of the post-tap-hole processing of the five furnace operation. In particular, alloy mass prediction helps to select a ladle with enough capacity for the anticipated tap mass and it makes it possible to plan a casting schedule. This study therefore aims to improve the prediction of the tapped alloy mass by inclusion of variables other than power efficiency. A data-driven approach is chosen and machine learning methods are used to identify the strongest predictors of the tapped mass.

The rest of the paper is structured as follows. Section "Background" presents the background for machine learning methods. Section "Data Description" describes the data used in this paper. Section "Data Embedding and ARX Models" outlines the models chosen for the analysis. Section "Results" presents the results. Sections "Discussion" and "Conclusions" present discussion and conclusions, respectively.

Background

Machine learning (ML) is a subfield of artificial intelligence that uses a data-driven approach to construct predictive models [3]. Such models vary from simple linear models, such as linear regression, to more complex nonlinear opaque models, such as artificial neural networks or support vector machines [4]. Normally, machine learning models perform one out of three common tasks: regression, classification, and data decomposition. Regression refers to prediction of continuous output, such as temperature or mass. Examples of regression models include linear regression, regression trees, feed-forward neural networks, Gaussian process regression [4, 5]. Classification is a prediction of a class of the output, e.g. "normal state" versus "fault state" or identifying a digit from a scanned image. The output of these models is discrete and finite. Commonly used classification models are logistic regression, linear decomposition analysis (LDA), k-nearest neighbor (kNN), classification trees, support vector machine (SVM), and others [4]. Finally, data decomposition refers to a large set of methods with the aim to somehow simplify the data: remove noise, remove redundant variables, or decompose signal to statistically independent components. Typical methods from this group include principal component analysis (PCA), self-organizing maps (SOM), and autoencoders [4, 6, 7]. Since the tapped alloy mass is a continuous variable, the model must be selected from a regression group.

The sequence of observations of an operating furnace may be important as the effect of the changes introduced at some point in time may only become apparent later. The dataset with such observations is referred to as a time series (multivariate time series if multiple variables are observed). Specialized ML models exist to construct

the predictions from time series data [8]. A typical task is to predict the next output based on its past values

$$y_{t_0+\Delta t} = f(y_{t_0}, y_{t_0-\Delta t}, \ldots) + \varepsilon,$$

where $f(\cdot)$ is some functional relation and ε denotes unaccounted effects (past and present).

Linear models of this form are known as auto-regressive moving average (ARMA) models. If additional m input variables, $x_{j,t}, j = 1, \ldots, m$, are considered with their past (lagged) values,

$$y_{t_0+\Delta t} = \sum_{i=1}^{p} \alpha_i y_{t_0-i\Delta t} + \sum_{i=1}^{q} \beta_i \varepsilon_{t_0-i\Delta t} + \sum_{j=1}^{m} \sum_{i=0}^{r} \gamma_{ji} x_{j,t_0-i\Delta t} + \varepsilon_{t_0},$$

where α_i, β_i, and γ_{ji} are regression coefficients, and p, q, and r define the furthest past values for auto-regressive, moving-average, and exogenous parts, respectively, such models are referred as ARMAX, ARMA model with exogenous inputs. Non-linear time series models can be also constructed. Long short-term memory (LSTM) machines are an example of such a model based on a recurrent neural network structure [9]. Since the dataset used in this study has a limited number of observations (783 observations, see section "Background" for more details), only linear models were considered.

Estimation of the parameters of an ARMAX model requires the solution of a non-linear optimization problem since both regression errors ε_t and regression coefficients β_i need to be estimated [8]. This problem can be simplified considerably if the effect of past errors is dropped (moving-average part) and the model is transformed to ARX (auto-regressive model with exogenous inputs):

$$y_{n+1} = \sum_{i=1}^{p} \alpha_i y_{n-i} + \sum_{j=1}^{m} \sum_{i=0}^{r} \gamma_{ji} x_{j,n-i} + \varepsilon_n, \tag{1}$$

where n refers to the time index, $t_0 = n\Delta t$, and is introduced to simplify the notation. This problem can be viewed as a simple linear regression problem where the set of predictors is augmented by their past values. This augmentation, i.e. the replacement of a single value $x_{j,n}$ by a vector of values $(x_{j,n}, x_{j,n-1}, \ldots, x_{j,n-r})$, is called *data embedding*. While embedding enables the capture of time evolution of the data sequence in the model, it also increases the dimensionality of the data: instead of m predictors, there are now $p+m(r+1)$ predictors. Such dimensionality expansion can hinder the learning process. Thus, some feature selection may need to be performed to produce an accurate model.

There are various ways to perform feature selection, including PCA, backward and forward stepwise selection, or using regularized models, such as ridge or least

absolute shrinkage and selection operator (LASSO) regressions [4]. Partial least-squares (PLS, sometimes also decoded as *projections to latent structure*) is another approach that automatically constructs the sequence of best (latent) predictors [4].

The quality of the model can be assessed using various metrics describing the goodness of fit and by analyzing the residuals. Coefficient of determination is commonly used to describe the goodness of fit of linear models:

$$R^2 = 1 - \frac{\sum_n \left(y_n - \hat{y}_n\right)^2}{\sum_n (y_n - \overline{y})^2},$$

where $\hat{y}_n$ is the value predicted by the model and $\overline{y}$ is the average value of the output [4]. R^2 can be interpreted as the portion of variance explained by the model. Mean absolute error (MAE),

$$\text{MAE} = \frac{1}{N}\sum_{n=1}^{N}\left|y_n - \hat{y}_n\right| = \frac{1}{N}\sum_{n=1}^{N}|\varepsilon_n|,$$

is another metric that is often used to complement R^2 [10]. Root-mean-squared error (RMSE) is yet another metric [4, 10]:

$$\text{RMSE} = \sqrt{\frac{1}{N}\sum\nolimits_{n=1}^{N}\left(y_n - \hat{y}_n\right)^2} = \sqrt{\frac{1}{N}\sum\nolimits_{n=1}^{N}\varepsilon_n^2}.$$

If the model incorporates all important predictors, the model residuals, ε_n, are expected to follow Gaussian distribution since Gaussian distribution arises when a large number of (small) independent random variables are added—random noise (central limit theorem, [11]).

Mutual information (MI) between two random variables X and Y is defined as follows:

$$I[X, Y] = -\iint p_{XY}(x, y)\ln\frac{p_X(x)p_Y(y)}{p_{XY}(x, y)}\mathrm{d}x\mathrm{d}y,$$

where p_X, p_Y and p_{XY} are probability density functions (PDF) of variable X, variable Y, and their joint distribution, and the integration is taken over all values of variables X and Y [12]. If variables X and Y are independent ($p_{XY}(x, y) = p_X(x)p_Y(y)$), their mutual information is zero. MI reaches maximum if two variables are connected by a functional relation, i.e. $Y = f(X)$, even if this relation remains unknown. The maximum of MI for a given variable X can be estimated by putting $Y = X$. For interpretability it is more convenient to introduce relative mutual information $RI[X, Y]$ as follows:

$$RI[X, Y] = \frac{I[X, Y]}{I[X, X]}. \tag{2}$$

Relative MI can be interpreted as the portion of variability of X explained by Y and it can be conveniently expressed as a percentage.

In this paper, three ARX models with different regularization procedures were tested for the prediction of tap alloy mass and predictor selection: full linear regression model with 20 predictors, LASSO linear regression and PLS model (section "Data Description"). Full linear regression is also referred as ordinary linear regression (OLS) to contrast it with LASSO regression and PLS. LASSO regression was selected over ridge regression since the former automatically identifies the most important predictors and removes unimportant variables from the model, whereas the latter tends to keep all the predictors. The results of the methods are examined and the set of the best predictors (additional to energy input) are identified (section "Results"). The model residuals are examined using mutual information (MI) to test if the accuracy can be further improved by the addition of non-linear features.

The analysis conducted in this paper used R programming language, `glmnet` package for LASSO regression [13], `pls` package for PLS [14], and `infotheo` package to compute mutual information [15].

Data Description

The data provided by Transalloys comprises tapped (1) alloy mass in tons, (2) energy input between consecutive tap starting times in MWh, (3) tap duration in minutes, and (4) tap interval in hours, for a single furnace producing silicomanganese alloy. Additionally, the recipes history gives the information on the (5) mass of ore in kg, (6) reductant in kg, and (7) flux in kg, used for this furnace. The recipes data was merged with tap data using zero-hold extension (last value carried forward) of recipes since tapping is performed more frequently than recipe change. The data spans the period of 130 days and consist of 783 taps.

As a standard (in ML) pre-processing step, all the variables in the data were standardized: the variable mean was subtracted and the values were re-scaled using standard deviation. The example of a few variables is shown in Fig. 2. Note that although the tap interval was set to 4 h on the plant, due to various reasons it may vary. Hence, *Tap Interval* was included as a separate variable.

Data Embedding and ARX Models

For the current study the embedding with lags $p = r = 2$ (see Eq. (1)) was used as it was not expected to pick up the effects that preceded the tap by more than 8 h. As a result, the original dataset with 7 variables and 783 observations was replaced by the

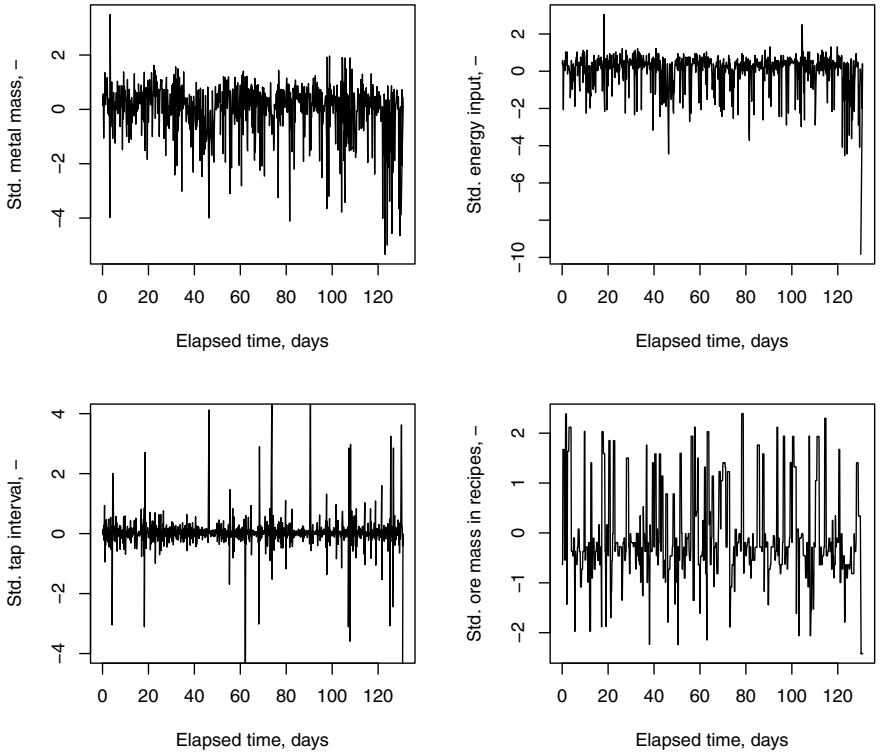

Fig. 2 An example of time series of four variables from the dataset used in the study

dataset with 21 variables (see Fig. 3) and 781 observations (the first 2 observations had to be removed since they do not have all lagged values). Out of 21 variables, 1 is the response (tapped metal mass) and other 20 form the set of predictors.

The full dataset of 781 observations was split to training data with 546 observations and testing data with 235 observations. The former was used to train the models and to fine-tune hyperparameters (see further below), whereas the latter was used to validate the models and to assess their accuracy.

The full linear regression model (or ordinary linear regression, OLS) fits the model of the form (Eq. (1) with $p = r = 2$):

$$y_n = A + \alpha_1 y_{n-1} + \alpha_2 y_{n-2} + \sum_{j=1}^{m} \sum_{i=0}^{2} \gamma_{j,i} x_{j,n-i} + \varepsilon_n. \tag{3}$$

LASSO model fits the same model as in Eq. (3) but it additionally constrains all the coefficients to satisfy the following condition:

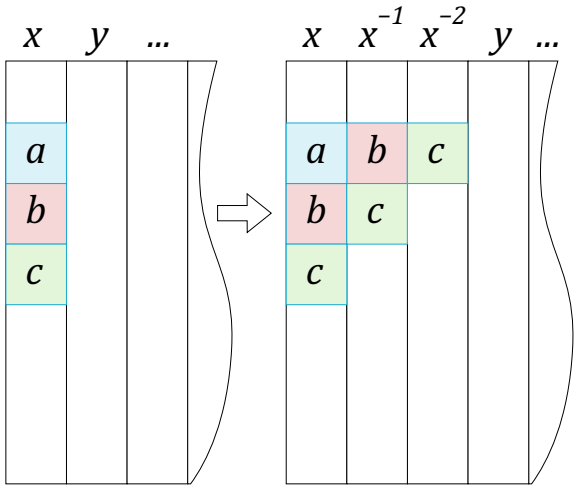

Fig. 3 Schematic representation of the embedding with two lagged values. Each variable x generates three variables: x itself, x^{-1} consisting of values x_{n-1}, and x^{-2} with values x_{n-2}

$$|A| + |\alpha_1| + |\alpha_2| + \sum_{j=1}^{m} \sum_{i=0}^{2} |\gamma_{j,i}| \leq \lambda,$$

where λ is the regression "budget" [5]. To satisfy the "budget", LASSO regression puts insignificant coefficients to zero, producing sparse models. Since the parameter λ needs to be specified upfront and cannot be learned by the regression procedure, it is a hyper-parameter that needs tuning. λ was tuned using tenfold cross-validation on the training data [5]. This tuned value then was used to perform LASSO regression.

Partial least squares (PLS), in contrast to OLS, first finds the directions (latent variables) in the predictors space that provide the best linear fit for the response. The number of latent variables for the method to use is a hyperparameter. This hyper-parameter is easy to fine-tune since the method is embedded: it finds an additional latent variable based on already found directions. Thus, the fine-tuning only requires the regression to be performed once with a large enough number of latent variables and then choosing the number of components once the resulting fit stops improving.

Results

Hyperparameter Fine-Tuning

Only LASSO and PLS regression methods required hyperparameter tuning. The value of λ for LASSO regression by itself is not informative, but it is worth mentioning that the values in the range from 0.001 to 100 were tested and the best value found (for this dataset) was 0.01.

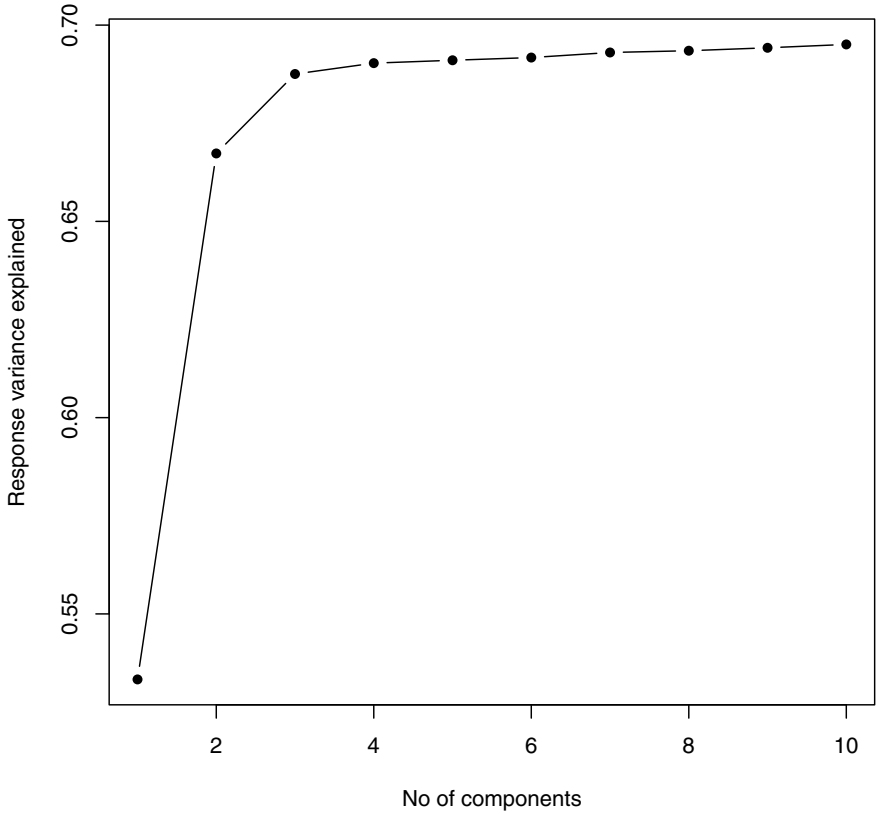

Fig. 4 Amount of the response variance explained in the training dataset based on the number of components of the PLS model

The PLS regression was performed with the maximum of ten components. The amount of variance explained for each number of components is shown in Fig. 4. It is obvious that using more than three components does not considerably improve the fit. Thus, three components were used for the rest of the analysis.

OLS and LASSO Predictors Selection

Ordinary least squares regression provides useful statistics associated with the regression coefficients. These statistics can be used to reduce the number of predictors. The OLS method applied to the tapping dataset resulted in (current) tap duration, energy input, energy input for previous tap, and the previously tapped alloy mass (lag of one step) being the most significant predictors.

Table 1 Comparison of the model performance on training and testing datasets using different metrics: coefficient of determination (R^2), MAE, and RMSE. The best-performing model according to each metric is highlighted

Metric	Model			
	Full OLS	LASSO	PLS	Reduced OLS
R^2, training	**0.71**	0.7	0.7	0.69
R^2, testing	0.71	0.72	0.71	**0.73**
MAE, training	**0.4**	0.41	0.41	0.41
MAE, testing	0.4	0.39	0.4	**0.38**
RMSE, training	**0.55**	0.56	0.56	0.57
RMSE, testing	0.51	0.5	0.51	**0.49**

LASSO regression additionally selected intercept A, current tap interval, the tapping duration of the last but one tap (lag 2), the last but one tapped alloy mass, and the last but one mass of the flux in the recipe.

Based on the results of the full OLS model, it was decided to train a reduced OLS linear model, using only predictors that were found significant by a full OLS model. The results reported in the next subsection include the results of this model.

Goodness of Fit

The goodness of fit for the models was tested on the testing portion data. For completeness, Table 1 shows the model performance on both training and testing data. It is evident that all models performed similarly. Although the reduced OLS model shows slightly higher errors on training data, it outperforms all other models on testing data.

Analysis of Residuals

Only the testing residuals from the reduced OLS model are presented here. The histogram of the residuals is shown in Fig. 5. Shapiro–Wilk test for the residuals has a p-value of 0.065 which for this test means that the residuals are unlikely to be normally distributed.

Relative mutual information (relative MI, see Eq. (2)) was computed for the residuals and all the predictors and the response (tapped alloy mass). It has a maximum for the current tap alloy mass (Table 2). It is considerably smaller for all the predictors, including power input.

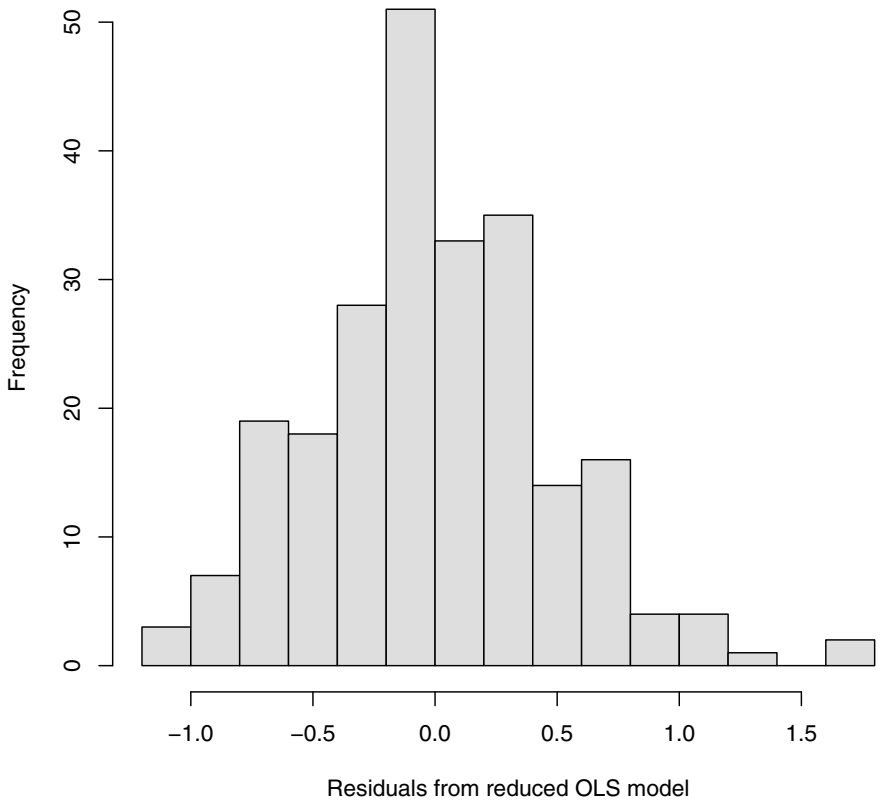

Fig. 5 Distribution of the reduced OLS model residuals

Discussion

The performance of all tested models is similar. This is expected since they are all linear models. The only difference is the selection of predictors. The reduction of the number of the components helps to avoid model overfitting. This is evident from the performance of the reduced OLS model: on the testing set, its performance is slightly superior to other models. PLS model has the least number of the predictors, 3. While it is possible that the addition of 1 or 2 more components will improve its performance, it has reduced explainability compared to other models since the regression is performed against latent variables.

As expected, current (before current tap) power input is the strongest predictor of the tapped mass: if it is used as a single predictor, its $R^2_{\text{test}} = 0.71$, which is only marginally worse than that for the reduced OLS model. Having said this, tap duration, previously tapped alloy mass and previous energy input are statistically significant predictors of the next tapped alloy mass.

Table 2 Relative mutual information (relative MI, see Eq. (2)) of the residuals of the reduced OLS model with other predictors. Relative MI with the predictors lagged by two steps is not shown due to their low values. Relative MI of the residuals and the tapped alloy mass (highlighted) has the maximum value among all the variables

	Tap duration	Energy input	Tapped metal mass	Tap interval	Reductant mass	Ore mass	Flux mass	Lagged tap duration	Lagged energy input	Lagged tapped metal mass	Lagged tap interval	Lagged reductant mass	Lagged ore mass	Lagged flux mass
Relative MI with residuals	3.1%	4.0%	13.6%	3.4%	1.9%	2.2%	3.0%	3.3%	2.7%	4.8%	2.7%	3.3%	4.7%	3.7%

Previously tapped alloy mass coefficient in the model is negative, meaning if the previous tap resulted in a large alloy mass, the next tapped mass will (likely) be smaller. This is unsurprising, since the average tapped mass is constrained by the material inlet flow, which remains relatively constant.

The energy input for the previous tap and the next tapped mass are positively correlated. This means that some of the energy that was put into the furnace carries over to the next tap.

Surprisingly, the tap duration is negatively correlated with the tapped mass. This correlation is weak but nonetheless present. A possible explanation for this is as follows: tap duration is usually set to 30 min and it is only extended if the flow from the tap is obstructed. However, the obstructed flow will still result in a lower tapped mass even with the extended tap duration.

The model residuals distribution (see Fig. 5) is far from Gaussian. The Gaussian distribution is expected if a random variable is comprised of the sum of many independent random variables. Therefore, it is possible that there are a few (hopefully) identifiable effects that can explain some variability of the residuals. Mutual information analysis has shown that these effects—linear or nonlinear—cannot be found among already considered predictors. Thus, the next step would be to consider the tapped alloy mass with more detailed recipes information and additional process monitoring variables (hearth temperature, current between electrodes, etc.).

Conclusions

The aim of this study was to identify the model and the predictors of the tapped alloy mass. Only linear models were considered due to the limited size of the available dataset. To incorporate the dynamics of the process, all the variables were considered together with the lagged values (embedded data). Embedding produced the dataset with 20 predictors. The LASSO model and PLS models showed that the number of predictors can be significantly reduced. Based on their results, reduced OLS model was proposed that only included four predictors. That model showed slight improvement of the performance, compared to the other models. Power input, as expected, is the strongest predictor of the tap alloy mass. Other predictors, such as current tap duration, power input for the previous tap and previously tapped alloy mass, have statistically significant but small contribution to the tapped mass prediction. Surprisingly, the recipe variables (ore, reductant, and flux masses) cannot act as reliable predictors. It is proposed to use more detailed recipe information and process monitoring data in order to find more precise tap alloy mass model.

Acknowledgements The financial assistance of the National Research Foundation (NRF) toward this research is hereby acknowledged. Opinions expressed and conclusions arrived at are those of the author and are not necessarily to be attributed to the NRF.

This paper is published by permission of Mintek and Transalloys.

Conflict of Interest On behalf of all authors, the corresponding author states that there is no conflict of interest.

References

1. Steenkamp JD, Maphutha P, Makwarela O, Banda WK, Thobadi I, Sitefane M, Gous J, Sutherland JJ (2018) Silicomanganese production at Transalloys in the twenty-tens. J South Afr Inst Min Metall 118:309–320
2. Matinde E, Steenkamp JD (2021) Metallurgical overview and production of slags. In: Piatak NM, Ettler V (eds) Metallurgical slags: environmental geochemistry and resource potential 2017. Royal Society of Chemistry, pp 14–58
3. Mitchell T (1997) Machine learning. McGraw-Hill, New York
4. James G, Witten D, Hastie T, Tibshirani R (2017) An introduction to statistical learning with applications in R. Springer
5. Schulz E, Speekenbrink M, Krause A (2018) A tutorial on Gaussian process regression: modelling, exploring, and exploiting functions. J Math Psychol 85:1–16
6. Kohonen T (1982) Self-organized formation of topologically correct feature maps. Biol Cybern 43:59–69
7. Kramer MA (1991) Nonlinear principal component analysis using autoassociative neural networks. AIChE J 37:233–243
8. Chatfield C (1996) The analysis of time series. An introduction, 5th edn. Chapman & Hall/CRC
9. Hochreiter S, Schmidhuber J (1997) Long short-term memory. Neural Comput 9:1735–1780
10. Willmott CJ, Matsuura K (2005) Advantages of the mean absolute error (MAE) over the root mean square error (RMSE) in assessing average model performance. Clim Res 30:79–82
11. Loeve M (1977) Probability theory I. Springer, New York
12. Bishop CM (2011) Pattern recognition and machine learning. Springer, New York
13. Friedman J, Hastie T, Tibshirani R (2010) Regularization paths for generalized linear models via coordinate descent. J Stat Softw. https://doi.org/10.18637/jss.v033.i01
14. Mevik B-H, Wehrens R, Liland KH (2020) pls: partial least squares and principal component regression. https://cran.r-project.org/web/packages/pls/index.html. Accessed 2 Sept 2021
15. Meyer PE (2014) infotheo: information-theoretic measures. https://cran.r-project.org/web/packages/infotheo/index.html. Accessed 2 Sept 2021

Slag Reduction and Viscosities Interaction in Ferromanganese Process

Tichaona Mukono, Maria Wallin, and Merete Tangstad

Abstract Slag reduction and viscosity are closely related in the practical operation of a submerged arc furnace for ferromanganese (FeMn) production. The viscosity of slag is dependent on temperature and its composition, and influences different aspects in the FeMn production process, namely reduction kinetics and final MnO content of slag, slag–metal separation, slag flow in the furnace, and ultimately furnace tapping. As such, it is paramount to establish knowledge about the relationship between slag reduction and viscosities. The kinetics of MnO reduction in FeMn slags based on Nchwaning, Comilog, and UMK ores were investigated between 1400 and 1550 °C. The extent of reduction was determined by thermogravimetry, slag morphology, and change during reduction was examined by electron probe micro-analyzer and slag viscosities calculated using FACTSage 8.1 thermochemical software. Results show that viscosity of primary FeMn slag is higher and decreases with increasing dissolution of solid phase into liquid as temperature increases.

Keywords Slag reduction · Kinetics · Viscosity · Ferromanganese

Introduction

The production and reduction of slag is a key aspect of the ferromanganese (FeMn) alloy production process [1]. In the high-temperature zone of the furnace, gangue minerals in the furnace feed materials, fluxes and residual MnO from the smelting reaction combine to form a slag which consists of a mixture of different oxides (e.g., MnO, SiO_2, Al_2O_3, CaO, and MgO) and is characteristically immiscible to the recovered FeMn alloy. Considering the process reactions in the submerged arc furnace (SAF), the prereduction zone involves the prereduction of higher manganese oxides and iron oxides (MnO_2, Mn_2O_3, Mn_3O_4 to MnO and Fe_2O_3, Fe_3O_4, FeO to Fe). However, final reduction of MnO in the high-temperature cokebed zone is by either solid carbon or carbon dissolved in alloy according to the following reaction:

T. Mukono (✉) · M. Wallin · M. Tangstad
Norwegian University of Science and Technology, Trondheim, Norway
e-mail: tichaona.mukono@ntnu.no

J. D. Steenkamp et al. (eds.), *Furnace Tapping 2022*, The Minerals, Metals & Materials Series, https://doi.org/10.1007/978-3-030-92544-4_12

$$MnO_{(l)} + C_{(s,l)} = Mn_{(l)} + CO_{(g)} \quad (1)$$

The kinetics of the reduction of MnO has been extensively studied by several researchers [2–7]. The reduction reaction has been modelled by the following reaction [3]:

$$\begin{aligned} R_{MnO} &= k_{MnO} \cdot A \cdot (a_{MnO} - a_{MnO,eq}) \\ &= k_{0,MnO} \cdot A \cdot \exp(-E_{MnO}/RT) \cdot (a_{MnO} - a_{Mn}/K_{eq}) \end{aligned} \quad (2)$$

where R_{MnO} is the reduction rate (g/min), k_{MnO} is the rate constant (g/min cm^2), k_0 is the pre-exponential factor, A is the reaction interface area (cm^2), E_{MnO} is the activation energy (kJ/mol), R is the ideal gas constant (J/mol K), T is the temperature (K), a_{MnO} is the activity of MnO in the slag, $a_{MnO,eq}$ is the equilibrium activity of MnO in the slag phase, a_{Mn} is the activity of Mn in alloy phase, and K_{eq} is the equilibrium constant at temperature T. The reaction rate constant follows the Arrhenius expression and ($a_{MnO} - a_{Mn}/K_{eq}$) is the driving force of the reaction. The MnO reduction reaction has been concluded to be controlled by interfacial chemical reaction and is highly dependent on temperature and ore chemical composition [3, 5, 8]. Tangstad [8] established that MnO reduction increases with increase in temperature and the reduction rate is rapid in the two phase region, i.e. when solid MnO coexists with a liquid slag phase saturated with MnO. This is due to the activity of MnO which will be high and constant until the complete dissolution of manganosite into liquid slag. Further MnO reduction through the completely liquid slag phase will take place at a rapidly decreasing rate resulting from the decreasing activity of MnO.

The reduction behavior of different ore materials in the FeMn process are different as they possess different ore chemistry, mineralogy, and melting properties. In addition, the dissolution behaviors are different which affects changes in slag viscosities during reduction [1, 6]. Slag viscosity has been reported by several researchers to be highly dependent on temperature and slag composition [9–11]. Jang et al. [9] studied the effect of controlling slag composition on the separation of alloy and slag in the refining stages of medium carbon FeMn alloy. It was reported that controlling the SiO_2 content in the slag to 32% lowered viscosities of the slag and thus increased fluidity and better metal/slag separation. In other works, Sunahara et al. [10] highlighted that slag drainage is a fluidization phenomenon dominated by viscosity in which the drainage rate decrease with increasing slag viscosity. An increase of MgO content in the slag was found to be effective in maintaining slag drainage under high Al_2O_3 concentrations in slag. The results from the published literature, commonly highlight that slag viscosity is an important variable in furnace operation which is indicative of the ease with which slag could be tapped from the furnace. Therefore, the composition of ferromanganese slag is important in determining the slag/metal equilibrium relations, MnO content of final slag, as well as slag viscosity which is expected to influence the furnace tapping process.

In the EU funded PreMa project [12], pretreatment of manganese ores is suggested with the main goal of reducing the overall energy consumption on the SAF process,

coke consumption, and CO_2 emissions. As part of PreMa, the effect of pretreatment, i.e., extent of prereduction of manganese ores on the metal producing reactions is investigated in this work. In the practical operation of a SAF for FeMn production, slag reduction and viscosity are closely related as they are both dependent on temperature and composition. They influence different aspects in the FeMn production process, namely reduction kinetics and final MnO content of slag, slag–metal separation, slag flow in the furnace, and ultimately furnace tapping. Therefore, the present study focuses mainly on the experimental investigation of the reduction behavior of different manganese ores. In the current work, slag viscosities are calculated using the FactSage 8.1 viscosity module as this method of estimating slag viscosities has been reported to be quite reliable [13].

Experimental

Preparation of Raw Materials

Three different manganese ores, namely UMK (United Manganese of Kalahari), Comilog, and Nchwaning ores were utilized in this work. The ores were ground and sieved into particle size fractions of 3.15–4 mm and were chemically analysed by SINTEF Norlab using X-ray fluorescence, while the oxygen amount connected to Mn oxides was obtained by titration for each ore type. Eltra (combustion-IR) was used to determine the amount of carbon, which was recalculated to CO_2 in the carbonate minerals. The composition of the raw materials is shown in Table 1. The raw materials in each experiment were weighed into charge mixtures consisting of 10 g ore and 2 g Polish coke as shown in Table 2. The Polish coke was used in the same size fraction as the ores. Each charge was mixed manually and loaded into a graphite crucible of 36 mm external diameter, 30 mm internal diameter, 70 mm height, and a depth of 61 mm.

TGA Furnace Experimental Procedure

The experiments were conducted in a vertical graphite tube furnace equipped with thermo-gravimetric (TG) balance. The filled graphite crucibles with a perforated closing lid were hooked to the balance and suspended inside the furnace chamber by a molybdenum (Mo) wire. The atmosphere in the furnace chamber was initially evacuated using a vacuum pump and subsequently replaced by a high purity 99.99% Ar gas stream up to 1 atm pressure. The Ar gas stream at 0.5 L/min was replaced by a CO gas at 0.5 L/min during the heating stage upon reaching 500 °C and Ar was reintroduced at the end of the experiment when the temperature had cooled down to 900 °C. Two alternative heating schedules were conducted. The samples were

Table 1 Chemical composition of raw materials (wt. %)

Material	MnO	MnO_2	SiO_2	Fe_2O_3	CaO	MgO	Al_2O_3	BaO	S	C	CO_2	H_2O	Total
UMK	25.96	26.52	5.59	11.04	13.29	2.89	0.44	0.11	0.02		16.0	1.53	103.4
Comilog	3.91	74.0	3.83	4.49	0.19	0.13	6.97	0.20	0.04		0.14	6.0	99.90
Nchwaning	31.19	34.36	6.07	14.36	6.22	1.09	0.38	0.45	0.15		3.10	1.0	98.37
Polish coke	0.04		5.6	0.86	0.42	0.22	2.97	0.03		87.68			97.64

Table 2 Amount of charge components and summary of the conducted experiments

Ore in charge	Basicity	Amount (g)					Experiments conducted
		UMK	Com	Nch	Coke	Total	
UMK		10	–	–	2	12	UMK-1400-30, UMK-1400-0, UMK-1500-30, UMK-1500-0, UMK-1550-30, UMK-1550-0
Com		–	10	–	2	12	Com-1400-30, Com-1400-0, Com-1500-30, Com-1500-0, Com-1550-30, Com-1550-0
Nch		–	–	10	2	12	Nch-1400-30, Nch-1400-0, Nch-1500-30, Nch-1500-0, Nch-1550-30, Nch-1550-0

rapidly heated at 25 °C/min up to 1200 °C and temperature held at 1200 °C for 30 min followed by a slow heating step at 4.5 °C/min. Alternatively, the fast heating stage was subsequently followed by a slow heating stage without holding temperature at 1200 °C. The two heating regimes were conducted to ascertain the effect of extend of prereduction on the final metal formation reactions. Final target temperatures were 1400, 1500, and 1550 °C for the two heating regimes. The initial rapid heating stage up to 1200 °C represents the prereduction of manganese oxides and iron oxides (MnO_2, Mn_2O_3, Mn_3O_4 to MnO and Fe_2O_3, Fe_3O_4, FeO to Fe, evaporation of bound water and decomposition of carbonates) and the calculated composition of a completely prereduced charge are shown in Table 3. Further heating to target temperatures represent the non-isothermal reduction of MnO in slag by carbon to form FeMn alloy. The temperature was recorded in two locations as shown in Fig. 1, with B-type thermocouple recording temperature in the hot zone at approximately 0.5 cm below the bottom of the graphite crucible and S-type thermocouple measuring

Table 3 Calculated compositions of charge completely prereduced at 1200 °C

Charge	MnO	SiO_2	CaO	MgO	Al_2O_3	Total	Basicity*
UMK	66.39	9.43	18.66	4.09	1.43	100	2.09
Com	83.22	6.44	0.36	0.23	9.76	100	0.04
Nch	79.19	9.61	8.43	1.52	1.25	100	0.92

*Basicity = $(CaO + MgO)/(SiO_2 + Al_2O_3)$

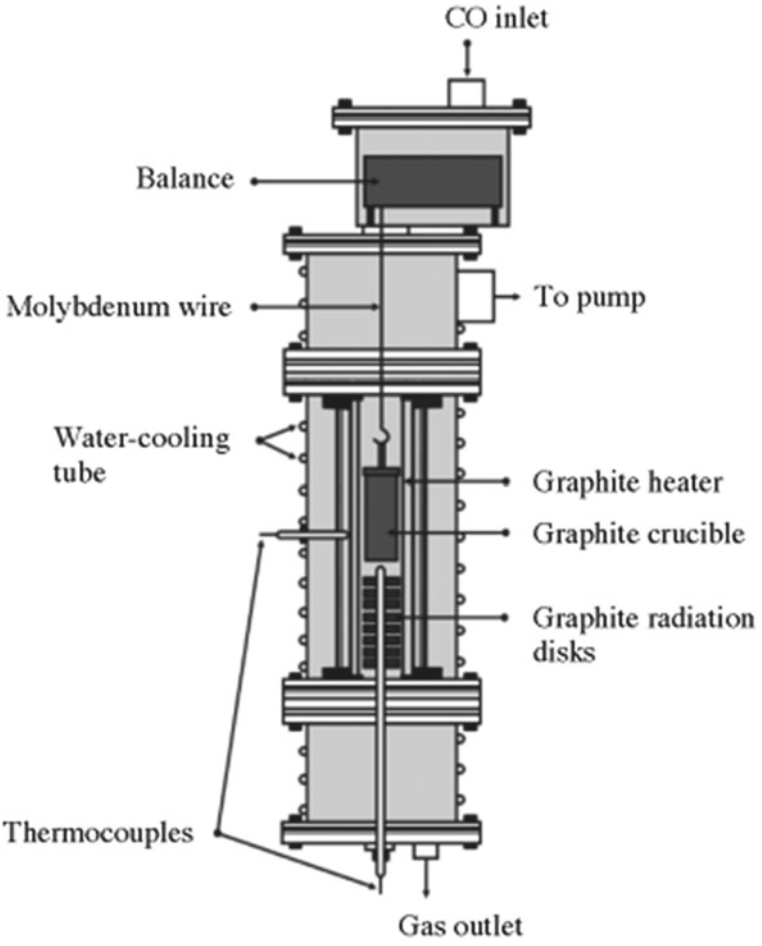

Fig. 1 Thermogravimetric furnace layout

furnace wall temperature. The weight loss of a sample is recorded every 5 s. After completing the experiment, the reduced sample is weighed and subjected to further characterization. The conducted experiments were named following the format; Mn Ore-Temperature-Holding time (mins) at 1200 °C as shown in Table 2.

Sample Characterization

After cooling, the crucibles containing reacted slag are casted in epoxy resin and then cut to expose the slag and metal. Prior to EPMA analysis, metallographic sample preparation and polishing was conducted to produce smooth surfaces. Samples

were embedded using epoxy resin curing for 12 h and the surface of the samples were initially ground using a SiC grinding paper, grit 220 before polishing using polyurethane based pads as the polishers (i.e., MD-Dac, 200 mm and MD-Nap, 300 mm) and an abrasive suspension, diamond water-based type as the polishing agent gradually decreased from 9, 3, and 1 μm particle size. The polished samples were cleaned by tap water using a cotton swab and dried in an oven for 12 h. After metallographic preparation, a high-resolution electron probe micro-analyzer (EPMA) JEOL JXA 8500TM, supported by wavelength dispersive spectroscopy (WDS) was used. EPMA/WDS provides high accuracy on quantitative analysis of the elements in observed phases of the samples as well as it can be used for imaging. On each of the observed phases of the samples, three points were analyzed, and backscattered images of the analyzed samples were recorded.

Thermochemical Calculations

FACTSage 8.1 thermochemical software was used to calculate equilibrium phases and compositions in the reduction process of UMK, Comilog, and Nchwaning ores. The equilibrium module in FACTSage 8.1 was used to calculate the equilibrium phase relations in the system MnO–SiO_2–Al_2O_3–FeO–CaO–MgO for the ores mixed with excess carbon in a carbon monoxide (CO) atmosphere as a function of temperature in the range 1100–1600 °C at intervals of 10 °C and atmospheric pressure set to 1 atm. The FactPS, FToxid, and FTmisc databases were used in all calculations. The primary slag composition presented in Table 3 were used as starting input values for equilibrium calculations. The viscosities of the three charges and their change during reduction were estimated using the viscosity module in FactSage 8.0. The viscosity calculations were performed with the chemical composition of the liquid determined from the equilibrium calculations. Viscosity is determined by both the liquid phase and content of solid phase. As such, viscosity of liquid was used to calculate the viscosity of the solid + liquid slag mixture according to Roscoe equation [1]:

$$\text{Viscosity}_{(\text{solid+liquid})} \approx \text{Viscosity}_{(\text{liquid})} \cdot (1 - R\phi_s)^{-n} \tag{3}$$

where Φ_s is the volume fraction of the solid phase, R and n are empirical parameters, which equal 1.35 and 2.5, respectively, assuming rigid spheres of equal size.

Results and Discussion

Reduction Behavior of UMK, Comilog, and Nchwaning Ores

The experiments were performed for the UMK, Comilog, and Nchwaning charges to ascertain the effect of extent of prereduction on the final metal reduction reaction and the extent of the reduction of MnO from the primary slag. This was done by having an isothermal section of 30-min holding temperature at 1200 °C compared to no isothermal section and the mass loss results for prereduction are shown in Table 4. Generally, the mass loss results up to 1200 °C show that maintaining samples at a heating plateau of 1200 °C for 30 min ensured a higher extent and complete prereduction compared to not holding.

The mass loss versus time and temperature profile for different charges is presented in Fig. 2. The prereduction curves at temperatures lower than 1200 °C overlap each other which is an indication of high accuracy in weight loss measurements for different experiments of the same ore type. The weight loss for Nchwaning ore is significantly lower than UMK and Comilog. This is mainly because Nchwaning is a Mn_2O_3-based ore with significantly lower O/Mn ratio of 1.4 compared to 1.9 for Comilog and less carbonates compared to UMK. UMK has significantly higher CO_2 content of 16% than Nchwaning and Comilog as shown in Table 1, therefore its mass loss is close to that of Comilog even though it has a lower O/Mn ratio of 1.3.

The weight loss in the MnO reduction stage is obtained by deducting the weight loss from prereduction from the total weight loss and is shown by Fig. 2d–f. The prereduction weight loss included the weight loss during holding for 30 min at 1200 °C for experiments including this isothermal stage. In general, holding for complete prereduction has been observed to have no effect on the overall weight loss in the metal producing reduction. As such, a greater extent of prereduction has been concluded to have no effect on the metal formation reaction. Weight loss at 1400 °C in the reduction of Nchwaning is higher followed by UMK and lastly Comilog. However, with an increase in temperature up to 1550 °C, Comilog shows the highest weight loss followed by Nchwaning and lastly UMK. This shows that

Table 4 Prereduction mass loss for experiments with and without holding for 30 min at 1200 °C

Experiment	Starting mass (g)	Prereduction mass loss (g)		Mass loss (%)
		30 min holding at 1200	No holding time at 1200	
UMK-1200-0	12		2.62	21.86
UMK-1200-30	12	2.84		23.65
Com-1200-0	12		2.58	21.51
Com-1200-30	12	2.85		23.74
Nch-1200-0	12		1.77	14.78
Nch-1200-30	12	2.23		18.62

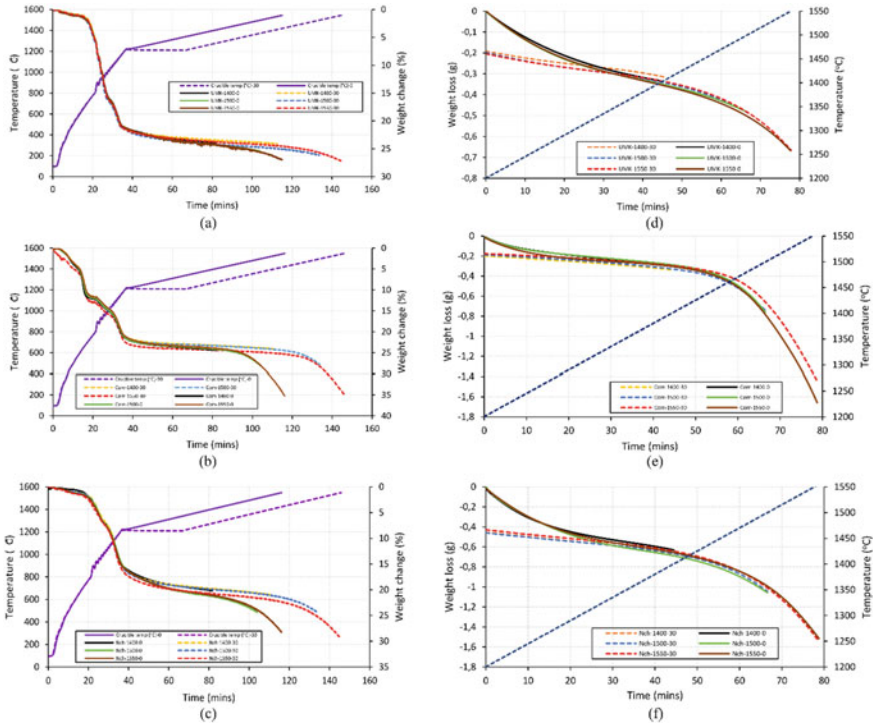

Fig. 2 TGA and temperature curves: **a** UMK series; **b** Comilog series and **c** Nchwaning series. Dashed lines represent the TGA and sample temperature for experiments with 30-min holding time at 1200 °C to complete prereduction and the solid lines represent experiments without holding for complete prereduction). Curves **d**, **e,** and **f** are the reduction curves for UMK, Comilog, and Nchwaning ores with weight loss before the second heating stage deducted, respectively

the reduction rate is higher for Nchwaning and UMK at low temperatures, whereas for Comilog, the reduction rate is significantly higher at higher temperature. This can also be seen in the calculated reduction rate curves versus temperature shown in Fig. 3. This is reasonably consistent with previous studies by Xiang et al. [6] though this study exhibits lower mass loss due to reduction for similar investigated temperatures.

The calculated reduction curves are presented in Fig. 4. In the calculation other ore components were neglected except for higher manganese and iron oxides, SiO_2, Al_2O_3, CaO, and MgO. Therefore, the primary constituents after complete prereduction were MnO, SiO_2, Al_2O_3, CaO, and MgO as presented in Table 3. Comilog ore contains very little CaO and MgO and the slag formed during the reduction process is very acidic. However, the slag is basic for UMK and Nchwaning ores as they contain significant amounts of CaO and MgO. The reduction curves are calculated based on weight loss due to the reduction of MnO in slag and the corresponding final slag compositions are shown in Table 5.

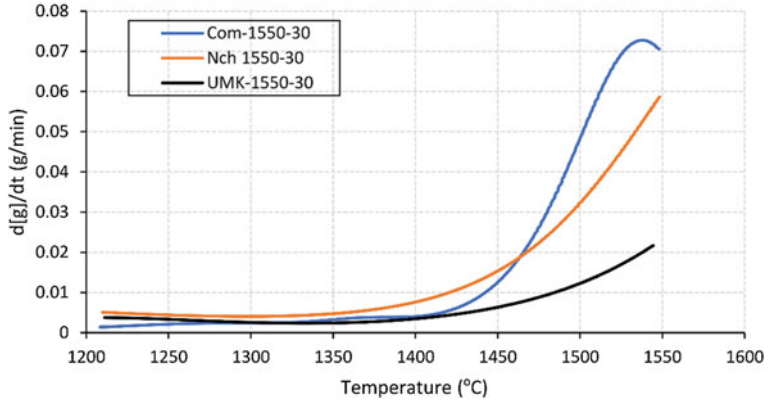

Fig. 3 Calculated reduction rate versus temperature for Comilog, Nchwaning, and UMK in the temperature range 1200–1550 °C

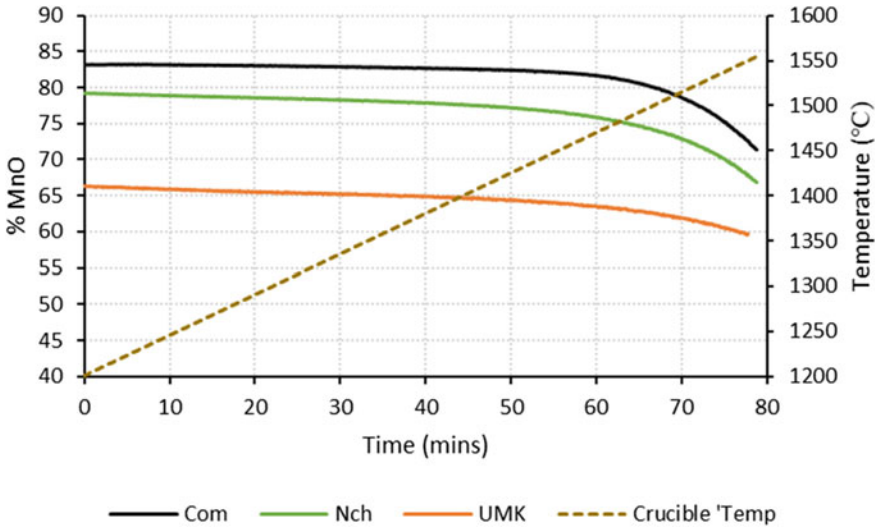

Fig. 4 Calculated % MnO during reduction for UMK, Comilog and Nchwaning

Slag Structure and Viscosities Variation During Reduction

MnO reduction occurs in liquid slag and typically the slag structure in ferromanganese process is a two-phase component of solid + liquid, which increases in liquid with dissolution of solid MnO. Therefore, the viscosity is a function of the structure of the slag system. The backscattered images from EPMA showing the slag morphology for UMK, Comilog, and Nchwaning slags as a function of temperature is shown in Fig. 5. The images shows that the slag contained a solid phase and liquid phase, and show that the reduction process has not reached the tapping slag

Table 5 Calculated slag composition based on reduction weight loss

Charge	MnO	SiO_2	CaO	MgO	Al_2O_3	Total
UMK-1400-30	64.85	9.86	19.51	4.28	1.49	100
UMK-1500-30	62.56	10.51	20.78	4.56	1.59	100
UMK-1550-30	59.76	11.29	22.34	4.90	1.91	100
Com-1400-30	82.44	6.74	0.37	0.24	10.22	100
Com-1500-30	74.47	7.87	0.44	0.28	11.94	100
Com-1550-30	71.45	10.95	0.61	0.39	16.60	100
Nch-1400-30	77.49	10.40	9.12	1.64	1.36	100
Nch-1500-30	74.22	11.91	10.44	1.88	1.55	100
Nch-1550-30	66.94	15.27	13.39	2.41	1.99	100

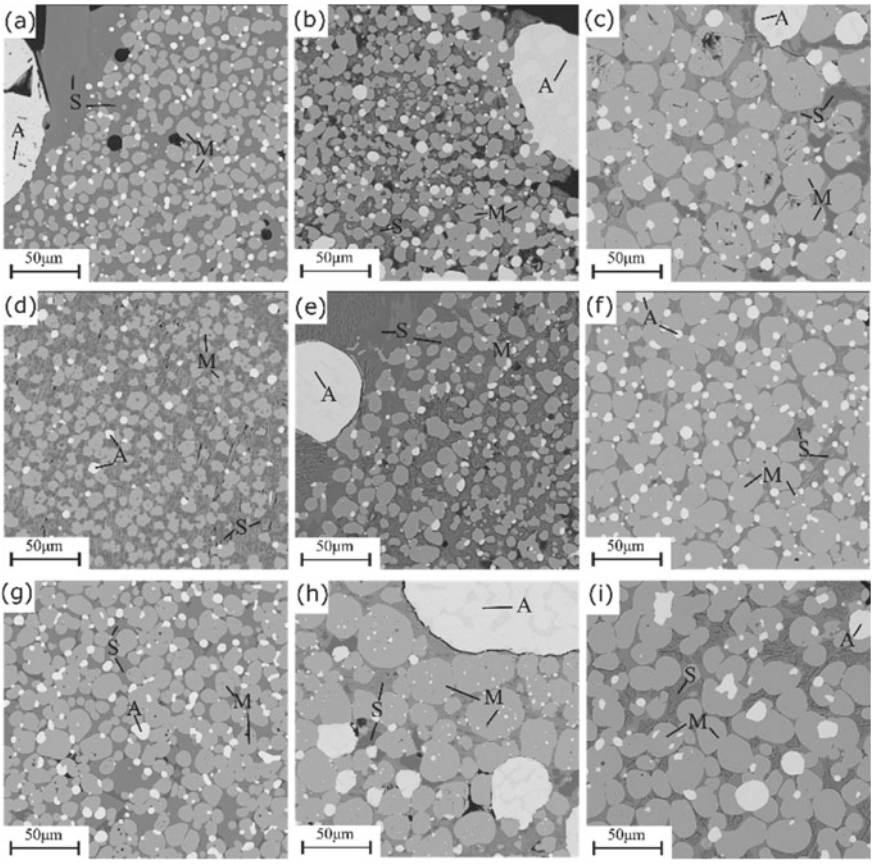

Fig. 5 BSE images of UMK slag (**a**–**c**), Comilog slag (**d**–**f**) and Nchwaning slag (**g**–**i**). The temperatures were 1400 °C (**a**, **d**, **g**), 1500 °C (**b**, **e**, **f**) and 1550 °C (**c**, **f**, **i**). Legend: A = alloy, M = monoxide phase; S = slag matrix

composition in these experiments. There has been no significant dissolution of solid MnO into liquid based on the experiments. The viscosity will hence be calculated according to the slag composition assumed down to tap composition. Therefore, the characteristic viscosity changes during reduction are mainly described based on equilibrium and viscosity calculations in FactSage 8.1. However, this creates significant discrepancies between calculated and mineralogically determined phases and compositions since the concentrations of chemical species are calculated under the assumption that compounds react to reach a state of chemical equilibrium which is hardly ever achieved.

In this work, the viscosity of the slag is calculated using the viscosity module in FactSage 8.1 from slag composition calculated from the equilibrium module. The melt database for the MnO–SiO_2–Al_2O_3–CaO–MgO system was used for the calculations and temperature was selected in accordance with the investigated experimental temperature range of 1400–1550 °C. Figure 6 shows the viscosity changes during reduction as function of temperatures. It can be noted that the viscosities are highly dependent on temperature, with increasing temperature resulting in a decrease in viscosity for the three ores. The initial primary slag will consist of a solid phase and a liquid slag having liquidus composition and the viscosity will vary with temperature. The content of solid phase decreases during reduction due to its dissolution in the liquid slag. As a result, the viscosity will decrease until the lowest viscosity is reached on the liquidus composition is reached and the viscosity will increase with further MnO reduction in the liquid. This is easily observed for the Comilog and Nchwaning viscosities curves. However, this is not the case for the UMK slag

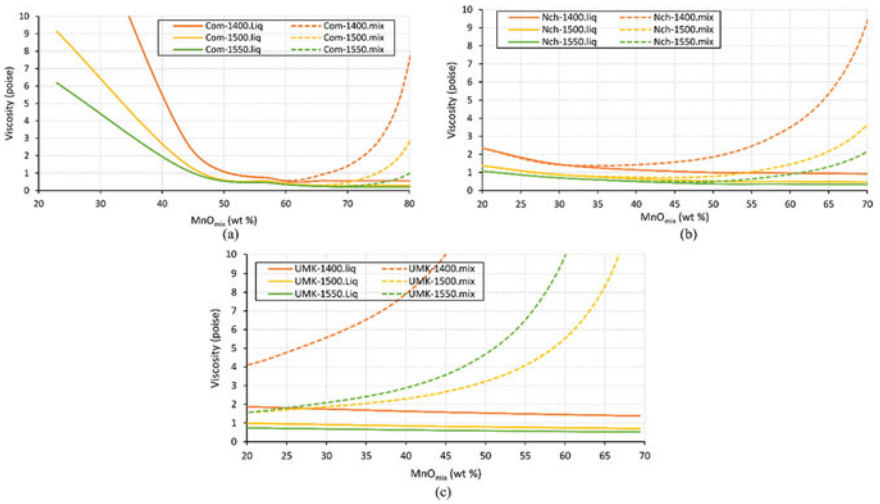

Fig. 6 Calculated viscosities as a function of temperature during reduction of **a** Comilog ore, **b** Nchwaning ore and **c** UMK ore. The calculated viscosities in the two phase area solid + liquid is indicated by dotted lines

system. Equilibrium calculations for the UMK slag systems shows that there is formation of high melting point silicates which are predominantly Ca_2SiO_4, Mg_2SiO_4, and Mn_2SiO_4. These silicates make the slag highly viscous and with dissolution of MnO in liquid during reduction, the silicates remain solid thus making the slag highly viscous. Comparison of the three slag systems shows that the viscosities in the two phase area, i.e., solid + liquid slag are high in UMK, followed by Nchwaning and, lastly, Comilog. However, Comilog shows a higher increase in viscosity with further reduction of MnO in one phase region, i.e., completely liquid slag. This is mainly due to a higher quantity of acidic oxides, $Al_2O_3 + SiO_2$ which are network forming oxides resulting in increased viscosity of the slag. Network forming oxides have been previously reported [14] to increase slag viscosity and the viscosities have been found to be minimum along the liquidus in the MnO-rich area, which is close to the chemical composition of tapped ferromanganese slags. The viscosity plays a key role in industrial operations. Slag viscosity contributes to the metal-slag separation efficiency, slag flow and furnace tapping. However, no direct relationship has been observed between the kinetics of reduction and calculated viscosity of slag.

The UMK ore, with its high basicity, will at a certain temperature, e.g., 1400 °C, have a higher viscosity at <20%MnO compared to Nchwaning at <20% MnO and Comilog at 40–50% MnO which are typical tapping compositions. The higher viscosity gives more tapping issues as described above. The UMK ore has additionally a lower reduction rate, and may end up with higher MnO content, increasing the viscosity and hence the tapping issues even more. This will be one of the reasons why UMK ore must be mixed with more acid ores.

Conclusions and Recommendations

It is of great importance to understand and control slag properties in order to improve the efficiency of the ferromanganese process. As such, the main concluding remarks from this work can be summarized as follows:

- The effect of pretreatment i.e., extent of prereduction on the metal formation reaction has been investigated by having a series of experiments with 30-min holding time at 1200 °C to ensure complete prereduction. This has been observed to have no effect on the overall weight loss in the metal producing reduction reactions. As such, the extent of prereduction has been concluded to have no effect on the metal formation reaction.
- Slag viscosity varies with slag reduction. The initial primary slag will consist of a solid phase and a liquid slag having liquidus MnO composition. The content of solid phase decreases during reduction due to its dissolution in the liquid slag. As a result, viscosity will decrease until the lowest viscosity on the liquidus composition is reached, and the viscosity will increase with further MnO reduction in liquid slag.

- The viscosities in the two phase area, i.e., solid + liquid slag is considerably high in UMK, followed by Nchwaning and, lastly, Comilog. However, Comilog shows a higher increase in viscosity with further reduction of MnO in liquid slag.

Acknowledgements This work is part of the PreMa project, which has received funding from the European Union's Horizon 2020 Research and Innovation Programme under Grant Agreement No 820561 and industry partners: Eramet, Ferrogroble, Transalloys, OFZ, and Outotec.

References

1. Olsen SE, Tangstad M, Lindstad T (2007) Production of manganese ferroalloys. Tapir Academic Press, Trondheim
2. Yastreboff M, Ostrovski O, Ganguly S (1998) Carbothermic reduction of manganese from manganese ore and ferromanganese slag. In: The eighth international ferroalloys congress, 1998, pp 263–270
3. Ostrovski O, Olsen SE, Tangstad M, Yastreboff M (2002) Kinetic modelling of MnO reduction from manganese ore. Can Metall Q 41(3):309–318. https://doi.org/10.1179/cmq.2002.41.3.309
4. Safarian J, Kolbeinsen L (2008) Kinetic of carbothermic reduction of MnO from high-carbon ferromanganese slag by graphite materials. ISIJ Int 48(4):395–404. https://doi.org/10.2355/isijinternational.48.395
5. Safarian J, Tranell G, Kolbeinsen L, Tangstad M, Gaal S, Kaczorowski J (2008) Reduction kinetics of MnO from high-carbon ferromanganese slags by carbonaceous materials in Ar and CO atmospheres. Metall Mater Trans B 39(5):702–712. https://doi.org/10.1007/s11663-008-9175-1
6. Li X, Tang K, Tangstad M (2020) Reduction and dissolution behaviour of manganese slag in the ferromanganese process. Minerals 10(2):1–16. https://doi.org/10.3390/min10020097
7. Olsø V, Tangstad M, Olsen SE (1998) Reduction kinetics of MnO-saturated slags. In: 8th international ferroalloys congress, vol 8, pp 279–283
8. Tangstad M (1996) PhD thesis, The Norwegian Institute of Technology, Trondheim, Norway
9. Jang HS, Ryu JW, Sohn I (2015) FeMn metal droplet behavior in the MnO-SiO2-CaO slag system. Metall Mater Trans B 46(2):606–614. https://doi.org/10.1007/s11663-014-0234-5
10. Sunahara K, Nakako K, Hosm M, Inada T, Komatsu S, Yamamoto T (2006) Effect of high A12O3 slag on the blast furnace operations. Tetsu-To-Hagane/J Iron Steel Inst Jpn 92(12):875–884. https://doi.org/10.2355/tetsutohagane1955.92.12_875
11. Tang K, Olsen S (2007) The effect of alumina in ferromanganese slag. In: The eleventh international ferroalloys congress: innovations in ferroalloy industry, 2007, pp 335–343
12. PreMa project. https://www.spire2030.eu/prema. Accessed 15 Aug 2021
13. Gregurek D, Wenzl C, Reiter V, Studnicka HL, Spanring A (2014) Slag characterization: a necessary tool for modeling and simulating refractory corrosion on a pilot scale. JOM 66(9):1677–1686. https://doi.org/10.1007/s11837-014-1070-4
14. Tang K, Tangstad M (2007) Modeling viscosities of ferromanganese slags. In: 11th international ferro-alloys congress. Ferro Alloy Ind., pp 344–357

Lab-Scale Physical Model Experiments to Understand the Effect of Particle Bed on Tapping Flow Rates

Varun Loomba, Hesam Pourfallah, Jan Erik Olsen, and Kristian Etienne Einarsrud

Abstract Optimal tapping of metallurgical furnaces is required for efficient furnace operation. Improper tapping can lead to metal and slag accumulation in the furnace thereby reducing the process efficiency. The mass flow rate of metal and slag during tapping in metallurgical furnaces is driven by the hydrostatic pressure head, i.e., the liquid level, and hindered by the porous particle bed formed by the raw materials in the furnace. To understand the effect of the particle bed, experiments were performed on a lab-scale tank fitted with a tap-hole using water and a mineral oil as fluids emulating the real furnace. The tank was filled with only water and both water and oil and their drainage rates were measured as they were emptied by gravity. The tank was then filled with glass beads to include the effect of the particle bed, adding an extra pressure drop due to the resistance offered by the glass beads and reducing the mass flow rate of the fluids. A significant effect of the particle bed was observed on the tapping flow rates. The presence of air bubbles in the oil and the water phase reduced the tapping flow rates of the phases even in the absence of the particle bed.

Keywords Physical model · Porous-media flow · Tapping experiments

V. Loomba · H. Pourfallah · K. E. Einarsrud (✉)
Department of Material Science and Engineering, NTNU, Trondheim, Norway
e-mail: kristian.e.einarsrud@ntnu.no

V. Loomba
e-mail: varun.loomba@ntnu.no

H. Pourfallah
e-mail: hesamp@stud.ntnu.no

J. E. Olsen
Process Technology Group, SINTEF AS, Trondheim, Norway
e-mail: jan.e.olsen@sintef.no

J. D. Steenkamp et al. (eds.), *Furnace Tapping 2022*, The Minerals, Metals & Materials Series, https://doi.org/10.1007/978-3-030-92544-4_13

Introduction

Drainage of fluids under gravity is a process applicable in several industries such as oil and gas, chemical processing, metallurgy, etc. [1]. Particularly in the metallurgical industry, the drainage of metals and slags, referred to as tapping process, plays an important role in deciding the efficiency of the furnace operation. The tapping flow rates mainly depend on the height of the liquid metal and slag accumulated in the furnace which defines the hydrostatic pressure head and the pressure drop created by the particle bed consisting of minerals and carbon rich particles (e.g. coal, coke, wood chips). The flow through the particle bed depends on both bed properties such as bed porosity and the particle size as well as fluid properties such as viscosity and density. Metal and particularly slag are highly viscous, thus making the flow through the particle bed the most crucial parameter limiting the tapping rates. Experimental determination of the effect of the particle bed on the tapping rates in the furnace is extremely difficult due to the large size of the furnace and the extreme high temperatures at which the flow occurs. Therefore, lab-scale experiments at room temperature are required to study the tapping process and the factors affecting it.

A significant amount of research has been done on drainage, but only quite few studies have been published on drainage through a particle bed. Vango et al. [2] studied the effect of sitting and floating particle bed on the tapping rates of water both experimentally and numerically, but did not consider the flow of two immiscible fluids and their interaction with the particle bed. Other researches with drainage of two immiscible fluids were performed on Hele-Shaw physical model, a 2D set-up where the flow occurs between two parallel plates places very close to each other [3, 4]. The fluids converge differently into a tap-hole compared to a slit as used in previous studies. The acceleration is important for the flow rate [5]. Thus, studies on a slit are useful, but care must be taken to apply the results directly for a tap-hole. He et al. [6] performed both 2D and 3D experiments with two immiscible fluids passing through a particle bed focusing on studying the gas–liquid interface behavior during tapping.

These studies have not focused on the effect of the particle bed on the drainage rates of the two immiscible fluids, occurring in real furnaces. Therefore, in this study a lab-scale plexiglass tank is constructed that replicates the region near the tap-hole to experimentally determine the effect of the particle bed on the tapping flow rates of single liquid and two immiscible liquids with density and viscosity ratios in the same range as that of the metal and the slag in the furnace. The experiments were performed both with and without the particle bed and the tapped mass of the fluids was recorded and compared.

Materials and Methods

In this study, a lab-scale physical model is constructed from plexiglass and has dimensions of 1 × 0.5 × 0.6 m. The tank is fitted with two outlets (the tap-holes) at each side of the tank of square cross-section with inner dimension of 0.02 × 0.02 m. One of the tap-holes is located at the bottom of the tank whereas the other one is 0.03 m above the bottom surface. Only the tap-hole located at the bottom surface is considered in this paper. L-shaped plexiglass pipes with same inner dimensions as the tap-holes are attached to each tap-hole. At the end of each tap-pipe, a ball valve (GF Type 546 pro) is fitted to regulate the flow through the tap-hole. The valve has a circular diameter (0.032 m) which is larger than the diagonal dimension of the tap-pipe to eliminate the effect of the pressure loss due to change in cross-sectional shape of the pipe. Figure 1 shows the schematic diagram, describing different lengths.

Water and a mineral oil are used as fluids to simulate the flow of liquid metal and slag in the furnace. These fluids are chosen as their physical properties' ratios are similar to that of the metal and the slag. The kinematic viscosities of model fluids correspond well to those encountered in the furnace, indicating that the flow regimes also will be similar. Considering the ratio of the Reynolds numbers for slag and metal (40.7) and water and oil (65.07), the relative flow rates are of the same order of magnitude, but water will drain slightly faster relative to oil, compared to metal and slag. Table 1 shows the physical properties of the fluids in the experiment and the fluids in a typical FeMn or SiMn-furnace. An important point to note here is that the physical properties of the metal and the slag mentioned in Table 1 are at furnace

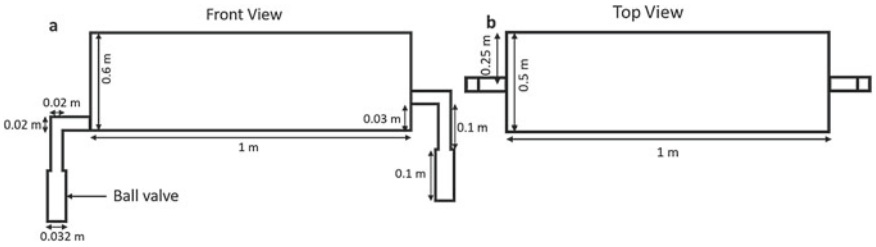

Fig. 1 Schematic diagram of the tank showing the **a** front view with width and height of the tank and **b** top view with width and the depth of the tank

Table 1 Physical properties of the fluids

Material	Density (kg/m^3)	Viscosity (kg/m-s)	Ratio of Re
Water	1000	0.001	65.07
Mineral oil	876	0.057	
Metal	6100	0.005	40.67
Slag	3000	0.1	

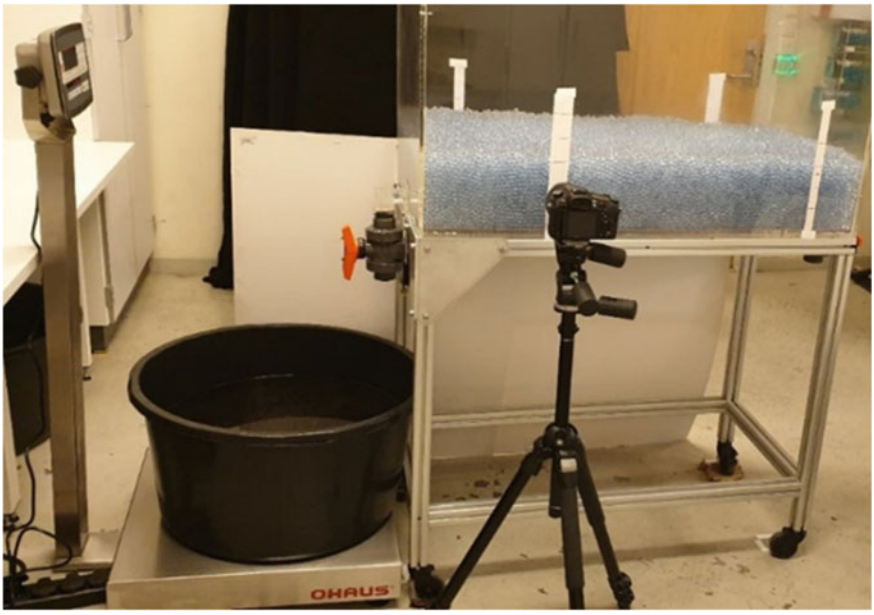

Fig. 2 Experimental set-up showing the tank, the weighing scale, the collection tub, and the camera

temperatures, typically 1400–1700 °C, whereas the water and the oil properties are specified at room temperature.

The mass of the tapped fluids is measured using an OHAUS Defender 5000 weighing scale, storing the data at a time interval of 1 s. Moreover, a high-speed camera is set up to record the video that tracks the movement of the water–oil, oil–air, or water–air interfaces. The captured video is used to determine the individual masses of the tapped fluids as the weighing scale can measure total mass of the liquids tapped at any time. Figure 2 shows the entire experimental set-up.

Glass beads of diameter 0.01 m are randomly added to incorporate the effect of the particle bed in the real furnace. It induces an additional pressure drop across the liquid column which affects the flow rate of the tapped fluid. Experiments are performed with and without the particle bed to analyze the effect of the particle bed on the tapping rates. The random distribution of mono-sized particles leads to a porosity between 0.35 and 0.45 [7]. The porosity was estimated by adding a known volume of water in the particle bed and calculating it from the measured height in the experiments and was found to be 0.39 and 0.325 for the bed heights of 0.1 and 0.16 m respectively (uncertainty based on 0.005 m error in reading bed heights, see Table 2). A plastic mesh is placed at the entrance of the tap-hole in order to stop the glass beads from flowing out of the tank. The size of each square on the mesh was 0.005×0.005 m since the purpose of the mesh is to keep the glass beads (diameter 0.01 m) from flowing out of the tank.

Table 2 Details of experimental conditions

	Height of water (m)	Height of oil (m)	Total height (m)	Particle bed height (m)	Porosity (± 0.02)
Exp 1	0.10	–	0.10	–	–
Exp 2	0.06	0.04	0.10	–	–
Exp 3	0.16	–	0.16	0.10	0.39
Exp 4	0.10	–	0.10	0.10	0.39
Exp 5	0.21	–	0.21	0.17	0.35
Exp 6	0.16	–	0.16	0.17	0.35
Exp 7	0.17	0.04	0.21	0.17	0.35

In the experiments without a particle bed, the tank is filled up to 0.1 m from the base of the tank. The water column has a height of 0.1 m when single phase experiments are performed, and 0.06 m when both the water and the oil are used. The oil phase has a height of 0.04 m therefore the total height of the column is the same in both cases for a fair comparison. A water-soluble coloring material is added to clearly distinguish the water–oil interface by the camera. When the particles are added, the experiments are performed with same hydrostatic pressure as without any particle bed leading to a smaller amount of liquid in the tank, and the same amount of liquid as without particle bed with a higher hydrostatic pressure. Table 2 describes all the tests performed all the conditions which have been evaluated.

Results and Discussion

All the experiments were performed at room temperature to avoid the changes in the viscosity of the materials among different tests. All experiments were performed at least 4–5 times in order to confirm the reproducibility of the results. Matlab® [8] was used for plotting all the results, and Matlab® and ImageJ® [9] were used for image analysis.

Single Phase Without Particle Bed

The mass flow rate of water depends on the density of the liquid, the acceleration due to gravity, and the height of the water column in the tank and can be explained by the Torricelli law which is derived from the Bernoulli's equation for an ideal fluid [10]. The flow rates estimated by the Torricelli's law are higher than the experimental results as the Torricelli's law is defined for an inviscid fluid without any friction losses, whereas in real experiments viscous shear and friction and other losses are inevitable. The first experiment was performed with only water filled up to a height of 0.1 m from the bottom surface of the tank, with and without the plastic mesh at

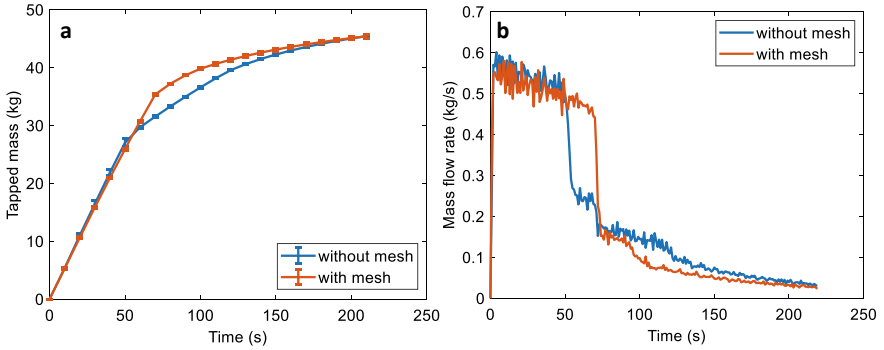

Fig. 3 Comparison of **a** tapped mass and **b** mass flow rate with and without mesh for only water phase. The curves in show the mean values, and the error bars indicate a single standard deviation

the outlet (Exp 1). Figure 3a shows the accumulated tapped mass of water both with and without mesh as measured on the weighing scale. Initially the water flows out continuously from the tap-hole at a linearly decreasing flow rate. After a certain time, the water–air interface near the tap-hole bends and air enters the tap-hole from the top, even though the average height of the water–air interface is above the tap-hole. The water flow rate decreases significantly when the air enters the tap-pipe, since the air will occupy some volume inside the pipe which then become unavailable for flow of water. The tap-pipe contains both water and air during this time as opposed to only water for the initial period. This leads to a lower slope of the curve for the rest of the experiment as shown in Fig. 3a. The plastic mesh at the outlet has an insignificant effect on the mass flow rate of the tapped water as evident by the similar slopes of the two curves in Fig. 3a before the air enters the tap-hole. The mesh, however, affects the bending of the interface and thus increases the time when the air enters the tap-hole. In absence of the mesh, it takes 52 s for the air to enter the tap-hole after opening the outlet valve, whereas 64 s in presence of the mesh. A sharper bend of the water–air interface was observed in the absence of the mesh causing the air to enter earlier than in presence of the mesh. The reduction in slope of the tapped mass vs time curve is sharper in the presence of the mesh due to lower hydrostatic pressure when air enters the tap-hole as the height of the liquid column is lower. In the end, the total mass of the tapped water is the same.

The mass flow rate of water linearly decreases in the beginning with decreasing height of the water column in the tank as the hydrostatic pressure across the liquid column depends on the height of the column. There is a sudden fall in the mass flow rate of water at 52 s after opening the valve in case of no plastic mesh and 64 s in case with the mesh. This fall corresponds to the bending of the water–air interface near the tap-hole and the air entering the tap-hole leading to a lower flow rate of water, as explained earlier. Once the air enters the tap-hole, the flow rate decreases suddenly and then continues to decrease almost linearly thereon as the height of the water column decreases continuously due to a lower hydrostatic pressure. The flow rate is higher in absence of the mesh, after the sudden fall, as the hydrostatic head

is higher. It can be inferred from Fig. 3a, b that the mass flow rate of water depends only on the liquid column height and the mesh does not induce an additional pressure loss but only affects the bending of the water–air interface leading to different times at which the air enters the tap-hole.

Two Phases Without Particle Bed

Adding the second phase to the system complicates the tapping flow as the hydrostatic pressure head changes due to density difference between the fluids. In these experiments (Exp 2), the water column accounts for 60% (0.06 m height) of the total volume of fluids inside the tank while the oil for 40% (0.04 m height) in the beginning of each experiment. The water starts flowing out of the tap-hole for the first 70 s on opening the valve as it forms the lower layer in the tank due to its higher density. Figure 4a shows the comparison of combined accumulated mass of water and oil tapped measured by the weighing scale over time with the previous case of only water. The initial flow rate of the water is the same in both cases as the two curves coincide with each other for first 15 s, as the hydrostatic pressure of the liquid column is the same. When these experiments are performed several times, air bubbles get entrapped inside the water phase, the oil phase as well as at the water–oil interface, causing different fluid flow profiles depending on the number, the size, and the location of these bubbles. The slope of the accumulated total mass of the liquids changes at 15 s after opening the tap-hole due to these air bubbles entering the tap-hole with water, creating turbulence inside the tap-hole causing the air to be sucked in from the outlet and forming an air bubble in the tap-pipe. This air forms a bubble inside the tap-hole which stays for the rest of the experiment, reducing the tapping flow rate. Therefore, the two curves separate after 15 s and the overall tapped mass of

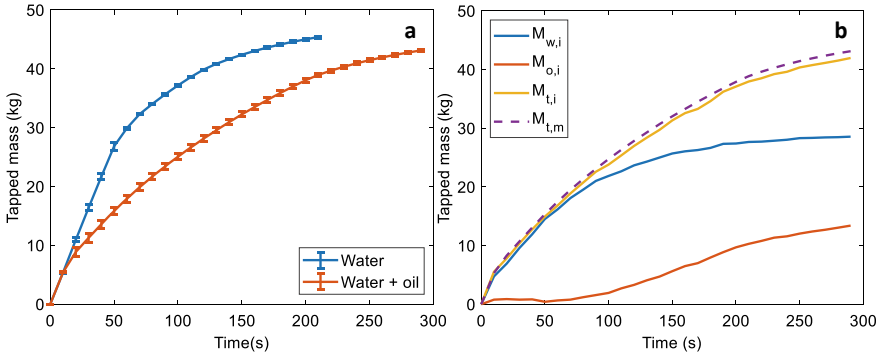

Fig. 4 Tapped mass of **a** water (Exp 1) and water + oil phase (Exp 2) **b** individual phases reconstructed from the image analysis for water + oil phase experiment (Exp 2). The curves in **a** show the mean values and the error bars indicate a single standard deviation. The image reconstruction is shown for a single experiment

the liquids at any instant is lower for the two-fluid system than only water. The time when the oil phase bends and oil starts flowing out of the tank is not evident from Fig. 4a, because the flow rate is already slower due to the air bubble that the decrease due to the change in fluid flowing out is not predominant. The oil finally starts to tap approx. 70 s after opening the tap-hole, when the water–oil interface close to the tap-hole bends, causing the oil to flow out even though the average water–oil interface height is higher than the height of the tap-hole.

Figure 4a shows the total mass of the water and the oil measured during the experiments but the individual masses cannot not be measured by the weighing scale. In order to calculate the individual masses of the phases, screenshots were taken at every 10 s from the video recording, and the interfaces were tracked via image analysis. The interfaces are located manually as there were reflections from the tank surface. These interface heights are then used to calculate the amounts of water and oil in the tank and the amounts tapped over time. As can be seen in Fig. 4b, initially only water is tapped ($M_{w,i}$, blue line) for the first 70 s and the oil begins to tap ($M_{o,i}$, red line) along with water. The line $M_{t,i}$ (the yellow line) is the reconstructed total mass calculated by adding the individual masses of the water and the oil at each time, which matches quite well with the measured total mass from Fig. 4a. In the beginning the total mass and the mass of water are same until the oil starts flowing out, thereby increasing the total tapped mass. The average error between the measured and the calculated total mass is within the acceptable range, approx. 5%, which is mainly an effect of the human error in locating the exact position of the interfaces in the images.

Single Phase with Particle Bed

The particle bed introduces a pressure loss in the liquid column due to the resistance offered by the glass beads. The liquids flow through the voids in the particle bed during tapping. Comparing the cases without particle bed (green dashed line, Exp 1) to all other cases with particle bed (Exp 3, Exp 4, and Exp 5) in Fig. 5a, the presence of the particle leads to a lower mass flow rate. Taking the same amount of liquid as in case of without the particle bed for a bed height of 0.1 m (blue line, Exp 3), the water–air interface takes 123 $\pm$ 5 s (standard deviation based on all experiments), compared to 64 s without particle bed, to reach the tap-hole. The slope of the initial stage of accumulated tapped mass over time (Fig. 5a) i.e., the time before the water–air interface reaches the tap-hole height, changed by 36% on due to the resistance offered by the particle bed. The pressure drop introduced by the particle bed depends on physical parameters such as particle bed porosity and particle diameter, fluid properties such as density and the viscosity of the fluids and flow properties such as fluid velocity.

For the same particle bed height (0.1 m) but different amounts of water in the tank (0.16 m (Exp 3) and 0.1 m (Exp 4)), hence having different hydrostatic heads, the slope of mass accumulated over time is reduced by only 8.5% (the blue and red

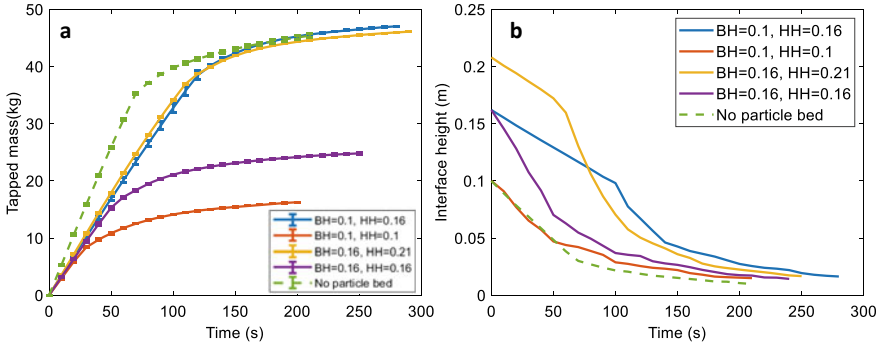

Fig. 5 Comparison of **a** tapped mass and **b** water–air interface heights with different particle bed heights for only water phase (BH = Bed Height, HH = Hydrostatic Head). The curves in **a** show the mean values and the error bars indicate the standard deviations

curve in Fig. 5a). This signifies that the resistance offered by the particle bed governs the flow rate rather than the hydrostatic head. On increasing the particle bed height from 0.1 to 0.16 m but keeping the same volume of water as without particle bed (hydrostatic head 0.21 m), the mass accumulated over time shows a similar profile (comparing blue (Exp 3) and yellow line (Exp 5) in Fig. 5a) with an increase in slope by 4.5% compared to the bed height of 0.1 m and same amount of water (hydrostatic head 0.16 m). The times required for the water–air interface to reach the tap-hole are similar as well because the overall hydrostatic head has increased from 0.16 to 0.21 m on increasing the height of the particle bed and the porosity decreased from 0.39 to 0.35, thereby increasing the resistance offered by the particle bed. The water–air interface moves faster inside the particle bed than in absence of the particle bed as the same hydrostatic head forces lesser volume of water (only in the voids in the particle bed) to flow through the bed, making it to move faster. Therefore, even with higher particle bed height in Exp 5, the water–air interface reaches the tap-hole height at a similar time compared to Exp 3.

When the water–air interface is above the particle bed, the interface height decreases linearly with time until the interface reaches the top of the particle bed as seen in Fig. 5b. The same trend is followed by the interface in absence of particle bed (green dashed line). As soon as the interface enters the particle bed, it starts to decrease exponentially, because the hydrostatic head is the same as without any particle bed which determines the tapping velocity whereas the amount of liquid is less as most of the volume in the tank is consumed by the particles. This is further clarified in experiments with same initial water–air interface height as particle bed height (red and purple lines in Fig. 5b), where the decline is exponential from the beginning of the experiment. Comparing this trend in absence of the particle bed, the interface height decreases linearly till the interface reaches the tap-hole height because the hydrostatic head is the same and the entire volume is occupied by water. Hereafter, the decrease in interface height is still linear but with a smaller slope. It should be noted that the change in slope in presence of particle bed occurs when

the interface reaches the top of the particle bed whereas when the interface reaches the tap-hole in absence of the particle bed. The time when the water–air interface reaches the tap-hole height is not visible from Fig. 5b.

Two Phases with Particle Bed

The flow of two fluids through the particle bed is even more complicated than a single phase, as the density and the viscosity of the two phases are different, the resistance offered by the particle bed on the fluids is also different. Another complication that arises when water and oil (two immiscible fluids) are passing through a particle bed is the accumulation of the air bubbles and the oil droplets in the small voids between particles in the water phase causing the flow to be trickier than in absence of the particle bed. Figure 6a shows the total mass accumulated of the two phases over time. The longer error bars signify higher standard deviation in the flow rates, which is a direct impact of the air bubbles and oil droplets trapped in the particle bed. The time when the oil starts tapping out varies from 52 to 96 s for different experiments depending on the bending of the water–oil interface near the tap-hole, which in turn depends on the amount and the locations of the air bubbles and the oil droplets trapped inside the particle bed. Therefore, the change in slope in the tapping flow rates, as seen in other cases, is smoothed out when the results averaged over several experiments in Fig. 6a. The total time required for both the fluids to be tapped is much higher in presence of the particle bed (35 min) compared to other cases, as the oil phase flows out extremely slowly compared to the water phase due to high viscosity. The difference between the cases with (Exp 7) and without (Exp 2) the particle bed is not significant as in single fluid case because the flow rate is reduced due to the air bubbles in the water and oil phases (as explained earlier)

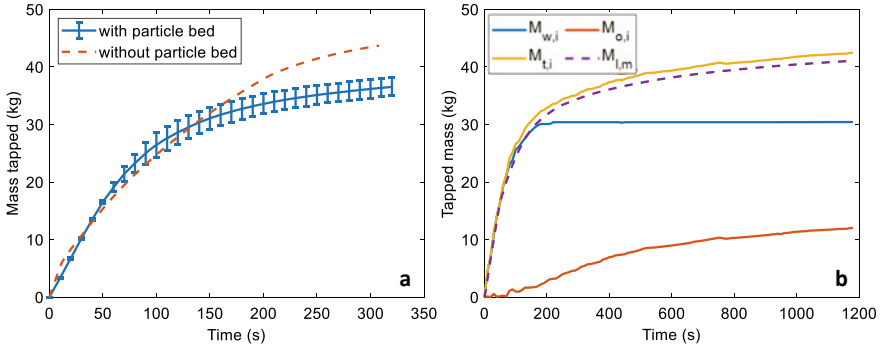

Fig. 6 Comparison of **a** total tapped mass with and without particle bed, and **b** tapped mass of individual phases calculated by the image analysis of water–oil and oil-air interface heights. The curves in **a** show the mean values and the error bars indicate a single standard deviation. The image reconstruction is shown for a single experiment

leading to a lower mass flow rate than expected, whereas the presence of the particle bed anyhow reduces the mass flow rate of the liquids. It can also be inferred that the mass flow rate of oil is more affected by the particle bed compared to water as the total mass accumulated are considerably lower in Fig. 6a at higher times when oil is being tapped compared to when water is tapped (in the beginning of the experiments). The flow rate of oil being extracted is much lower and consequently the total mass accumulated increases slowly in comparison with water tapping. This can be explained by the higher viscosity of oil which increases the pressure drop of the particle bed.

In order to calculate the mass flow rates of individual phases, again image analysis was performed on the video tracking the movement of the water–oil and oil-air interface. Figure 6b shows the individual tapped masses of water and oil over time, and the total tapped mass over time calculated by adding the masses of individual phases. In the beginning only water is tapped for first 150 s, while there is no oil phase being tapped. The tapped mass of water phase (blue line) and the total mass tapped (yellow line) coincide (or very close to each other). The oil starts to flow out after 150 s and then is continuously tapped whereas most of the water is tapped by then. It can also be seen that the water flows rapidly through the bed while the oil flows slowly due to high viscosity of oil. There average difference between the total mass calculated from image analysis and measured with weighing scale is around 6%, which is in the acceptable range.

Conclusions and Outlook

A detailed experimental study of the tapping mass flow rates in presence and absence of a particle bed for single phase and two-phase flow has been presented. The fluids drain out under gravity and the flow rate is driven by the height of the liquid column. The main conclusions derived from this study are as follows:

(1) The flow rate of the fluids decreases when the air enters the tap-hole. The air can enter from the top when the top interface bends near the tap-hole or can be sucked up from the outlet due to turbulence in the tap-pipe.
(2) The plastic mesh placed at the tap-hole to prevent the particles to flow out of the tap-hole, has an insignificant effect on the tapping flow rates of the fluids but it does affect the bending of the interface in the tap-hole region.
(3) The presence of the particle bed reduces the tapped mass flow rates of water due to an additional pressure drop. The entrapment of gas bubbles in the water and the oil phase reduced the mass flow rates of the phases in absence of the particle bed, whereas the flow of oil phase was considerably slower due to the high viscosity of the oil in presence of the particle bed.

An experimental quantitative data set for the drainage of a single and two immiscible fluids in the presence and absence of a particle bed has been presented. It includes the experimentally measured total mass of the tapped fluids, interface heights

of the fluids in the tank and the individual tapped masses of the fluids calculated from the interface heights. This can further be used for model validation for any numerical study on tapping flow rates. A computational validation of this system is in progress which upon validation can further be used to simulate the real furnaces.

References

1. Wang CY, Cheng P (1997) Multiphase flow and heat transfer in porous media. In: Hartnett J et al (eds) Advances in heat transfer 1997. Elsevier, pp 93–196
2. Vångö M, Pirker S, Lichtenegger T (2018) Unresolved CFD–DEM modeling of multiphase flow in densely packed particle beds. Appl Math Model 56:501–516
3. Liu W, Shao L, Saxén H (2020) Experimental model study of liquid–liquid and liquid–gas interfaces during blast furnace hearth drainage. Metals 10(496)
4. Tanzil WBU et al (1984) Experimental model study of the physical mechanisms governing blas furnace hearth drainage. Trans ISIJ 24:197–205
5. Olsen JE, Reynolds QG (2020) Mathematical modeling of furnace drainage while tapping slag and metal through a single tap-hole. Metall Mater Trans B 51(4):1750–1759
6. He Q et al (2006) Free surface instability and gas entrainment during blast furnace drainage. Dev Chem Eng Mineral Process 14(1/2):249–258
7. Guo Z et al (2017) Radial porosity peak at the centerline of packed beds with small tube to particle diameter ratios. Powder Technol 319:445–451
8. MATLAB 9.7.0.1190202 (R2019b) 2019: Natick, Massachuesetts
9. Rasband WS (1997–2018) ImageJ. U.S.N.I.o. Health, Editor. 1997–2018: Bathesda, Maryland, USA
10. Bird RB, Stewart WE, Lightfoot EN (2002) Transport phenomena. Wiley, New York

The Interaction of Slag and Carbon on the Electrical Properties

Gerrit R. Surup, Kseniia Koseniuk, and Merete Tangstad

Abstract Renewable reducing agents are intended to replace significant amounts of fossil-fuel-based reductants in submerged arc furnaces in the upcoming decades. In this study, the interaction of a manganese slag to a charcoal, a semi-coke, and a metallurgical coke was investigated. In a first series, the wettability of the slag was measured, while the electrical resistivity of carbon particles was measured by a four-point measuring technique. It was shown that the contact resistant between the carbon materials significantly decreased by void and pore filling. The results were validated by measuring the bulk resistivity of carbon-slag blended bed. While the slag is nonconductive below melting temperature, electrical current is highly conducted in the molten phase. The higher electrical resistivity of charcoal compared to the fossil-fuel-based reductants improves the local heat generation in the carbon bed, concomitant reducing the viscosity of the slag, which may be beneficial for tapping of the furnace. While the work described here is not specifically on furnace tapping, the work is linked to good furnace operation, hence indirectly relevant.

Keywords Charcoal · Coal char · Metallurgical coke · Ferromanganese slag · Wettability · Electrical resistivity

Introduction

The increasing average living standard and demand for metals can hamper the aim to be climate neutral by 2050. Industrialized countries are expected to adjust their economies to be greenhouse gas (GHG) neutral by the middle of the century, by which time a transition from fossil-fuel-based technologies to renewables can decrease current anthropogenic CO_2 emissions; the metallurgical industry will play an important role in decarbonization, yet it also needs to reduce its carbon emissions. The

G. R. Surup (✉) · K. Koseniuk · M. Tangstad
Norwegian University of Science and Technology (NTNU), 7491 Trondheim, Norway
e-mail: gerrit.r.surup@ntnu.no

M. Tangstad
e-mail: merete.tangstad@ntnu.no

J. D. Steenkamp et al. (eds.), *Furnace Tapping 2022*, The Minerals, Metals & Materials Series, https://doi.org/10.1007/978-3-030-92544-4_14

Norwegian process industry estimated a reduction of ≈75% CO_2 emissions which could potentially be achieved by the use of biomass and its derivatives [1].

A large portion of special elements is required for alloying steels. While on average about 3–5% of alloying elements are used in steel production, high alloy steels can contain more than 12% alloying elements [2]. Most of these elements are produced by carbothermal or electrolytic production, for example, in blast furnaces, submerged arc furnaces (SAF), electric arc furnaces (EAF), or in electrolytic cells. Reduction of metal oxides to the metallic form in SAF and EAF is carried out by solid carbon, such as woodchips, charcoal, coal, anthracite, or metallurgical coke.

Carbon reductants in SAF operations have two main purposes: 1. to reduce the metal oxides and quartz to the metallic form and 2. to form a conductive bed to conduct current and provide the necessary heat through the Joule effect. The electrical resistivity of carbon materials is essential to ensure a stable operation of the SAF, in which more than 50% of the required thermal energy is provided by electrical power [3]. While several publications deal with the use of raw carbon materials [4–7], only limited knowledge of wetted coke beds or the interaction between renewable reductants and slag has been published.

In SAF and EAF, electrical energy dissipation occurs by both micro-arcing and resistive heating, for example, there is less than 5% arcing occurring in chrome production [8], with up to 15% occurring in silicomanganese production [9]. Silicon and ferrosilicon, on the other hand, exhibit much larger electrical dissipation by arcing, in which a crater below the electrode tips is formed, transferring between 20 and 60% of the electrical energy [8]. Thus, the electrical properties of the carbon bed are important in order to maintain stable heat generation and operation of SAFs.

In this study, the interaction between ferromanganese (FeMn) slag and charcoal was investigated and compared to blends of FeMn slag to coal char and metallurgical coke. Blends of fossil-fuel-based carbon reductants and high-carbon ferrochromium have shown that the electrical resistivity is significantly affected by the volume fraction of slag [10].

Similar results were obtained for blends of metallurgical coke and charcoal at low temperatures [11]. The aim of this study was to investigate: (1) the behavior of charcoal, coal char and metallurgical coke towards FeMn slag; (2) determine the slag intrusion into packed carbon beds; and (3) to measure the electrical resistivity of partially wetted carbon beds. In this paper, wetted carbon refers to a carbon bed that is in contact with a molten slag.

Materials and Methods

A metallurgical coke, a coal char and an industrial charcoal were selected as representative carbon materials for examining the behavior of an FeMn slag produced in a pilot test. The coal char and industrial charcoal were obtained from a local silicon producer, while the metallurgical coke was the same as used in the production of ferromanganese. The carbon material also had been used in a previous study and had

Table 1 Proximate and ultimate analyses of carbon feedstocks

	Unit	Metallurgical coke	Charcoal	Coal
Moisture	wt%, ar	<0.1	0.9	0.6
Ash	wt%, db	12.1	2.4	3.8
Volatile matter	wt%, db	<0.5	<0.5	<0.5
Carbon content	wt%, daf	98.9	99.1	99.2
Hydrogen content	wt%, daf	<0.1	<0.1	<0.1
Nitrogen content	wt%, daf	<0.5	<0.5	<0.5
Oxygen content	wt%, daf	<0.5	<0.5	<0.5
Sulfur content	wt%, daf	0.3	–	0.3

ar As received basis, *db* dry basis, *daf* dry ash free basis

been heat treated to 1650 °C [7]. The analyses of the carbon feedstocks after heat treatment are summarized in Table 1.

Sessile Drop Test

Prior to each experiment, the crushed slag sample was split using a sample splitter, ground to a particle size less than 100 μm, and then compacted to form a small cylinder (diameter: 4 mm; height: 4–5 mm). The cylinder was placed on the carbon substrate (graphite, charcoal, coal char, or metallurgical coke), which had been heat treated at 1600 °C prior to the experiment. The specimen was placed on the sample arm and positioned in the center of the sessile drop furnace, schematically shown in Fig. 1. The chamber was closed, evacuated to less than 0.3 mbar, and consecutively purged by 0.15 l min^{-1} of argon to render the chamber inert. The furnace was heated at a heating rate of 300 K min^{-1} to 900 °C and further heated at a constant heating rate of 10 K min^{-1} to a final temperature of 1700 °C. At temperatures above 900 °C, the substrate temperature was measured by a pyrometer in addition to the furnace

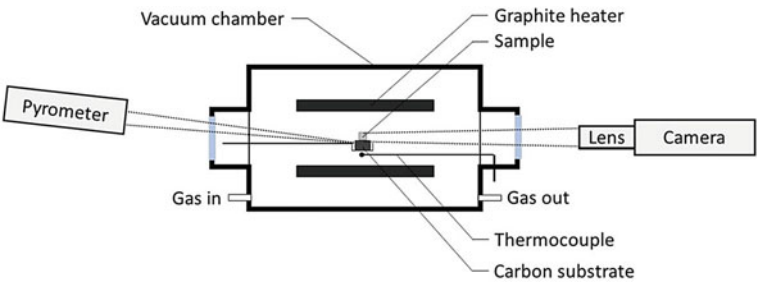

Fig. 1 Schematic of the sessile drop test

temperature, which was measured by a thermocouple type C. After the heating cycle was completed, the sample was cooled to room temperature, the sample and substrate removed and stored in sample containers.

The sessile drop test was carried out to determine the interaction between the manganese slag and the different carbon substrates, as well as the ash fusion temperatures, which are composed of the deformation temperature (IDT), softening temperature (ST), hemispheric temperature (HT), and flow temperature (FT, also called fluid temperature). The sample and substrate were cast in iodized resin, cut, and further investigated by scanning electron microscopy.

Slag Intrusion Measurement

The interaction of the slag and the dry carbon bed (coke bed) was determined at temperatures up to 1550 °C in an argon atmosphere. Carbon fines with a particle size less than 2 mm were blended with wood tar and water at a ratio of 100:35:65, homogenized and compacted inside an alumina crucible. The compacted sample was dried overnight at 105 °C to remove moisture and volatile components from the tar binder, concomitantly increasing the mechanical stability of the pellet. A channel (diameter: 2.5, 4, and 5 mm) and a chamfer of 60° were machined into the sample, schematically shown in Fig. 2a. Slag particles of 1.5–1.75 g were placed on top of the channel to simulate dense particle packing.

Three samples were placed in a graphite crucible in an induction furnace IF75 (Inductotherm Europe, Droitwich Spa, UK), as presented in Fig. 2b. Argon (purity 5.0) was purged continuously at a constant flow rate of 1 l min^{-1} to render the atmosphere in the crucible inert. The furnace control thermocouple was positioned

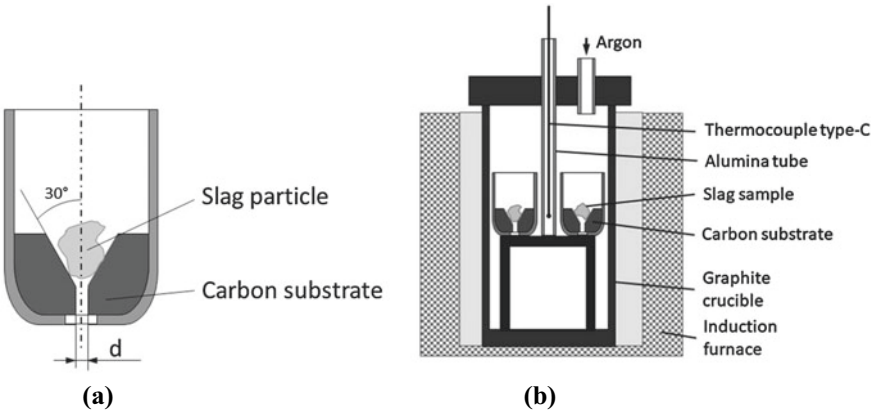

Fig. 2 Schematic of the slag intrusion experiment. **a** Compacted carbon material with defined chamfer and channel and **b** installed setup in induction furnace

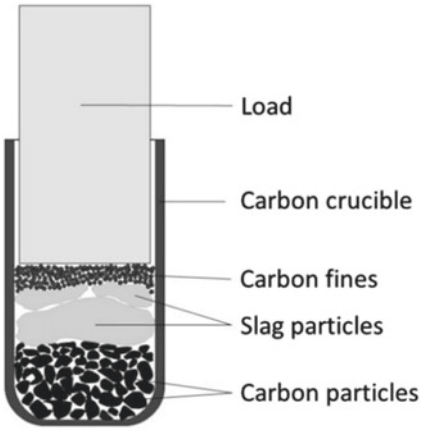

Fig. 3 Schematic of the load introduced intrusion experiment

at the sample height to minimize any temperature gradient between the furnace and sample. The furnace was heated at a heating rate of 15 K min^{-1} to 900 ºC and kept at this temperature for 10 min to minimize the temperature gradient in the sample. The sample was subsequently heated to 1550 ºC at a constant heating rate of 10 K min^{-1} and kept at the final temperature for 30 min. After the heating program was finished, the furnace was turned off and the samples were cooled in an argon atmosphere to room temperature.

To simulate the burden load on the carbon bed in a SAF, an additional load (compaction pressure ≈ 10 kPa) was introduced on the slag sample, schematically shown in Fig. 3. Carbon particles with particle size 2–4.75 mm were filled in a graphite crucible (height 67 mm, diameter 40 mm, wall thickness 4 mm) to a height of 30 mm and compacted by vibrating compaction. A slag layer was added above the carbon samples to a height of ≈15 mm. Carbon fines (dp < 250 μm) were installed above the slag layer to ensure an evenly distribution of the additional load. The height of the load was noted and monitored over the heating program to analyze the melting and the void filling of the carbon bed. The crucible was placed in the center of the induction furnace called IF75 and heated, following the same heating procedure described in the previous paragraph.

Electrical Resistivity

Electrical resistivity measurements were performed using a four-point probe measurement system (SINTEF, Trondheim, Norway) installed in the induction furnace IF75 as described elsewhere [7]. 150 g of slag sample (dp ≤ 2 mm) was blended into the carbon feedstock (4.75 mm ≤ dp ≤ 9.5 mm) and distributed homogeneously in the measurement zone and also slightly above it, resulting in a slag carbon ratio of 7:3 for metallurgical coke, 5:3 for coal char and 1:1 for charcoal. A

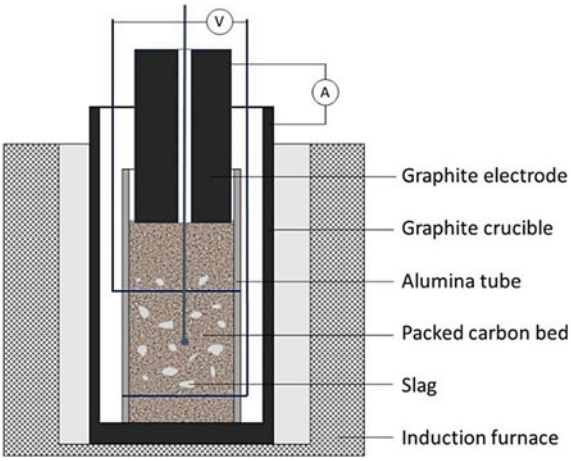

Fig. 4 Schematic of the electrical measurement setup at NTNU/SINTEF

schematic of the setup is shown in Fig. 4. The furnace was heated with a constant heating rate of 15 K min^{-1} to 900 °C and kept at this temperature for 15 min to minimize the radial temperature gradient in the packed bed. Furthermore, the furnace was heated at a heating rate of 10 K min^{-1} to 1650 °C and kept at that temperature for 30 min. The electrical resistivity of the packed bed was investigated for each 25 °C temperature increase in the center of the bed.

Single Particle Interaction with Slag

The effect of slag on the contact resistance between single particles was investigated by using a graphite cylinder (diameter: 16 mm, length: ≈ 25 mm) in the induction furnace IF75. A hole (diameter: 10 mm, depth: 15 mm) was drilled in the upper cylinder and partially filled with slag, schematically shown in Fig. 5.

Scanning Electron Microscopy

Scanning electron microscopy was performed on the residue from sessile drop test and slag intrusion experiments using a high-resolution microscope ULTRA 55 (Zeiss, Oberkochen, Germany) under a high vacuum to investigate the change in the structure in the contact region.

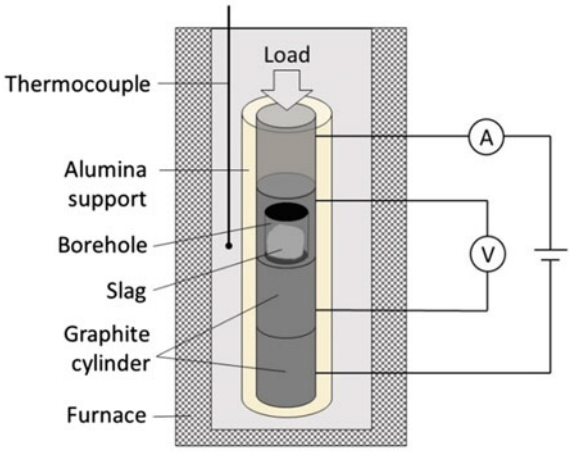

Fig. 5 Schematic of the four-point measurement of single particles

Results and Discussion

The interaction between the slag and different carbon substrates and the ash melting behavior was investigated in the sessile drop test as shown in Fig. 6. The first ash deformation and hemispheric temperature were measured at ≈1190 °C and 1220–1240 °C, respectively. These values are generally in agreement with reported values in the literature [12]. The lower melting temperature compared to manganese ores indicates that the MnO content in the slag was reduced to ≤40% in the pilot-scale experiment [13]. This hemispheric shape was kept at a temperature of 1700 °C for graphite and coal substrates, whereas the slag surpassed the flow temperature for metallurgical coke and charcoal at temperatures above 1680 °C, schematically as shown in Fig. 6d, f.

A further gas formation in the slag droplet was observed for temperatures above 1300 °C for all carbon substrates, resulting in a volume increase up to 200% of its melting volume. The non-wetting behavior of graphite and carbon materials below 1600 °C and the further reduction on carbon substrates is also in agreement with information in the published literature [14, 15].

Scanning electron microscopy on a cross section of the charcoal and metallurgical coke substrates revealed that some of the slag diffused into the carbon matrix, as shown in Fig. 7. The slag intrusion into the carbon bed increases at temperatures above 1600 °C [13], in which slag reduction and a lower viscosity at elevated temperature increase the slag flow and intrusion into the void fraction and pore structure. The composition of the carbon substrate, the surface layer, and the outer slag was investigated using EDS with the results summarized in Table 2. The EDS analysis confirmed that some surface layer slag was further reduced to its metallic form, whereas the composition of the main slag droplet above the carbon substrate remained nearly constant. The EDS results for the slag intrusion experiments deviated from the results from sessile drop test by ≤4% points.

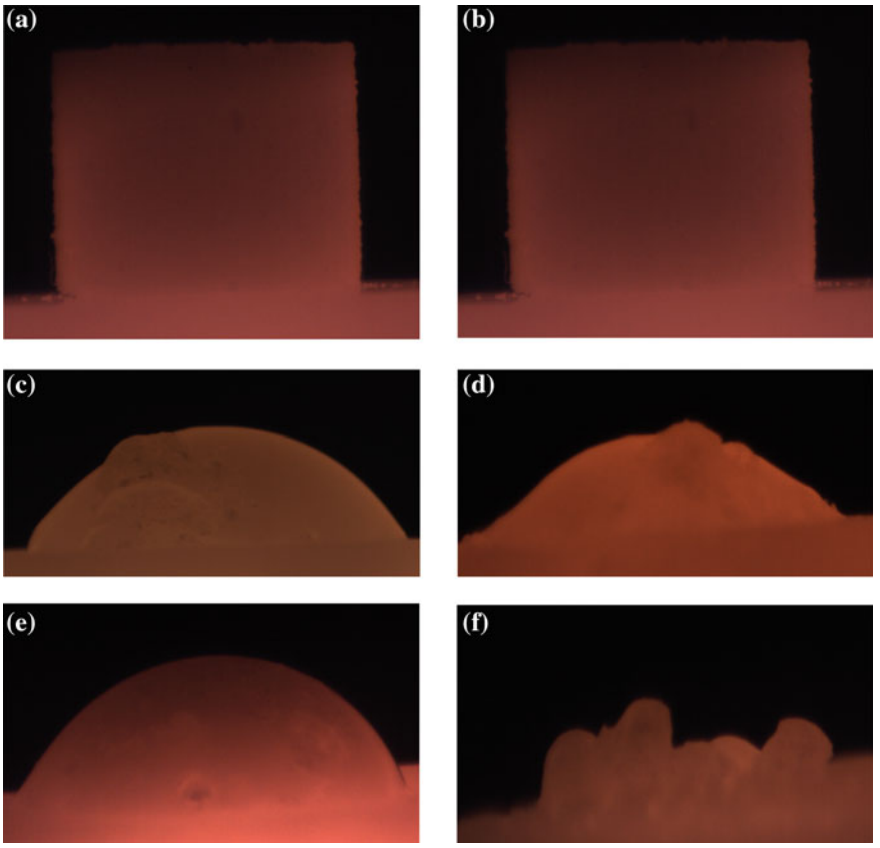

Fig. 6 Ash–carbon interaction of FeMn slag with different carbon substrates in sessile drop test **a** First deformation at 1190 °C on graphite substrate, **b** Hemispheric temperature at 1239 °C on graphite substrate, **c** shape at 1696 °C on graphite substrate. **d** shape at 1698 °C on metallurgical coke, **e** shape at 1698 °C on coal char and **f** shape at 1699 °C on charcoal

The slag intrusion was measured for channel diameter larger of 2.5, 4, and 5 mm. At a channel diameter of 4 mm, some of the slag passed through the channels for metallurgical coke, whereas no slag flow was observed for charcoal and coal char samples. However, at a channel diameter of 5 mm, the complete slag droplets passed through the channels of all carbon substrates. The non-wetting properties of charcoal, coal char and metallurgical coke towards FeMn will decrease the slag flow into the void. However, it may be possible that small slag droplets pass into the void fraction with smaller openings before they coalescence to larger slag clusters inside the packed bed, inhibiting a further flow through the bed.

The burden of raw material in the SAF introduces a load on the molten slag, which can potentially press or force the molten slag into the void. However, the current experiments showed that a compaction pressure of 10 kPa was not sufficient

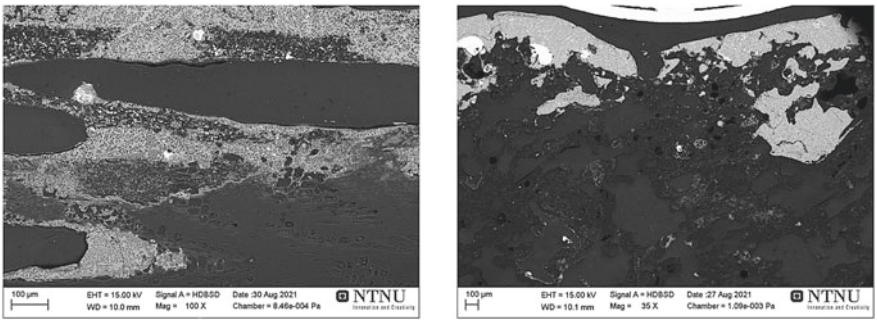

(a) **(b)**

Fig. 7 SEM images of the cross section of the carbon substrate from sessile drop test: **a** charcoal top layer and **b** metallurgical coke top layer

Table 2 EDS spot analysis of charcoal and metallurgical coke substrate and slag from sessile drop test

Element, %/%	Charcoal substrate			Metallurgical coke substrate		
	Carbon	Surface layer	Slag	Carbon	Surface layer	Slag
C	100	13.0	8.1	98.7	18.1	8.9
O		5.8	41.4		6.3	42.1
S				0.4		
Al		0.4	8.9	0.5	0.4	8.2
Ca			9.5	0.4	1.1	11.0
Si		17.3	9.3			5.0
Mn		40.0	22.8		48.3	24.8
Fe		23.5			11.3	

to compress the molten slag into the void fraction of fines or small carbon particles (3.35–4.75 mm).

For coal char and charcoal particles, the molten slag formed an additional layer on top of the carbon bed, whereas small amounts of slag were found at the bottom of the crucible for metallurgical coke, as shown in Fig. 8. Fine particles in carbon blends can therefore hamper the slag transport in the upper region of the dry coke bed. Fine formation will increase with the addition of mechanical weak material in carbon blends, for example, charcoal in metallurgical coke.

Figure 9 presents the electrical resistivity measurements for graphite cylinders with a partial slag layer in the contact region. A graphite rod (length: 100 mm, diameter: 16 mm) was used as a reference for the material property. It is seen that the electrical resistivity further decreases at temperatures above about 1200 °C, corresponding to the partial slag melting for the top carbon particle. In addition, the electrical resistivity became more stable, in which the standard deviation of the

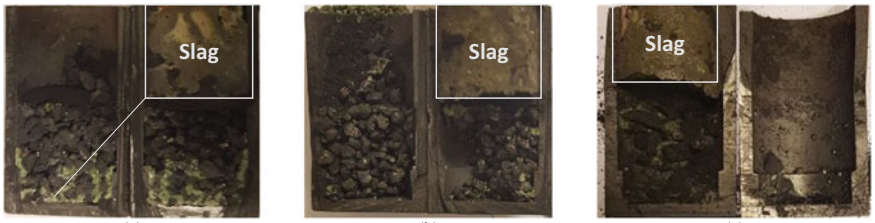

Fig. 8 Images of **a** metallurgical coke, **b** coal char and **c** charcoal packed beds with a top layer of FeMn slag. Parts of the packed beds of charcoal were removed prior to the image to investigate possible slag intrusion in the packed bed

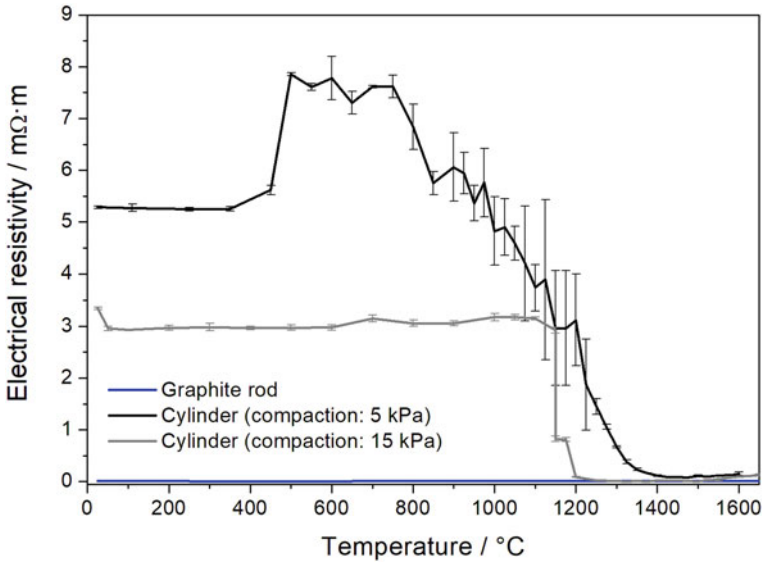

Fig. 9 Electrical resistivity of graphite cylinders with FeMn slag at the contact area. The graphite rod was investigated to measure the electrical resistivity of the carbon material

measurements decreased by a factor of $\geq$5. The large standard deviation is related to the weak contact by the low compaction pressure [7]. The increased stability and decreased electrical resistivity indicate that the compaction pressure and contact resistance are of less importance in the wetted carbon bed, respectively, that most of the electrical energy dissipation takes place in the dry coke bed.

The electrical resistivity of the carbon–FeMn slag packed beds is shown in Fig. 10. At temperatures below 1000 °C, the electrical resistivity of the carbon–slag blends was $\approx$50% larger than that of the dry carbon material, whereas a lower electrical resistivity was measured at temperatures above about 1200 °C.

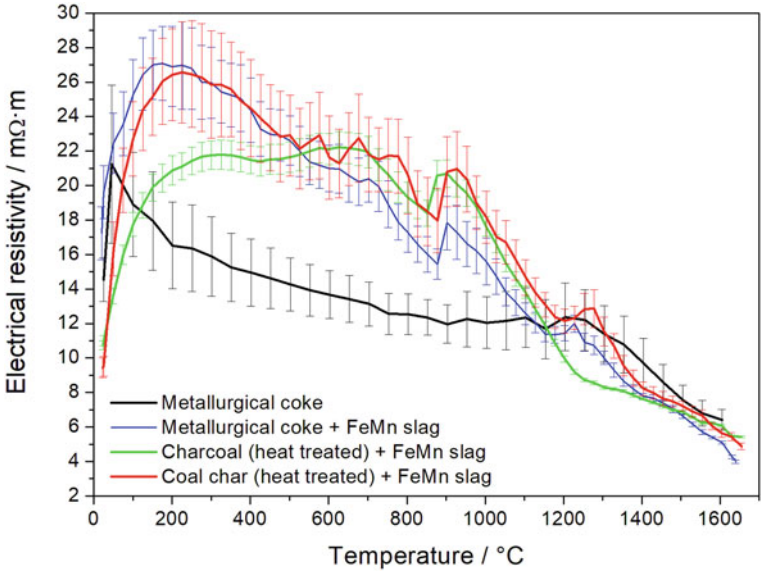

Fig. 10 Electrical resistivity of different carbon–slag packed beds at temperatures below 1650 °C

It is hypothesized that the higher electrical resistivity is related to the replacement of carbon by slag particles, decreasing the amount of possible current paths through the packed bed [10]. At higher temperatures, the nonconductive slag becomes conductive and reduces the contact resistance between the particles.

Figure 9 also shows that the contact resistance between graphite particles was almost rendered of little consequence due to the molten slag forming between the particles at elevated temperature. COMSOL simulations have shown that the current density at the contact area of particles in wetted carbon beds is the highest at the contact point [16]. Current paths through the FeMn slag would increase the current density at the contact areas between the particles. A similar electrical resistivity of FeMn slag and metallurgical coke was reported for 1200–1400 °C, in which the electrical conductivity increases with increasing temperature [17]. However, further reactions between the molten slag and the carbon bed can result in gas formation at the contact area and may result in an interference of the current paths.

Despite the poor transport of FeMn slag in the preliminary experiments, ≈33–50% of the slag was recovered below the measurement zone. Thus, slag droplets, which did not coalesce with other droplets, passed through the carbon bed. In addition, some of the droplets exhibited a metallic appearance and will be further investigated. It is expected that an increased void filling of the wetted carbon bed will result in a further decrease of the electrical resistivity. An increased electrical conductivity between the carbon particles will decrease the risk of micro-arcs and arcs in the carbon bed, decreasing the energy dissipation in wetted carbon beds [9]. The investigated

carbon species resulted in a more equal electrical resistivity in the wetted carbon bed compared to the dry carbon bed, which differed by a factor of 2–3 [4, 11, 18, 19].

The results are promising in that renewable reductants (e.g., charcoal) can replace fossil-fuel-based reductants without negatively affecting the heat generation in a SAF. Heat generation in the dry carbon bed is further increased by the larger electrical resistivity of charcoal, whereas the electrical resistivity in wetted carbon beds remain nearly constant. The local heat generation near the electrodes may improve the temperature profile in a SAF, enhancing the flow properties of the slag by tapping the furnace. Furthermore, the low electrical resistivity of charcoal at temperatures less than 1000 °C will minimize possible current paths in the burden.

Conclusion

The electrical resistivity of wetted carbon beds was measured for FeMn slag in charcoal, coal char, and metallurgical coke packed beds and was determined to 5.5–6.5 mΩ m at 1550 °C. Thus, the difference in the electrical resistivity of wetted carbon beds was reduced to less than 1 mΩ m at elevated temperature, whereas dry carbon beds can differ by more than 10 mΩ m (e.g., 6 mΩ m for metallurgical coke and 18 mΩ·m for charcoal). The slag between single particles rendered the contact resistance between the particles to a low level resulted in an electrical resistivity to be close to that of the pure material. Thus, a wetted carbon bed has a lower electrical resistance than that of the pure carbon materials in dry coke beds.

Charcoal, coal char and metallurgical coke exhibited a non-wetting behavior for temperatures less than 1650 °C. The high surface tension in combination with the not-wetting properties resulted in a minimum channel diameter of 4 mm for FeMn to pass into the void fraction. Large slag droplets and coalescence of small droplets can hinder the flow through the carbon bed and void filling. Pressure applied to the burden did not enhance the flow into a charcoal or coal char matrix, whereas small amounts of slag were recovered in the metallurgical coke bed. It was confirmed in sessile drop experiments that FeMn slag penetrated the outer layers of the carbon particles at temperatures above 1600 °C for charcoal and metallurgical coke. It is assumed that the macro-porosity of metallurgical coke and charcoal and the partial consumption of surface carbon increased the flow into the carbon matrix.

The results indicate that renewable reductants can, in all likelihood, replace fossil-fuel-based reductants in the wetted carbon bed without negatively affecting the electrical properties in the lower part of the SAF. The larger electrical resistivity of the dry carbon (charcoal) bed will further increase the heat generation close to the electrodes, possibly decreasing slag viscosity by an increased temperature.

References

1. Norsk Industri (2016) The Norwegian process industries' roadmap-combining growth and zero emissions by 2050. Available online: https://www.norskindustri.no/siteassets/dokumenter/rapporter-og-brosjyrer/the-norwegian-process-industries-roadmap-summary.pdf (accessed on 10 September 2018).
2. Carvill J (1994) Mechanical engineer's data handbook, Butterworth-Heinemann, 1st(edition), p 352
3. Tangstad M (2013) Metal production in Norway, 1. ed., Akademika, p 240
4. Eidem PA, Tangstad M, Bakken JA (2007) Measurement of material resistivity and contact resistance of metallurgical coke. In: Proceedings of the INFACON XI, New Delhi, India, pp 561–571
5. Eidem P, Tangstad M, Bakken J (2008) Determination of electrical resistivity of dry coke beds. Metall Mater Trans B 39(1):7–15
6. Eidem PA, Tangstad M, Bakken JA (2008) Determination of electrical resistivity of dry coke beds. Metall Mater Trans B 39B:7–15
7. Surup GR, Pedersen TA, Chaldien A, Beukes JP, Tangstad M (2020) Electrical resistivity of carbonaceous bed material at high temperature. Processes 8(8):933
8. Barker I, RennieM, Hockaday C, Brereton-Stiles P (2007) Measurement and control of arcing in a submerged-arc furnace. In: Proceedings of the INFACON XI. New Delhi, India, pp 685–694
9. Steenkamp JD, Hockaday CJ, Gous JP (2016) Analysis of electrical energy dissipation in submerged-arc furnaces producing silicomanganese. In: 11th European electric steelmaking conference & expo (EEC2016), Venice, Italy, pp 1–11
10. Dijs H, Smith D (1980) Factors affecting the resistivity and reactivity of carbonaceous reducing agents for the electric-smelting industry. J S Afr Inst Min Metall 80:286–296
11. Surup GR, Smith-Hanssen N, Tangstad M (2021) The properties of carbon blends in submerged arc furnaces. In: Proceedings of the 16th international ferro-alloys congress (INFACON XVI), Trondheim, Norway, pp 1–11
12. Gaal S, Lou D, Wasbø S, Ravary B, Tangstad M (2015) Melting phenomena in ferromanganese production. In: Proceedings of the INFACON XI. New Delhi, India, pp 247–257
13. Ringdalen E, Gaal S, Tangstad M, Ostrovski O (2010) Ore melting and reduction in silicomanganese production. Metall Mater Trans B 41B:1220–1229
14. Safarian J, Kolbeinsen L (2008) Kinetic of carbothermic reduction of MnO from high-carbon ferromanganese slag by graphite materials. ISIJ Int 48(4):395–404
15. Safarian J, Tangstad M (2010) Slag-carbon reactivity. In: INFACON XII, Helsinki, Finland
16. Eidem PA (2008) Electrical resistivity of coke beds. PhD thesis, Norwegian university of science and technology, Trondheim, Norway, ISBN 978-82-471-1258-8
17. Miyauchi Y, Mochida M, Fuchi Y (2001) High thermal electrical property of manganese ore in the production of high carbon ferromanganese. In: Proceedings of the INFACON IX, Quebec City, Canada, pp 236–243
18. Monsen B, Tangstad M, Solheim I, Syvertsen M, Ishak R, Midtgaard H (2007) Charcoal for manganese alloy production. In: Proceedings of the INFACON XI, New Delhi, India, pp 297–310
19. Monsen B, Tangstad M (2004) Use of charcoal in silicomanganese production. In: Proceedings of the INFACON X, Cape Town, South Africa, pp 392–404

Electrical Resistivity of Transformed Carbon Materials in the Silicon Furnace

H. Hoover, G. Saevarsdottir, and M. Tangstad

Abstract Optimal current paths through the silicon furnace depend on the electrical properties of the charge materials. It is essential for good tapping conditions that sufficient current is supplied to the arc and lower part of the furnace. As such, the electrical resistivity of the charge mix as it is transformed in the furnace is investigated. Various carbon materials (coal, charcoal, and char) are partially transformed at high temperatures to silicon carbide (SiC) through reactions with silicon monoxide (SiO) gas. The temperature gradient in the crucible creates layers of varying degrees of conversion. These layers are separated and characterized based on SiC, carbon, and Si content. The electrical resistivity of each layer is then measured from 25–1600 °C. When the majority of the material is transformed to SiC, it will raise the resistivity compared to the carbon material, until silicon forms, when it will decrease again. The original structure appears to be more important to the resistivity than the transformation to SiC.

Keywords Silicon production · Electrical resistivity · Silicon carbide · Carbon materials

Introduction

Silicon is produced through the carbothermic reduction of quartz in electric arc furnaces. Reactions 1–3 are a summary of the main chemical processes happening in the furnace. The silicon (Si) production process requires large amounts of electrical energy supplied to the system via carbon electrodes. The high temperature zone

H. Hoover (✉) · M. Tangstad
NTNU, Trondheim, Norway
e-mail: haley.hoover@ntnu.no

M. Tangstad
e-mail: merete.tangstad@ntnu.no

G. Saevarsdottir
Reykjavik University, Reykjavik, Iceland
e-mail: gudrunsa@ru.is

J. D. Steenkamp et al. (eds.), *Furnace Tapping 2022*, The Minerals, Metals & Materials Series, https://doi.org/10.1007/978-3-030-92544-4_15

(lower in the furnace) requires sufficient energy to sustain the electric arc, as well as the relevant endothermic reactions [1]. In general, most of the current should pass from the electrode to the metal/slag pool at the bottom of the furnace or to the crater wall consisting of primarily silicon carbide. However, additional current paths through the furnace depend on the electrical properties of the charge materials [2]. The charge mix will be exposed to various temperatures and silicon monoxide (SiO) gas as it enters and moves down the furnace. Subsequent transformations and chemical changes will change the electrical properties of the material, which can affect the furnace's efficiency [3, 4]. As explained by Magnessun [4], the relationship between electrical and metallurgical conditions is often neglected as they are usually studied separately, despite knowing one directly affects the other. The efficiency of the furnace is directly related to the tapping process. It is important that tapping does not negatively affect the electrical conditions in the reaction zones and vice versa. Poor tapping conditions in the furnace can lead to clogging and accumulation of materials, mainly silicon, which can cause the reverse of Reaction 2. Furthermore, silicon can react with carbon and disrupt the electrical balance in the furnace and create unstable electrode positions and gas blows [5]. These issues can take substantial time to correct and lead to lowered Si yield. Direct studies on the electrical properties of the charge mix are rare, as current literature usually focuses on pure materials or does not study high temperatures. For example, Eidem [6] explored the resistivity of coke beds at high temperature and studied the effects of contact resistance, whereas Krokstad [7] studied single particles from industrial samples of both mixed and pure materials. Krokstad found that samples of industrial α-SiC had a resistivity less than 20mΩm around 1600 °C which was lower than intrinsic SiC. Eidem concluded that contact resistance is responsible for much of the bulk resistivity, but its contribution decreases with increasing temperature.

There is no knowledge of the resistivity of partly transformed materials, except for the preliminary findings of Hoover et al. [8, 9] where the electrical resistivity of the bulk charge mix as it is transformed to SiC in the furnace is investigated from 25–1600 °C. This work seeks to build on this work using three carbon materials (C) (coal, charcoal, and char) that are partially transformed at 1850 °C to silicon carbide (SiC) through reactions with SiO gas. The temperature gradient in the crucible creates layers of varying degrees of conversion. The material is characterized based on SiC, C, and Si content. Hoover et al. concluded that there is a large variation in the bulk resistivity of partially transformed coal at low temperature, but at high temperature, the range becomes comparable, with factors such as mechanical strength and bulk density having a large effect. In some cases, this work uses the same material, and it is indicated when appropriate. The results are compared to all previous works mentioned to compare [7–9].

$$SiO_{(g)} + 2C = SiC + CO_{(g)} \tag{1}$$

$$SiO_2 + Si = 2SiO_{(g)} \tag{2}$$

Table 1 Composition of raw carbon materials in SiC production

Carbon materials	Fixed %C	%Ash	%Volatiles
charcoal	85.9	3.97	15.9
coal (heat-treated)	95.3	2.28	0.4
char	88.5	5.87	5.4

$$SiC + SiO_{(g)} = 2Si + CO_{(g)} \tag{3}$$

Experimental Methodology

SiC Production

SiC was produced in the laboratory using three different carbon materials (charcoal, coal, and char) as well as a mixture of quartz (SiO_2) and Si. The method is based on the work of Jayakumari [10]. The compositions of the raw carbon materials can be found in Table 1. The mixture of SiO_2 and Si was added to a 40 cm tall graphite crucible with an inner diameter of 11.5 cm. A graphite sieve of the same diameter was placed on top to allow for better SiO gas permeation and separation of the carbon material. The carbon material as well as a graphite tube housing the thermocouple was placed on top of the sieve. An induction furnace was used to heat the raw materials to the target temperature of 1850 °C and the holding time was varied from 60–120 min. The setup is shown as an illustration in Fig. 1. Samples were sent for chemical analysis to Degerfors Lab in Sweden to determine SiC, C, and Si content for each.

Temperature Gradient

The temperature gradient in the graphite crucible is shown in Fig. 2. The gradient was measured from the top of the sieve (~6 cm from the bottom of the crucible) to the top of the carbon layer in increments of 2 cm. While the height of the caron layer may vary slightly, it is usually around 10–15 cm. The temperatures measured during one experiment are shown in Fig. 2. The middle thermocouple (TC3) is excluded due to a malfunction in the early stage of the experiment. The temperature profile shows approximately 100 °C change for every 2 cm of height change in the crucible.

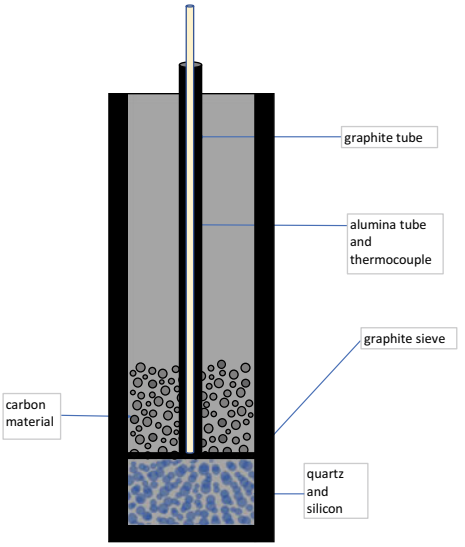

Fig. 1 Schematic of the experimental setup for SiC production including the crucible, sieve, and raw materials

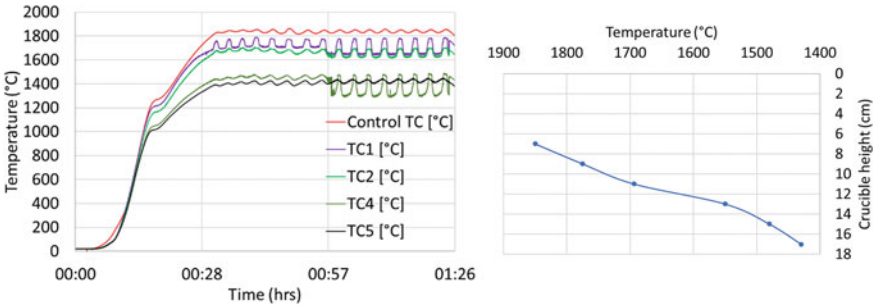

Fig. 2 Temperature profile for SiC formation in the graphite crucible setup from Fig. 4 (left) and the temperature versus crucible height (right). The profile shows approximately 100 °C for every 2 cm of height change in the crucible. Figures made by Sethulakshmy Jayakumari

Electrical Resistivity

Bulk resistivity is measured using the apparatus shown in Fig. 3, based on Pedersen [11]. The four-point method, explained by Singh [12] and used for low resistance materials, measures the voltage and current in two different places to eliminate contact resistance between the electrical contact points and the sample. The outermost crucible is made of graphite and acts as the container for the setup, as well as the bottom electrode. Inside is another crucible made from alumina, which contains the sample and insulates it from the graphite. Molybdenum (Mo) wires define the measuring zone (8 or 10 cm) as the voltage drop is measured between them. They are placed across the 8 cm wide alumina crucible such that the sample covers both

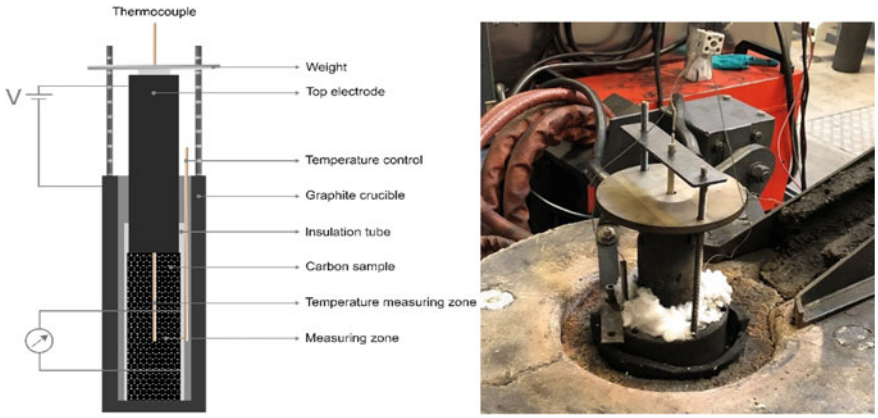

Fig. 3 Schematic of the resistivity measurement setup (left) and a picture from the lab (right). Borrowed with permission from INFACON [9]

wires. There are two thermocouples in the system, one embedded in the center of the sample to determine the temperature in the sample and another between the walls of the alumina crucible and graphite crucible. This thermocouple controls the furnace's heating rate. Additionally, a graphite block is placed on top of the sample and acts as the top electrode, and above that is a stainless-steel weight. All samples are compacted using this weight and gravity from 40 consecutive 10 cm high drops onto shock absorbent material to obtain similar compaction. The system is connected to a power source that applies current pulses every 25 °C, where the difference between the voltages measured in the top and bottom Mo wires, along with the geometry of the setup, allows for the resistivity to be calculated via Eq. 1, where (ΔV) is the voltage drop, (A) is the cross sectional area, (h) is the height of the measuring zone or the distance between the Mo wires, and (I) is the current [13].

$$\text{bulk resistivity} = \frac{\Delta V \cdot A}{h \times I} \tag{1}$$

Results and Discussion

SEM Morphology and EPMA

Scanning electron microscopy (SEM) imaging from different regions of the crucible from each carbon material was used to examine the surface morphology as the carbon is converted to SiC. This is shown in Figs. 4, 5, and 6 (note that the magnification will be varying). In addition, the back scattering (BSE) images are included in Figs. 7, 8, and 9, to show the distinct phases more clearly. Electron probe microscopic analysis

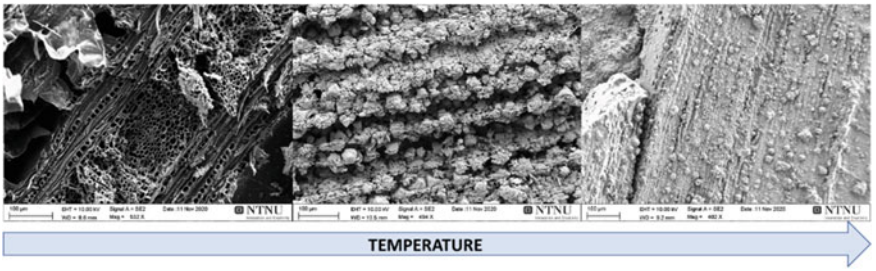

Fig. 4 SEM images of the top (left), middle (middle), and lower (right) areas of the crucible of material from coal

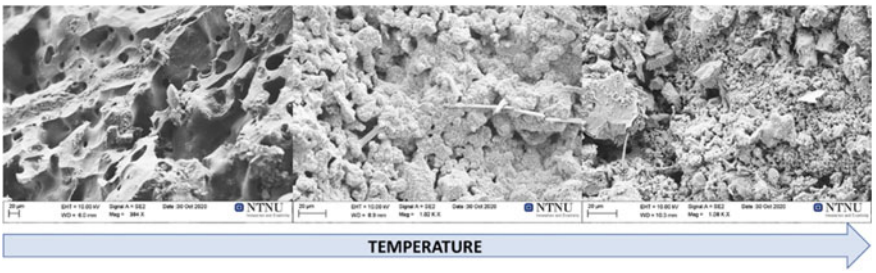

Fig. 5 SEM images of the top (left), middle (middle), and lower (right) areas of the crucible of material from charcoal

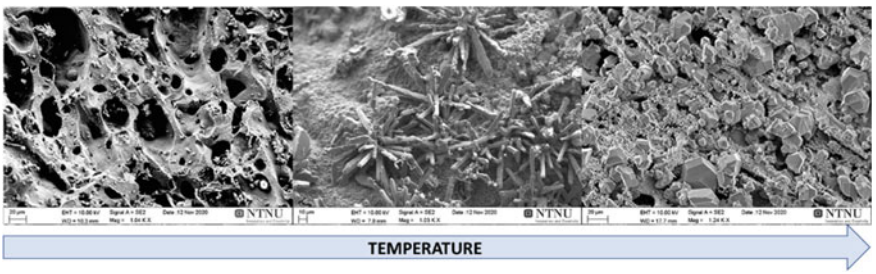

Fig. 6 SEM images of the top (left), middle (middle), and lower (right) areas of the crucible of material from char. Images taken by the author and Sethulakshmy Jayakumari

(EMPA) is shown in Figs. 10, 11 and 12 to see the Si, C, and iron (Fe) in the samples. Iron is only present in sizeable quantities in the samples from char. In the top region of the crucible, SiC is not found, as it is mostly unreacted carbon material with insufficient temperature and SiO pressures to form SiC. Further down in the crucible SiC formation is seen in the form of crystals. At the bottom of the crucible, where the material is exposed to the highest temperatures and SiO pressures, most of the carbon is transformed and Si begins to form in the SiC particles. All materials were

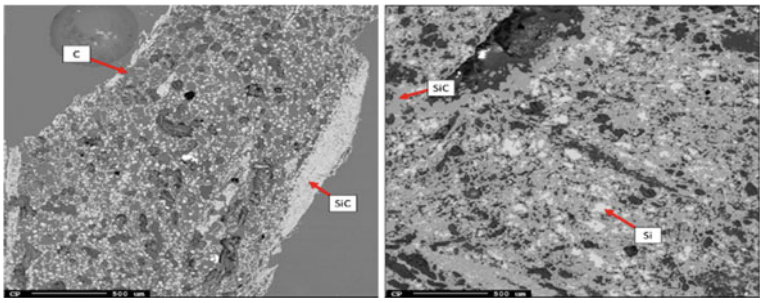

Fig. 7 BSE images (same as Fig. 10) of the middle (left) and lower (right) areas of the crucible of SiC made from coal. Three phases of C, SiC, and Si are seen. Carbon is dark gray, SiC is medium gray, and Si is light gray. Shown with permission from INFACON [9]

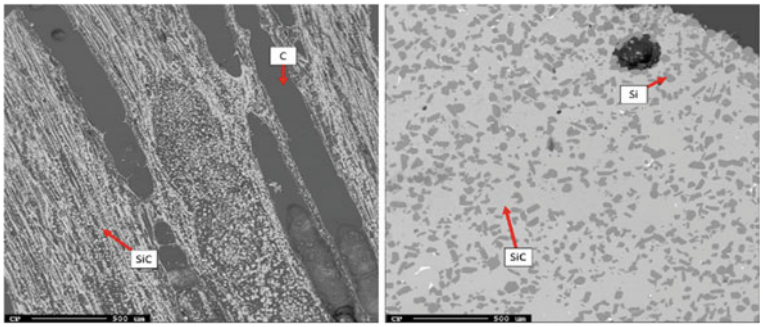

Fig. 8 BSE images (same as Fig. 12) of the middle (left) and lower (right) areas of the crucible of SiC made from charcoal. Three phases of C, SiC, and Si are seen. Carbon is dark gray, SiC is medium gray, and Si is light gray

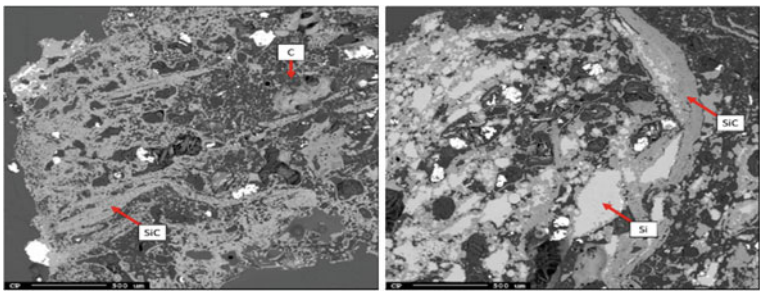

Fig. 9 BSE images (same as Fig. 11) of the middle (left) and lower (right) areas of the crucible of SiC made from char. Three phases of C, SiC, and Si are seen. Carbon is dark gray, SiC is medium gray, and Si is light gray

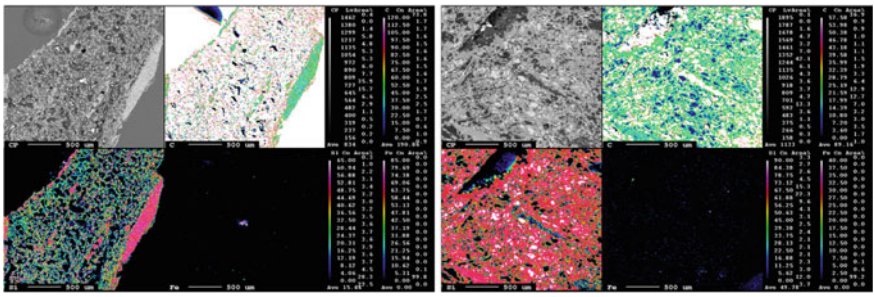

Fig. 10 EMPA of the middle (left) and lower (right) areas of the crucible of SiC material from coal. Elemental mapping shows the carbon and silicon distribution, as well as the presence of smaller iron impurities. Shown with permission from INFACON [9]

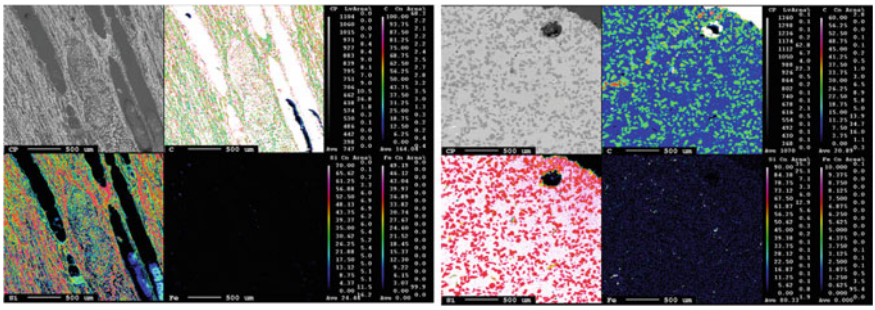

Fig. 11 EMPA of the middle (left) and lower (right) areas of the crucible of SiC material from charcoal. Elemental mapping shows the carbon and silicon distribution, as well as the presence of smaller iron impurities

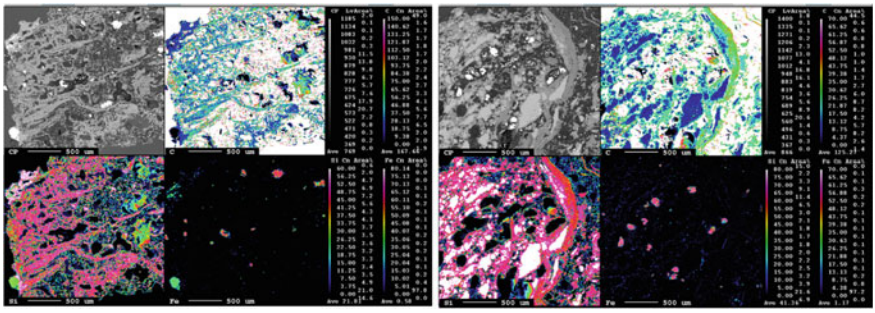

Fig. 12 EMPA of the middle (left) and lower (right) areas of the crucible of SiC material from char. Elemental mapping shows the carbon and silicon distribution, as well as the presence of smaller iron impurities

held at 1850 °C for 60–120 min, but due to the temperature gradient silicon is only expected in this part of the crucible where the temperature is over 1800 °C and can support the silicon forming reaction, just as in the industrial furnace [14].

Electrical Resistivity

Figure 13(left) shows the electrical resistivity of SiC from coal using an 8 cm measuring zone. Lines without markers indicate measurements published by Hoover et al. [8, 9]. Run numbers indicate how many times the sample has been measured, and letters indicate if the packing of the bed is the same. The 30%SiC sample has the lowest resistivity. The 69 and 72% samples are comparable in their SiC content, but the 72%SiC sample contains 7% elemental Si. This likely explains why the 69%SiC is at a higher resistivity, since silicon is both a good conductor and it is filling up the pores, both of which will lower resistivity. The general trend shows that increasing the SiC content increases the resistivity, until elemental Si begins to form, wherein the resistivity is lowered. There is a similar trend seen in Fig. 13(right), which shows the resistivity of four of the coal samples using a 10 cm measuring zone. However, elemental Si is not present in any of those materials and the 30%SiC sample is lower than the heat-treated coal (0%SiC). Since the SiC content is so low in the 30%SiC sample, the unreacted carbon (heat-treated coal) could be the controlling factor for the resistivity, meaning the sample consists of mainly of coal has that been heat-treated three times in total (calcination, partial conversion to SiC, and heating to 1600 °C for resistivity measurements).

Figure 14 shows the electrical resistivity of the materials from charcoal. Charcoal (0%SiC) as seen in Hoover et al. [8] is also shown in blue without markers. The 54%SiC has the lowest resistivity and the initial run of the 60%SiC has the highest resistivity. Both SiC materials contain elemental Si, with the 54%SiC and 60%SiC containing 6% and 36% respectively. However, since their SiC contents are

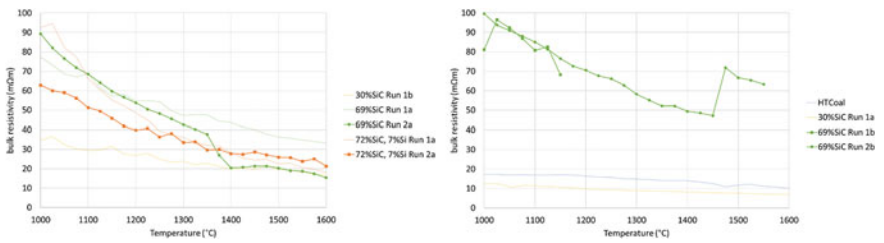

Fig. 13 Bulk resistivity vs. temperature for SiC material from coal using an 8 cm measuring zone (left) and 10 cm measuring zone (right). The 30%SiC sample has the lowest resistivity. The 69% and72% samples are comparable in their SiC content, but the 72%SiC sample contains 7% elemental Si. Since the SiC content is so low in the 30%SiC sample, the unreacted carbon (heat-treated coal) could be the controlling factor for the resistivity

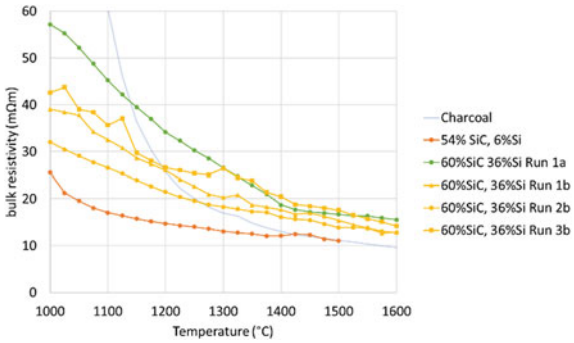

Fig. 14 Bulk resistivity vs. temperature for SiC material from charcoal. The 54%SiC has the lowest resistivity and the initial run of the 60%SiC has the highest resistivity. Both SiC materials contain elemental Si, with the 54%SiC and 60%SiC containing 6% and 36%, respectively

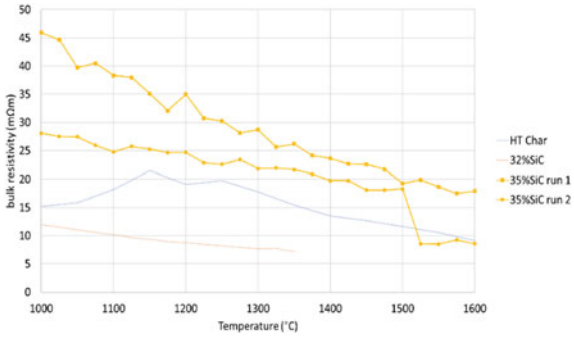

Fig. 15 Bulk resistivity vs. temperature for SiC material from char. There is higher variation here compared to other materials, as the SiC content is almost the same for all materials. The 35%SiC samples have a good agreement, but the 32%SiC sample does not

comparable, the Si content is likely the main factor affecting the resistivity, through for example increasing the density. Conversely, the amount of unreacted carbon in the 54%SiC sample is higher, 36% compared to 1.9%. Based on the resistivity of charcoal, the higher unreacted carbon content in the 54% sample could explain the lower resistivity. The 60%SiC sees larger variations at 1000 °C with multiple runs, but this difference is smaller at the high end of the temperature range. This could be uncertainty in the measurement method; however, the high temperature range is more important as there will not be SiC in the industrial furnace at 1000 °C.

Figure 15 shows the resistivity of materials from char. Lines without markers indicate measurements published by Hoover et al. [8]. There is higher variation here compared to other materials, as the SiC content is almost the same for all materials. The 35%SiC samples have a good agreement, but the 32%SiC sample does not.

Resistivity During Cooling

The resistivity of materials as they cooled from 1600 to 1000 °C was measured in some cases. Figure 16 shows the cooling of 69%SiC from coal, 60%SiC from charcoal, and 35%SiC from char. In general, cooling results in lower resistivity, with the gap widening as the temperature decreases. However, as can be seen in the coal

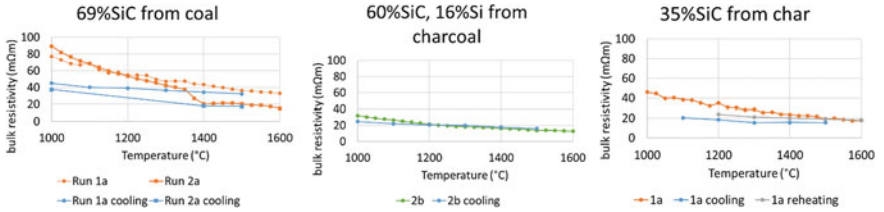

Fig. 16 Bulk resistivity vs. temperature for 69%SiC from coal, 60%SiC from charcoal, and 35%SiC from char including resistivity during cooling. The cooling curves have a lower resistivity, and the gap widens as the temperature reaches the lower limit of 1000 °C. Reheating or subsequent runs with the same packing see the resistivity rise again

and char samples, upon reheating or performing another measurement, the resistivity rises again. This could be due to better contact points at high temperatures that are able to remain as the material cools to 1000 °C but disappear as the material is cooled to room temperature and must be formed again upon reheating.

Comparison to Other Works

Figure 17 shows the resistivity at 1500 °C for all materials compared to their SiC content, as well as the ranges seen in the work of Krokstad [7]. This is based on results presented by Hoover et al. [9], with additional runs and materials from char and charcoal added. Coal is blue, charcoal is orange, and char is green. Krokstad's SiC samples from the industrial crust (shaded blue) had a range of approximately 0–20 mΩm; however, he measured the particle resistivity and not the bulk resistivity. The lack of contact resistance explains why it remains lower. The highest variation is seen in the coal samples; however, these used two different measuring zones (8 cm and 10 cm). Additionally, some samples from the coal contain elemental silicon, and some do not, diamond markers indicate the presence of Si. The 35%SiC from char and

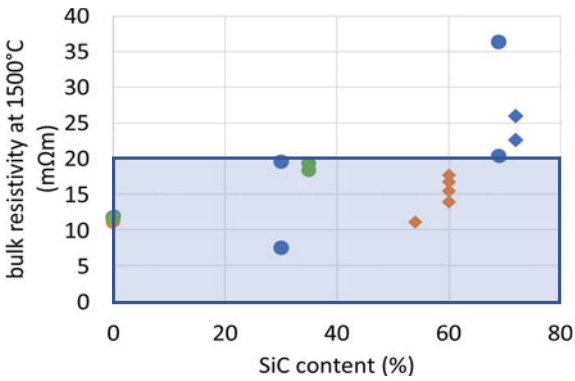

Fig. 17 Bulk resistivity at 1500 °C vs. %SiC for all materials, with diamond markers for those containing Si. Coal is blue, charcoal is orange, and char is green. The shaded blue region indicates the range of Krokstad's results (less than 20 mΩm). High variation is seen in the coal samples. The total range for all the samples is from around 7–36 mΩm (Color figure online)

60%SiC from charcoal have good agreement among their repetitions, which supports the conclusion that at higher temperatures the variations in resistivity become smaller even with multiple runs and different packings. Similarly, the total range for all the samples is from around 7–36 mΩm, which is relatively narrow and approximately the same as previous findings [9], and there is no change to this range among the different carbon materials. The similarities among the SiC from different carbon materials are interesting when considering the differences in bulk density, where for example the charcoal is significantly less dense than the other materials and previous works have concluded density has a large effect on the resistivity [5, 8, 15]. This also applies to mechanical strength, as charcoal is well known to have weak mechanical strength [16] and pure SiC is known for its strength [17]. Therefore, the original structure, not the transformation to SiC, seems to be the more determining factor for resistivity. A similar conclusion was described by Krogerus et al. [18] where changing the composition of gas cokes and chars for ferrochrome production had little effect on the conductivity. The effect of these factors cannot be ruled out, however, because they are all changing during the transformation to SiC, so it is difficult to isolate them. However, even though all materials seem to be of the same magnitude once 1500 °C is reached, previous figures in this work show there are higher variations at lower temperatures. This could be due to compaction or differences in the packing of the particles. However, in the industrial furnace, little SiC would be expected at 1000 °C, so the higher temperature results are more relevant. The general trend that increasing SiC content increases resistivity and the presence of Si will lower resistivity is still apparent.

Conclusions

It is essential for good tapping conditions that sufficient current is supplied to the arc and lower part of the furnace. A highly resistive charge mix can ensure this takes place by directing the energy into the arc. Similarly, adequate tapping can minimize the accumulation of silicon and prevent back reactions or gas blows leading to unstable electrode positions. As such, the electrical resistivity of the charge mix as it is transformed in the furnace was investigated. When most of the material is transformed to SiC, it will raise the resistivity compared to the carbon material, until silicon forms, when it will decrease again. At temperatures at the end of the measured range (1500 °C), all materials had the same magnitude, with a range of 7–36 mΩm, and the choice of carbon material had little effect. Therefore, the original structure, not the transformation to SiC, seems to be the more determining factor for resistivity.

References

1. Schei A, Tuset JK, Tveit H (1998) Production of high silicon alloys. Tapir Forlag, Trondheim, vol 1, pp 139–162

2. Sævarsdottir G, Bakken J (2010) Current distribution in submerged arc furnaces for silicon metal/ferrosilicon production. Ferrosilicon Smelt 717–728
3. Hasannezhad H, Meysami A (2018) Effects of porosity and electrical resistance of metallurgical coke and semicoke on silicon recovery in a electric arc furnace. Electr Arc Smelt 336–341
4. Magnussen T (2018) Basic paramters in the operation and design on submerged arc furnaces, with particular reference to production of high-silicon alloys. J S Afr Inst Min Metall 118:631–636
5. de Oliveira V (2018) Tapping of metallurgical silicon furnaces—a brief. In: Furnace tapping 2018, Kruger National Park, pp 1–13
6. Eidem PA (2008) Electrical resistivity of coke beds. NTNU, Trondheim, pp 9–41
7. Krokstad MA (2014) Electric resistivity in industrial SiC-slag. NTNU, Trondheim, pp 22–24
8. Hoover H, Pedersen T, Sævarsdottir G, Tangstad M (2020) Bulk resistivity of SiC and carbon materials in the silicon furnace. In: Silicon for the chemical and solar industry XV, Trondheim, pp 65–74
9. Hoover H, Saevarsdottir G, Tangstad M (2021) Electrical resistivity of partially transformed silicon carbide made from coal. In INFACON XVI, Trondheim, pp 1–14
10. Jayakumari S (2020) Formation and characterization of B- and a-silicon carbide produced during silicon/ferrosilicon process. NTNU, Trondheim, pp 78–108
11. Pedersen T (2019) Method for measuring bulk resistivity in particulate carbon materials. in: Conference paper, Trondheim, pp 29–39
12. Singh Y (2013) Electrical resistivity measurements: a review. Int J Modern Phys 745–756
13. Heaney MB (2003) Electrical conductivity and resistivity. In: Electrical measurements, signal processing, and displays. CRC Press LLC, Berkeley, pp 7–1–7–14
14. Tranell G, Andersson M, Ringdalen E, Ostrovski O, Steinmo J (2010) Reaction zones in a FeSi75 furnace—results from an industrial excavation. In: Twelth international ferroalloys congress, Helsinki, pp 709–715
15. Pedersen T (2020) Electrical resistivity in carbon materials converting to SiC, NTNU, Trondheim, pp 20–24
16. FAO (1985) Industrial charcoal making. Food and Agricultural Organization of the United Nations, Rome, pp 20–22
17. Izhevskyi V, Genova L, Bressiani J, Bressiani A (2000) Silicon carbide structure, properties, and processing. Ceramica 46(297):4–14
18. Krogerus H, Lintumma T, Jokinen P (2006) Laboratory investigations of the electrical resistivity of cokes and smelting charge for optimizing operation in large ferrochrome furnaces. S Afr Pyrometall 309–328

Part III
Session III

PGM, Nickel, and Copper Tapping: An Updated Industry Survey

I. Nolet, L. Rodd, S. Straub, J. Du Toit, T. Futterer, and W. Taylor

Abstract An industry survey of PGM-Ni matte tapping practices was published in 2014 with the aim of providing high-level information on matte tap-hole design, operation, and maintenance practices at different smelting operations. Since then, various innovation trends have been developing within the industry, with regards to safety and automation, environmental considerations, and design and monitoring technological advances aiming at enhancing tap-hole campaign life, minimizing tapping risks, and generally bringing the industry towards safer tapping. Hatch has conducted an updated industry survey, this time including PGM, Nickel, and Copper producers, with an extended view into those industry developments with specific objectives to encourage cross-pollination across industries and organizations and provide a useful reference documenting best practices in matte and metal tapping operations in the base metals and PGM industry.

Keywords Tapping · Benchmarking · Matte/Metal tapping practices

Introduction

In continuous smelting operations, the tapping of molten matte or metal is one of the most critical tasks performed by operations personnel due to the safety risk of potential exposure to molten metal or matte. The ability to tap metal or matte from a furnace tap-hole both safely and reliably is dependent on both the tap-hole design but is also critically dependent on the way in which the tap-hole is operated and maintained. Across industries, tap-hole design, operation, and maintenance strategies are typically tailored to suit the process conditions encountered as well as the required

I. Nolet (✉) · J. Du Toit
Hatch, 158 Emerald Pkway, Greenstone Hill, South Africa
e-mail: isabelle.nolet@hatch.com

L. Rodd · S. Straub · T. Futterer
Hatch, 2800 Speakman Drive, Missisauga, Canada

W. Taylor
Hatch, 61 Petrie Terrace, Brisbane, Australia

J. D. Steenkamp et al. (eds.), *Furnace Tapping 2022*, The Minerals, Metals & Materials Series, https://doi.org/10.1007/978-3-030-92544-4_16

tapping duty (or frequency of taps). This is particularly notable in PGM smelting where matte superheats up to 600 °C result in highly intense conditions during tapping, requiring a water-cooled tap-hole design to prolong the life of the tapping channel refractory, as well as frequent repairs, to ensure both the safety of personnel and reliability of the tap-hole. FeNi smelting operations, which typically involve much lower metal superheats (usually less than 100 °C), also utilize water-cooled tapblock designs but generally have lower requirements for repairs and maintenance.

In 2014, Nolet [1] published a survey of matte tapping practices and tap-hole repair strategies associated with PGM and Ni matte smelting operations, covering four key areas of matte tapping: tapblock design, tap-hole maintenance, tapblock monitoring, and tapping practices. The current paper provides an update to Nolet's survey and summarizes the results from a recent survey that was expanded to include Cu matte and FeNi smelting operations, in addition to PGM and Ni matte smelting previously covered in the 2014 paper. The ranges of metal or matte properties and production rates across these operations are summarized in Table 1.

A survey was developed, building upon the previous survey developed in 2014, including additional details relating to the same key areas of metal and matte tapping outlined above. The survey was distributed to several smelting operations across the PGM, Ni, and Cu industries, with the intent that the results would be published anonymously. The results of the survey are summarized by commodity in Tables 2, 3, and 4.

Table 1 Overview of matte/metal temperatures and compositions—range reported and average value

		PGM matte	Cu matte	Ferronickel	Ni matte
Metal/matte production (t/d)		58–210	648–2150	70–250	200–270
Metal/matte tapping Temperature (°C)		1250–1430 (1371)	1245–1265 (1255)	1400–1485 (1449)	1185–1370 (1260)
Estimated superheat, calculated (°C)[1]		215–498 (413)	150–225 (182)	20–218[2] (73)	58–375 (167)
Composition (weight %)	Ni	12–43 (20)	–	12–40 (29)	25–48 (33)
	Cu	10–28 (14)	62–69 (64.0)	0.03–0.68 (0.22)	0–12.5 (4.7)
	S	24–32 (30)	20–23 (22)	0.1–1.0 (0.4)	9–27 (19)
	C	–	–	0.02–3 (0.79)	–
	Cr	0–0.3 (0.1)	–	0.03–2 (0.54)	–
	Si	0–4.7 (1.2)	–	0.01–4 (1.0)	–
	Fe	3.8–43 (34.3)	6.5–13.2 (10.1)	59–79 (68)	21–64 (41)

Notes

[1] Liquidus temperatures were calculated using FactSage™ using various databases for mattes and alloys

[2] High FeNi superheat corresponds to high reduction FeNi smelting operations producing high C, high Si-containing FeNi

Table 2 Survey data for PGM furnaces

Parameter	Units	PGM—Ref A	PGM—Ref B	PGM—Ref C1	PGM—Ref C2	PGM—Ref C3
Info on plant, type of furnace, and matte/metal produced						
Tapping temperature	°C	1315	1250	1430	1430	1430
Composition: Ni	wt%	12	43	15	15	15
Cu	wt%	10	28	10	10	10
S	wt%	29	24	32	32	32
Fe	wt%	39	4	43	43	43
Matte/metal production						
Dedicated slag and metal/matte tap-holes	Y/N	Y	Y	Y	Y	Y
Nominal metal/matte production	t/d	58	210			
Total number of matte/metal tap-holes	#	2	2	2	2	2
Number of matte/metal taps	#/d	12	16			
Ladle capacity	Tonnes	12	20	16	16	16
Total mass matte/metal per ladle (typical)	Tonnes	8	12	14	14	14

(continued)

Table 2 (continued)

Parameter	Units	PGM—Ref A	PGM—Ref B	PGM—Ref C1	PGM—Ref C2	PGM—Ref C3
Number of ladles used per tap	#	1	1	1	1	1
Tapping duration (typical)	Min	15	8			
Minimum tapping duration (towards end of tap-hole campaign life)	Min	8	10	8 min per ladle		
Matte/metal temperature measurement device	–	Handheld optical pyrometer	Handheld optical pyrometer	Fixed/mounted optical pyrometer	Fixed/mounted optical pyrometer	Fixed/mounted optical pyrometer
Matte/metal temperature measurement frequency	–	Every tap	Every tap	Every tap	Every tap	Every tap
Tapblock and launder design						
Tapblock design includes removable/replacement faceplate	Y/N	Y	Y	Y	Y	Y
Tapblock design includes extension/"bullnose"	Y/N	N	N	N	N	N
Is the tapblock a dog house design?	–	Full tapblock	Full tapblock	Full tapblock	Full tapblock	Full tapblock

(continued)

Table 2 (continued)

Parameter	Units	PGM—Ref A	PGM—Ref B	PGM—Ref C1	PGM—Ref C2	PGM—Ref C3
Lintel cooler above tap-hole	Y/N	Y	N	Y	Y	Y
Total depth of tapping channel	mm	1250	535	750	750	750
Location of the tapblock on the perimeter of the furnace	–	N/A (circular)	N/A (circular)	Endwall	Endwall	Endwall
Integration of the tapblock in the furnace design	–	Tapblock positioned above skew/hearth brick	Integrated into skew/hearth brick	Integrated into skew/hearth brick	Integrated into skew/hearth brick	Integrated into skew/hearth brick
Tap-hole centreline elevation above hearth invert (or top of hearth)	mm	640				
Tap-hole centreline elevation above the top of the skew brick	mm	451				
Number of modules/bricks along the depth of tapping channel	#	7	3	5	5	5
Initial tapping channel diameter (fabricated hole dia thru tapping module block)	mm	60	75			
Tap-hole refractory type used	–	Alumina-based	Carbon-based	Magnesia-based	Magnesia-based	Magnesia-based

(continued)

Table 2 (continued)

Parameter	Units	PGM—Ref A	PGM—Ref B	PGM—Ref C1	PGM—Ref C2	PGM—Ref C3
Where is mortar used in the tap-hole arrangement?	–	Brick surfaces in contact with copper	Between inserts			
Furnace includes an emergency/drain tap-hole	Y/N	N	N	N	N	N
Length of launder	m		5.8 + 7.6			
Launder angle to horizontal	Degrees					
Lining type	–	Refractory	Refractory	Refractory	Refractory	Refractory
Water-cooled launder	Y/N	N	Y	N	N	N
Launder configuration	–	One bend	Straight	Straight	Straight	Straight
Launders equipped with fixed burners	Y/N	N	N	N	N	N
Tapping practices						
Tap-hole opening practice (drilling, lancing, or combination)	–	Combination	Combination	Lancing	Lancing	Lancing
Tap-hole closing practice (manual plugging or mud gun)	–	Mud gun	Mud gun	Manual plugging	Manual plugging	Manual plugging

(continued)

Table 2 (continued)

Parameter	Units	PGM—Ref A	PGM—Ref B	PGM—Ref C1	PGM—Ref C2	PGM—Ref C3
Number of mudgun/drilling units on matte/metal side	#	2	2	N/A	N/A	N/A
Primary driver for furnace tapping schedule	–	Furnace levels	Batch operation	Cycles of downstream equipment	Cycles of downstream equipment	Cycles of downstream equipment
Maximum allowed metal level above tap-hole centreline	mm	260	2700			
Minimum required metal level above tap-hole centreline	mm	260	800	500		
Slag tapped from matte/metal tap-hole at end of tap	–	Occasionally	Yes (to monitor levels at the end of every tap)	Never	Never	Never
Tap-hole closing material—binder type	–	Resin	Other	Other		
Tap-hole closing material—type of aggregate used (material composition)	–	Carbon-based	Other	Other	Other	Other
Typical closing material volume used	L	9	5			

(continued)

Table 2 (continued)

Parameter	Units	PGM—Ref A	PGM—Ref B	PGM—Ref C1	PGM—Ref C2	PGM—Ref C3
Maximum closing material volume used (towards the end of tap-hole campaign life)	L	15	8			
If drilling:				N/A	N/A	N/A
Drill diameter	mm		45			
Average drilling depth	mm		500			
Type of percussion used on the drill	–	Hydraulic	Hydraulic			
Criteria to stop drilling (if drilling then lancing)		Target drill depth reached	Target drill depth reached			
If lancing:						
Is the lancing manual or is there a lancing machine (if so, how many)?	–	Manual	Manual	Manual lancing	Manual lancing	Manual lancing
Lance guide	Y/N	Y	N	N	N	N
Typical number of lances used	#	2	2			

(continued)

Table 2 (continued)

Parameter	Units	PGM—Ref A	PGM—Ref B	PGM—Ref C1	PGM—Ref C2	PGM—Ref C3
Lance type	–	Open pipe	Open pipe	Open pipe	Open pipe	Open pipe
Lance pipe segment length	mm	600	4500			
Lance diameter	mm	12	8			

Table 3 Survey data for Cu furnaces

Parameter	Units	Cu—Ref A	Cu—Ref B	Cu—Ref C	Cu—Ref D	Cu—Ref E
Info on plant, type of furnace, and matte/metal produced						
Tapping temperature	°C	1265	1263	1245	1250	1250
Composition: Ni	wt%	–	–	Not available	–	–
Cu	wt%	68.5	64	62.8	63	62
S	wt%	20	23	Not available	20.7	22.7
Fe	wt%	7	10	10	11	13
Matte/metal production						
Dedicated slag and metal/matte tap-holes	Y/N	Y	Y	Y	Y	Y
Nominal metal/matte production	t/d	2150	1300	648	1600	1050
Total number of matte/metal tap-holes	#	5	7	7	6	5
Number of matte/metal taps	#/d	0	45	18	50	20
Ladle capacity	Tonnes	N/A	35	42	40	65
Total mass matte/metal per ladle (typical)	Tonnes	N/A	28	36	33	44
Number of ladles used per tap	#	N/A	1	1	1	2
Tapping duration (typical)	Min	120	15	10	30	12

(continued)

Table 3 (continued)

Parameter	Units	Cu—Ref A	Cu—Ref B	Cu—Ref C	Cu—Ref D	Cu—Ref E
Minimum tapping duration (towards the end of tap-hole campaign life)	Min	120	8	8	–	8
Matte/metal temperature measurement device	–	Quick immersion thermocouple	Quick immersion thermocouple	Quick immersion thermocouple	Quick immersion thermocouple	Other
Matte/metal temperature measurement frequency	–	Every tap	Every tap	Every tap	Every tap	Never
Tapblock and launder design						
Tapblock design includes removable/replacement faceplate	Y/N	Y	Y	Y	Y	N
Tapblock design includes extension/"bullnose"	Y/N	Y	N	N	N	N
Is the tapblock a dog house design?	–	Full tapblock	Full tapblock	Doghouse tapblock + lower cooler	Full tapblock	Full tapblock
Lintel cooler above tap-hole	Y/N	N	N	Y	N	N
Total depth of tapping channel	mm		875	230	560	750
Location of the tapblock on the perimeter of the furnace	–	Sidewall	Sidewall	Sidewall	Sidewall	Sidewall

(continued)

Table 3 (continued)

Parameter	Units	Cu—Ref A	Cu—Ref B	Cu—Ref C	Cu—Ref D	Cu—Ref E
Integration of the tapblock in the furnace design	–		Integrated into skew/hearth brick	Integrated into skew/hearth brick		Integrated into skew/hearth brick
Tap-hole centreline elevation above hearth invert (or top of hearth)	mm	450	230	0 and 200 mm		200
Tap-hole centreline elevation above the top of the skew brick	mm		0	0 and 200 mm		−159
Number of modules/bricks along the depth of tapping channel	#		4	3	12	3
Initial tapping channel diameter (fabricated hole dia thru tapping module block)	mm	50/60	70	70	55	90
Tap-hole refractory type used	–	Other	Magnesia-based	Magnesia-based	Magnesia-based	Magnesia-based
Where is mortar used in the tap-hole arrangement?	–		Usually not used around the tapblock	NA	–	The mortar is used around the channel brick and to adjust to the copper cooling block
Furnace includes an emergency/drain tap-hole	Y/N	Y	N	Y	N	N
Length of launder	m	10	From 5.6 to 6.6	5.57 and 6.9	4.66	9.3

(continued)

Table 3 (continued)

Parameter	Units	Cu—Ref A	Cu—Ref B	Cu—Ref C	Cu—Ref D	Cu—Ref E
Launder angle to horizontal	Degrees	15	6–7.3–8.5	Not available		6
Lining type	–	Refractory	Refractory	Refractory		
Water-cooled launder	Y/N	N	N	N	Y	N
Launder configuration	–	Straight	Multiple bends	One bend	Multiple bends	One bend
Launders equipped with fixed burners	Y/N	Y	N	N	N	N
Tapping practices						
Tap-hole opening practice (drilling, lancing, or combination)	–	Lancing	Lancing	Lancing	Lancing	Lancing
Tap-hole closing practice (manual plugging or mud gun)	–	Manual plugging	Manual plugging	Manual plugging	Manual plugging	Manual plugging
Number of mudgun/drilling units on matte/metal side	#		1	N/A	9	N/A
Primary driver for furnace tapping schedule	–	Furnace levels	Cycles of downstream equipment	Furnace levels	Furnace levels	Cycles of downstream equipment
Maximum allowed metal level above tap-hole centreline	mm		800	35 cm	740	800
Minimum required metal level above tap-hole centreline	mm		N/A	19 cm	600	

(continued)

Table 3 (continued)

Parameter	Units	Cu—Ref A	Cu—Ref B	Cu—Ref C	Cu—Ref D	Cu—Ref E
Slag tapped from matte/metal tap-hole at end of tap	–	Never	Occasionally	Never	Never	Occasionally
Tap-hole closing material—binder type	–	Other		Other	Other	
Tap-hole closing material—type of aggregate used (material composition)	–	Other		Other	Alumina-based	
Typical closing material volume used	L		1	0.5	0.3	±0.8
Maximum closing material volume used (towards the end of tap-hole campaign life)	L		Undetermined	0.75		
If drilling:			N/A			
Drill diameter	mm		N/A	N/A		
Average drilling depth	mm		N/A	N/A		
Type of percussion used on the drill	–					
Criteria to stop drilling (if drilling then lancing)						
If lancing:			–			
Lance guide used	–	Manual	Manual	Manual	Manual	Manual

(continued)

Table 3 (continued)

Parameter	Units	Cu—Ref A	Cu—Ref B	Cu—Ref C	Cu—Ref D	Cu—Ref E
Is a lance guide being used for alignment purposes?	Y/N	Y	N	N	N	N
Typical number of lances used	#	4	1	4–7	2	5
Lance type	–	Open pipe	Lances with internals/fillers	Open pipe	Open pipe	Open pipe
Lance pipe segment length	mm	6000/9000	3000	6000	5500	6000
Lance diameter	mm	10	6.4	6.4	10.5	6.4

Table 4 Survey data for FeNi and Ni matte furnaces

Parameter	Units	FeNi—Ref A	FeNi—Ref B	FeNi—Ref C1	FeNi—Ref C2	Ni—Ref A	Ni—Ref B	Ni—Ref C
Info on plant, type of furnace, and matte/metal produced								
Tapping Temperature	°C	1485	1445	1465	1400	1370	1225	1185
Composition: Ni	wt%	24.9	38.5	40	12	26.5	48	24.5
Cu	wt%	0.68	0.08	0.1	0.03		1.5	12.5
S	wt%	0.22	0.95	0.3	0.1	9	27	20.5
Fe	wt%	73.2	59.7	59.4	78.8	63.5	21	39
Matte/metal production								
Dedicated slag and metal/matte tap-holes	Y/N	Y	Y	Y	Y	Y	Y	Y
Nominal metal/matte production	t/d	216		70	250	221	270	200
Total number of matte/metal tap-holes	#	2	2	2	2	2	6	2
Number of matte/metal taps	#/d	8	5	9	9	11	42	4
Ladle capacity	Tonnes	50	47	40	40	21	15	26
Total mass matte/metal per ladle (typical)	Tonnes	45	46	34	34	21	13	26
Number of ladles used per tap	#	1	1	1	1	3	1	2
Tapping duration (typical)	min	35	30	10	30		12	30

(continued)

Table 4 (continued)

Parameter	Units	FeNi—Ref A	FeNi—Ref B	FeNi—Ref C1	FeNi—Ref C2	Ni—Ref A	Ni—Ref B	Ni—Ref C
Minimum tapping duration (towards the end of tap-hole campaign life)	min	20					6	30
Matte/metal temperature measurement device	–	Quick immersion thermocouple	Quick immersion thermocouple	Quick immersion thermocouple	Quick immersion thermocouple	Quick immersion thermocouple	Handheld optical pyrometer	Handheld optical pyrometer
Matte/metal temperature measurement frequency	–	Every tap	Every tap	Every tap	Every tap	Every tap	Every tap	Every tap
Tapblock and launder design								
Tapblock design includes removable/replacement faceplate	Y/N	Y	Y	Y	Y	Y	Y	Y
Tapblock design includes extension/"bullnose"	Y/N			Y	Y	N	Y	
Is the tapblock a dog house design?	–	Full tapblock	Doghouse tapblock + lower cooler	Full tapblock	Doghouse tapblock	Full tapblock	Full tapblock	Full tapblock
Lintel cooler above tap-hole	Y/N	Y	N	N	N	Y	N	

(continued)

Table 4 (continued)

Parameter	Units	FeNi—Ref A	FeNi—Ref B	FeNi—Ref C1	FeNi—Ref C2	Ni—Ref A	Ni—Ref B	Ni—Ref C
Total depth of tapping channel	mm	1154	1035	1400	1600	762	335	690
Location of the tapblock on the perimeter of the furnace	–	Sidewall	N/A (circular)	Endwall	Endwall	N/A (circular)	Endwall	N/A (circular)
Integration of the tapblock in the furnace design	–	Tapblock positioned above skew/hearth brick	Tapblock positioned above skew/hearth brick	Tapblock positioned above skew/hearth brick	Tapblock positioned above skew/hearth brick	Tapblock positioned above skew/hearth brick	Tapblock positioned above skew/hearth brick	Integrated into skew/hearth brick
Tap-hole centreline elevation above hearth invert (or top of hearth)	mm	1023		685	200	y	370	709
Tap-hole centreline elevation above the top of the skew brick	mm	451	114	75	Straight under	y	112	189
Number of modules/bricks along the depth of tapping channel	#		6	7	7	5	4	6
Initial tapping channel diameter (fabricated hole dia thru tapping module block)	mm	50	50	32	40	50	50	30
Tap-hole refractory type used	–	Magnesia-based	Magnesia-based	Alumina-based	Alumina-based	Magnesia-based	Carbon-based	Carbon-based

(continued)

Table 4 (continued)

Parameter	Units	FeNi—Ref A	FeNi—Ref B	FeNi—Ref C1	FeNi—Ref C2	Ni—Ref A	Ni—Ref B	Ni—Ref C
Where is mortar used in the tap-hole arrangement?	–		Module installation and side refractory plates	Bricks along the depth of tapping channel	Bricks along the depth of tapping channel	In between tapblocks	Minimal mortar used to fill gaps between replaceable components /bricks	Graphite plates are coated with clay before being inserted in the tap-hole
Furnace includes an emergency/drain tap-hole	Y/N	N	N	N	N	N	Y	N
Length of launder	m		4					4
Launder angle to horizontal	Degrees		15			7		5
Lining type	–		Refractory			Refractory	Refractory	Graphite
Water-cooled launder	Y/N	N	N			N	Y	N
Launder configuration	–		Straight			Straight	Straight	Straight
Launders equipped with fixed burners	Y/N	N	N			N	N	N
Tapping practices								
Tap-hole opening practice (drilling, lancing, or combination)	–	Combination	Combination	Drilling	Drilling	Combination	Combination	Lancing

(continued)

Table 4 (continued)

Parameter	Units	FeNi—Ref A	FeNi—Ref B	FeNi—Ref C1	FeNi—Ref C2	Ni—Ref A	Ni—Ref B	Ni—Ref C
Tap-hole closing practice (manual plugging or mud gun)	–	Mud gun	Mud gun	Mud gun	Mud gun	Mud gun	Mud gun	Mud gun
Number of mudgun/drilling units on matte/metal side	#		2	1	1	1 mud gun /furnace	2	1
Primary driver for furnace tapping schedule	–	Batch operation	Furnace levels	Furnace levels	Furnace levels	Furnace levels	Batch operation	Furnace levels
Maximum allowed metal level above tap-hole centreline	mm	200	201	1060	760	304.8	420	
Minimum required metal level above tap-hole centreline	mm		101	780	600	101.6	70	
Slag tapped from matte/metal tap-hole at end of tap	–	0	Occasionally	Occasionally	Never	Never	Never	Occasionally
Tap-hole closing material—binder type	–	Pitch	Other	Pitch	Pitch	Water	Resin	Water
Tap-hole closing material—type of aggregate used (material composition)	–	Magnesia-based	Alumina-based	Carbon-based	Carbon-based	Alumina-based	Carbon-based	Alumina-based
Typical closing material volume used	L		10	10	10	10–15		

(continued)

Table 4 (continued)

Parameter	Units	FeNi—Ref A	FeNi—Ref B	FeNi—Ref C1	FeNi—Ref C2	Ni—Ref A	Ni—Ref B	Ni—Ref C
Maximum closing material volume used (towards the end of tap-hole campaign life)	L			20	20	15		
If drilling:								
Drill diameter	mm	45		32	32	25	50	
Average drilling depth	mm	1000	700–850	800	1000	610		
Type of percussion used on the drill	–	Pneumatic	Pneumatic	Pneumatic	Pneumatic		None	
Criteria to stop drilling (if drilling then lancing)		Resistance	Resistance	Prevent matte\metal contact with drill bit	Prevent matte\metal contact with drill bit	Other	Target drill depth reached	
If lancing:								
Is the lancing manual or is there a lancing machine (if so, how many)?	–	Manual	Manual				Manual	Manual
Lance guide used for alignment purposes	Y/N	N	N			N	Y	N
Typical number of lances used	#		1–3			3–10	1–2	
Lance type	–	Open pipe	Open pipe			Open pipe	Open pipe	
Lance pipe segment length	mm	5000	6000			4000		
Lance diameter	mm	6.35	16			9.52		

Matte/Metal Production Data

As shown in Fig. 1, the range of reported furnace production per tap-hole is lower for the PGM (29–105 tonnes/day per tap-hole) and Ni (35–125 tonnes/day per tap-hole) furnaces. The furnace type with the largest productivity range is the Cu furnaces (92–430 tonnes/day per tap-hole). In addition to having the highest productivity per taphole, the Cu smelting furnaces surveyed have the highest number of tap-holes (5–7 tap-holes).

The PGM, Cu, and Ni matte furnaces included in this survey operate with matte/metal tapping temperatures within the range of 1185 to 1430 °C, whereas the FeNi furnaces operate within a much higher tapping temperature range of 1400 to 1485 °C.

As shown in Fig. 2 tapping duration is typically in the range of 10 to 30 minutes. Cu – Ref A is an outlier at a two-hour tapping duration. Average tapping rates vary from approximately 0.3 to 4.4 tonnes/min. Average tapping rates were calculated based on daily production, taps per day, and total tap duration.

Furnaces that are coupled with downstream equipment (e.g., converters) are generally tapped as needed to match the cycles of that equipment. For furnaces that are decoupled from downstream equipment, tapping frequency is driven by furnace levels or it is a batch process.

Figure 3 shows total matte/metal production in tonnes per day and identifies the primary driver for the furnace tapping schedule. Most respondents reported level as the primary driver for tapping. Often, tapping is driven by multiple factors. For

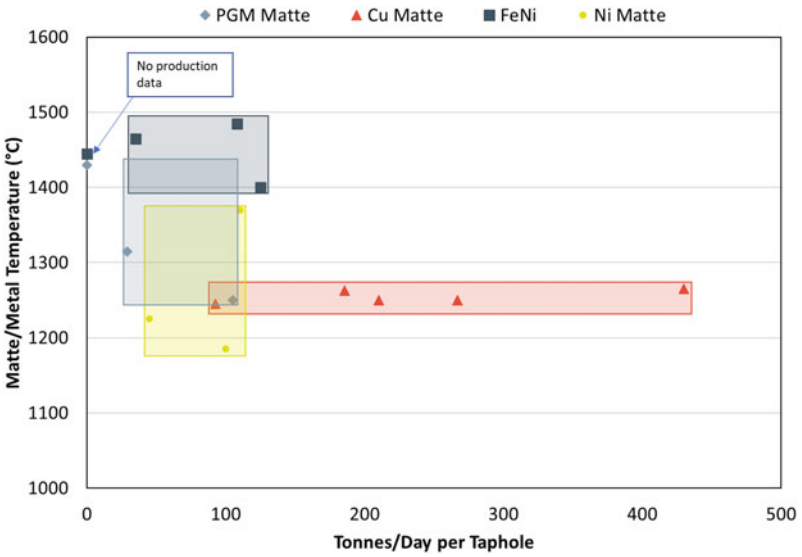

Fig. 1 Matte/metal tap-hole productivity versus temperature for various commodities

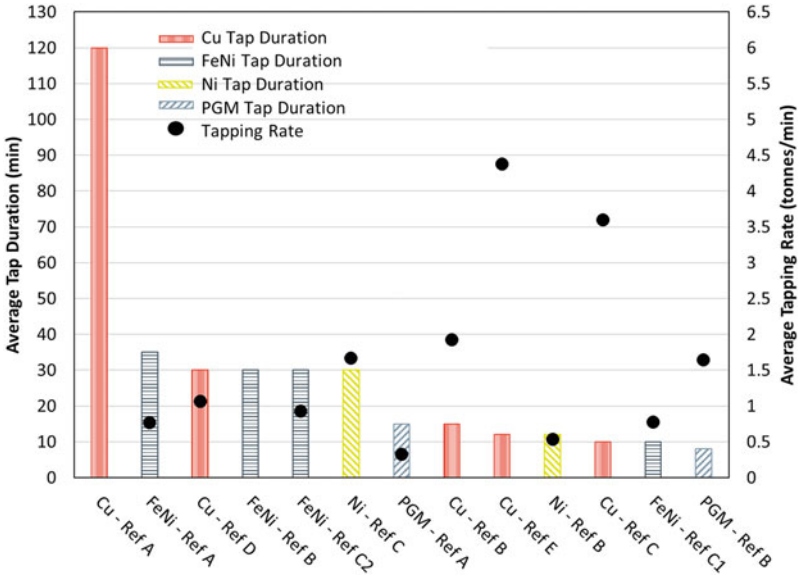

Fig. 2 Tap duration and tapping rate

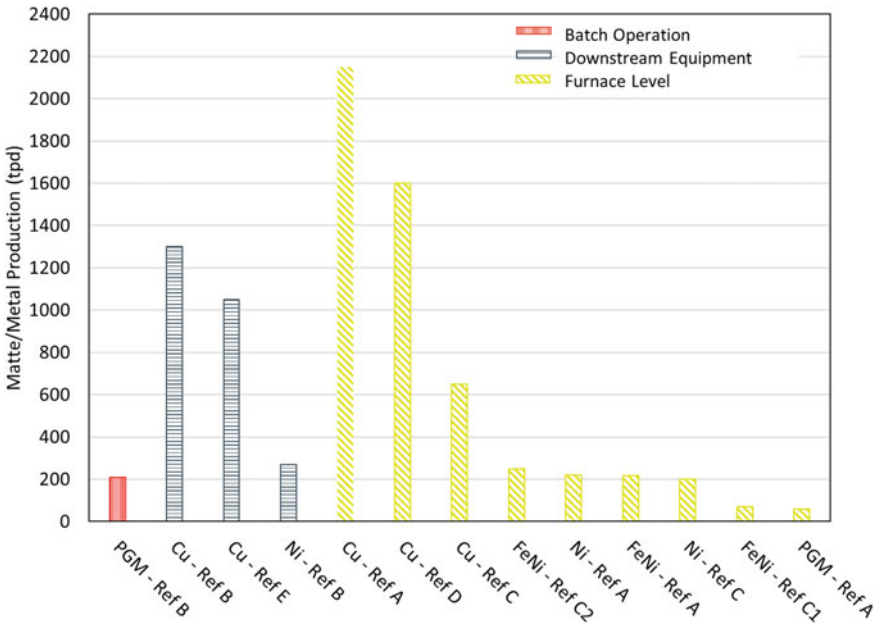

Fig. 3 Primary driver for furnace tapping schedule

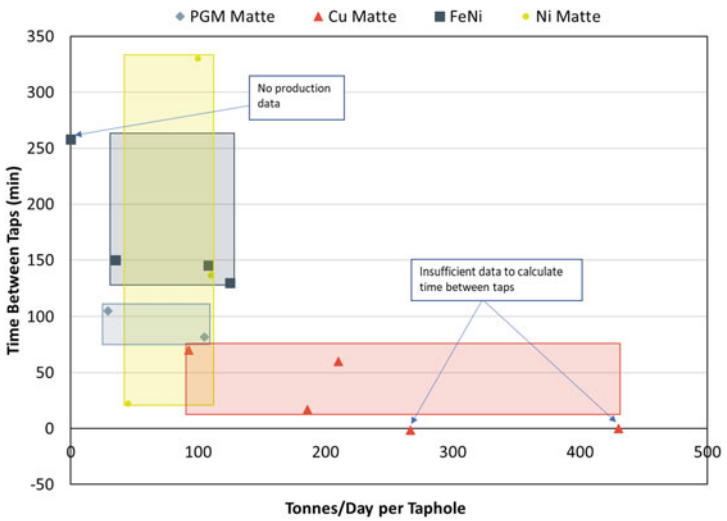

Fig. 4 Time between taps versus tap hole productivity

example, Ni matte—Ref B is driven by converter availability when operating a high matte levels, and by concentrate supply when operating at low matte levels.

The number of taps per day varied significantly from 4 up to 50. As expected, there is a strong relationship between tapping frequency and total daily production. Fig 4 shows the time between taps versus the furnace productivity by tap-hole. Time between taps ranged from approximately 15 minutes up to 5.5 hours. The Cu furnaces tend to have a shorter duration between taps.

Tap-Hole Design

All participating smelters use a water-cooled copper block surrounding the refractory tapping channel. 82% of respondents use a full tapblock design where the tapblock copper is one piece around the module bricks. The remaining have a variation of the doghouse design where the top and sides of the module bricks are covered by a one-piece, inverted U-shaped tapblock, while the bottom either has no coverage or a separate copper cooler interfacing with the main doghouse cooler above.

94% of respondents have a removable / replaceable faceplate. They are used to retain the refractory tap-hole modules against the internal hydrostatic bath pressure, and the pull out force of the drill (where used). At the same time, the faceplate provides a flat face for the mudgun to bear against, ensuring a good seal for closing.

44% use a lintel cooler above the tapblock (this can assist in the replacement of the tapblock without disturbing the sidewall above). 31% have bullnose extensions,

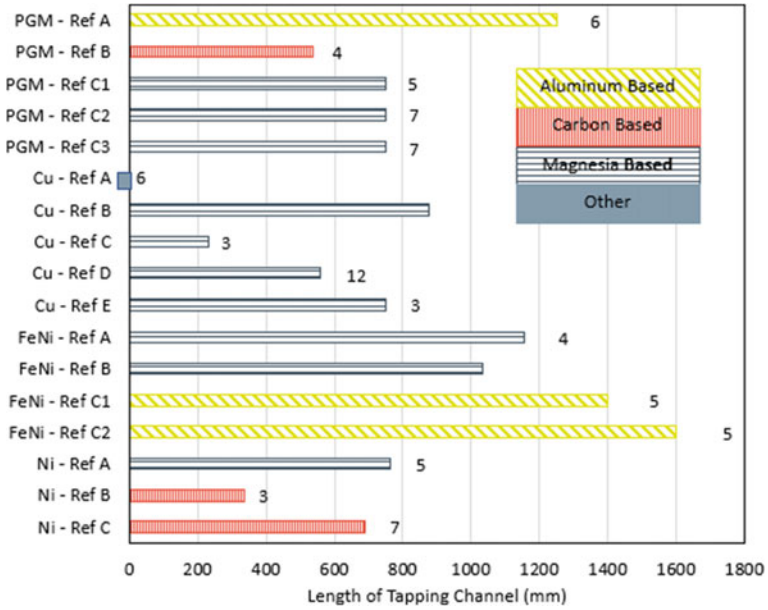

Fig. 5 Length of tapping channel, number of tap-hole bricks, and type of refractory

allowing for a shorter tapblock proper while maintaining a long tapping channel length.

All participating smelters use multiple bricks in their tap-holes, allowing sequential repairs and requiring deep tap-hole repairs only very infrequently. The number of tap-hole bricks varies between 3 and 12 (Fig. 5), depending on the length of the tapping channel and refractory design. Note that there may be some inaccuracies in the number of bricks and tapping channel length, depending on how the participating smelter defines those parameters. Some of the shorter tapping channel lengths reported were checked against client drawings and found to only include the length within the cooled tapblock, while ignoring the channel length through the remaining wall refractory. Without drawings of each furnace, it was not possible to validate and ensure consistent reporting of these values.

In the 2014 survey [1], most respondents used magnesia-based refractory. A similar proportion of respondents (56%) currently report to use magnesia-based refractory. Alumina usage is lower (19% in 2021 vs. 44% in 2014). An equal number (19%) of smelters are also using carbon-based materials, compared to none in 2014. One smelter used an undisclosed refractory material. As seen in Fig. 6, the carbon materials are currently used on lower temperature tap-holes. Although the data suggests a growing use of carbon-based refractories, there are insufficient respondents that were common between the two surveys to make this conclusion. Future

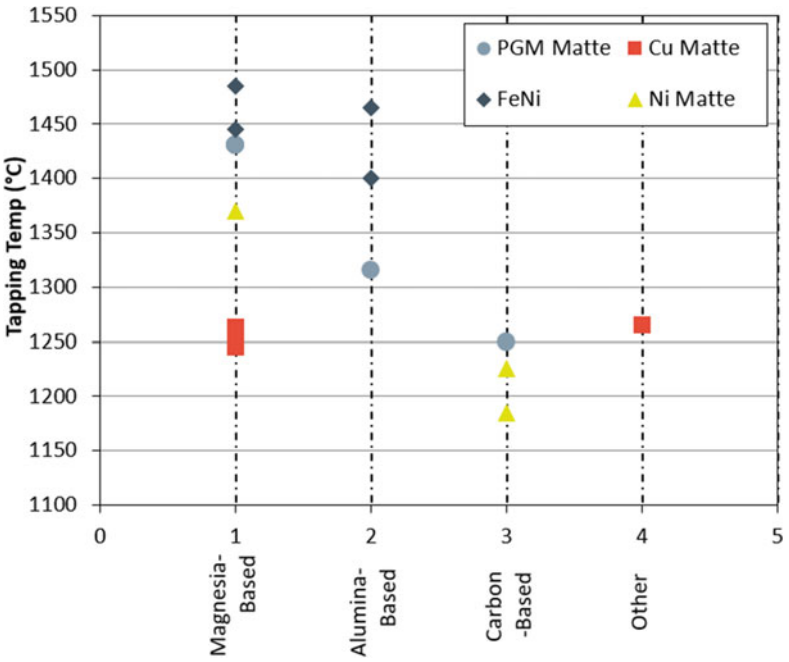

Fig. 6 Matte tapping temperature versus tap-hole brick type

revisions of this survey will aim to expand the data set to confirm these industry trends.

Figure 7 shows a plot of launder slope versus length. If the data lies on an axis, it is because data for the other axis was not available. Most Cu respondents had one or more bends, while the majority of PGM and Ni respondents had straight launders. All respondents stated their launders were refractory-lined, with one Ni matte respondent stating their lining was graphite. Only one respondent (Cu) stated their launder was equipped with burners.

Operation and Tapping Practices

The majority (53%) of the participating operations use only lancing for tap-hole opening, while 12% use a drill-only method and the remaining 35% use a combination of drilling and lancing (Fig. 8). Of the 15 furnaces using lancing, only 3 furnaces use lance guides.

For the operations that use only lancing, the reported number of lances used per tap is in the range of 4–7, except for one operation reporting the use of a single lance per tap. The operation using a single lance uses lances with internals/fillers. In

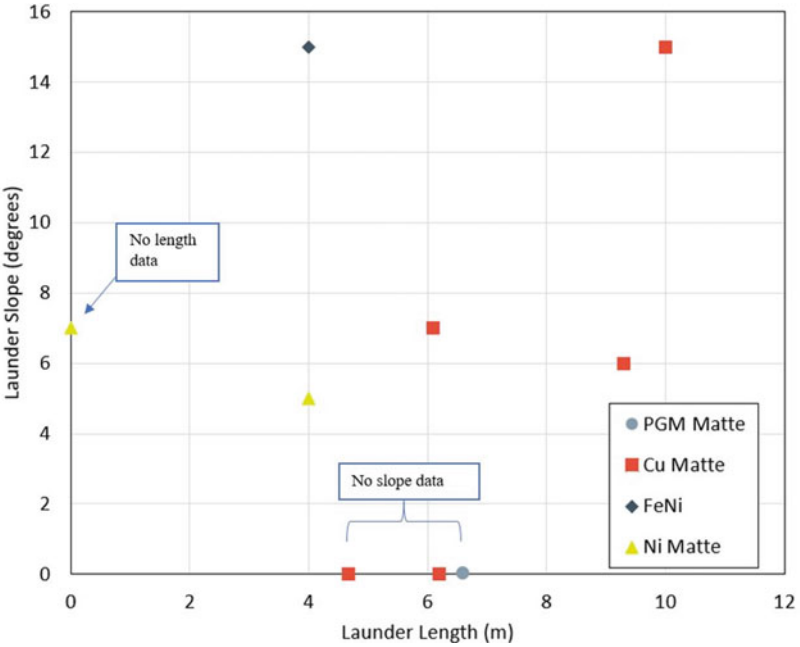

Fig. 7 Launder slope versus length

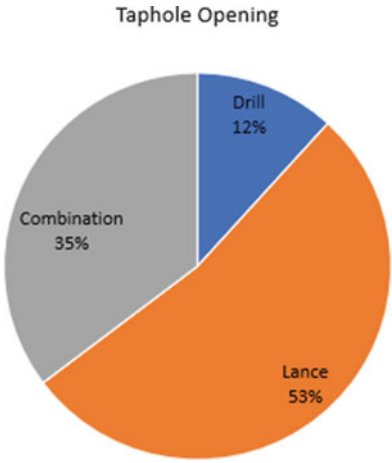

Fig. 8 Tap-hole opening method

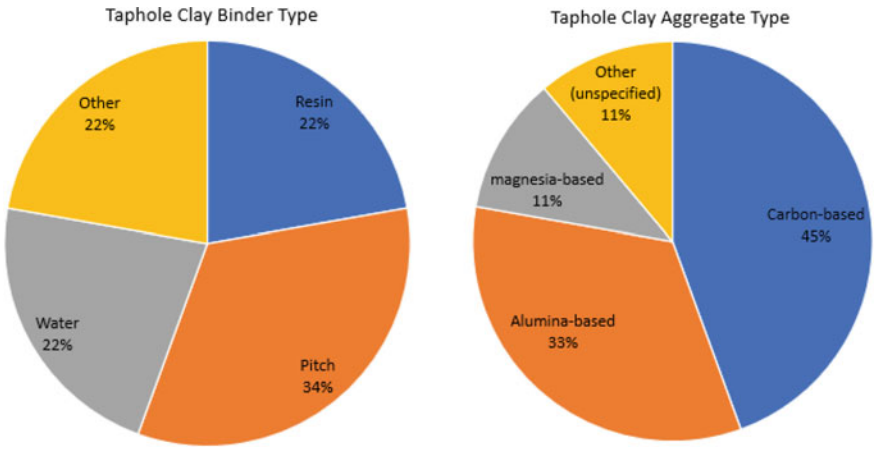

Fig. 9 Tap-hole clay binder and aggregate type

contrast, for the operations using a combination of lancing and drilling, the lances per tap decrease to around 2 lances per tap.

The considered operations are split almost equally between using mud guns (53%) and manual plugging (47%). The respondents using manual plugging typically did not specify the binder and aggregate of the tap-hole clay used. From the respondents using a mud gun for tap-hole closure (9 respondents) pitch was still most widely used as binder (34%), with resin, water, and unspecified binders accounting equally for the remaining 66% (Fig. 9). The respondents using mud guns showed a preference for carbon-based tap-hole clay aggregates (45%), followed by alumina-based (33%), and a single operation reported the use of magnesia-based aggregate in the tap-hole clay (Fig. 9). Magnesia-based and other aggregates accounted for the remaining 22%.

Industry Trends

Although the survey describes significant manual lancing or reliance on traditional drill and mud guns, the current industry trend is to avoid manual lancing where possible to reduce exposure of operators to hot molten metal (from the tapped material or the lance combustion products themselves). Manual plugging is generally undesirable for similar reasons.

One surprising result was the number of operators present on the tapping floor during tapping events, reported between 2 and 6. It is typically preferable to minimize the number of employees exposed during tapping operations to the minimum and to have clear functions or responsibilities for each of them. Protection for tappers is highly variable between smelters ranging from no protection, to protective curtains, to a full enclosure, up to a control room with CCTV/camera feedback for operators.

Ideally, tap-holes are drilled open as this gives the most uniform tapping channel and avoids module brick or tap-hole damage typically experienced with lancing. Traditional drilling machines are used in PGM, Cu, and Ni industries; however, they are generally not capable of fully opening a metal/matte tap-hole due to frozen metal/matte being too difficult to drill (or damage to the drill bit if it does fully open it). Ideally, a deep clay plug is achieved by the mud gun to minimize the size of any frozen metal/matte plug. Most respondents make use of a mudgun unit to close the tap-hole, except for 5 Cu operations and 1 PGM operation.

Several smelters are investigating or trialing automated lancing machines, either for the complete tap-hole opening or to complete the final opening after drilling. Hatch has been involved in many of these projects recently and has seen the following methods investigated (some of these have been in operation for over 10 years):

- Lancing using industrial robots (both via pre-programmed paths or remotely operated via haptic feedback).
- Lancing using dedicated lancing machines, there are 2 different styles in use by multiple vendors;
  - A coil lance reel which is straightened as it is fed.
  - Straight lances, manual or auto fed.
- Adaption of rodding devices to feed lances.
- Other innovative solutions such as adapting a lance connection into the drill machine.

In general, survey respondents are showing a high level of interest in technologies aiming at reducing operator exposure to tapfloor hazards. The main challenges encountered to the implementation of such solutions are the availability of proven technologies, space constraints on the tapping floor, and costs (Fig. 10).

One key trend in the survey responses is that most operations record or log a significant number of manual parameters related to tap-hole integrity monitoring, including tapping rate and/or duration, the mass of metal tapped, metal temperature, drilling depth, number of lances used, the quantity of closing material used, wear measurements, and photos of tapping channel during repairs. Such data is invaluable when monitoring, evaluating, and optimizing tap-hole integrity: the use of digital platforms in which the data can be logged and be made accessible via dashboards to metallurgists, production engineers, and senior management will be of great significance in the near future (Fig. 11).

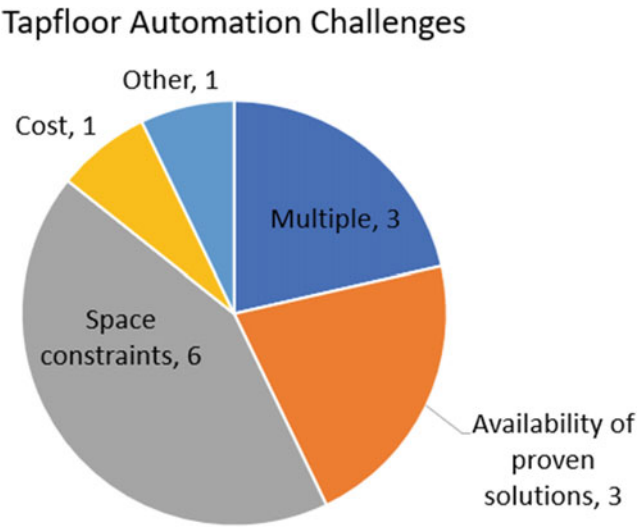

Fig. 10 Major tapfloor automation challenges as per survey responses

Fig. 11 Examples of digital platforms/dashboards for tap-hole monitoring data consolidation and visualisation

Conclusions

As with the previous 2014 survey, a survey of this nature provides the means for a comparison of matte tapping practices across operations and across industries. This recent survey expanded the commodities covered and also provides a more recent snapshot of the current state of the industry. Note that the data set is still relatively small, so trends apparent in the respondents are not necessarily reflective of the industry as a whole or by commodity. An example of this is tapping practices in copper smelters, where all respondents use manual lancing, while Hatch's experience with numerous other copper smelters covers various levels of automated drilling and lancing operations.

The intent is to keep updating this tapping database and to involve more participants across a wider range of smelting industries. Anyone wishing to participate in this effort is invited to contact the author at isabelle.nolet@hatch.com.

Acknowledgements All participants of this survey are gratefully acknowledged for the time taken to respond to the questionnaires. Special thanks to Hatch colleagues who helped reach out in the industry: Tom Gonzales, Ray Cardoza, Anastasiya Mitsui, Yan Elksnis, Anton Vernigora, Ross Forzatti, Evan Deng, Daan Sauter, Afshin Sadri, and Andrew Munsch. Thanks also to Mike Bodley for providing FactSage™ calculations.

We wish to sincerely thank the TMS Organizing Committee for a special invitation to submit a full survey to the *JOM* Special Topic on Furnace Tapping in 2022.

Reference

1. Nolet I (2014) Tapping of PGM-Ni mattes: an industry survey. In: Furnace tapping conference, SAIMM

Kansanshi Copper Smelter ISACONVERT™ Furnace Tapping System Design, Operation, and Improvements

Trevor Mwanza, Matthias Eggert, Winson Chirwa, Mark Prince, Nurzhan Dyussekenov, and Dennis Marschall

Abstract In 2019, the construction and commissioning of what was to be the world's first commercially operated ISACONVERT™ furnace was completed at the Kansanshi Copper Smelter. Between 2019 and 2021, the ISACONVERT™ furnace was operated in four campaigns in which the matte treated steadily increased from an average of 35 tonnes per day to an average of 245 tonnes per day. Manual blister and slag tapping were among the areas that had challenges and initially had a significant impact on the plant availability. Frequent failures to close the tap-holes occurred and hot metal spills were experienced as a result, giving rise to safety concerns. Several changes were implemented that resulted in a significant improvement in safety for the tappers, as well as a reduction in plant down time. This paper describes the design and operation of the ISACONVERT™ blister and slag tapping systems, and the improvements that led to successful operation of the furnace.

Keywords ISACONVERT™ · Blister tapping · Modified polish plugs · Tap-hole

Introduction

The ISACONVERT™ is a continuous copper matte converting process based on the ISASMELT™ technology, designed and supplied by Glencore Technology (formerly Xstrata Technology and MIM Process Technologies) [1, 2]. Kansanshi Mining Plc (KMP) constructed and commissioned the first commercial-scale ISACONVERT™ furnace in Solwezi, Zambia, to prove the technology and reduce the operational and technical risks in order to provide scale-up data for the design of a larger ISACONVERT™ furnace for a potential expansion of the existing smelter. The

T. Mwanza (✉) · M. Eggert · W. Chirwa · N. Dyussekenov
Kansanshi Mining Plc, Old Congo Road, Solwezi, Zambia
e-mail: trevor.mwanza@fqml.com

M. Prince
Glencore Technology, Brisbane, Australia

D. Marschall
Independent Consultant, Phoenix, AZ, USA

J. D. Steenkamp et al. (eds.), *Furnace Tapping 2022*, The Minerals, Metals & Materials Series, https://doi.org/10.1007/978-3-030-92544-4_17

installed furnace was designed to treat 12 tph of solid crushed matte at 60–64 wt% Cu producing about 81,000 tonnes of blister copper per annum.

The ISACONVERT™ furnace is a vertical furnace, supported on a concrete base. The hearth and lower furnace walls are in contact with the blister copper and are lined with magnesia chrome refractories. In the slag region, above the blister area, the furnace has copper cooling elements. The calcium-ferrite slag system of the ISACONVERT™ is known to be aggressive on any refractory materials, hence contact of slag with the bricks is minimised in the design [3]. In the section above the coolers, the furnace is again lined with magnesia chrome refractories.

The blister copper is tapped from the furnace via one of the two tap-holes that are both located 150 mm above the hearth. The hearth has a flat surface so the 150 mm offset serves as a sump. Each of the blister tap-holes is equipped with a water-cooled copper block that has a refractory insert to protect the copper blocks from direct contact with molten blister. Blister copper is transferred into copper moulds via 13-m-long, refractory lined, launders. A maximum of four ingots, each weighing up to three tonnes, are cast per tap. The launders are equipped with covers and diesel burners to minimise molten material freezing during tapping.

The furnace is equipped with one slag tap-hole located at an elevation of 1550 mm above the hearth. Slag skimming is performed through a water-cooled copper block installed in one of the copper cooling elements. The original slag launder was lined with refractory and required frequent cleaning and refractory repair. Therefore, it was soon replaced with an uncooled steel launder. Slag is skimmed directly into a ladle with a holding capacity of up to 50 t. Filled ladles are transported to a cooling area, using a Kress Hauler, to allow for slag to be slow cooled in the ladle. The slow cooled slag is then crushed for recycling to either the ISASMELT™ or ISACONVERT™ processes as coolant. Figure 1 shows the ISACONVERT™ plant flow sheet.

Both blister tap-holes and the slag tap-hole are opened by manual oxygen lancing and also closed manually by plugging with a Modified Polish Plug (MPP).

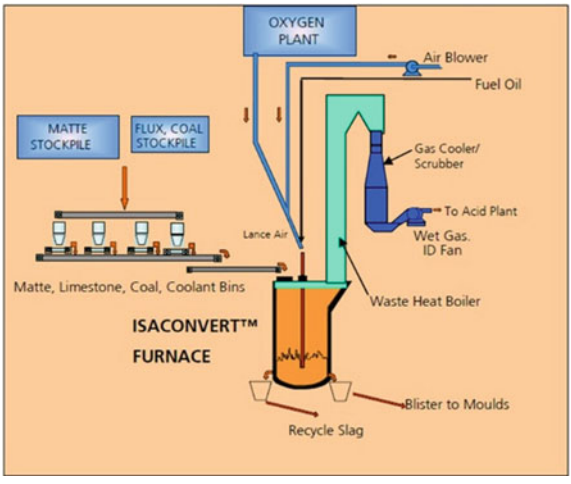

Fig. 1 Kansanshi ISACONVERT™ process flowsheet

One of the main challenges during initial operation was to establish reliable operation for blister tapping and slag skimming. A number of failures to close the blister tap-holes resulted in molten material spills and furnace draining. The material selection for blister tap-hole inserts was key to the tap-hole closing success rates as well as the life of the inserts. Determining a method that would allow monitoring of the wear of the inserts was another important aim for achieving the desired process efficiency and safe operation. Another challenge was the freezing of the slag and blister on the respective launders resulting in plant downtime for cleaning and refractory repair. This paper mainly describes the challenges experienced around slag skimming and blister tapping operation and the changes made to overcome these.

Blister Tapping

Blister Tap-Hole Refractory Insert Life

Unlike slag or copper matte, blister cannot be tapped through a water-cooled copper element. Contact of molten blister with a water-cooled copper element typically results in a rapid dissolution of the copper element, which eventually may cause a steam explosion or furnace leak with serious consequences [4]. A proven practice for tapping blister is tapping the blister copper through a refractory insert installed in the water-cooled copper block [2]. Material selection for the refractory insert was an important consideration for achieving reasonable life and tap-hole closure success. The materials used across other established copper smelter operations are varied and based on their experience, together with some theoretical considerations. The Kansanshi team considered two different materials for the inserts.

Each of the Kansanshi ISACONVERT™ blister tap-holes includes two water-cooled copper blocks, shown in crosshatch in Fig. 2. The inner copper block is installed through the shell of the furnace and butts up against the cold face of the refractory bricks (shown in orange). The outer copper block is butted up to the cold face of the inner copper block. This serves as a locking mechanism for the conical refractory inserts (shown in yellow), which fit inside the copper elements. The blister tapping channel consists of two refractory blocks inside the furnace (shown in purple) and the two refractory inserts in the copper blocks.

The inserts installed in the inner and outer copper blocks can be changed while the furnace is hot with only partial bath draining required. The tap-bricks (purple in Fig. 2) can be changed from outside the furnace if the bath is completely drained and the material in the sump is frozen. To date the tap-bricks have not been changed due to insignificant wear observed throughout the operational period. The initial tap-hole diameter for the refractory inserts and tap-bricks was 40 mm. The tap-hole diameter of the inserts was later increased to 45 mm to accommodate larger diameter MPPs and to increase the initial tapping rates after an insert replacement.

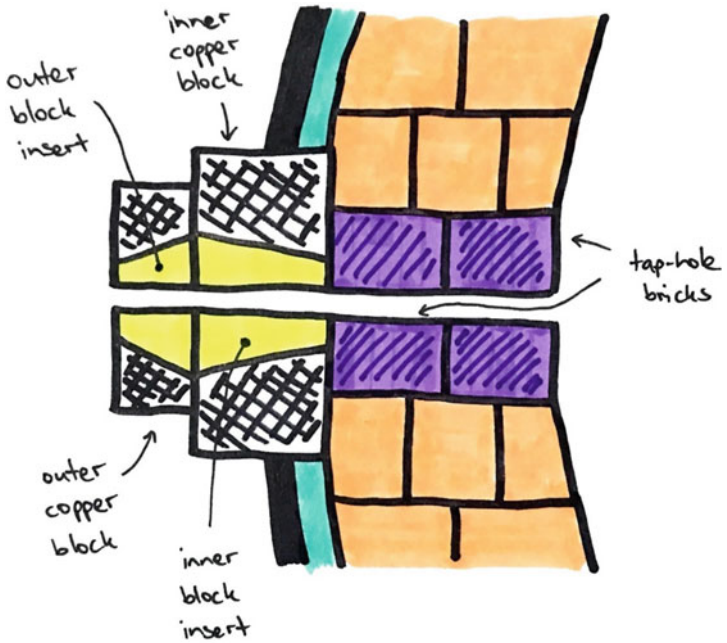

Fig. 2 Sketch of blister tap-hole arrangement

The initial operation started with fused magnesia chrome inserts and tap-bricks. An unacceptably fast wear rate of the outer inserts was observed. The tap-hole diameter of the outer insert increased from 40 mm initially to 100 mm after only 45 taps. At that rate the inserts had to be replaced weekly, which resulted in significant downtime. As a result, graphite was trialled on the outer inserts of both tap-holes. The graphite outer inserts resulted in a significantly improved insert life. It was further observed that the wear rate was not linear, with the highest wear rate being in the beginning of new insert operation. The tap-hole size was much more stable after a few days in operation. Figure 3 shows the cumulative taps achieved with the magnesia chrome outer inserts compared to the graphite outer inserts.

Blister Level Control

The level of the blister copper/slag interface is one of the most critical parameters to measure and manage in order to achieve steady converting in the ISACONVERT™ furnace. This furnace has a relatively small blister holding capacity of about two (2) cubic meters, which at the nominal feed rate would require a blister tap every 60–90 min. The main constraint to the blister capacity is the water-cooled copper elements installed in the slag region. The superheated blister copper could melt

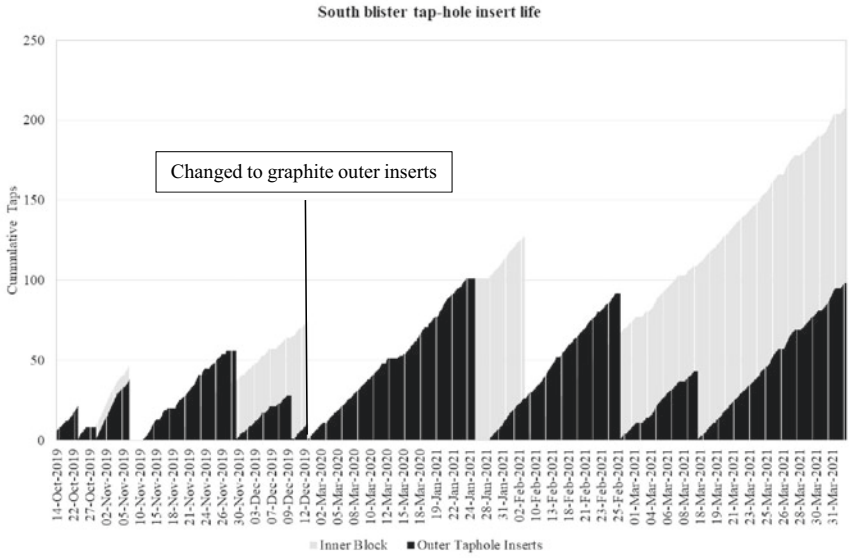

Fig. 3 Blister tap-hole insert life

the copper coolers rapidly and cause a catastrophic failure (furnace leak or steam explosion) if the molten blister comes into contact with these coolers [4]. On the other hand, operating with a low blister level in the furnace would increase the occurrences of tapping slag through the blister tap-hole, potentially accelerating the wear rate of the tapping channel.

An electromagnetic-level measuring instrument was installed for online blister-level measurement. A mass balance calculation was also incorporated in the Distributed Control System (DCS) for blister-level calculation. The electromagnetic-level instrument readings were not stable or reliable and sometimes deviated significantly from the calibration curve. Even though the mass balance calculations were more reliable, the operation was still required to stop after several blister taps to dip the furnace and confirm the blister level, so that the calculation could be reset. This caused production delays but was necessary to ensure safe operation of the furnace.

The original strategy for continuous blister-level control was to remove all of the blister during every blister tap, and then reset the blister-level calculation in the DCS to zero. It was later observed that closing the blister tap-hole with significant quantities of slag in the stream was difficult and regularly led to molten material spills with a high risk of completely draining the furnace. The wear rate of blister tap-hole inserts also increased when high quantities of slag were tapped through them. A new strategy was adopted where the tap-hole was closed immediately once the first sign of slag was observed floating on top of the blister in the moulds. This method was more effective in preventing blister tap-hole closing failures and improved the tap-hole insert life. It is believed that this strategy worked well because by the time the

tap-hole is shut, most of the stream would still be blister, which would freeze easily on the MPP. When the blister stream already consists of mostly slag it would not freeze as fast and more molten material spills would be experienced. It was therefore of utmost importance to close the blister tap-hole as fast as possible once the first slag was observed on the mould.

Modified Polish Plugs, MPPs

Modified Polish Plugs (MPPs) are used to close the blister tap-holes on the ISACONVERT™ furnace as they allow them to be opened relatively quickly via oxygen lancing. If blister tap-holes are plugged completely with clay they are difficult to open by means of manual oxygen lancing. However, if the tapping channel is not entirely filled, then blister will freeze in the tap-hole channel and result in long durations to open the tap-holes. This increases the potential for more damage in the area. This is because blister is very heat conductive and thus not easy to oxy-lance. Opening the blister tap-holes using a drilling machine is also extremely challenging if the tapping channel contains frozen blister, as this material is malleable and causes extremely high wear on drill bits.

Polish plugs are named after the Glogów smelter in Poland where they were invented [5]. Traditionally, a Polish plug is a steel bar with clay formed around it. The assembly is then held inside the end of an extended stopper bar that is used to insert the polish plug into the open tap-hole to stop the flow. The actual seal is frozen blister in the tapping channel. This is achieved by interrupting the blister stream for sufficient time for the cooling applied through the inserts to freeze the blister stream. The steel starter bar in the middle of the plug then serves as guide during oxygen lancing and assists with opening the tap hole.

The unique difference between the MPP at Kansanshi Smelter and conventional Polish plugs is the use of a hollow steel pipe, instead of a steel bar, in the construction of the MPP barrel. When opening the tap-hole on the next tap, the steel pipe of the MPP acts as sleeve through which the oxy-lance slides. This guides the oxy-lance through to the end of the tapping channel, reducing burn time and minimising opportunities to damage the inserts whilst still providing ignition for burning the tap-hole open.

An MPP is made using a mild steel pipe of 20 mm nominal bore with a length of 850 mm, which is the approximate length of the blister channel. The objective when inserting the MPP is to displace as much blister as possible from the channel, leaving 50–100 mm of the MPP protruding out of the tapping channel when fully inserted. Ceramic rope is wrapped around the pipe to protect the pipe from burning out during closing. Clay is applied to the rope in a thin coating. The clay is formed into a cone at the rear end of the MPP for plugging. The front 200 mm of the pipe is filled with clay to stop blister from flowing out through the pipe. Figure 4 shows an MPP loaded on a stopper bar just prior to use.

Fig. 4 An MPP just before closing a blister tap-hole

As the MPP is inserted into the tap-hole, the front pipe blocks most of the flow and displaces the blister from the tapping channel. Upon full insertion by tapping the MPP inwards with a hammer, the clay cone at the back stops the remaining blister copper flow. An air spear is directed at the tap-hole around the back of the MPP to promote cooling and solidification of blister at the tap-hole front face.

As blister tapping experience and operator discipline increased, the benefits of using the MPP became apparent. Minimal downtime from delays in blister tap-hole opening was experienced, closing failures reduced to almost zero, and insert life nearly doubled. As confidence grew over time, the operators were able to change the diameter of the MPP to match the tap-hole wear by increasing the amount of ceramic fibre rope that was wrapped around the barrel of the MPP. Typically, it takes 10–15 s to close the blister tap-hole using an MPP.

Blister Launders

The refractory lined blister launders are equipped with burners to preheat the launder before tapping and to help prevent build-up forming during tapping. The launders had several cold spots initially and unmanageable levels of material were building up as a result, which led to several extensive plant stoppages for launder cleaning. It was difficult to distribute the heat evenly because of the geometry of the launders and transitional section from the tapping floor to the level below. This is highlighted in Fig. 5. The transition area between steep and shallow launder angle had the largest

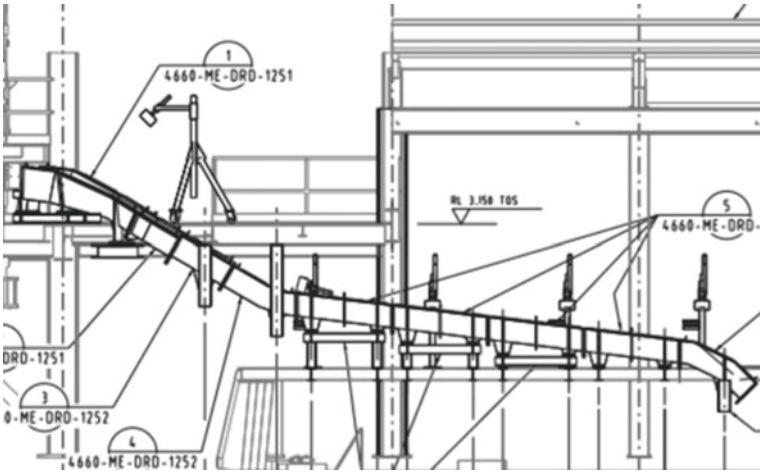

Fig. 5 Blister launder geometry

build-ups and was the most difficult to clean. Crow bars and jack hammers were used for launder cleaning, which came at the cost of refractory damage. Launders had to be repaired in the damaged sections after only a few days of operation.

One additional diesel burner per launder was installed to target the transitional section. Refractory lined steel covers were added to the entire launder to retain and distribute heat more efficiently, but the success was limited to the lower launder sections—after the transition area. The burner orientation on the launders was changed from perpendicular to counter-current to the blister flow, but this did not bring any significant improvement.

The operation strategy to manage launder cleaning was to use one launder for several consecutive taps while cleaning the other launder. This was done successfully for short times. It was found that the more consecutive taps were done on one launder, the bigger the build-ups grew, and the more time was required to clean them.

It is planned to trial a graphite blister launder in the future. It is known that graphite has low wettability to blister copper, which is expected to substantially reduce cleaning requirements and increase plant availability. It would also not require burners and hence a saving on diesel. The graphite launder material is expected to have a high life, which would cut the cost of castable required for launder repairs.

Currently, the blister flow and burner flame arrangement is counter-current. Concurrent burner arrangements have been considered, to assist the blister flow, instead of the possible impediment to blister flow from the counter-current burner arrangement.

Blister Mould Availability

Blister copper is cast into copper moulds. The moulds are sprayed with barium sulphate and preheated to drive off all moisture before casting starts. The cast blister solidifies and cools inside the mould in ambient air. A water cooling system was installed for the ingots but its use was discontinued for safety reasons.

Initially, the blister ingots were removed from the moulds after cooling with ambient air. These ingots were more subject to stick inside the moulds, causing low mould availability and plant downtime. The other major factors contributing to blister ingots sticking in the moulds were high blister tapping temperature and poor mould quality. High blister temperature caused partial melting of the mould surface, which would then fuse with the ingot. The average tapping blister temperature was in the range of 1180–1230 °C. On rare occasions blister temperatures of up to 1270 °C were recorded, which would damage the moulds. Recovering stuck ingots took several days of work with an excavator and hydraulic hammer moil.

Rejected anodes and copper chunks from the casting area were placed inside the moulds before casting to help overcome this problem. These worked as a sacrificial surface and a heat sink, but were viewed as a short-term solution only, due to the resulting reduction in new blister volume in each mould. The process of putting heat sink material inside the mould was also laborious. The blister cart carrying the moulds was also kept moving at very low speed while casting blister. This was to reduce fusing of blister to the mould by shifting the impact zone on the mould base.

The solidified ingots are now removed from the moulds using an overhead crane before cooling down to ambient temperatures. This practice significantly reduced the number of ingots sticking in moulds. This was believed to be because the ingots were still malleable enough to tear away from any areas where they were fused to the mould.

Blister Mould Casting

Initial attempts to cast blister moulds were problematic. Blister moulds were cast in a cast steel master mould that had the core, the body of the pig, fixed to the top. This presented two major problems with the moulds being cast. Firstly, there was very little control over the end point of casting causing shallow moulds and irregular mould heights. Secondly, with the core fixed to the top of the blister mould, the fire-refined copper was channelled between the mould and the core edge. As such, the pour rate was reduced causing some blister to freeze in the extreme corners of the master mould. It was also not possible to skim the impurities off the surface, which later caused pitting on the surface of the moulds being cast. Pitting in moulds provided anchor points and increased the likelihood of fusing the blister ingot to the mould after casting.

During the fourth ISACONVERT™ campaign, a new master mould was designed and used to alleviate the two major flaws of the first master mould. Again, a cast steel tub was used, but this time the core was affixed to the bottom of the master mould. This allowed for faster casting, in which the copper did not freeze in the mould before the end of cast. Also, impurities in the fire-refined copper floated to the surface, which was now the bottom of the mould and not the inner surface of the mould. This provided for consistent and full volume moulds with a much-improved inner surface.

Slag Tapping System

The target maximum total bath depth in the furnace is 2.2 m above the hearth. The slag tap-hole is situated at 1.55 m above the hearth. The slag tap-hole is opened when the total bath height reaches about 2.0 m and is kept open until there is little or no flow of slag from the tap-hole. Blister tapping is normally initiated directly after slag tapping with the aim of reducing the head pressure during blister tapping. The slag tap-hole is closed using an MPP and opened by means of oxy-lancing.

Slag Tap-Hole Life

The slag tapping channel consists of a copper block that is mounted in one of the intensively cooled copper elements. Poorly aligned oxygen lancing, high copper oxide levels in the slag, and blister entrainment in slag were initially causing significant damage to the copper block. A lance guide was used to assist the tappers to centre the lance inside the tap block. Blister entrainment was evident with thin layers of blister copper found on the frozen slag buttons. After just 2 months of operation, the damage on the front block was significant, as shown in Fig. 6. Tighter control of copper oxide levels in the slag will require improvements to the feed blending practices during future campaigns. A drill could be used in the future to reduce the damage from oxy-lancing. Although space was reserved for a tap-hole drill, it was not installed during the initial plant construction for cost reasons.

Slag Launder

Initially, a refractory lined launder was used for removing slag from the furnace. This launder had to be cleaned frequently. Using a non-cooled cast steel launder for slag skimming improved the availability as it required less cleaning. The downside was that the cast steel slag launder wore out in several areas when the process was not well controlled. Slag tapping temperatures sometimes exceeded 1280 °C. Hot slag would then start to form a gouge on the bottom of the launder that would eventually

Fig. 6 A slag tap block after 2 months in operation

burn through. High copper content in the slag, or blister entrainment in the slag, would worsen the situation. The launder was in such cases temporarily patched with refractory castable while a complete launder replacement was scheduled (Fig. 7).

Fig. 7 A damaged slag launder viewed from inside the furnace

Conclusion

Improvements on both the blister and slag tapping floors have led to improved performance of the ISACONVERT™ furnace. Not only was the uptime, throughput, and efficiency improved, but the operation of the furnace was also made safer. Further improvements should make increases to the continuous converting periods in the ISACONVERT™ possible and there are several opportunities that can be further explored.

Acknowledgements The authors would like to thank Kansanshi Mining Plc. for granting permission to publish this work.

The authors also acknowledge Glencore Technology for their support, without which this success would not have been possible.

References

1. Nikolic S, Edwards J, Burrows A, Alvear G (2009) ISACONVERT—TSL continuous copper converting update paper presented at the annual meeting and exhibition of the minerals, metals & materials society, San Francisco, California. International Peirce-Smith Centinnial (2009), pp 407–414
2. Edwards J, Alvear G (2007) Converting using ISASMELT technology. In: Paper presented at the sixth international copper-cobre conference, Toronto, Ontario. Copper 2007, Carlos Diaz Symposium on Pyrometallurgy, vol 3, book 2, pp 17–28
3. Jahanshahi S, Sun S (2003) Some aspects of calcium ferrite slags. In: Paper presented at the 132nd annual meeting and exhibition of the minerals, metals & materials society (TMS), San Diego, California. Yazawa International Symposium. vol 1, pp 227–245
4. Nelson L, Hundermark R (2016) The Tap-hole—key to furnace performance. J S Afr Inst Min Metal 116:465–490. https://doi.org/10.17159/24119717/2016/v116n5a12
5. George-Kennedy D, Walton R, George D, Nexhip C (2005) Flash converting after 10 years. In: Paper presented at the 11th international flash smelting congress, Bulgaria-Spain. Proceeding of the 11th Flash smelting congress, Bulgaria/Spain, pp 79–97

Successful Development and Optimisation of Lead ISASMELT™ Furnace Slag Tapping System at Kazzinc Ltd.

Benjamin Hogg, Mark Prince, Mark Letchford, Alistair Burrows, Timur Tokzhigitov, and Turarbek Azekenov

Abstract The first application of the ISASMELT™ furnace in the mid-1980s targeted the treatment of MIM lead-based feeds in a two-furnace oxidation–reduction combination. The first furnace originally transferred molten slag to the second furnace via a water-cooled copper block tap-hole. The next installation of the primary lead ISASMELT™ furnace technology occurred in the 2000s, this time feeding molten slag to a casting machine for solidification. This design had a number of learnings that were incorporated into a recent primary lead ISASMELT™ furnace, built and commissioned in 2012 at the Kazzinc Ltd Metallurgical Complex in Ust-Kamenogorsk, Kazakhstan. This paper presents the patented tapping system developed by Glencore Technology as applied to the lead ISASMELT™ furnace at Kazzinc. It focuses on the development process of this simple and effective tapping system, the current application, and how it has been optimised during the past 10 years of operational experience.

Keywords ISASMELT™ · Lead smelting · Tapping · Furnace tapping · Freeze lining · Slag chemistry · Continuous tapping · Slag casting · Tapping block · Tapping floor · Water-cooled copper block

Introduction

ISASMELT™ technology is based on vertical submerged lance injection technology to provide highly efficient mixing and reaction of feed materials in the molten slag bath. The result of the injection of the air directly into the molten bath is an intense smelting process in a highly turbulent bath [1]. The technology has been applied to treat a variety of materials including nickel [2], lead [3], and copper [4] concentrates and secondary materials [5].

B. Hogg (✉) · M. Prince · M. Letchford
Glencore Technology Pty Ltd, 10/160 Ann St, Brisbane 4000, Australia
e-mail: ben.hogg@glencore.com.au

A. Burrows · T. Tokzhigitov · T. Azekenov
Kazzinc Limited, Ulitsa Promyshlennaya 1, Ust'-Kamenogorsk 070000, Kazakhstan

J. D. Steenkamp et al. (eds.), *Furnace Tapping 2022*, The Minerals, Metals & Materials Series, https://doi.org/10.1007/978-3-030-92544-4_18

The design and operation of a lead ISASMELT™ tap-hole requires unique considerations. Most furnaces and processes in pyrometallurgy require the slag to be superheated above the liquidus temperature for safe and stable operation. However, the highly turbulent bath of the ISASMELT™ furnace technology, as can also occur with other bath smelting systems, allows operation at sub-liquidus conditions and as such, the tapping of these furnaces is vastly different.

This paper summarises some practical experience interwoven with a few minor digressions into the field of theoretical research. It is also the story of numerous beneficial, but accidental and unexpected, discoveries and their real-world applications. The topic of the paper is a tapping system in Kazakhstan but the learnings span three countries, four decades, many tap-holes, and engineers beyond counting.

The Process

The lead ISASMELT™ process, developed in the mid-1980s at Mount Isa Mines Ltd [6], now a subsidiary of Glencore plc, has been implemented in Australia, China, and Kazakhstan. The closely related ISASMELT™ process for recycling lead–acid batteries was developed in the late 1980s and has additionally been operated in England and Malaysia [7]. In each case, lead-rich feeds are smelted and slags are created that are rich in lead oxide. Removal of the slag through a tap-hole in the wall of the furnace has been the subject of numerous efforts of design, improvement, re-design, and modification.

Freezing Liquid Flow

The 1980s and 1990s in Australia was a period characterised by numerous innovative developments in the fields of mineral processing, hydrometallurgy, and pyrometallurgy. Some developments thrived and some withered on the vine. The large number of innovations was undoubtedly due in part to industry participation in, and support for, the research that was conducted during that period. (Disclosure: one of the present authors started his career that way and may be somewhat biased.)

One of the more innovative pieces of research that occurred was an attempt to mathematically formulate the relationship between freezing of high-temperature liquids and their flow [9], and then to use the mathematical formulation to engineer relevant smelter tapping equipment. Numerous industry participants chipped in to sponsor the work. Mount Isa Mines Ltd. assisted the researchers to perform field experiments evaluating the heat transfer and freezing phenomena of slag flowing inside a ‘U’-shaped slag launder but the researcher, John Pitsillos, was more ambitious than that. He wanted to develop a valve to control the flow of molten materials. His concept was to use external cooling to achieve a controlled amount of freezing of liquid inside a tube. The choice of, and flow rate of, coolant would be selected appropriately to control the molten liquid flow rate out of the furnace, as shown in Fig. 1.

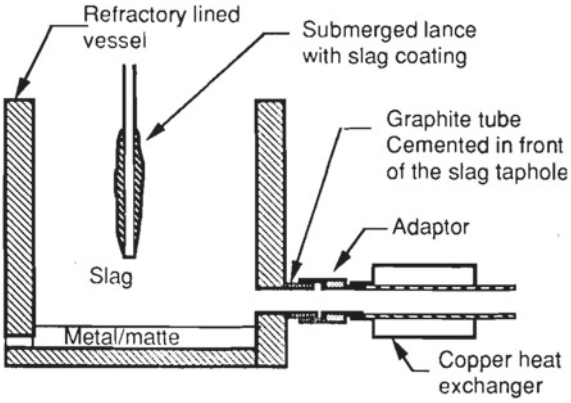

Fig. 1 Schematic diagram of slag tapping system attached to a SIROSMELT reactor [9]

The ambition of the researcher's vision extended beyond the imagination of the industry sponsors of that time, companies who variously smelted lead, copper, and nickel. Management in each of the industry sponsors was, respectively, operating and developing world-leading smelting technologies. But what happened when they were confronted with a concept, such as the diagram shown in Fig. 2, for completely automated furnace tapping in a base metal smelter?

This idea was among those that 'withered on the vine'. So far as the authors are aware, no manager of an industrial smelting plant has ever embarked on a field experiment in an effort to demonstrate the potential application of slag flow rate control using only externally applied heating and cooling. Furnace tapping is a field

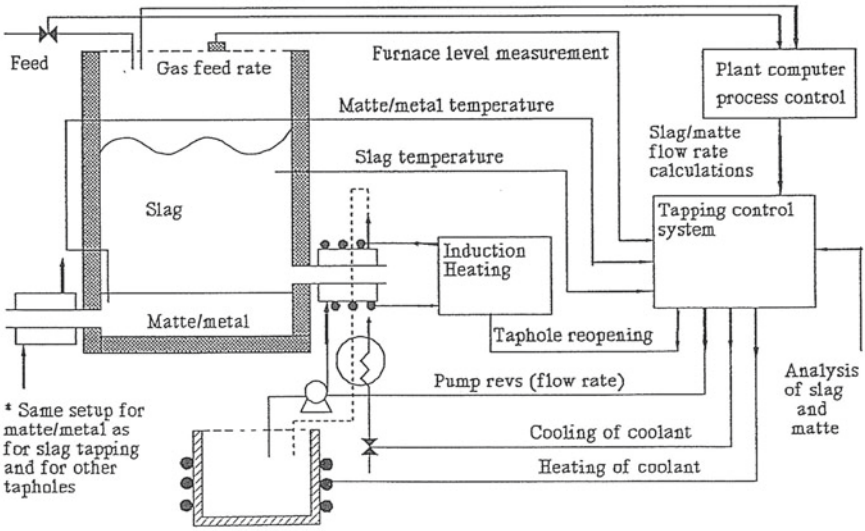

Fig. 2 Schematic diagram of automatic furnace tapping system [8]

where improvements tend to be made in small increments, and where the practical consequences of failed experiments can be severe if there is a loss of containment.

The Slag

As outlined in Matthew et al., lead-rich slag from the ISASMELT™ starts melting at around 950 °C, which is a temperature far lower than more reductive modes of smelting [10]. At the same time, it was also disclosed that smelting temperatures in the range 1170–1200 °C could be employed with bricks on the furnace side wall having negligible wear over many years. These two plant observations do not usually occur together. These incongruous features become still more mysterious when considering the aggressive nature of litharge slags, which is known to affect the ISASMELT™ furnace when used for recycling lead–acid batteries [11].

A then-young Ph.D. student shed light on this mystery in some industry-supported research in the mid-1990s. Eugene Jak, now a distinguished professor at the University of Queensland, demonstrated that at typical smelting temperatures the ISASMELT™ slag in the lead smelter at Mount Isa Mines Ltd. was not a homogenous liquid. As shown in Fig. 3, slags obtained by careful sampling, followed by rapid quenching, contain a mix of reaction products in both solid and liquid states as a result of the smelting process.

Thus, the lead ISASMELT™ furnace at that time operated, as those still operating do today, below the slag liquidus temperature. Tiny particles of solids, in addition to floating in the bath of high-density slag, gradually accumulate on solid surfaces inside the furnace that are exposed to splashed slag. The liquid part of the slag drains off quickly, leaving behind a few solid particles each time, similar to the way the surface of your car accumulates dirt when you drive through muddy puddles. The accretion that develops from the left-behind particles of spinel offers good protection for the

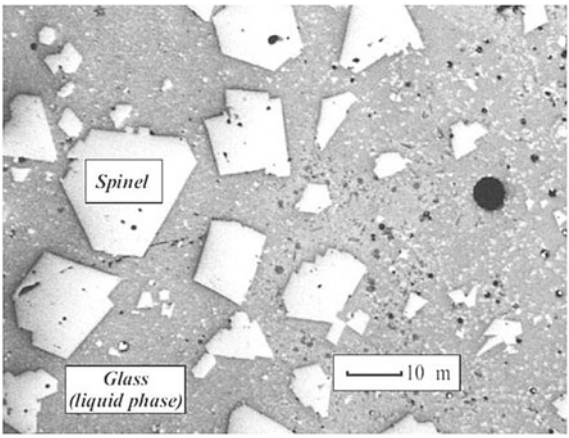

Fig. 3 Photomicrograph of slag from the lead ISASMELT™ process [12]. Many euhedral spinel particles, up to a particle size of 10 μm, are suspended inside a liquid

Fig. 4 Lead ISASMELT™ furnace side wall bricks, exposed mid-campaign, showing widespread spinel coating

furnace side wall refractory. A view inside a nicely spinel-coated ISASMELT™ furnace is shown in Fig. 4.

With the lead ISASMELT™ process, once the correct metallurgical recipe has been obtained, side wall brick-wear is almost eliminated from the list of problems a smelter manager has to worry about. Indeed, most of the bricks have an indeterminately long life. In similar smelting processes where spinel-forming compounds do not exist, such as in the ISASMELT™ process for lead–acid battery recycling, this mechanism of refractory protection is not possible.

While this representation of lead ISASMELT™ slag helped generations of metallurgists to control the chemistry of their furnace better, it did not shed much light on how best to tap the slag out of the furnace. If a liquid has already started to freeze inside your furnace, how do you reliably tap it out?

Choked Flow

The problem of flow rate control for already-freezing slag changed from a theoretical to a practical topic for Mount Isa during a period when the industrial-scale lead ISASMELT™ furnace was being commissioned. As explained by Player et al., the intended mode of operation required a continuous and steady flow of slag from the oxidation furnace to the reduction furnace, refer to Fig. 5 [13]. The tap-hole in the oxidation furnace was to be operated as an overflow tap-hole, with a minimum head of liquid slag inside the oxidation furnace.

One lesson learned during commissioning was that if process constraints (unrelated to tapping) dictated that the oxidation furnace had to be fed with a low feed rate, then it became very difficult to maintain the continuous flow of lead-rich slag out of the oxidation furnace, down the launder and into the charge port of the reduction furnace. Under these conditions, it was found to be easier in practice to continuously feed the oxidation furnace and continuously smelt the feed, and then to tap the slag batchwise into the reduction furnace where a batch reduction would be performed.

The phenomenon that a ‘small’ flow of slag is harder to consistently maintain than a ‘large’ flow of slag is well known to furnace tappers all around the world. When the phenomenon is characterised in the mathematics of Pitsillos, then with a fixed

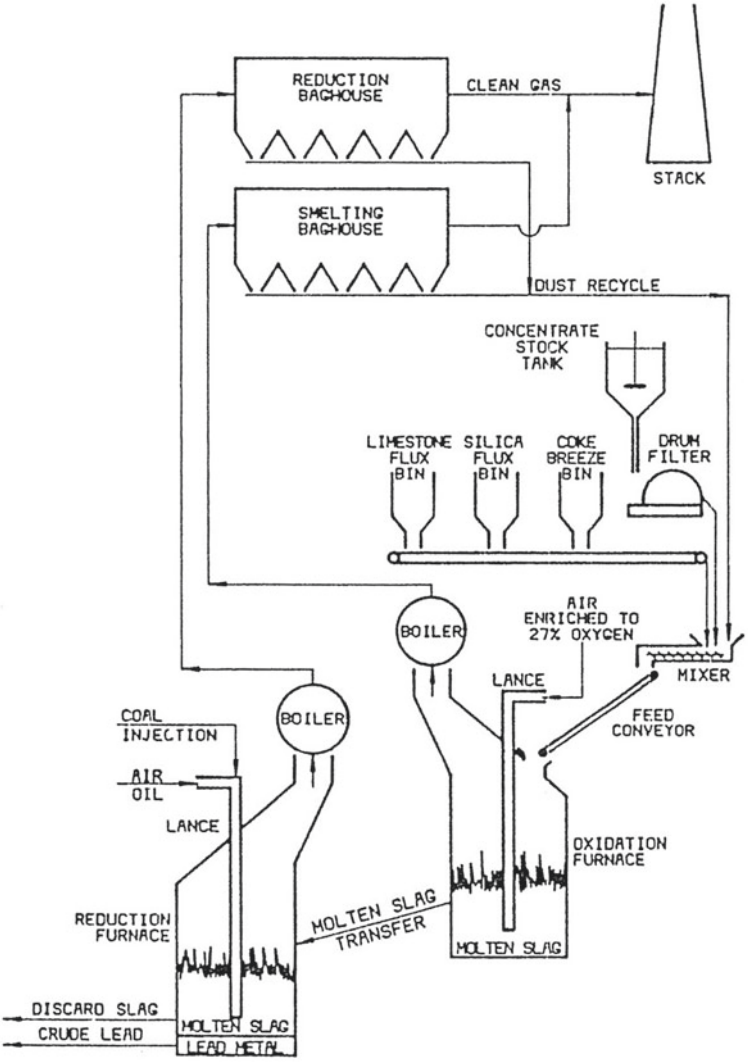

Fig. 5 Flow sheet for MIM's 60,000 tpy (of lead bullion) ISASMELT™ plant [13]

amount of cooling and a sub-liquidus slag, there is a unique L/D ratio of the tap-hole that is suitable for maintaining any particular slag flow rate. If you choose the ratio of L/D incorrectly for your furnace (or if you apply too much cooling) then you are forced to increase the flow of slag if you want to avoid the slag tap-hole closing by itself.

Later during the operation of the lead ISASMELT™ plant at Mount Isa, the smelter operators discovered that plant availability could be further increased by removing the water-cooled copper tapping block from the oxidation furnace slag tap-hole and

replacing it with some sacrificial bricks [14]. The reduced operator interventions and a reduction in plant downtime caused by self-closing tap-holes outweighed the extra maintenance introduced by the sacrificial bricks.

Going Global

Tapping sub-liquidus slag was next tried in China when the Isa-YMG process was commissioned in Qujing [15]. Although the production capacity of Chihong Zinc & Germanium Company's smelter in China was intended to be greater than that at Mount Isa Mines, there was a comparatively reduced amount of lead-rich slag owing to the high grade of concentrate being smelted and the production of some lead bullion inside the ISASMELT™ furnace, as shown in Fig. 6.

Some of the lessons from the Mount Isa Mines plant a decade earlier had been learned. In anticipation of the low hourly rate of slag production, the ISASMELT™ plant at Qujing was equipped with generously sized slag casting equipment and the method of slag tapping was designed to be short batches. But other lessons from Mount Isa may have been lost over the passage of time. The L/D ratio of the tap-hole in the water-cooled copper tapping block was not appropriate for the slag flow rate. Self-closing tap-holes again featured prominently among the list of production delays in the first few months of operation.

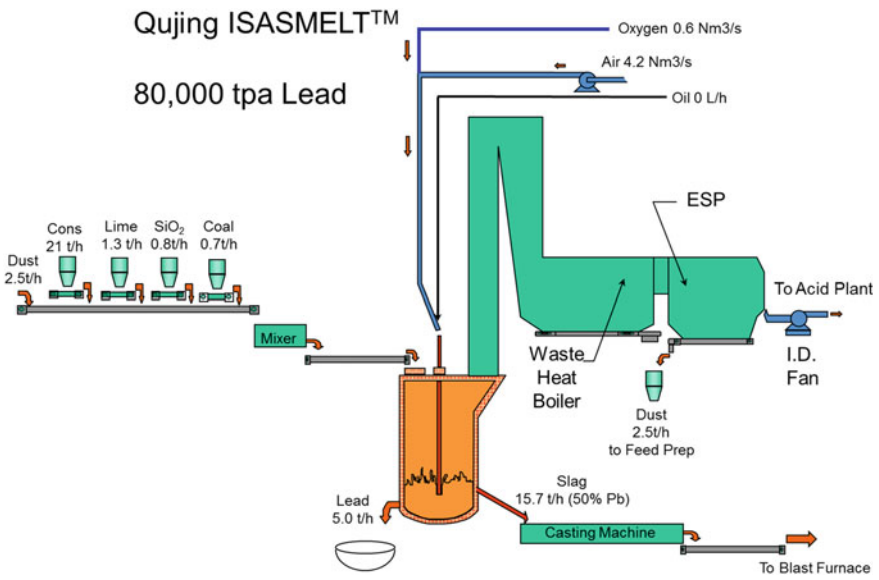

Fig. 6 Schematic of flowsheet for Chihong Zinc & Germanium Company's ISASMELT™ plant at Qujing, Yunnan Province, PRC

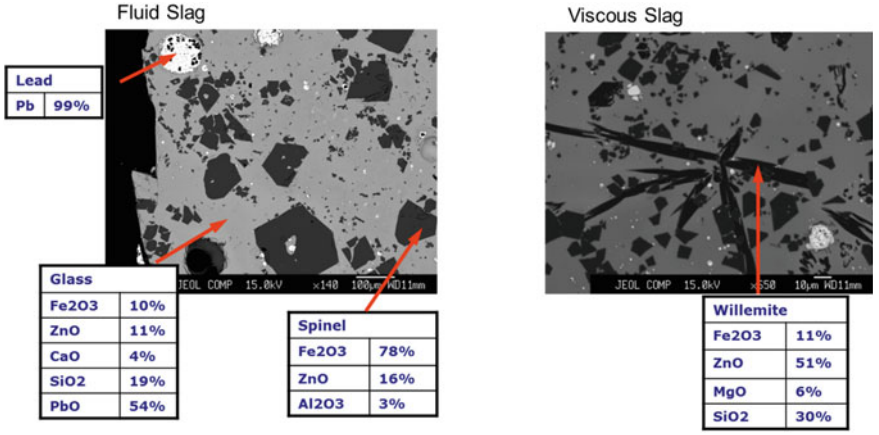

Fig. 7 Photomicrographs of slags, tapped at sub-liquidus temperatures, from Qujing lead ISASMELT™ furnace. The absence of acicular crystals was found to be a prerequisite for achieving a reliable slag flow

There was also a tendency for the slag at Qujing to change from 'tappable' to 'untappable' throughout the day, with little apparent change in temperature or bulk composition. This phenomenon was investigated further. Through some sponsored research it was identified that at the microscopic level fluid slags tended to look very similar to those at Mount Isa a decade earlier: a slurry of spinel particles suspended in a lead-oxide-rich liquid. But viscous slags looked different. There were some additional particles with the approximate composition of willemite. The crystals of willemite tended to appear as acicular needles, which were very different from the shape of spinels, as shown in Fig. 7.

It was already known that the presence and crystal shape of the suspended solid particles in a sub-liquidus lead-oxide-rich slag could vary with slag composition. Zhao et al. reported this observation with respect to melilite particles [16]. Accumulated knowledge about sub-liquidus crystal types now seemed to be knowledge that was transportable to the more practical application of understanding whether a slag would exhibit good tapping behaviour at sub-liquidus temperatures. What was needed was a method of communicating this information effectively so that it was understandable. Separately, just such a communication method was being developed.

The Campforts Diagram

In a series of published papers [17–19], Mieke Campforts calculated the proportion of phases present at various temperatures using the FactSage™ package [20]. The proportion of solids was graphically presented as pseudo-unary phase diagrams, as shown in Fig. 8. With a variation in the slag bulk composition, the nature and

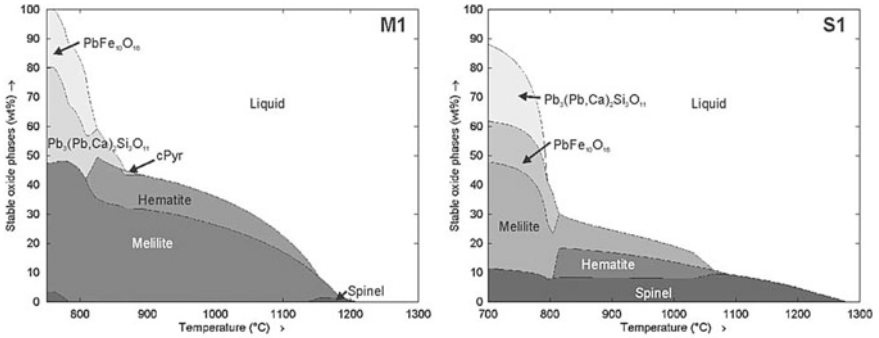

Fig. 8 Campforts diagrams for two different slags (denoted M1 and S1) [19]

proportion of solids changes, with a unique pseudo-unary diagram for each slag composition and oxygen partial pressure. It was a useful method to explain her topic of freeze lining formation. By chance, it is also a useful method to explain the chemistry of sub-liquidus slags. In the interests of brevity, and because these cited papers are the first in which the authors saw this type of diagram, it is referred to hereafter as the 'Campforts Diagram'.

For two different slags rich in lead oxide, Campforts predicted different proportions of stable condensed oxide phases at each temperature [19]. Compositions of slags M1 and S1 are shown below.

Slag	CaO	SiO_2	PbO	ZnO	Fe_2O_3	Al_2O_3
M1	10.57	13.81	45.79	3.28	20.28	6.27
S1	3.70	9.56	55.80	4.44	21.35	4.90

For both of these slags, it was predicted that only about 90% of the mass of condensed oxides is going to be in liquid form at the temperature of 1150 °C. However, it was also predicted that there were significant differences in the solid phases present. Referring to Fig. 8, it is clear that for slag M1 at 1150 °C the solids are predicted to be mostly melilites, whereas for slag S1 at the same temperature those solids will be exclusively spinels.

In the experiments performed by Campforts and under the conditions investigated, melilite was observed to form acicular crystals that were able to be interlocked, while spinel was observed as individual and isolated crystals. This ability for spinel crystals to form individual phases whilst crystals involving silica formed interlocking structures was consistent with that observed by other researchers in other slag systems [21]. From experience with sub-liquidus slag tapping, and informed by the Campforts diagrams of these two slags, it is possible to predict that slag M1 will need to be tapped at a temperature of about 1200 °C, but it would be possible to tap slag S1 at a temperature of 1100 °C. Note that this is completely the opposite of the conclusions that would be drawn if the liquidus temperature alone were considered, i.e. slag S1

has a higher liquidus temperature than slag M1, but it is possible to tap slag S1 at a lower temperature.

Kazzinc's Lead ISASMELT™

In 2006 Kazzinc Ltd., a subsidiary of Glencore plc, began to design a refurbishment of its Lead Plant at the Ust-Kamenogorsk Metallurgical Complex. Avrachov et al. have described the refurbishment previously [22]. Some key parts of the new plant are shown in Fig. 9. The footprint of the plant was constrained by the available space on site, and the total length of the plant was not negotiable, which meant that the length of the dual strand slag casting machine (shown in gold in Fig. 9) had to be chosen to fit the site, rather than to fit the process. The predicted solidification capacity of the slag casting machine was 45 t/h of cast slag.

Sub-liquidus temperatures for slag tapping would become a key feature for the success of the ISASMELT™ furnace at Kazzinc. In addition to the predictable advantages of saving the cost of fuel and minimising the cooling capacity of the off-gas system, the ability to tap sub-liquidus slags would maximise the rate of cast slag production for a plant built with a fixed limit on slag solidification capacity.

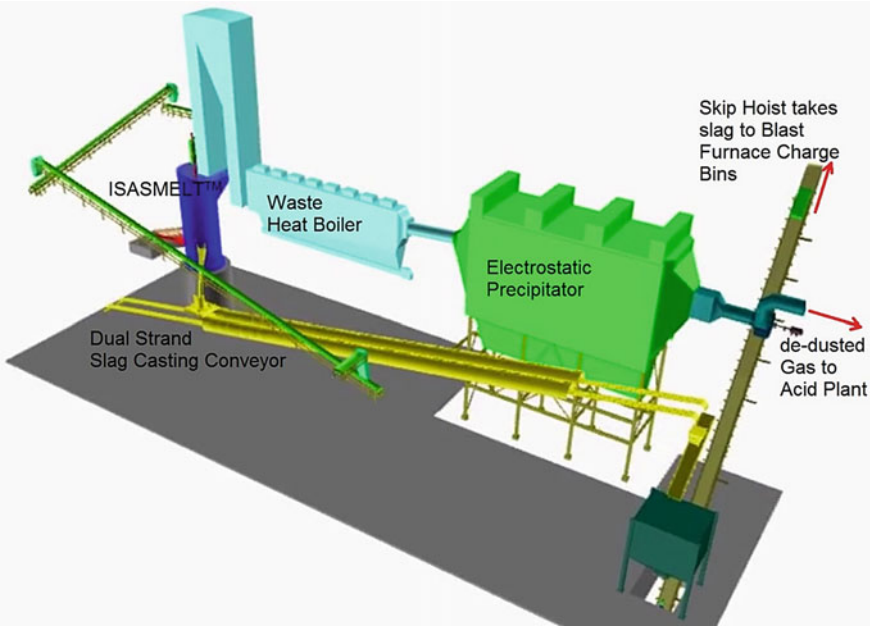

Fig. 9 Layout of Kazzinc's lead ISASMELT™ plant

Some features of the lead ISASMELT™ at Ust-Kamenogorsk have been described previously [23] but it has not been reported before now that Glencore Technology (then known as Xstrata Technology) designed a tap-hole system specially for sub-liquidus tapping at a flow rate of about 40 t/h. It is a submerged tap-hole near the free surface of the slag bath, such that slag continuously flows through it. In a practical application of the ideas of Pitsillos, informed by a Campforts Diagram calculated by Glencore Technology as shown in Fig. 10, and combined with past experience, both the slag composition and the tap-hole were engineered so that exactly sufficient externally applied cooling would exist to produce an effective tap-hole L/D ratio suitable for the production rate [24]. The concept is that inside the tapping block a protective freeze lining would form, circumscribing a channel with the desired diameter to provide an adequate slag flowrate for continuous operation. The advantage of this method is that the tap-hole has low risk of either blockage or wear and requires minimal operator intervention when in use. A cross section of the tap-hole is shown schematically in Fig. 11.

At the time of publication, the tap-hole of Kazzinc's lead ISASMELT™ furnace will have been operating for nearly 10 years. The copper tapping block has been changed twice in that time, and on neither occasion was the replacement attributable to internal wear. The frozen slag creates a zero-cost, wear-resistant lining for the flowing slag. Taken after shutdown and partial drainage of the furnace, the photograph in Fig. 12 shows what this feature looks like in practice.

For every novel design feature, engineers are apprehensive of the future performance, and Glencore Technology was no different. Additional mechanical aids [24] were designed and installed to assist tapping of Kazzinc's new lead ISASMELT™ furnace, but in practice they have not been required. Control of slag composition and furnace temperature has been sufficient to make the slag-lined tap-hole an effective

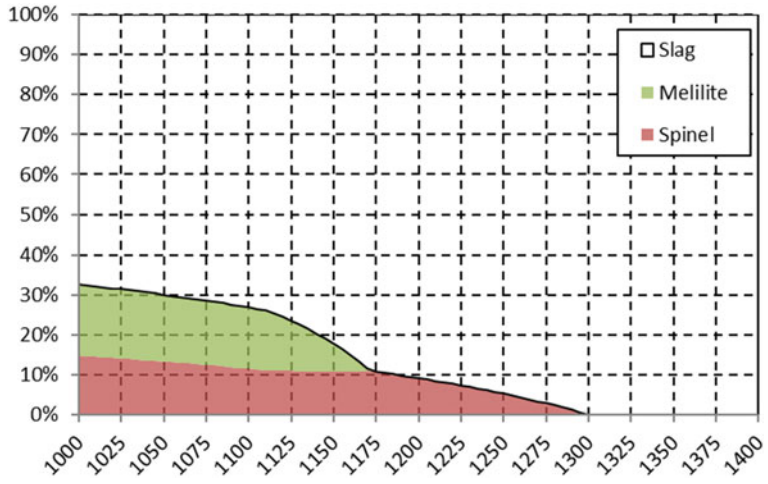

Fig. 10 Calculation of the pseudo-unary phase diagram in FactSage™

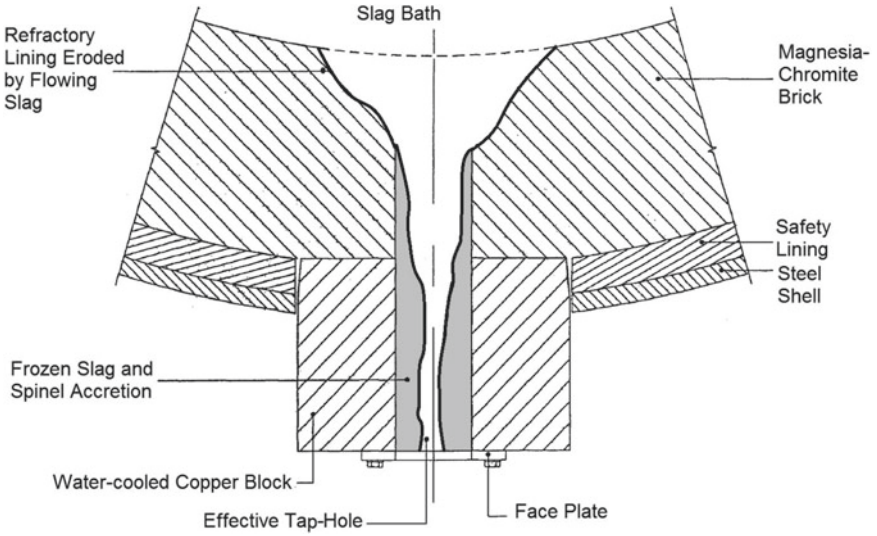

Fig. 11 Artist's impression of cross section through Kazzinc's slag tap-hole, during operation

Fig. 12 Frozen slag defining the effective tap-hole, inside a partially dismantled slag tapping block

and enduring success. The annual production of lead-oxide-rich slag from the lead ISASMELT™ at Ust-Kamenogorsk is shown in Table 1. The original design intent of 40t/h of solidified slag has been demonstrated together with consistent operation above the design rate.

Table 1 Annual mass of slag tapped from lead ISASMELT™ furnace ('000 t)

	Slag Tapped
2015	211
2016	302
2017	306
2018	287
2019	325
2020[a]	271

Note [a] Re-brick year

An additional design feature of Kazzinc's tapping system is that the tapping block was designed to be easily removable and the bricking arrangement behind it was designed to be self-supporting and replaceable. The 16 individual bricks adjacent to the inlet of the slag tap-hole are among the only bricks in the furnace that need repair (as depicted in Fig. 11). Typical service life for these bricks is 4000–6000 h of operation. Repairs are normally scheduled to coincide with a major plant shutdown (e.g. for a repair of the Acid Plant) and are conducted with the inside of the furnace at around 400–600 °C. *In extremis*, a hot replacement of the worn bricks could be conducted in a 16-h duration, if required.

The Kazzinc lead-slag tapping system avoids or resolves many of the technical issues and operational inconveniences experienced by other base metal tap-holes. The 'self-managing' system requires minimal operator intervention to manage the discharge from the tap-hole or accretion in the tapping launder. If the slag temperature rises the hole will enlarge itself, but the overflow of slag out the tap-hole remains consistent with the generation of slag inside the furnace. With the ideal relationship between surface area and applied cooling, the freeze lining is easily maintained for weeks at a time in both the tapping channel and the launder, see photographs in Fig. 13. The tap-hole rarely requires 'closing' as the bath height drops slightly after

Fig. 13 Freeze lining in lead ISASMELT™ tapping launder at Kazzinc Ltd.

smelting ceases and the lance is withdrawn from the bath. This effectively stops the slag overflow until smelting resumes. Removal of the unused mechanical aids (drill machine, rock-breaking device, and clay gun) has enabled simpler and more effective secondary gas capture in the area. It has also allowed superior access for inspections and maintenance. The tapping area labour requirement is low compared to similar smelters. There is minimal exposure of workers to the hazards of molten metal, moving machinery, and manual handling.

Conclusion

ISASMELT™ technology's vertical submerged lance injection, with a resulting highly turbulent bath, allows for a different approach to be taken for the design and implementation of a furnace tapping system. For the lead ISASMELT™ furnace specifically, the development of a reliable sub-liquidus tapping system has taken many years and relied on numerous theoretical and practical developments. The first application transferred molten slag to a second furnace and this was a key focus of the design team. The next installation was feeding a molten slag to a casting machine for solidification. The design learnings and subsequent theoretical investigations were incorporated into Kazzinc Ltd.'s plant at Ust-Kamenogorsk, Kazakhstan. Over almost 10 years of operation, this tapping system has proven itself to be reliable. Both the tapping area labour requirement and the exposure of personnel to the hazards of molten metal are low when compared to similar smelters using alternative technology.

Acknowledgements The authors wish to acknowledge Kazzinc Limited and Glencore Technology for permission to publish this paper.

References

1. Hogg B, Nikolic S, Voigt P (2018) ISASMELT™ technology for sulfide smelting. Paper presented at extraction 2018 symposium, Ottawa, Canada, 26–29 Aug 2018
2. Bakker ML, Nikolic S, Mackey PJ (2011) ISASMELT™ TSL—applications for nickel. Miner Eng 24(7):610–619
3. Errington W, Arthur P, Wang J, Dong Y (2005) The ISA-YMG lead smelting process. In: Fujisawa T et al (eds) Paper presented at the international symposium on lead and zinc processing, Kyoto, Japan October 2005. MMIJ, pp 581–599
4. Arthur PS, Hunt SP (2005) ISASMELT™—25 years of continuous evolution. In: Nilmani M, Rankin WJ (eds) Paper presented at floyd international symposium on sustainable development in metals processing. NCS Associates (Australia), pp 73–94
5. Alvear GRF, Nikolic S (2013) ISASMELT for recycling of valuable elements contributing to a more sustainable society. Paper presented at REWAS 2013: enabling materials resource sustainability. TMS Annual Meeting, San Antonio, Texas, USA
6. Errington WJ, Fewings JH, Keran VP, Denholm WT (1987) The Isasmelt lead smelting process. Trans Instn Min Metall Section C 96:1–6

7. Errington B, Hawkins P, Lim A (2010) ISASMELT™ for lead recycling. Paper presented at lead-zinc 2010, TMS 2010, Seattle, United States, 14–18 Feb 2010
8. Pitsillos JS (1992) Modelling of phase change with fluid flow—flow rate control of molten liquids. PhD Thesis, University of Melbourne
9. Pitsillos JS, Gray NB (1991) Handling of slags leaving metallurgical vessels. Paper presented at EPD congress '91, TMS 1991, New Orleans, United States, 17–21 Feb 1991
10. Matthew SP, McKean GR, Player RL, Ramus KE (1990) The continuous ISASMELT™ lead process. Paper presented at lead-zinc '90, TMS 1990. Anaheim, United States, 18–21 Feb 1990
11. Errington WJ, Edwards JS, Hawkins P (1997) ISASMELT™ technology—current status and future development. J South Afri Inst Mining Metall 97:161–167
12. Jak E, Liu N, Lee HG, Hayes PC (1994) Application of phase equilibria studies to describe behaviour of lead smelting slags. Paper presented at the 6th AusIMM extractive metallurgy conference, Brisbane, Australia, 3–6 July 1994
13. Player RL, Fountain CR, Nguyen TV, Jorgensen FR (1992) Top-entry submerged injection and the ISASMELT™ technology. Paper presented at Savard/Lee international symposium on bath smelting TMS 1992. Montreal, Canada, 18–22 Oct 1992
14. Boag G (2008) Personal communication
15. Errington B, Arthur P, Wang J, Dong Y (2005) The ISA-YMG lead smelting process. Paper presented at international symposium on lead and zinc processing, Kyoto, Japan, 17–19 Oct 2005
16. Zhao B, Errington B, Yang G, Wang J, Dong Y, Jak E, Hayes PC (2005) Characterisation of ISASMELT™ slag and lead blast furnace sinters. Paper presented at international symposium on lead and zinc processing, Kyoto, Japan, 17–19 Oct 2005
17. Campforts M, Verscheure K, Boydens E, Van Rompaey T, Blanpain B, Wollants P (2007) On the microstructure of a freeze lining of an industrial nonferrous slag. Metall Mat Trans B 38B:841–851
18. Campforts M, Verscheure K, Boydens E, Van Rompaey T, Blanpain B, Wollants P (2008) On the mass transport and the crystal growth in a freeze lining of an industrial nonferrous slag. Metall Mat Trans B 39B:408–417
19. Campforts M, Blanpain B, Wollants P (2009) The importance of slag engineering in freeze-lining applications. Metall Mat Trans B 40:643–655
20. Bale CW, Pelton AD, Thompson WT (2007) Facility for the analysis of chemical thermodynamics. Ecole Polytechnique de Montreal. http://www.crct.polymtl.ca
21. Hidayat T, Henao HM, Hayes PC, Jak E (2012) Phase equilibria studies of Cu-O-Si systems in equilibrium with air and metallic copper and Cu-Me-O-Si systems (Me = Ca, Mg, Al, and Fe) in equilibrium with metallic copper. Metall Mater Trans B 43B:1290–1299
22. Avrachov A, Saltykov P, Strecker JJF, Dobersek A, Moskalenko SN (2015) ISASMELT™-based reconstruction of a lead plant. Paper presented at Pb-Zn 2015, Dusseldorf, Germany, 14–17 June 2015
23. Burrows AS, Azekenov TA, Zatayev R (2015) Lead ISASMELT™ operations at Ust-Kamenogorsk. Paper presented at Pb-Zn 2015, Dusseldorf, Germany, 14–17 June 2015
24. Prince MJ, Letchford MK (2011) Method for removing slag from a furnace. WO 2011/060483

Simulation-Based Approaches for Optimized Tap-Hole Design

Guenter Unterreiter, Anton Ishmurzin, Hans U. Marschall, and Alfred Spanring

Abstract For efficient operation of an electric arc furnace, the tap-hole region is one of the most important parts. It experiences thermal stresses, creep, and erosion. To consider these effects in a virtual design process, it is necessary to use sophisticated thermo-mechanical and fluid dynamics models. We demonstrate application of finite element analysis, computational fluid dynamics, and optimisation methods to obtain tailored refractory tap-hole design. We use linear-elastic and creep models to perform structural mechanics numerical analyses of a geometrically simplified tap-hole area. An experiment-based methodology to obtain Norton-Bailey creep parameters is presented. The significance of considering creep during the design process is demonstrated. Using computational fluid dynamics (CFD) and optimisation methods, we perform a shape optimization of a tap-hole channel. A multi-objective optimisation of mass flow rate and area-averaged wall shear stress with respect to the funnel angle at the beginning of the tapping channel is performed.

Keywords Tap-hole · Optimisation · Flow · Creep · Refractory · Virtual · Design · Process · Thermo-mechanical stresses

Introduction

Designing a durable tap-hole area and therefore applying proper materials is one of the most crucial stages during the engineering process of complex electric arc furnaces (Fig. 1). Optimised operating conditions, greater output, and efficiencies push refractories to their limits. The tap-hole area is particularly exposed to high thermal and mechanical loads [1].

G. Unterreiter (✉) · A. Ishmurzin · H. U. Marschall
Technology Center Leoben, RHI Magnesita, 8700 Leoben, Austria
e-mail: Guenter.Unterreiter@RHIMagnesita.com

A. Spanring
Technical Marketing, RHI Magnesita, 1120 Vienna, Austria

J. D. Steenkamp et al. (eds.), *Furnace Tapping 2022*, The Minerals, Metals & Materials Series, https://doi.org/10.1007/978-3-030-92544-4_19

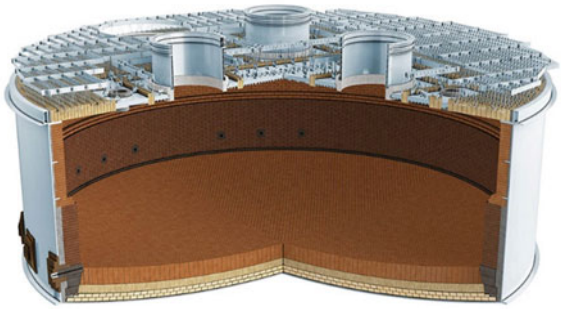

Fig. 1 Refractory lining of an electric arc furnace for the non-ferrous and ferroalloy industry

Virtual prototyping is a fast and effective method used during the product development process. On the basis of numerical simulations, a tailored design with optimised operating behaviour can be developed in an efficient manner.

To meet demands of modelling and simulation for the purposes of designing such a complex system, it is necessary to combine structural mechanics and fluid dynamics. The first part of this article deals with the structural mechanics side of the problem, while the second part addresses the CFD-based shape optimisation of the tapping channel.

Structural Mechanics

In the first half of structural mechanical section of the presented research, two different tap-hole designs were compared based on finite element method (FEM) calculations using linear-elastic material model. The applicability limit of the linear-elastic material model is demonstrated. Hence, the importance of considering creep behavior by sophisticated material models was shown.

In the second half section, a methodology and testing device for measuring and extracting Norton-Bailey creep parameters is presented. A tailored design with optimised operating behaviour can be found in a rapid and effective way, based on numerical simulations with advanced material models and concepts of virtual prototyping.

The impact of two different designs (Fig. 2) is investigated in terms of thermo-mechanical stresses after heat-up and during tapping by using linear-elastic material model.

Furthermore, using a simplified geometry (Fig. 3), a Norton-Bailey creep model was implemented and the corresponding reduction of the Mises stresses in the steel shell is shown in Fig. 12.

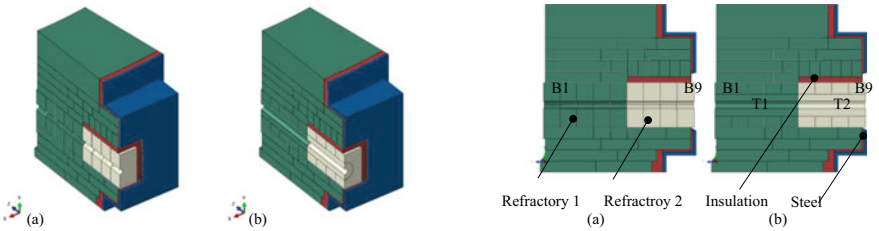

Fig. 2 A half of the symmetric design **a** "single brick" and **b** "tube tapping channel" design including refractory lining, insulant, and steel shell

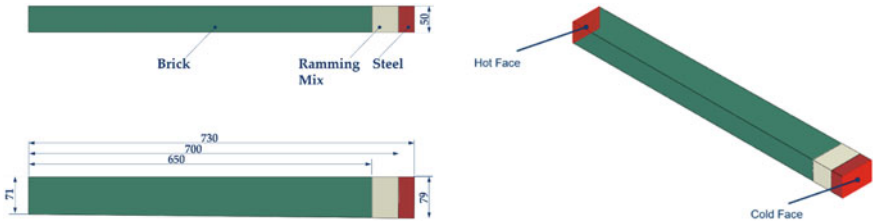

Fig. 3 Simplified geometry for considering creep in the refractory material and the impact of creep on the Mises stresses in the steel shell [2]

Structural Mechanics—Materials and Methods

In material science, creep is defined as the deformation of a material over a period due to combined influence of temperature and an applied load [3]. Although significant information is available on the effect of additives, corrosion process, and thermal behaviour of refractories [4, 5], significantly less data exists on the creep response of refractories at elevated temperatures in the range of 1200–1500 °C. However, this data is required for highly sophisticated material models which describe the creep behaviour of the structure. It should be noted that computations considering creep behaviour are more time-consuming than linear-elastic model.

In previous research [2], the importance of addressing Norton-Bailey creep model was demonstrated. There are a variety of creep models which can be selected for implementation in finite element codes [6]. The applicability of the Norton-Bailey creep equation to characterise the creep behaviour of refractories has been demonstrated in previous studies [7–9].

However, it should be noted that most refractory structures do not experience creep under constant load. In most cases, the global loads, not considering local stresses, e.g., due to thermal shock, are caused by restrictions of the refractories' thermal expansions due to rigid external structures (e.g., steel shell). In those cases, the creep of the material will decrease the load. Once the suppressed thermal expansion is compensated by creep, there is no significant load on the material and the creep process is stopped before reaching the tertiary creep stage.

Refractory creep can be described by the Norton-Bailey creep law shown in Eq. (1). According to the Norton-Bailey strain hardening/softening formulation, the creep strain rate is a function of temperature, stress, and creep strain:

$$\dot{\varepsilon}_{cr} = K(T) \cdot \sigma^{n} \cdot \varepsilon_{cr}^{a} \tag{1}$$

Exponent a is in the case of strain hardening (primary creep) negative and in the case of strain softening (tertiary creep) positive. Secondary creep occurs if the strain exponent a is zero. The parameter K is a temperature function and n is the stress exponent [8]. The tertiary creep contribution is of minor importance for the design, as tertiary creep is followed by failure of the component and should be avoided [10]. In this presentation, the contribution of the secondary and tertiary creep stages is neglected, and the creep strain is described by so-called primary creep.

The measurement results used for this work include the elastic and viscoplastic creep deformation and have been published [2]. The creep testing device (CTD) for high-temperature uniaxial compressive creep application and an efficient methodology to identify the creep law parameters used in this work were developed by the Chair of Ceramics (Montanuniversität, Leoben, Austria) [8]. The creep testing device shown in Fig. 4 and the experimental procedure of determining the strain–time curves were published in [2]. The procedure for identifying the parameters K, n, and a for the Norton-Bailey creep law has been described in [8].

The numerical model of parts of the lining shown in Fig. 2 and the simplified geometry for considering creep shown in Fig. 3 were created with the FEM software package Abaqus CAE/2018 [11]. The problem was formulated as sequentially coupled pure thermo-mechanical. Phenomena such as infiltration or chemical reaction which would alter the material properties were neglected. The goal was to show the influence of the tap-hole design on thermo-mechanical stresses, resulting in a comparison of tap-hole lining designs using linear-elastic material model.

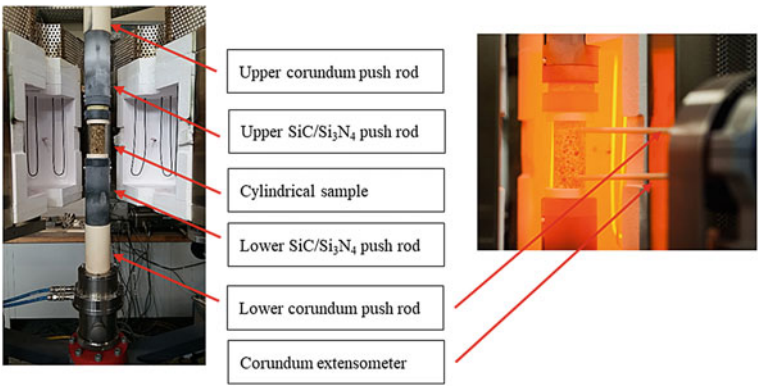

Fig. 4 Internal view of the high-temperature compressive creep testing device located at the Research and Development Centre Leoben [2]

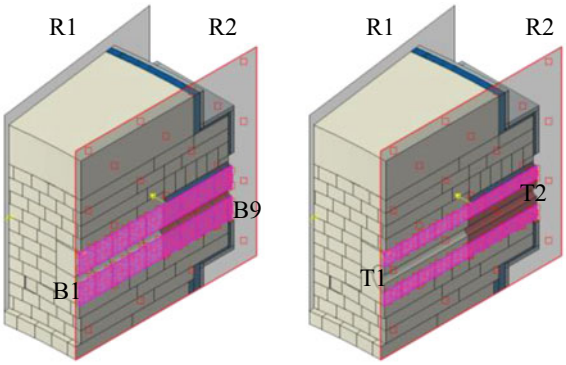

Fig. 5 Rigid plane R1 used as rigid boundary condition during heat up. Rigid plane R2 is acting as symmetry plane everywhere except the violet-coloured area which is also considered as a rigid wall

In general, the used linear-elastic model overestimates stress magnitudes as it does not account for stress relaxation. However, in reality, plastic deformations occur which lower the resulting stresses. Thus, an accurate description of the acting stresses and strains is only possible by considering creep. However, for a comparative study, the linear-elastic approach is admissible as the order of the tensile stresses is identified and different designs can be compared based on the magnitude of the tensile stresses [1].

Due to the particular susceptibility of refractory materials to fail under tensile loads, the tensile stresses were used for design quality assessment. Generally speaking, as the elastic model overpredicts stresses, they cannot be used as a damage criterion. Nevertheless, the stresses can be used for the assessment whether a design is favourable.

A representative section of the tap-hole area was modelled as shown in Fig. 2. The displacement that occurs mainly due to thermal expansion was constrained by the rigid wall R1. The violet-coloured area of wall R2 also behaved as a rigid wall. The remaining surface was defined as a symmetry boundary condition. Hence, tap-blocks B1–B9 in Fig. 5 were not modelled considering symmetry, in contrast, the cylindric refractory bricks T1 and T2 were modelled considering symmetry.

Sections of the refractory lining inside the furnace were also considered as interacting parts. The thermal boundary conditions outside the furnace considered natural convection on the furnace surface with a constant heat transfer coefficient of 50 W m^{-2} K^{-1} and an emissivity of 0.8 for surface radiation. The ambient temperature outside the furnace was defined as 20 °C (Fig. 6).

Firstly, the heat-up process was modelled as steady state and the hot face boundaries were assigned a constant temperature of 1600 °C. Then a tapping sequence with a tapping time of 40 min and a constant temperature at the channel of 1600 °C was considered and modelled transient. In Tables 1, 2, and 3, the temperature-dependent physical properties of the considered materials are provided.

In the case where no data is available for a specific temperature, the given values were extrapolated to higher or lower temperatures.

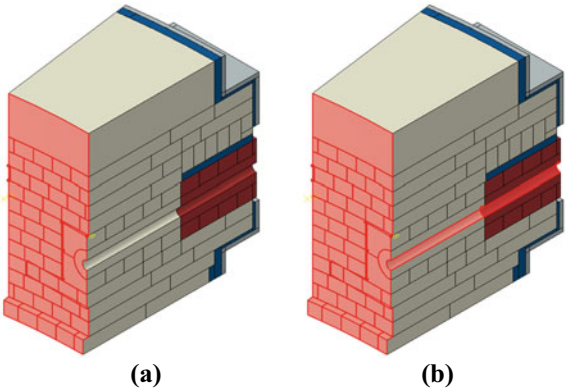

Fig. 6 Thermal boundary conditions. Hot faces during steady-state heat-up are shown in (**a**) hot faces during transient taping process are shown in (**b**)

Table 1 Temperature-dependent specific heat of materials in J kg^{-1} K

Material	20 °C	100 °C	200 °C	500 °C	1500 °C	1800 °C
Refractory 1	920	1042	1127	1230	1346	1373
Refractory 2	750	890	970	1110	1260	1200
Ramming mix	710	930	1170	1630	2020	2050
Steel	430	500	540	690		

Table 2 Temperature-dependent thermal conductivity of materials in W m^{-1} K^{-1}

Material	20 °C	100 °C	200 °C	500 °C	750 °C	1000 °C	1200 °C	1400 °C
Refractory 1				7.7	5.9	4.6	3.8	3.5
Refractory 2				4.55	3.95	3.65		
Ramming mix	16					16		
Steel	57	57	54	42				

Table 3 Physical data of material used in the model

Material	Density (kg m^{-3})	Young's modulus (GPa)	Poisson's ratio (1)	Thermal expansion coefficient (10^{-6} K^{-1})
Refractory 1	3000	20	0.2	14
Refractory 2	3400	17	0.2	7.9
Ramming mix	1730	10	0.2	3
Steel	7850	209	0.28	12

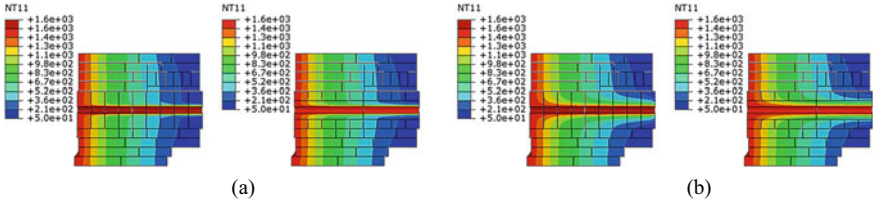

Fig. 7 Temperature fields after **a** 90 s and **b** 40 min of tapping

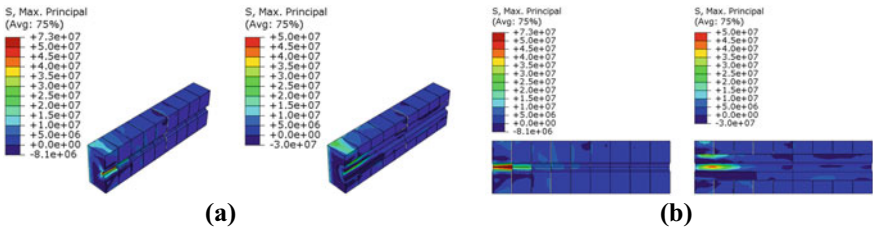

Fig. 8 Maximum principal stresses after steady state is reached during heat-up simulation

Structural Mechanics—Results

The nomenclature of the tapping bricks under discussion is hereinafter as follows: the first tapping brick is considered as Brick 1 (B1) subsequent Brick 2 (B2) till Brick 9 (B9) (Figs. 2 and 5). The tubes acting as tapping channel are labelled as Tube 1 (T1) and Tube 2 (T2) (Figs. 2 and 5).

The steady-state temperature distribution after heat-up and after 40 min of tapping is shown in Fig. 8a. The material considered showed creep behaviour during the compression creep test at about 1200 °C [2]. Only the first two bricks of the hot side and the vicinity of the tapping channel are subjected to creep since their temperature is above 1200 °C as it can be seen in Fig. 7.

In Fig. 7a, b, instantaneous temperature distributions after a tapping sequence of 90 and 2400 s are shown. Due to the steep temperature gradient in the vicinity of the tapping channel there is a certain risk for thermal shock.

The maximal principal stresses calculated during steady-state heat are shown in Fig. 8. The largest occurring maximal principal stresses appear in both designs at the hot face, which is in contact with the melt. Since linear-elastic material model was used, the magnitudes of the calculated stresses are overpredicted. In reality, it is expected that a significant reduction of the stresses over time will occur due to creep. Thus, to calculate a more realistic stress distribution, a time-dependent calculation and creep material model must be used. However, the highest tensile stresses in the linear-elastic approach are nevertheless decisive during a design optimisation.

In Fig. 8, it can be seen that the stress distribution has a steep change between Brick 1 and Brick 2. The magnitudes of the stresses in the single brick model are about 50% higher than in the tube-brick model. However, without using a creep model on the base of a transient calculation no quantitative prediction of the occurring stresses

can be done. The stress distribution is continuous in the tube model at the beginning of Tube 1. Moreover, in tube model, tensile stresses can be found not only near the channel at the inner surface of the tapping channel but also in the upper part of Tube 1, indicating bending. The bending can be explained by different thermal expansion of the first and the second half of the tapping channel. The single brick design is significantly more flexible, and bending does not occur.

The single brick design shows that after 90 s of tapping the highest tensile stresses are located at Brick 1 in Fig. 9. Bricks 4 and 5 also show high tensile stresses above and below the centreline, indicating that the reason for these high stresses was not bending (Fig. 9). For the tube-brick approach, the highest maximum principal stresses occur at the inlet and at the end of Tube 1. Also, at the end of Tube 2, the maximum principal stresses occur above and below the centreline indicating that these stresses do not originate from bending of the tube. The regions which show temperatures above 1200 °C and elevated tensile stresses are prone to creep and a detailed investigation considering creep is recommended.

For the single brick design at 40 min, the tensile stresses at the tapping channel inlet were in the same order of magnitude as after 90 s (Figs. 9 and 10). The stresses in Brick 3, 4, and 5 are relaxing. Contrary to that, the maximum principal stresses at Tube 1 where stresses remain. In Brick 9 at the right end, tensile stresses appear. For the tube-brick approach, the tensile stresses on the left side (T1) are increasing. In Tube 2, the stresses at 40 min tapping are slightly dissipated compared to the state at 90 s.

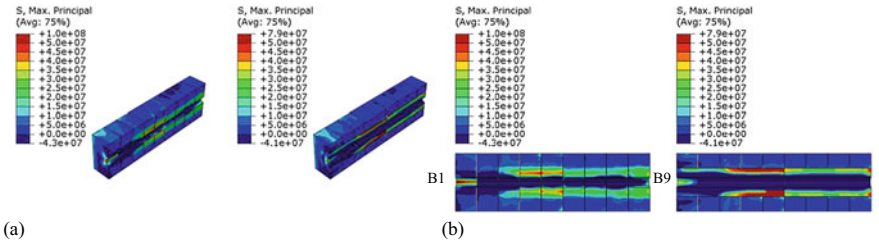

Fig. 9 Maximum principal stresses after 90 s tapping

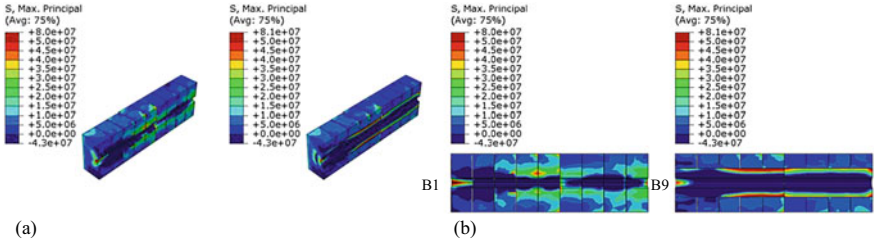

Fig. 10 Maximum principal stresses after 40 min tapping

Experimental Work for Estimation of Creep Parameters

In a previous study [2], the creep parameters of refractory materials were measured by the compressive CTD shown in Fig. 4. The measured and extracted Norton-Bailey creep parameters were used to extend the linear-elastic simulation approach by considering creep. The load applied on the testing sample was constant for the whole testing period of 5 h. The measurements were carried out in the operating temperature range of refractory materials of interest from 1150 to 1500 °C.

The two extensometer pairs recorded the deformation due to compression. Based on these data a total strain–time curve under constant loads and temperatures were obtained (Fig. 11). For a specific temperature, different compression loads were used, resulting in characteristic total strain–time curves as shown in Fig. 11. In a previous research [2], the curves presented in Fig. 11 [2] were used to evaluate the Norton-Bailey creep law parameters by an inverse estimation method.

To show the effect of considering creep in refractory material on the stresses in steel shell, a geometrically simplified (Fig. 3) uniaxial thermo-mechanical simulation was conducted. The thermal expansion due to the heat-up process and the restraint of the refractory material by the external steel shell were considered. As it can be seen in Fig. 12, considering creep in refractory material also leads to significantly lower stresses in the steel shell.

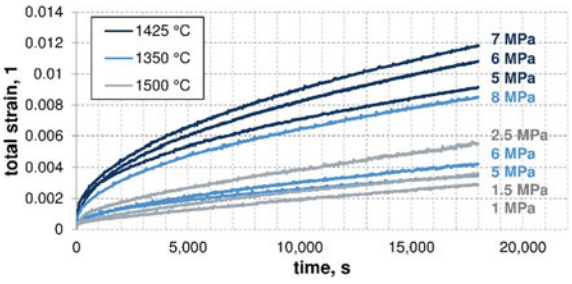

Fig. 11 Total strain–time curves of a fired magnesia brick from experiments at 1350, 1425, and 1500 °C and with varying compressive loads 1–8 MPa [2]

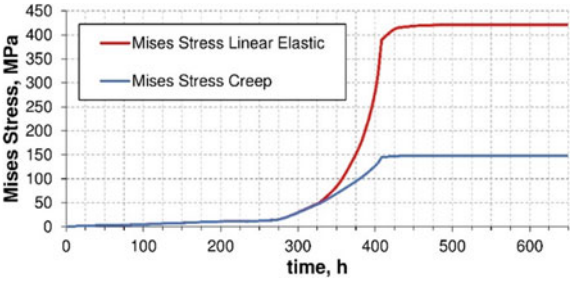

Fig. 12 Mises stresses in the steel shell for the simplified quarter brick model shown in Fig. 3 considering creep in the refractory material [2]

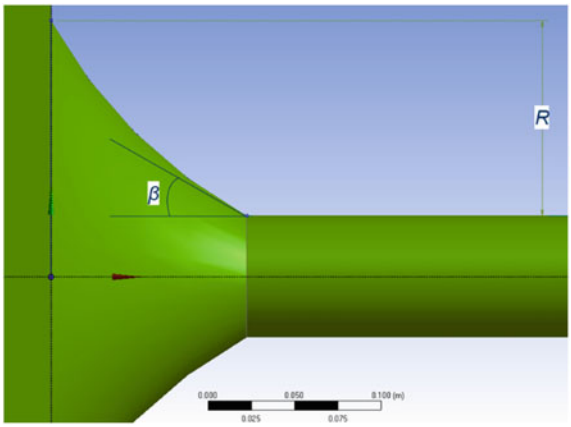

Fig. 13 Tapping channel geometry with geometric input parameters

Shape Optimization of a Tapping Channel

It is known that tapping channel is in contact with hot flowing media like metal or slag and it is subjected to their erosive action. In the following text, we investigate a possibility to minimise the erosion wear of the refractory material of the channel and maximize the mass flow rate by changing channel geometry. We optimise the shape of the channel using CFD simulations and optimisation methods provided by Ansys OptiSLang [12] and Ansys Fluent [12]. We considered a hypothetical tap-hole channel geometry with geometric input parameters R and β shown in Fig. 13.

Parameterisation

The geometric input parameter R is the difference between the inner and outer radii of the funnel, and we let it vary in the range from 0.03 m to 0.01 m. The geometric input parameter β is the angle formed by the tangent of the generatrix circle and the narrow part of the channel. We permit a variation from 0° to 45°. The radius of the rest of the channel was 0.035 m. The total length of the channel including the funnel was 1.4 m.

We considered two output parameters: the area-averaged wall shear stress τ along the channel surface and the mass flow rate q. We would like to find such an angle beta β and radius R that ideally should minimise the area-averaged shear stress τ and maximise the mass flow rate q.

CFD Evaluation of a Parameter Set

The boundary conditions for the prepared template CFD simulations in Ansys Workbench were as follows. We assumed a constant pressure at the top of the liquid bath and zero pressure at the exit from the channel. For a single parameter set evaluation, a transient two-phase VOF simulation was run until the relative changes in both mass flow rate and area-averaged wall shear stress along the channel were below 0.001. A single simulation required 4–5 min on average to complete.

A parameter set of the form (β_i, R_i, F_i), where F_i is one of surrogate models given in Eqs. (2) and (3) by means of a simulation as described above will be called a *design* in the further text and diagrams. Here i is the number of the design.

Optimisation

Using the template simulation described above, we employed Ansys OptiSLang [12] to produce anisotropic kriging [13, 14] surrogate models of the form:

$$\tau = \tau(\beta, R) \tag{2}$$

$$q = q(\beta, R). \tag{3}$$

To produce these surrogates, we employed a sampling strategy available in OptiSLang that iteratively improves the surrogate quality estimation expressed as local coefficient of prognosis [15] so that its minimal value is at least 90%. It took 59 simulation evaluations to satisfy this criterion.

After the surrogate models were computed, their explaining power in terms of the total effects [16] was evaluated. The 2D surrogate response surface plots for surrogate models (2) and (3) are shown in Figs. 14 and 15, respectively.

As it can be seen, the explaining power of the input parameter r is very low, it explained only 1.9% of variation in (2) and 2.7% in (3). We can conclude there was no dependence of either τ or q on r found. From this point on, we decided to consider only the angle β as the only input parameter.

As it can be seen from Figs. 14a and 15a, the change in the angle β affects the output parameters in the opposite way. As the angle β increases, the mass flow rate decreases, and at the same time the area-averaged wall shear stress τ along the channel surface decreases as well. It is not possible to minimise both shear stress and maximise mass flow rate at the same time, since the decrease of the value of one output parameter leads to increase in the other and vice versa.

To understand this relationship between τ and q, we performed a multi-objective optimisation using Ansys OptiSLang [11], where minima of both of τ or q were sought. For the multi-objective optimisation, the evaluations of surrogate models (2) and (3) were used instead of real simulation calls. The results of the multi-objective

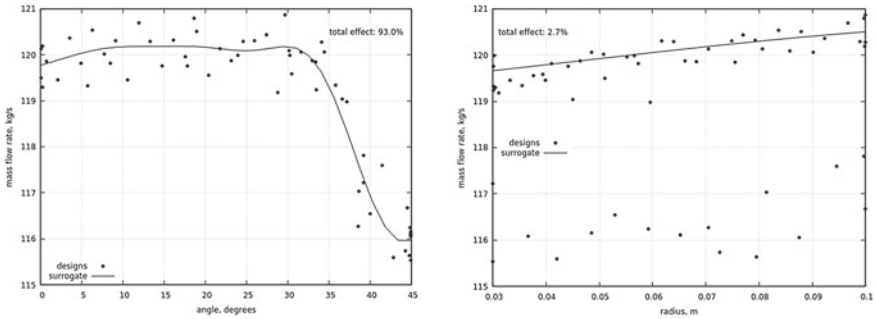

Fig. 14 Anisotropic kriging approximation of mass flow rate of the tapping channel shown in Fig. 13. The total effect of each variable is indicated. Black dots represent real simulation evaluations

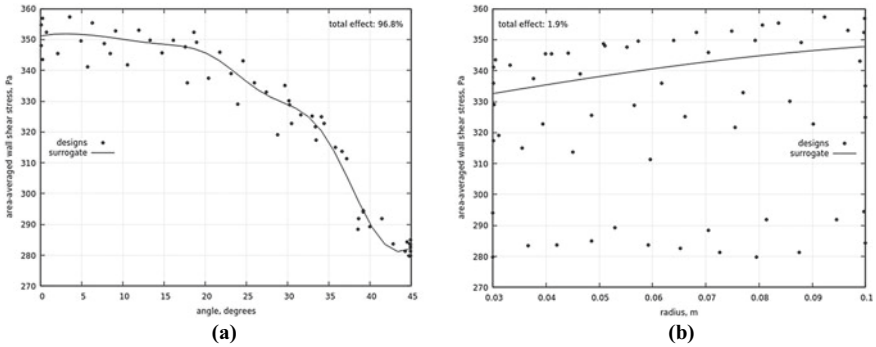

Fig. 15 Anisotropic kriging approximation of area-averaged wall shear stress of the tapping channel shown in Fig. 13. The total effect of each variable is indicated. Black dots represent real simulation evaluations

optimisation are shown in Fig. 16. The multi-objective optimisation was performed using a genetic algorithm [11], which produced 2279 designs, of which a Pareto front was calculated, which is also shown in Fig. 16. After that, 18 real simulation evaluations were used to evaluate the position of the Pareto front. This is also shown in Fig. 16. In Fig. 16, the real simulation validations (blue triangles) show the existence of the tendency predicted by the calculated Pareto front.

CFD Optimisation Results and Discussion

From the Pareto front in Fig. 16 we can see that a relatively small change in mass flow rate, from 121 to 116 kg/s (4% change), leads to a change in area-averaged wall shear stress from 323 to 278 Pa which amounts to a 14% change. In this way, the

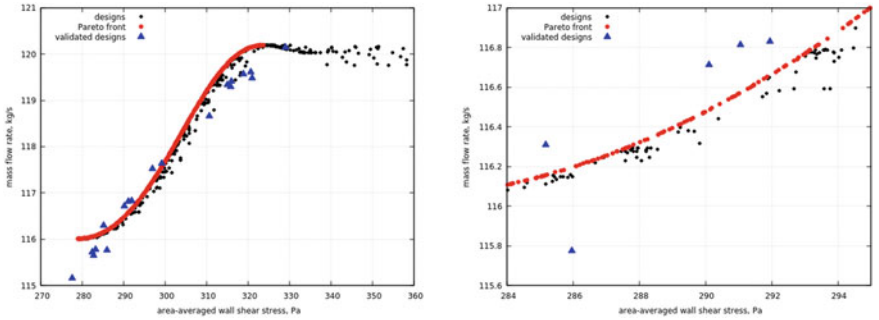

Fig. 16 Pareto front (**a**) and a zoomed area of Pareto front (**b**). Black dots represent evaluations based on surrogate models (2) and (3). Blue triangles represent real simulation evaluations (Color figure online)

Pareto front provides information by how much of the flow rate q should be sacrificed to gain benefit in terms of lowering the area-averaged wall shear stress τ.

Let us say we are prepared to sacrifice 5 kg/s or 4% of the mass flow rate to achieve the highest possible reduction in wall shear stress along the channel. The enlarged diagram in Fig. 16b shows the evaluated design points which can be considered as the ones which provide maximal minimisation of the wall shear stress. The validated design (blue triangle) in the left lower corner in Fig. 16b with approximate coordinates (285.2 Pa; 116.3 kg/s) lies above the predicted Pareto front which can be considered as the one providing maximal minimisation of the area-averaged wall shear stress. The angle which corresponds to this design was $\beta = 38.5°$. The resulting wall shear stress distribution in this design is shown in Fig. 17.

Since we could not find a significant dependence of either of the output parameters τ or q on the radius r, it can be chosen based on other reasons which are beyond the scope of this publication.

The whole optimisation process computation took less than 7 h: 59 simulation evaluations for producing surrogate models (2) and (3) took approximately 295 min, evolutionary algorithm for multi-objective optimisation required approximately 20 min and final validation simulation evaluations took approximately another 90 min.

Conclusions

Structural Mechanics

Two geometrical different tap-hole designs were analysed with respect to the occurring maximum principal stresses. After the steady-state heat-up and during the tapping sequence at 90 s and 40 min, the maximum principal stresses were detected.

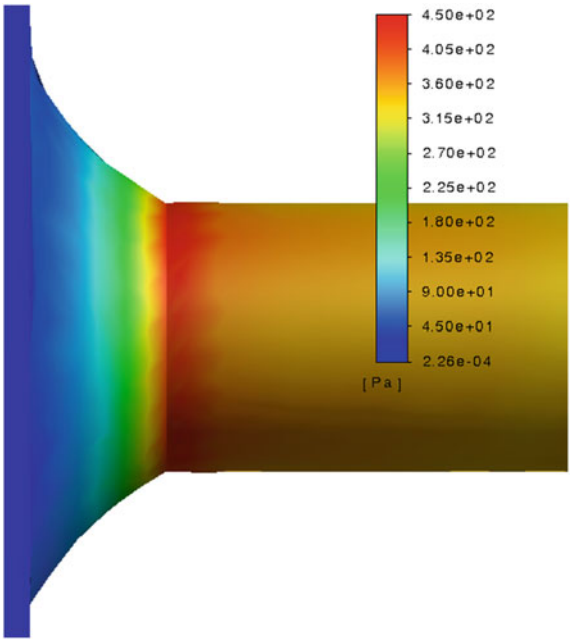

Fig. 17 The resulting geometry and the wall shear stress distribution

In the case of single brick arrangement after steady-state heat up, a step change in the distribution of the stresses at the first and second brick of the tapping channel was shown. After 90 s transient tapping, exaggerated stress magnitudes occurred on the upper area of the tapping channel, as well on the lower zones. These peaks were reduced at 40 min of tapping. This is a specific result caused by the geometry, the chosen material, and process conditions. In this case, the thermal shock predominates the geometrical constrains. As shown in prior research, specific process conditions can lead to a predominance of the geometrical constraint, which would cause the higher stresses at the end of the tapping period. Depending on the chosen design (single brick or tube), in the surrounding of the tap-blocks inlets, a characteristic and maximum stress pattern occurs. The mechanically more flexible configuration of the single brick design shows a kind of star-shaped pattern whereas the more rigid tube design shows a kind of radial stress distribution with lower stress magnitudes.

In the case of the mechanically stiffer tube-brick design, on the second half of Tube 1 areas with high principal maximum stresses occur. In the area of the transition of Tube 1 and Tube 2 stresses are significantly reduced. After 40 min the stress pattern of the tube-brick design is qualitatively similar than after 90 s. At the very end of the tube (outlet) spots with high stresses were detected.

A previously published established method to measure and extract Norton-Bailey creep parameters from refractory material was presented [1, 8]. By a simplified quarter brick model, the influence of considering creep in the refractory material on the calculated Mises stresses in the steel shell was demonstrated. The calculated

stresses in the steel shell were reduced by approximately a third. This is very reasonable and depending on the steel grade used, much closer to reality than the results of the linear-elastic approach which were in the order of 420 N mm^{-2}.

The results have shown that the application of material creep models implemented in finite element analysis of refractory materials improve the prediction of stresses and strains. Especially it shows more realistic stress values in the steel shell compared to the linear-elastic material model commonly used in industry. It should be mentioned that considering creep in FEM model will lead to a nonlinear, transient, and much more time-consuming calculations than the linear-elastic approach.

CFD Optimisation

Although the evaluated designs were quite scattered around the predicted Pareto front, the dependency between the mass flow rate and area-weighted average wall shear stress appears to exist, and a compromise must be made: the funnel shape that provides higher mass flow rates will at the same time experience shear stresses.

We were able to find the value of the funnel angle β that provides the most reduction of average wall shear stress, while sacrificing a small fraction of mass flow rate.

For a more realistic shape optimisation of a tapping channel in the future, we will have to consider more geometric parameters, for instance, different inlet and outlet radii of the channel after the funnel as well as channel inclination.

Fluid dynamics analyses with Ansys Workbench together with Ansys OptiSLang provide us with a powerful tool to study and improve the geometry and flow characteristics in functional a timely manner.

References

1. Kreuzer D, Marschall U, Wagner C (2018) Numerical simulation—a tap-hole refractory design study. Paper presented at the furnace tapping 2018, South Africa, 14–17 Oct 2018
2. Unterreiter G, Kreuzer D, Lorenzoni B, Marschall H, Wagner C, Machhammer R, Hackl G (2020) Compressive creep measurements of fired magnesia bricks at elevated temperatures including creep law parameter identification and evaluation by finite element analysis. MDPI Ceram 3(2):210–222. https://doi.org/10.3390/ceramics3020019
3. Richerson DW (1992) Modern ceramic engineering: properties, processing and use in design, 2nd edn. Marcel Dekker, Inc., New York, p 834
4. Afshar S, Allaire C (1996) The corrosion of refractories by molten aluminium. JOM 48:23–27
5. Allahevrdi M, Afshar S, Allaire C (1998) Additives and the corrosion resistance of aluminosilicate refractories in molten Al-5Mg. JOM 50:30–34. https://doi.org/10.1007/BF03222938
6. Hosseini E, Holdsworth S, Mazza E (2012) Creep constitutive model considerations for high-temperature finite element numerical simulations. JSA 47:341–349. https://doi.org/10.1177/0309324712450542

7. Mammar AS, Gruber D, Harmuth H, Jin S (2016) Tensile creep measurements of ordinary ceramic refractories at service-related loads including setup, creep law, testing and evaluation procedures. Ceram Int 42:6791–6799. https://doi.org/10.1016/j.ceramint.2016.01.056
8. Jin S, Harmuth H, Gruber D (2014) Compressive creep testing of refractories at elevated loads—device, material law and evaluation technique. J Eur Ceram Soc 34:4037–4042. https://doi.org/10.1016/j.jeurceramsoc.2014.05.034
9. Dusserre G, Valentin O, Nazaret F, Cutard T (2016) Experimental and numerical investigation of the asymmetric primary creep of a fibre reinforced refractory concrete at 1200 °C. J Eur Ceram Soc 36:2627–2639. https://doi.org/10.1016/j.jeurceramsoc.2016.03.007
10. Munz D, Fett T (2001) Ceramics mechanical properties, failure behaviour, material selection. Springer, Berlin/Heidelberg, Germany, pp 227–229
11. Dassault Systems. https://www.3ds.com/products-services/simulia/products/abaqus/. Accessed 16 Sept 2021
12. Ansys Platform web page Ansys Platform | Digital product development tools. https://www.ansys.com/products/platform. Accessed 13 Sept
13. Oliver MA, Webster R (1990) Kriging: a method of interpolation for geographical information systems. Int J Geogr Inf Syst. https://doi.org/10.1080/02693799008941549
14. Hansen RO (1993) Interpretive gridding by anisotropic kriging. Geophysics 58(10):1491–1497. https://doi.org/10.1190/1.1443363
15. Will J, Most T (2009) Metamodel of optimized prognosis (MoP)—an automatic approach for user friendly parameter optimization. https://doi.org/10.13140/2.1.4946.9122
16. Most T, Will J (2011) Sensitivity analysis using the metamodel of optimal prognosis. Weimar Optim Stochastic Days 8:24–40

Part IV
Session IV

Tap-Hole Refractory Issues and Remedies

Dean Gregurek, Christine Wenzl, Jürgen Schmidl, and Alfred Spanring

Abstract Post-mortem investigations of used refractories have proven to be a crucial tool for evaluating process conditions and their effect on the lining. Despite these experiences, refractory samples from tap-holes are often neglected and do not get too much attention—there is a general opinion: "tap-hole refractory wear is due to tapping operations and there is no room for optimization". However, closer investigations of tap-hole samples provide some valuable insights into wear phenomena and optimization potential (e.g., slag corrosion, non-oxide infiltration, and microstructural changes due to high-temperature load). Even though the possible changes to the actual tapping operations might be limited, it is worth considering, e.g., refractory upgrades. Additional possibilities for optimized tap-hole refractory performance and general tapping procedures are various additional technologies, e.g., sensor technologies.

Keywords Refractories · Wear phenomena · Sensor technologies

Introduction

Post-mortem investigations of used refractories are an established tool for studying failure mechanisms and optimizing lining concepts. Such investigations (visual and mineralogical) offer valuable insights into the process conditions and the process/refractory interactions. Although numerous lining samples are investigated every year, tap-hole refractory samples only account for a very small portion: usually, wear and failure in this region are commonly seen as process-inherent and unavoidable. Even though it is true that there are certain limits to changing tapping procedures, it is possible to optimize tap-hole refractory performance: both by optimizing the material and applying additional tools and technologies. Tap-holes are found in almost all furnace types, in various metal production processes, with refractory

D. Gregurek (✉)
Technology Center Leoben, RHI Magnesita, Magnesitstrasse 2, 8700 Leoben, Austria
e-mail: dean.gregurek@rhimagnesita.com

C. Wenzl · J. Schmidl · A. Spanring
RHI Magnesita, Kranichberggasse 6, 1120 Vienna, Austria

J. D. Steenkamp et al. (eds.), *Furnace Tapping 2022*, The Minerals, Metals & Materials Series, https://doi.org/10.1007/978-3-030-92544-4_20

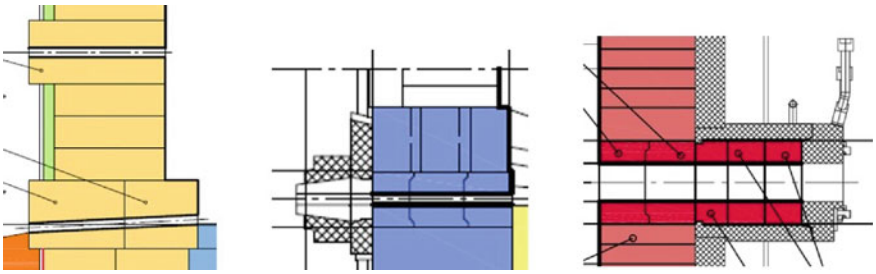

Fig. 1 Sideview sketches of design examples in various complexities depending on specific parameters—**a** simple design, e.g., pilot-plants; **b** and **c** advanced design options applied on numerous applications in NFM processes (e.g., Cu, Fe-Alloys) [7]

materials optimized for the specific furnace and process—some example designs are shown in Fig. 1.

Regarding tap-hole refractory wear, design and tap-hole opening practice are important to understand [4, 5]:

- Sliced tap-hole blocks versus single-block options;
- Cooled tap-holes with the aim of freeze lining formation at the hot face versus non-cooled solutions;
- Opening with combination drilling/lancing versus lancing only;
- Selection of lancing material: Fe-pipe versus wire-filled Fe-pipe versus specifically designed cross-section of thermal lance;
- Contact pressure: thermal lances have the best performance when in contact with the material to be tapped, but excessive pressure (causing mechanical damage) has to be avoided;
- Oxygen flow control: The optimum flow rate is a proportional amount of iron in the cross-section of the lance and excess oxygen flow can even decrease the performance of the lance (quite often it gives the impression that the tap-hole is penetrated faster as a consequence of the noise generated and material projected).

The observed wear phenomena through post-mortem investigations can generally be subdivided into continuous and discontinuous wear [1]. Continuous wear is characterized by continuous mass loss as a function of time. It is caused by chemical, thermal, and mechanical load that can occur as single or interrelated wear factors [3, 6].

The continuous wear is caused by corrosion of the refractory by dissolution in melts/slags with additional hot erosion due to hot metal. In industrial furnaces, dissolution in melts/slags occurs at the direct refractory hot face. Increased temperatures, as well as the metal infiltration into the brick microstructure, are further phenomena on the thermal wear side. Mechanical load includes already mentioned hot erosion which is primarily caused by the movement of the metal bath, slag, and charging material.

Discontinuous wear is mainly characterized by mechanical failure prepared by thermal/chemical load occurring discontinuously over time. It is associated with mass loss. Further discontinuous wear phenomena include (structural) spalling, thermal shock failure, and bursting reactions (alkali, carbon, forsterite, etc.). Thermal shock is mainly due to changes in the temperature and partial pressure during the furnace operation. Stresses in the brickwork due to improper lining procedures additionally contribute to damages of the refractory by mechanical load.

The current paper describes post-mortem investigations on tap-hole samples with focus on ferroalloy furnaces, as well as suggestions for optimizing tap-hole and tapping performance.

Observed Wear Phenomena in Tap-Holes

Slag Corrosion

Generally, the corrosion of the refractories by slag attack manifests itself in three ways [2, 3].

(a) Dissolution reaction occurring at the immediate brick hot face: The driving force here is the lower activity of the refractory oxides like MgO in the slag. The dissolution process, at least in the closed system, will continue until the liquid slag has reached saturation. However, in practice, the point of saturation is never reached, and dissolution continues until the entire refractory has been consumed.

The dissolution of the refractory can be expressed by the first Fick's law that basically postulates that the refractory dissolution is proportional to the diffusion coefficient and difference in the concentration gradient and can be expressed through the following equation (Eq. 1):

$$j = \frac{D}{\delta}(c_S - c_0)$$

where j represents mass flux of dissolving species, c_S solubility (concentration at the interface), c_0 bulk concentration distant from interface, δ effective diffusive boundary layer thickness, and D effective binary diffusion coefficient, respectively.

(b) Dissolution and chemical reaction within the refractory microstructure: Infiltrating slag will dissolve magnesia, especially from the fines, according to the respective phase equilibrium. This will not directly contribute to corrosive wear which takes place at the immediate refractory hot face. Nevertheless, it will contribute to wear by preparing hot erosion due to a loss of brick bonding.

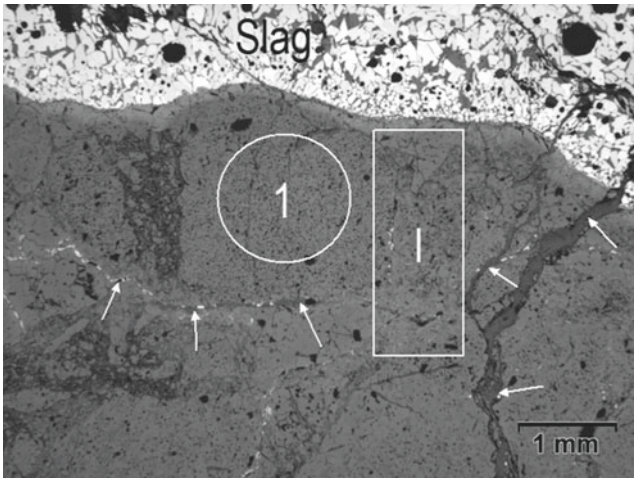

Fig. 2 Slag layer on the immediate brick hot face. Below the slag coating partly infiltrated brick microstructure (I). Magnesia (1). Cracks running parallel and diagonal to the hot face sometimes filled with slag (arrows)

(c) Kinetics of slag infiltration: Kinetics of slag infiltration causing processes mentioned above depends on several parameters like temperature, viscosity, pore size distribution, and wetting angle.

On a microscopic scale, several zones can be distinguished at the brick hot face:

- Adhering slag layer, frequently covering the immediate brick hot face (Fig. 2).
- Below the slag layer, an infiltrated and corroded brick microstructure Within the infiltrated brick microstructure, due to corrosion of sintered magnesia and the interstitial phase, the main reaction products include Ca-Mg-silicates (monticellite, $CaMgSiO_4$ and merwinite, $Ca_3MgSi_2O_8$) and some MA-spinel ($MgAl_2O_4$) (Fig. 3). Additionally, in the infiltrated microstructure the periclase (MgO) in sintered magnesia is enriched with iron- and manganese oxide.

Non-oxide Infiltration

In addition to acidic slag, also other components such as FeMn, FeNi, FeCr, and iron infiltrate the brick microstructure (Fig. 4). Generally, non-oxide infiltration only densifies the brick's microstructure without any corrosive attack on the brick components. Similar to the acidic slag, the degree of infiltration depends on the surface tension, the boundary angle in contact with the refractory oxides, the temperature, the bath height, and the size/distribution of the brick pores.

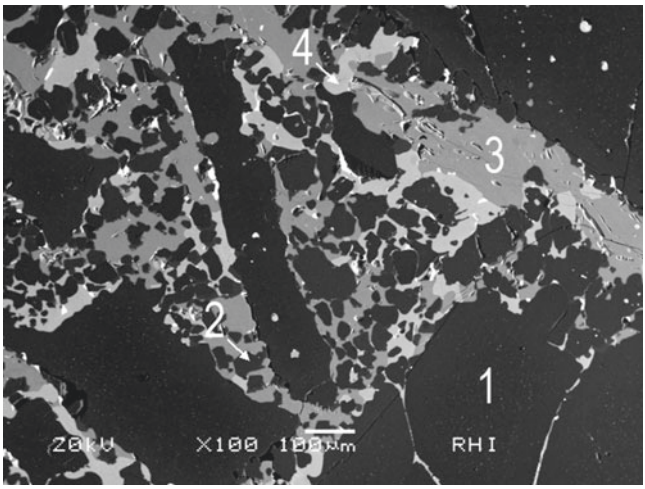

Fig. 3 Below the slag layer infiltrated brick microstructure. Corroded magnesia (1). MA-spinel (2). Monticellite (3). Monticellite (4)

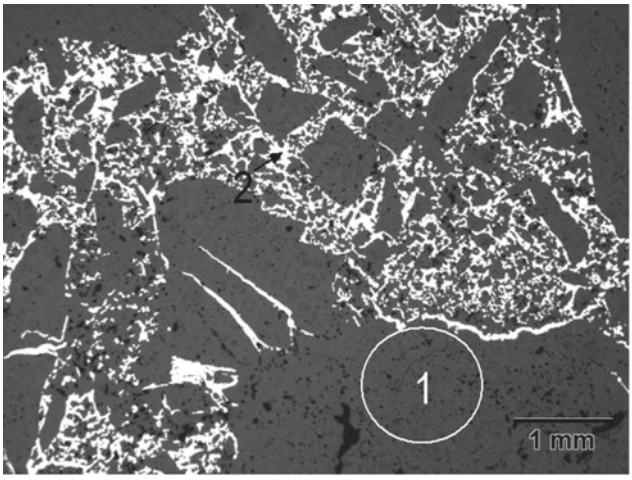

Fig. 4 Pore filling infiltration of the brick microstructure. Sintered magnesia (1). Iron (2)

Microstructural Changes Due to High-Temperature Load

Although the temperatures in most furnaces for nonferrous metal production are typically quite below the maximum service temperature of the as-delivered refractory materials, the temperature plays an important role in the continuous wear of the bricks. The higher degradation rate, caused by the reduced viscosity and higher

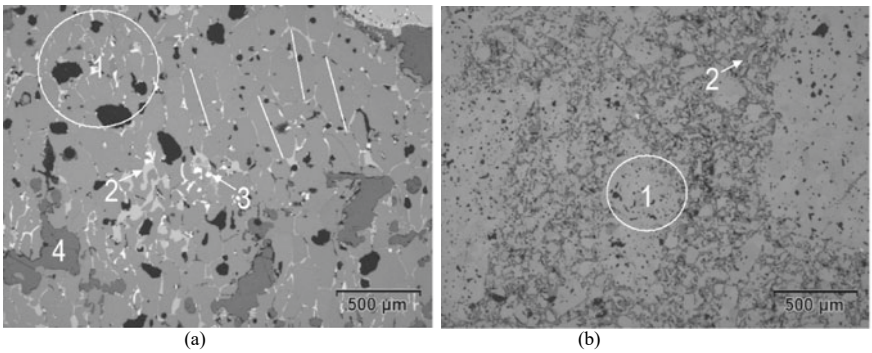

(a) (b)

Fig. 5 **a** Extreme elongation of periclase crystals (epitaxial crystal growth) towards the thermal gradient (lines). Magnesia (1). Mg-titanate (2). Ca-titanate (3). Coarse pores (4) formed due to severe degeneration of the brick microstructure (Fig. 5b). For comparison to Fig. 5a, original brick microstructure at the same magnification. Magnesia (1). Pores (2)

diffusivity associated with an overheated melt, clearly demonstrates the effect of temperature.

On the microscopic level, a very characteristic feature for this wear phenomenon is periclase crystal growth and lengthening towards the thermal gradient (several mm long crystals). The crystal size of the single periclase crystals within the original sintered magnesia is usually up to 140 µm [6]. However, in highly degenerated brick microstructure the single grains, as well as the classical ceramic microstructure with coarse grains and matrix fines, cannot be observed anymore. In addition to this, also the supplied oxide components such as nickel-, iron- and manganese-oxide act as mineralizing agents, thus strongly supporting the periclase crystal growth.

Within the first 10 mm from the hot face the brick microstructure is highly degenerated. There is coarse pore formation and partly elongation of periclase crystals along the thermal gradient (Fig. 5a).

In such a highly degenerated brick microstructure, the coarse grains and the matrix fines cannot be recognized. For comparison, the microstructure of an unused refractory at the same magnification is shown in Fig. 5b.

Such microstructural changes are quite typical for ferroalloy furnaces where the operating temperature is much higher than in base metal production.

According to observations on-site, the wear could be caused by jack-hammering in combination with excessive oxygen lancing in the tap-hole channel.

Decarburization

In refractory materials, carbon is used either in the form of carbon blocks or magnesia-carbon bricks. While it is the main component in the former, it provides the binder phase and determines brick properties in the latter. However, carbon is oxidized by

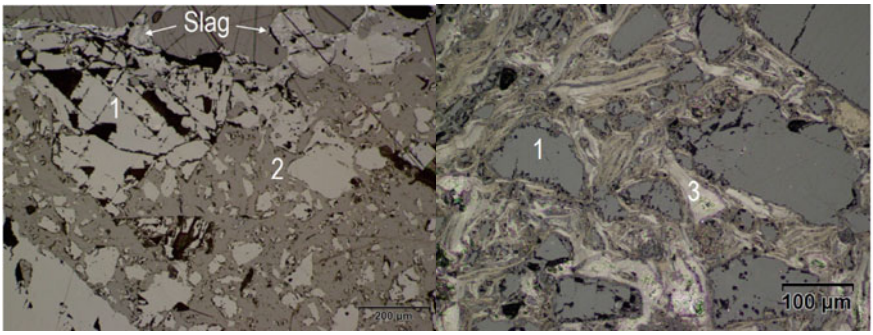

Fig. 6 Completely bondless microstructure of a used magnesia-carbon brick (left figure). Complete loss of carbon binder and graphite due to oxygen lancing. In comparison (right figure) original and non-oxidized microstructure of the magnesia-carbon brick. Fused magnesia (1). Pore space filled with preparation resin (2). Graphite (3)

oxidic phases (slags) and also by oxygen lancing procedures for tap-hole opening. Such oxidation negatively affects the brick integrity and can lead to premature lining failure.

In Fig. 6, completely disintegrated microstructure of the magnesia-carbon brick is compared with the original/non-oxidized microstructure. The carbon bonding and flake graphite are completely lost due to oxygen accesses (oxygen lancing), thus the single fused magnesia coarse grains and the matrix fines are bondless.

Brick Damage by Hydration

Although magnesia bricks provide high refractoriness compared to other refractories, there is still a great concern regarding their vulnerability when exposed to water vapor at low temperatures and subsequent hydration. Typical origins of hydration can be transportation and storage, as well as improper heat-up and/or combination with water-cooled cooling elements.

Generally, hydration of magnesia-chromite bricks can occur in humid atmospheres typically at temperatures between 40 and 120 °C [6]. It is characterized by the transformation of periclase into brucite ($Mg(OH)_2$) according to the reaction:

$$MgO + H_2O \rightleftharpoons Mg(OH)_2$$

This reaction is associated with an increase in volume of up to 115% [6]. Additionally, the formation of brucite is accompanied by an expansion of the crystal lattice because of the oriented growth of the hexahedral brucite on the cubic periclase—the space between the magnesium ions within the brucite is larger than in the periclase.

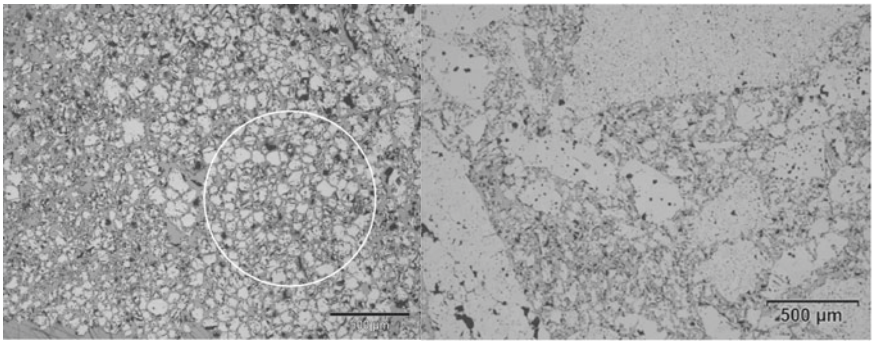

Fig. 7 (Left figure) Brick damage by hydration of the periclase (circle). In comparison (right figure) original microstructure at the same magnification

Due to this reaction, the periclase crystals are separated along the natural, crystallographic cleavage planes. The resulting "microcracks" represent new reaction surfaces, which again show a high tendency towards hydration. This leads to a chain reaction which, starting just from a few centers, can finally cause extensive, characteristic crack formation and in extreme cases a sand-like disintegration of the whole brick. Influencing factors having an effect on hydration are humidity, temperature, and time. The hydration process can occur during storage, drying after installation, or during service. Microstructural image of typical hydration and comparison to the original non-hydrated brick microstructure are shown in Fig. 7.

Cracks

As in any type of refractory materials, also in tap-hole refractories, cracks can cause early brick damage and failure. The origins of cracks can be manifold, e.g., production process, transportation, storage, installation, heat-up, as well as thermal shocks during furnace operation. Crack formation before installation has to be avoided by the refractory producer, as well as following instructions for transportation and storage of materials. Well-trained staff as well as professional supervision of installation work and following defined and furnace-specific heat-up procedures help to avoid crack formation during these stages. Cracks resulting from furnace and tapping operations are usually due to thermal cycling, and their reduction requires a thorough review of these processes.

Discontinuous Wear by Thermal Shocks

In the case of batch-wise processes, the refractory lining is exposed to high thermo-mechanical load. The infiltration and corrosion of the refractory microstructure increase the structural brittleness. Temperature changes due to discontinuous furnace operation (even when charging and operation is continuous, tapping is mostly discontinuous) create stresses in the brick lining which can only be absorbed in limited extent, thus leading to crack formation, as soon as microstructural strength is exceeded.

Static tension which arises through inadequate brick lining or failure in the heating procedure leads to serious deformation of the brick lining and crack formation.

Measures

In the previous sections, common wear phenomena as observed in tap-hole refractories were described. Even though not all of them can be eradicated completely, there are some measures to reduce tap-hole refractory wear and prolong lifetime. The cost/benefit ratio of such measures is always a crucial factor for industrial applications, therefore profound process and refractory wear knowledge are required before selecting meaningful measures to optimize the performance of tap-hole refractories.

The most obvious measure is adaption and optimization of the refractory material quality, e.g., changing to higher-quality components to reduce infiltrations and corrosion. Depending on the specific process and its requirements, this is only possible to a limited extent.

Wherever applicable and available, it is of utmost importance to follow the refractory supplier's instructions for transportation, storage, and handling of the refractories, as well as proper installation and heat-up.

The tap-hole opening procedures need to be reviewed in order to find a good balance between drilling and lancing, minimizing the latter as far as possible to reduce its detrimental effect on the tap-hole refractories (i.e., thermal shocks, overheating, and decarburization).

Temperature monitoring is vital for the detection and prevention of process-related overheating of tap-hole refractories, as well as reduction of infiltrations.

Besides these more obvious and straightforward measures, it also makes sense to consider new technologies.

Alternative tap-hole opening/closing technologies, namely the use of slide gates (as widely used in various vessels in the Steel industry), help to reduce stresses on tap-hole refractories caused by oxygen lancing.

Sensor technologies for furnace-level measurement (such as RHIM's EMLI FurnaceProfile and EMLI SmelterLevel) allow for objective and repeatable monitoring of the material levels in the furnace. This information is used to determine the optimum tapping time and schedule, namely when the right amount of material is available in the furnace and not tap more often than required. This does not reduce

the thermal shock associated with tapping per se, but helps to reduce the number of such events (thereby prolonging tap-hole refractory life).

Sensor technologies are also available for metal and slag detection during the tapping process (such as RHIM's EMLI MetalSlag and VISIR MetalDetect)—this not only reduces metal losses (and improves safety in case of subsequent slag water-granulation) but also reduces corrosion by slag.

Sensors can also be applied for tap-hole monitoring, detecting (metal) infiltrations, and assisting with tap-hole repair.

Conclusion

Post-mortem investigations of refractory samples are a well-established tool to understand the reasons for refractory wear. Such investigations on tap-hole refractories are often neglected, however they provide valuable insights and a basis for optimization. Despite the more obvious measures like upgrading refractory qualities, it also makes sense to investigate the furnace and tapping process as a whole and consider the use of new technologies. The evaluation of the most appropriate measures has to include the cost/benefit ratio and needs to be carried out for each individual process.

References

1. Barthel H (1981) Wear of chrome magnesite bricks in copper smelting furnaces. Interceram 30:250–255
2. Gregurek D, Reinharter K, Majcenovic C, Wenzl C, Spanring A (2015) Overview of wear phenomena in lead processing furnaces. J Eur Ceramic Soc 35:1683–1698
3. Harmuth H, Vollmann S (2014) Refractory corrosion by dissolution in slags—challenges and trends of present fundamental research. Iron Steel Rev 58(4):157–170
4. Morales D, Morales C, Nunez S (2018) Tap-hole opening: advances and improvements. In: Proceeding to furnace tapping conference 2018. SAIMM, pp 231–249
5. Nelson LR, Hundermark RJ (2016) The tap-hole—key to furnace performance. SAIMM 116:465–490
6. Routschka G, Wuthnow H (2012) Handbook of refractory materials, 4th edn. Vulkan-Verlag, Essen
7. RHI Magnesita internal publication

Sensor Technologies for Optimized Tapping Procedures

Christine Wenzl, Magnus Persson, and Ladislav Koncik

Abstract Decision-making to tap is often based on experience and mass balance calculations. However, better methods are available to optimize the tapping efficiency, making sure tapping occurs at the best moment with minimum losses. Metal tapping should occur at a precise moment when the correct amount is available in the furnace and before overfilling. This moment can be difficult to determine without proper level monitoring. Even for slag tapping, the right timing is difficult to assess and even worse, it often leads to metal value losses and represents a safety hazard. RHI Magnesita offers sensor technologies to help you control levels and detect metal losses. These are used for fact-based decision-making ensuring optimized tapping procedures. The paper will describe and discuss the technologies as well as how to implement them in the furnace operation and what benefits can be achieved.

Keywords Sensor technologies · Process optimization · Level measurement · Metal detection

Introduction

Furnace operations today are still widely based on experience, calculations, and/or estimations. However, there are more reliable and objective tools available today that allow one to move from educated guessing and gut feeling to fact-based decision-making.

Tapping processes are found in all metal production processes and various furnace types, and represent an equally important and potentially hazardous process step: removing the right amount of process phases at the right time with maximum control of the liquid materials leaving the furnace. Therefore, good knowledge of the material levels in the furnace, as well as monitoring of the liquid material streams exiting the furnace, are decisive factors for efficient tapping procedures. RHIM's "beyond refractories" technology portfolio comprises various tools to achieve optimum process

C. Wenzl (✉) · M. Persson · L. Koncik
RHI Magnesita, Kranichberggasse 6, 1120 Vienna, Austria
e-mail: Christine.wenzl@rhimagnesita.com

J. D. Steenkamp et al. (eds.), *Furnace Tapping 2022*, The Minerals, Metals & Materials Series, https://doi.org/10.1007/978-3-030-92544-4_21

stability and safety, including sensor technologies that can be applied in a wide range of furnaces. Such sensor technologies must not be considered a standalone tool, but allow for data collection and subsequent analysis to stabilize and optimize processes, including tapping operations. This is a further step towards enabling automation of processes and finally the introduction of Industry 4.0.

The present paper will discuss some typical challenges in tapping operations, as well as how sensors can assist in the optimization of the processes, regarding efficiency and safety.

Typical Issues

Furnaces are typically designed for specific levels of furnace contents, e.g., slag and metal. Based on these theoretical levels, the lining concept is designed, considering the optimum refractory for each zone (e.g., metal, slag, and freeboard) based on the expected wear phenomena in the specific zones. Therefore, it is important to keep the material levels in the designed zones to avoid unexpected and excessive refractory wear, which in turn can lead to shorter furnace campaigns or, in the worst case, even breakouts. The most critical case, from a refractory perspective, would be too high slag levels, i.e., when slag reaches the freeboard area which is normally not lined with highly slag-resistant material. A similar situation occurs in the case of too low metal levels, i.e., with slag reaching the defined metal area.

While too high metal levels in the furnace are not that relevant regarding excessive refractory wear, this is a crucial parameter for overall metal production, affecting not only the specific furnace operation but also the coordination with downstream processes.

The most common methods nowadays for determining material levels in the furnace are still mass balance calculations and/or manual dip bar measurements. The latter is highly subjective and dependent on the operator's experience. Therefore, there are several uncertainties about the material amounts in the furnace, leading to suboptimal tapping regarding timing and quantities.

Tapping comprises several aspects: the right timing, tap-hole opening, and the actual tapping including handling liquid material streams. All these aspects affect the process and operator safety: optimized timing and tapping quantities ensure that the safety-critical tapping procedure is only carried out as often as required, thereby also prolonging the lifetime of the refractories in the tap-hole area, and providing an adequate and defined amount of material for the downstream process. When handling liquid material streams, it is of utmost importance to differentiate between metal and slag: metal losses during slag tapping not only reduce efficiency and lead to monetary losses, but in cases of subsequent water-granulation represent a significant safety risk in case of explosions. Therefore, it is important to have not only good knowledge of the material levels in the furnace but also a good overview of what materials are exiting the furnace.

How to Tackle Typical Issues

When performing manual sounding bar measurements, there are a number of factors that will have an impact on the measurement performances. The bar will be inserted and kept in the furnace for a short period as the metal heats up the bar and the slag may freeze on its surface. When the bar is removed, the transition between slag and metal is usually quite difficult to observe and even more difficult to measure precisely. The angle of the bar, the unclear transition, and the thermal bending of the bar will have a huge impact on the measurement itself. Therefore, operators rely a lot on their experience and judgment when performing such measurements.

During tapping procedures, it is important to make sure only the wanted material phase is tapped. This is usually done solely by observations and sometimes using tools to split the tapping stream and observe the materials inside or in the "back" of the stream. Obviously, this is a very difficult and heavily operator-dependent task.

Both sounding bar practices and tapping observations are critical to furnace operations and efficient tapping procedures. They, however, both come with a doubtful accuracy which is heavily dependent on the operators' judgement and provide a safety hazard to the personnel.

Short Overview of Systems and Technologies Available

RHI Magnesita offers systems for monitoring, measurement, and control in almost all stages of the liquid phase of the production process. The Sensors portfolio is based on several technologies ranging from optical to electromagnetic systems (Fig. 1). While

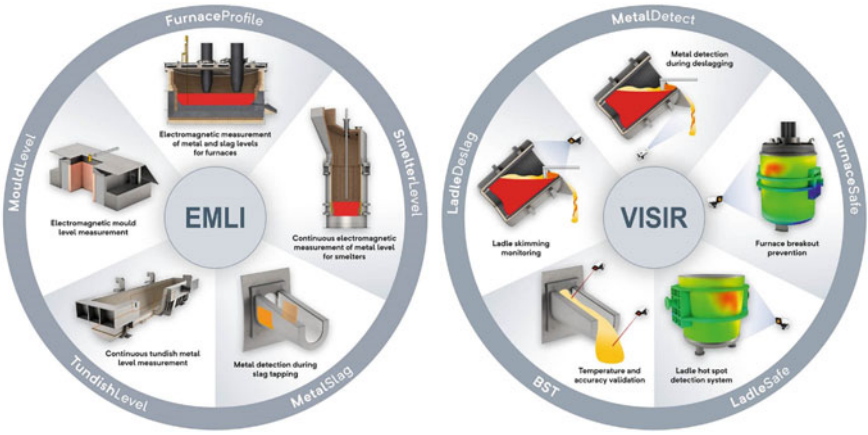

Fig. 1 Overview—RHIM's sensor technologies (left: electromagnetic/EMLI; right: visual and infrared/VISIR)

optical systems are usually used to monitor objects or processes from the outside, electromagnetics can be used to monitor inside tap-holes and inside furnaces.

Precise Furnace Levels (EMLI FurnaceProfile)

The EMLI FurnaceProfile (Fig. 2) system is a patented technology used to create a precise profile of the materials contained inside a furnace. The technology is capable of distinguishing between material electrical conductivities and can, as such, identify and map the different levels inside the furnace.

The system is engineered to replace the standard sounding bar measurements and can often be installed in the same location with the same footprint. The system is composed of a sensor-equipped lance that is inserted inside the furnace in the same fashion as one would insert a sounding bar. The lance movement is controlled by a very precise automated and remotely operated winch device making sure the measurement sequence is made in a timely and safe manner.

As the sensor travels inside the furnace, it detects the different material layers and transition zones between them, providing an instantaneous material profile. The results are displayed on an operator screen and transmitted automatically to the plant PLC system. A measurement sequence takes about 15–30 s and will typically result in a slag level, metal level, alloy level if present, and a local bottom build-up. The accuracy of detection will depend on the delivery system, the process, and conductivity characteristics of the present materials. Typical accuracy for metals is usually in the millimeter range.

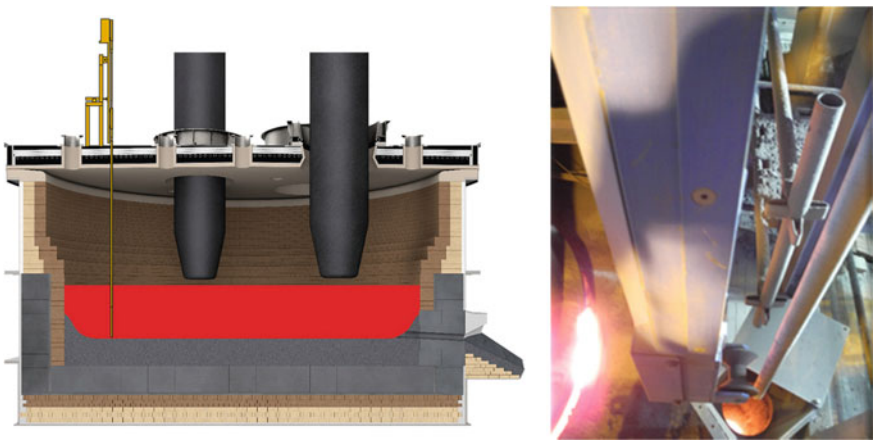

Fig. 2 EMLI FurnaceProfile (left: schematic with EMLI system depicted in orange; right: lance entering furnace through hole in furnace roof) (Color figure online)

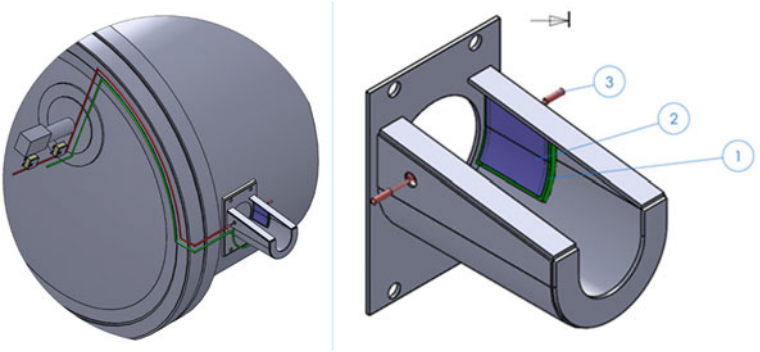

Fig. 3 EMLI MetalSlag (left: overview; right: detail with (1) sensor frame, (2) sensor cover, (3) sensor cable)

Differentiate Metal from Slag During Tapping (EMLI MetalSlag)

During tapping of slag, it is of utmost importance to make sure only slag is being tapped and avoid accidental metal losses. The EMLI MetalSlag (Fig. 3) is precisely engineered to monitor a slag tap-hole and make sure no metal is inadvertently tapped. A sensor installed in the surroundings of the tap-hole or slag runner is continuously monitoring the material passing within its electromagnetic field. The appearance of metal triggers an alarm on the operator's displays and can be used to trigger an additional action via the customer's PLC system. The system's sensitivity can be adjusted to limits fitting the actual process.

How to Use the Data

Precise and on-time measurement of all liquid phases in different furnaces is an important step for the following production chain and must be done as accurately and independently as possible. Calculated or visually observed level measurements can be influenced by significant errors, having negative consequences for the production.

The EMLI FurnaceProfile system not only provides accurate information about the different levels of the metal or slag in the furnace but also can provide information about the speed of the melting process itself or build-ups on the furnace bottom (Fig. 4). Intermediate layers of partially melted material can be created between the slag and melted phase or can be floating on the top of the slag. The EMLI FurnaceProfile system can reliably detect these layers which can be useful information for optimizing the feed rate of the raw materials and maintain the correct operating levels of the various phases in the furnace.

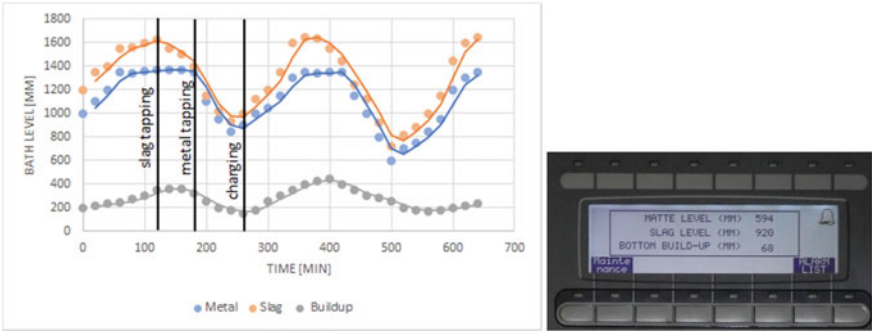

Fig. 4 Material levels in furnace over time (left); operator view (right)

In addition, the system can be equipped with different additional sensors like temperature, O_2-potential measurement, or a slag/metal sampling device, which could further enhance the value for the customer and increase the safety of the operators.

The Benefits

The usage of the data from the EMLI FurnaceProfile and EMLI MetalSlag systems can clearly improve the metallurgical process and exclude the subjective experience of the furnace operator which significantly reduces the risk of production mistakes. In addition, several production steps like metal or slag sampling, temperature and bath level measurement can be combined in one operation step which improves the efficiency, accuracy and safety of the employees.

The main benefits of using sensor-assisted furnace operations and tapping are

- Safety improvements;
- Avoiding unnecessary metal losses;
- Keeping levels within the operational range;
- Improved tap-to-tap times;
- Reduced refractory wear;
- Improved coordination with downstream processes;
- Improved quality assurance capabilities.

Improving just some of the above aspects has a significant economic impact on production. For example, by using EMLI technology in batch processes, a 12% decrease in process time has been reported.

Conclusions

Furnace and tapping operations require process knowledge to ensure smooth processes. Today, the respective decisions are widely based on experience and calculations. However, this traditional approach can be significantly improved by implementing new technologies. Sensor technologies are a useful tool to measure furnace levels and monitor tap streams, as well as provide valuable data for fact-based objective decisions. Consequently, operations can be optimized, leading to positive economic and safety impacts.

While sensors are a reliable tool for measurement and data collection, for realizing the benefits it is essential to not only collect data but also use and analyze them. Only then can data assist in gaining a better process understanding and finally process optimization.

Today, such novel sensor technologies as the EMLI FurnaceProfile and EMLI MetalSlag described in the present paper might seem “exotic” and unusual: their value might not be obvious and easily understandable, or might even be seen as a threat to reduce headcount. However, it is important to understand the benefits of such new technologies and their contribution to ensuring competitiveness, namely by optimizing processes, efficiency, working conditions, and safety.

Automated bath-level measurement—possibly in combination with sampling and temperature measurement as one single automated step—not only provides reliable data for optimized process control but also saves time, which can be used to change the focus of interest for the next improvements in the plant.

The Evaluation of Chemical Wear of Carbon-Based Tap-Hole Refractories in Ferrochrome Production

M. B. Sitefane and J. D. Steenkamp

Abstract In ferrochrome (FeCr) production, the tap-hole refractory represents the highest wear area. Preliminary desktop FactSage modelling work conducted by Steenkamp (J South Afr Inst Min Metall 119(8):537–544, 2019) indicated that both alloy and slag had the potential to chemically wear the carbon-based tap-hole refractory material. The current study sought to build on the modelling work, by performing laboratory-scale experiments aimed at validating the modelling outcomes. Experimental work was conducted using a cup test approach, in an induction furnace, at 1450–1650 °C for the alloy-refractory, and 1550–1700 °C for the slag-refractory. Experimental results confirmed the potential for both FeCr alloy and slag to chemically wear the refractory. Tapping temperature was also found to have a marked effect on the extent of the wear.

Keywords Refractory · Chemical wear · Ferrochrome · Carbon refractories · Tap-hole

Introduction

Ferrochrome (FeCr) is an alloy composed mainly of chromium (Cr) and iron (Fe), and some amount of carbon (C) impurity. Two FeCr grades, categorised based on the amount of Cr in the alloy, are produced during the FeCr smelting process. High carbon ferrochromium (HCFeCr) is one such grade, and typical contains 60–70%

M. B. Sitefane (✉)
Researcher, Pyrometallurgical division, Mintek, 200 Malibongwe Drive, Randburg 2125, South Africa
e-mail: martinsi@mintek.co.za

M. B. Sitefane · J. D. Steenkamp
School of Chemical and Metallurgical Engineering, University of Witwatersrand, Johannesburg, South Africa

J. D. Steenkamp
Technical Specialist, Pyrometallurgical division, Mintek, 200 Malibongwe Drive, Randburg 2125, South Africa
e-mail: joalets@mintek.co.za

J. D. Steenkamp et al. (eds.), *Furnace Tapping 2022*, The Minerals, Metals & Materials Series, https://doi.org/10.1007/978-3-030-92544-4_22

Cr (with 4–6% C) [1]. The other grade, which is produced in South Africa (S.A.) is charge chrome, and typically contains 50–55% Cr (with 6–8% C) [1]. Recently, charge chrome with Cr levels below 50% have been reported [1].

In FeCr production, the tap-hole has been reported to be the highest wear area [2–4]. As a case in point, in June 2017, at a planned maintenance shutdown of a FeCr producing smelter based in S.A., the carbon-lined (C-based) tap-hole refractories of its 63 MVA submerged arc furnace (SAF) were observed to have been severely worn [4]. The observed wear was so extensive that little to no refractory remained. Tap-hole refractory wear has a negative impact on the process economics, especially since about 55% of maintenance costs are as a result of refractory repair and some smelters have reported that refractory wear accounts for 10–12% of process downtime [5–7]. Any viable solution based on a fundamental understanding of the cause of C-based tap-hole refractories in FeCr production, could potentially have a significantly positive impact on FeCr process economics.

In 2018, Dr Joalet Steenkamp performed a desktop based study to evaluate the potential chemical wear of C-based tap-hole refractory by FeCr alloy and slag [4]. Her study found that based on thermodynamic modelling, there lied a potential for the refractories to be worn by either alloy or slag [4]. However, she proposed that further work in the form of controlled laboratory experiments be conducted to verify her findings, especially considering that her study made a number of assumption, e.g. process equilibrium and pure molten species [4]. The current study is aimed at building upon Steenkamp's work, with the following research questions focussed upon:

1. Does the laboratory experiments also indicate a potential for chemical wear of the C-based refractory by both alloy and slag?
2. Is there a relationship between wear and temperature?
3. How does the laboratory experimental results compare with Steenkamp's [4] desktop evaluation?

The remainder of the paper briefly reviews literature data that relates to the study, the experimental procedure adopted, and the findings of the study in light of the aforementioned research questions.

Literature Review

Chemical Wear of C-Based Refractories in FeCr Production

Chemical wear (also referred to as 'corrosion wear') occurs when a system is not at equilibrium [8]. In FeCr production, desktop modelling studies have shown that both alloy and slag have the potential to chemically wear C-based refractories [4]. The chemical wear mechanisms at play for the alloy and slag as highlighted by

Table 1 Summary of the chemical wear mechanism of carbon tap-hole refractory by alloy and slag as modelled by Steenkamp [4] (where: '<M>' specie in solid phase; '(M)' specie in liquid phase; 'M' specie in solution; 'M' specie in gas phase)

Alloy-refractory (1450–1650 °C)	Slag-refractory (1550–1750 °C)
A. Dissolution (main mechanism) • Reaction: <C> ↔ (C) Solid carbon dissolves in the alloy • Dissolution limited by saturation	A. Chemical reaction • 4 <C> + (SiO_2) ↔ 2 <SiC> + 2CO SiC formation • <C> + (FeO) ↔ (Fe) + CO Formation of metallic iron • <C> + (CrO) ↔ (Cr) + CO Formation of metallic chromium Iron and chromium combine as the alloy formed
B. Chemical reaction • 2 <C> + 3(Cr) + 3(Fe) ↔ <Cr, Fe)$_3C_2$> C can also be in solution Reaction forms a Cr–Fe carbide precipitate	
Overall details • Phases observed: alloy, refractory, and chrome-iron carbide below 1475 °C • Refractory consumption increases with temperature increases • Low overall refractory consumption	Overall details • Phases observed: liquid slag, spinel, refractory. Alloy forms at all temperatures, SiC around 1600–1650 °C • Refractory consumption increases with temperature

Steenkamp [4] are summarised in Table 1. The indicated temperatures were derived from plant data gathered from a S.A. FeCr producer [4].

Static tests are favoured over dynamic tests for the examination of chemical wear because of the ability to exclusively examine chemical wear without the interference of other more dynamic factors [9]. The induction cup tests is one such semi-static tests favoured for these experiments [10].

Refractory Wettability and Penetration

Wettability of a refractory refers to an alloy or slag (molten constituents) to adhere to the surface of the refractory. Wettability is an important consideration in chemical wear evaluation studies, since chemical wear of refractory requires that the refractory be wetted by the molten constituents that it is in contact with [11]. Wettability can be assessed either experimentally using the sessile drop method [11], or by observation of the refractory crucible after the cup tests [10].

Refractory penetration is caused by alloy or slag infiltrating the pores and/or reacting with the refractory [4]. Scanning Electron Microscope (SEM) can be used to assess the penetration depth of the alloy or slag [9]. A highly penetrated refractory has the potential to undergo chemical wear not only at the alloy/slag-refractory interface but also within the refractory structure. This can result in severe refractory wear and subsequent refractory failure.

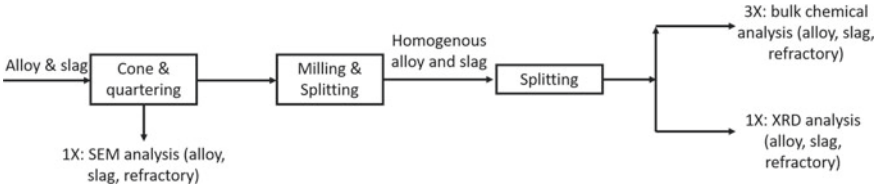

Fig. 1 Flowsheet showing sample preparation procedure for starting alloy and slag

Experimental Procedure

Sample Preparation

A batch of ~7.5 kg of alloy and 11.6 kg of slag, which were previously sourced from a S.A. FeCr producer, were used as the starting materials for this study. FeCr alloy had a mixed particle size distribution (particles with diameter as large as 50 mm and others <1 mm). FeCr slag was fine, that is, all particles were <4 mm in diameter.

The same sample preparation procedure, as presented in the flowsheet (Fig. 1), was employed for both alloy and slag. The procedure entailed firstly applying the cone and quartering technique to extract a representative sample for SEM characterisation. The remaining sample was further homogenized through a combination of milling (using a TS250 vibratory disc mill) and splitting (using a 2407002 Kendrion rotary splitter). Further splitting was undertaken using the aforementioned splitter. From this a total of four sub-samples, along with refractory samples, were collected for bulk and phase chemical characterisation.

Characterisation

Bulk chemical analysis of the alloy and slag was undertaken using an inductively coupled plasma-optical emission spectrometry (ICP-OES) produced by a ThermoFisher Scientific iCAP 7600; carbon and sulphur in the alloy were determined using CS744 and CS230 LECO instruments; and phosphorus was determined using a Nanocolor UV/VIS spectrophotometer. The carbon-based refractory was analysed using undisclosed proximate and ultimate analysis techniques. All bulk chemical analyses were undertaken in triplicates.

Bulk chemical phase characterisation was undertaken by X-ray diffraction (XRD), using a Bruker D8 advance diffractometer. The instrument was run from 0° to 80° 2θ, at a wavelength of Co K-alpha 1.7902 Å.

Specific chemical phase characterisation was undertaken a Zeiss Evo MA15 SEM instrument which generated backscattered (BSE) micrographs at 20 kV. The SEM was equipped with a Bruker X-Flash detector for Energy-Dispersive Spectroscopy (EDS) which enable determination of specific phase compositions.

Cup Tests

A C-based refractory provided by Carboquip Manufacturing, was employed for the laboratory experimental work. The cup was provided pre-machined to 50 mm height and outer diameter, 30 mm internal diameter, and 20 mm bottom thickness.

The preparation procedure entailed firstly weighing the empty refractory cup. The cup was then packed to the top with either alloy only (amounting to ~70 g), or slag only (amounting to 40 g). The packed cup was weighed, before being loaded into a cold 30 kVA induction furnace. An empty cup was also placed alongside the packed crucible and served as a reference. A schematic diagram showing the induction furnace set-up is presented in Fig. 2. The set-up consisted mainly of two B-type thermocouples (two thermocouples served to ascertain the temperature gradient and acted as back-up in the event of breakdown of either), an argon (Ar) gas port (where Ar gas was purged to maintain an inert atmosphere throughout the test), and a gas outlet port (a designated port to allow for formed gases to escape).

Smelting tests were conducted by heating the furnace from cold, in 1.5 kW/h intervals, until the targeted temperature had been reached. Once the target temperature was reached, the input power was adjusted accordingly to ensure that the target temperature was maintained, within a ±10 °C deviation, for a duration of 1 h. At the end of the holding time, the furnace was switched off. Argon purging was maintained until the next day when the furnace had cooled down. At this point, the cup content was removed, filled with resin, and then vertically sectioned. Photographs were taken of the sections using an Olympus Stylus F2.0 camera. Some of the photographs were printed and used to construct a wear profile through thickness measurements using a

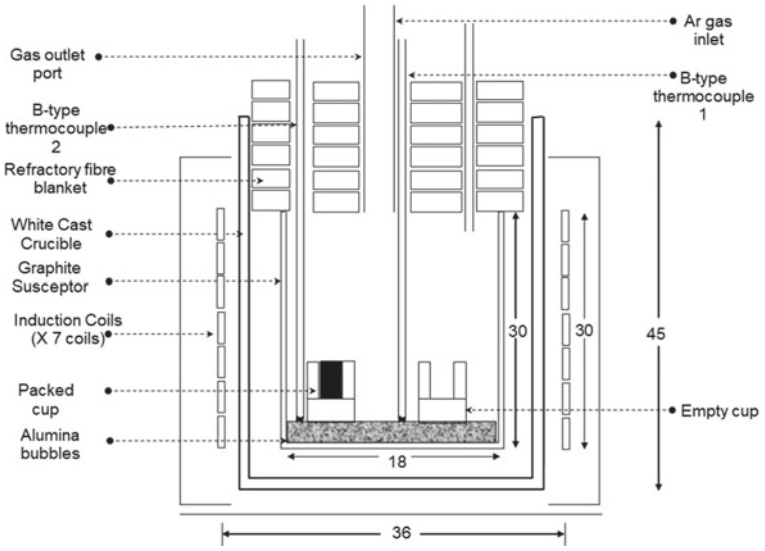

Fig. 2 Schematic diagram of 30 kVA induction furnace used for the experiments

digital 150 MM Insize Vernier Caliper. Ten Vernier caliper measurements were taken in 3-mm intervals across the right side of crucible. These were used to compute the thickness loss according to Eq. 1 (maximum thickness loss was used). A microscopic evaluation of the refractory cup in contact with alloy/slag was also undertaken using SEM–EDS.

$$\%\text{loss} = \frac{100(\text{initial thickness} - \text{final thickness})}{\text{initial thickness}} \quad (1)$$

Results

Characterisation

Alloy and Slag

The bulk chemical compositions of the starting FeCr alloy and slag are presented in Tables 2 and 3, respectively. As expected, the alloy consisted mainly of Cr, Fe, Si, and C. The Cr (48 ± 0.5%) and C (6.3 ± 0.02%) contents where typical of the charge chrome specifications presented previously.[1] Micrographs of the alloy revealed that the alloy was virtually pure, with various alloy compositions formed within the alloy structure (see Fig. 3—left). A Cr–Fe–C carbide was also detected by XRD. FeCr slag consisted mainly of SiO_2 (32.3 ± 0.5%), Al_2O_3 (28.4 ± 0.4%), and MgO (19.2 ± 0.3%). Cr and Fe were also present. A combination of SEM–EDS and XRD confirmed that the Cr and Fe were distributed among the entrained alloy, a partially reduced Cr–Fe-oxide, and as part of some slag compositions (see micrograph Fig. 3c).

Table 2 Bulk chemical composition of starting alloy (Avg. means average; SD means standard deviation over three measurements; – means not obtainable)

Component	Cr	Fe	Si	C	S	P	Mg	Al	Ca
(%) Avg.	48.5	36.5	3.6	6.3	<0.01	0.12	0.1	0.1	<0.05
(%) SD	0.5	0.3	0.1	0.02	–	0.04	0.01	0.01	–

Table 3 Bulk chemical composition of starting slag

Component	Al_2O_3	CaO	Cr_2O_3	FeO	MgO	MnO	SiO_2	TiO_2
(%) Avg.	28.4	3.5	9.4	4.6	19.2	0.2	32.3	0.7
(%) SD	0.4	0.1	0.2	0.1	0.3	0.01	0.5	0.01

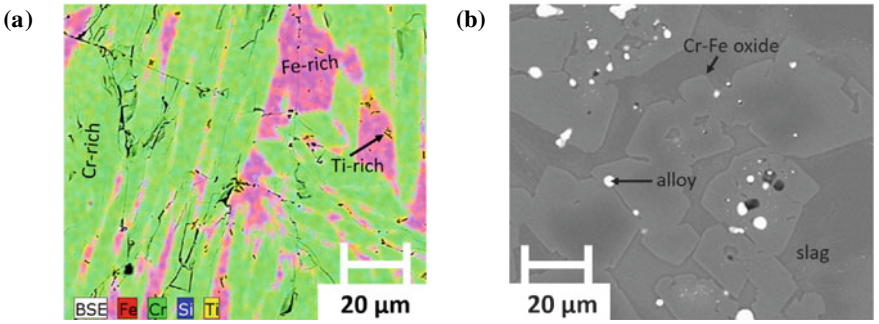

Fig. 3 **a** Micrograph of alloy showing several phases rich in Cr, Fe, and Ti (left); **b** Cr–Fe bearing species including entrained alloy in slag micrograph

Refractory

The bulk chemical composition of the C-based refractory is presented in Table 4. The composition showed that the refractory was almost pure carbon. This is typical of graphite material that has undergone treatment. A micrograph of the refractory showed that it had a fairly consistent texture with minimal impurities (see Fig. 4).

Table 4 Bulk chemical composition of C-based refractory (IM means inherent moisture; S means sulphur; H means hydrogen; N means nitrogen)

Component	C	Ash	IM	Volatiles	S	H	N
(%) Avg.	99.7	<0.1	0.2	–	0.05	0	0
(%) SD	0.2	–	0.1	–	0.0	–	–

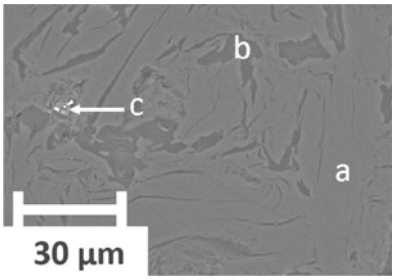

Fig. 4 Micrograph of refractory showing a clean and consistent structure (left); EDS analysis results of point 'a', b', and 'c' included (right)

Cup Tests

Macroscopic Observations

Figure 5 presents photographs of the refractory in contact with alloy at 1500 °C (left), and the in contact with slag at 1600 °C (right). The photographs are used as a sample, since all the tests regardless of temperature, presented the same macroscopic appearance. Wettability of the refractory by alloy was observed—indicated by a red circle in Fig. 5a—at all temperatures. The same observation wasn't as obvious in the slag-refractory cup tests.

Thickness loss results as graphically presented in Fig. 6. The results showed that thickness loss (and thus wear quantified by reduced sidewall thickness), tended to increase with temperature. The exception was in the case of the alloy starting at 1600 °C.

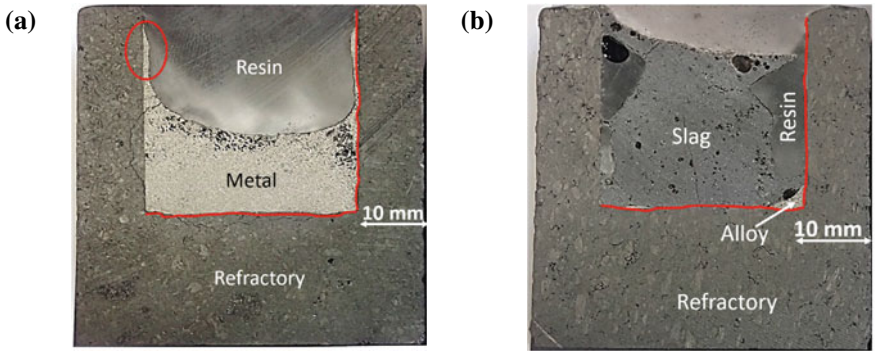

Fig. 5 **a** Photograph of alloy-refractory cup at 1500 °C and **b** slag-refractory cup at 1600 °C

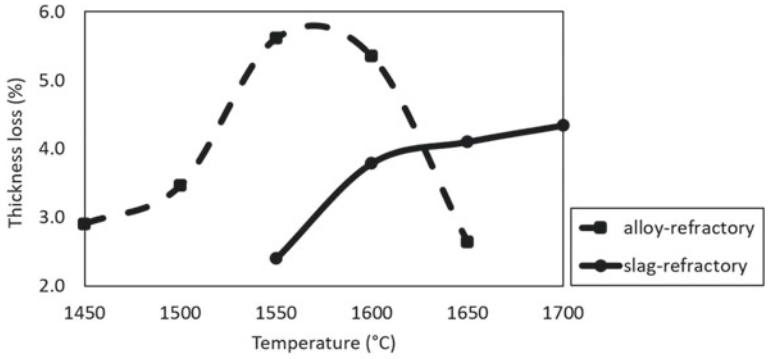

Fig. 6 Refractory thickness loss (in length %) as a function of tapping temperature

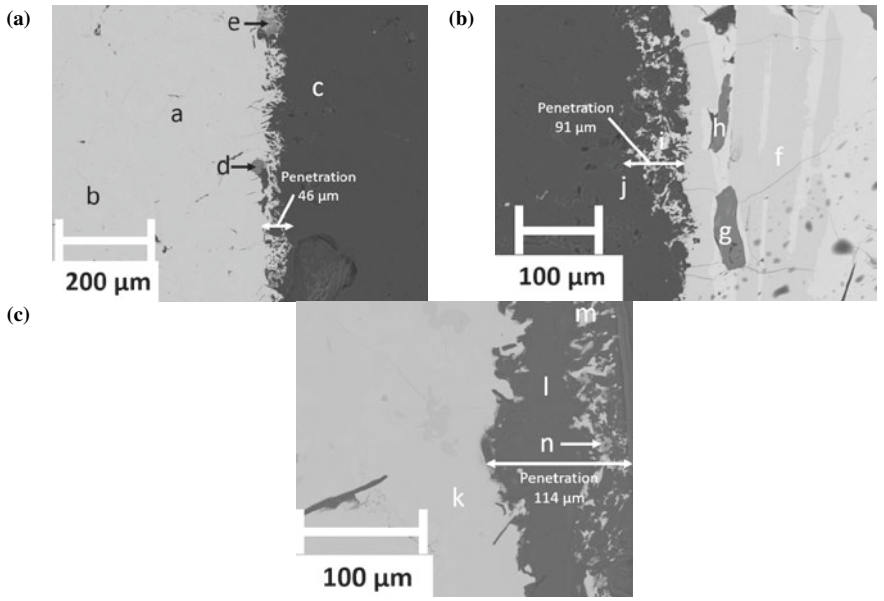

Fig. 7 Micrograph showing alloy-refractory interaction at: **a** 1450 °C, **b** 1500°, and, **c** 1650 °C

Microscopic Observations

SEM BSE micrographs of alloy-refractory interaction at 1450, 1500, and 1650 °C are presented in Fig. 7. For each micrograph, the alloy penetration depth was measured. EDS analyses of the various phases are presented in Table 5. The following main observations were made:

- At all temperatures, the main phases present were alloy (a Cr–Fe–C phase—'b and k'—and a Cr–Fe–Si–C phase—'a and m'), pure C-refractory, and two mixed phases (probably oxides due to the high presence of Mg, Ca, Si species).
- At 1650 °C, a phase labelled 'n' containing 37.2% Ti, 11.3% Cr, 2.1% Fe, and 19.5% C was detected. Its composition points to it being a carbide that formed through local precipitation of the alloy that had penetrated through the refractory.
- The alloy penetration depth was observed to increase with increase in temperature.

SEM BSE micrographs of slag-refractory interaction at 1550 and 1700 °C are presented in Fig. 8. EDS analyses of the same are subsequently presented in Table 6. The following main observations were made:

- At all temperatures, the main phases observed were C-refractory ('e' and 'j'), slag of various compositions, and a Cr–Fe–C alloy phase—'a'—which formed as a result of a slag-refractory interaction. The formed alloy was observed at all temperatures and at increasing volumes with increasing temperature.
- In addition to the conventional phases, SiC was formed at 1700 °C.

Table 5 EDS point analyses of phases labelled 'a' to 'n' in Fig. 7 (* not verified)

Component	C	O*	Mg	Al	Si	Ca	Cr	Fe	Ti
Alloy 'a'	7.5				8.8		32.2	51.4	
Alloy 'b'	11.0						65.5	23.5	
Refractory 'c'	100								
Mix 'd'	20.1	31.5	2.7	14.0	28.8	2.8			
Mix 'e'		40.8	7.1	3.1	20.3	24.0	2.6	1.6	
Alloy 'f'	17.4						76.0	6.6	
Mix 'g'		44.1	40.2		15.3	0.5			
Mix 'h'	2.5	40.1	4.3	7.4	9.5	1.7	14.6	19.8	
Alloy 'I'	9.5				8.5		36.9	45.1	
Refractory 'j'	100								
Alloy 'k'	11.5						64.5	23.9	
Refractory 'l'	100								
Alloy 'm'	7.6				9.5		33.9	49.0	
High Ti 'n'	19.5						11.3	2.1	37.2

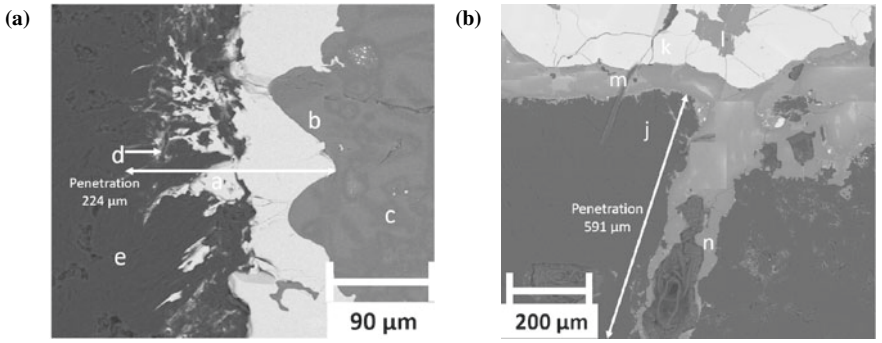

Fig. 8 Micrograph showing slag-refractory interaction at **a** 1550 °C and **b** 1700 °C

- Between 1550 and 1650 °C, only the formed alloy was observed to penetrate through the refractory. Penetration depths increased from 224 µm at 1550 °C to 465 µm at 1650 °C. At 1700 °C, slag was observed to penetrate the refractory at a depth of 591 µm.

Table 6 EDS point analysis of phases labelled 'a' to 'n' in Fig. 8 (* not verified)

Component	C	O*	Na	Mg	Al	Si	Ca	Cr	Fe
Alloy 'a'	15.7							50.8	32.6
Slag 'b'		42.0	0.9	6.0	16.8	24.4	9.8		
Slag 'c'		43.7		17.4	33.5			5.4	
Mix 'd'	38.8	29.9				3.9	1.5	6.4	19.5
Refractory 'e'	100								
Refractory 'j'	100								
Alloy 'k'	7.9				20.9		2.2	54.6	14.3
SiC 'l'	32.8				67.2				
Slag 'm'		44.5	8.08	11.8	19.6	16.0			
Slag 'n'		44.6	20.0	35.4					

Discussion

Does the Laboratory Experiments Also Indicate a Potential for Chemical Wear of the C-Based Refractory by Both Alloy and Slag?

Laboratory experiments clearly indicated a potential for chemical wear of C-based refractory by both alloy and slag. In both cases, chemical wear was indicated mainly by the reduction of the C-refractory sidewall thickness (see Fig. 6). The reduction in wall thickness was further highlighted by the non-linear phase boundary indicating that some parts of the refractory had been consumed (max 5.6% for alloy, and 4.3% for slag—see Figs. 7 and 8). In the case of the slag-refractory tests, formation of a C-bearing FeCr alloy also proved that the C-refractory reduced the Cr–Fe oxide in the slag phase. This chemical wear mechanism was also reported by Steenkamp [4]. Furthermore, the formation of Ti-carbides (in the alloy-refractory test) and SiC (in the slag-refractory test), also pointed to chemical wear of the C-refractory by both alloy and slag.

Is There a Relationship Between Wear and Temperature?

A relationship was observed between wear and temperature. An increase in the temperature resulted in a corresponding decrease of the refractory thickness (see Fig. 6). An exception to this was observed from 1600 °C for the alloy-refractory tests. Reasons for these were unknown and would make for a worthy investigation in the future. Another observed effect of temperature was that increasing the temperature increased the penetration depth of the alloy/slag in the refractory. Penetration of the

refractory by alloy or slag is undesirable not only because it increases the potential of wear as a result of thermal expansion disparities between the alloy/slag and refractory but also because the penetrated alloy/slag can act as incipient points for internal chemical wear of the refractory.

How Do the Laboratory Experimental Results Compare with Steenkamp Desktop Evaluation?

In many respects the present laboratory experimental results were similar to those obtained during Steenkamp [4] desktop. Firstly, in the case of the slag-refractory tests, C-bearing FeCr alloy formation occurred at all temperatures. Secondly, refractory consumption tended to increase with temperature. Thirdly, SiC formation was also observed for the slag-refractory tests.

Conclusion

An experimental investigation into the potential chemical wear of C-based refractories by FeCr alloy and slag has been conducted. The experimental results indicated that both FeCr alloy and slag have the potential to chemically wear the C-based refractory at 1450–1650 °C for the alloy, and 1550–1700 °C for the slag. Temperature was observed to intensify the extent of wear. In many respects the results were in agreement with previous FactSage thermodynamic modelling work conducted by Steenkamp [4].

Acknowledgements The work is presented with permission from Mintek.

References

1. Gasik M (2013) Handbook of ferroalloys: theory and technology. Elsevier, Amsterdam
2. Coetzee C et al (2010) No taphole—no furnace. Paper presented at the refractory 2010 conference, Muldersdrift, Johannesburg, 16–17 March 2010
3. O'Shaughnessy P et al (2014) Tap-hole repair: the UCAR®V repair solution. Paper presented at the furnace tapping 2014, Muldersdrift, Johannesburg, 27–29 May 2014
4. Steenkamp JD (2019) Wear analysis of tap-holes at two ferrochromium production furnaces. J South Afr Inst Min Metall 119(8):537–544
5. Deo B (2017) Wear and dissolution of MgO–C refractory lining in belly and top cone regions of BOF vessel. Trans Indian Inst Metals 70(8):1965–1971. https://doi.org/10.1007/s12666-016-1018-1
6. Nolet I (2016) Tapping of PGM-Ni Mattes: an industry survey. J South Afr Inst Min Metall 116(1):11–16. https://doi.org/10.17159/2411-9717/2016/v116n1a2

7. George-Kennedy D et al (2005) Flash converting after 10 years. Paper presented at the 11th international flash smelting congress, Bulgaria/Spain, October 2005
8. Steenkamp JD (2014) Chemical wear of carbon-based refractory materials in a silicomanganese furnace tap-hole. PhD thesis, University of Pretoria
9. Thethwayo BM (2019) Interaction of carbon based refractories with liquid PGM-furnace melt. PhD thesis, University of Pretoria
10. Schacht C (2004) Refractories handbook. CRC Press, Boca Raton
11. Steenkamp JD, Pistorius PC, Tangstad M (2015) Wear mechanisms of carbon-based refractory materials in SiMn tap-holes—Part II: in situ observation of chemical reactions. Metall Mater Trans B 46(2):668–679. https://doi.org/10.1007/s11663-014-0276-8

Investigation of Melting Behavior and Viscosity of Slags from Secondary Ferromanganese Production

David Scheiblehner, Christoph Sagadin, Stefan Luidold, Helmut Antrekowitsch, and Dieter Offenthaler

Abstract Viscosity and melting behavior are two of the most important properties of industrial slags as they directly impact the yield of metallurgical processes. Too high fluidity may cause losses during tapping or infiltration of refractory while too viscous liquids can lead to problems regarding the smelting of charged material or metal inclusions. This paper comprises the determination of melting behavior and viscosity of slags as functions of their composition. Therefore, 19 mixtures of different oxides have been prepared and melted by means of an induction furnace. An analysis of the resulting slags in a hot stage microscope and the computation of the corresponding viscosities allow an evaluation of the most important parameters. Significant variations of viscosity and characteristic temperatures can be measured as functions of the content of manganese oxide and the ratio between calcium oxide and silicon dioxide, respectively, besides a strong temperature dependency and a major influence of network-forming oxides.

Keywords Pyrometallurgy · Viscosity · Melting behavior · Slags

Introduction

The re-utilization of residuals and the optimization of processes in terms of energy consumption and amount of used raw materials are gaining in importance due to economic and ecological reasons. Especially, metallurgical operations can benefit from these measures as conservation of natural resources, and a reduction of the required energy is obtained by increasing efficiency and re-using materials such as

D. Scheiblehner (✉) · C. Sagadin · S. Luidold
CD-Laboratory for Extractive Metallurgy of Technological Metals, Nonferrous Metallurgy, Montanuniversitaet Leoben, 8700 Leoben, Austria
e-mail: david.scheiblehner@unileoben.ac.at

H. Antrekowitsch
Nonferrous Metallurgy, Montanuniversitaet Leoben, 8700 Leoben, Austria

D. Offenthaler
Batrec Industrie AG, 3752 Wimmis, Switzerland

J. D. Steenkamp et al. (eds.), *Furnace Tapping 2022*, The Minerals, Metals & Materials Series, https://doi.org/10.1007/978-3-030-92544-4_23

slags or fly ashes. Furthermore, the amount of waste which requires disposal or incineration declines and various advantages regarding greenhouse gas emissions can be achieved [1–3].

Ferromanganese is indispensable for the production of steel and cast iron as it acts as a deoxidizing and strongly sulfur-binding agent and serves as an important alloying element. The manufacture of this alloy takes place primarily in low shaft furnaces by carbothermic reduction of manganese ores. As mentioned before, facilities for extracting the alloy from metal containing residuals, for example, in the field of recycling of used electric devices, are in use additionally. This study therefore characterizes slags produced in processes for recycling batteries by determining their melting behavior. Furthermore, it includes an examination of the slag viscosity as well as the impact of manganese oxide and the CaO/SiO_2 ratio, respectively, on these properties by means of thermodynamic calculations. The outcome enables a greater insight into the occurring reactions and allows an improvement in efficiency [4–6].

In modern metallurgy, slags do not represent unwanted by-products but rather important phases which take an active part in performed reactions. One of the main functions is the removal of undesirable tramp elements and non-metallic inclusions. An appropriate composition ensures a sufficient capacity for the absorption of impurities. In addition, the temperature range in which slag forming takes place can be controlled by adjusting the amounts of contained elements. Therefore, the chemical and physical properties of slags have a great influence on the duration and yield of metallurgical procedures. Especially, flow properties and viscosity as well as the influence of temperature and specific compounds on these attributes must be evaluated precisely [6–8].

With molecular and ionic theory, there are two existing models which can be used to describe the structure of slags and the reactions which occur in them and with them. The molecular theory assumes that slags consist of separate oxides, sulfides, fluorides, etc., for instance, SiO_2, CaO, Al_2O_3, and CaF_2. However, inconsistencies are emerging in measurements of electrical conductivity as a sharp decrease in the slags' resistance can be observed at solid/liquid transition. This behavior cannot be described with the mentioned structure. The ionic theory provides an adequat explanation for the abrupt change in the slags' conductivity. The latter states that slags are built up of positively and negatively charged ions. The constituents can be divided into three categories. The first one comprises metallic cations, for instance, Ca^{2+}, Mn^{2+}, Fe^{2+}, Fe^{3+}, and Mg^{2+}. These components are comparably small and can be moved easily. The second category contains non-metallic anions, for example, O^{2-}, S^{2-}, and F^{2-}, and the third group anion complexes which are more difficult to move such as SiO_4^{4-}, PO_4^{3-}, AlO_3^{3-}, and FeO^{2-} [7, 9–11].

The structure of crystalline silica rests upon SiO_4^{4-} tetrahedrons. Four O^{2-} ions surround every Si^{4+} ion whereat each O^{2-} ion connects two Si^{4+} ions and forms an oxygen bridge. In this way, widespread networks with high energetic bonds are formed which can even be found, at least in part, in liquid phases. The viscosity of silica slags therefore strongly depends on the size and related movability of the emerging long-chain entities. However, the presence of other ions and ion complexes,

departing from SiO_4^{4-}, heavily influences the degree of polymerization along with fluidity. Correspondingly, oxides can be classified as follows. The first category consists of oxides, such as SiO_2, P_2O_5, and TiO_2, that tend to form networks and act as O^{2-} acceptors according to the equation [7, 9]:

$$SiO_2 + 2O^{2-} \rightleftharpoons SiO_4^{4-} \tag{1}$$

An addition of network-modifying oxides of the second group leads to a weakening of the intermolecular bonds until the long-chained structures eventually break down to smaller-sized complexes which are more mobile. Components such as Na_2O, MgO, and CaO belong to this category and act as donators according to the following equation [7, 9]:

$$CaO \rightleftharpoons Ca^{2+} + O^{2-} \tag{2}$$

Some oxides, such as MnO, FeO, CoO, and NiO, cannot be categorized clearly. They act either as acceptors or donators, depending on the amount of free oxygen in the slag [9].

As mentioned above, viscosity represents one of the most important properties of metallurgical slags. However, determining the fluidity of these liquids relates to difficulties especially as the measurements must take place at high temperatures. The occurring problems can only be overcome by increased expenditure. Modern measuring devices rely on the usage of special equipment, for example, high-temperature viscosimeters. In these apparatuses, the quantification of viscosity occurs by means of rotary measuring systems. A cylindrical object submerged in the liquid to be investigated rotates at specific angular speeds. Plotting the torque which is necessary to carry out this rotational movement enables a calculation of fluidity. As the usability of all construction units at operating conditions of metallurgical processes can only be guaranteed by extensive financial input and planning efforts, the development of models for the computation of the rheological features exhibits great interest. Several methods are in use to estimate the viscosity of multicomponent systems which are in general applicable for specific slag compositions, respectively [12, 13].

The viscosity module of the software FactSage 7.3 which is applied in this work computes viscosities of single-phase melts and glasses by defining a correlation between their fluidity and structure. Information about structure, in turn, is obtained implementing the modified quasi-chemical model. The latter extends classical theories, which assume ideal mixtures and calculate thermodynamic properties as enthalpy or entropy using simple polynomial expressions, by furthermore taking effects due to structural ordering into consideration. Nevertheless, the model rests upon several parameters that must be fitted to experimental data for selected unary, binary, and ternary oxide systems. The compositions at which these effects obtain maximal impact are defined independently for each respective system which is highly significant especially in silica slags. Applying the viscosity module, a model based on data gathered from experiments with either melts or glasses can be chosen

depending on the investigated range of temperatures. Above liquidus temperature, the melts model delivers more accurate results whereas at or near liquidus temperature both methods give similar values. For investigations below liquidus temperature, the application of the glasses database represents the preferred approach to obtain the most precise outcomes [14–17].

Materials and Methods

Experimental Design

A statistical design of experiments was compiled by means of the software MODDE® 12. Accordingly, 19 different samples were created. The content of MnO varies within 40.94 and 69.77 wt.%, that of SiO_2 and CaO within 8.32 and 18.71 wt.% and 8.31 and 19.04 wt.%, respectively. The limits for Fe_2O_3 were set at 0.00 and 7.71 wt.%. The fractions of MgO and Al_2O_3 are kept constant at values of 4.20 and 9.40 wt.%, respectively. Fe_2O_3 was chosen for the mixture instead of FeO because of its defined composition and better availability. The provided experimental plan was defined based on analyses of industrial slags from battery recycling.

Preparation of Slags

To avoid distortion of the measuring results triggered by undesirable moisture absorption due to the hygroscopic nature of calcium oxide, an annealing procedure at 1100 °C for 8 h was implemented in a muffle furnace in air prior to the mixing of components. Afterwards, a homogenization executed in a swing mill ensures a uniform composition of the samples. Sagadin et al. [7] showed that significantly differing results can be measured depending on whether the tests are conducted with or without premelting. Melting the mixtures prior to analyzing them guarantees comparable results. In addition, this treatment allows an approximation of experimental conditions to factual process conditions. In the following step, the samples were therefore melted in a graphite crucible by means of an induction furnace. The point of exceeding liquidus temperature was defined visually. Afterwards, the synthetic slags were cast into a steel mold for rapid cooling. Subsequently, the samples are ground in a swing mill to obtain a homogenous powder with sufficiently low grain sizes.

Immediately prior to the analysis in a hot stage microscope (HSM), the prepared slags must be pressed in a cylindrical form with a diameter of 3 mm and a height of 3 mm. To ensure a uniform compression for all investigated oxide mixtures, a spring-loaded metal stamp was used for carrying out this operation. Afterwards, the samples were moved onto a pad consisting of 99.7 wt.% Al_2O_3 with a thickness

of 1.5 mm. To avoid undesired interactions between refractory and specimen material, a sheet consisting of PtIr10 with a thickness of 1.12 mm rested in between. The assembly was then positioned inside a refractory tube (99.7 wt.% Al_2O_3), and argon (100 vol.%) flooded the oven chamber to exclude possible reactions with the surrounding air. Before starting the experiment, several essential parameters had to be defined. The selected heating rate amounted to 10 °C/min and the gas flow rate to 0.15 l/min. The evaluations of the experimental results were performed according to Hesse Instruments (based on DIN51730:1984). As soon as the flow temperature was exceeded by 10 °C or the highest achievable oven temperature of 1700 °C was reached, the test ended.

Analysis of the Melting Behavior in a Hot Stage Microscope

The change of shape with gradually increased temperature of a cylindrical sample made from the material to be investigated can be analyzed by means of a hot stage microscope. According to the normative specifications of Hesse Instruments (based on DIN51730:1984), several characteristic temperatures have been defined. The starting temperature T_1 indicates the temperature at the beginning of the measuring process. The sample's dimensions at this state serve as a reference for the following determination of characteristic points. If high demands on accuracy are required, this state must be defined more precisely. The deformation temperature DT occurs as soon as first indications of softening, for instance, inflation of the cylinder or rounding of its edges, can be detected. At spherical temperature ST, the sample's height equals its width and its silhouette resembles a round form. The hemispherical temperature HT appears when the sample's form can be described as hemispherical and its height equals half of its width. The flowing temperature FT is defined as the point at which the object's height equals one-third of its initial dimension. Figure 1 illustrates these definitions. Schnideritsch [18] defines the liquidus temperature at a point at which the actual projected sample area equals between 35 and 30% of its initial size. As this gives a temperature range rather than a specific temperature in this work, liquidus temperatures were calculated in FactSage 7.3.

Figure 2 depicts the temperature-dependency of the height automatically recorded by the HSM software as well as the measured characteristic points for a synthetic slag from the experiments consisting of 55.36 wt.%. MnO, 13.52 wt.% SiO_2, 13.68 wt.%. CaO, 3.85 wt.%. Fe_2O_3, 4.20 wt.% MgO, and 9.40 wt.% Al_2O_3. The first section of the plot up to a temperature of approximately 1200 °C gives no significant changes in cylinder height. A moderate increase can indicate thermal expansion. The second section shows a rapid decrease in the graph, and the characteristic temperatures can be determined.

Additional to the experimental determination of hemispherical and flow temperature and the computation of the liquidus temperatures, the viscosities of the synthetic

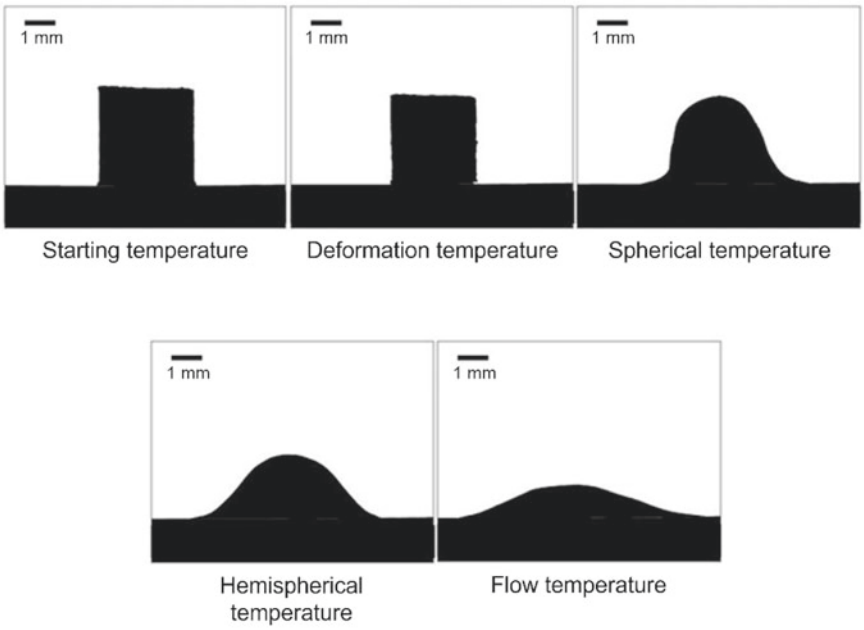

Fig. 1 Exemplary shape of a cylindrical sample at characteristic temperatures

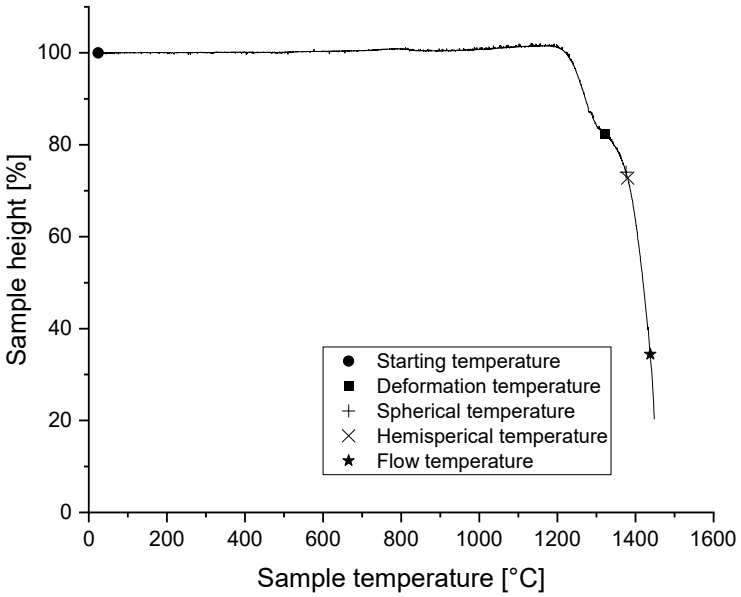

Fig. 2 Temperature-dependency of sample height and characteristic points according to Hesse Instruments (based on DIN51730:1984) for a sample containing 55.36 wt.%. MnO, 13.52 wt.% SiO_2, 13.68 wt.%. CaO, 3.85 wt.%. Fe_2O_3, 4.20 wt.% MgO, and 9.40 wt.% Al_2O_3

slags at liquidus temperature were calculated by means of FactSage 7.3. This temperature was chosen for the determination of the viscosities to ensure that the computation is performed in a region where no solid fraction is left.

Results

Experimental Results

The measured hemispherical and flow temperatures as well as the calculated liquidus temperatures and viscosities at liquidus temperature are listed in Table 1 besides the varying contents of SiO_2, CaO, Fe_2O_3, and MnO. As mentioned above, the amounts of Al_2O_3 and MgO remain constant at values of 9.40 and 4.20 wt.%, respectively. Experiments of samples containing large percentages of manganese oxide showed tendencies to result in higher characteristic temperatures while a reduced MnO content leads to lower values. The flow temperatures of samples 1 and 10 which represent

Table 1 Oxide contents, experimentally determined characteristic temperatures as well as liquidus temperatures (LT) and viscosities at 1850 °C, computed with FactSage 7.3

Sample number	SiO_2 [wt.%]	CaO [wt.%]	Fe_2O_3 [wt.%]	MnO [wt.%]	HT [°C]	FT [°C]	LT [°C]	Viscosity at LT [dPa s]
1	8.32	8.31	0.00	69.77	1440.70	–	1790.02	0.060
2	18.71	8.31	0.00	59.38	1348.30	1406.30	1607.68	0.210
3	18.71	19.04	0.00	48.65	1328.00	1397.70	1670.25	0.200
4	8.32	8.31	7.71	62.06	1437.70	1480.80	1675.41	0.090
5	18.71	8.31	7.71	51.67	1341.00	1416.70	1434.99	0.380
6	8.32	19.04	7.71	51.33	1353.00	1413.50	1714.18	0.100
7	18.71	19.04	7.71	40.94	1308.70	1402.30	1475.31	0.420
8	8.32	19.04	2.57	56.47	1352.30	1418.50	1813.36	0.070
9	8.32	19.04	5.14	53.90	1341.70	1417.30	1763.43	0.090
10	8.32	11.89	0.00	66.19	1416.00	–	1811.92	0.070
11	8.32	15.46	0.00	62.62	1384.00	1445.00	1835.02	0.070
12	11.78	19.04	0.00	55.58	1359.70	1418.00	1803.31	0.090
13	15.25	19.04	0.00	52.11	1353.30	1416.30	1741.81	0.130
14	18.71	13.68	3.86	50.16	1305.00	1411.00	1546.93	0.280
15	13.52	8.31	3.86	60.72	1392.80	1450.70	1640.80	0.130
16	13.52	13.68	7.71	51.50	1376.30	1435.30	1594.96	0.170
17	13.52	13.68	3.86	55.36	1381.30	1438.30	1667.57	0.130
18	13.52	13.68	3.86	55.36	1391.30	1437.50	1667.57	0.130
19	13.52	13.68	3.85	55.36	1380.30	1438.50	1667.57	0.130

the mixtures with the highest fractions of manganese oxide exceed the realizable oven temperature. Therefore, their measurement was not possible in these experiments. At 0.420 dPa s, the highest value of viscosity can be calculated for sample 7 with the lowest content of MnO whereas the minimum figure of 0.060 dPa s is recorded for sample 1 which contains the most manganese oxide. The liquidus temperatures vary between 1434.99 and 1835.02 °C whereat no correlation to the content of manganese oxide is obvious.

Evaluation of the Results

The statistical software MODDE® 12 allows a description of measured and calculated values by simple mathematical functions due to multiple linear regression. Thus, coefficients are defined which can be used to specify an equation that is applicable within the range of slag compositions investigated in this work. The evaluations focused on the effect of various parameters on hemispherical and flow temperature.

Accordingly, the impact of an increasing percentage of one specific oxide at the expense of manganese oxide on the flow temperature was determined. A significant decrease in hemispherical and flow temperatures became apparent as silicon oxide is added. A similar pattern can be observed for calcium oxide, while no strong effect appears for a variation of the Fe_2O_3 content within the investigated ranges.

The alteration of the flow temperature due to an addition of calcium oxide at the expense of silicon oxide for different contents of manganese oxide at 5.00 wt.% Fe_2O_3 is depicted in Fig. 3. The amounts of MgO and Al_2O_3 remain constant at values of 4.20 and 9.40 wt.%, respectively. Figure 4 shows the analogous plot for the hemispherical temperature. In both diagrams, a rise in temperature can be observed as the amount of calcium oxide increases at low CaO/SiO_2 ratios. With a further decrease in the silicon oxide content, a less pronounced decline occurs. Addition of manganese oxide accompanied with a simultaneous reduction of the amounts of calcium oxide and silicon oxide leads to a rise of the characteristic temperatures.

Figure 5 shows the alteration of viscosity as calculated using FactSage 7.3 with an increasing CaO/SiO_2 ratio for various MnO contents at liquidus temperature. The amounts of Fe_2O_3, MgO, and Al_2O_3 are kept constant at values of 5.00, 4.20, and 9.40 wt.%, respectively. The graph depicts a steady decline in viscosity with rising contents of calcium oxide. However, this tendency weakens as more and more CaO is added at the expense of SiO_2. Especially for mixtures containing high amounts of manganese oxide, the change in viscosity with decreasing SiO_2 contents at CaO/SiO_2 >1.5 becomes less significant. Furthermore, addition of manganese oxide leads to higher fluidity.

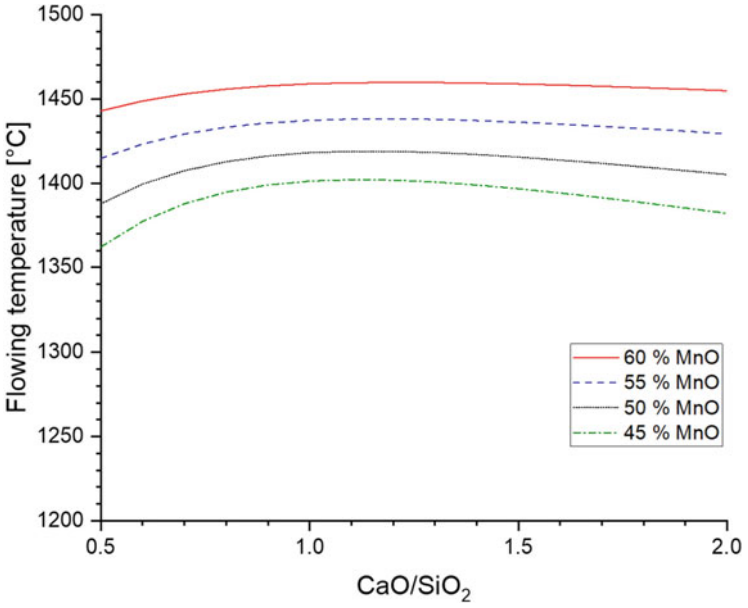

Fig. 3 Alteration of flow temperature with increasing CaO/SiO_2 ratio for various MnO contents and 5.00 wt.% Fe_2O_3, 4.20 wt.% MgO, and 9.40 wt.% Al_2O_3

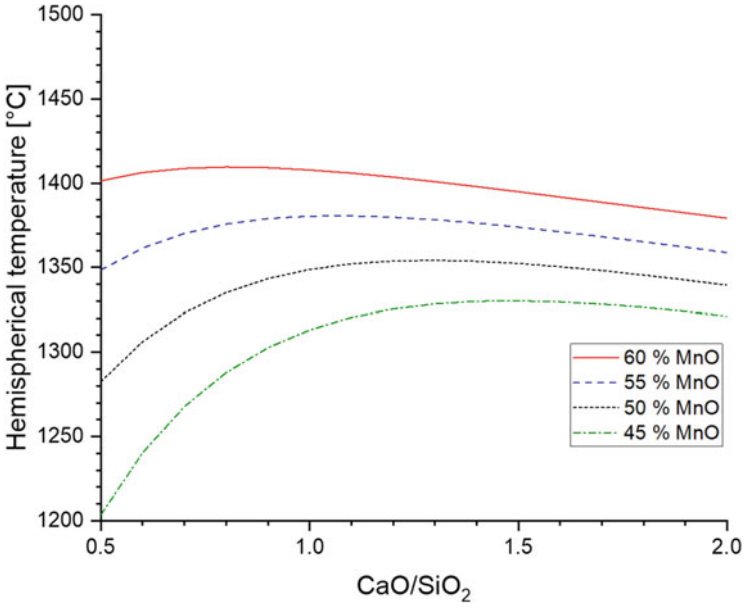

Fig. 4 Alteration of hemispherical temperature with increasing CaO/SiO_2 ratio for various MnO contents and 5.00 wt.% Fe_2O_3, 4.20 wt.% MgO, and 9.40 wt.% Al_2O_3

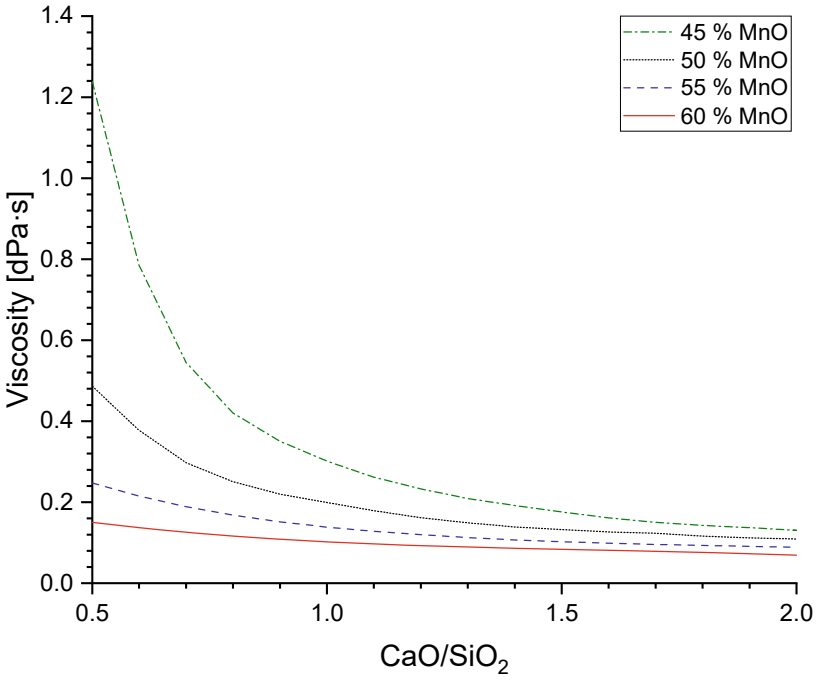

Fig. 5 Alteration of viscosity at LT with increasing CaO/SiO_2 ratio for various MnO contents and 5.00 wt.% Fe_2O_3, 4.20 wt.% MgO, and 9.40 wt.% Al_2O_3 at 1850 °C

Discussion

The process of premelting the slags ensures a homogenous composition and leads to reproducible results. However, an alteration of the components due to reactions with the crucible carbon is possible. Computation of the potential of such reactions was not performed in this case but guarantees the accuracy of results in further studies.

Figures 3 and 4 show an increase of the characteristic temperatures as calcium oxide is added at low CaO/SiO_2 ratios. A maximum occurs at approximately $CaO/SiO_2 = 1.1$. At higher ratios, a decrease in the observed temperatures becomes apparent. At higher contents of manganese oxide, the total amount of silicon oxide and calcium oxide is smaller which leads to a significantly reduced impact of a variation of the CaO/SiO_2 ratio.

The diagram in Fig. 5 emphasizes the influence of network-forming and network-modifying oxides on the viscosity of the slags at flow temperature. At 45 wt.% MnO, a decrease in viscosity of 1.110 dPa s can be measured as the ratio of CaO/SiO_2 increases from 0.5 to 2.0 whereas for a slag containing 60 wt.%, the decline is less pronounced with a value of 0.080 dPa s. As described by Sagadin et al. [7], the observed decrease in viscosity can be quantified as a result of broken bonds due to a higher amount of network-modifying calcium oxide and thus a better movability of

molecules. The effect of an alteration of the CaO/SiO_2 ratio is greater at lower MnO contents for similar reasons outlined above.

Defining all influences on the depicted variation of characteristic temperatures seems relatively complex as a great number of factors must be taken into consideration. Initially, the impact of the slags' viscosities was analyzed. Furthermore, the effect of liquidus and solidus temperatures and therefore the amount of remaining solid components at a specific temperature within the two-phase region must be investigated. Figure 5 compares the flow temperature with the liquidus temperature calculated with the equilib module of FactSage 7.3 and the viscosity computed with the viscosity module of FactSage 7.3 at liquidus temperature as functions of the CaO/SiO_2 ratio at 45 wt.% MnO and 5.00 wt.% Fe_2O_3, 4.20 wt.% MgO and 9.40 wt.% Al_2O_3. At $CaO/SiO_2 = 0.5$, a flow temperature of 1362.10 is calculated. The characteristic temperature increases by the addition of calcium oxide and reaches its maximum value of 1402.03 °C at $CaO/SiO_2 = 1.1$. Afterwards, a decline becomes apparent whereby at $CaO/SiO_2 = 2.0$ a temperature of 1382.10 °C can be determined. As CaO is added to increase the CaO/SiO_2 ratio from 0.5 to 2.0, the liquidus temperature rises steadily from 1304.59 to 1719.39 °C, whereas the viscosity declines from 1.240 to 0.130 dPa s. No linear correlation between characteristic temperatures and liquidus temperature can be determined. At $CaO/SiO_2 < 0.6$, the flow temperature even exceeds liquidus temperature, an effect caused by a combination of increased viscosity and other parameters, for instance, high surface tension of the slag and poor wettability of the platinum sheet during the experiments.

Conclusion

Ecological and economic trends for an effective enhancement of processes lead to increased re-usage of former waste material. In this work, melting behavior and viscosity were investigated by means of a hot stage microscope and thermodynamic calculations. The results should help to optimize effectiveness and reduce losses. The main objective is the determination of a relation between manganese oxide content and the mentioned parameters. Therefore, 19 synthetic slags with statistically chosen compositions have been produced. The experiments are designed to deduce conclusions about the characteristic temperatures of the samples. Additionally, viscosities of the different mixtures have been calculated and compared with the temperature variation. The investigated slags' compositions differ from those of representative HCFeMn and SiMn slags as noted by Muller [19] and Muller et al. [20]. Particularly noticeable are higher contents of manganese oxide. Jones et al. [21] give a value of 4.5 dPa s as an approximate upper limit of the viscosity for tapping slags. Figure 6 shows that viscosities of slags in the investigated ranges are below this value at liquidus temperature. However, as operating temperatures in typical processes implemented in the production of HCFeMn or SiMn are below 1650 °C especially slags with greater CaO contents, therefore, higher liquidus temperatures must be evaluated critically. If these cases are of interest, the calculations must be

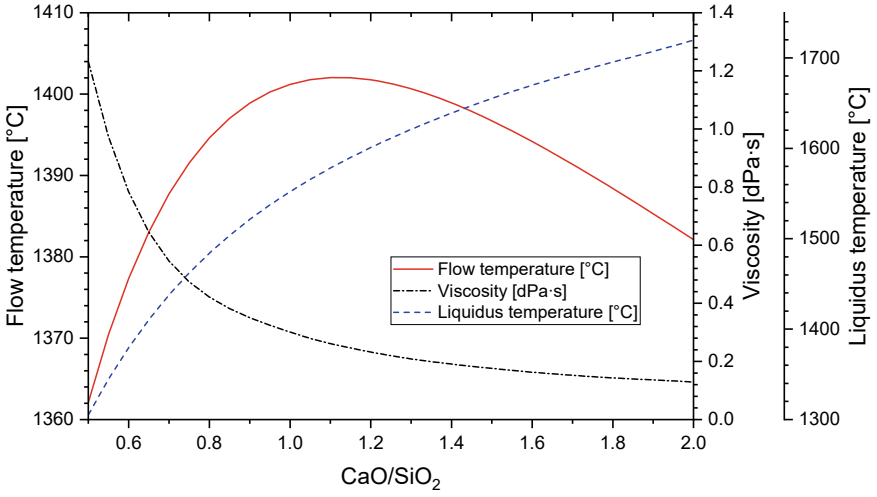

Fig. 6 Flow temperature, liquidus temperature (calculated in the equilib module of FactSage 7.3), and viscosity at 1850 °C (calculated in the viscosity module of FactSage 7.3) as functions of the CaO/SiO_2 ratio for a slag containing 45 wt.% MnO and 5.00 wt.% Fe_2O_3, 4.20 wt.% MgO and 9.40 wt.% Al_2O_3

adjusted accordingly as the remaining solid percentage at tapping temperatures shifts viscosities to higher values.

Mills [9] states that manganese oxide may act either as an O^{2-} acceptor contributing to the formation of widespread networks or as an O^{2-} donator shifting viscosities to lower values, depending on the composition of each particular slag. However, in this work a tendency to a decreased viscosity can be observed by addition of MnO and simultaneously decreasing amounts of CaO and SiO_2 (cf. Figs. 5 and 6). Hence, MnO may be classified as a network-modifying molecule within this range of composition.

An addition of CaO leads to a raise of the characteristic temperatures at a low CaO/SiO_2 ratio. With further increase of the CaO amount, a slight drop in the measured temperatures can be observed. The viscosities are decreasing steadily with a gradual subtraction of SiO_2 for reasons outlined above.

The results illustrate the highly non-linear correlation between liquidus and flow temperatures. Besides an investigation of viscosity, a determination of various other parameters such as interfacial tension must be implemented in order to increase the accuracy of predictions regarding the melting behavior of slags.

The combination of experimental results with computed values from thermodynamic calculations provided in this work gives extensive information about slags which are typically used in recycling processes of batteries and offers an opportunity to classify them based on their composition. Thus, their viscosity and melting behavior can be estimated, and conclusions regarding the occurring processes during the periods of smelting and reduction and the influence of slag composition on

required time and parameters to be set may be drawn. An adaption to a broader range of slags can be subject to further investigation.

Acknowledgements The financial support by the Austrian Federal Ministry for Digital and Economic Affairs, the National Foundation for Research, Technology and Development, and the Christian Doppler Research Association is gratefully acknowledged.

References

1. Martens H, Goldmann D (2016) Batterierecycling. In: Martens H (ed) Recyclingtechnik. Springer Vieweg, Wiesbaden, pp 1–2
2. Raghupathy L, Chaturvedi A (2013) Secondary resources and recycling in developing economies. Sci Total Environ 461–462:830–834
3. Eric RH (2014) Production of ferroalloys. In: Seetharaman S (ed) Treatise on process metallurgy. Elsevier, Amsterdam, pp 477–532
4. Gregurek D, Ressler A, Reiter V, Franzowiak A, Spanring A, Prietl T (2013) Refractory wear mechanisms in the nonferrous metal industry: testing and modeling results. JOM 65(11):1622–1630. https://doi.org/10.1007/s11837-013-0758-1
5. Espinosa DCR, Bernardes AM, Tenório JAS (2004) An overview on the current processes for the recycling of batteries. J Power Sources 135(1–2):311–319. https://doi.org/10.1016/j.jpowsour.2004.03.083
6. Espinosa DCR, Mansur MB (2019) Recycling batteries. In: Goodship V, Stevels A, Huisman J (eds) Waste electrical and electronic equipment (WEEE) handbook. Elsevier, Cambridge, pp 371–391
7. Sagadin C, Luidold S, Wagner C, Wenzel C (2016) Melting behaviour of Ferronickel slags. JOM 68(12):3022–3028. https://doi.org/10.1007/s11837-016-2140-6
8. Grothe H (1949) Metallhüttenkunde. Carl Winter Universitätsverlag, Heidelberg, pp 69–70
9. Mills KC (1981) Structure of liquid slags. In: Verein Deutscher Eisenhüttenleute, Schlackenatlas. Slag atlas. Verlag Stahleisen, Düsseldorf, pp 2–6
10. Frohberg MG (1961) Die Anwendung der Ionentheorie auf metallurgische Schlacken unter besonderer Berücksichtigung der Sauerstoff- und Schwefelverteilung. Arch Eisenhuettenwes 32(9):597–606. https://doi.org/10.1002/srin.196103250
11. Sagadin C, Luidold S, Wagner C, Spanring A, Kremmer T (2018) Phase reactions between refractory and high-acidic synthetic CaO-Ferronickel slag. JOM 70(1):34–40. https://doi.org/10.1007/s11837-017-2619-9
12. Ji FZ (2001) Experimental studies of the viscosities in CaO-MnO-SiO_2 and CaO-FenO-MnO-SiO_2 slags. Metall Trans B 32(1):181–186. https://doi.org/10.1007/s11663-001-0020-z
13. Park JH, Ko KY, Kim TS (2015) Influence of CaF_2 on the viscosity and structure of manganese ferroalloys smelting slags. Metall Trans B 46(2):741–748. https://doi.org/10.1007/s11663-014-0269-7
14. Wiesner VL, Vempati UK, Bansal NP (2016) High temperature viscosity of calcium-magnesium-aluminosilicate glass from synthetic sand. Scr Mater 124:189–192. https://doi.org/10.1016/j.scriptamat.2016.07.020
15. Bale CW, Bélisle E, Chartrand P, Decterov SA, Eriksson G, Gheribi AE, Hack K, Jung IH, Kang YB, Melançon J, Pelton AD, Petersen S, Robelin C, Sangster J, Spencer P, van Ende MA (2016) FactSage thermochemical software and databases, 2010–2016. Calphad 54:35–53. https://doi.org/10.1016/j.calphad.2016.05.002
16. Pelton AD, Blander M (1986) Thermodynamic analysis of ordered liquid solutions by a modified quasichemical approach—application to silicate slags. Metall Mater Trans B 17(4):805–815. https://doi.org/10.1007/BF02657144

17. Pelton AD, Chartrand P (2001) The modified quasi-chemical model: Part II. Multicomponent solutions. Metall Mater Trans A 32(6):13551360. https://doi.org/10.1007/s11661-001-0226-3
18. Schnideritsch H (2010) Schmelz- und Reduktionsverhalten komplexer Sekundärrohstoffe. PhD thesis, Montanuniversität Leoben
19. Muller J (2013) Evaluation of HCFeMn and SiMn slag tapping flow behaviour using physiochemical property modelling and analytical flow modelling. PhD thesis, University of Pretoria
20. Muller J, Zietsman JH, Pistorius PC (2015) Modeling of manganese ferroalloy slag properties and flow during tapping. Metall Mater Trans B 46:2639–2651. https://doi.org/10.1007/s11663-015-0426-7
21. Jones RT, Erwee MW (2016) Simulation of ferro-alloy smelting in DC arc furnaces using Pyrosim and FactSage. Calphad 55(1):20–25. https://doi.org/10.1016/j.calphad.2016.05.003

Metal and Slag Extraction from Different Zones of a Submerged Arc Furnace with Non-uniform Porous Bed Using CFD

Varun Loomba, Jan Erik Olsen, and Kristian Etienne Einarsrud

Abstract A submerged arc furnace (SAF) is generally used in the production of ferroalloys (referred to as metal in this study). Viable production of ferroalloys requires a consistent tapping process where metal and slag are extracted from the furnace. The tapping flow rates depend on various in-furnace conditions such as the height of the metal and slag column, presence of a porous coke bed (particle bed), crater pressure, and the physical properties of the fluids. In order to understand the difference in drainage of metals and slags produced in different zones of the furnace, a computational fluid dynamics (CFD) study is performed. Variations in the tapping of metal and slag from the different zones would lead to accumulation in the furnace, thus reducing its efficiency. A comparison between the tapping rates for the metal produced in the front or the back zone of the furnace is performed for a uniformly distributed coke bed and a coke-free bottom region. The tapping rates of slag produced in different zones of the furnace for a uniformly distributed particle bed are also compared. The results showed that the furnace reached a quasi-steady state quicker for the coke-free bottom region compared to the uniformly distributed particle bed, whereas the tapped metal comes equally from all zones of the furnace. It took longer for the simulation to reach a quasi-steady state for extraction of slag produced in different zones due to higher initial volume of slag. At the quasi-steady state, the slag was tapped equally from all zones of the furnace.

Keywords CFD · Porous media flow · Tapping · Furnace simulation

V. Loomba · K. E. Einarsrud (✉)
Department of Material Science and Engineering, NTNU, Trondheim, Norway
e-mail: kristian.e.einarsrud@ntnu.no

V. Loomba
e-mail: varun.loomba@ntnu.no

J. E. Olsen
Process Technology Group, SINTEF AS, Trondheim, Norway
e-mail: jan.e.olsen@sintef.no

J. D. Steenkamp et al. (eds.), *Furnace Tapping 2022*, The Minerals, Metals & Materials Series, https://doi.org/10.1007/978-3-030-92544-4_24

Introduction

Efficient furnace operation depends on several factors where one of the crucial processes is tapping i.e., extraction of the molten metal and slag from the furnace. Poor tapping could lead to metal and slag accumulation in the SAF, reducing the efficiency of the entire process. The metal and the slag drain out of the furnace due to gravity, therefore their flow rates depend on the height of the liquid column accumulated in the furnace. In batch tapping, the tap-hole is opened when a significant amount of metal and slag have accumulated in order to facilitate their flow out of the furnace. The unreacted coke particles in the furnace hinder the flow of the metal and the slag by offering resistance to the flow, lowering their flow rates. It is not clarified whether the coke bed floats on top of the metal, the coke bed forms a bridge due to interlocking between the particles, or this observation is caused by a phenomenon occurring after the furnace shuts down. Regardless of the reason for the absence of a coke bed at the furnace bottom, it is worthwhile to verify if this affects the flow of metal and slag towards the tap-hole. Experimentation on the furnace tapping process is difficult due to the huge size and the extremely high temperatures at which the furnace operates. Computational fluid dynamics (CFD) is an excellent tool to study these kinds of processes without dealing with extreme industrial conditions.

CFD has previously been used intensively in the metallurgical industry to simulate the flow of metals and slags under various operational conditions, to understand various aspects of the tapping process [1–8]. In some studies, a uniform distribution of the particle bed has been considered [1–4], whereas others considered the presence of a coke-free region at the bottom of the furnace [5–8]. Further details of several studies implementing CFD for tapping process in SAF have been described by Bublik et al. [9].

The tap-hole is generally present on one side of the furnace, therefore the metal and the slag produced in the other side must travel through the entire furnace in order to be tapped. If remained untapped, the metal and the slag will consume some volume which will not be utilized for production, lowering the process efficiency. Therefore, in this study the extraction of the metal and the slag from different zones of the furnace is studied to better understand the accumulation of the fluids. Our previous study (Loomba et al. [10]) includes the effect of uniform and a non-uniform distribution of particle bed inside the furnace on the tapping flow rates of the metal produced in different zones of the furnace. A comparison of the metal tapping flow rate produced in the back of the furnace relative to the metal from the front of the furnace has been shown in detail. In this paper, we continue the research to include the coke-free bottom region to study the metal tapping rates produced in different zones of the furnace relative to the metal from the front. Further, the extraction of slag from different zones of the furnace is also considered.

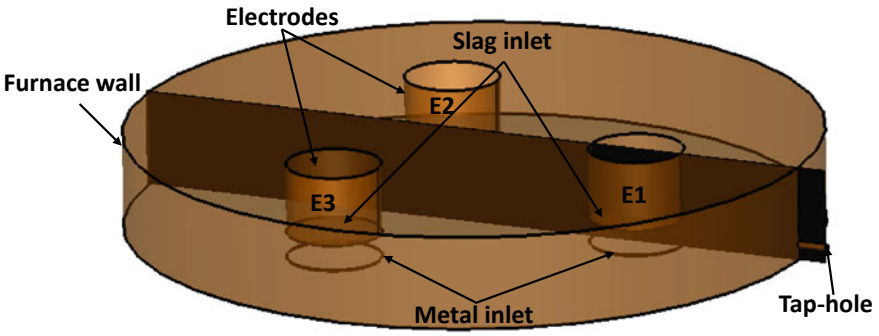

Fig. 1 Furnace design describing the different parts. The plane is used for analysis of metal and slag volume fractions in the results section

Materials and Methods

All flows can be mathematically represented by the Navier–Stokes equations [11], which are a set of partial differential equations describing the velocity of a fluid in all directions, including all the physical processes that facilitate the flow. These equations cannot be solved analytically for complex flow systems, which is the case in most flow systems. Computational Fluid Dynamics (CFD) is a technique to solve these equations numerically for all possible flow situations [12].

The simulated furnace in this study is an industrial-scale furnace, 10 m in diameter and 4 m high which represents a ferromanganese (FeMn) furnace. Since all the liquids are present in the bottom part of the furnace, only 1.5 m height is considered in the simulations. The furnace consists of three electrodes (E1, E2, and E3) that generate an electric arc to heat the materials, but from the fluid dynamic purpose, they act as solid walls present 0.5 m above the base of the furnace. The tap-hole is present on one side of the furnace near one of the electrodes with a diameter of 0.1 m. The tap-hole is located 0.1 m above the bottom surface of the furnace. A square cross-section tap-pipe is considered in these simulations to improve the mesh quality. Figure 1 shows the schematic diagram with the location of each of the components. The metal and the slag inflow are calculated based on the production rates of 300 and 200 tonnes/day.

Simulation Setup

Three fluid phases (the metal phase, the slag phase, and the gas) are defined in the simulations. The metal being the densest forms the bottom layer followed by the slag and the gas forming the top layer. The physical properties of the fluids are specified in Table 1 [8]. Since there are three immiscible fluids in the furnace, a multiphase volume of fluid (VOF) approach is used in the simulations [13]. In this approach, the

Table 1 Physical properties of the fluids

Material	Density (kg/m^3)	Viscosity (Pa s)
Metal	6,100	0.005
Slag	3,000	0.1
Gas	1	1×10^{-5}

interface between each phase is tracked along with the velocity profile calculation. The metal and the slag are produced in the entire bottom part of the furnace but for the simulation purposes, slag inlet is defined on the bottom surface of the electrodes whereas three discs are defined on the bottom surface of the furnace under each electrode which serve as metal inlets as shown in Fig. 1. The furnace is divided into three zones, one under each electrode (E1, E2, and E3), in order to realize whether the metal (or slag) being tapped comes from which region of the furnace. To determine in which zone of the furnace the fluids being tapped are produced, a separate fluid phase (metal or slag) is defined in each zone in order to identify the tapped fluid (but with the same physical properties as in other zones). This is explained in detail in the following sections.

The geometry of the furnace was designed using Gambit 2.4.3 software and the simulations were performed in OpenFOAM®. MultiphaseInterFoam module of OpenFOAM® was used for these simulations which implements the VOF multiphase approach. The Navier–Stokes equations are solved in this method for calculating the velocity profiles which are shared by all the phases. Additional equations (derived from continuity equations) are solved to track the interface between the phases. Therefore, adding more phases leads to additional equations being solved, slowing down the simulations. The dam break tutorial in OpenFOAM was used as the basis to build up the model. The geometry and mesh, the boundary and initial conditions, and the physical properties of the fluids were replaced in order to define our case. Finally, a topoSet file was added to define the porous region and a fvOptions file was added to include the resistance from the particle bed.

Several real-time tapping and production periods were simulated, where each tapping period is 20 min long and the production period is 2 h long. There is no outlet during the production period and the fluids are accumulated in the furnace during this time. The fluids are symmetrically distributed in the furnace at the beginning, which is not the usual case, i.e., after a certain operational time, the metal (or slag) produced at the back of the furnace will reach the other zones of the furnace. Therefore, several tapping and production cycles are required to reach the quasi-steady state, i.e., when the ratio of mass flow rates of each metal and the slag does not vary significantly in successive taps.

Porosity Distribution

The unreacted coke particles form a porous particle bed creating a resistance to the flow of the metal and the slag. This additional resistance is added to the Navier–Stokes equations using the Ergun equation, added as a sink term thereby reducing the velocity of the fluids through the fvOptions methodology in OpenFOAM. The Ergun equation describes the pressure drop across the bed as a function of the properties, the fluid physical properties, and the flow properties as shown in Eq. 1:

$$-\frac{\Delta P}{L} = \frac{150\mu_f(1-\varepsilon)^2}{d_p^2\varepsilon^3}u + \frac{1.75\rho_f(1-\varepsilon)}{d_p\varepsilon^3}u^2 \tag{1}$$

where ε is the particle bed porosity, d_p is the particle diameter, μ_f and ρ_f are the fluid viscosity and density, and u is the fluid velocity. The negative sign in Eq. 1 signifies the pressure loss created by the particle bed. The first term of the equation describes the viscous pressure loss, and the second term includes inertial effects. The Ergun equation is reduced to the Kozeny–Carman equation when the second term in Eq. 1 is excluded. Several researchers in the metallurgical field have used the Kozeny–Carman equation for the flow through the porous bed, arguing that the flow is laminar for highly viscous fluids such as the metal and the slag, but Olsen and Reynolds [14] showed that better results were obtained when the Ergun equation is used instead of Kozeny–Carman equation. For most of the particle bed, the flow is laminar. However, in front of the tap-hole where liquids accelerate into the tap-hole, the flow becomes turbulent. This is important for pressure loss.

Simulation Cases

Two separate cases are simulated, one to determine the extraction of metal from different zones of the furnace and the other to determine the extraction of slag phase.

Base case: Extraction of metal from different zones of the furnace for uniformly distributed particle bed.

Three metal phases are defined under each electrode (named metal1, metal2, and metal3 corresponding to the electrodes E1, E2, and E3 from Fig. 1) and only one slag phase as the focus is on metal tapping, in order to speed up the simulations. The metal enters the furnace constantly whereas there is no slag inlet. The velocity of metal is defined at the inlet based on the production rate of the metal, and the amount of slag produced during each tapping and production period is added on top to have the same hydrostatic head. The atmospheric pressure is defined on the top surface of the furnace, and wall boundary conditions (no slip for velocity and no flux for pressure) are defined at the furnace walls, tap-hole pipe walls, and the slag inlet. The outlet boundary conditions change from pressure outlet (atmospheric

pressure) during tapping to wall boundary during the production period. A uniformly distributed particle bed is defined with a porosity of 0.45 and a particle diameter of 0.03 m. This case has been explained in detail in our paper Loomba et al. [10]. All the boundary conditions used in this simulation are shown in Table 2. A static adaptive mesh was used for the simulation with more number of elements in the bottom region where most of the flow is happening and fewer elements in the top region as it is covered by the gas. This allows the use of coarser mesh without compromising the accuracy of the results, in order to save the simulation time. Since several tapping and production simulations are required, the mesh cannot be extremely fine in order to constrain the simulation time, therefore 286,000 mesh elements were used for these simulations with minimum cell volume 1.455×10^{-6} m^3, maximum cell volume 3.7×10^{-3} m^3, and average cell volume 3.9×10^{-4} m^3.

Case 1: Extraction of metal from different zones of the furnace with non-porous bottom region.

The previous case is extended to add a non-uniformity by adding a coke-free bottom region to the furnace. The particle bed is removed from the bottom of the furnace till the bottom of the tap-hole. The particle bed properties in the rest of the furnace are the same as in the base case. The boundary conditions and the mesh properties used for this case are the same as used in the base case and specified in Table 2. The initial distribution of the metal and the slag phases is shown in Fig. 2.

Case 2: Extraction of slag from different zones of the furnace.

In this case, three slag phases (named slag1, slag2, and slag3 corresponding to the regions below the electrodes E1, E2, and E3 from Fig. 1) and one metal phase are considered as the focus is on tapping of slag rather than metal. Both metal and

Table 2 Boundary conditions used in the simulation for the base case

Boundary	Tapping	Production
Metal inlet	Velocity inlet (calculated from production rates)	Velocity inlet
Slag inlet	Wall	Wall
Furnace wall	Wall	Wall
Outlet	Pressure outlet	Wall
Surface	Atmospheric pressure	Atmospheric pressure

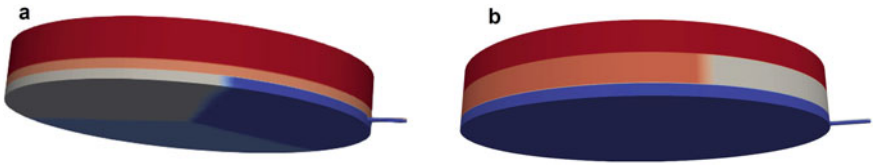

Fig. 2 **a** Case 1: 3 metal phases, 1 slag phase with non-porous bottom region and uniformly distributed porosity in the top region ($\varepsilon = 0.45$ and $d_p = 0.03$ m), **b** case 2: 1 metal phase, 3 slag phases with uniformly distributed porosity in the entire furnace ($\varepsilon = 0.45$ and $d_p = 0.03$ m)

Table 3 Boundary conditions used in the simulation of case 2

Boundary	Tapping	Production
Metal inlet	Velocity inlet (calculated from production rates)	Velocity inlet
Slag inlet	Velocity inlet (calculated from production rates)	Velocity inlet
Furnace wall	Wall	Wall
Outlet	Pressure outlet	Wall
Surface	Atmospheric pressure	Atmospheric pressure

slag inlets are defined in this case, metal from the disc at the bottom (as in previous cases) and the slag from the bottom surface of the electrode wall. The initial amount of slag in this case is double that of the previous cases such that the slag level in the furnace should always remain above the height of the slag inlet, in order to avoid any divergence in the solution. Particle bed is uniformly distributed, the same as the base case. Figure 2 shows the metal and the slag distribution in each case. The slag inlets are defined with a velocity calculated from the mass production rate of the slag (similar to metal inlet velocity). All other boundary conditions used are the same as in the base case. Table 3 shows the list of boundary conditions used for these simulations. The initial level of the slag in the furnace is higher in this case than in the previous case, therefore a coarse mesh cannot be used in the top region of the furnace, hence 722,000 mesh elements were used in this case: minimum cell volume 1.25×10^{-6} m^3, maximum cell volume 7.3×10^{-4} m^3, and average cell volume 1.56×10^{-4} m^3.

Results and Discussion

Simulations were performed using an open-source CFD software called OpenFOAM® version 7 [15], whereas plotting was performed in Matlab [16].

Flow Profiles

The flow patterns of all cases are similar. Figure 3 shows the volume fractions of each phase for all cases at the beginning of the first tap and at the end of the fourth tap. The plane shown in Fig. 3 passes through the middle of the tap-hole and perpendicular to the base of the furnace (as shown in Fig. 1). On the backside of the furnace, this plane passes through the interface between metal2 and metal3 (or slag2 and slag3). On opening the tap-hole, the fluids start flowing out of the furnace due to the hydrostatic pressure of the accumulated liquid column in the furnace. The initial level of the metal is above the tap-hole, therefore only metal should flow out of the furnace in the beginning until the metal–slag interface reaches the tap-hole height,

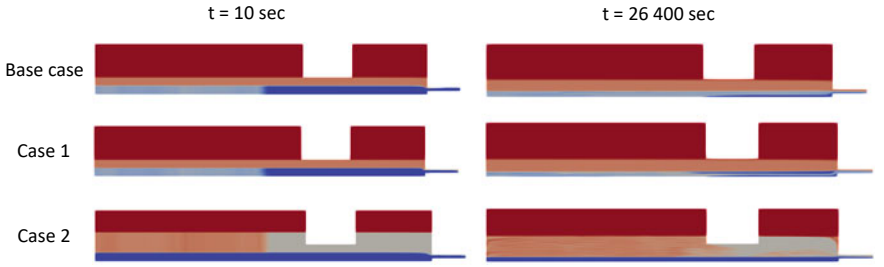

Fig. 3 Volume fraction along the plane perpendicular to the base of the furnace, passing through the center of the tap-hole (as shown in Fig. 1) for both cases at 10 s (tap 1) and 26,400 s (tap 4) from the beginning

but the metal–slag interface near the tap-hole bends due to the high viscosity of the slag and the slag also flows out from the beginning. This is evident from the first column in Fig. 3a where the bending of the metal–slag interface is visible even 10 s after opening the tap-hole. As metal1 covers the region near the tap-hole in the base case and case 1, only metal1 is tapped in the beginning whereas metal2 and metal3 come closer to the tap-hole. Since the bottom region (where metal1, metal2, and metal3 are produced) is free of particle bed in case 1, the metals flow faster than the base case with particle bed at the bottom of the furnace. Therefore, metal2 and metal3 also start flowing out towards the end of the first tap in case 1. It takes two taps for metal2 and metal3 to reach the tap-hole and be tapped for the base case due to the resistance by the particle bed. At the end of the fourth tap (second column in Fig. 3), it can be seen that metal2 and metal3 have been tapped for both cases. Similarly, slag1 covers the region near the tap-hole in case 2 and it starts flowing at the beginning of the first tap. The slag is always passing through the particle bed and due to the higher viscosity of the slag, the resistance offered to the slag is also higher compared to the metal. Since the slag has much higher volume in case 2 compared to the other cases, more number of taps are required for the slag at the back of the furnace to reach the tap-hole. Therefore, even at the end of the fourth tap (the second column in Fig. 3), most of the region near the tap-hole is still covered by slag1, and only small amounts of slag2 and slag3 are visible in the tap-hole pipe. This shows that more number of taps will be required for the furnace to reach the quasi-steady state for case 2 compared to the other cases.

Mass Extracted in Each Tap

Figure 4 shows the comparison of the tapped mass of each metal phase in each tap for the base case and case 1. Metal2 and metal3 are not tapped in the first tap for the base case as the region near the tap-hole is covered by metal1. In case 1, however, metal2 and metal3 are tapped even in the first tap because the metal phases

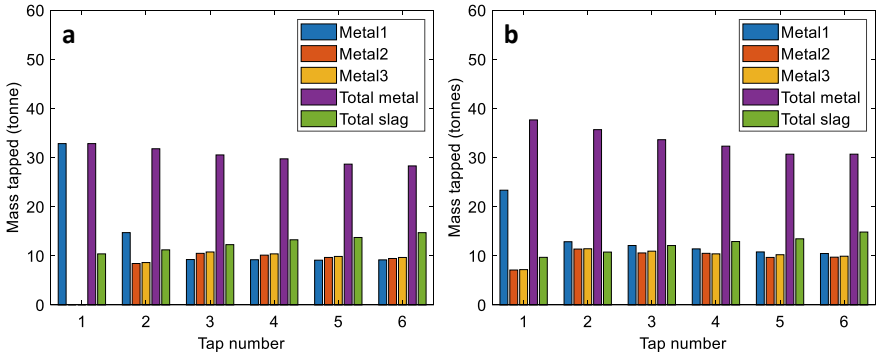

Fig. 4 The mass of metal1, metal2, metal3, and the slag phase in each tap for **a** the base case and **b** case 1

are moving faster in the absence of the resistance offered by the particle bed. The total amount of metal tapped in each tap is also larger for case 1 compared to the base case, due to fast-moving metal in the bottom region of the furnace, but it will become constant if the simulations run for longer times due to mass conservation. The total amount of slag tapped is similar for the base case and case 1 because the slag phase is always flowing through the particle bed in both cases. It is also evident that it takes at least three taps for the furnace to reach a quasi-steady state, after which the ratios of metal1, metal2, and metal3 remain constant for the subsequent taps, and only two taps are required for case 1. This again can be explained by the fast-moving metal at the bottom region of the furnace; the metal from the back can reach the tap-hole faster compared to the base case. At quasi-steady state, the amounts of metal1, metal2, and metal3 extracted are similar for case 1 signifying that once the furnace reaches its steady state, metal extracted in each tap comes equally from all zones of the furnace and not just the metal produced in the region near the tap-hole. Table 4 shows the amounts of each of the metal phases and the slag phase extracted in each tap for case 1. It can be confirmed from Table 4 that the amounts of metal1, metal2, and metal3 tapped become constant from the second tap onwards signifying that the furnace has reached the quasi-steady state. A significant amount of metal2 and metal3 are extracted in the first tap compared to only metal1 being extracted for the base case. The amounts of all three metal phases extracted become constant in the

Table 4 Mass of metal and slag extracted in each tap for case 1 in kg

Material	Tap 1	Tap 2	Tap 3	Tap 4	Tap 5	Tap 6
Metal1	23,370	12,875	12,104	11,417	10,797	10,474
Metal2	07,116	11,382	10,590	10,512	09,681	09,730
Metal3	07,194	11,442	10,955	10,405	10,227	09,924
Total metal	37,680	35,699	33,650	32,335	30,705	30,128
Slag	09,696	10,769	12,099	12,916	13,468	14,846

second tap for case 1 compared to the third tap in the base case. The fast movement of the metal in the porous free zone leads to the shorter time required for reaching the quasi-steady state.

As mentioned, earlier the initial amount of slag in case 2 is double that of the base case, therefore more taps are required for the furnace to reach the quasi-steady state. Figure 5 shows the comparison between the base case and case 2. In the first three taps, only slag1 is tapped because a larger volume of slag1 is covering the region near the tap-hole compared to the base case. Slag2 and slag3 start flowing out from the fourth tap, and it takes at least seven taps to reach the quasi-steady state compared to three taps in the base case. In the first three taps, the total slag tapped is equal to the amount of slag1 tapped. Once the furnace reaches the quasi-steady state, the amounts of slag1, slag2, and slag3 tapped are similar. The total amount of slag extracted in each tap is higher for case 2 compared to the base case and case 1 because of the higher hydrostatic head of the liquid column in case 2. A similar pattern occurs for the total metal extracted in each tap due to the same reason (Table 5).

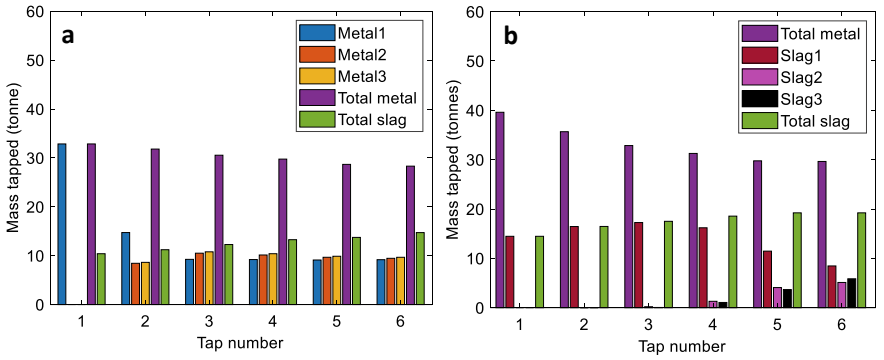

Fig. 5 The mass of different metal and slag phases in each tap for **a** the base case and **b** case 2

Table 5 Mass of metal and slag extracted in each tap for case 2 in kg

Material	Tap 1	Tap 2	Tap 3	Tap 4	Tap 5	Tap 6
Metal	39,606	35,669	32,862	31,266	29,766	29,641
Slag1	14,471	16,451	17,259	16,197	11,466	08,465
Slag2	0	6	112	01,298	04,083	05,118
Slag3	0	13	138	01,064	03,675	05,856
Total slag	14,471	16,469	17,509	18,560	19,225	19,441

Mass Flow Rate of Individual Metal and Slag Phases in a Single Tap

It can be inferred from the previous sections that the amount of each metal and slag phases extracted in each tap is constant once the furnace reaches a quasi-steady state. The mass flow rates of the metal and slag phases also become constant once the quasi-steady state is reached. Figure 6 shows the fifth tap for the three cases when the furnace has reached the quasi-steady state for the base case as well as case 1 and not yet for case 2. More taps are required for case 2 to reach the quasi-steady state. For the base case, metal1 (which is produced under the electrode E1) forces metal2 and metal3 from the previous tap present near the tap-hole to be tapped first, therefore peaks are seen in their mass flow rates at the beginning of the tap. The flow of metal1 is hindered by the particle bed leading to a time-lag in the extraction of metal1. The tapping flow rate increases for the metal1, once it reaches the tap-hole, whereas the tapping flow rate for the other two metal phases decreases. Towards the end of the tap when most of metal1 is tapped, its flow rate starts decreasing and allowing the other metal phases to be tapped. A similar flow profile to the base case is also observed in case 1 with a difference that the peaks for each of the metal phases appear sooner than the base case. The peaks have higher amplitude and lower standard deviation than the base case because of the resistance-free flow of the metal phases. The total amount of metal1 (calculated by integrating the curve in Fig. 6) extracted is slightly higher for case 1 compared to the base case, due to its fast movement, whereas the amounts of metal2 and metal3 are similar. When most of metal1 is tapped, its tapping flow rate starts decreasing and the tapping flow rates of metal2 and metal3 start increasing. The tapping rates of the slag are the same for both case 1 and the base case because the hydrostatic head is the same for both cases and the slag phase is always flowing through the particle bed, experiencing equal amount of resistance in both cases. The mass flow rates of metal1 dip down to a low value but not zero as some metal1 remains at the end of the tap. The mass flow rate profile of each of the slag phases in case 2 is similar to the total slag tapping flow rate in the base case and case 1 because a large amount of slag phases was assumed at the beginning of the first tap. The total slag tapped in case 2 is higher than the total slag phase in the

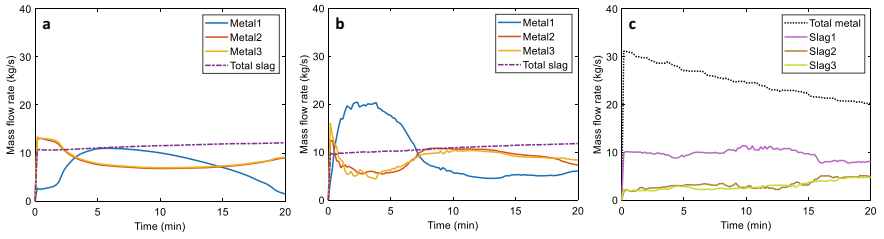

Fig. 6 The mass flow rates of the individual metal and slag phases for **a** the base case, **b** case 1, and **c** case 2 for the fifth tap

Table 6 Residence time (seconds) for individual metal and slag phases

Case	Metal1	Metal2	Metal3	Slag1	Slag2	Slag3
Base case	1,180	5,661	5,570	–	–	–
Case 1	1,643	4,284	4,139	–	–	–
Case 2	–	–	–	1,955	15,904	15,271

base case and case 1 because of the higher hydrostatic head. The total metal phase flow rate for case 2 is also higher than the base case (both have the same porosity distribution) due to the higher liquid column in case 2 leading to a higher hydrostatic pressure head.

Residence Time of Individual Metal and Slag Phases

The residence time of individual phases in the furnace is the average time spent by each phase inside the furnace. It can be quantified by considering the initial mass of each phase at the beginning of the tap, dividing it by the average mass flow rate of the respective phase. The residence time for each of the phases is shown in Table 6. The residence time for metal1 is less than metal2 and metal3 as the latter need more time to reach the tap-hole compared to metal1 which is formed closer to the tap-hole. The same pattern is seen for all three cases. The reason for higher residence time for metal1 and lower residence time for metal2 and metal3 for case 1 (porous free bottom region), compared to the base case, is the fast movement of the metal in the bottom region of the furnace. Metal2 and metal3 reach the tap-hole sooner, thereby substituting metal1 while tapping, compared to the base case. A similar trend is observed in the residence times for different slag phases in case 2; the residence time for slag1, slag2, and slag3 are 1,955, 15,904, and 15,271 s, respectively. These values are specified for the sixth tap, although the furnace has not reached the quasi-steady state yet. High values for slag2 and slag3 are observed because the initial volume of the slag is higher in case 2 compared to the other two cases and the furnace has not reached a quasi-steady state by the sixth tap. These values are shown in Table 6.

Conclusions and Outlook

A systematic numerical study of tapping of metal and slag from a SAF has been presented. The flow rate of the metal and the slag depends on the height of the liquid column accumulated in the furnace and the resistance offered by the particle bed to the flowing fluids. Three different cases have been discussed: the first is the base case with uniform porosity distribution in the furnace where metal extraction from different zones has been studied, in the second case the bottom region is a coke-free

region and the particle bed is uniformly distributed in the top part of the furnace, and the third case with similar porosity configuration as the base case but extraction of slag from different zones of the furnace is discussed. The main conclusion from this study is that the metal and slag produced in the back part of the furnace is extracted equally relative to the metal and the slag produced in the front side once the quasi-steady state is reached. The other following conclusions that can be drawn from this study are as follows:

(1) The furnace reaches the quasi-steady state faster for case 1 (coke-free bottom region) compared to the base case (uniformly distributed porosity) in the furnace as the metal moves faster in the bottom region where there is no particle bed.
(2) At steady state, the metal flows on average equally from all zones of the furnace, therefore there is no apparent accumulation of metal with the chosen porosity distribution for the furnace.
(3) Similarly, the slag extracted at a quasi-steady state in case 2 (uniform porosity distribution) is also on average tapped in equal amounts from all zones of the furnace. It takes longer for the furnace to reach a quasi-steady state with respect to tapping of slag due to the higher initial amount of slag and the higher viscosity of slag as compared to metal.
(4) When studying a single tap at a quasi-steady state, we see that the metal and slag produced at the electrode close to the tap-hole is drained first and then the products from the far electrodes towards the end. If the tap-hole is open sufficiently long, there will be an overall equal amount of tapping from each zone of the furnace.

In reality, there will be temperature gradients and cold spots where metal and in particular slag can solidify and accumulate. There is a higher likelihood for that to happen with metal and slag produced at the electrodes away from the tap-hole since these have longer residence times in the furnace than the metal and slag produced close to the tap-hole.

The methodology for predicting the tapping flow rates of metals and slags produced in different zones of the furnace has been presented. This can further be extended to include other non-uniformities that might be detected in the industrial furnaces. Further, it can be extended to calculate the shear stress on the furnace walls and thus the erosion of the furnace walls can be calculated. Once the flow profiles are calculated, the temperature profiles inside the furnace can be estimated by including the energy equation along with the flow equations.

References

1. Dash SK et al (2001) Optimum taphole length and flow induced stresses. Ironmak Steelmak 28(2):110–116
2. Dash SK et al (2004) Optimisation of taphole angle to minimise flow induced wall shear stress on the hearth. Ironmak Steelmak 31(3):207–215

3. Nishioka K, Maeda T, Shimizu M (2005) A three-dimensional mathematical modelling of drainage behavior in blast furnace hearth. ISIJ Int 45(5):669–676
4. Kadkhodabeigi M, Tveit H, Johansen ST (2011) Modelling the tapping process in submerged arc furnaces used in high silicon alloys production. ISIJ Int 51:193–202
5. Nishioka K, Maeda T, Shimizu M (2005) Effect of various in-furnace conditions on blast furnace hearth drainage. ISIJ Int 45(10):1496–1505
6. Guo BY et al (2008) CFD modelling of liquid metal flow and heat transfer in blast furnace hearth. ISIJ Int 48:1676–1685
7. Shao L, Saxén H (2012) Numerical prediction of iron flow and bottom erosion in the blast furnace hearth. Steel Res Int 83(9):878–885
8. Reynolds QG et al (2019) Phase effects in tap-hole flow—a computational modelling study. J South Afr Inst Min Metall 119(6):527–536
9. Bublik S et al (2021) A review of ferroalloy tapping models. Metall Mater Trans B 52(4):2038–2047
10. Loomba V, Olsen JE, Einarsrud KE (2021) Simulation of metal and slag in a Si-Mn furnace during production and tapping. In: Infacon XVI. Trondheim
11. Drazin PG, Riley N (2006) The Navier-Stokes equations: a classification of flows and exact solutions. London mathematical society lecture notes series. Cambridge University Press
12. Versteeg HK, Malalasekera M (2007) An introduction to computational fluid dynamics: the finite method, 2nd edn. Pearson Education Limited, Essex, England
13. Hirt CW, Nichols BD (1981) Volume of fluid (VOF) method for the dynamics of free boundaries. J Comput Phys 39:201–225
14. Olsen JE, Reynolds QG (2020) Mathematical modeling of furnace drainage while tapping slag and metal through a single tap-hole. Metall Mater Trans B 51(4):1750–1759
15. Foundation O (2020) OpenFOAM v7 user guide. https://cfd.direct/openfoam/user-guide
16. MATLAB, 9.7.0.1190202 (R2019b) (2019) Natick, Massachusetts

Tapblock Refractory Wear Monitoring and Hearth Refractory Design Optimization in Metallurgical Furnaces

Cameron Soltys, Jayant Borana, Hamid Ghorbani, Richard MacRosty, Tom Plikas, and Chad Van der Woude

Abstract Monitoring the refractory wear in the tapblock is key to achieving extended tap-hole and furnace hearth life by informing operation and maintenance plans. The utility of a tapblock condition assessment system can be maximized by enhancing thermal monitoring, using an online monitoring system, data processing, and first-principles process modeling to develop a robust model of the tapblock condition. Another key factor impacting furnace campaign life is the refractory design, which requires balancing of competing priorities such as cost, performance, and constructability. Structural assessment of a hearth system can be used to quantify and optimize these features while identifying potential fatal flaws in a design, avoiding short campaign life. This assessment can be used to determine the impact of design changes, providing confidence in refractory design decisions. This paper will present examples of wear monitoring in the tap-hole region of a flash converting furnace and refractory design optimization for electric arc furnaces.

Keywords Online monitoring · Refractory assessment · Campaign life · Refractory life · Campaign extension · Tapblock · Design optimization · Refractory wear

Introduction

The furnace hearth is a complex heterogeneous system comprised of refractory bricks, castables, ramming mixes, and expansion allowances. This complexity is most evident in the tap-hole region, where extreme thermal cycling and 3D heat transfer effects put this critical part of the refractory system under particularly aggressive conditions. The refractory condition in the tap-hole region is frequently the limiting factor on campaign life, so developing well-performing refractory designs and monitoring the tap-hole condition are critical to the safe operation of a furnace and achieving business objectives.

C. Soltys (✉) · J. Borana · H. Ghorbani · R. MacRosty · T. Plikas · C. Van der Woude
Hatch, 2800 Speakman Drive, Mississauga, ON L5K 2R7, Canada
e-mail: cameron.soltys@hatch.com

J. D. Steenkamp et al. (eds.), *Furnace Tapping 2022*, The Minerals, Metals & Materials Series, https://doi.org/10.1007/978-3-030-92544-4_25

Monitoring the refractory wear in the tapblock is key to achieving extended tap-hole and furnace life by informing operation and maintenance plans. While thermocouple sensors are installed on the tapblock for this purpose, the data is often challenging to analyze and interpret for engineering assessment and diagnosis of tapblock health, including the state of refractory wear. The utility of a tapblock condition assessment system can be maximized by enhancing thermal monitoring, using advanced sensors, online monitoring, data processing, and first-principles process modeling to develop a robust model of the tapblock condition. The functionality and robustness of this diagnostic tool are demonstrated through case studies from plant installations.

Another key factor impacting furnace campaign length is the refractory design, which requires balancing of competing priorities such as cost, performance, and constructability. In addition, the design must be tolerant of material variation and deviation from the installation procedure, both of which are all-but-inevitable with refractory materials. Structural assessment of a hearth system can be used to quantify and optimize these features while identifying potential fatal flaws in a design, avoiding short campaign life. This assessment can be used to determine the impact of design changes, helping to ensure that a new refractory system will improve operation, or to provide confidence in a substantial redesign.

Tap-Hole Wear Monitoring

The metal/matte tap-hole is a key area to monitor in the furnace as it undergoes severe wear from the molten material repeatedly drained through it, the associated thermal cycling, opening and closing of the tap-hole, and refractory impregnation by the metal/matte. The high wear rate around the tap-hole means downtime is necessary to perform refractory repairs. Typical maintenance practice for the tap-holes is time- or production-based, with regularly scheduled repairs of the tapping channel refractory brick or replacement of the entire tap-hole. Time/production-based maintenance, by necessity, is very conservative to avoid safety concerns and typically results in repairs being performed well before they are required. A data-driven model that can predict the state of tap-hole involves collecting operational data, contextualizing and analyzing the data, and providing performance indicators to decision-makers while in operation. A good understanding of the tap-hole condition allows the operators to take a condition-based maintenance approach to maximize safety and production.

Assessment Methodology

Hatch has developed an assessment methodology to ensure that a range of variables associated with tap-hole that could affect the heat transfer are captured for both design and operating conditions, including

- Refractory thickness,
- Tap-hole thermal resistance,
- Thermal conductivity of refractory,
- Cooling water supply temperature,
- Cooling water flow rate,
- Bath temperature, and
- Bath convection properties.

The following are the steps taken for assessment incorporating the influence of the abovementioned variables on the condition of tap-hole:

- Data collection: Instrumentation and process data is collected using advanced sensors for larger spatial coverage at given operating conditions.
- Data storage: building a single repository for data collected from various sensors and sources.
- Contextualizing: thermal modelling to provide context to the measured values to understand the condition of the refractory.
- Analyzing: combining data collected through mathematical models and/or real-time data for multivariate statistical modelling for soft-sensing, predictive analytics, etc., applications.
- Decision-making: undertaking necessary steps by operators based on the guidance provided on the state of tap-hole using data analysis.

Case Study—Flash Converting Furnace

Sidewall accretion in a smelting furnace plays an important role in furnace integrity as it provides protection to the sidewall cooling elements, and thereby, extends the furnace campaign life. The extreme thermal and mechanical stresses in the furnace and changes in the slag chemistry can cause the sidewall accretion to melt or break away, decreasing the lining protecting the cooling elements.

A case study presented here discusses using of high spatial resolution thermal data (collected from fibre optic temperature arrays) to assess the tapblock condition. A soft-sensor application based on thermal modelling for abnormal condition detection, diagnosis, and monitoring through prediction of sidewall accretion thickness is discussed.

Fiber Optic Temperature Monitoring for Tap-Holes

Fiber optic technology allows the installation of numerous sensors in locations that are very sensitive to refractory thickness, thereby providing information previously unavailable with traditional sensors. The key benefits of the fiber optic temperature sensors are the small size of the fiber and the ability to install many sensors along a

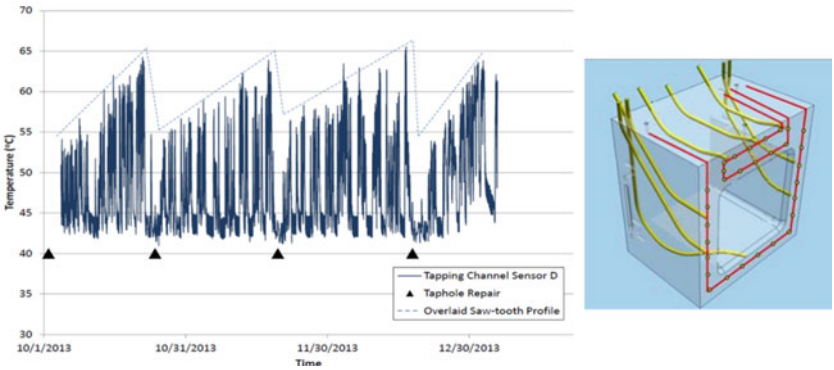

Fig. 1 Saw-tooth temperature profile inside tapping channel between brick repairs (left) and taphole showing location of thermowells/thermocouples and fiber optic cables (right)

single fiber optic strand. In addition to the benefits of increased spatial coverage, the small diameter of the fiber allows the sensors to be located such that sensitivity can be optimized.

In the case of the tap-holes, the fibers are installed across the hot face, on or just below the surface of the copper. Figure 1 shows an example of an installation with two fiber strands (in red) on the copper surface. The traditional method for monitoring a tap-hole would be eight to twelve thermocouples embedded in the copper; the fiber optic sensors provide a much denser measurement grid.

The saw-tooth pattern traced out by the peak temperatures during tapping is quite evident in Fig. 1 and corresponds closely to the brick repair schedule. The pattern generally starts out with relatively low peak temperatures (55 °C) when the refractory is new and over time it increases, tending towards 65 °C just before the next repair. This increase in temperature is consistent with the tap-hole increasing in size and/or the impregnation of the refractory with a more conductive metal. The thermal modelling with the data collected can be used to optimize the repair schedule such that operational efficiency can be maximized.

Thermal Modelling for Soft-Sensor Applications

To seal the furnace after tapping, the tap-hole is plugged with clay that cures and hardens as it contacts the hot metal/matte. It is opened by drilling and oxygen lancing to allow the flow of molten material for tapping. During tapping, the tap-hole is subjected to high heat loads and the resulting thermo-mechanical stress will cause the refractory to deteriorate over time. In addition, every time the tap-hole is plugged with clay, agitation caused by the gas bubbles that evolve during the curing of the clay plug causes wear of the refractory lining and accretion on the hot face. A detailed thermal model based on 3D geometry (see Fig. 2) used mass, momentum, and heat

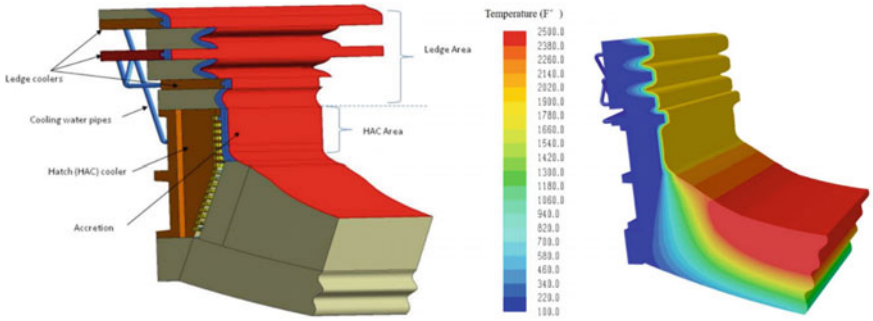

Fig. 2 Thermal model for a section of furnace sidewall (left) and sample results of a thermal model simulation (right)

transfer relationships to establish the conditions within the tap-hole hot-face at the uptake shaft end of a Flash Converting Furnace (FCF).

The high-fidelity model was used to simulate the thermal response for a range of refractory wear and bath conditions. To develop an online model that can predict conditions in real time, a multivariate statistical model was developed from these simulations. Initially, non-tapping and tapping models were calibrated using non-tapping and tapping data, respectively; subsequently, a combined model was calibrated with both non-tapping and tapping data to produce one multivariate statistical model that was validated for both conditions. These results eliminated the necessity of switching models between the tapping and non-tapping conditions. The accretion prediction of about 275 mm on the tap-holes during normal furnace operation matched reasonably well with the accretion measurement of 300 mm taken during a rebuild at that time.

An additional benefit of multivariate statistical models used for accretion thickness prediction is their ability to detect abnormal process conditions and identify the variables contributing to such conditions. Multivariate models are typically built using normal operation data and therefore any condition that is not seen in the calibration data can be identified; as an abnormal condition. From an operational perspective an abnormal condition may be a process upset that requires human intervention, e.g., process drifts away from normal operation and noisy data due to faulty instruments.

An example for faulty instrument detection and diagnosis is illustrated here. The field measurements and model predictions over a two-day period are shown in Fig. 3. Looking at the field measurements, the flow rate on circuit A is highly noisy (possibly a faulty instrument), while the flow rates on circuit B, TDIs, and Tis are all very stable. In this case, it was identified that the noise was due to an instrumentation issue. However, a leaking circuit or real thermal anomaly would also have been quickly identified.

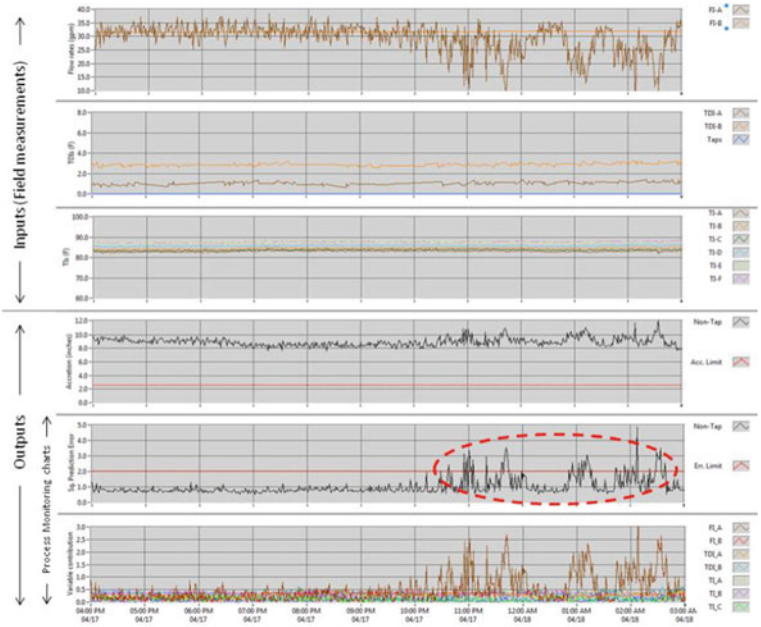

Fig. 3 Abnormal outputs encircled in red dotted line (Color figure online)

Refractory Structural Assessment

Detailed monitoring of the state of the tap-hole during operation can support the more economical operation of the furnace, with reduced downtime and better usage of tap-hole refractory. The best outcomes for furnaces can be achieved when detailed monitoring is combined with a good underlying refractory design, maximizing refractory life and minimizing operational difficulties.

The design of furnace refractory is often based on experience, "rules of thumb," and hand calculations. These methods can be effective at capturing the approximate behavior of the refractory in a furnace, especially the behavior of a single course, assuming it is unaffected by the movement of adjacent courses, other structures, or other parts of the furnace. However, the interaction between courses and the complex relationship between bricks and expansion joints cannot be captured. A 3D structural refractory assessment offers a comprehensive approach to evaluate the performance of a hearth design, with the ability to simulate scenarios and observe the impact of the complex interactions that occur due to differential thermal and mechanical loads in the hearth.

Assessment Methodology

Hatch has developed a methodology for capturing the 3D behaviour of refractory systems, including

- Brick–Brick and Brick–Mortar interactions,
- Gap opening between bricks,
- Closure of expansion joints,
- 3D elastic–plastic behavior of ramming materials, and
- Brick crushing, cracking, and creep.

By capturing all these effects, it is possible to understand how the bricks will move and interact during heating and operation, and identify possible refractory failures such as gap opening, causing infiltration; brick failure, causing instability; and expansion joint closure, causing excessive stress in the refractory system and/or furnace shell.

Case Study—Electric Arc Furnace

Hatch assessed the impact of a new hearth refractory design on a ferronickel electric arc furnace (EAF). The refractory changes were seen as minor as shown in Fig. 4 (different refractory materials with similar composition, addition of mortar joints in the wash zone, change of expansion joint material from card to pitch-impregnated paper, and minor geometric changes), so only minor changes in the refractory behavior were expected.

To evaluate the impact of the changes, Hatch assessed both the existing and new refractory designs so that comparative assessments between the two designs could be performed.

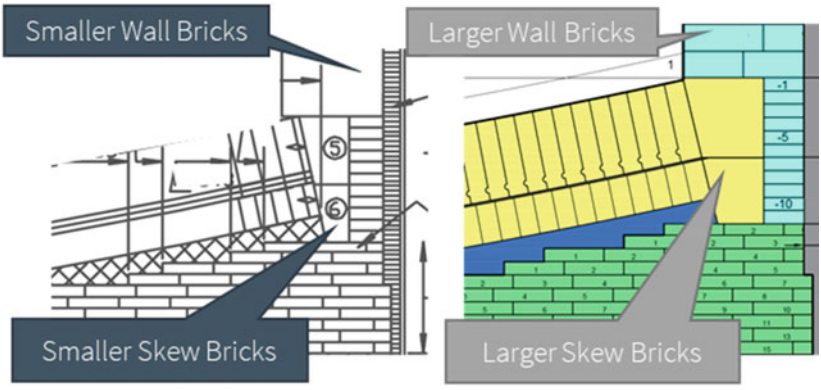

Fig. 4 Geometric design changes between (L) original design and (R) new design

Assessment of Hearth and Skew Bricks

The skew bricks are critical for transferring the load from the hearth to the wall of the refractory system, and ultimately the shell. In the original hearth design, the expansion allowances of the hearth and the refractory bricks were oriented such that load was transferred from the shell to the hearth via the skew brick, resulting in a tight hearth, as seen on the left in Fig. 5. Conversely, the expansion allowance in the new design did not align the expansion between the hearth and the skew brick. As a result, load was not transferred effectively in the new design, and the confinement of the hearth was reduced (Fig. 5 Middle). If this new hearth design had been implemented, it is likely that the furnace would have experienced significantly more infiltration of the hearth than the existing design.

Based on the findings of the assessment, the relative expansion allowance in the hearth and the skew bricks was revised, resulting in a design that provided improved hearth confinement (Fig. 5 Right). The final expansion design of the hearth was not as high as in the original design, but additional assessments of the new design showed that the hearth was expected to remain tight even if the installation or process details were slightly changed, minimizing infiltration.

The same incompatibility between the hearth and the skew bricks would have introduced additional loads into the skew bricks, seen in Fig. 6 Left versus Middle. In this scenario, the skew bricks may have crushed due to the expansion load, leading to even lower confinement, higher infiltration, and progressive failure of the refractory system; this could have significantly limited the campaign life of the refractory, and caused operational issues and production losses through increased stoppages for refractory repairs. By adjusting the expansion design, the stress in the skew brick was reduced so that crushing was not expected (Fig. 6 Right).

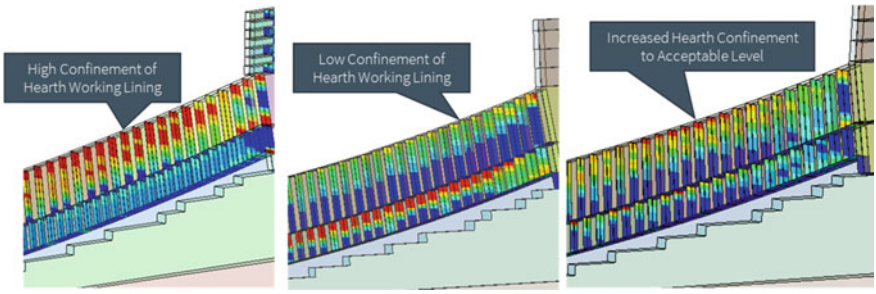

Fig. 5 Confinement of the hearth working lining in (L) original design, (M) initial new design, and (R) final new design

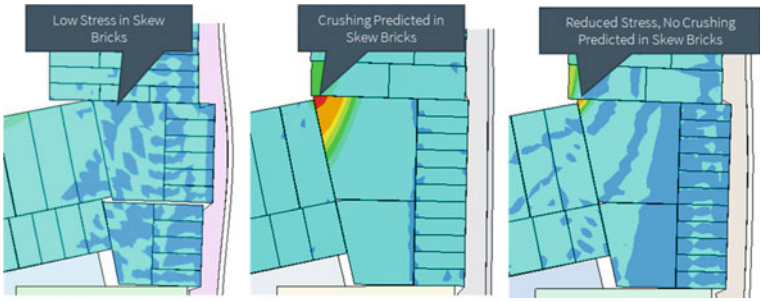

Fig. 6 Stress in the skew bricks of (L) original design, (M) initial new design, and (R) final new design

Ring Beam Assessment

Refractory structural assessments can also be used to inform design choices. For instance, in the same EAF discussed above, the client was considering installing a ring beam at the roof of the furnace to increase the confinement pressure in the furnace wall by transferring the weight of the furnace roof to the refractory wall, instead of the shell.

In general, determining the impact of a ring beam on a refractory system can be done using hand calculations to determine the impact of the additional load on the wall refractory. However, in this application, concerns had been raised about the impact that the additional load would have on the skew brick and the wall in the skew brick area; given the 3D nature of the refractory loads in this area and the interaction between the skew brick, wall, and hearth, hand calculations could not assess all impacts that this loading could produce.

By comparing the behavior of the refractory with and without the ring beam, the structural assessment was able to demonstrate that the addition of the ring beam would not negatively impact the behavior of the bricks in the wash zone and skew area (see Fig. 7). Therefore, the client was able to move forward with the ring beam

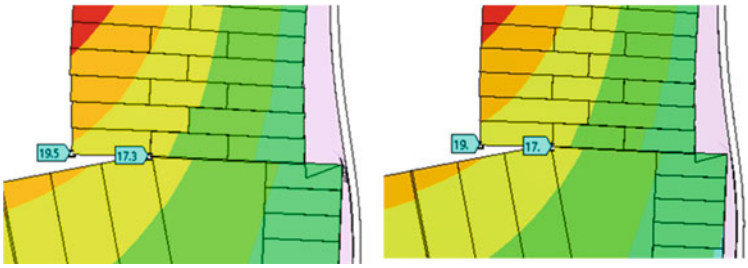

Fig. 7 Movement of the skew and wash zone bricks in mm (L) without and (R) with a ring beam installed

design in the roof area with confidence that it would not cause issues in other areas of the hearth.

By performing a structural assessment of the refractory, it was possible to identify that apparently minor changes in the expansion design of the hearth can lead to significant changes in refractory behavior. Even more critically, the assessment allowed the long-term negative campaign life and operational impacts of the refractory changes to be understood and alternate details developed.

Conclusion

Extreme thermal cycling and 3D heat transfer effects in the tap-hole region put this critical part of the furnace hearth refractory system under particularly aggressive conditions. The refractory condition in the tap-hole region is frequently the limiting factor on campaign life. Hence, developing well-performing advanced refractory designs and high-fidelity monitoring tools using advanced sensors, data collection/processing, multivariate statistical modelling to gather insights from the collected data for the tap-hole condition are critical to the safe operation of a furnace and achieving business objectives. Monitoring the refractory wear in the tap-holes is key to achieving extended tap-hole and hearth campaign life by informing operation and maintenance plans. Two applications of multivariate statistical models were presented here to inform operation and maintenance plans. First, the application of a soft sensor for evaluating the sidewall accretion condition on an operating furnace, thus allowing the operators/engineers to monitor sidewall integrity. Second, the ability of the accretion monitoring system to detect and diagnose abnormal conditions, e.g., conditions arising from faulty instruments were highlighted.

Refractory structural assessments can also be used for a variety of purposes to extend the campaign life of lining and minimize operational difficulties. They allow issues with refractory to be identified, including interactions between different refractory courses or structures that cannot be captured by traditional hand calculations. Furthermore, the assessment can be used to develop design changes to avoid fatal flaws or improve performance during the initial design phase, minimizing the cost of altering the design.

Refractory structural assessments can also be used to study the impact of other furnace changes on the hearth structure, such as the application of new loads or alterations to the furnace shell design. This can help operators reduce the risk associated with upgrades and relines, even if the operator has no experience with the new design or reference to use for comparison.

Slide Gate Technology for Slag Tapping

Goran Vukovic

Abstract With environmental, energy-saving, and legislation considerations becoming increasingly important, there is a need for a major improvement in slag handling. The metallurgical industry is directing its efforts into minimizing and processing the slags to achieve sustainable development and a circular economy. An important pillar for the advanced slag treatment is an automated and smooth tapping operation. A well-functioning tap-hole is an essential requirement for stable melting/refining processes as well as for reliable smelter operation. Slag should be tapped from the furnace balancing between production rate, capacity of the downstream vessels, and safety of the operators. In stationary vessels, tapping flow rate and slag flow behavior are dependent on conditions in the furnace (e.g. pressure, bath level, and liquid properties) as well as on tap-hole geometry and its wear level. In conventional slag tapping there can be challenges in maintaining a steady flow. The S-TAP Slag Slide Gate Technology is a solution that enables an accurate regulation of the slag tapping flow rate and quick reaction by tap-hole closing. This implies controlled and steady slag flow, minimized splashing around the tap-hole surroundings, improved safety due to an immediate tap-hole closing in case of an emergency, and brings a higher degree of automation in a metallurgical plant. A vision towards fully automated tapping is also presented in the paper.

Keywords Slide gate · Slag tapping · Flow control · Automation

Introduction

Metallurgical slags are produced in the pyrometallurgical process in quite large amounts, and if not properly treated and utilized, they are a large source of waste [1]. A target of the current metallurgical industry is to recycle and utilize all their by-products, to close the sustainable production loop, and to reach zero emissions and zero waste [2, 3]. Use and recycling of the steel industry's slags have increased

G. Vukovic (✉)
RHI Magnesita GmbH, Kranichberggasse 6, 1120 Vienna, Austria
e-mail: goran.vukovic@rhimagnesita.com

J. D. Steenkamp et al. (eds.), *Furnace Tapping 2022*, The Minerals, Metals & Materials Series, https://doi.org/10.1007/978-3-030-92544-4_26

significantly over the last 20 years due to innovative technology developments and synergies with other industries which have brought the steel industry, for example, close to its goal of zero waste to landfill [3, 4]. More than 400 million tonnes of iron and steel slag are produced worldwide each year which are mainly used for the manufacturing of high-quality products for the cement and building materials industries, aggregates for road construction, fertilizers, hydraulic engineering, etc. [3].

However, the non-ferrous metals (NFM) industry is still challenged with achieving efficient utilization of large quantities of generated slags. Generally, due to process complexity as well as lower metal content in concentrates treated relative to those feeds in iron ore processing, a large amount of slag is generated from NFM production. As an illustration, to produce one tonne of copper or ferro-chrome, approximately 2.0–3.0 tonnes of copper slag [5] and 1.1–1.6 tonnes of ferro-chrome slag [6], respectively, are generated as a by-product material. A conservative estimation is that more than 50 million tonnes of NFM slag are produced worldwide each year [7]. Copper slags are usually considered as a waste and are typically noted by a producer by reference to the final copper content [8]. Forecasts show that, for example, copper demand could exceed 35 million tonnes annually by 2030, increasing to 50 million tonnes annually by 2050 [9]. Large and increasing quantities of slag are being produced and disposed of near the metallurgical plants [8]. With environmental, energy-saving, and legislation considerations becoming increasingly important, there is a need for a major improvement in slag handling. The metallurgical industry is directing its efforts into minimizing and processing the slags in order to achieve sustainable development and a circular economy [1–9]. This may be achieved through multi- or cross-disciplinary approaches by changing the process paradigm by designing new, novel, and integrated solutions.

The ability of a solidified slag to be a component of an environmental-friendly product is a function of its chemical and physical properties (e.g. chemical composition, the crystalline phase assemblage, and the particle size distribution). Even though slags from different smelters may have somewhat different compositions, most NFM slags consist of similar phases that vary by relatively small amounts [1, 7]. A good understanding of the properties of these slag phases would enable adjustment of furnace operating parameters and slag tapping conditions to improve and optimize downstream post-tap-hole treatment of the slag and to facilitate its final application [10]. An important pillar for the advanced slag treatment in the early metallurgical stage is an automated and smooth slag tapping operation.

As has been stated: “Tap-holes are key for furnace success”—a well-functioning slag/metal tap-hole is an essential requirement for stable melting/refining processes as well as for reliable smelter operation over time [11]. Tap-holes are subjected to severe operating conditions (thermal and mechanical load, erosion, and chemical attack) and consequently are typically the most regularly maintained part of the furnace [12]. The tapping procedure covers the following activities: opening, tapping, and closing. To open a tap-hole, the commonly used practice is to use lancing or in some cases, drilling and in many cases a combination of both. Closing is done manually using a clay stopper (mud plugs) or with a machine (mud gun). Manual tap-hole closing

may seem relatively simple but requires a direct interface of the operator with a hot tapping stream (safety issue). On the other hand, machine-closing if incorrectly controlled may lead to a destructive (but often hidden) action on the tap-hole and furnace surroundings—excess clay may increase the amount of gas emitted around the tap-hole clay (damage to the furnace lining and tap-hole channel), but on the other hand, use of an insufficient amount of clay can mean poor tap-hole closing (safety issue) [11, 13].

Continuous progress in tap-hole design, tapping equipment, and related monitoring systems are key factors to meet strategic operational performance. Selecting a suitable tap-hole design concept based on on-site experience combined with advanced computer simulations is one of the most important tasks in the refractory lining engineering process for a furnace, as a reliable and safe operation depends on the overall tap-hole performance [11–13]. Besides tap-hole refractory design, there are constant enhancements reported in the literature in tap-hole cooling practice [14, 15], improvements of tapping devices and equipment [16–18], and in the integration of different monitoring technologies [19, 20]; all must not only provide a smooth and safe tapping procedure but also allow for easy maintenance work.

While some tapping equipment, devices, and systems have already been introduced, further effort is required to improve the safety and productivity of tapping operations. In the flow control sector, RHI Magnesita with its Technology Centre, INTERSTOP®, provides the entire life cycle for systems & solutions: from the development of new systems to marketing, customized engineering, commissioning as well as after-sales support for steel and non-ferrous industries [21–24]. RHI Magnesita has also developed an innovative solution to open and close a slag tap-hole with a slide gate system which allows also an accurate control of the tapping process.

This paper presents the new slide gate system (S-TAP) for slag tapping in detail, shows the advantages and benefits in operation, as well as discusses a further developmental vision towards fully tapping automation.

Operator Slag Tapping Challenges

Slag should be tapped from the furnace balancing among production rate (accumulation in the furnace may affect the metal recovery, production yield, or potentially lead to dangerous conditions for workers in the tapping area), capacity of the downstream vessels (for example, too high a tapping rate may accidentally divert slag into unwanted areas, possibly causing damaging of the surrounding equipment and also contribute to loss of production), and the safety of the operators. In stationary vessels, the tapped flow rate and its flow behavior are strongly dependent on conditions in the furnace (e.g. pressure, bath level, and liquid properties) as well as on tap-hole geometry and its wear level. These conventional tapping procedures can imply potentially uncontrolled and unsteady flow of hot slag, splashing around the furnace surroundings (safety issue and production losses), and possible lack of options for an immediate tap-hole closing (e.g. in case of an emergency).

Commonly, operator slag tapping challenges reported in the literature [10–20] may be summarized as follows:

- Slag tap-holes are considered as a so-called "black box" where the actual operational status is mainly estimated by the experience of furnace operators.
- No supplier presently provides complete tap-hole solution due to its design and function complexity in terms of design, refractory, equipment, monitoring, and maintenance.
- Slag tapping is performed without real and accurate flow regulation and control, potentially causing issues in the furnace, as well as in downstream processes/vessel, slag splashing, and safety concerns.
- A lot of manual handling work and hence undue exposure of the operators to the harsh environment on the tap-hole platform where unpredicted incidents may occur (safety issue).
- Potential lack of fast tap-hole closing (e.g. in case of an emergency).
- Uncontrolled metal carryover.
- Decreased yield by leaving a high amount of slag in the furnace.

S-TAP—Slide Gate Solution for Slag Tapping

The S-TAP slide gate technology is a solution that enables accurate regulation of the slag tapping flow rate and quick reaction for tap-hole closing [25]. This implies controlled and steady flow of hot slag, minimizing splashing around the tap-hole surroundings, and improved safety due to an immediate tap-hole closing in case of an emergency. Although at some smelters, space constraints around the tap-hole area may define appropriate tapping equipment, this device can find application in such cases due to its compact design (Fig. 1). It is a high-performance device with considerable potential, allowing safe, fast, and simple operation and handling. Short downtimes of the furnace and consequential savings on energy are a result of this solution.

The S-TAP slide gate is a one-plate, linear, hydraulically driven system [25]. There are two different sizes available, S-TAP70 and S-TAP90 with some key parameters presented in Table 1.

Integration of the S-TAP slide gate at a facility does not normally require expensive structural modification on the existing installation and may be implemented on a vertical as well as an inclined steel shell as well as be fitted onto almost any tap-hole design (Fig. 2). The cold side of the copper cooling element or copper block should be adjusted to host the base plate and enable smooth moving of the insert plate over its surface (Fig. 3). The base plate is designed to fit on the copper cooling element or copper block and is fixed to the furnace steel shell via four supports. The slide gate housing (frame) is bolted onto the base plate through four tension elements. A heat shield mounted on the slide gate frame protects the slide gate and the hydraulic cylinder from slag splashing and heat radiation from a launder (Fig. 3).

Fig. 1 S-TAP installation

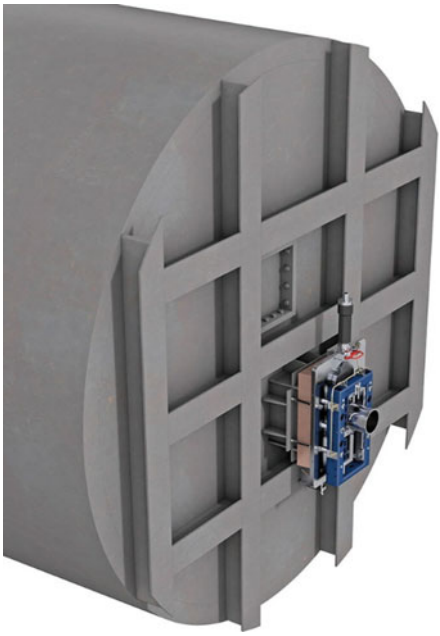

Table 1 S-TAP70 and S-TAP90 parameters

Description	S-TAP70	S-TAP90
Dimensions (incl. hydraulic cylinder), L × W × H [mm]	820 × 340 × 1587	870 × 455 × 1830
Weight [kg]	450	710
Maximum tap-hole diameter [mm]	Ø110	Ø230

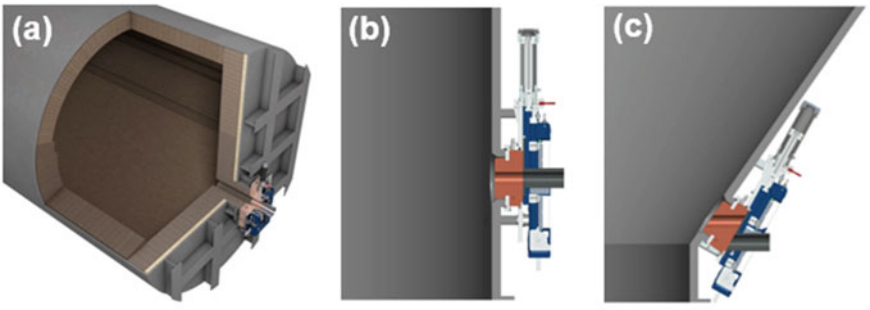

Fig. 2 S-TAP installation: **a** vertical installation on the tap-hole with refractory lining concept and copper cooling element or copper block; **b** vertical installation on the tap-hole with slag freeze lining concept and copper block; **c** inclined installation on the tap-hole with slag freeze lining concept and copper block

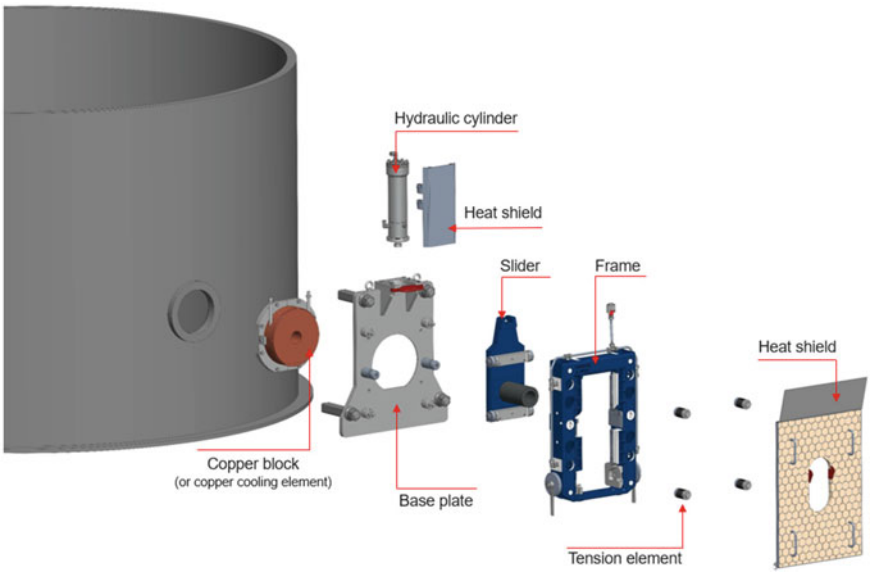

Fig. 3 S-TAP main components

The S-TAP slide gate is a compact system, engineered with only two main components: the housing (frame) and the slider (Fig. 3). The user-friendly design of the slide gate allows a quick and simple exchange of the components. The slider can be completely lifted vertically downward and removed if the guides are placed into the appropriate (slider changing) position (Fig. 4). If needed, the outer nozzle can easily be changed by removing it from the slider. The insert plate can be exchanged by swiveling the movable slider outwards over the rollers, rails, and guides that also function as a stroke stopper (Fig. 4). Following the plate exchange, the slider is swiveled back into the normal working position (Fig. 4). For tap-hole maintenance, the S-TAP may be easily dismounted to enable the repair of the tap-hole channel (Fig. 3).

The defined tension force of the system is generated through four pre-set tension elements, which are equipped with high-temperature-resistant spiral disc springs and integrated into the housing (Fig. 3). The spring-loaded housing presses the slider and simultaneously the insert plate and nozzle against tap-hole copper block or copper cooling element. The design ensures the tension is distributed evenly over the tap-hole. The contact surface between the copper block and the insert is large enough and symmetric to enable safe operation and overlapping of the interface of the copper block and insert plate with the slide gate in the closed as well as in the open position (Fig. 2). Hydraulically driven movement of the slider, together with the insert plate over the copper block into the working position, activates the tensioning of the system. Normally, tension is automatically applied over four rollers that roll onto a ramp of a rail when moving the slider (Fig. 5).

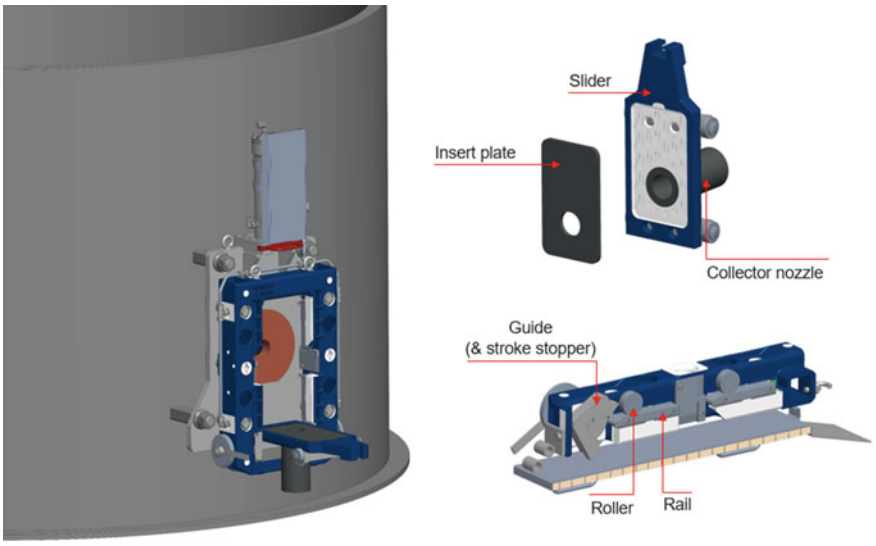

Fig. 4 S-TAP main components

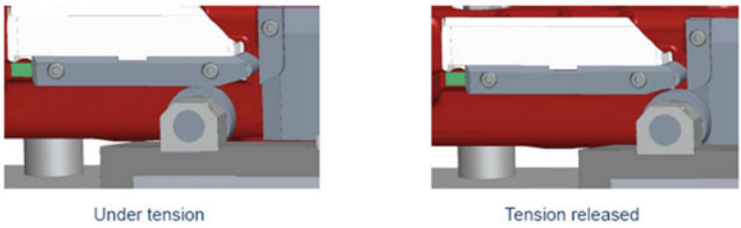

Fig. 5 S-TAP automatic system tensioning

The material of construction for the insert plate and the collector nozzle is determined according to the slag properties (Fig. 4). The outer nozzle, also called the collector nozzle, gives a concentrated slag stream and minimizes slag splashing. The S-TAP components subjected to regular maintenance (insert plate, collector nozzle, and slider) are delivered ready to use to allow for a quick change out. No tools are needed and there is no additional machining work in a workshop required. Therefore, the position of the system components and their tolerances are exactly defined.

The S-TAP is a hydraulically driven system, and its position (open, close, and throttle) is actuated from the operator room or from the tapping platform by a set of push-button controls, with control of the slag gate being an operator-controlled task (Fig. 6). A combination of the feedback from the tapping as well as from the downstream process is used from the furnace operator to decide about preformed action on the slide gate. The S-TAP system operational overview is presented in Fig. 6. The hydraulic cylinder is directly mounted at the slide gate and connected to

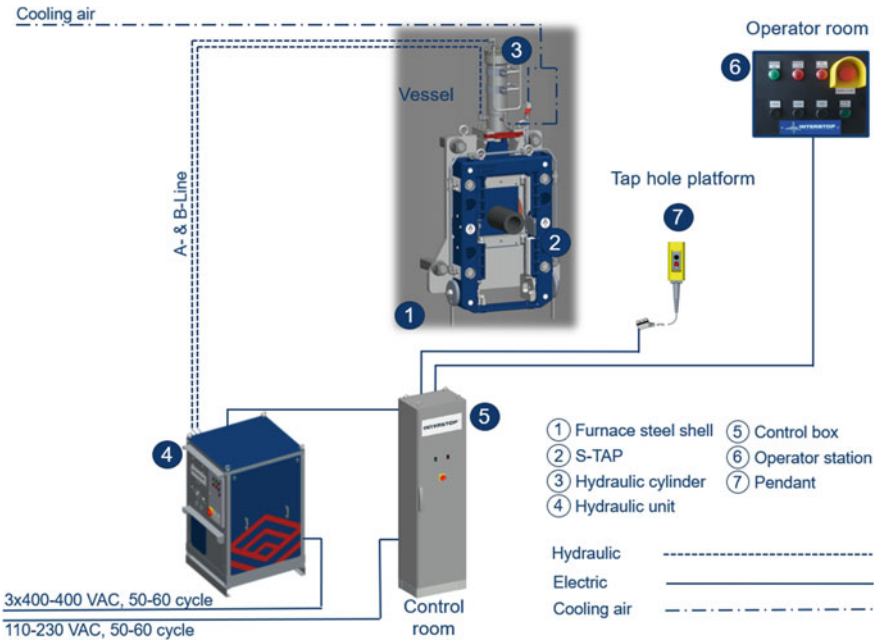

Fig. 6 S-TAP system operational overview

the hydraulic unit. Cooling air is applied for the cooling of tension elements in the slide gate frame.

Benefits of S-TAP Application

Due to its robust design, the S-TAP slag slide gate system may be integrated with other standard tapping equipment and devices such as copper cooling elements, a tap-hole drilling machine, and lances. Its compact design and installation directly on the tap-hole at the furnace steel shell enable the replacement of a mud gun with advantages in investment costs and required space. Remotely controlled, hydraulically driven, the slag slide gate system is a solution that enables an accurate regulation of the slag tapping flow rate and quick reaction by tap-hole closing in case of emergency. S-TAP can be operated in vertical and horizontal positions and is suitable for any furnace type (e.g. slag cleaning furnace, smelting furnace, converting furnace, refining furnace, holding furnace, and many others) with minor modifications. The benefits of S-TAP installation may therefore be summarized as follows.

General

- S-TAP slide gate system for slag tapping can be operated in vertical and horizontal positions and is suitable for any furnace type.
- It is compatible with other tapping equipment and devices.

Increased safety standard

- User-friendly design for simple, fast, and safe operation.
- Rapid tap-hole closing (e.g. in case of an emergency).
- Reduced manual handling work and hence exposure of the operators to the harsh tap-hole environment.
- Higher degree of automation—the first step towards tapping automation

Improved process control

- Accurately controlled and steady slag flow for each tapping condition.
- Regulated slag tapping rate for downstream process/vessels.
- Maintaining appropriate drain of the furnace to improve metal recovery and yield (unwanted accumulation in the furnace is avoided).
- Collector nozzle leads slag directly into launder (reduced splashing/slag losses), and improves the guidance of different tools and devices directly through the slag tap-hole channel (e.g. oxygen lances and drills).
- Can minimize metal tapped with slag using the EMLI sensor (refer later in the text).

S-TAP Installation and Operation

In 2018, RHI Magnesita was invited to design and supply a slide gate for the slag tap-hole on a stationary slag cleaning furnace used to treat slag for metal recovery at a European plant; tapped slag was to be directed to granulation. The unit (model S-TAP70) was commissioned the following year. The granulated slag is currently mainly supplied for sand blasting, but considerable R&D has been carried out to identify other uses.

The furnace design included shell cooling providing a slag freeze lining. The slag is tapped out through the tap-hole channel and copper block to a water-cooled launder. The copper block without any applied cooling has an outer surface temperature between 600 and 750 °C during tapping. Tapped slag at 1200 °C is typical of NFM iron silicate slags. The slag flow was initially controlled by the slag valve which created a number of issues to the operators over time and affected attaining smooth tapping operation. The problems were evaluated as follows: inadequate tensioning in the slide gate valve causing the sticking of its mechanism and avoiding slag flow regulation, as well as closing and opening of the tap-hole when needed; inappropriate integration of the hydraulic cylinder that moves the valve; frequent damaging of the copper block by tap-hole opening by drilling due to lack of slag valve outer nozzle which guides the drill correctly through the copper block channel.

The corrections to the initial slag valve included a more robust design of a new system located in the challenging environment with a long lifetime of the components and user-friendly design for safe, fast, and simple operation and handling as well as space limitations in the tap-hole area, were the key requirements.

The slag slide gate S-TAP70 was successfully commissioned and fully integrated with other devices and equipment on-site (Fig. 7). The interface with the furnace is the above-mentioned copper block, which is not cooled, showing the outer surface operational temperature between 600 and 750 °C and has about 10 weeks in operation before it is changed. The designed tensioning system enables optimal tightness between the copper block and slide gate for smooth sliding of the insert plate over the copper block surface. No slag leakage or any S-TAP handling and operational issue is identified. Operational figures and S-TAP system parameters are presented in Table 2.

It is a big advantage to be able to fully open the slag gate to allow quick filling of the launder before freezing can occur and then to throttle the slag flow back to optimise the granulation process. Throttling flow regulation mode is mostly applied at the beginning of tapping as the slag level in the furnace is typically high. Accurate control of the slag flow is of utmost importance for efficient water granulation

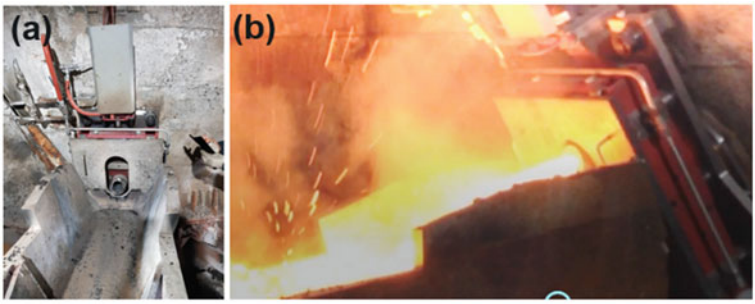

Fig. 7 S-TAP **a** installed; **b** in operation

Table 2 Operational figures and S-TAP parameters

Description	Unit	Value
Tap-hole diameter	mm	80
S-TAP70 dimensions (incl. hydraulic cylinder), L × W × H	mm	820 × 340 × 1587
S-TAP70 weights	kg	450
Slag flow rate	t/h	80–140
Tapping duration	h	1
Tapping frequency	tap/day	3–4
Tapped slag	kt/year	120
Slag tapping temperature	°C	1200

treatment. Additionally, this system offers a secure cut-off in case of an emergency during tapping and removes the need for operators in this area. A drilling machine is successfully integrated for removal of any frozen slag after the opening of the S-TAP, but in some cases, if not working properly lancing is also applied. The S-TAP position (open, close, and throttle) is actuated from the operator room by a set of push-button controls.

The collector nozzle, insert plate, and slider are the S-TAP components exposed to wear. Oxygen lancing—when applied in cases when drilling is inadequate for tap-hole opening—may impact the life of the insert plate and the slider and cause their premature changeover. Otherwise, their changing is performed by planned relining stoppages; in this circumstance, it is two times per year, after about 60 kt of tapped slag. The most wear is presented on the collector nozzle where the slag starts to freeze, and the flowing slag destroys the nozzle, especially its lower part. Collision of the outer nozzle with frozen slag in the launder just below slide gate during its closing movement is often the reason for the mechanical damaging, and nozzle early changing. Therefore, the wear of the collector nozzle is reduced compared to the insert plate and the slider, and a life of about 10 days is obtained which means about 4.5 kt of tapped slag. Nevertheless, reported maintenance results show that the components exposed to wear may be changed within one hour in hot furnace conditions which indicates simple and fast handling during maintenance.

Further Developments—Fully Automated Tapping Platform

Continuously increasing requirements with respect to safety, process reliability, and product quality in the NFM industry are also driving the need not only for the regulation of the tapping process but also for its full automation and continuous monitoring. Diagnostics systems and devices such as metal content detection in slag tapping stream are considered as important contributors for reliable tapping technologies. The tap-hole area is a place where critical tasks are carried out by operators under very harsh conditions. Heat, dust, and time pressure can influence the performance quality, in addition to a constant issue with safety. Developments are ongoing, working towards a fully automated tap-hole platform.

Process Automation/Robotic Support for Slag Tapping

As the tap-hole area is one of the areas with the highest safety concerns where “the man meets the hot slag”, hence, automated and remotely controlled tapping systems and devices are nowadays of utmost importance. While some tapping equipment have already been introduced, further effort is required to realize such an ideal working environment—a fully automated tap-hole area without the presence of operators.

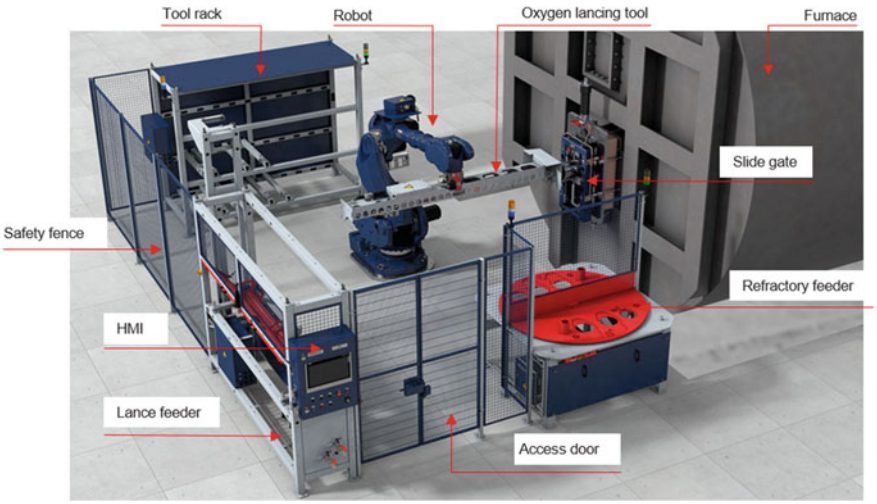

Fig. 8 RHI Magnesita's vision of the robotic support for slag tapping

For slag slide gate systems, solutions are under development at the tapping platform that allow for manual and robotic operation (Fig. 8). The full package contains the S-TAP, fully equipped with a hydraulic system and devices, all being operated by a customized robotic system.

However, the challenge is that the robot requires different designs to allow a high degree of automation in the tapping area and hence, a re-examination of current practices may be necessary for some process steps. Also, a robot implementation at the tapping platform may require a certain amount of space, which may not be always available at a plant where conventional manual tapping practice is in place.

Robotic application in slag tapping practice would be used for tap-hole opening with automated oxygen lancing of the tap-hole channel. Also, automated sample taking, temperature measurement as well as checking the status of the tap-hole may be performed. Coupling and uncoupling of different devices, sensors, and media is part of the automation.

Applying such devices and add-ons to the slag slide gate ensures automatic handling by robots, and incorporates smart features resulting in a number of benefits:

- Increased safety for employees;
- Reproducible quality level of task;
- Prevention of breakthroughs by increasing process stability;
- Reduction of production costs through constant monitoring of system;
- Increased production efficiency;
- Integration of "smart" solutions for better planning of maintenance;
- High degree of automation (minimize presence of people at the tap-hole area).

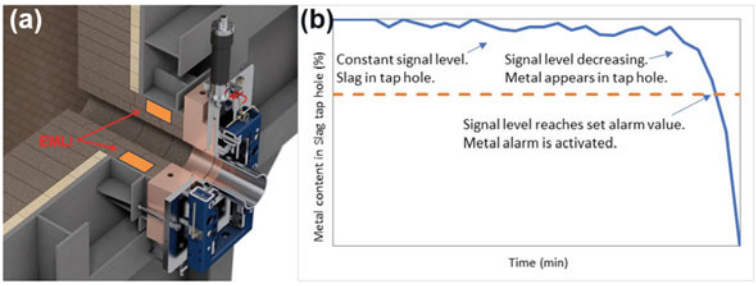

Fig. 9 **a** Sketch of possible EMLI sensor integration in the tap-hole equipped with S-TAP. **b** Example of EMLI-MetalSlag output signal

Monitoring of Tapping Operation

The EMLI-MetalSlag (Electromagnetic metal detection system in slag tapping streams) developed by the Agellis Group of RHI Magnesita can detect by an electromagnetic signal that changes when some amount of metal is present in the tapped slag stream. This unit can withstand higher heat exposure (up to approximately 500 °C) compared with other available systems. The unit is based on electromagnetic technology, which is an operator-safe, accurate, and reliable monitoring method. The EMLI sensors are so located that they enable early detection of the metal in the slag tapping stream, but the final design can depend on the overall tap-hole design as well as on process aspects (Fig. 9a). The sensors are connected via a flexible cable to the electronic components that can continuously monitor the slag flow during tapping, and provide an alarm signal having a fast response time at the onset of detection of metal in the stream. This signal can be used to immediately end tapping by the S-TAP unit, while also giving visual and audible alarms (Fig. 9b). This is beneficial to the operators as they no longer need to visually monitor the operation to detect metal. The monitoring of the tapped slag stream is indicated by a displayed signal, which can also show the gradual onset of metal in the stream (Fig. 9b). In this way, unwanted situations in downstream processes and/or vessels in terms of operator safety and damaging of equipment can be avoided.

Process Traceability and Data Mining

Each furnace tapping process may be recorded in the system over time. This enables operators to follow up on the tapping performance for any specific charge, which is an important quality assurance function. Also, as vessel tapping data is collected continuously in the database, the information is available for any process or production optimization and improvement purposes.

Conclusion

From the first installation, it can be seen that the S-TAP slide gate system developed for slag tapping mainly in the non-ferrous metals industry meets operational and safety requirements. This technology provides an accurate regulation of the slag tapping flow rate and quick reaction by tap-hole closing. This implies controlled and steady slag flow, minimized splashing in the tap-hole surroundings, improved safety due to an immediate tap-hole closing in case of an emergency, and brings the next level of slag tapping in a metallurgical plant. Further innovations, initiatives, and new developments are ongoing, resulting from the exciting opportunities automation and digitalization are offering.

References

1. Reuter M et al (2004) Recycling and environmental issues of metallurgical slags and salt fluxes. Paper presented at the II international conference on molten slags fluxes and salts, The South African Institute of Mining and Metallurgy, 2004
2. Sykes C et al (2020) Report: zero emission copper mine of the future. The Warren Centre for Advanced Engineering. Zero Emission Copper Mine of the Future (usyd.edu.au).pdf
3. World Steel Association (2020) Public policy paper: steel industry co-products. World Steel Association. https://www.worldsteel.org/publications/position-papers/co-product-position-paper.html
4. Horckmans L et al (2017) Chromic: new processes to recover metals from carbon steel, stainless steel and ferrochrome slags. Paper presented at the the 9th European slag conference Euroslag 2017, Metz, France, 11–13 October 2017
5. Sim S, Jeon D, Kim DH, Yum WS, Yoon S, Oh JE (2021) Incorporation of copper slag in cement brick production as a radiation shielding material. Appl Radiat Isot 176:109851. https://doi.org/10.1016/j.apradiso.2021.109851
6. Niemelä P et al (2007) Production, characteristics and use of ferrochromium slags. Paper presented at the Infacon XI, New Delhi, India, 18–21 February 2007
7. Wang GC (2016) The utilization of slag in civil infrastructure construction. Woodhead Publishing, Cambridge
8. Sánchez M, Sudbury M (2013) Physicochemical characterization of copper slag and alternatives of friendly environmental management. J Min Metall Sect B-Metall 49(2) B:161–168
9. Kulczycka J, Lelek Ł, Lewandowska A, Wirth H, Bergesen JD (2017) Environmental impacts of energy-efficient pyrometallurgical copper smelting technologies. J Ind Ecol 20(2):304–316
10. Fleischanderl A et al (2018) Dry slag granulation—the future way to granulate blast furnace slag. Paper presented at the AISTech conference proceedings PR-374-192
11. Nelson LR et al (2014) 'The tap-hole'—key to furnace performance. Paper presented at the SAIMM furnace tapping conference, Misty Hills Country Hotel, Muldersdrift, 27–29 May 2014
12. Kreuzer DR (2018) Numerical simulation—a tap-hole refractory design study. Paper presented at the SAIMM furnace tapping conference, Nombolo Mdhluli Conference Centre, Kruger National Park South Africa, 15–16 October 2018
13. van Beek WSB (2014) An overview of the design, operation, and maintenance practices relating to tap-hole management of a PGM smelting furnace. Paper presented at the SAIMM furnace tapping conference, Misty Hills Country Hotel, Muldersdrift, 27–29 May 2014
14. Dougall IMC (2014) Water-cooled tap-hole blocks, Paper presented at the SAIMM furnace tapping conference, Misty Hills Country Hotel, Muldersdrift, 27–29 May 2014

15. Belford BN et al (2018) Development, installation, and operation of a full-copper, deep-cooled slag tap-block for a six-in-line copper slag-cleaning electric furnace. Paper presented at the SAIMM furnace tapping conference, Nombolo Mdhluli Conference Centre, Kruger National Park South Africa, 15–16 October 2018
16. Essack SC (2014) Closing your slag tap-hole. Paper presented at the SAIMM furnace tapping conference, Misty Hills Country Hotel, Muldersdrift, 27–29 May 2014
17. Morales D et al (2018) Tap-hole opening: advances and improvements. Paper presented at the SAIMM furnace tapping conference, Nombolo Mdhluli Conference Centre, Kruger National Park South Africa, 15–16 October 2018
18. Dienenthal A (2014) A short history of the development of tapping equipment. Paper presented at the SAIMM furnace tapping conference, Misty Hills Country Hotel, Muldersdrift, 27–29 May 2014
19. Persson F et al (2015) Electromagnetic slag detection system stabilizes furnace slag carryover and improves effective secondary metallurgy at Höganäs Atomizing Plant in Halmstad. Paper presented at the AISTtech conference—the 7th international conference on the science and technology of ironmaking, Cleveland, Ohio USA, 4–7 May 2015
20. Braun W et al (2014) Tap-hole monitoring technologies. Paper presented at the SAIMM furnace tapping conference, Misty Hills Country Hotel, Muldersdrift, 27–29 May 2014
21. Ehrengruber R, Bühlmann R, Schmidt V, Persson M (2021) Influence of the trends robotics and digitalization on ladle slide gate development. China's Refract 30(2):30–34
22. Gamweger K (2012) Slide gate systems for copper tapping. Paper presented at the 141st TMS annual meeting—3rd international symposium on high-temperature metallurgical processing, Orlando, Florida, 11–15 March 2012
23. Vukovic G et al (2020) Slide closure on the spout of a metallurgical vessel. US Patent US10,799,949B2. Granted on October 13, 2020
24. Manhart C et al (2017) Method and device for the detection of quantities in the outlet of a metallurgical vessel. EP Patent EP3326735B1. Granted on June 1, 2017
25. Vukovic G et al (2020) Sliding closure for a metallurgical vessel. Patent application WO2021144088A1. Filing date 11.21.2020

Tap-Hole Clay Technologies for Ferroalloy Reduction Furnaces

Tomás Moreira de Oliveira, Wagner Moulin-Silva, Humberto Chiaretti Bassalo, Aloísio Simões Ribeiro, and Modestino Alves de Moura Brito

Abstract Tap-hole clay is a very important material to seal tap-holes in ferroalloy reduction furnaces. Different types of this refractory are available for the ferroalloy industry and to decide which would be the most appropriate material may be a difficult task. This paper shows a comparison between the properties of four different types of tap-hole clays that were designed for ferroalloy furnaces, focusing on the application in metal tap-holes. The goals are to improve the knowledge regarding these materials and guide ferroalloy producers when deciding what type of tap-hole clay should be used. The analyzed mixes differ from each other mainly in terms of the type of aggregate (basic or non-basic) and type of binder (tar, resin, or synthetic oil).

Keywords Tap-hole clay · Reduction furnace · Ferroalloy

Introduction

Tap-hole clay is mainly known as a refractory material used to seal blast furnace tap-holes at the end of casting. However, it is also a very important material to seal tap-holes in other types of smelter operations, such as ferroalloy reduction furnaces. In blast furnaces, it should present three main functions [1]: (1) after plugging, assure the closure of the blast furnace tap-hole; (2) at the moment of casting, allow its drilling and assures a regular drainage of the hot metal and slag; and (3) contribute to the hearth refractory protection ("mushroom") in the tap-hole region. Although blast furnaces and ferroalloy reduction furnaces operate in a much different way, the functions of the tap-hole clay are the same for both.

Different types of tap-hole refractory mixes are available for the ferroalloy industry and to decide which would be the most appropriate material may be a difficult task. Differences, such as bonding type, may have significant impact on refractory properties, depending on what is chosen.

T. M. de Oliveira (✉) · W. Moulin-Silva · H. C. Bassalo · A. S. Ribeiro · M. A. de Moura Brito
RHI Magnesita, Vienna, Austria
e-mail: tomas.oliveira@rhimagnesita.com

J. D. Steenkamp et al. (eds.), *Furnace Tapping 2022*, The Minerals, Metals & Materials Series, https://doi.org/10.1007/978-3-030-92544-4_27

This paper shows a comparison between the properties of four different types of tap-hole clays that were designed for ferroalloy furnaces, focusing on the application in metal tap-holes. The goals of this study are to improve the knowledge regarding these materials and guide ferroalloy producers when deciding what type of refractory mix should be used. The analyzed mixes differ from each other mainly in terms of type of aggregate (basic or non-basic) and type of binder (tar, resin, or synthetic oil).

Experimental Procedure

Materials Tested

Table 1 shows the identification and description of each tap-hole clay tested in this study. All of them are currently in use in metal tap-holes of ferroalloy reduction furnaces and were brought from different manufacturing plants to be analyzed. NT is a tar bonded non-basic material from Brazil, BT is a tar bonded basic (magnesia based) material from Brazil, BO is an oil bonded basic (doloma based) material from USA, and NR is a resin bonded non-basic material from Argentina. The chemical analysis (based on ISO 12677) of these refractories can be seen in Table 2.

Table 1 Identification of tested tap-hole clays

Identification	Description
NT	Non-basic tap-hole clay bonded by tar
BT	Basic tap-hole clay bonded by tar
BO	Basic tap-hole clay bonded by synthetic oil
NR	Non-basic tap-hole clay bonded by phenolic resin

Table 2 Chemical analysis of tested tap-hole clays based on ISO 12677

Component	Amount (wt.%)			
	NT	BT	BO	NR
Al_2O_3	34	18	1	29
SiO_2	39	14	1	43
MgO	0	42	39	0
CaO	0	0	58	0
SiC + C	23	23	0	24
Others	4	3	1	3

Physical and Mechanical Properties

For physical and mechanical tests, samples were moulded in a press with 8.5 MPa in the shape of rectangular blocks with 160 × 40 × 40 mm^3 and then cured at 350 °C/5 h and coked at 1200 °C/5 h in resistance heated furnaces. The coked samples were involved by a bed of fine coke particles before heating to avoid carbon oxidation.

The tests of bulk density (BD) and apparent porosity (AP) were carried out according to the standard ASTM C20–00 (Reapproved 2005). Modulus of rupture (MOR) and cold crushing strength (CCS) according to ASTM C133–97 (Reapproved 2008).

Hot Modulus of Rupture

For hot modulus of rupture (HMOR), samples were moulded in a press with 8.5 MPa in the shape of rectangular blocks with 160 × 40 × 40 mm^3 and then cured at 350 °C/5 h in a resistance heated furnace. Samples were coked for 5 h before the tests at the same temperature of the HMOR (800, 1000, 1200, and 1485 °C) in resistance heated furnaces and were enveloped in nickel sheets to avoid carbon oxidation. Samples were tested in a three-point bending test according to the standard ASTM C583–05 (Reapproved 2009).

Thermogravimetric Analysis

The thermogravimetric analysis was carried out in a thermobalance METTLER TOLEDO HB43S. Green tap-hole clay samples of 50 g each were hand molded as a cylinder and put on the scale inside an electric furnace. The material was then heated at 3 °C/min from room temperature until 600 °C and kept at 600 °C for 3 h in air. The weight loss was measured every minute.

Curing Test

Tap-hole clay samples were molded in a press with 8.5 MPa to form a cylinder of 50 mm diameter and 50 mm height and were kept in a resistance heated furnace at 400 °C during 20 and 40 min in air. After heating, the samples were immediately removed from the furnace and CCS was measured after they were cooled to room temperature. This test, called curing test, has been important to evaluate the increase of tap-hole clay strength after fast heating [2].

Hot Plasticity

The hot plasticity test was carried out to estimate the plasticity of the tap-hole clays during heating. Cylinder samples of 50 mm diameter and 50 mm height were prepared and placed into a universal testing machine for hot testing (MTS MATERIAL TEST SYSTEM model MTS 810). From the beginning, the samples were compressed at 0.17 mm/min, while they were heated at 2.5 °C/min until 300 °C in air. The load demanded to compress the samples was measured over the test [2].

Extrusion Index Over Time

The tap-hole clay plasticity stability was measured over 180 days after production using the extrusion index test (standard ABNT NBR 9881). In this case, a special apparatus is used for the test, so that a certain quantity of clay is pushed by a piston under constant displacement rate (55 mm/min) through an orifice of standardized diameter for 30 s. The mould and tap-hole clay are at 50 °C during the test. The extrusion index is a pressure value, which consists of the force registered in a load cell attached to the piston after 30 s divided by the area of the orifice in which the sample has been extruded. The test method is schematically shown in Fig. 1 [3].

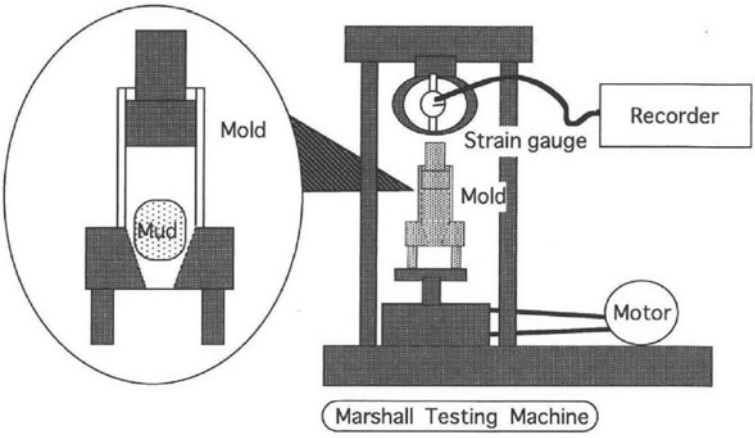

Fig. 1 Apparatus for measuring extrusion index of tap-hole clays [3]

Table 3 Tap-hole clays' physical and mechanical properties measured after curing at 350 °C/5 h and after coking at 1200 °C/5 h

After curing at 350 °C/5 h	NT	BT	BO	NR
Bulk density (g/cm^3)	1.90	1.98	2.67	1.98
Apparent porosity (%)	15.2	17.6	12.2	15.5
Modulus of rupture (MPa)	2.2	2.9	2.5	9.3
Cold crushing strength (MPa)	5	9	7	26
After coking at 1200 °C/5 h	NT	BT	BO	NR
Bulk density (g/cm^3)	1.83	1.89	2.77	1.88
Apparent porosity (%)	27.7	31.9	17.0	27.5
Modulus of rupture (MPa)	1.5	1.3	11.4	2.0
Cold crushing strength (MPa)	5	3	21	9

Results and Discussion

Physical and Mechanical Properties

Table 3 shows the tap-hole clays' physical and mechanical properties that were tested after curing at 350 °C/5 h and after coking at 1200 °C/5 h. The lower density of the tar and resin bonded clays (NT, BT, and NR) is believed to come from the presence of carbon as binder. The loss of volatiles during coking resulted in an increase in open porosity. The MOR and CCS values show that NR forms at low temperature a hard structure. Resin bonded tap-hole refractory mixes are known for its fast curing (resin polymerization) and higher mechanical resistance [4–6]. After firing at high temperature, the deterioration of the thermosetting bonds of the resin and the loss of volatiles of tar result in a more porous and weaker structure of the clay. In the case of BO, the absence of fixed carbon from the oil after coking enables the onset of sintering, increasing the MOR and CCS.

Hot Modulus of Rupture

Although the carbon bond is weak at room temperature, it brings much higher strength at high temperatures. This is easily verified in Fig. 2, which contains the results from HMOR tests. Resin bonded material (NR) is the strongest material at temperatures above 1000 °C, which could represent higher liquid metal erosion resistance on the upside and on the downside, difficulty in drilling if a weak drilling machine is available. BO presents very low strength at the tested temperatures, with some improvement only at 1200 °C, reflecting the sintering of the material. At very high temperatures, close to metal tapping, all materials present similar values within the detection limit of the apparatus employed.

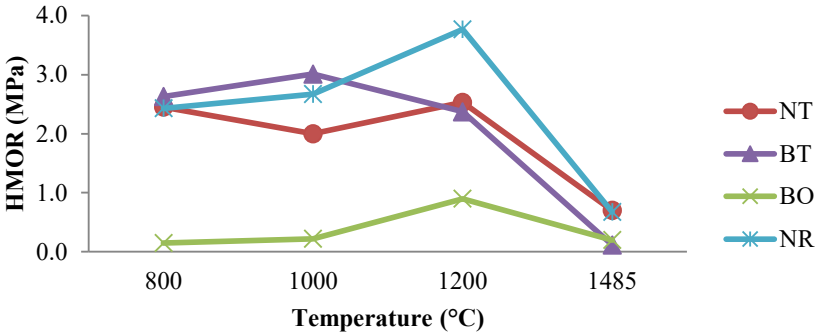

Fig. 2 Hot modulus of rupture of tap-hole clays at different temperatures

Thermogravimetric Analysis

Figure 3 shows the weight loss behavior of each tap-hole clay when heated until 600 °C. The weight loss is read in the graphic axis on the left side and temperature on the right side. The behavior of the three bonding systems is significantly different.

BO presented very low weight loss below 400 °C, when a sudden release of volatiles is observed and all the oil is removed from the sample. Thus, at the range of 400 °C, it is expected that the material will present its lowest physical integrity. The lack of binder at high temperatures and the release of less volatiles (~5%) favor sintering, which contributed for higher MOR and CCS and lower AP after 1200 °C as seen in Table 3.

On the other hand, the carbon bonded materials lost weight continuously up to approximately 20%. The tar bonded clays (NT and BT) presented continuous evolution of volatiles, which should lead to smooth property gradient inside the tap-hole. The resin bonded clay (NR) presented a mixture of both behaviors: at approx.

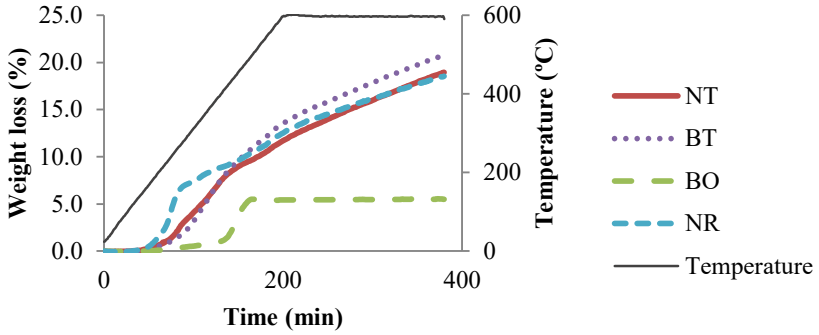

Fig. 3 Weight loss behavior of tap-hole clays when heated until 600 °C

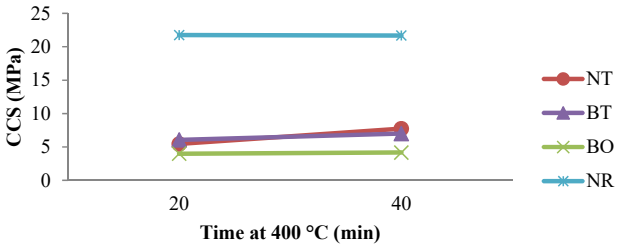

Fig. 4 Tap-hole clays CCS after fast curing at 400 °C

200 °C there is a large volatile evolution, linked to the process of polymerization of the phenolic resin. Afterwards, there is a continuous loss of weight.

Curing Test

The curing test results can be seen in Fig. 4. NR was the only material that presented high CCS after 20 and 40 min at 400 °C, due to fast curing of resin. Thus, when higher mechanical resistance needs to be achieved in a short time and at low temperature (>200 °C), resin bonded tap-hole clay is a good option.

Hot Plasticity

Figure 5 shows the results from the hot plasticity test. The load is read in the graphic axis on the left side and temperature on the right side.

Both tar bonded materials kept excellent plasticity over the whole duration of the test. At approximately 250 °C, the resin bonded clay hardens and the dolomitic clay has a two-step hardening process: a slight and continuous stiffening initiated at ~200 °C and a total hardening shortly before reaching the 300 °C temperature.

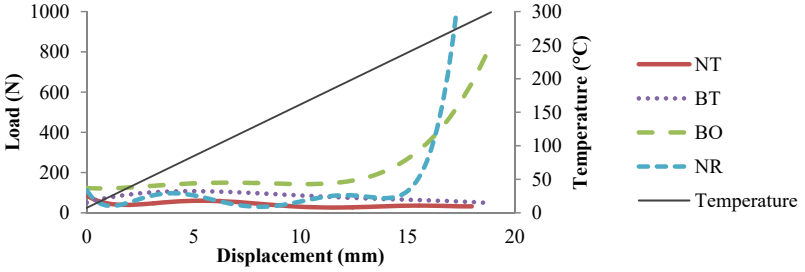

Fig. 5 Tap-hole clays plasticity behavior during heating until 300 °C

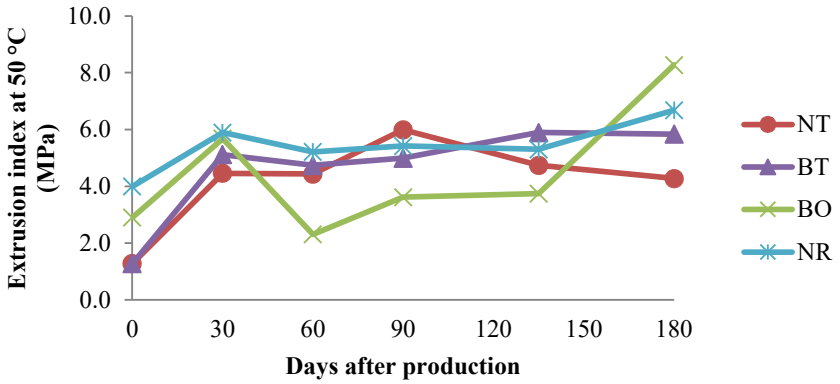

Fig. 6 Evolution of tap-hole clays plasticity over time, by measuring their extrusion index at 50 °C with Marshall test

Thus, tar bonded clays should allow better spreading of the refractory inside the tap-hole and should be less subjected to curing inside the clay gun than materials bonded by resin or oil, which is a major concern especially for resin bonded clay users. Besides that, tar is known for its adhesiveness on solid refractory [7], which favors the tap-hole clay adhesiveness on the tap-hole.

Extrusion Index Over Time

The evolution of extrusion index over time of each tap-hole clay can be seen in Fig. 6. All tested clays were very stable and retain their plasticity after 6 months of storage. Although tar bonded materials' aging stability were high in the test, this type of tap-hole clay is known to require heating (temperatures above 50 °C) to be properly injected after a long time in storage.

Properties Summary

Each laboratory test result can be associated with an important operational property from the tap-hole clay and based on the analysis of all results from this study a summary with the main operational properties of each tested tap-hole clay was built (Fig. 7). This summary is a basic guide for ferroalloy producer to decide which type of tap-hole refractory mix should be used in their metal tap-hole, according to their needs and operating conditions.

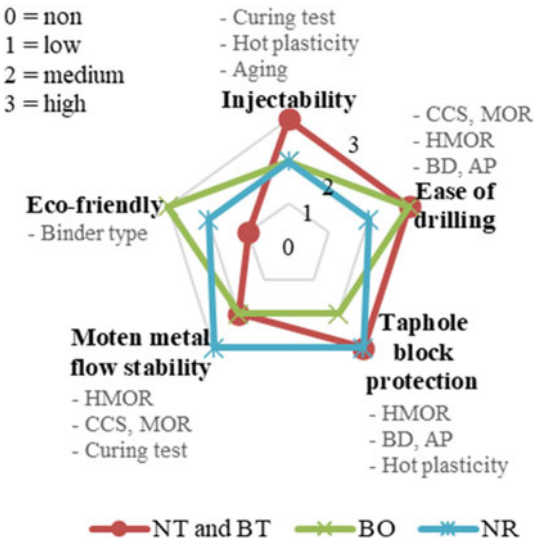

Fig. 7 Operational properties summary of tested materials with the main parameters that were considered to evaluate each property

Conclusions

The conclusions are as follows:

(1) The type of binder has been proven to have high impact on the properties of tap-hole clays and no relevant differences were noticed on the materials properties regarding aggregate type (non-basic and basic).
(2) A basic guideline (Fig. 7) was prepared to aid the ferroalloy producer to select the material that best suits their needs.

Acknowledgements The authors thank Oscar Sigueru, Norberto Bellandi, Steve Gruver, and Vanderlucio Madalena for contributing to this research.

References

1. Bassalo HC, Bittencourt LRM (2002) Massas de tamponamento para furos de corrida de altos-fornos – tipos, projeto de desenvolvimento e adequação às condições operacionais. Paper presented at the XXXII Seminário de Redução de Minério de Ferro, pp 349–357
2. Ribeiro AS, Bassalo HC, Brito MAM, Lenz-Silva GFB (2010) New generation of tap-hole tar mixes for small blast furnaces. Paper presented at the advances in refractories V, pp 153–160.
3. Hamasaki Y (1997) Paper presented at the Dai 23-kai Tekkoukougaku Semina Tekisuto, The Iron & Steel Institute of Japan, pp 129–135
4. Muroi N (1999) New tap-hole mud for blast furnace. Taikabutsu Overseas 19(3):24–27
5. Bassalo HC, Bittencourt LRM, Brito MAM (2002) Evolution of monolithics for blast furnace cast houses in South America. Paper presented at the 45th international colloquium on refractories, pp 93–97

6. Gisbert A, Duarte AK, Amado H, Bassalo HC (1998) Desenvolvimento de massas ligadas a resina para tamponamento de furo de corrida de altos-fornos. Paper presented at the XXVII Congresso Alafar, pp 199–208
7. Bitencourt CS, Pandolfelli VC (2013) Refratários contendo carbono: propriedades, características e variáveis em sua composição. Cerâmica 59:84–114

Health-Friendly Plugging Repair Pastes

A. De Pretto and L. Lindstad

Abstract A well-functioning tap-hole is critical for most furnaces and it is important to have a plugging repair paste that contributes to maintain this. Plugging materials mainly containing carbon and oxides have been studied. The best working pastes in this system often contain Coal Tar Pitch high temperature (CTPht) which has been defined as a substance of very high concern under the European Chemicals Legislation (European Chemicals Agency in Annex XIV (authorization list), 2017). Tap-hole pastes that are without CTPht or large amounts of polycyclic aromatic hydrocarbons (PAH) have been developed in this work. An important part has been to develop test and measurement techniques to compare properties of new tap-hole materials with old well-working pastes. Three of these have been, plate viscometry, rapid heat up of samples with or without pressure in simulated tap-holes keeping temperatures up to 1200 °C. From these, properties of the paste and it's repairing effect on surrounding materials could be measured.

Keywords Plugging paste · Repair paste · Health friendly · CTPht free

Introduction

The tap-hole is probably the most important part of a furnace and work developing a comprehensive overview of it and its importance to the smelting industry has been comprehensively covered by Nelson & Hundermark in their 2016 paper titled "the tap-hole – key to furnace performance". It is the most critical part of the furnace lining that should keep melted raw materials, slag, metal, and process gas inside the furnace lining. The tap-hole should be easy to open and give a controlled tapping speed of metal and slag in the wanted direction. Closure of the tap-hole should be possible to do quickly and safely at any time. Different stages for the tap-hole are shown in Fig. 1.

A. De Pretto (✉) · L. Lindstad
Elkem, Oslo, Norway
e-mail: antonio.de.pretto@elkem.com

J. D. Steenkamp et al. (eds.), *Furnace Tapping 2022*, The Minerals,
Metals & Materials Series, https://doi.org/10.1007/978-3-030-92544-4_28

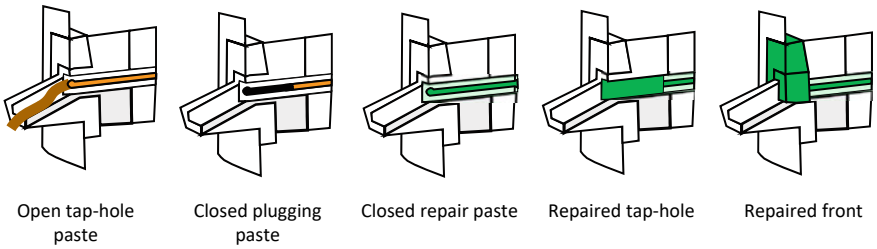

Fig. 1 The tap-hole in different stages [8]

The tap-hole is normally made of blocks and bricks or from monolithic plugging, self-flowing, or ramming materials. The materials can be oxides, carbide, nitrides, or carbon materials. In self-flowing, ramming and plugging paste, plasticity and binding often comes from high-temperature coal tar pitch (CTPht) due to good technical performance and low cost [7]. CTPht is made from several PAH components which have boiling points spread over a temperature range of close to 400 °C. Due to this the pressure of baking gases is kept low even during rapid heat up as in tap-hole [8]. CTPht-containing materials also repair surrounding materials due to CTPht ability needs to easily wet these.

Many producers are developing products in which CTPht is replaced with more health- and environmentally friendly solutions. It is important to reduce exposure of people to PAH and PAH emissions to the environment. The target for this project has been to develop a repair paste without CTPht or large amounts of polycyclic aromatic hydrocarbons (PAH). This paste should

- be easily placed inside a plugging gun and extruded into the tap-hole;
- cure quickly to obtain physical strength without gas cavities;
- repair surrounding tap-hole materials; and
- stand against metal, slag, and oxygen.

Each of these properties has been tested with improved equipment and procedures, or with totally new equipment and classification methods to identifying and simulate behaviour within a tap-hole.

Plate viscometer. Test the paste for use in plugging gun and extraction into the tap-hole. This is tested on a parallel plate viscometer under isothermal conditions chosen to replicate the temperatures along a plugging gun and measures the rheology of the pastes.

Rapid heat up of simulated tap-holes and measurement of paste at heated temperature (Infacon.2021). Test how quickly the paste obtains strength and if gas cavities are obtained in the material.

Rapid heat up of simulated tap-holes under pressure. Strength of binding to surrounding materials can be measured together with the strength of the surrounding material before and after repair.

Table 1 Showing list of tap-hole clays and reference terms for them

Paste no.	Paste manufacturer	Referred to name	Distinguishing characteristics
1	Elkem	Eltap™ G THL car	Low softening point—carbohydrate binder
2	Elkem	Eltap™ G THL bio	Low softening point—biopolymer binder
3	Competitor 1	Paste A	Low softening point—current industrial use
4	Competitor 2	Paste B	Low softening point—current industrial use
5	Competitor 3	Paste C	Low softening point—current industrial use

Cup testing and gas reactivity testing. Cup testing is to measure strength against metal and slag. Gas reactivity testing is done with air and CO_2 against material heat treated to different temperatures.

Three commercial pastes currently in use within the Ferro- and Silica- Manganese (FeMn, SiMn) and Ferrosilicon (FeSi) industries were compared to a new developed product from Elkem as shown in Table 1.

A target of this project was to determine the practicality of the results obtained from the newer classification methods toward the data and usage of these pastes in the physical tap-hole within a smelting plant.

Development Work of a Tap-Hole Characterisation Framework

In order to develop a new healthy, environmentally friendly hybrid plugging and repair paste for the tap-hole, it was first necessary to understand what applicable testing should be done on these pastes. A measure that is often reported for tap-hole pastes is the workability index of them [9, 15]. Considerable work was performed on observing the various methods of measuring this value and its applicability in measuring the flow properties of the tap-hole pastes. Steenkamp in her work showed the inconsistency within the industry on test methods for this and the variation of the usable workability index values for commercial tap-hole pastes. For this project, it was decided to do an in-depth characterisation of the tap-hole pastes that focused on readings outside of the workability index. The project thus commenced by developing a characterisation framework that would allow for any new tap-hole plugging pastes to undergo a structured testing methodology prior to scaling-up testing to an industrial scale. As it can be observed from the simplified schematic of this framework in Fig. 2, it is based on an iterative, tiered loop where if a new mixture of paste does not satisfy set parameters, the recipe was altered, and the testing commenced again.

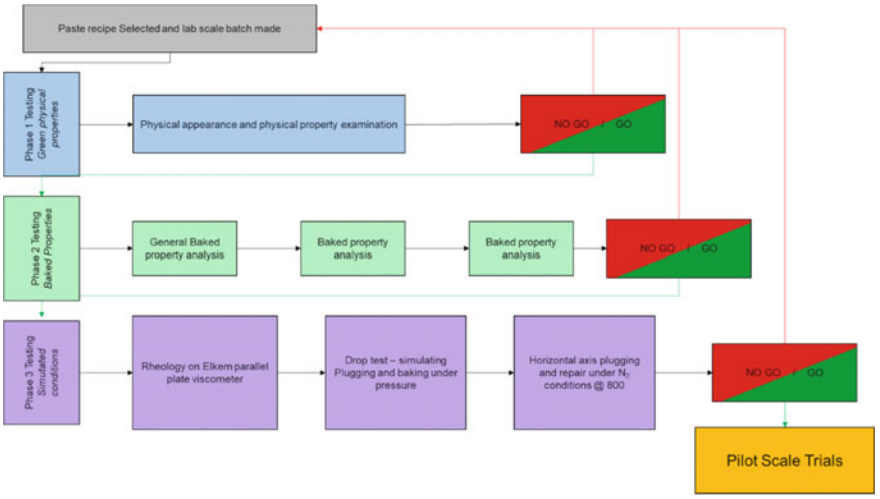

Fig. 2 A summarized characterisation framework for developing and testing tap-hole pastes

The characterisation framework allowed for any new tap-hole paste to be evaluated against other known pastes as well as against any required specifications before scaling-up testing to a pilot-scale trial on an industrial furnace tap-hole. This framework is based on an iterative tiered approach with the first tier consisting of basic observations of the green paste properties such as the workability on an automated Fischer sand rammer [15], green density, and qualitative analysis of the softening point of the paste.

The second tier of this framework involves baking samples of the paste under controlled conditions to temperatures from 950 to 1200 °C due in part to equipment limitations, but also selected from thermal measurements of industrial tap-holes during rebuild and usage. These baked samples are tested mainly for their reactivity to air and CO_2 and their compressive strength as these values are most pertinent to their usage within the furnace tap-hole [3, 10].

The final tier of the framework is one where the conditions the paste would experience within the tap-hole are partly simulated. For this application, three tests were developed to simulate

- the flow of material under pressure within the tap-hole,
- the behaviour of the paste as it baked under pressure at the high temperatures of the tap-hole, and
- the behaviour of paste as it bakes horizontally within the tap-hole channel.

The first two tests were developed in house within Elkem Carbon and will be discussed in detail. The final test, which is of the horizontal baking behaviour, has been covered in past work [11] and as such and will not be discussed further in this paper.

Test Methodology and Results

Baked Properties

As was stated by numerous papers including [10] wherein some of the most important properties of a tap-hole paste are that it should have sufficient strength to properly plug and close the furnace tap-hole as well as to have minimal erosion when the paste reacts to with air and CO_2 gases. During the second tier of the laboratory-scale characterisation framework samples of the tap-hole pastes were prepared by baking them to various temperatures above and including 950 °C through a controlled and steady temperature ramp up. The baked properties of the tap-hole clays were measured by following the procedures given below:

- Compressive strength—ISO 18515:2014.
- Air Reactivity—ISO 12989-1.
- CO_2 reactivity—ISO 12988-1.

The results of the testing on Eltap™ G THL and Pastes B and A can be viewed in Fig. 3.

The results showed that paste B and G THP bio performed similarly to each other with respect to the Air Reactivity Residue (ARR), while paste A is a lot weaker. All pastes give measurements in the same range for CO_2 Reactivity Residue (CRR). G THP bio has a much higher compressive strength than the two others.

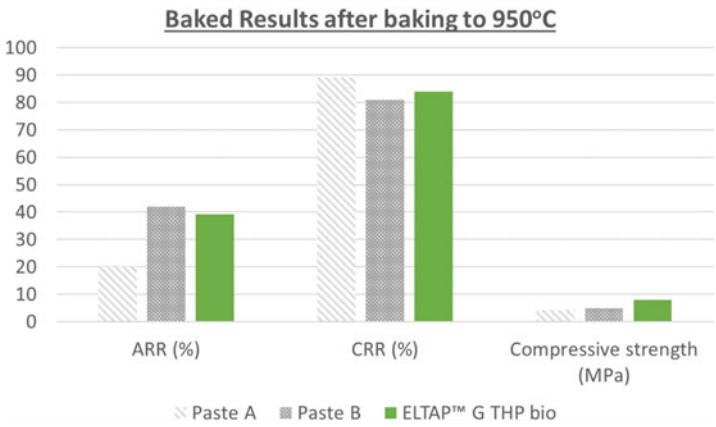

Fig. 3 Baked properties of various tap-hole pastes at 950 °C

Simulated Characterisation Methods—Plate Viscometer

After the previous work done by Steenkamp et al. [15] on the current method of calculating workability of the tap-hole clays and pastes and the inconsistencies within these methods between suppliers and users, it was decided that a potentially more comprehensive method of classifying the flow properties of the tap-hole pastes would be to determine the viscosity of the plugging pastes at various shear rates. This is an area within Elkem Carbon that had readily and frequently been used to observe the viscosity of Søderberg electrode pastes as recently shown by Skjeldestad [14]. Furthermore, significant work had already been done in determining the correct form of measurement as it was highlighted in numerous works such as Nordbø [12], Engmann et al. [5], TA Instruments [16], Torklep [17]. All sources showed that the best method for analysing the viscosity of a plugging paste at various shear speeds would be that of an axisymmetric squeeze flow method. It was based on these sources that an axisymmetric, compressive, parallel plate viscometer was developed by Elkem Technology initially for use in measuring the viscosities of various concrete mixtures and paste for aluminium anodes. This equipment was used to measure and compare the viscosity curves of the various plugging pastes.

This parallel plate viscometer consists of two temperature-controlled parallel plates with a diameter of 200 mm. The bottom plate remains stationary while the top plate is able to lower at a constant speed ranging up to a maximum of 10 mm/min. The equipment has the capability of being able to measure and record the viscosity, change of height, and force on a sample placed between the two plates at a set temperature that is controlled within the cabinet to ensure that all measurements occur in isothermal conditions.

Each plugging paste type was subjected to testing of the viscosity at various plate speeds to observe the effect that the different speeds would have on the maximum viscosity and the shear rates experienced by the pastes. Due to the construction of the machine, a set of plate speeds ranging from the maximum allowable on the machine to the minimum with a median point between were selected. This led to the following plate speeds being tested at 2, 5, 10 mm/min.

Once this was complete, the plate viscometer was preheated to various temperatures and the tap-hole paste samples were tested with the same plate speeds at these temperatures. The temperatures selected were based on measurements taken around the furnace tap-hole area and plugging gun installations at various Elkem Ferrosilicon smelters within Norway along with the ambient temperature in the testing lab. The three temperatures selected for testing were 22, 45, and 65 °C.

The result of the viscosity curves generated from the parallel plate viscometer was plotted against the shear rates that were calculated at the various plate speeds and temperatures. The reasoning for this was to enable a comparison to be made between the flow of the different paste types as well as to determine the thermo-viscous effect of each paste. In order for the results to be put into a form for comparison, it was first pertinent to calculate the shear rates and shear stress of each paste to ensure that the flow behaviour was similar.

The shear rate was calculated previously for the parallel plate viscometer [17] and was later refined and incorporated for the Elkem plate viscometer [12]. The shear rate, when using the Elkem plate viscometer, can be expressed by Eq. 1, wherein the shear rate becomes a function not only of the sample height and plate speed, but also of the volume (and by definition, density) of the samples of paste themselves.

$$\gamma = \frac{3v}{h^2}\sqrt{\frac{V}{\pi h}} \tag{1}$$

Nomenclature

γ shear rate (s^{-1}),
v plate velocity (m s^{-1}),
h height of the sample/distance between plates (m), and
V volume of sample (m^3).

This was then used to plot the calculated sheer stress against the shear rate for each paste to determine the type of flow behaviour it exhibited.

From the plot in Fig. 4, it can be seen that almost all of the tap-hole pastes exhibited visco-elastic properties as the profile of the plot of shear stress against shear rate follows that shown in literature for a visco-elastic material with shear-thinning behaviour [13, 16]. The exception to this is the Eltap™ G THL car which was shown to follow along a profile of a more Newtonian fluid. This could be attributed to the carbohydrate binder phase in use within this tap-hole paste that is a Newtonian fluid [1].

The results for the testing enabled a comparison of the viscosity changes at various shear rates to be observed and compared between various different tap-hole pastes. It should be noted that only a portion of these results will be highlighted here as test

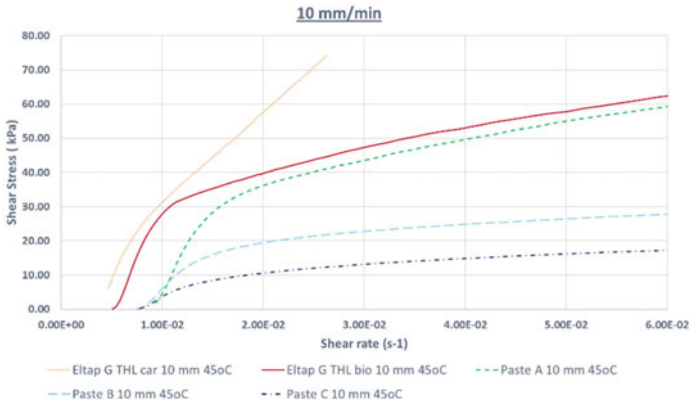

Fig. 4 Flow characterisation of the various pastes

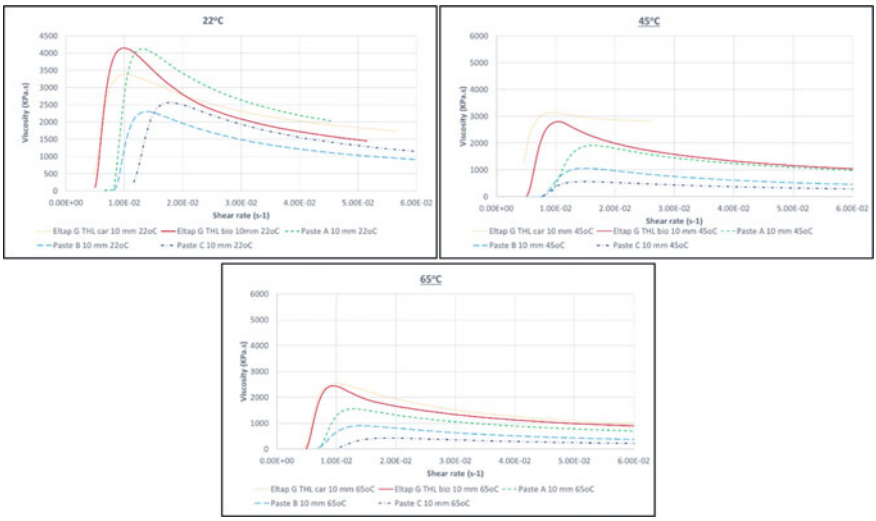

Fig. 5 Individual paste viscosity curves at 10 mm/min plate speed and various temperatures

results at plate speeds of 2 and 5 mm/min were deemed to be too dissimilar to the speeds experienced by paste within an industrial plugging gun [2, 4].

From the viscosity curves that were plotted in Fig. 5, a shear-thinning behaviour was observed in all the pastes.

This behaviour is characterised by the viscosity gradually decreasing as the shear rate increases, after first having experienced and overcome a maximum viscosity. Practically this implies that the pastes will have elastic behaviour and oppose plastic flow until a maximum viscosity is overcome. Thereafter the pastes will begin to flow to a greater extent as the shear rate, and by implication the shear stress increases.

From observing the trends of the viscosity at the increased temperatures, the temperature dependency of the viscosities for all pastes was observed. This temperature dependency was experienced to be much more pronounced at the lower temperatures between 22 and 45 °C as the change in viscosity was much greater in the tap-hole paste samples between these temperatures, with particular significant changes observed on Paste A.

This temperature dependency becomes much less evident at slightly higher temperatures as can be observed form the changes in viscosities between the temperatures of 45 and 65 °C. This may in part be due to the binder phases of the tap-hole clays becoming more thermally stable with increased temperature, the exact effect of which would have to be studied further. The major exception to this observed temperature dependency, however, is the Eltap™ G THL car paste which was observed to have a viscosity that remained quite consistent regardless change in temperatures. This tap-hole paste, while having a higher viscosity than the other pastes, seemed to be much less affected by thermal fluctuations than the other pastes.

All the tap-hole pastes showed similar flow behaviour. Eltap™ G THL bio was showing similar viscosities and trends to some of the commercially available pastes.

Simulated Characterisation Methods—Rapid Heat Up of Plugging Paste in a Simulated Tap-Hole Under Pressure

A further test method from the third tier of the characterisation framework was a method that was developed earlier by my colleagues Lindstad, Bryntesen, and Lindstad. This was the method that aimed to simulate baking of the tap-hole paste under pressure within the tap-hole through use of a "drop" test. This method is used to determine several factors, namely:

- How the tap-hole pastes flow out and fill the tap-hole under pressure at an immediate high temperature.
- Properties of tap-hole paste after baking at conditions similar to a tap-hole.
- The ability of the plugging paste to attach to the tap-hole walls of carbon, graphite, or SiC.
- The ability of the paste to repair surrounding materials.

An experimental set-up was developed wherein a hollow partly graphitized Søderberg electrode paste cylinder was heated within a convective heating furnace to temperatures in the range of 800–1200 °C. The electrode was not protected against air for a period and the surface oxidized as materials in a real tap-hole will do. Into this a smaller cylinder(s) of tap-hole paste was directly inserted into the hollow space of the paste cylinder with a SiC crucible on top of it. Into the SiC crucible a metal rod was placed that extended through the roof of the furnace. Finally, a weight of up to 60 kg was added to simulate two bars of pressure on the paste. The set-up is shown in Fig. 6.

In most experiments, the plugging paste is left under pressure for 1 hour. After this the weight and rod are removed before the hollow electrode and sample is taken out of the oven for cooling. Sample is protected against air during this cooling.

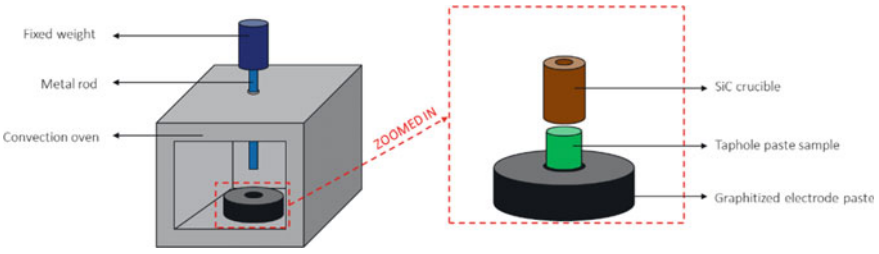

Fig. 6 Experimental design sketch showing the Elkem "drop" test

Fig. 7 Pictures showing results of the Elkem baking "Drop" test and the performance of the Eltap™ G THL

With the Eltap™ G THL bio the samples were removed and were shown to have adhered completely to the graphitized electrode paste cylinder. Core samples had to be drilled out as the paste would not allow for removal from the cylinder. The adherence between the graphitized electrode paste and the Eltap™ G THL was so complete that there was no visible differentiation between the tap-hole paste and the cylinder. Furthermore, a sample was extracted from a separate test and the adherence to the SiC crucible was so complete that the tap-hole paste sample had to be cut away from the SiC to sample. All these observations can be viewed in Fig. 7.

The method shows very promising results for the new plugging repair paste, but these will need to be validated with plant-scale experiments. This test methodology should after some further refinement increase the speed for development and improvement of new plugging pastes. The new method should also stop some materials with wrong properties from test at a real tap-hole where it could give dangerous malfunction.

Plant-Scale Pilot Tests

The final test for a plugging paste is normally first to test the flow of the paste in the plugging gun and just push the paste out of the gun without putting it against a tap-hole. If this works well, the next test is to plug a tap-hole that is tapping metal or slag. We performed these tests at an Elkem FeSi furnace in Norway. This furnace was chosen as it had an intermittent tapping wherein the furnace was tapped every 1.5 h and both slag and metal were tapped out of the same tap-hole. It was also chosen due to Paste B being in current use at the furnace which would allow for a good comparison.

In order to evaluate the effectiveness of the developed Eltap™ G THL in actual furnace performance, it was decided that two main factors would be evaluated. These were the drilling length used to reopen a tap-hole and the thermocouple temperatures along the copper cooled tap block installed 40 cm into and around the tap-hole.

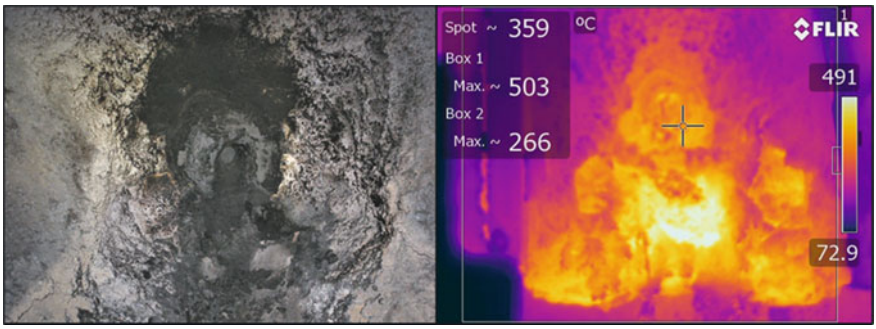

Fig. 8 Photo and infrared image of the trialed tap-hole successfully closed with Eltap™ G THL tap-hole paste

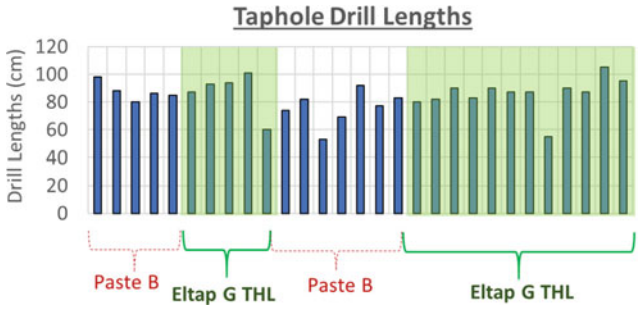

Fig. 9 Graph showing the drilling lengths on the trial furnace with different tap-hole pastes

The closure of this furnace's tap-hole is shown in the picture and corresponding thermal image in Fig. 8.

From the trends of the drilling length of the tap-hole shown in Fig. 9, some interesting trends can be observed. The tap-hole was plugged in oscillating campaigns of Paste B followed by the Eltap™ G THL. The usage of Eltap™ G THL showed elongating drill lengths. The two drill lengths in these periods under 60 cm were due to slag blocking the tap-hole and were not attributed to issues with the closure with the tap-hole paste.

In Fig. 10, some of the temperatures from the thermocouples along the copper water-cooled tap block were observed during the trial periods of Eltap™ G THL. Any increasing trend in this temperature would mean that the tap-hole was expanding and degrading. This would, of course, be expected through regular usage of the tap-hole.

After the plugging with Eltap™ G THL, especially the second trial period, the temperatures within the tap block were seen to remain at a constant, even with a slight trend of the temperatures decreasing. This was taken as a sign of the tap-hole paste repairing the tap-hole.

Both the drill lengths and copper cooled tap block temperatures confirmed that the paste that tested well in lab-scale experiments had the same properties and functioned

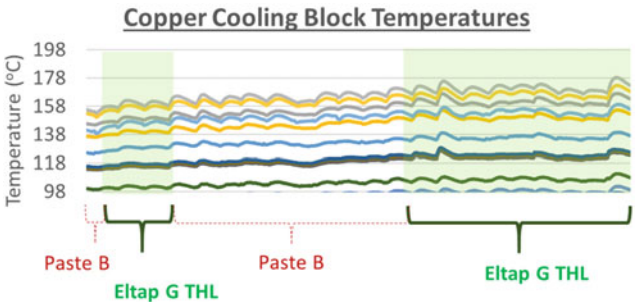

Fig. 10 Graph showing the copper cooled tap block temperatures for different paste usage

well within the plugging gun and furnace tap-hole. While the results were promising, it was decided that a much longer trial campaign of over a month would be needed to observe and confirm any repair properties of the paste.

Conclusions

When this project commenced, and a characterisation framework was drawn up the aim was twofold. The first was to develop a no CTPht-containing, hybrid plugging and tap-hole repair paste that could perform equally well as other commercially available tap-hole pastes. The second goal while characterising this paste during development against other pastes was to validate the practicality of these characterisation methods to actual behaviour of these pastes within a physical tap-hole at a smelting furnace.

Development of a hybrid, environmentally friendly plugging paste—From initial results from the characterisation framework and from subsequent initial plant-scale trials, it can be concluded that the Eltap™ G THL bio seems to show promising results. While it is too early to conclude on the long-term effects of repair on a tap-hole. More data on this will be available shortly when a month-long tapping campaign will be completed with this paste. The paste with completely green biopolymeric binder was shown to have similar and for several areas, stronger properties when compared with commercial pastes.

Validity and practicality of use of the Elkem parallel plate viscometer—The use of the parallel plate viscometer provides a new method of observing the rheology of various tap-hole plugging and repair paste that can be made precludes to the validity of the use of the Elkem parallel plate viscometer and how it could be used practically to give more information in characterising plugging pastes. The method, while needing some refinement and further work in certain aspects, could undoubtedly be used as a comparative tool to compare various flows of pastes. This could be used in many different practical applications; an example would be in development of a specialized flow plugging paste with suitable viscosities at

specified set points. Further use of this method could pertain to understanding the maximum viscosities at a range of temperatures and understanding the equipment and force required to overcome these maximum viscosities before the paste will start to exhibit shear-thinning behaviour and start flowing.

The parallel plate viscometer—The use of the parallel plate viscometer provides a new method of observing the rheology of various tap-hole plugging and repair pastes and can provide a more dynamic insight as to what temperatures and shear stresses are required to sufficiently extrude a paste from a furnace mud gun. The method does have some limitations, however, with regard to the maximum plate speed and temperature that can be run on it; however, to simulate the flow of plugging pastes out of a mud gun, this shows some promising results as testing equipment.

The simulated baking test under pressure—The simulated baking test at high temperatures with an in situ dropping of plugging paste into an annulus under pressure shows some promise as a test method to quantitatively observe the behaviour of pastes in the tap-hole and to observe the repair properties of the tap-hole plugging pastes against any potential material that a tap-hole could be constructed out of. This not only allows more flexibility as future materials are developed for furnace and tap-hole linings, but allows the potential to observe the behaviour of these pastes under varying temperatures and pressures. While this test is in its infancy when compared with other more well-defined tests, there is a large potential for it in characterising paste behaviour and also to make it more qualitative.

Further Work

While a lot of work was covered within the paper, there is some important work that could be performed to better characterise the flow characteristics of the paste. Two of the most pertinent suggestions for further work are listed below:

- *Parallel plate viscometer*—a collaborative research is suggested wherein a small-scale mud gun with metering along it to record pressure and speeds could be used to confirm the measurements obtained from the viscosity measurements on the plate viscometer. This would allow a more comprehensive correlation to be drawn up between the measurements in the laboratory-scale experiments and what is actually experienced in a mud gun.
- *Simulated baking test*—further work to be done to refine this would be to better define the measurement criteria after removing the dropped in sample. This could include use of an Optical Light Microscope (OLM) or analysis under a Scanning Electron Microscope (SEM) to determine the exact nature of the bonds between the paste and the surrounding material. Another improvement is to measure the force that is needed for pushing the baked plugging paste out of the tap-hole.

References

1. Bowitz O, Eftestol T, Selvik RA (1960) New methods for testing raw materials for anode carbon paste. In: Extractive metallurgy of aluminium, vol 2. Wiley, p 19
2. Dango & Dienenthal Maschinebau GMBH (1994) Combined DDS clay gun and taphole drills with hydraulic drives specifications. s.l.:s.n
3. Dash SR (2009) Doctoral thesis: development of improved tap hole clay for blast furnace tap hole. Department of Ceramic Engineering, National Institure of Technology, Rourkela, Rourkela
4. Dienenthal A (2014) A short history of the development of tapping equipment. In: The Southern African Institute of Mining and Metallurgy—furnace tapping conference 2014
5. Engmann J, Servais C, Burbidge AS (2005) Squeeze flow theory and applications to rheometry. J Nonnewton Fluid Mech 132:1–27
6. European Chemicals Agency (2017). Annex XIV (authorization list). https://echa.europa.eu/authorisation-list. Accessed 2021
7. Lindstad L (2018) More health-friendly materials for the tapping area. Kruger Nation Park, Southern African Institute of Mining and Metallurgy, pp 95–100
8. Lindstad L, Lindstad C, De Pretto A (2021) Health friendly materials for use in taphole and runner. In: Sixteenth international ferroalloys congress 2021, 27–29 September
9. Lungmus Feverfest (2006) Lungmus tap hole clays. s.l.:s.n
10. Nelson LR, Hundermark RJ (2016) The tap-hole—key to furnace performance. J South African Inst Mining Metall 116:465–490
11. Nightingale S et al (2006) Assessment of the structural development of resin bonded taphole clay. Int Conf Sci Technol Ironmak 2006:251–255
12. Nordbø T (2013) Some rheological properties of highly viscous pastes with large particles. Elkem As Technology, Kristiansand, Norway
13. Schramm G (1998) A practical approach to rheology and rheometry, 2nd edn. Gebrueder HAAKE GmbH, Karlsruhe
14. Skjeldestad A (2019) Doctoral thesis: electrode paste behaviour in Søderberg electrodes in ferroalloys production. Norwegian University of Science and Technology, Trondheim
15. Steenkamp JD, Mnisi M, Skjeldestad A (2018) The workability index of three tap-hole clays. In: International ferro-alloys congress 2018, 25–28 February
16. TA Instruments (2019) www.tainstruments.com. https://www.tainstruments.com/wp-content/uploads/Boston-Rheology-Training-2019.pdf. Accessed 5 Jan 2021
17. Torklep T (1988) Viscometry in paste production. TMS

Author Index

J. D. Steenkamp et al. (eds.), *Furnace Tapping 2022*, The Minerals, Metals & Materials Series, https://doi.org/10.1007/978-3-030-92544-4

Subject Index

J. D. Steenkamp et al. (eds.), *Furnace Tapping 2022*, The Minerals, Metals & Materials Series, https://doi.org/10.1007/978-3-030-92544-4